Effets d'environnement sur la fatigue de l'acier inoxydable 304L en milieu primaire REP sous chargement cyclique

Nicolas Huin

Nicolas Huin. Effets d'environnement sur la fatigue de l'acier inoxydable 304L en milieu primaire REP sous chargement cyclique. Autre. ISAE-ENSMA Ecole Nationale Supérieure de Mécanique et d'Aérotechique - Poitiers, 2013. Français. NNT : 2013ESMA0009 . tel-00835093

HAL Id: tel-00835093
https://theses.hal.science/tel-00835093v1

Submitted on 18 Jun 2013

THESE

Pour l'obtention du Grade de

DOCTEUR DE L'ECOLE NATIONALE SUPERIEURE DE
MECANIQUE ET D'AEROTECHNIQUE

(Diplôme National - Arrêté du 7 août 2006)
Ecole doctorale :
Sciences et Ingénierie en Matériaux, Mécanique, Energétique et Aéronautique
Secteur de recherche: Mécanique des solides, des matériaux, des structures et des surfaces

Présentée par :

Nicolas HUIN

****

Environmental effect on cracking of a 304L austenitic stainless steel in PWR primary environment under cyclic loading

****

Directeurs de thèse: José Mendez & Gilbert HENAFF

Thèse soutenue le 19 Février 2013

****

Jury

Pr D. DELAFOSSE	Professeur, ENSM-SE, St Etienne	Président
Pr J.Y.BUFFIERE	Professeur INSA, Lyon	Rapporteur
Dr J.M. OLIVE	Chargé de recherche CNRS HDR, Université Bordeaux 1	Rapporteur
Pr J.MENDEZ	Directeur de Recherche CNRS, ISAE-ENSMA, Poitiers	Examinateur
Pr G. HENAFF	Professeur, ISAE-ENSMA, Poitiers	Examinateur
Dr T.COUVANT	Ingénieur Chercheur, EDF, Les Renardières	Examinateur
Dr A.LEFRANCOIS	Ingénieur Chercheur AREVA, La Defense	Examinateur

Remerciements

En premier lieu, je tiens remercier les membres du jury pour l'intérêt qu'ils ont porté à ce travail et en particulier Monsieur David Delafosse de m'avoir fait l'honneur de présider ce jury.

Je suis très reconnaissant à Messieurs Jean Marc Olive et Jean Yves Buffiere d'avoir accepté la charge d'évaluer ce travail.

Je souhaite également témoigner ma gratitude à Monsieur André Lefrançois de m'avoir fait l'honneur de siéger dans mon jury et de l'attention particulière qu'il a bien voulu porter sur mon travail en plusieurs occasions.

Je tiens à remercier chaleureusement Gilbert Henaff et José Mendez pour leurs compétences et conseils avisés sur le plan professionnel et humain.

Je tiens à assurer de toute ma reconnaissance Ellen Mary Pavageau ainsi que Hubert Catalette, chefs du groupe Chimie Corrosion, pour m'avoir accueilli au sein du groupe.

Je tiens aussi à remercier Jan Van Der Lee pour m'avoir accompagné dans la grande aventure du MAI.

Un grand merci à François Vaillant, Antoine Ambard, Jean-Christophe Le Roux, Jean-Michel Stephan, Jean-Paul Massoud, Romain Beaufils, Salem Miloudi, Gabriel Ilevbare, Mohammad Behravesh, Kenji Sato, Yuichiro Sueishi, Teruhisa Tatsuoka, Christian Cossange, Michel Mahé, Felix Arnoldi, Didier Leclaire, Solène Gicquel, Denis Chollet, Véronique Bordier et Jérôme Langlais.

Je tiens à remercier plus particulièrement Thierry Couvant, qui m'a proposé ce sujet et m'a apporté énormément de connaissances dans ce domaine, pour son optimisme et son dynamisme constant ainsi que pour la convivialité de nos rapports.

Une attention toute particulière à Kazuya Tsutsumi à qui je dois ce travail, depuis ma motivation et mon énergie jusqu'aux résultats et sans qui cette thèse n'aurai pas été ce qu'elle est.

Un grand merci aux membres du laboratoire de microscopie électronique, Laurent Legras, Dominique Loisnard, Lucie Saintoyant, Frederic Delabrouille pour leurs qualités professionnelles et humaines auxquelles j'ai été très sensible.

Un grand merci aux (ex-)doctorants d'EDF, Arnaud, Pauline, Laurence, Bruna, Aurélie, Nina, Christophe, Mickael, Mi, Anaïs, Pr Diawara, Jau-man, Ricardo.

Un grand merci à tous les compagnons de route croisés en chemin.

A ma famille

INTRODUCTION

Management of nuclear power plant aging is increasingly considered to be a key energy challenge worldwide. By 2020, one third of the world's nuclear fleet will be older than 40 years. In 2030, this figure will increase to 80%. Since short term replacement of current generation capacity without a massive increase in CO_2 emission is not technically feasible, ensuring the safety of nuclear plant operations beyond 40 years is currently considered by worldwide nuclear utilities to be the best option.

In 2012, the average age of EDF generation units in France is 28 years. EDF has successfully managed this fleet without any major incidents, integrating safety measures during construction and optimizing them during the operating, maintenance and dismantling phases. However, during the operating phase, power plants experience material aging that may alter availability and safety if not controlled and counteracted [1].

1. Background

1.1. Pressurized water reactors

In Pressurized Water Reactors (PWR) (Figure 1), the nuclear fuel in the reactor vessel is engaged in a fission chain reaction, heating the water in the primary coolant loop by thermal conduction through the fuel cladding. The primary water remains liquid despite the high temperature due to the high pressure in the primary loop. The pressure is maintained by a pressurizer, a separate vessel connected to the primary circuit and partly filled with water which is heated to the saturation temperature (boiling point) by submerged electrical heaters. To achieve a pressure of around 155 bars, the pressurizer temperature is maintained at 345 °C. The hot primary coolant is pumped into a heat exchanger named steam generator, where heat is transferred to the lower pressure secondary coolant, which evaporates to pressurized steam.

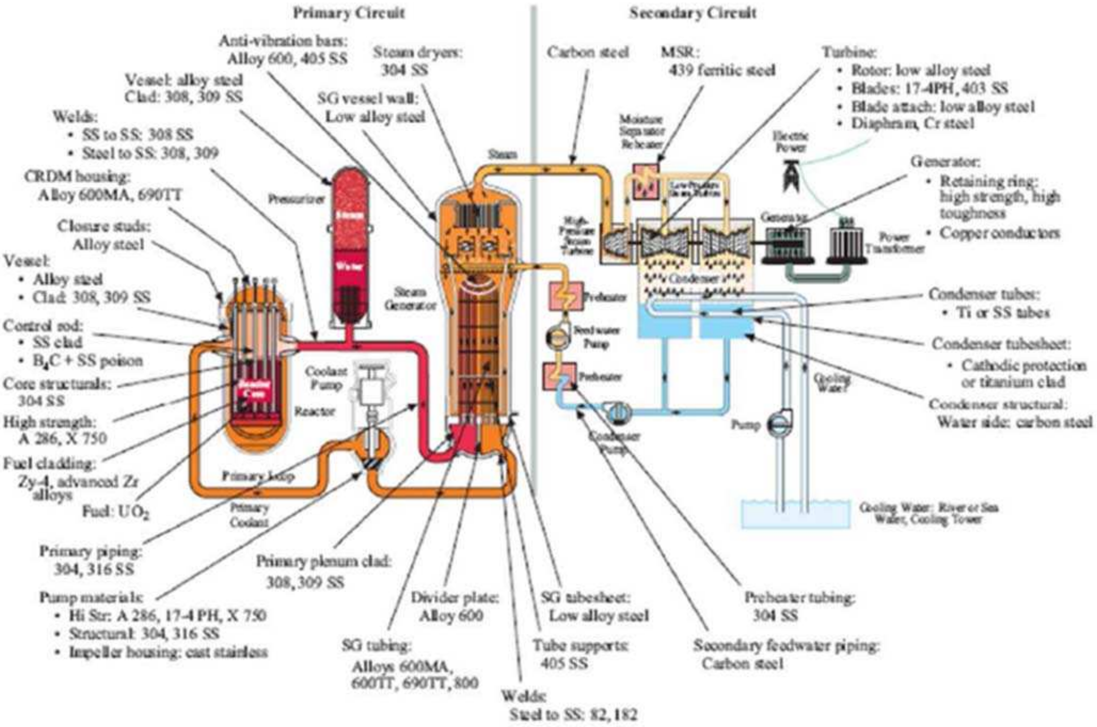

Figure 1- PWR Reactor [2].

1.2. Corrosion of PWRs

The French field experience (Figure 2) on metallic material (Figure 3) of materials in PWRs reveals that the major degradation is Flow Accelerated Corrosion (FAC). Stress Corrosion Cracking (SCC) seems to be minor but it is highly generic and has a large impact on safety because it may occur in the second containment barrier. Fatigue and Corrosion of PWR materials are significant contributors to plant unavailability and maintenance costs.

Thermal fatigue is considered as a potential problem in case of thermal stratification inside surge line and steam generator feedwater lines, thermal striping in isolable or un-isolable piping sections and also thermal fatigue in hot and cold water mixing areas.

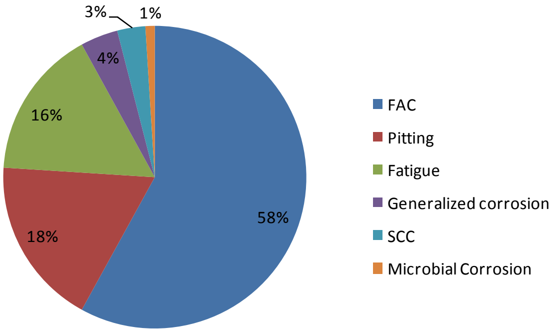

Figure 2 - French operational field experience of metallic material degradations [3].

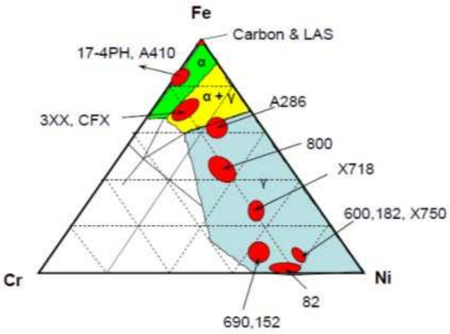

Figure 3 - Simplified Ternary Equilibrium Diagram for Iron, Chromium and Nickel at 400 °C [3].

Corrosion Fatigue (CF) or Environmentally Assisted Fatigue (EAF) is a degradation resulting in a damage induced by a crack initiation at the surface followed by a crack growth. It results from the combined effects of cyclic mechanical loads and the environment. EAF is characterized by a reduction of fatigue life and generally an increase of crack growth rates. EAF results from the superposition of two types of damage that do not depend on the same parameters: the mechanical damage due to fatigue mainly depends on loading amplitude and frequency and temperature. The corrosion mechanisms are very time and temperature sensitive, so it is at low frequencies and high temperature that the phenomenon is the most significant.

1.3. Fatigue of stainless steels in PWR primary circuits

The international field experience includes cases of fatigue crack initiation in stainless steels exposed to PWR primary water. Detailed observations are presented in Appendix 1. After examinations, it was never concluded that the root cause of the degradations was EAF, except at Loviisa 2 where a crack growth assisted by the environment was reported [4]. In addition, it can be noticed that loading and environmental conditions that lead to degradations observed at Mihama 2 [5] and Genkai 1 [6] are in good agreement with the current international codification of EAF (Figure 4). Civaux [7] and Genkai 1 degradations involved weld metals which usually exhibit residual stresses and may be susceptible to primary water stress corrosion cracking (PWSCC). It is important to notice that EAF cracks are often overlooked in component examinations due to the fact that fracture surface looks like SCC or Fatigue features. In addition, EAF underlying mechanisms remains unclear.

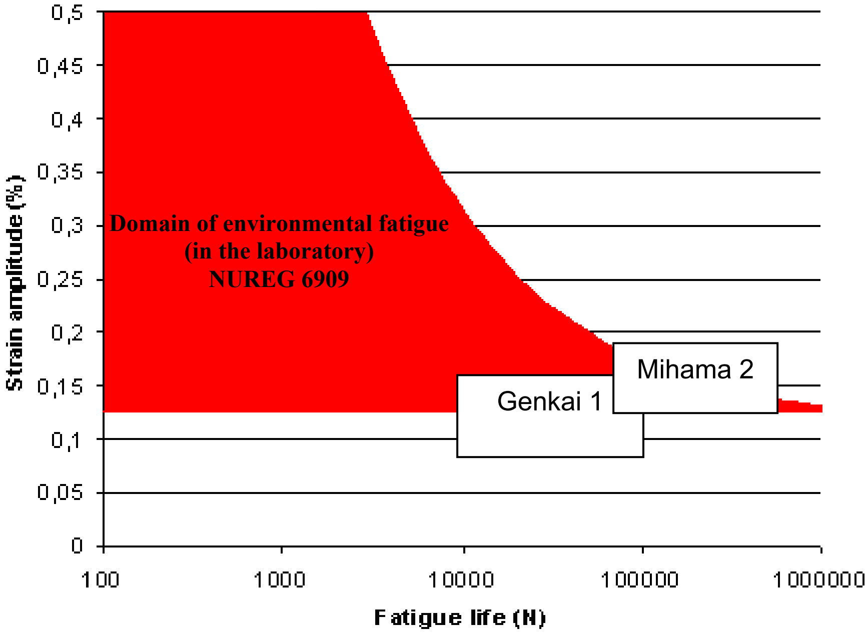

Figure 4 International field experience (Genkai 1 and Mihama 2) compared to the NUREG 6909 [8].

The French Nuclear Safety Authorities imposes the survey and the justification of the mechanical behavior of components exposed to PWR water under cyclic loading without explicitly taking into account the potential deleterious effect of the environment.

By contrast, the United States Nuclear Regulatory Commission (USNRC) and the Japan Nuclear Energy Safety (JNES) organization impose an environment factor Fen to take into account the effect of PWR primary environment on fatigue life. [8,9]

In addition, a lack of understanding of environmental effects on fatigue was pointed out in the degradation matrix proposed by EPRI [10]. Indeed phenomenological observations describe the observed macroscopic behavior for a certain set of macroscopic test condition parameters. Understanding of the underlying mechanisms is a way to better understand the physics that controls the phenomenon based on the microscopic behavior. Understanding the underlying mechanisms should allow us to extrapolate results outside the boundaries of phenomenological test matrix.

2. Objectives and approach

In response to the above background, the EDF launched environmentally-assisted fatigue studies in the framework of the COPRIN 2 and the COFAT projects (MAI).

The two main objectives of this work were separated into:

- A codification support study

The current codification compares fatigue lives obtained in PWR primary and air environments. It is proposed to indentify some relevant key gaps (Chapter 1) in the current codification and to evaluate their effect on the fatigue life in air (Chapter 3) and in PWR primary environment (Chapter 4). The results will be confronted in the Chapter 5.

- A mechanism understanding study

It is proposed to increase out the understanding of the underlying mechanisms on EAF (Chapter 3-4) through multiple microscopy techniques (Chapter 2). Indeed fatigue life of a material is usually separated in several cracking steps: initiation, micro propagation, propagation and failure. The understanding of fatigue life differences between several loadings, environment and material conditions may be achieved through the understanding of each cracking steps. Results will be discussed in the Chapter 5.

---

[1] www.themai.org

[2] **R.G. BALLINGER**, “Light Water Reactors: Materials of Construction and their Performance: Characteristics that Impact Degradation” International conference on plants materials degradations : Application to the stress corrosion cracking of Ni base alloys; The Materials Ageing Institute, EDF, Moret Sur Loing, France, November 2008.

[3] **P. SCOTT, F. VAILLANT**, « Degradation Modes & Remedies in Operating Plants », Materials Degradation Course for Engineers in the Nuclear Industry, Moret sur Loing, France, May 3-6, 2011

[4] **Y. HYTÖNEN**, "Two leakeages induced by thermal stratification at the Loviisa power plant ", Experience with thermal fatigue in LWR piping caused by mixing and stratification, 1998.

[5] **P. HIRSCHBERG**, “Operating Experience Regarding Thermal Fatigue of Unisolable Piping Connected to PWR Reactor Coolant Systems” (MRP-25), EPRI, Palo Alto, CA: 2000. 1001006.

[6] **S. SHIRAHAMA**, “Failure to the RHRS suction line pipe in Genkai unit 1 caused by thermal stratification cycling”, Experience with thermal fatigue in LWR piping caused by mixing and stratification, 1998.

[7] **O. GOLTRANT, E.HERBEZ**, "CNPE de CIVAUX - Tranche 1 - Expertise du coude RRA situé en aval de la vanne RRA071VP" Final report, Note EDF D5710/ECH/1998/009885/01, Août 1999.

[8] **O.K. CHOPRA, W.J. SHACK** , "Effect of LWR Coolant Environments on the Fatigue Life of Reactor Materials," Final Report, NUREG/CR-6909, ANL-06/08, Feb. 2007.

[9] **Japan Nuclear Safety Organization**, “Final report of EFT project”, 07-kizaiho-0002, 2007.(in Japanese)

[10] **EPRI**, “Primary System Corrosion Research Program; EPRI Materials Degradation Matrix, Revision 2”, Final Report, August 2010.

CHAPTER 1: Literature review

List of acronyms

AFM: Atomic Force Microscope
ASME: American Society of Mechanical Engineers
BWR: Boiling Water Reactors
CC: Cubic Centered
CEAT: Centre d’Essais Aeronautique de Toulouse
COFAT: COdification en FATigue
COPRIN 2 : COrrosion en milieu PRimaire des INconels et des aciers inoxydables
DDD: Discrete Dislocation Dynamics
DH: Dissolved Hydrogen
DO: Dissolved Oxygen
EAC: Environmentally Assisted Cracking
EAF: Environmentally Assisted Fatigue
ECCS: Emergency Core Cooling System
ECP: Electro Chemical Potential
EFD: Environmental Fatigue Data
EFEM: Environmental Fatigue Evaluation Method
EFT: Environmental Fatigue Testing
EPRI: Electric Power Research Institute
FCC: Face Centered Cubic
GE: General Electric
HCF: High Cycle Fatigue
HEDE: Hydrogen Enhanced Decohesion
HELP: Hydrogen Enhance Localized Plasticity
HWC: Hydrogen Water Chemistry
IG: Intergranular
IGSCC: Intergranular Stress Corrosion Cracking
JAPEIC: Japan Power Engineering and Inspection Corporation
JNES: Japan Nuclear Energy Safety
JSME: Japan Society of Mechanical Engineers
K-S: Kurdjumov-Sachs
LCF: Low Cycle Fatigue
LWR: Light Water Reactors
MAI: Material Ageeing Institute
MITI: Ministry of International Trade and Industry
NG: Nuclear Grade
NPP: Nuclear power plant
OWC Oxygen Water Chemistry
PLM: Plant Life Management
PSB: Persistent Slip Bands
PVRC: Pressure Vessel Research Council
PWR: Pressurized Water Reactor
PWSCC: Primary Water Stress Corrosion Cracking
RCC-M : Règles de Conception et de Construction des matériels Mécaniques des îlots nucléaires REP
RHRS: Residual Heat Removal System
SCC: Stress Corrosion Cracking
SFE: Stacking Fault Energy
SS: Stainless Steels

SSRT: Slow Strain Rate Tensile Tests
TENPES: Thermal and Nuclear Engineering Society
TG: Transgranular
TGSCC: Transgranular Stress Corrosion Cracking
USNRC: United States National Regulatory Commission
UTS: Ultimate Tensile Stress
WM: Weld Metals
Ys: Yield Stress

Summary

1. Industrial context and current codifications

Fatigue life curves provide the design basis for nuclear power plant (NPP) components. The French safety authority does not impose that the effects of high temperature PWR primary environment on fatigue life of components are explicitely being taken into account. However, low cycle fatigue data, obtained by laboratory testing demonstrate that fatigue life reductions may occur in such an environment. The validity of current fatigue design curves for components exposed to PWR primary environment must therefore be assessed.

In this chapter, an overview of the current existing codifications in Japan and in the US will be presented. Another section will address the main factors that can affect the fatigue life in PWR primary environment. The following section presents a state of the art concerning the EAC. The last part will focus on the identifications of key gaps related to factors that can affect the fatigue life in light water reactors (LWRs) environment.

1.1. Overview on the existing codifications of EAF

1.1.1. NUREG report CR-6909

The U.S. Nuclear Regulatory Commission (USNRC) issued NUREG/CR-6909 [1] and Regulatory Guide 1.207 [2] in March 2007. These are guidelines for evaluating fatigue analyses which incorporate the life reduction of metallic components due to the effects of the LWR environment.

In these guidelines, the potential effects of the PWR primary water environment on fatigue life have been defined with:

- the **S-N curves** as a function of strain amplitude, temperature, dissolved oxygen content and strain rate as shown in Equation 1.
- the □**Fen**□parameter, ratio between fatigue life in air at ambient temperature and fatigue life in the PWR primary water at the same strain amplitude (Equation 2) and at a given temperature. In these two equations, the dissolved oxygen content (*DO*) has a constant deleterious effect on the resistance to fatigue: *O** is constant. Figure 1 shows the original data used to calibrate O*.

$$Ln(N) = 6.157 - 1.920Ln(\varepsilon_a - 0.112) + T^* O^* \dot{\varepsilon}^*$$ **Equation 1**

$$F_{en} = \frac{N_{air,RT}}{N_{water,T}} = e^{(0.734 - T^* O^* \dot{\varepsilon}^*)}$$ **Equation 2**

With $T^* = 0$ (T<150°C)

$T^* = \frac{T - 150}{175}$ (150°C< T< 325°C)

$T^* = 1$ (T>325°C)

$O^* = 0.281$ (For all *DO* content)

$\dot{\varepsilon}^* = 0$ ($\dot{\varepsilon}$ > 0.4 %/s)

$\dot{\varepsilon}^* = \ln\left(\frac{\dot{\varepsilon}}{0.4}\right)$ (0.0004 %/s < $\dot{\varepsilon}$ < 0.4 %/s)

$\dot{\varepsilon}^* = \ln\left(10^{-3}\right)$ ($\dot{\varepsilon}$ = 0.0004 %/s)

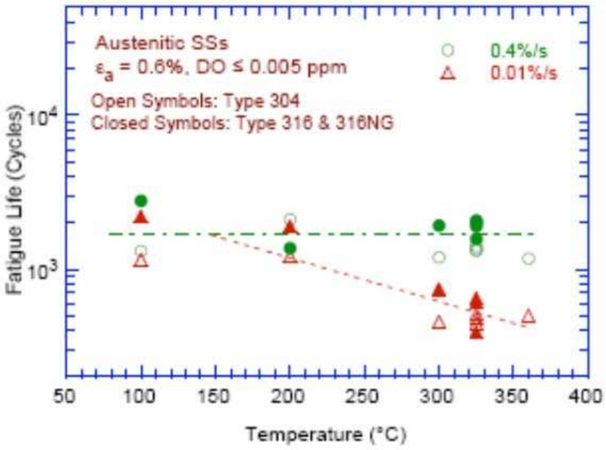

Figure 1 - Change in fatigue lives of austenitic stainless steels in PWR primary environment $\Delta\varepsilon_t/2=0.6\%$ [1].

According to [1] and [2], a need emerged to amend the current ASME code, since the ASME Section III code does not take into account environmental effects. The following sections state on ASME Section III Subgroup on Design Plan for Code Changes to Implement Environmental Fatigue Evaluation Methods [3].

It is planned to introduce environmental effects on fatigue in the ASME section III subgroup providing guidance on acceptable methods for evaluating reactor water environment effects on reactor coolant pressure boundary components.

The action plan was developed by the Subgroup on Design to coordinate activities necessary for changes that will provide to the user the necessary tools to evaluate the effect of reactor water environment on fatigue life of components. The action plan lies out a strategy for a staged implementation of analysis methodologies, needed research, analysis guides, sample problems, and an assessment of the impact of the new rules upon the industry. The ultimate goal of the Subgroup on Design is to develop a new non-mandatory appendix that provides guidance to the user when evaluating reactor water environmental fatigue effects on Class 1 components.

1.1.2. JSME S NF1-2006, EFEM-2006

In Japan, after 1990s, the Environmental Fatigue Data Committee (EFD) of the Thermal and Nuclear Power Engineering Society (TENPES), the Project on Environmental Fatigue Testing (EFT Project) supported by the Japan Power Engineering and Inspection Corporation (JAPEIC) and the Japan Nuclear Energy Safety organization (JNES) and some utility joint studies investigated the environmentally assisted fatigue (EAF).

In September 2000, the Nuclear Power Generation Safety Management Division of the Agency for Natural Resources and Energy, Ministry of International Trade and Industry issued "Guidelines for Evaluating Fatigue Initiation Life Reduction in the LWR Environment" (hereafter, called "the MITI Guidelines") [4]. These guidelines included an equation to evaluate environmental fatigue and require electric utilities to consider the environmental effects in their Plant Life Management (PLM) activities. However, the MITI Guidelines did not provide specific and practical techniques for evaluating environmental fatigue under actual plant conditions. Therefore, TENPES took on the task to produce a technique. In 2002 TENPES issued the "Guidelines on Environmental Fatigue Evaluation for LWR Component" [5,6], called "the TENPES Guidelines", based on the techniques developed by the EFD Committee.

Finally, a set of Rules, called the Environmental Fatigue Evaluation Method (EFEM), was established in the Codes for Nuclear Power Generation Facilities — Environmental Fatigue Evaluation Method for Nuclear Power Plants (JSME S NF1-2006, EFEM-2006) [7], which was issued in March 2006, based on the final outcome of EFT project

[8]. The EFEM revised version was drafted by incorporating the updated knowledge and was issued by the end of 2009.

In the following Equation 3 to Equation 9 are the latest equations proposed to evaluate Fen on austenitic stainless steels in PWR primary environment [7].

$$Ln(F_{en}) = (C - \dot{\varepsilon}^{*})T^{*}$$ **Equation 3**

$$\varepsilon_a = 23.0 \times N^{-0.457} + 0.11$$ (AIR) **Equation 4**

With $C = 3.910$ **Equation 5**

$$T^{*} = 0.000782 \times T$$ (T<325°C) **Equation 6**

$$T^{*} = 0.254$$ (T> 325°C) **Equation 7**

$$\dot{\varepsilon}^{*} = \ln(\dot{\varepsilon})$$ ($\dot{\varepsilon}$ < 49.9 %/s) **Equation 8**

$$\dot{\varepsilon}^{*} = \ln(49.9)$$ ($\dot{\varepsilon}$ > 49.9 %/s) **Equation 9**

1.1.3. Comparison of evaluation methods NUREG-6909 vs JSME S NF1-2006

The history of studies on environmental fatigue in LWR water and the recent activities on standardization of these studies were reviewed [9]. Three environmental fatigue evaluation methods, JSME methods [7] and NUREG-6909 [1] were compared.

The major differences and several remaining issues are listed as follows:

- The JSME and the NUREG-6909 methods are essentially comparable, but many differences are observed in the strain rate threshold (Figure 2), as well as in the effects of temperature (Figure 3) and *DO* (Figure 4).
- Regarding the effect of strain rate (Figure 2), the JSME provides a separated *Fen* for BWR and PWR water, but the other methods do not. The Pressure Vessel Research Council (PVRC) equations are the same as those proposed by Chopra in 2000 [10], and the F_{en} is about 50% larger than the one given in NUREG-6909. The NUREG-6909 line is higher than the JSME BWR line and lower than the JSME PWR line.
- The NUREG 6909 consider a strain rate threshold of 0.0004%/s.
- The JSME consider a strain rate threshold of 0.00004%/s for cast stainless steel and 0.0004 %/s for the other stainless steels. The fast strain rate threshold is the value at which F_{en} reaches 1.0 for JSME, but it is 0.4%/s for the other methods. Thus, the lowest F_{en} reaches 2.08 for NUREG-6909.

- With respect to laboratory data, the NUREG-6909 limit is not conservative in PWR water. Additionally, no lines are conservative at very slow strain rates.
- Higuchi proposed the slow strain rate threshold to be changed from 0.0004%/s to 0.00004 %/s to improve the conservatism in this region [11]. However, this transition seems to be difficult to be definitely identified because of the huge data scatters. Further testing data would be needed.
- Regarding the effect of temperature (Figure 3), the NUREG-6909 limit increases exponentially above 150°C and is constant below 150°C. JSME provides separate limits for BWR and primary PWR environments, and these limits increase exponentially with increasing temperature.
- With respect to the effect of *DO* (Figure 4), the NUREG-6909 exhibits a constant DO dependency in NUREG-6909. The NUREG-6909 limit is located between the BWR and PWR limits of JSME.
- The effects of water flow rate, strain waveform and strain holding on environmental fatigue life are not yet taken into account in the existing methods.

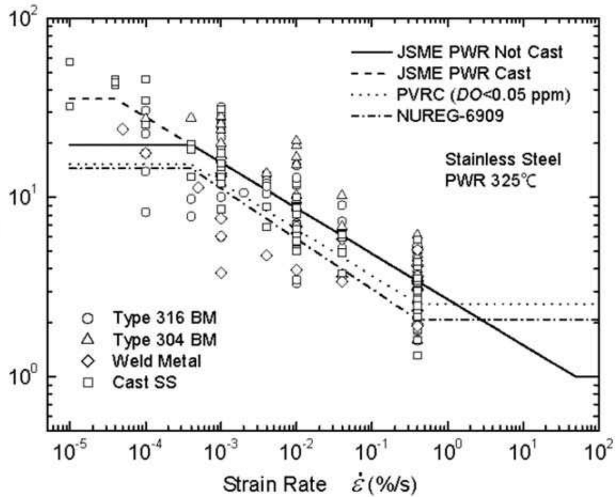

Figure 2 □Fen vs. strain rate for stainless steels in PWR primary water [9].

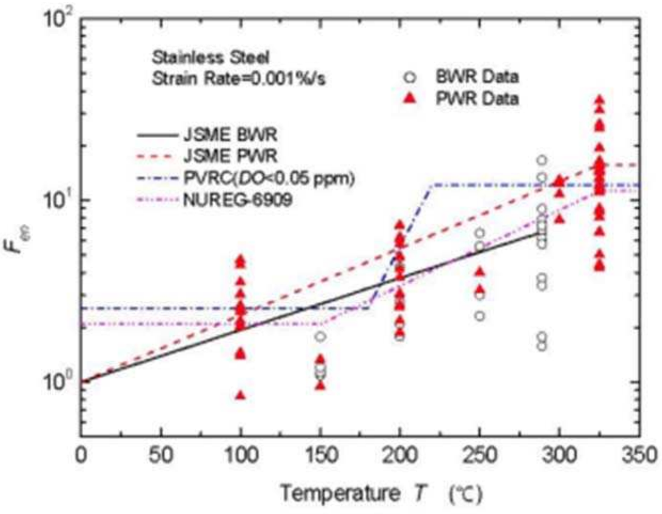

Figure 3 □Fen vs. temperature for stainless steels in LWR water [9].

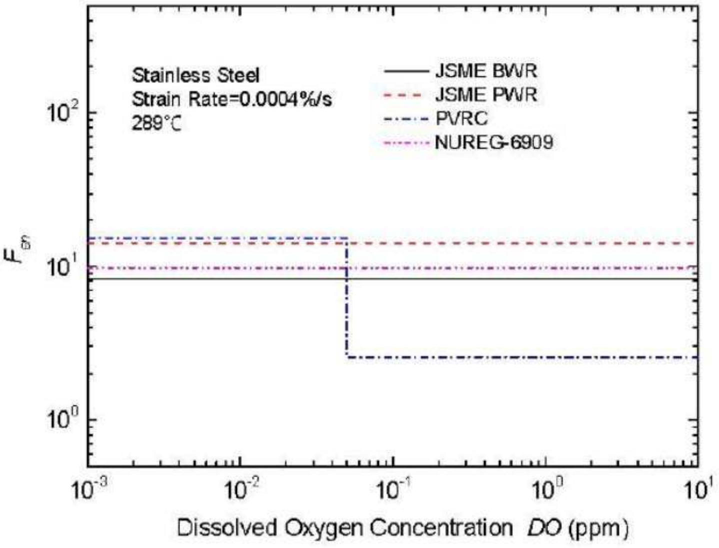

Figure 4 □Fen vs. dissolved oxygen concentration for stainless steels in LWR water [9].

1.2. Current status in France

The effect of primary water on thermal fatigue curves is not taken into account explicitly by RCC-M French requirement, even if environmental effects cannot be excluded.

1.3. Understanding of environmentally assisted fatigue mechanisms

EPRI [12] recently pointed out the lack in the mechanisms understanding in the current EAF approach. Indeed, EPRI mentioned that phenomenological observations describe the observed behavior for a certain set of test conditions in terms of macroscopic measurements. The applicability of these results is directly limited by the size of the test matrix. Mechanistic understanding is developed from the underlying synergies between the material, the environment and the applied mechanical loading. These synergies are often related to microscopic interactions. Mechanism understanding enables phenomenological observations to be extrapolated outside the boundaries of the phenomenological test matrix.

1.4. Conclusion on the industrial context

EAF has been codified in the US and Japan. The impact of the PWR primary environment is taken into account by considering a fatigue life reduction factor □Fen□ This factor has been calibrated using several macroscopic factors. At the moment, no clear mechanism is proposed. A potential way to improve our knowledge on the EAF field may consist in applying the fundamental knowledge and general approach used in the Stress Corrosion Cracking (SCC) and more generally in the Environmentally Assisted Cracking fields. The environmental assisted cracking (EAC) results from a complex synergy between 3 main parameters. Indeed, the environment, the material and the loading parameters are well known to be the driven force governing the EAC.

The first objective of this chapter is to describe each of these factors separately:

- Section 2 will present some material considerations focusing on the different phases that can be observed in a 304L stainless and their relationship with the fatigue damage.
- Section 3 will focus on the cyclic stress-strain behavior and the associated microstructure.
- Section 4 will present an overview of the wet corrosion and more specifically the PWR primary environment corrosion. Section 5 will address some fundamental knowledge on the environmentally assisted cracking. It will start on a quick overview on the fatigue damage in air, followed by some considerations of the impact of strain localization on oxidation processes. This section will end with an overview of the factors related to fatigue life reductions on PWR primary environment. The goal is to identify some relevant key gaps on the current codification.

2. Material: 304L austenitic stainless steel

Figure 5 presents an overview of the metallic materials used in a PWR power plant. The field experiences related to fatigue degradations [12] are mainly located in the auxiliary pipes connected to the primary piping. These circuits are mainly made of 304 and 316 austenitic stainless steels.

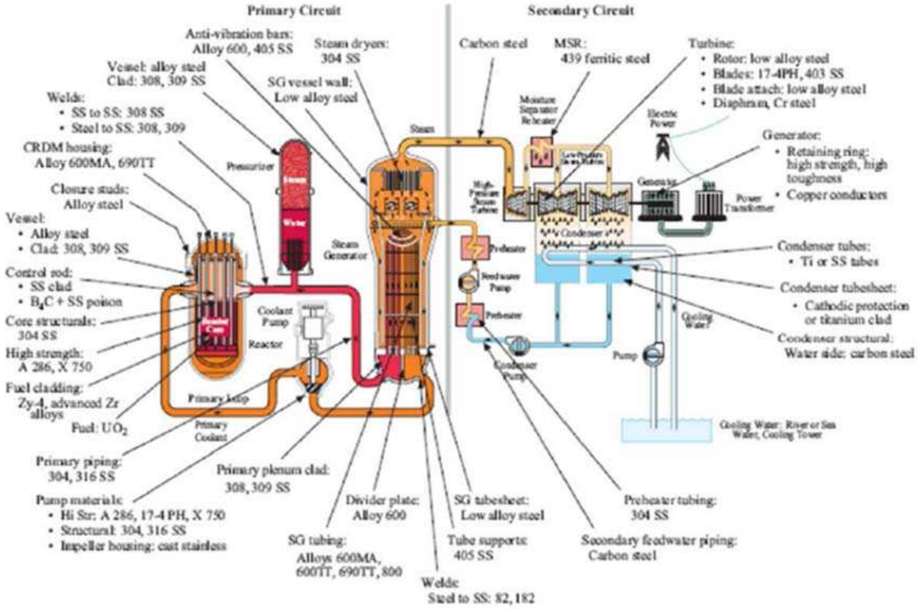

Figure 5- PWR Reactor [13].

Austenitic stainless steels have high ductility, low yield stress (Ys) and relatively high ultimate tensile strength (UTS) due to their face-centered cubic (FCC) crystallographic structure, compared to conventional carbon steels. These properties make them ideal for PWR pipes. The high chromium content is introduced to reduce uniform corrosion. However, at the same time, it stabilizes the residual cubic centered (CC) ferritic structure. Therefore, it is necessary to introduce nickel in order to maintain the material fully austenitic during cooling.

2.1. Austenite

Austenite is a FCC crystallographic structure with a lattice parameter of 3.59 nm defined by an elementary lattice of 4 atoms (1 at the origin, the 3 others at the center of cube faces). Austenite is a stacking of compact dense planes, in which atoms can be placed into equilateral triangles. Compact stacking structure is obtained by superposition of these two dense planes aligning a vacant position of one with the atom of a neighbor (Figure 6). Atoms of the third layer can adopt two different configurations. The first one is a direct positioning in front of the first layer which corresponds to a AB-type Hexagonal Compact (HC) stacking. The second one corresponds to atoms that can move, which corresponds to an ABC-type FCC stacking (Figure 7) [14].

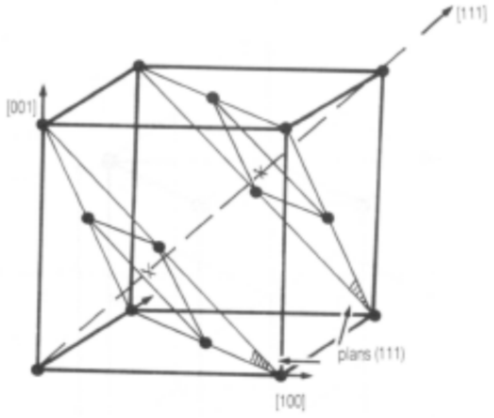

Figure 6 - FCC with dense direction <110> and dense planes {111} [14].

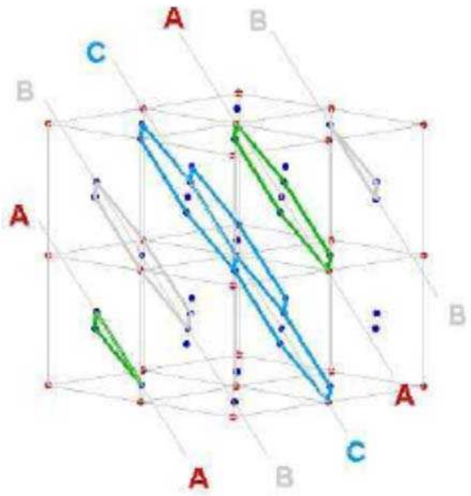

Figure 7 - FCC ABC compact stacking [14].

The deleterious effect of intergranular corrosion in austenitic stainless steels is avoided thanks to the low carbon content (less than 0.03%) [15]. This is sufficient to prevent intergranular precipitation of chromium carbides that promotes chromium depletion at grain boundaries. However this reduction of carbon content reduces the mechanical properties of the material. This is the reason why nitrogen is introduced to increase the yield stress. Manganese is introduced to increase nitrogen solubility in the metal. Austenitic phase is not stable at room temperature. To avoid carbides precipitation and to retain a metastable austenitic phase at low temperatures, an austenization (at typically 1040°C) recovery is carried out in order to increase the carbon and nitrogen solubility into FCC structure and homogenize the solute atoms distribution, followed by a water quench to substain a metastable austenitic structure at room temperature.

The residual ferrite content in austenitic stainless steels mainly depends on the chemical composition of the material and the heat treatment (cooling rate). This value can be evaluated using an empiric law developed for austeno-ferritic stainless steels (Equation 10 and Equation 11) where x_i is the fraction number of element i [16].

$$\delta(\%) = 21.8R^2 - 5.96R + 3.39$$ **Equation 10**

With

$$R = \frac{x_{Cr} + x_{Mo} + 0.065x_{Si} - 17.6}{x_{Ni} + 20x_C + 8.3x_N + 0.08x_{Mn} - 5.18}$$ **Equation 11**

Austenite and ferrite have different crystallographic structures: respectively FCC and BCC. The relation between austenite and ferrite follows Kurdjumov-Sachs (K-S) relation $\{111\}_\gamma // \{110\}_\delta$ and $<110>_\gamma // <111>_\delta$.

In most of the case, fatigue cracking mechanisms are related to microstructural evolution of the austenite. This aspect will be described in a specific section. However residual δ-ferrite can create strain incompatibilities (Figure 8) enhancing initiation of fatigue cracks at the austenite-ferrite interfaces (Figure 9) [17].

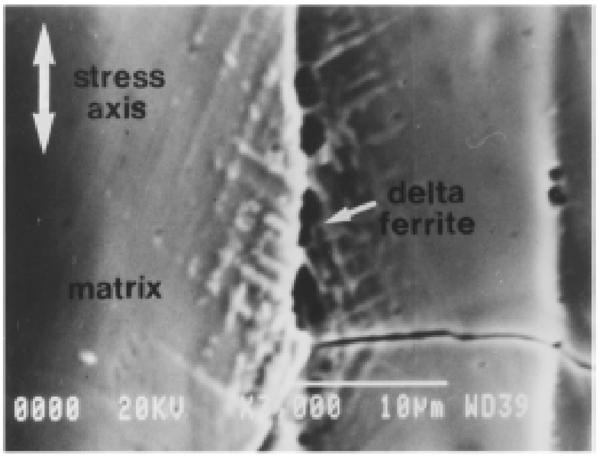

Figure 8 - Slip pattern near the interface between the matrix and δ-ferrite $\Delta\varepsilon_t/2=0.2\%$, $\Delta\varepsilon_t/dt=0.4$ %/s [17].

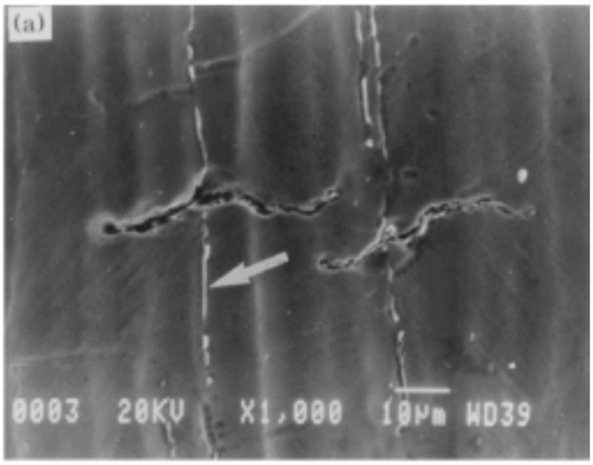

Figure 9 - Crack initiation near δ-ferrite after a LCF test at 600°C $\Delta\varepsilon_t/2=0.2\%$, $\Delta\varepsilon_t/dt=0.4$ %/s [17].

2.2. Stacking fault energy

Stacking fault energy (SFE) of stainless steels is related to the chemical composition of the material (Equation 10) and can be evaluated using the following empiric law [18]:

$$SFE(mJ.m^{-2}) = 25.7 + 2x_{Ni} + 410x_C - 0.9x_{Cr} - 77x_N - 13x_{Si} - 1.2x_{Mn}$$ **Equation 12**

In FCC lattice, SFE determines the character of dislocation slip : planar or cross.

- At low SFE (SFE < 10 $mJ.m^{-2}$) dissociation into partial dislocations is favored, which leads to a planar slip, which in turn promotes strain localization.

- At high SFE (SFE > 30 mJ.m^{-2}) dissociation into partial dislocations is difficult, therefore cross slip is promoted. The movement of screw dislocations is easier, which induces a more homogeneous three-dimensional organization of dislocations.

Austenitic stainless steels, despite their intermediate SFE, can exhibit cross-slip at high strain amplitude strain and planar slip at low strain amplitude. Depending on the strain rate between 150°C and 400°C the slip can be planar or cross. At high temperature (>600°C) the slip is mainly cross [19] [20][21] [22][23].

2.3. Martensitic transformation

The austenite phase in 304L austenitic stainless steels is metastable: indeed martensitic transformation can occur during cooling or due to plastic deformation (Figure 10). Two types of martensite can be observed:

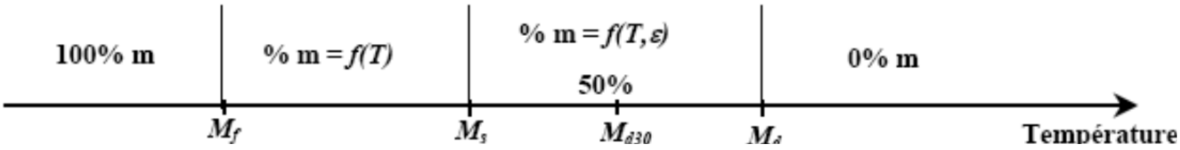

Figure 10 □Martensite fraction (m) as a function of temperature (T) and plastic strain (ε).

- Martensite ε

Martensite diffraction patterns denote that martensite is an hexagonal compact (HC) phase. This HC phase has a lattice parameter of 2.54 nm and its planes and dense directions are respectively {0002} <2-1-10>. Martensite ε is developed from the austenitic phase with a specific orientation between the two phases: {111} // {0001} <1-10> // <11-20>. This phase usually appears at low temperature [24].

- Martensite α□

Martensite α□is a metastable and ferromagnetic phase. Martensitic transformation consists in a change in the crystal lattice from a FCC phase to a quadratic phase as described in Figure 6. In the case of 304L, the martensite α□has the same Cubic Centered (CC) structure than ferrite. Its planes and dense directions are respectively {110} or {112} and <111>. Between the crystal lattice of austenite and martensite, there are specific Kurdjumov-Sachs orientations as {111} // [101] <1-10> // <11□1> (Figure 11) [25].

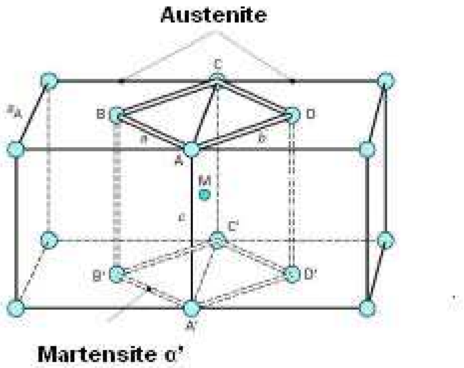

Figure 11 Creation mechanism of quadratic martensite α' from FCC austenite [25].

The susceptibility to martensite transformation of 304L stainless steel under cyclic loading is presented in Figure 12. The material presents an increase of the volume fraction of the martensite phase as a function of the applied number of cycles [26].

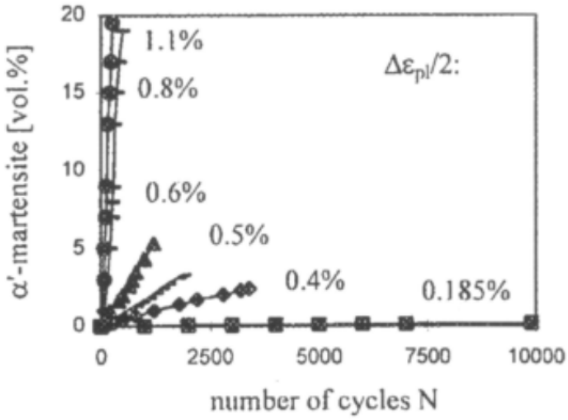

Figure 12 Effect of strain amplitude and applied number of cycle on martensitic transformation [26].

Some authors have found that a strain-induced martensitic transformation occurs at the tip of fatigue cracks formed in metastable austenitic stainless steel submitted to cyclic loading at room temperature. Bathias [27] reported that the presence of martensite at the crack tip increases fatigue life, because the associated hardening reduces the plastic strain amplitude that is then better accommodated.

Another explanation for such a beneficial effect is the increase in volume occurring during the transformation of austenite into martensite. Hornbogen [28] and Hennessy et al [29] noted that this change in volume introduces compressive residual stresses that can delay crack growth rate.

Stolarz [30] noted that the compressive stresses, related to the presence of martensite in fatigued samples, delays the initiation of fatigue cracks at room temperature. Moreover, he observed that martensite tends to limit slip activity at the surface.

These mechanisms associated with a martensitic transformation allows a noticeable improvement of the material resistance to cyclic strain. Indeed, the energy available for cracking in the case of a stable structure is dissipated by the martensitic transformation.

Austenite (FCC) can transform into α′-martensite (CC) due to a rapid cooling from 1050-1100°C. This transformation can occur for a starting temperature (Ms) depending on the chemical composition of the material (Equation 4) [18].

$$M_s(°C) = 502 - 810x_C - 1230x_N - 13x_{Mn} - 30x_{Ni} - 12x_{Cr} - 54x_{Cu} - 6x_{Mo} \qquad \textbf{Equation 13}$$

Metastable austenite can also change into α′-martensite for a temperature Ms < T < Md. In this case, α′-martensite volume fraction is a function of temperature and plastic strain. Md30 is the temperature at which 30% of plastic strain produces 50% of α′-martensite fraction. Md30 can also be calculated as a function of the chemical composition of the material with an empiric law (Equation 5) [18].

$$M_{d30}(°C) = 497 + 462(x_C + x_N) - 9.2x_{Si} - 8.1x_{Mn} - 13.7x_{Cr} - 20x_{Ni} - 18.5x_{Mo} \qquad \textbf{Equation 14}$$

3. Mechanical behavior: low cycle fatigue properties

The French field experience on PWRs over the last decade has highlighted cracking of austenitic stainless steel components attributed to thermal fatigue. These are mainly emergency core cooling system (ECCS) circuits, and residual heat removal system (RHRS). EDF has undertaken numerous studies dedicated to thermal fatigue and mechanical fatigue. Following these works, it became necessary to consolidate the knowledge of the phenomenon of fatigue in order to allow the control of its potential impact on the PWR power plant integrity.

The following section will provide several definition and observation, in order to better understand the underlying mechanisms related to the fatigue of stainless steels.

3.1. Cyclic behavior

3.1.1. Microstructural evolution during cycling

3.1.1.1. Cyclic strain hardening in single crystal

In a single crystal subjected to a particular stress σ, plastic flow can operate by slip on one or several slip systems. For a given stress, the 12 slip systems of the FCC structure are oriented differently with respect to the principal stress axis. Plastic flow initiates by dislocation glide on active slip systems where the resolved shear strain γ_r reaches a critical value τ_r, related to the tensile yield stress according to the Schmid law:

$\tau_r = m\sigma$, where m is the Schmid factor defined as $m = \cos\phi \cos\lambda$ (Figure 13)

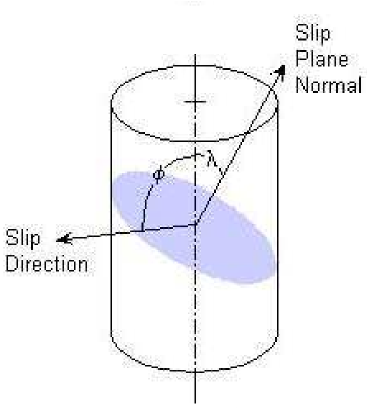

Figure 13 □Orientation of slip plane and slip direction in a single crystal [31].

During fully reversed loading fatigue test at a fixed plastic shear strain γ_{pl}, typical hysteresis loop indicate an initial hardening followed by a stabilization hysteresis loop after N cycles. The maximal shear stress is denoted τ_s. A plot of peak τ_s as a function of γ_{pl} provides a stress-strain curve for a single crystal (Figure 14). There are three different stages which exhibit distinctly different strain hardening characteristics and dislocations organization.

At low values of plastic strain amplitude ($\gamma_{pl} < \gamma_{pl,AB}$), hardening occurs during cycling loading. This hardening is almost due to the accumulation of primary dislocations such as alignments, pile-ups, dipoles or veins.

At middle range ($\gamma_{pl,AB} < \gamma_{pl} < \gamma_{pl,BC}$) values of plastic strain amplitude, a saturation of the stress amplitude is observed. The saturation stress τ_s is independent of γ_{pl} up to $\gamma_{p,BC}$.

Under these conditions, Persistent Slip Bands (PSBs) emerge at the surface. These PSBs first appear at $\gamma_{pl,AB}$ and their volume fraction increases linearly to nearly 100% at $\gamma_{pl,BC}$.

At high values of plastic strain amplitude ($\gamma_{pl} > \gamma_{pl,BC}$) dislocation structures evolve to three-dimensional dislocation structure such as cells.

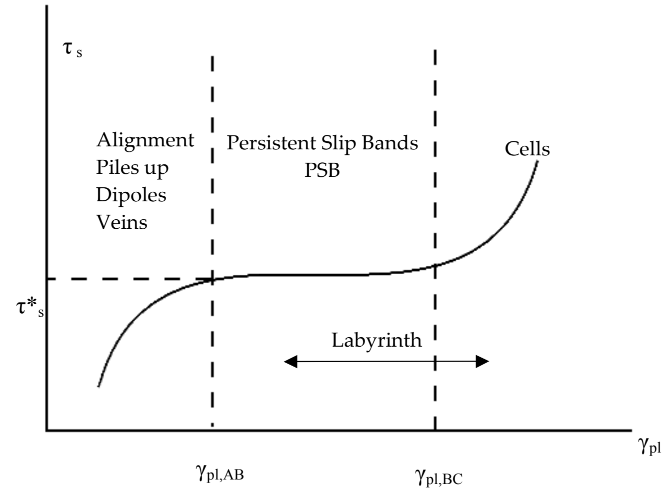

Figure 14 □Schematic diagram showing different regime of the saturation stress-strain curve [38].

3.1.1.2. Dislocation alignments and pile-ups

At very low strain amplitude, materials with low SFE (SFE <10 MJ.m^{-2}) form planar structures of dislocations such as alignments in the slip planes, stacks at grain boundaries or twin boundaries [38]. Generally, if the imposed strain amplitude is high, the creation of these structures is still observed at the beginning of cycling.

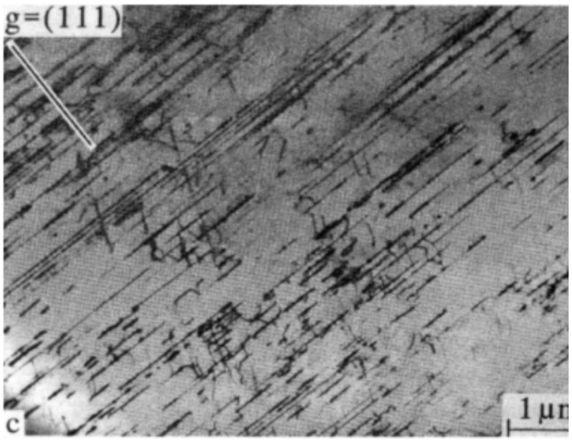

Figure 15 □Dislocation alignment in 316L. $\Delta\varepsilon_p/2=5.10^{-5}$, $\Delta\varepsilon_p/dt=0.1\%/s$, 20°C [32].

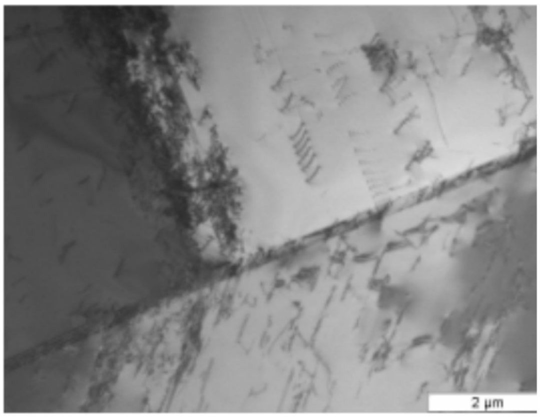

Figure 16 - Dislocation stack at grain boundaries XY182, $\Delta\varepsilon_t/2=0.1\%$, $\Delta\varepsilon_t/dt=0.4\%/s$, run Out, 150°C [33].

3.1.1.3. Dislocation dipoles

In high SFE materials, fully reversed cycling loading produces approximately equal numbers of positive and negative edge dislocations. When such dislocations of opposite signs encounter over small distances, their strong attractions tend them to combine, creating dislocation dipoles. Only edge dislocations can form that kind of dipoles because opposed screw dislocations are mutually annihilated during cycling [34].

Since only a few number of slip systems are activated, these dislocations block each other and are responsible for the first stage of strain hardening.

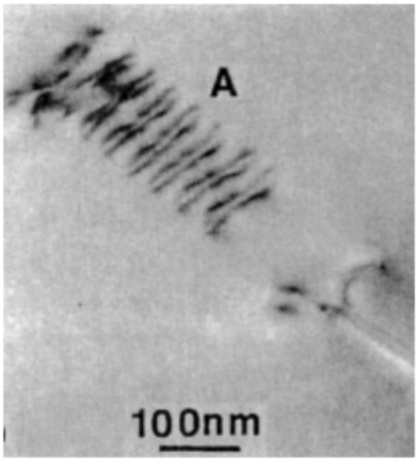

Figure 17 Dislocation dipoles 310 stainless steel [34].

3.1.1.4. Dislocation vein-like structure

The vein-like structure (Figure 18, Figure 19, Figure 20) develops just after planar dislocation structure, such as dipoles, when plastic strain increases. Veins result of tangles of dislocations after a few cycles. They contain a high density of dislocations and are principally composed of dislocation dipoles. These veins (also called loop patches or bundles) occupy 50% of the matrix and are separated by low density dislocation areas called channels.

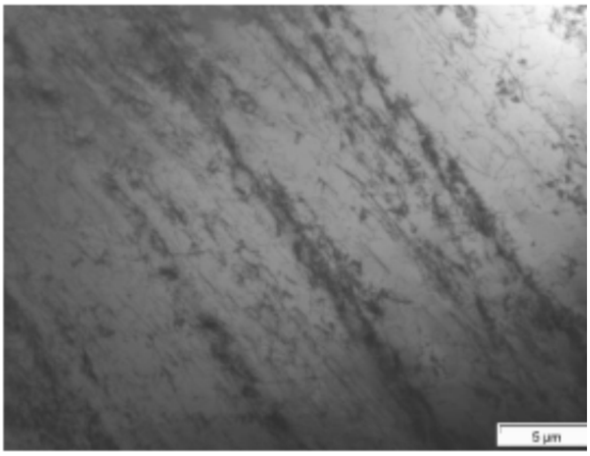

Figure 18 Veins-like structure XY182, $\Delta\varepsilon_t/2=0.15\%$, $\Delta\varepsilon_t/dt=0.4\%/s$, N=63000 cycles, 300°C [33].

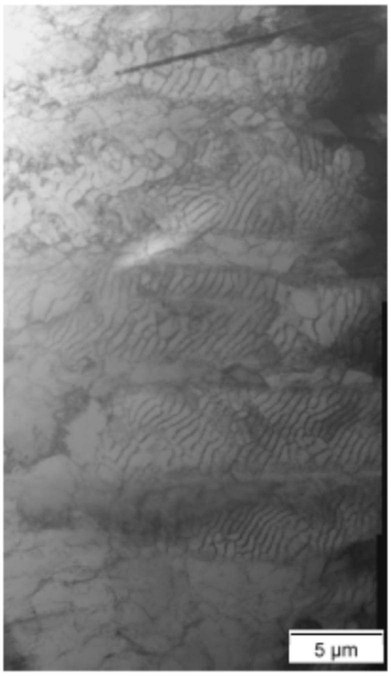

Figure 19 Vein-like structure XY182, $\Delta\varepsilon_t/2=0.15\%$, $\Delta\varepsilon_t/dt=0.4\%/s$, N=63000 cycles, 300°C [33].

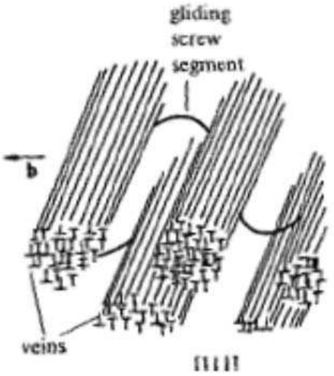

Figure 20 Theorical vein-like structure [38].

3.1.1.5. Persistent slip bands

During cycling, veins and channels are transformed into PSBs, a structure of dipolar walls that often appears in the case of copper in the ladder-like structure. Figure 21 clearly shows that veins-like structures condense into dipole structure walls consisting in edge dislocations in dipole position (Figure 22). PSBs follow primary slip plane, i.e. dipolar walls mainly composed of dislocations with a Burgers vector that corresponds to the direction of the maximum resolved stress τ_s. In case of austenitic stainless steels, PSB ladder-like structures are thicker than in copper and distance between bars is less regular (Figure 22). These structures often partly cover the grain by contrast with the case of copper where they are located at the grain boundaries where strain incompatibilities can create stress concentrations [35]. The rest of the grain is either composed of planar structure for low strain amplitudes, or walls at high strain amplitudes [35].

This structure is the same as the matrix one (veins and channels) and can be treated as a composite consisting of hard areas (walls) with a high density of dislocations and soft areas (channels) that contain very few dislocations. By contrast, in the case of PSBs, the density ratio of walls structure compared to channels is 1to10 [36]. Strain is thus localized in PSBs, which are much more deformable than the matrix [23].

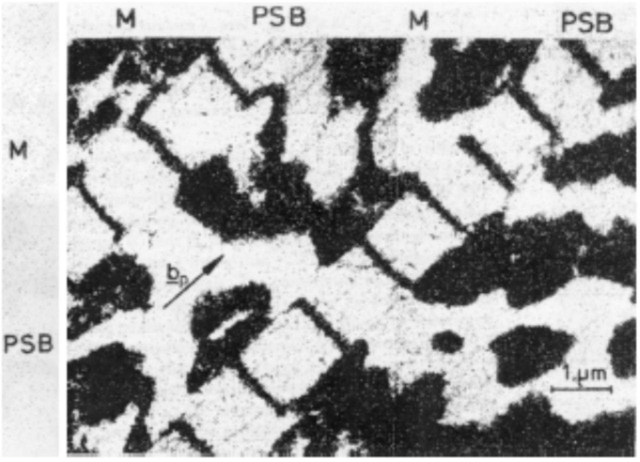

Figure 21 □PSB in copper [36].

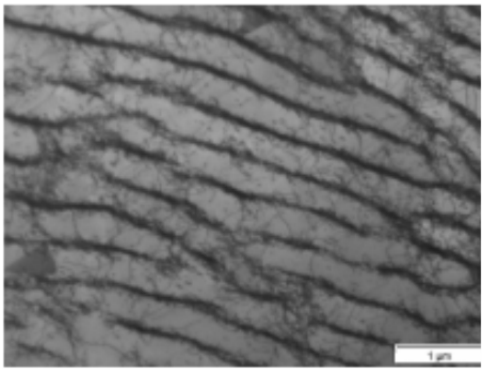

Figure 22 □PSB in XY182, $\Delta\varepsilon_t/2=0.1\%$, $\Delta\varepsilon_t/dt=0.4\%/s$, at failure, 300°C [33].

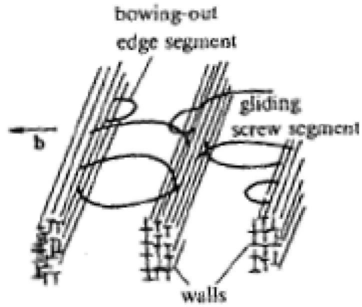

Figure 23 □Enlarged view of the theorical dipolar walls within a PSB [38].

3.1.1.6. Dislocation labyrinth structure

For the labyrinth structure, intermediate between cell and walls, only two different Burgers vectors are required. The cumulative plastic strain has to be sufficient to activate a secondary slip system. The transformation of the structure of walls in labyrinths is due to a density gradient of secondary dislocations (Figure 24) [37].

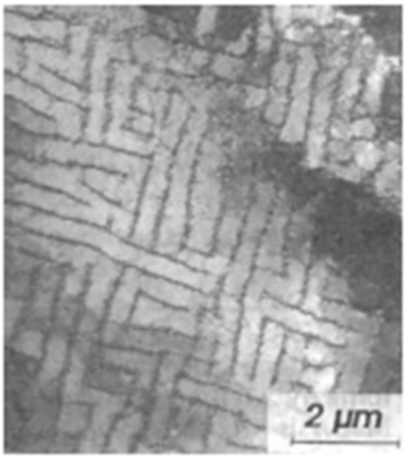

Figure 24 □Wall and channels structure evolving to labyrinth structure in XY182 [37].

3.1.1.7. Dislocation cells

When the plastic strain amplitude is quite high (> 5.10^{-4}), the dislocations are reorganized into cells directly by transformation of the wall and channel structures, or indirectly through an intermediate conversion into labyrinths (Figure 25, Figure 26). For this final three-dimensional configuration, associated with cyclic hardening, several active slip systems have to be involved [14].

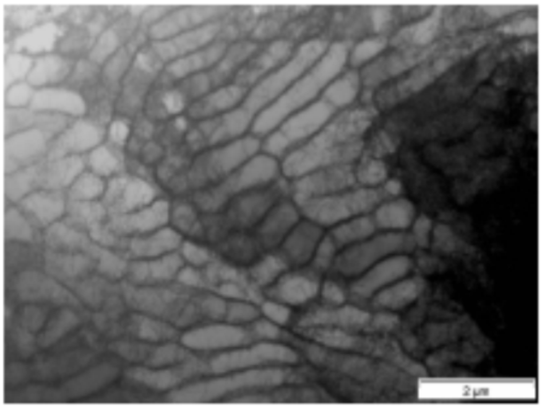

Figure 25 - PSB changing into cells XY182 on the bulk, $\Delta\varepsilon_t/2$=0.1%[3], $\Delta\varepsilon_t/dt$=0.4%/s, at failure, 300°C [33].

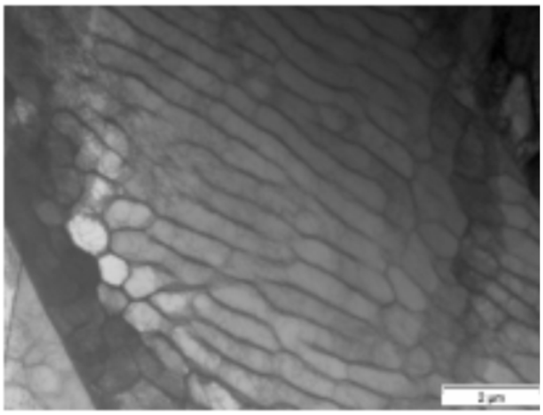

Figure 26 - PSB changing into cells XY182 near a grain boundary, $\Delta\varepsilon_t/2$=0.1%, $\Delta\varepsilon_t/dt$=0.4%/s, at failure, 300°C [33].

3.2. Cyclic stress-strain behavior of 304L stainless steel

The cyclic stress-strain behavior of 304L is typically characterized by a short period of primary hardening corresponding to the multiplication of dislocations and structural arrangement of dislocations in volume, followed by a period of softening and then a quasi-stabilization of stress. Finally, a secondary hardening may eventually appear (Figure 27) [38].

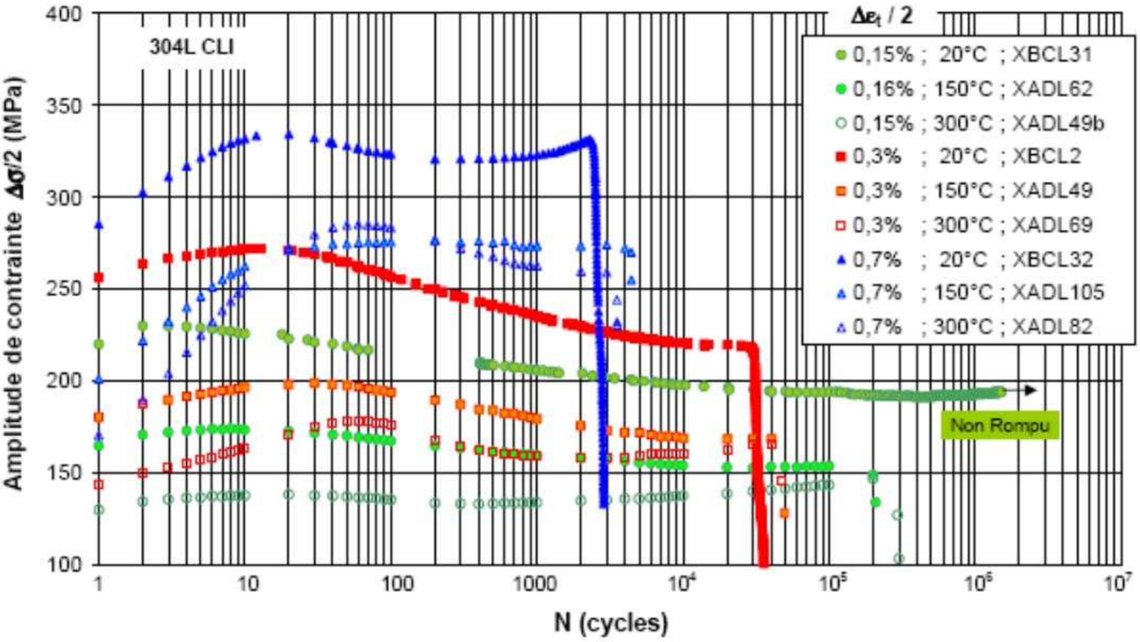

Figure 27 - Evolution of stress amplitude in function of number of cycle at different strain amplitude levels at room temperature, 150°C and 300°C, on heat XY182 (T218) [39].

Mechanisms of cyclic damage observed in ductile single crystals are also known to be generally applicable to the deformation of near surface grains in polycrystalline metals. However presence of grain boundaries, twin boundaries in polycrystalline materials may significantly deviate from those discussed for single crystal solids.

- Primary hardening

The duration and intensity of primary hardening increase with the amplitude of imposed deformation. This is due to the interaction between dislocations and solute atoms. These interactions are of course more important when the dislocation density increases (i.e. for higher amplitudes of deformation) and the concentration in solute atoms increases [38].

- Softening stage

Softening stage, in case of austenitic stainless steels, is due to a rearrangement of dislocations, leading to more stable structures. This is an annealing process assisted by cyclic deformation that causes a relaxation of internal stresses. From a microstructural point of view, softening, that occurs after the stage of hardening, is associated with the rearrangement of dislocations, initially in veins, in order to accommodate more plastic deformation, such as persistent slip bands (PSB) [38].

Observation within the bulk of a cyclically deformed polycrystalline 304L shows that persistent slips bands (PSBs) are confined to a single slip system in a channel and wall structure which is similar to that identified in the bulk of copper single crystals [33], although PSBs can cross low misoriented grains.

Matrix (vein-like structure) is a structure that can be hardly deformed. Therefore, during cycling, the volume fraction of PSBs increases up to occupy the whole grain. The generation of these PSBs will play an important role on the fatigue damage and this aspect will be describe in the dedicated section.

4. Environment: PWR primary water

In PWR plants, the primary water is composed of pure water, boric acid, lithia and dissolved hydrogen (25-50 ml/kg) at a temperature that mainly evolves between 290°C and 345°C under operation. Pure water is used as a heat transfer fluid. Boric acid is used to absorb neutrons coming from the nuclear reaction. But it decreases the pH. Lithia is introduced in order to rise the pH up to $pH_{320°C} = 7.2$ (neutral $pH_{320°C} = 5.8$) to avoid generalized corrosion. Hydrogen is used to avoid water radiolysis which produces oxidant species. The electrochemical potential is close to -600 mV/NHE (1). Most of the degradation in PWR power plants are related to corrosion and oxidation processes.

In contact with aqueous solutions, many materials are thermodynamically unstable and their tendency to oxidize results in "wet corrosion" processes. This oxidation occurs either by dissolution in the aqueous solution or by formation of more or less adherent oxides and hydroxides (passivation). This results in a loss of thickness or in the creation of more localized types of corrosion. In the case of austenitic stainless steels, the oxidation kinetics is slowed by the formation of a thin and adherent passive film, which tends to minimize the risk of component degradation by loss of material. However, the risk of localized corrosion can be increased in some situations. The study of aqueous corrosion of metallic materials is the study of reactions and associated processes that lead to an increase of resistance or degradation of materials in contact with aqueous environment.

---

(1) Normal hydrogen electrode.

4.1. Oxidation

Corrosion is an electrochemical process that results from the interaction of a material with its environment, resulting in the degradation of this material. This electrochemical reaction is due to the coupling of anodic and cathodic reactions. In the case of wet corrosion of a metallic material, the anodic reaction is the oxidation of the metal, resulting in its dissolution:

Anodic Reaction $M \rightarrow M^{n+} + ne^-$

In an aqueous environment, the cathodic reaction progress as follows in the case of Hydrogen Water Chemistry (HCW) and Oxygen Water Chemistry.

Cathodic reaction	Neutral HCW	$\mathbf{2nH_2O + 2ne^- \rightarrow nH_2 + 2nOH^-}$
	Neutral OWC	$\mathbf{nO_2 + 2nH_2O + 4ne^- \rightarrow 4nOH^-}$

The anodic reaction is specific to an environment-material couple. It is characterized by its electrochemical potential E, created by the decrease of the Gibbs energy of the atoms of the metal going into the solution and represents the energy available for reaction. The anodic reaction is also characterized by the dissolution current I, which is proportional to the number of atoms dissolved per unit time and the valence n. It represents the kinetics of the anodic reaction. The dissolution of the atoms is a thermally activated process. If no external potential is imposed (under free potential), anodic and cathodic reactions are balanced and the total current is zero. A more or less complex oxide or hydroxide layer forms at the surface of the material, in agreement with the E-pH (Pourbaix) diagrams [40].

According to its structure and composition, and in given ranges of potential, this layer can be stable and limit the current of dissolution. This layer is then named passive film.

In the absence of disturbances, the material covered by a passive film is protected from its environment. Nevertheless, the mechanical loading can damage the passive film, for example by the emergence of shear bands at the surface. The fresh material is then exposed to the environment where a rupture of the passive film occurs. This local oxidation is the root cause of many phenomena such as EAF and SCC. Chêne and Brass noted that in aqueous environments, the cathodic reaction has a high probability to lead to a hydrogen discharge [41], because hydrogen is partly adsorbed in the metal.

$$M + H^+ + e^- \rightarrow MH_{ads}$$

$$MH_{ads} \rightarrow \begin{cases} MH_{ads} \rightarrow MH_{ads} \\ 2MH_{ads} \rightarrow 2M + H_2 \end{cases}$$

At the crack tip, the local failure of the passive film is also promoted.

4.2. Oxidation of stainless steels in PWR primary water

In PWR environment, the oxide film formed on 304L has a duplex structure with a Cr-rich inner layer, adherent and compact, and an outer iron reach layer, porous, discontinuous [42] [43] [44]. The inner layer is suspected to be chromite ($(Fe,Ni)Cr_2O_4$) and the external layer magnetite ($Ni_xFe_{3-x}O_4$). It is considered that the inner oxide layer growth from the interface to the bulk due to an anionic growth. The outer layer growth from a cathionic mechanism with an eventual contribution of ions present in the environment.

5. Fatigue and Environmentally assisted cracking

As shown previously, the oxidation process of austenitic stainless steels is slowed by the formation of a thin and adherent passive film. However the passive film can be broken due to the combined action of the material and the loading. This process is the primary cause of the EAC process and depends on the nature of the environment, the material, the mechanical loading, and sometimes on irradiation. These effects cannot be treated separately: EAF and SCC are synergistic phenomena. Fundamental knowledge on the fatigue damage and the EAC are presented below.

5.1. Fatigue damage

5.1.1. Fatigue damage overview

The fatigue life can be divided in two parts:

- Fatigue crack initiation

The definition of initiation depends on the observation scale. From the engineering point of view, initiation corresponds to the minimal crack depth that can be detected in a structure using non destructive examination. From a more physical point of view, initiation corresponds to the nucleation of micro cracks at the surface. In most of the cases, preferential crack initiation sites are located where local accumulation of plastic strain and dislocations during cycling is high, as at twin or grain boundaries or at PSBs. Cracks initiate at the surface because dislocations are more mobile in this area. Environment can also contribute to initiate fatigue cracks [45].

- Fatigue crack propagation

Propagation stages are presented in Figure 28:

- Stage 1 (fatigue crack growth)

After initiation, cracks propagate at a 45° angle from the loading axis corresponding to a typical Mode 2 shear process orientation that can change due to obstacles (inclusion, twin boundaries,□).

- Stage 2 (crack growth and fatigue striation)

At higher stress intensity range values, the plastic area ahead of crack tip encompasses many grains. Crack growth involves at least two symmetrical slip systems. This duplex slip mechanism results in a planar Mode 1 crack path normal to the tensile axis.

Only a limited amount of stage 1 cracks propagate on stage 2. In the 1960's, Paris [46] postulated, in the hypothesis of small scale yielding, that the range of stress intensity factor (ΔK) controls the sub-critical crack growth under fatigue loading (Equation 15).

$$\frac{da}{dN} = C\Delta K^{n}$$

Equation 15

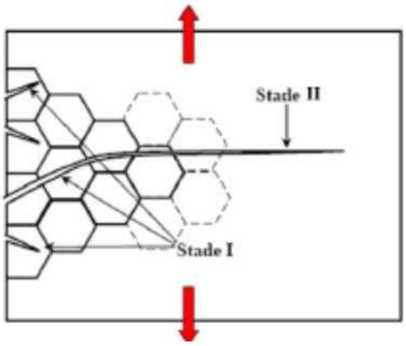

Figure 28 - Propagation regime.

5.1.2. Crack initiation in a single crystal

Free surfaces are preferential regions for fatigue crack initiation. Indeed PSBs, produced by cyclic deformation, induce the formation of intrusions-extrusions thus creating a surface relief (Figure 29).

In order to better understand damage accumulation mechanisms in austenitic stainless steels, three-dimensional discrete dislocation dynamics simulation (DDD) has been conducted both to simulate the dynamic evolution of the dislocation microstructure and the topography of the free surface where the plastic deformation is localized. Computations indicate that the intrusion-extrusion relief at free surface develops due to walls, composed of dipoles, and channel dislocation structure [47].

Therefore it can be considered that intrusions play the role of micro notches that induce stress concentrations where cracks can initiate.

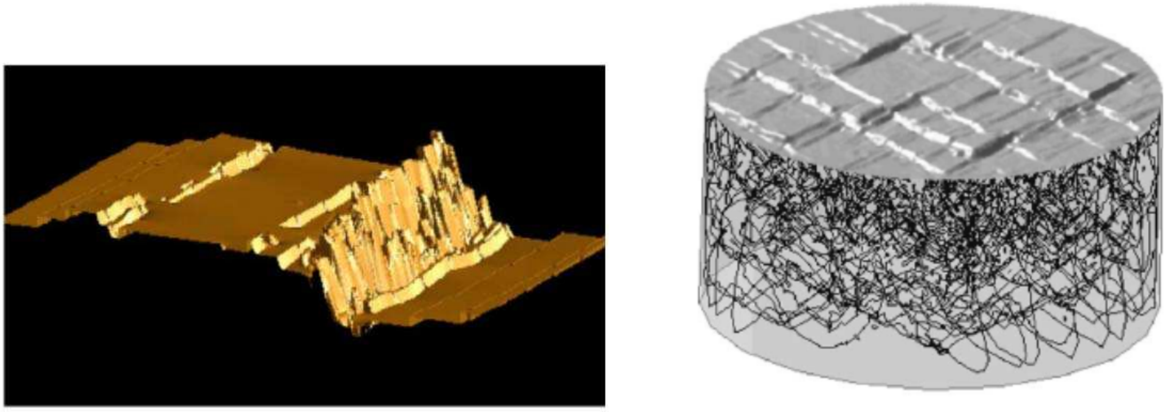

Figure 29 - Surface topography associated to dislocation microstructure and extrusion/intrusion at the strain localization in 316L. Discrete dislocation dynamics [47].

5.1.3. Initiation sites in polycrystals

As previously described, the surface of the material plays an important role in fatigue crack initiation. Preferential crack initiation sites are areas where local strain induced by cycling is high. The crystallographic orientation of each individual grain plays an important role in the process of emerging PSBs. Indeed, during a fatigue test, some grains are not so much plastically strained, while others are strongly deformed, with essentially only one slip system being activated (Figure 30) [48].

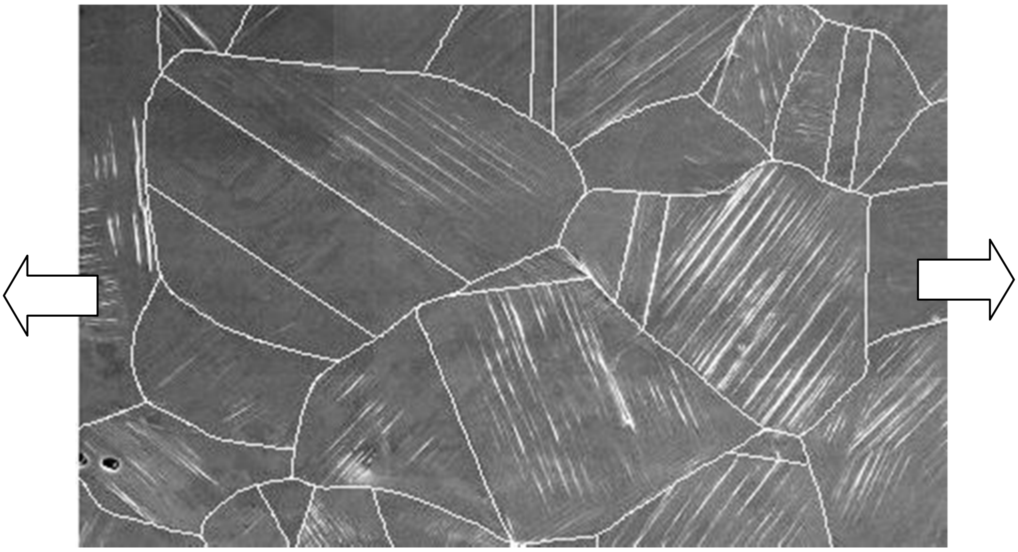

Figure 30- Slip occurring at the surface, 316L, 20°C, $\Delta\varepsilon_p/2 = 0.2\%$ [48].

The Schmid factor can be used to quantify the probability of initiation of fatigue cracking in air. A statistical evaluation on a 316L stainless steel at 20°C loaded at $\Delta\varepsilon_p/2 = 0.2\%$, with a Schmid factor calculated using the <110>{111] slip system, has been performed. The results presented in Figure 31) show that for a 316L austenitic stainless steel, 90% of cracked grains exhibit a Schmid factor higher than 0.41.

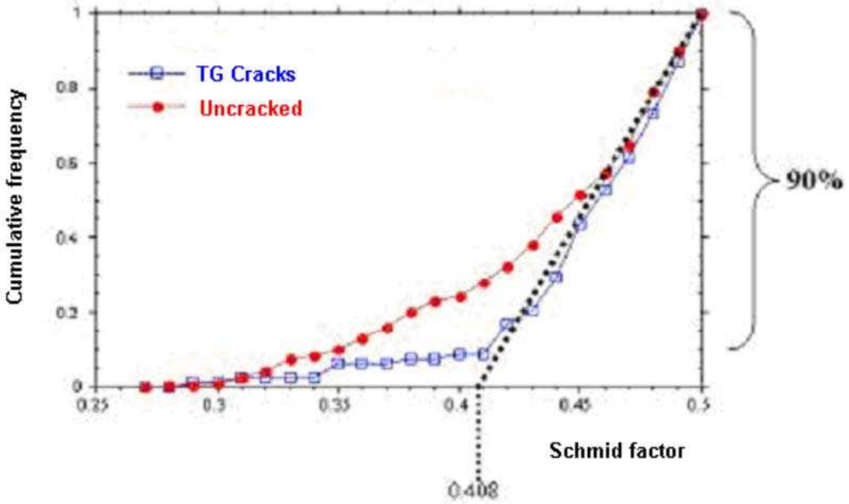

Figure 31 - Distribution of Schmid factors of untracked grains (red) and grains presenting TG cracks, 316L, 20°C, $\Delta\varepsilon_p/2 = 0.2\%$ [49].

Atomic Force Microscopy studies (AFM) can help to clarify the process of emergence of slip bands during cycling (Figure 32) [48]:

- Slip bands create nanoscale basic steps.
- Thick bands form at the slip band/matrix interface, then extrusions composed of {111} planes are produced.
- Activity in the previously formed band thickness leading to a highly irregular extrusion profile extrusions. Several examples of extrusion/intrusion are presented in Figure 33.
- PSB growth rate has been established to be equal to 40 nm/1000 cycles at $\Delta\varepsilon_p/2 = 0.2\%$.

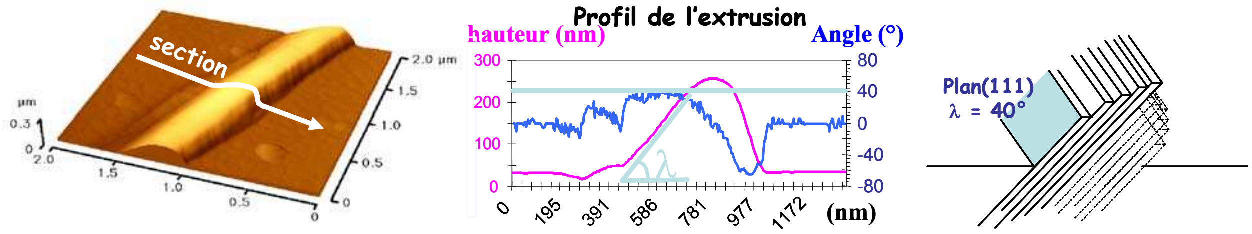

Figure 32 - AFM images of a PSB profile , 316L, 20°C, $\Delta\varepsilon_p/2 = 0.2\%$ [48].

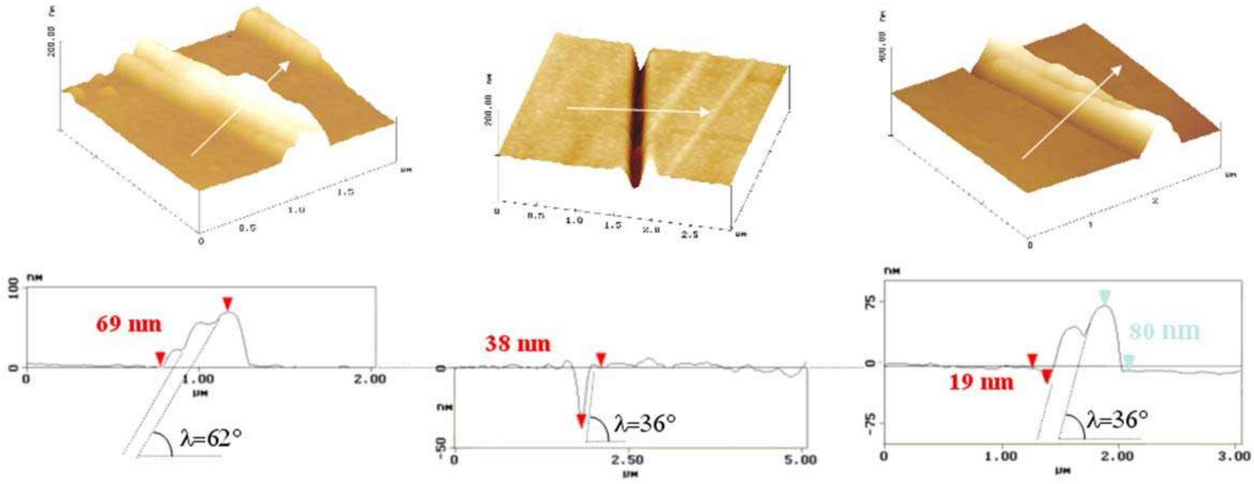

extrusion

intrusion

extrusion - intrusion

Figure 33 Examples of intrusion/extrusion configuration 316L, 20°C, $\Delta\varepsilon_p/2 = 0.2\%$ [48].

All the following reported fatigue tests were performed under tension-compression for $\Delta\varepsilon_p/2 = 0.2\%$ at 20°C. They were carried out under vacuum or in air to identify the mechanisms of initiation and to establish intrinsic differences due to the action of the air environment. 3 main types of initiation sites have been observed (Figure 34).

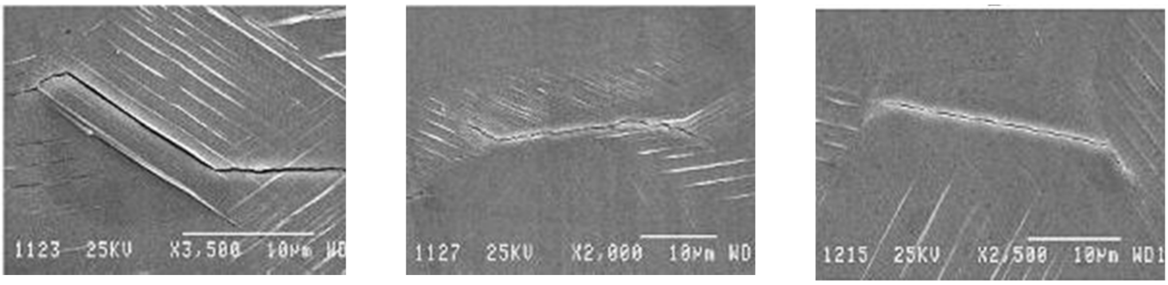

Persistent Slip Bands Grain boundaries Twin boundaries

Figure 34 □Initiation localization on a 316L SS, 5000 cycles, 20°C, $\Delta\varepsilon_p/2 = 0.2\%$, air [49].

A statistical study of several hundred cracks (given in number of initiation) showed that transgranular (TG) cracks can be observe in vacuum (33%) and are dominant (73%) in air, while intergranular (IG) cracks dominate under vacuum (57%). The fraction of IG cracks drastically decreases in air, due of an environmental effect promoting TG cracks, however no clear explanation is given by the authors.

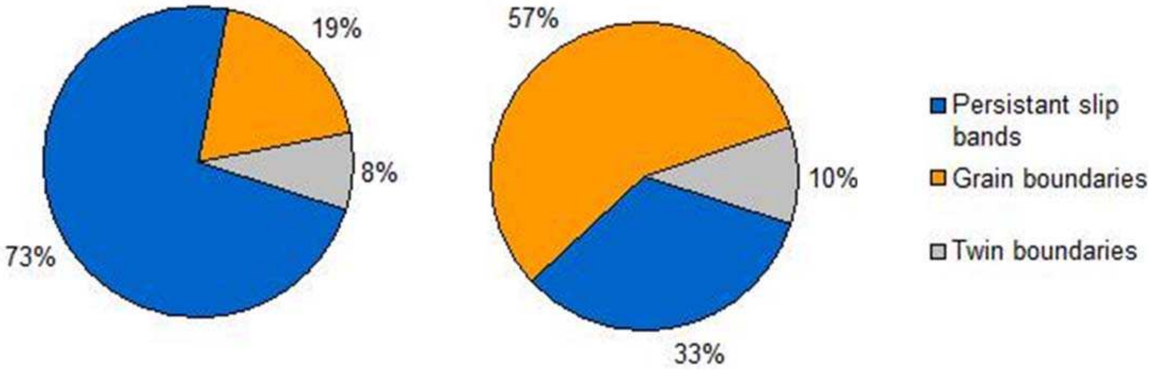

Air Vaccum

Figure 35 □Statistical analysis of initiation localization on a 316L , $\Delta\varepsilon_p/2 = 0.2\%$, 20°C, air [49].

Mineur [49] noted the strong susceptibility to initiate transgranular cracks in the grains oriented for single slip, promoting plastic strain localization. Grains that are favorably oriented for multiple slip, are somewhat less favorable to initiation. The role of the grain orientation at the surface of the specimen was highlighted. Thus the transgranular crack initiation is particularly favored for PSBs emerging with an angle relative to the surface between 40 ° and 60 ° (Figure 36).

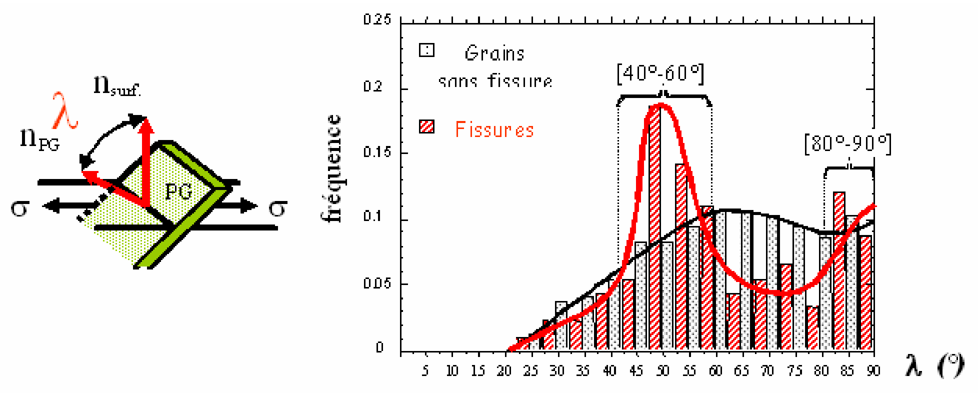

Figure 36 □Crack initiation as a function of PSB emergence angle 316L , $\Delta\varepsilon_p/2 = 0.2\%$, 20°C, air [49].

5.2. Interaction between strain localization and oxidation of stainless steels in PWR primary water

The stability of the protective passive film can be compromised by emerging shear bands [50] especially, when the film is thin and brittle. The base metal is then attacked by local dissolution. An example is given for the EAF damage of a duplex austenitic-ferritic stainless steel in a 30g/1 NaCl solution at pH 6.5 [50]. During the first few cycles, there is an increase in the peak current density J_T in tension and the peak current density J_C in compression corresponding to the multiplication of shear bands at the specimen surface and their local dissolution. The peak decrease corresponds with the repassivation of the material (Figure 37). When slip localization takes place, Jt and Jc decrease and then stabilize (Figure 38) until the microcracking process occurs, this makes repassivation more difficult.

The mechanism of depassivation depends on the rate and the amplitude of plastic strain, while the kinetics of repassivation material is environment/potential and time dependent (Figure 39). The current density level also increases when the strain rate increases, leading in this particular material/environment conditions to a decrease of fatigue life.

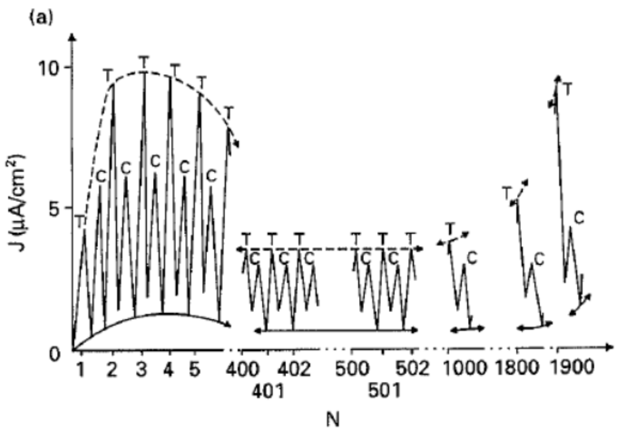

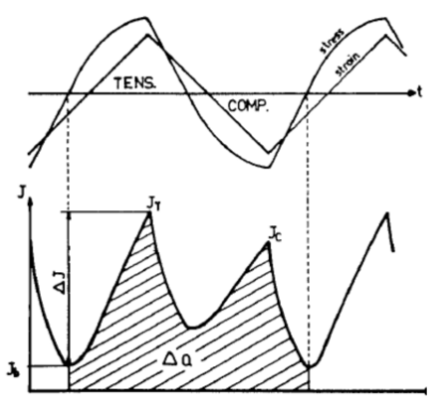

Figure 37 □Cyclic evolution of the corrosion current density J on the dupex austenitic stainless steel at $\Delta\varepsilon_p/2=0.4\%$ and $\Delta\varepsilon_p/dt=0.01\%/s$ (NaCl 30g/l) [50].

Figure 38 □Measurement of current transient characteristics at imposed potential of a passivated material [50].

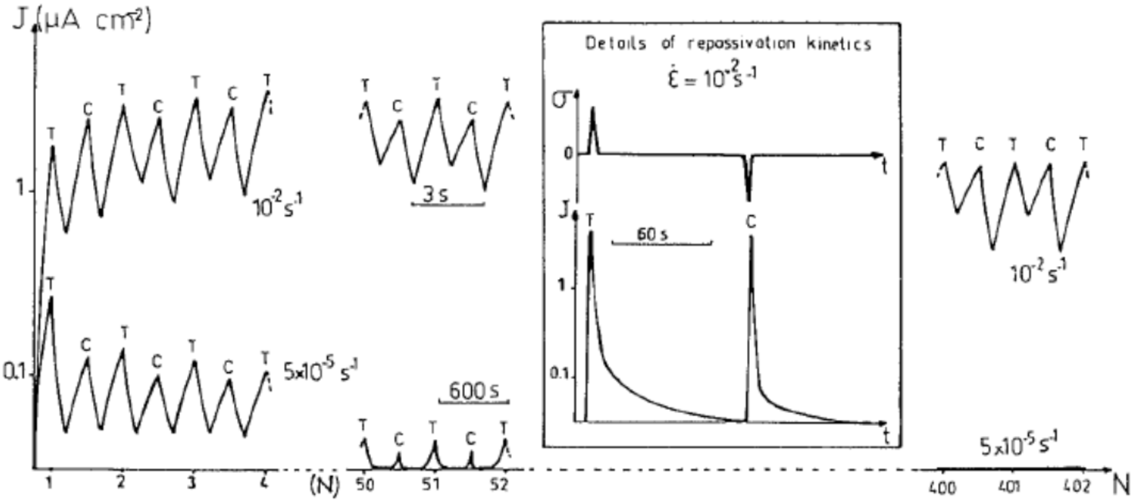

Figure 39 □Influence of strain rate on the cyclic evolution of J for different values of N and two different strain rates at $\Delta\varepsilon_p/2=0.4\%$ of a Fe-26Cr-1Mo alloy in 30g/l NaCl [50].

Figure 40 shows the typical aspect of an oxide layer formed at the surface of a strain hardened stainless steel sample exposed to primary water at 360°C during a SCC constant elongation rate test [51]. Duplex oxides are observed. Magnetite spinels grew on the inner Cr-rich oxide layer by precipitation of dissolved iron cations and cationic growth.

The inner passive Cr-layer is composed of fine-grained crystals with an epitaxial relation with the underlying metal: this is most likely the result of the progressive oxidation of the metal, retaining its original orientation. Microstructural defects of the metal, serving as transport shortcuts, shape the oxide grain-like structure, and offer preferential penetrations.

An increase of plastic strain leads to an increase of the Cr-rich oxide thickness (Figure 41) [52].

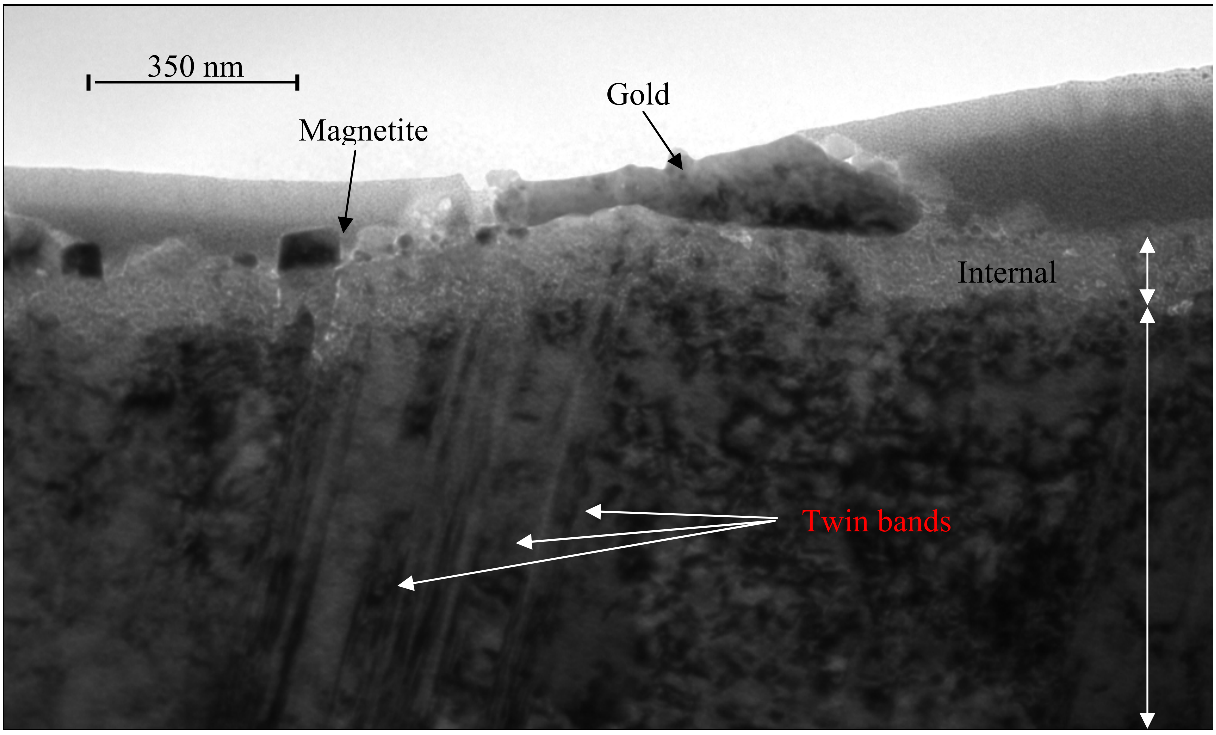

Figure 40 - Oxide observation (STEM, bright field) at the surface of a 304L specimen exposed to the primary water (360°C during 500 h □$2x10^{-8}.s^{-1}$, Constant Elongation Rate Test) [51].

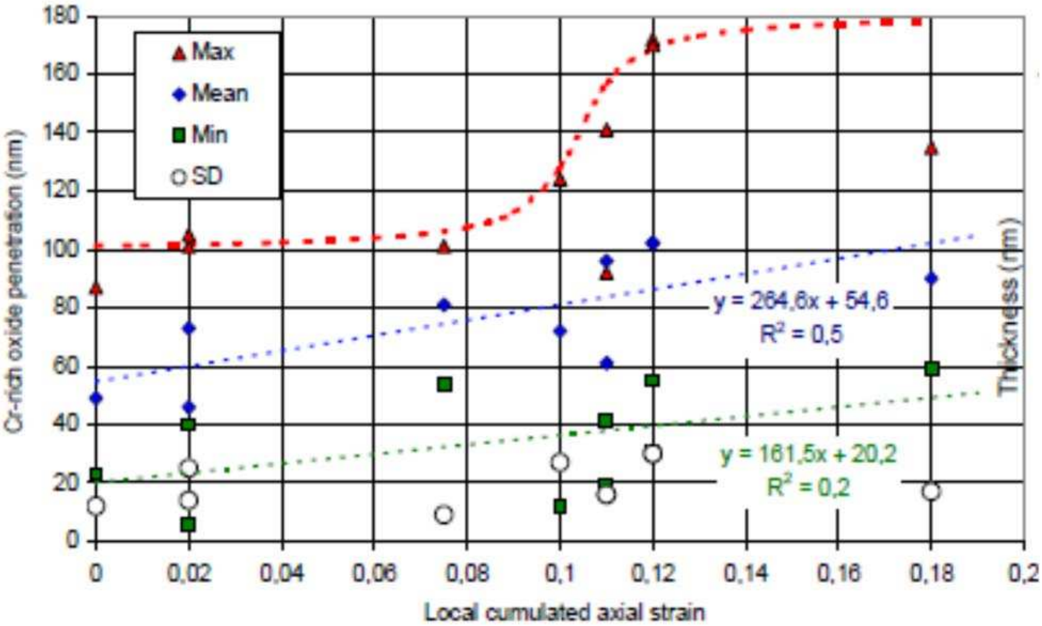

Figure 41 - Cr-rich oxide penetration against local cumulated strains of stainless steels [53].

5.3. Modeling EAC

Several authors postulates different model predicting the EAC. Such work are presented in the following section.

5.3.1. Slip dissolution and slip oxidation models

The slip-dissolution model originally proposed by Logan for SCC was taken up and developed by Ford [54] [55] [56] and modified by Shoji [57]. It postulates that dynamic plastic strain at the crack tip fractures a brittle oxide film, allowing a burst of metal dissolution prior to re-establishment of the film. Repetition of this sequence extends the crack. The kinetics of crack advance depends on the amount of dissolved metal during the dissolution step (Figure 42).

Parameters that govern the slip dissolution model are:

The strain rate, $\dot{\varepsilon}_{CT}$, at crack tip that induces a number of events that break the film.

The charge density Qf exchanged during the transient current dissolution-passivation following each event of rupture of the film.

Applying Faraday's law, an expression of the crack growth rate, $\dot{a}$, is written:

$$\dot{a} = \frac{MQ_f}{z\rho F t_f} = \frac{MQ_f \dot{\varepsilon}_{CT}}{z\rho F \varepsilon_f} \qquad \textbf{Equation 16}$$

where M and ρ are the atomic mass and density of the metal dissolved at the crack tip, F is the Faraday constant, z is the number of electrons being involved in the oxidation reaction of metal, t_f the film breaking periodicity, ε_f is the strain to fail the passive film.

There is a competition between the dissolution rate and the passivation rate: a slow passivation the stops propagation by blunting the crack, while a too fast passivation leads to negligible crack propagation rate. During transient, the expression of the crack rate, using current densities is the following:

$$\dot{a} = \frac{M}{z\rho F}\frac{i_o t_o^{\ m}}{(1-n)\varepsilon_f^{\ m}}\dot{\varepsilon}_{CT}^{\ m} = A(n)(\dot{\varepsilon}_{C} \qquad \textbf{Equation 17}$$

where i_0 the current density exchange at the crack tip at t_0, when the oxide film breaks, and m a constant:

$$i(t) = i_0\left(\frac{t}{t_0}\right)^{-m} \qquad \textbf{Equation 18}$$

The theorical plastic strain distribution at the crack tip along the crack line for growing crack in an elastic plastic strain hardening material was given by Gao & al

$$\varepsilon_{CT} = \left(\frac{\sigma_y}{E}\right)\left[\ln\left(\frac{A}{r}\right)\right]^{\frac{n}{n-1}} = \beta\left(\frac{\sigma_y}{E}\right)\left\{\ln\left[\left(\frac{\lambda}{r}\right)\left(\frac{K}{\sigma_y}\right)^2\right]\right\} \qquad \textbf{Equation 19}$$

where n is the strain hardening exponent defined as $\varepsilon_{pl} = c(\sigma - \sigma_y)^n$, σ_y is the yield stress, E is the young modulus, A is assumed to be equivalent to the plastic zone area, r is the distance from a growing crack tip, λ and β are constants for plastic strain calculation, K is the stress intensity factor.

$\dot{\varepsilon}_{CT}$ is given by derivation of ε_{CT} by t:

$$\dot{\varepsilon}_{CT} = \frac{\beta\sigma_y n}{E(n-1)}\left(2\frac{\dot{K}}{K} + \frac{\dot{a}}{r_0}\right)\left\{\ln\left[\frac{\lambda}{r_0}\left(\frac{K}{\sigma_y}\right)^2\right]\right\} \qquad \textbf{Equation 20}$$

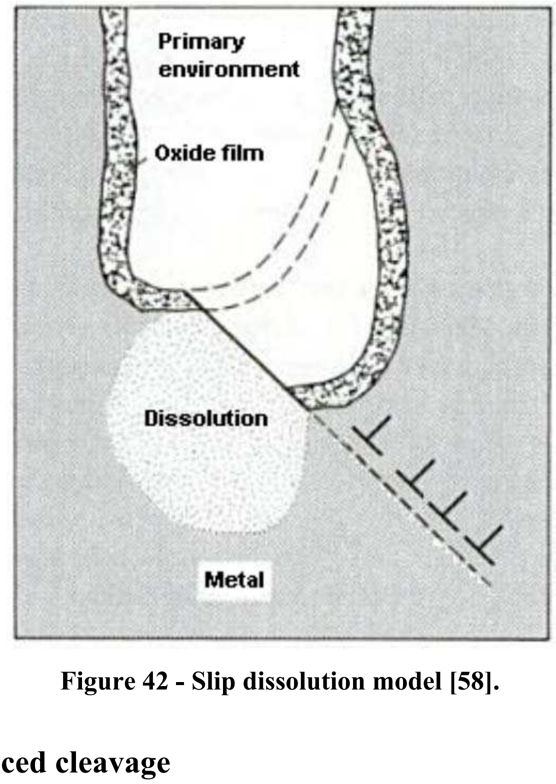

Figure 42 - Slip dissolution model [58].

5.3.2. Film-induced cleavage

The film-induced cleavage model has been proposed by Sieradzki and Newman in 1985 [59]. A description of this model and its applications has been presented by Cassagne

[60]. This model has been previously developed for Transgranular Stress Corrosion Cracking (TGSCC) of FCC systems, but it can be extrapolated to other systems (Figure 43).

The model is divided into three steps:

- Formation of a brittle oxide film under the action of a corrosive environment (i.e. porous layer established by selective dissolution).
- Cleavage cracking of the film, crossing the metal-oxide interface up to a distance of several micrometers.
- Crack blunting by dislocation emission. Under the effect of applied stress, the crack opens.

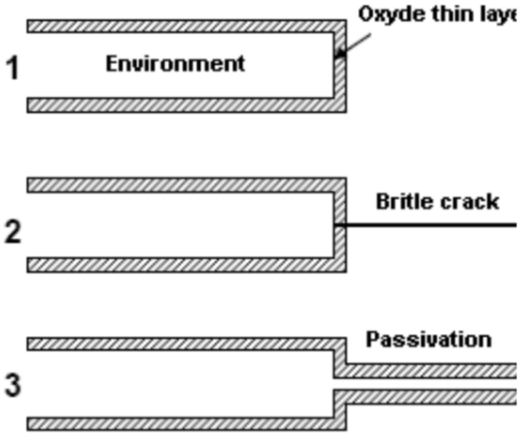

Figure 43 - Film induced cleavage model [60].

Crack front moves forwards by an oxidation process that is controlled by the same rate-determining steps as those in the slip-dissolution model, but when the film rupture occurs after an increment of strain, the crack extents of a*, into the underlying metal matrix (a* can reach from 1 µm to 10 µm). Thus the crack propagation rate of Shoji model is modified:

$$\dot{a} = A(n)(\dot{\varepsilon}_{CT})^m + a^* \frac{\dot{\varepsilon}_{CT}}{\varepsilon_f}$$ **Equation 21**

5.3.3. Surface mobility mechanism

The surface mobility mechanism postulates that environmentally induced crack propagation is due to the coalescence of vacancies at the crack tip. Crack grows by diffusion of metal atoms (which may be combined with ions or molecules in the environment) from the crack tip to the lips (i.e. vacancies catch at the bottom of the crack cause their advance). Elastic stress concentration at the tip of the crack, promotes the diffusion gaps [61].

Tensile test is known to reduce the free energy for the formation of vacancies according to the following relation:

$$\Delta F^0 = -\sigma.a^3$$ **Equation 22**

where σ is the tensile stress and a is the atomic size. This equation leads to the equilibrium concentration of vacancies in the stressed region:

$$C = C^0 e^{\left(\frac{\sigma.a^3}{k.T}\right)}$$ **Equation 23**

where C_0 is the concentration of vacancies in the free bulk metal, T is the temperature in K, k is the Boltzmann constant.

The relaxation time necessary to reestablish an equilibrated vacancy concentration is expressed by:

$$\tau \approx \frac{\lambda^2}{D}$$ **Equation 24**

where D is the vacancy diffusivity and λ is the distance to the nearest vacancy source (crack tip). However, when the temperature is lower than a half of the melting temperature the value of D is very low and consequently the relaxation time is very long.

The surface mobility mechanism assumes that, because of the action of the environment, only the first atomic layers of the metal are susceptible to move. Each time the stressed lattice at crack tip captures a vacancy, the crack propagates over an atomic distance, and a surface depletion of vacancies will be created. The diffusion of these vacancies along the surface will be the rate controlling process, leading to the following equation for the crack propagation rate:

$$\dot{\alpha} = \left(\frac{D_s}{L}\right)\left(e^{\left(\frac{\sigma.a^3}{k.T}\right)} - 1\right)$$ **Equation 25**

where D_s is the surface self-diffusion coefficient, L the diffusion distance of the vacancies. This model can be summarized as in the next Figure 44.

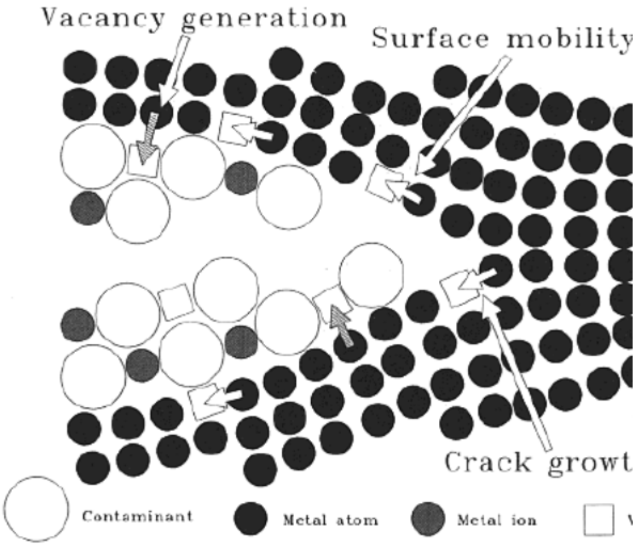

Figure 44 □Surface mobility mechanism [61].

The surface mobility mechanism is actually subjected to controversy [62] [63] because they are based on a coefficient D_s which is largely "amplified" at crack tip.

5.3.4. Internal oxidation

The Internal oxidation model [64] was proposed as a plausible mechanism of intergranular stress corrosion cracking (IGSCC) of the nickel base alloy 600 in PWR primary environment. The internal oxidation was originally developed to explain the degradation of 600 nickel alloys at high temperatures (T> 800°C).

The internal oxidation is based on the embrittling action of oxygen from the hydrolysis at grain boundaries by diffusion of oxygen atoms and is described in Figure 45. This model is supported by measurements of oxygen penetration using Nano-SIMS [65] that reveal an oxygen penetration at grain boundaries (Figure 46).

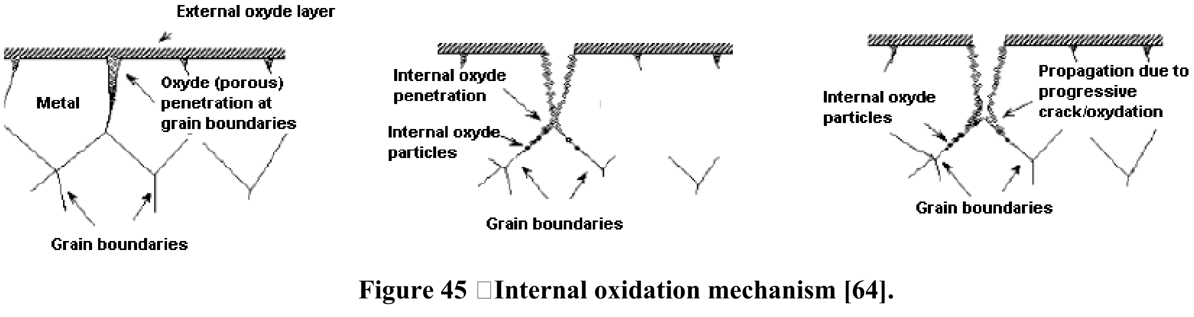

Figure 45 □Internal oxidation mechanism [64].

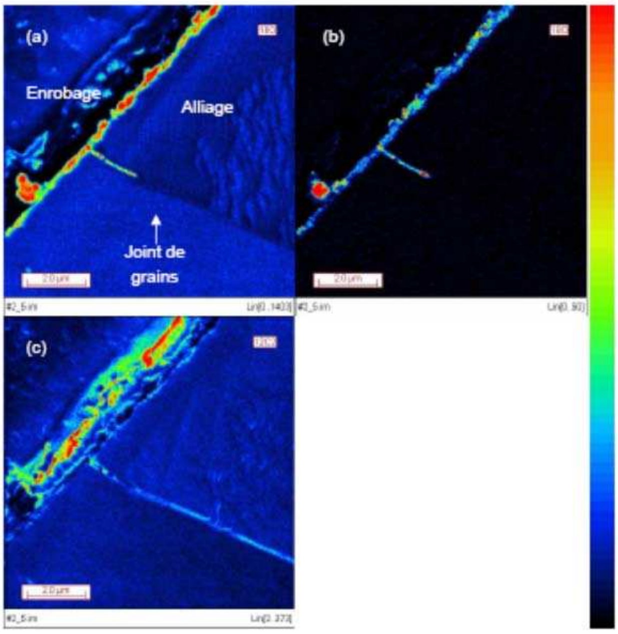

Figure 46 - Nano SIMS maps of 16O(a) 18O(b), and Carbon (c) of a 600 alloy after 1340h at 325°C [65].

5.3.5. Hydrogen assisted cracking

5.3.5.1. Internal pressure

This theory proposed by Zapffe [66] is based on the formation of molecular hydrogen in microcracks or microstructural defects (cavities, grain boundaries, ...) which results in raising the internal pressure to very high values, 10^6 to 10^8 bars so as to increase stress concentrations and promoting SCC.

5.3.5.2. Hydrogen Enhanced Decohesion

This theory proposed by Oriani [67] on the generic name Hydrogen Enhanced Decohesion (HEDE) is linked to the diffusion of mono-atomic hydrogen on the crystal lattice where there is a high stress triaxiality, i.e., at the crack tip. It assumes that hydrogen reduces the energy required for the separation of two atomic planes so as to increase the intrinsic brittleness of the material.

5.3.5.3. Adsorption induce dislocation emission

This theory was proposed by Lynch [68] it relies on the presence of micro-cavities similarly observed on the fracture surfaces of different alloys submitted to SCC. This model implies a weakening of atomic bonds induced by adsorbed hydrogen atoms on the surface. This adsorption facilitates the emission of dislocations from the crack tip.

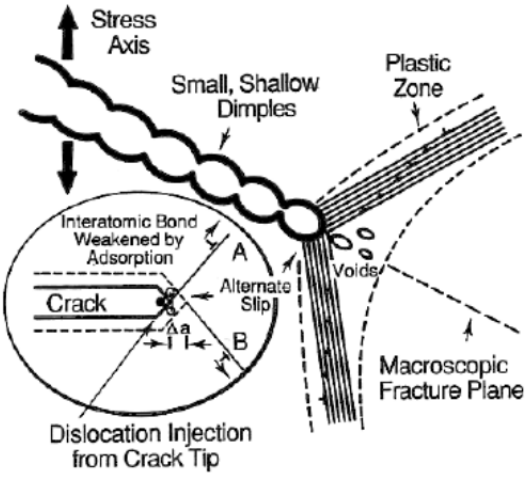

Figure 47 □Adsorption induced dislocation emission [68].

Adsorbed hydrogen promotes the successive emission of dislocations in two symmetric planes (A and B) causing a crack advance of □Δa□

This process is linked with a strong activity of slip ahead of the crack, which results in the formation of micro-gaps on precipitates or at the intersection of slip bands. These micro cavities coalesce and contribute to the spread of the crack. The crack extends as well as the plane bisecting the two slip planes activated A and B.

5.3.5.4. Hydrogen-plasticity interactions

This theory has been proposed by Bastien and Azou [69] and is based on hydrogen transport by dislocations to gaps and/or microcracks on the material. It assumes that hydrogen diffusion kinetics at a given temperature are comparable to dislocation velocity. In this case, embrittlement is due to recombining hydrogen and vacancies that increase internal pressure and stresses. Stroh [77] suggest that hydrogen embrittlement is due to a hardening at crack tip induced by dislocation stuck by hydrogen. By contrast, Beachem [70] suggests that hydrogen locally softens the material and so promotes deformation and fracture.

5.3.5.5. Adsorption

This theory has been proposed by Petch [71] and postulates that hydrogen embrittlement reduces free surface energy due to its adsorption. Indeed, according to Griffith theory the ultimate stress is proportional to the surface energy. This theory has been criticized by Coudreuse [72] arguing that other species like O_2, H_20, N_2 that have higher adsorption energy could counteract the hydrogen embrittlement.

5.3.5.6. Jones modeling

This theory has been formulated by Jones in order to propose a unified mechanism of stress corrosion and fatigue corrosion [73]. Jones suggests that the anodic dissolution causes a local softening of the material where the passive layer breaks down, thereby reducing the stress required to cracking, which will promote crack initiation and propagation due to micro cleavage.

Jones assumed that the cyclic strain induces a softening by generating a vacancy supersaturation. This supersaturation, in the case of monotonic loading, is induced by adsorption of specific species such as chlorides (Cl). This supersaturation results in the formation of bi-vacancies which have sufficient mobility to interact with dislocations near the crack tip, causing a reduction of the hardening. Crack propagation is a result of bi vacancies accumulation on {100} or {110} planes.

However this model is not able to predict brittle shearing on {111} plane. Moreover, Magnin [74] disagree about the role attributed to vacancies.

5.3.5.7. Corrosion enhanced plasticity model

This theory proposed by Magnin et al [74] also considers the effect of a localized anodic dissolution on the plasticity at crack tip. In this model, Magnin suggests that dissolution may facilitate the movement of dislocations near the surface, creating a synergy between corrosion and plasticity and leading to a brittle-type fracture. The corrosion enhanced plasticity model accounts of the micro-cleavage and intergranular fractures observed in case of 316L austenitic stainless steels in boiling $MgCl_2$ environment and has been summarized by Delafosse et al [75] as follows (Figure 48):

The activation of dislocation sources at the crack tip depassivates the metal and a localized dissolution takes place on the activated slip plane.

Vacancies and hydrogen atoms produced by the electrochemical reactions at the crack tip diffuse along this plane and produce an enhanced mobility of the dislocations. Blunting is then reduced, because of the slip localization in planes intersecting the very crack tip.

During deformation, the material is hardened. Further away from the crack, emitted dislocations interact with forest obstacles previously formed. Hence, two zones form: a diffusion zone (enhanced plasticity) near the crack and a hardened zone further away. The interface between these two zones moves along the slip plane while diffusion occurs. A pile-up forms against pre-existing microstructural barriers when they are reached by this mobile interface, and a significant part of the crack tip stress concentration is transferred at the head of the pile-up [76].

Due to the presence of hydrogen segregation on dislocations, the local K_{Ic} decreases and can be reached at the head of the pile-up. A crack's embryo forms by a Stroh-type mechanism [77].

Hydrogen lowers the decohesion energy of the slip plane, and the crack opens along this plane under the normal stress. Dislocations are emitted on a symmetrical plane, shielding the new crack tip. Depending on the crystallographic orientation and on the local stress triaxiality, cracking may occur along {111} or {110} planes.

This process is expected to lead to periodic changes of crack planes. A zigzag microcracking can occur, involving {111} planes.

The role of dissolution is essential but indirect. First, hydrogen absorption requires the existence of a critical defect in a passivated metal [21]. This defect is created by dissolution at the slip line emergence site, which is always experimentally observed [16].

Secondly, local vacancy injection (coming from cathodic reactions) most likely participates in the local plastic softening and strain localization at the crack tip. Vacancies may also act as hydrogen trapping sites, thus increasing the local concentration at the crack tip. In this model, fracture occurs because of the enhanced plasticity along one slip plane, inducing the formation of a pile-up and a local decrease of the cohesion energy due to the presence of hydrogen.

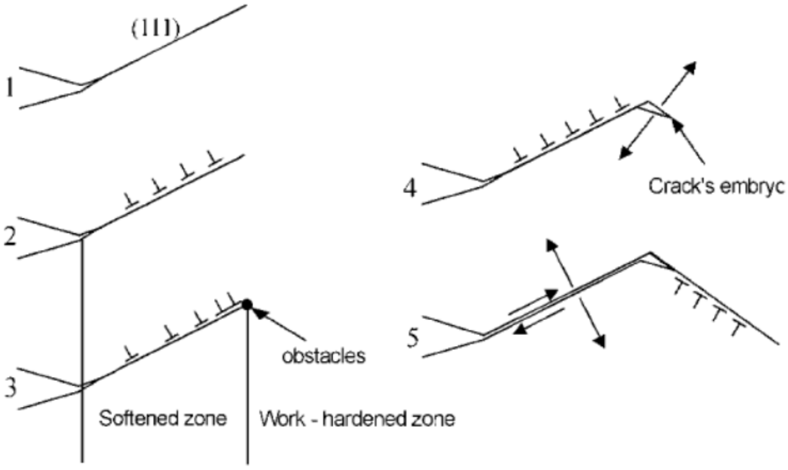

Figure 48 Corrosion enhanced plasticity model [74].

5.3.5.8. Hydrogen Enhance Localized Plasticity (HELP)

Some authors believe that the hydrogen enrichment at the crack tip promotes plastic strains. Beachem [78] suggests that with the presence of hydrogen the emission and the propagation of dislocations take place to relatively low stresses. This plasticity increased ahead of the crack is followed by an extremely localized ductile fracture. More recently, Birnbaum and Sofronis [79] have developed this idea in the Hydrogen Enhanced Localized Plasticity model (HELP). This mechanism, mainly supported by the TEM observations, is based on the modification of dislocations behavior due to hydrogen [80, 81]. The authors believe that hydrogen tends to increase the "mobility" of dislocations.

Sirois and Birnbaum [82] evoqued that hydrogen, reduces the area of dislocation activation in the nickel and nickel-doped carbon and facilitates the movement of dislocations. According to the authors, this effect results from the formation of hydrogen atmospheres around dislocations.

Sofronis simulations [83] of hydrogen-dislocation interactions shows that the contribution of the hydrogen atmosphere on the resolved shear stress present the same singularity 1 / r than the contribution due to dislocations but of an opposite sign and a lower amplitude. Therefore, hydrogen screens elastic interactions between dislocations resulting in a decrease of the applied stress required to move the dislocations. This screening may reduce the repulsive interactions between dislocations that can lead to the increase of dislocation density.

Hydrogen penetration at crack tip tends to increase strain localization. In addition, hydrogen diffusion along shear bands. Propagation then occurs by successive shearing along these shear bands.

6. Related factors affecting fatigue in LWR environment

Over the last 20 years, many laboratory tests were carried out and revealed the deleterious role of the primary water on fatigue life. The followings will give the fundamental knowledge about EAF on each factor.

6.1. Technological factors

6.1.1. Effect of the design of the specimen

In Japan, two types of specimens were mainly used for EAF tests in high temperature water: one is a common solid-type specimen (Figure 49), used for fatigue tests in air. The other one is a hollow cylindrical-type specimen (Figure 50). The solid type specimens are tested in an autoclave connected to a recirculating loop.

The environment circulates inside the specimen: only the inner surface of the specimen is exposed to the water. The outer surface is free for deformation measurement.

Figure 51 shows the good agreement between results obtained with the two different types of samples presented before.

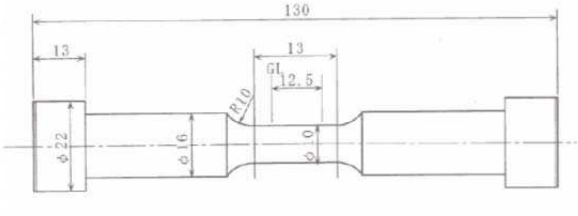

Figure 49 □Solid type specimen, dimension in mm [8].

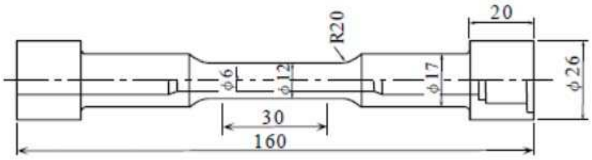

Figure 50 □Hollow cylindrical type specimen, dimension in mm [8].

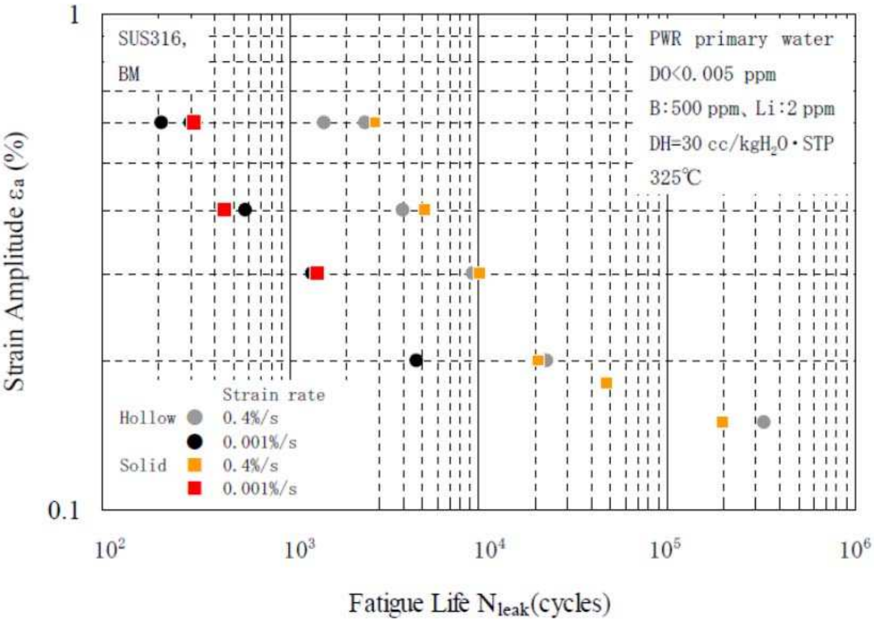

Figure 51 - Effects of specimen geometry on fatigue life of Type 316 SS in PWR water [8].

6.1.2. Effect of the surface finishing

This section is based on NUREG-6909 [1].

Fatigue tests have been conducted on Types 304 and 316NG SS specimens that were intentionally roughened with #50 grid sandpaper, to produce circumferential cracks and an average surface roughness of 1.2 µm. For both steels (Figure 52), the fatigue life of roughened specimens is slightly lower than that of the smooth specimens, in air and in PWR primary water at 289°C. No effect of the roughness was observed on stainless steels exposed to BWR simulating environment. Consequently the effect of the surface finishing was not explicitly introduced in the expression of the Fen; it is actually included in the sub factor for □surface finishing and environment,□which is applied in addition to the Fen.

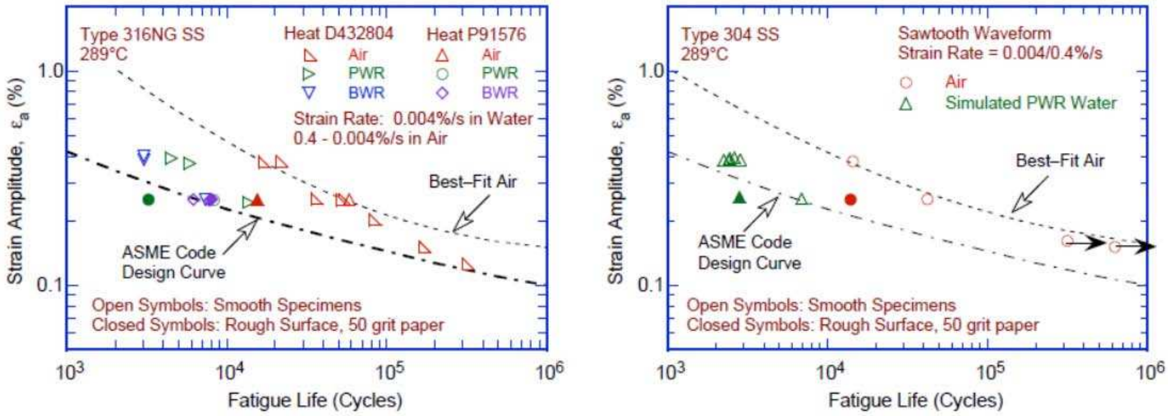

Figure 52 □Effect of surface roughness on fatigue life of 316NG (left) and 304 (right) SS in air and high-purity water [1].

Interesting tests with respect of this effect were also conducted by AREVA NP [84] [85] [86].

Figure 54 compares fatigue lives of polished and ground specimens under triangular loading signals, at a strain rate of 0.01 %/s [86]. A negligible effect of surface finish was noticed for the highest strain amplitude of ± 0.6%. For the lowest strain amplitude of ± 0.3%, the fatigue life was reduced by a factor of 2 when ground samples were tested. While NUREG/CR-6909 recommended to decrease the evaluation of the fatigue life of non-polished austenitic stainless steels by a factor of 2 to 3.5, AREVA NP concluded that these recommended factors are very severe compared to the test results shown in Figure 54.

AREVA NP proposed a more representative S-N mean curve based on test results (Figure 55) obtained in PWR primary environment on ground specimens cyclically loaded using a loading signal (Figure 53) simulating a cold thermal shock. The roughness Rt of the ground specimens was close to 70 μm. AREVA NP indicated that a margin of about 2.5 still remained in Figure 55 between the mean S-N curve and the current ASME and RCC-M design curves.

Figure 53 Typical strain history of cold and hot thermal shocks corresponding to a safety injection transient (SIS) [84].

Figure 56 compares the current ASME and RCCM design curves with the main experimental data obtained by AREVA NP. AREVA NP concluded that both environmental and surface finish effects are covered by the design curves, with sufficient margins: material variability of ~2.5 and scale effects of 1.1 for ground surface or 1.3 for polished specimens.

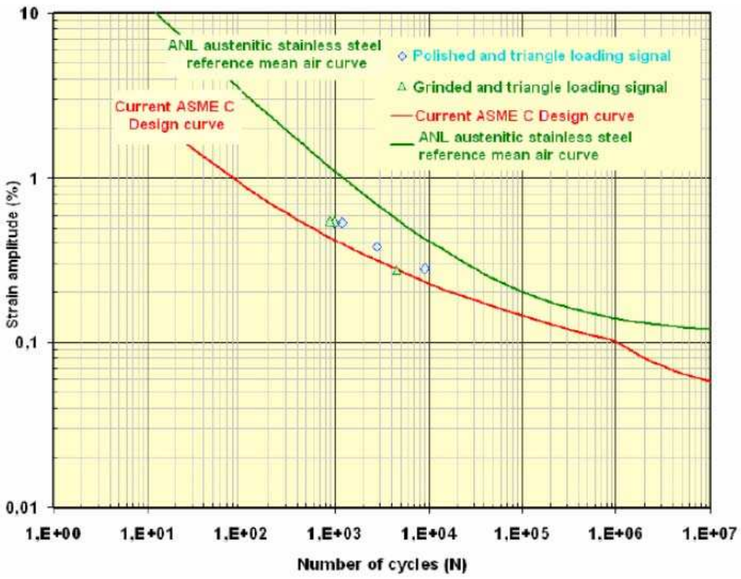

Figure 54 Comparison of LCF test results obtained on polished and ground specimens in PWR environment. (Triangle loading signals with ε'= 0.01 %/s) [86].

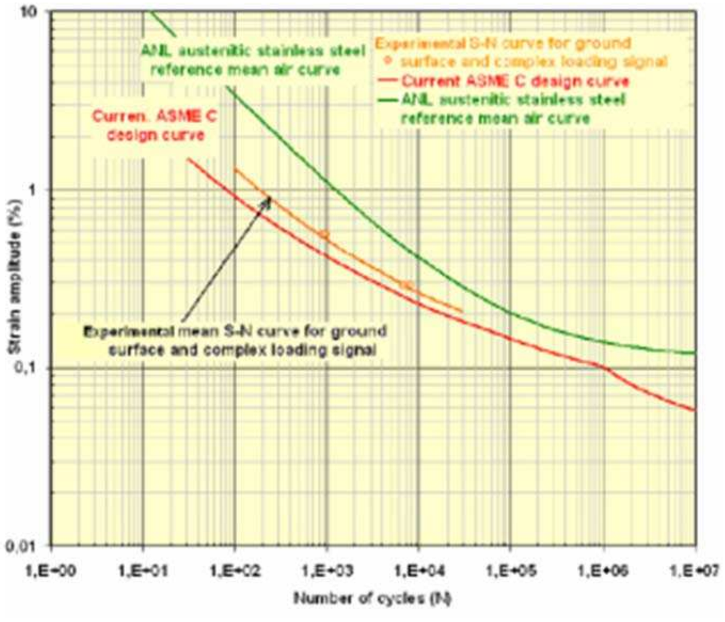

Figure 55 - Experimental mean S-N curve obtained in PWR environment for ground specimens (Rt ~70 µm) cyclically loaded with representative complex loading signals [86].

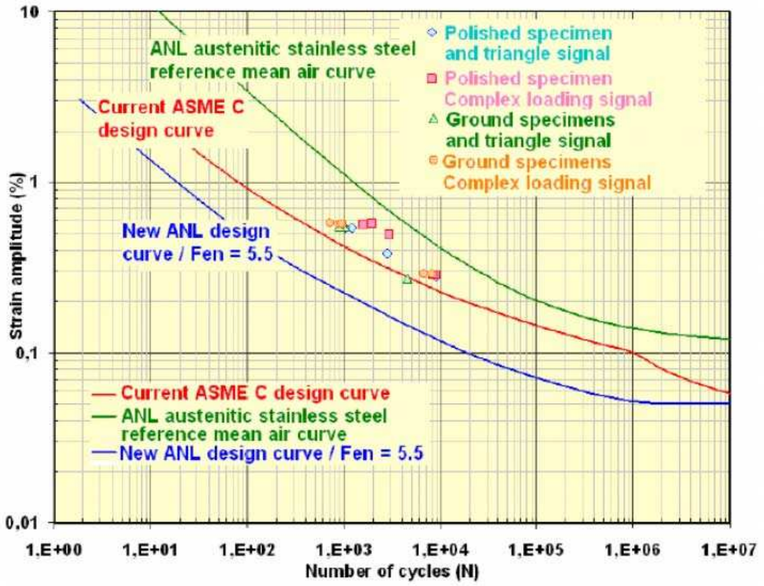

Figure 56 - Comparison of LCF test results obtained in PWR environment with mean and design S-N curves [86].

6.2. Material factors

6.2.1. Effect of material parameters

Fatigue lives at 325°C in simulated PWR primary water are plotted in Figure 57 as a function of the strain amplitude and strain rate for type 316 and 304 austenitic stainless steel base and weld metals [8]. At high strain rate, fatigue lives of weld metals are equivalent to or slightly longer than those of base metals. Whereas, at low strain rate, weld metals exhibited a better resistance to environmentally assisted fatigue compared with base metals, especially with 304 weld metals.

In Figure 58, the Fen dependency to strain rate is shown for different materials: trends are summarized as follow:

□Type 316 (PWR): Fen = 2.18 (Δε/dt) -0.315
□Type 304 (PWR): Fen = 3.02 (Δε/dt) -0.286
□SS Weld Metal (PWR): Fen = 2.25 (Δε/dt) -0.223
□Cast SS (PWR): Fen = 1.95 (Δε/dt) -0.397
□All data (PWR): Fen＝2.50 (Δε/dt) -0.257

The lowest Fen is observed for the weld metal while the largest Fen is noticed for 304 stainless steel base metal. However, the current regulations do not take into account such difference and the mean Fen shown with the solid line in Figure 58 is considered as the representative line for austenitic stainless steels in PWR water.

The material effect on fatigue life is definitely lower than the strain amplitude and strain rate effects in the LCF region. In the HCF region, results indicate that the fatigue limit of a weld metal is higher than a base metal. It should be noted that mechanical properties of stainless steel weld metals are completely different from base metals (Table 1).

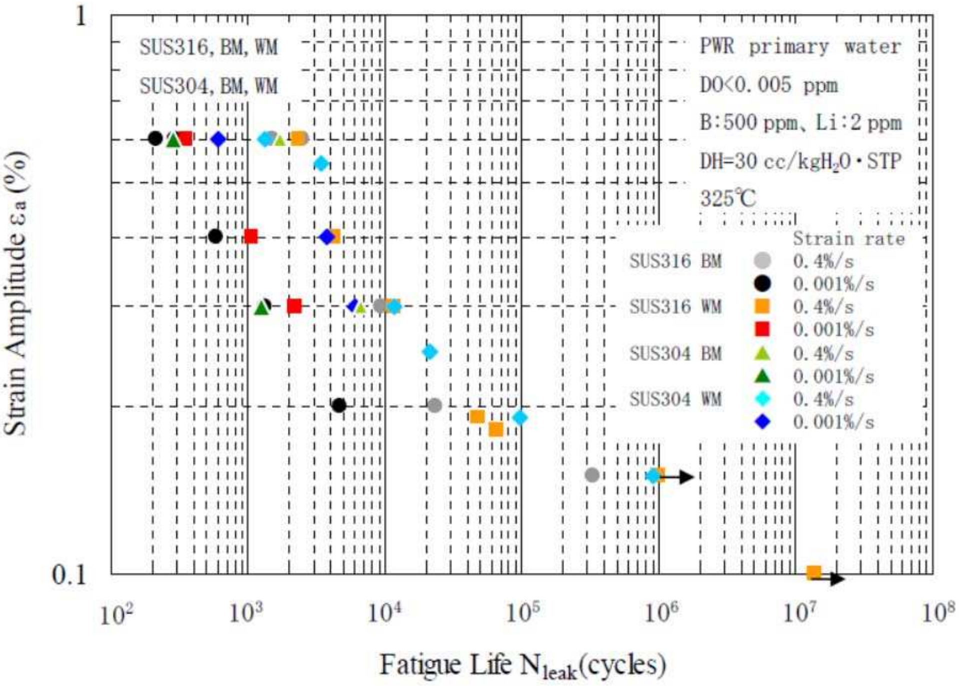

Figure 57 □Effect of materials on fatigue life for austenitic stainless steels in PWR water [8].

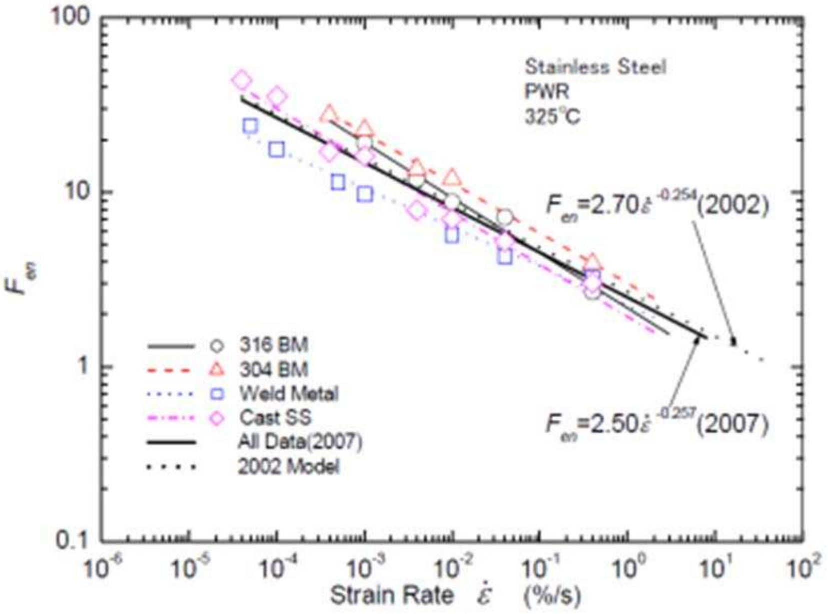

Figure 58 □Relation of strain rate to Fen for austenitic stainless steels in PWR water (average value) [11].

Table 1 □Mechanical properties of various base and weld stainless steels (WM: weld metal) [100,39]

	Ys (MPa)	UTS (MPa)
316 MHI	150	465
316WM D3P1 MHI	400	465
316WM G3P1 MHI	340	520
304 D4A1 MHI	160	450
304 D4B1 MHI	130	430
304WM MHI	237	367
316W MJNES	385	422
304 JNES	164	476
304WM JNES	324	417
304 XY182	138	401
316 forged	170	476

6.2.2. Effect of the sensitization of materials

Figure 59 shows the relation between Fen and strain rate for type annealed (2) and sensitized (3) 304 base metal in BWR water. The goal of the sensitization is to introduce a Cr depletion at grain boundaries. As seen in Figure 59, Fen for sensitized material is slightly higher than that of solution treated material, especially at low strain rate. However, because

---

(2) heat treatment at 1100ºC then water quenching.

(3) 100 min at 750ºC, then furnace cooling, then 1700 h at 400ºC then air-cooling.

even data for the sensitized material are present close to a trend line for solution 304SS given with the dot line, the sensitization has not been considered as harmful factor on *F*en in BWR water [87].

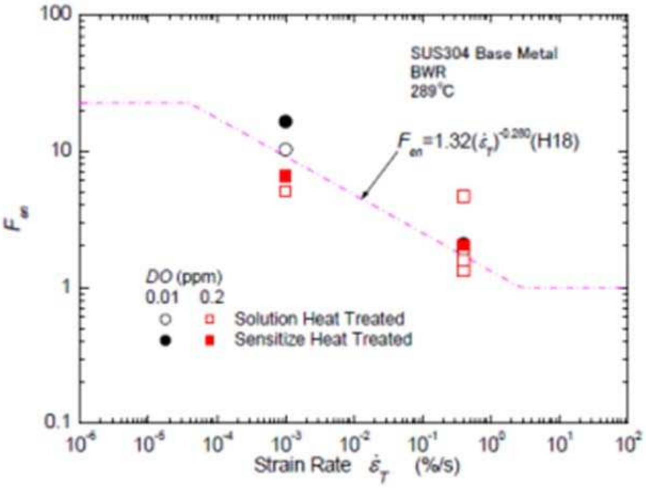

Figure 59 - Effect of sensitization on the relation of Fen to strain rate for SS in BWR environment [87].

6.2.3. Effect of pre hardening

The effect of a pre hardening on fatigue life in air and in LWR environment is not yet clear and not present in current codifications. Field experience degradations related to SCC reveals that a pre hardening increases the SCC susceptibly of components made of austenitic stainless steels or Alloy 600 Ni base alloy (Figure 60, Figure 61) [88].

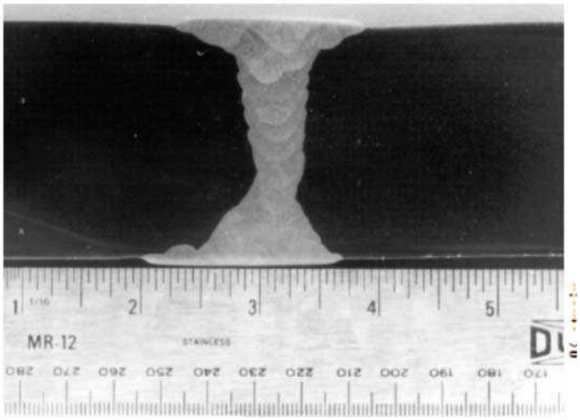

Figure 60 - BWR weld core shroud [88].

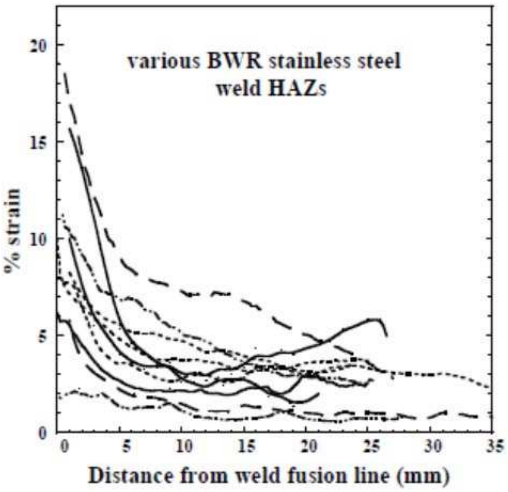

Figure 61 - Evolution of residual strains in various HAZ of SS welds in BWR environment [88].

It is well known that in LWR environment pre hardening has a deleterious effect on SCC [89]. A pre hardening significantly reduces the time to SCC crack initiation. Indeed, in BWR environment Kuniya [90] performed slow strain rate tests using various level of cold rolled 304 stainless steel. An increase of SCC crack length was observed while the non-hardened material was insensitive to SCC (Figure 9).

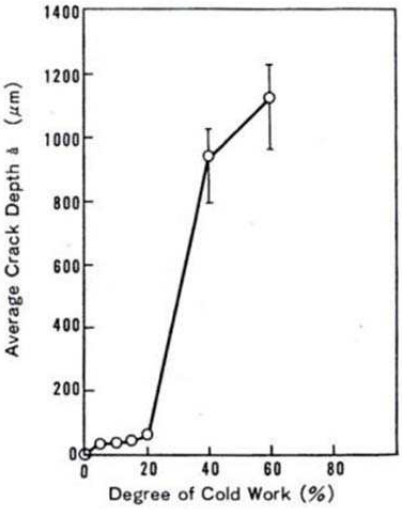

Figure 62 - Evolution of crack length as a function of the degree of cold work of a 304 SS in BWR environment [90].

Whether the material is sensitized or not, a prior strain hardening increases crack growth rates obtained in a purely static loading (Figure 63) [91] or slightly cyclic loading (Figure 64) [92]. For very high levels of strain hardening (Ys > 700 MPa), the crack growth rate seems to be an increasing function of the yield strength (Figure 11). Same tendency can be found in PWR environment [93].

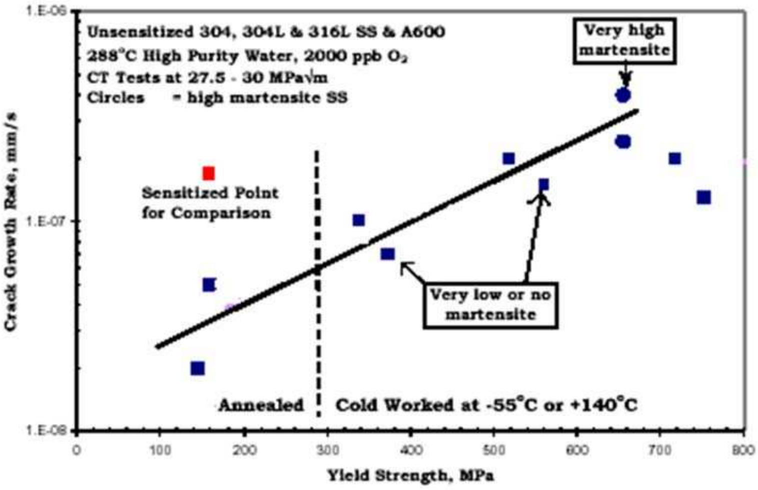

Figure 63 - Influence of Ys on CRG, constant load, K = 30MPa√m, R=0 [91].

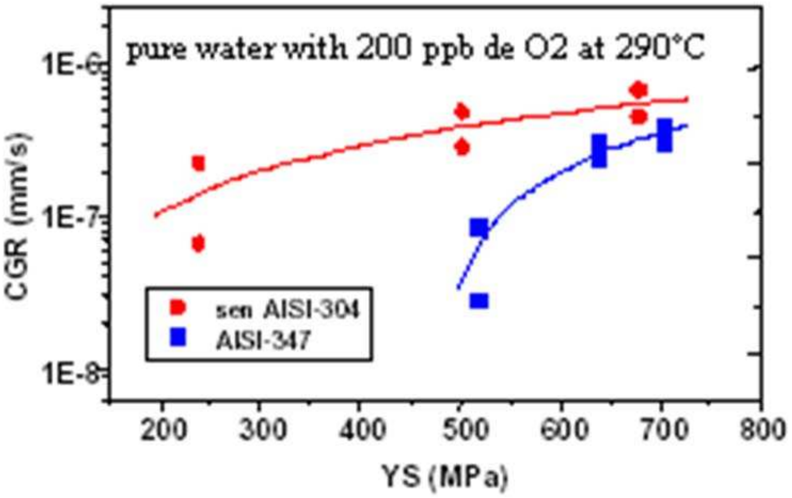

Figure 64 - Influence of Ys on crack growth rate (trapezoidal signal, K_{max} = 35MPa√m, R = 0.7, Tm = 2.5 h) [92].

Under cyclic loading, the austenitic stainless steels may keep the memory of a pre-hardening on their elastic plastic behavior which is observed through the dependence of the cyclic mechanical response on pre-hardening [94]. In case of a 304L SS tested at room temperature, a monotonic pre hardening (16% tension) and a cyclic pre hardening (10 cycles, at a strain amplitude of 1.9%) may reduce fatigue life in strain-controlled test (Figure 65) and increase it in stress-controlled test (Figure 66).

A possible explanation in air environment is given by Taheri [94]. His conclusion was that the formation of a hard structure may create an important internal stress which creates barriers to dislocation movement. Under stress-controlled, as the applied stress is the same before and after pre-hardening, this internal stress greatly reduces mean free path of dislocations. So, under stress-controlled, the increase of lifetime may be attributed to a difficulty in forming softening structures as veins, spaced out walls and PSBs. While in strain control after pre-hardening the same deformation has to be obtained under higher internal stress which needs more total energy compared to the non pre-hardened case, which therefore creates more damage.

Taheri also mentioned that a monotonic pre hardening results in a decrease of fatigue limit. However the test protocol did not mention any polishing after pre-deformation in tension. The surface roughness of the sample pre tensioned is then completely different from an as-received sample. A difference of surface roughness is critical for fatigue life in the high cycle region [95].

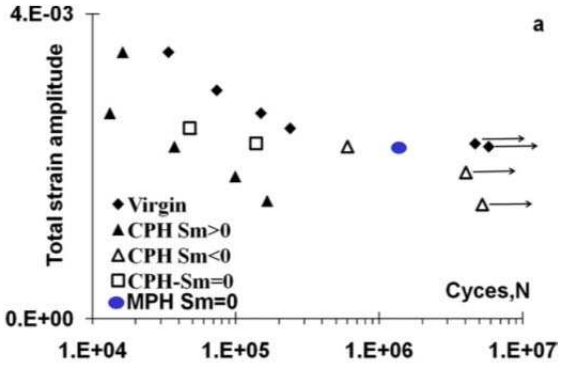

Figure 65 - Effect of pre hardening on the fatigue life 304L SS for strain control tests, detrimental effect on fatigue life [94].

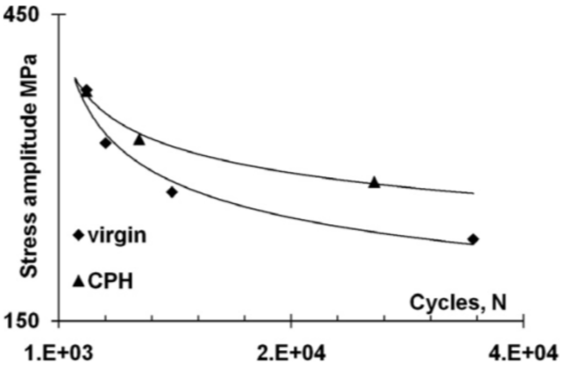

Figure 66 - Effect of pre hardening on the fatigue life 304L SS for stress control tests, beneficial effect on fatigue life [94].

6.3. Influence of loading parameters

6.3.1. Effect of strain amplitude

Figure 67 show basic S-N data observed in air and in simulated PWR primary water at 325°C [100] , involving several kinds of material and two levels of strain rate. The fatigue life increased with lowering strain amplitude in all materials and at all strain rates, as shown by data obtained in air.

The same type of initiation test was carried out on a 304L material (heat XY182) under constant strain rate (Figure 68) [96]. Clear strain amplitude and environmental effects on fatigue life can be distinguished. These results are in good agreement with data shown in Figure 67 and revealed the presence of a strain amplitude threshold below which it is assumed that, the environment has no effect on fatigue life.

However these conclusions suffer from a lack of data especially at strain rates below 0.4%/s. Several authors mentioned that [97] [98] fatigue life as well as fatigue limit in the HCF region highly depends on the environment (Figure 69 to Figure 71). It seems interesting to provide such data in PWR primary water at a frequency compatible with corrosion kinetics i.e. below 0.4%/s. Another aspect presented in Figure 67 is that both fatigue life and fatigue limit in case of weld metal are different from those obtained in case of base metal.

In PWR primary environment, the codifications include a total strain threshold of about 0.11% below which PWR primary environment has no effect on fatigue life, i.e., $F_{en} = 1$.

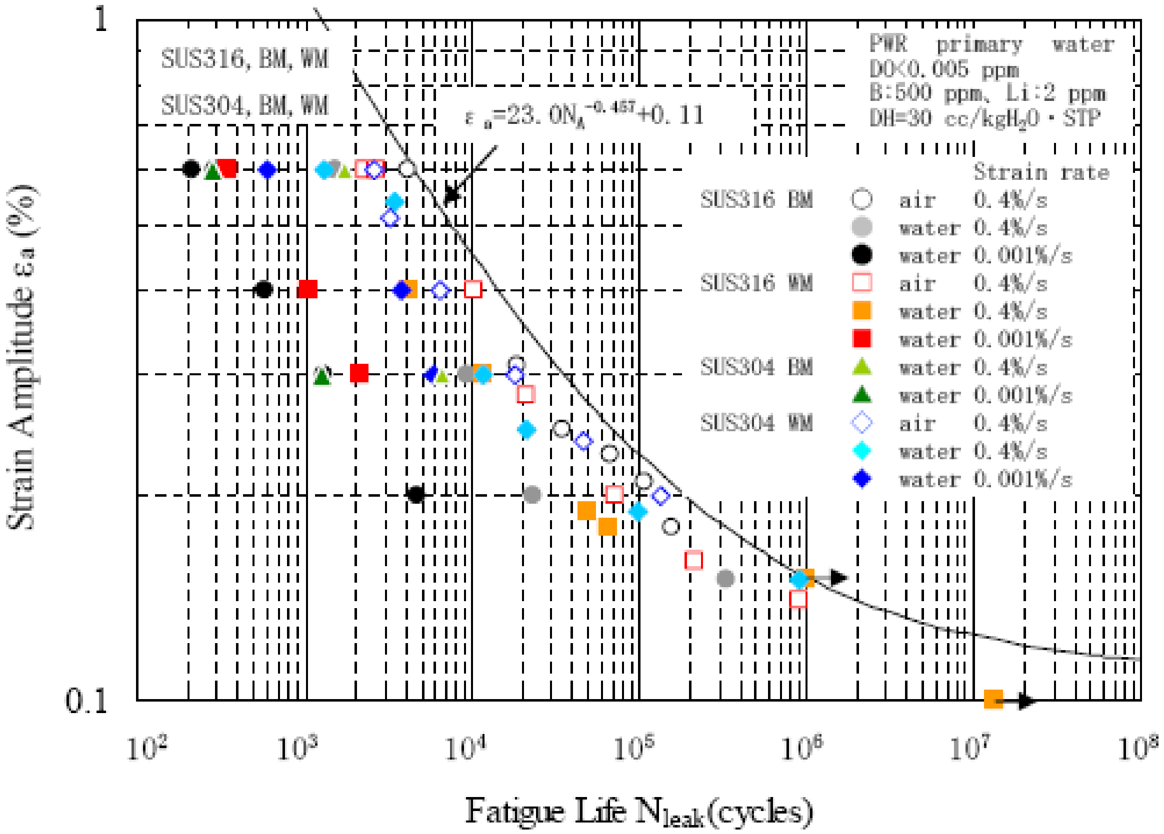

Figure 67 PWR primary environmental effect on fatigue life at 325°C [100].

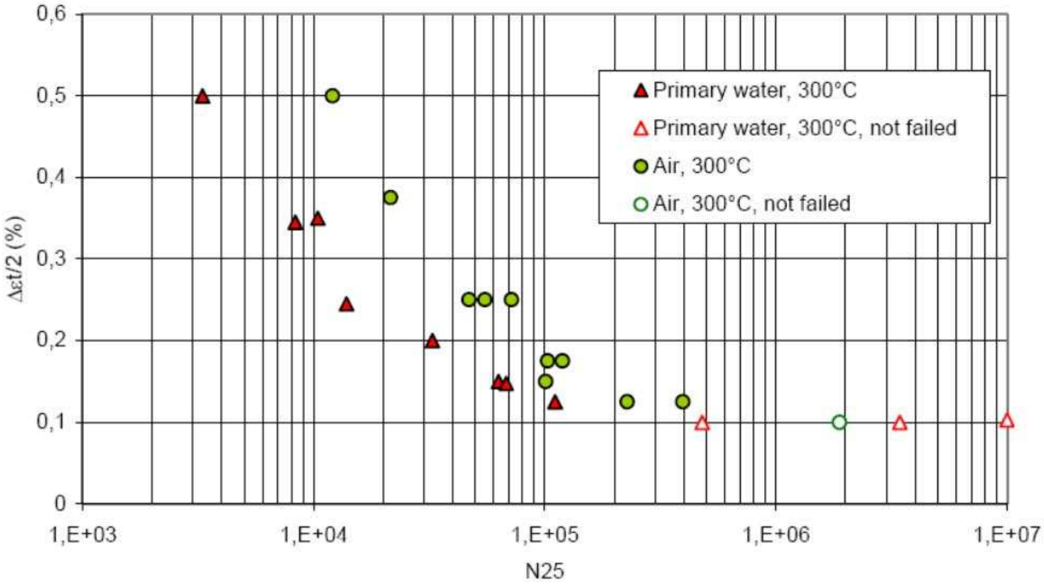

68 - Environmental effect (1000 ppm B, 2 ppm Li, 25-35 cm3.kg-1 $\Delta\varepsilon_t/dt$=0.4%/s R=-1) on fatigue life at 300°C [96].

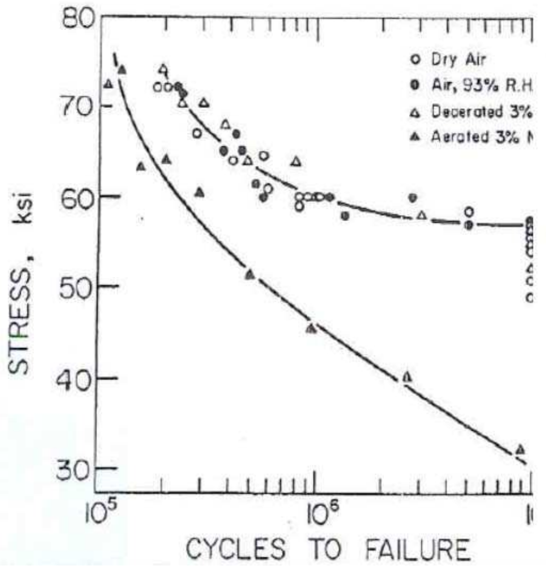

Figure 69 - Low yield strain carbon steel (HRC=20) in various environments [98].

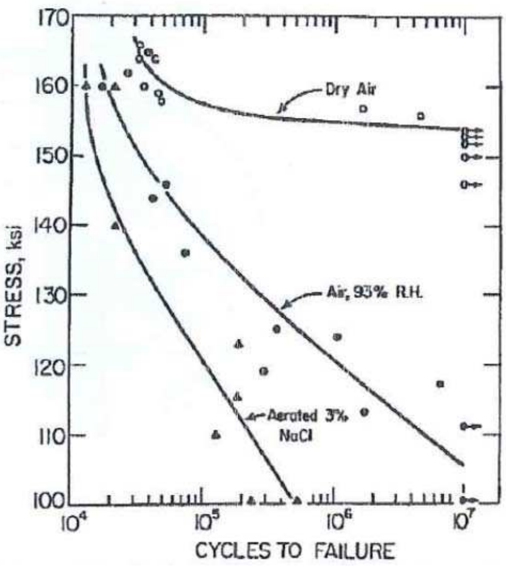

Figure 70 - High yield strain carbon steel (HRC=52) in various environments [98].

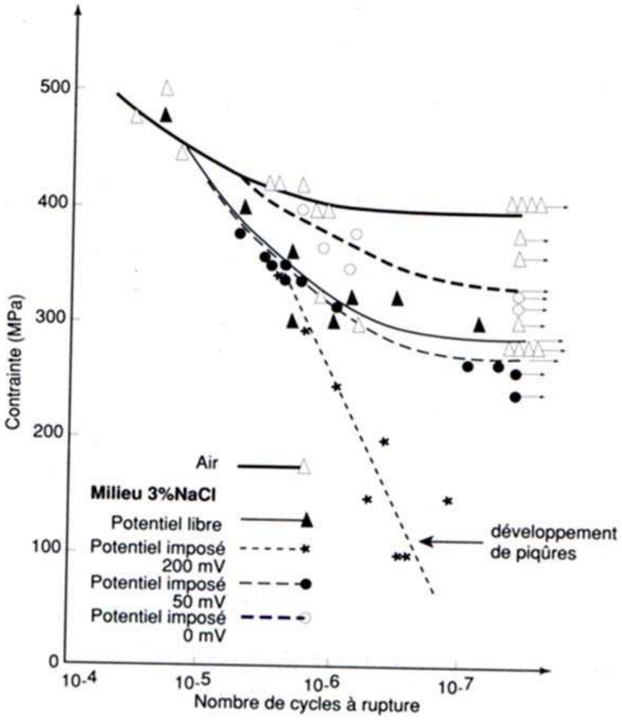

Figure 71 □Environmental effect on fatigue of Z2 CNDU 21-07 in NaCl environment and in air [97].

6.3.2. Effect of strain rate

As shown in Figure 67, the tension strain rate is one of the most deleterious factors that can affect fatigue life. Figure 72 and Figure 73 show respectively the Fen in PWR environment and the fatigue life in PWR environment of 304L and 316 stainless steels, as a function of strain rate. Fatigue life decreases almost linearly with decreasing strain rate in a log-log diagram. The authors suggested the “saturation” of the environmental effect in very slow strain rate region. DeBaglion confirm the presence of a saturation strain rate [99]. The saturating strain rate was found to be induced by the saturation of the micro crack propagation kinetics between the different strain rate conditions ($\Delta\varepsilon_t/dt=0.01\%/s$ and $0.001\%/s$ at $\Delta\varepsilon_t/2=0.6\%$). However, additional data would be required to confirm such assumed transition in PWR primary water (due to the current huge data scatter), especially because under BWR condition (Figure 74), such a transition was not clearly observed.

Another possible origin of this saturation could be the combination of EAF and SCC effects. Indeed, in PWR primary environment, most of the cracks observed were transgranular (TG), whereas in BWR condition a transition in crack morphology that evolves from TG cracks at high strain rate to a mixed mode TG/IG at lower strain rate is observed.

Some additional tests were carried out to better understand the effect of strain rate in compression [8]. In Figure 75, ε_T and ε_c indicate the strain rate in tension and the strain rate in compression respectively. Data obtained at slow strain rate in compression (solid marks) are very close to those collected at fast strain rate in compression (open symbols). Consequently, most of the following tests were performed for a strain rate in compression fixed at 0.4 %/s in order to shorten test durations. Considering that strain rate in compression has only a negligible effect on fatigue life. Some other tests have been conducted [8] to understand which part in a given loading signal has a deleterious effect on the fatigue life of a 316SS in PWR primary water (Figure 76 and Figure 77).

Results indicate that below a strain amplitude threshold between -0.3% and -0.4% strain rate has no effect on fatigue life. After this transition point, fatigue life increases with an increasing knee point (Figure 76 and Figure 77). In other words, after the -0.3% -0.4% threshold, the lower is the strain rate the lower is fatigue life. No mechanistic explanation was given by the authors. However, considering the results of Magnin reported in Figure 37 and Figure 38 and results obtained by Le Roux [39] (Figure 77), it seems that in loading domain higher than the -0.3% to -0.4% transition, stresses are positives. The fact that stresses are positive may correspond with an increase of current density which promotes dissolution.

For a given loading signal, it is then possible to identify in which portion the strain rate has a deleterious effect on fatigue life (Figure 78). However, Magnin [50] evoked that vacancy generation at crack tip due to localized dissolution can induce cyclic softening effects and that hydrogen absorption can also be enhanced by the local plasticity. Therefore, other model such as presented in section 5.3 may be taken into account.

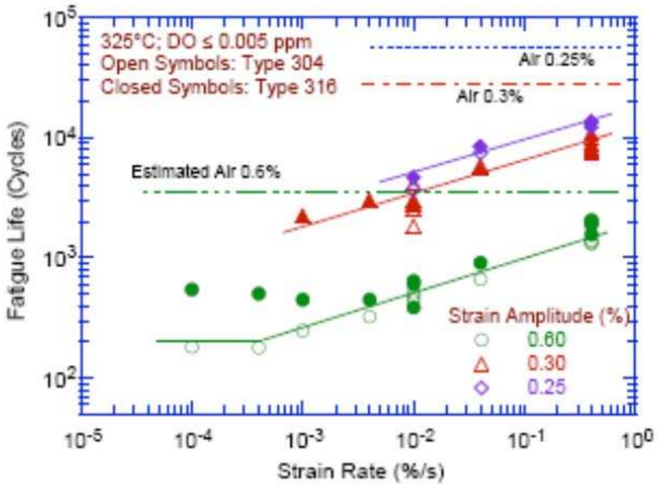

Figure 72 □**Effect of strain rate in fatigue life of stainless steels in PWR primary environment focusing on saturation (R=-1) [1].**

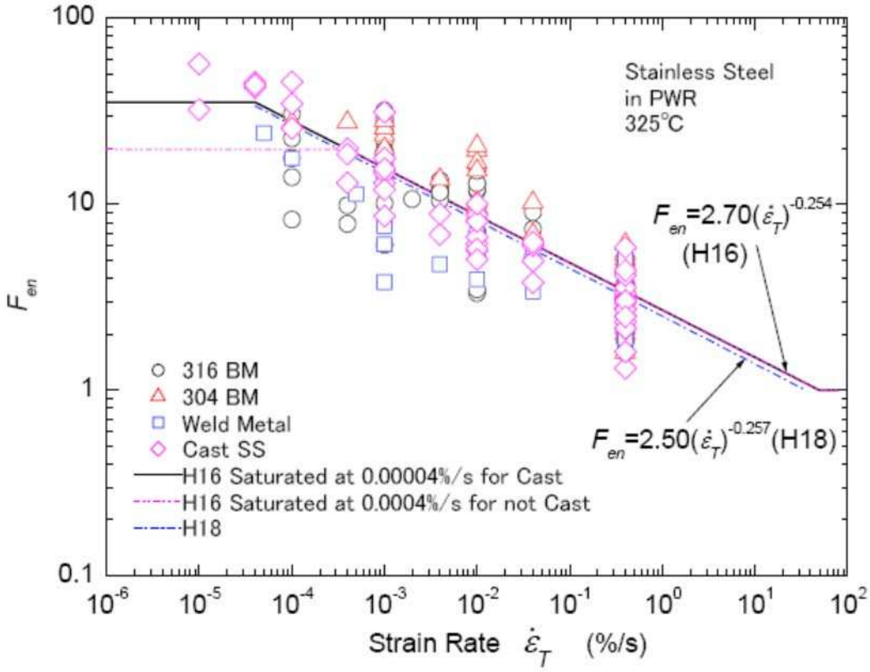

Figure 73 □Effect of strain rate in Fen of stainless steels in PWR primary environment ($\Delta\varepsilon_t/2$= 0.2-0.6 *R*=-1) [100].

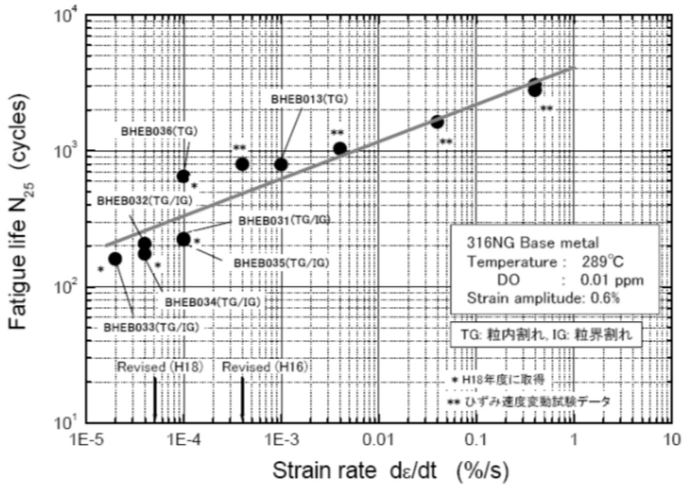

Figure 74 Effect of strain rate in fatigue life of stainless steels in BWR conditions(*R*=-1) [100].

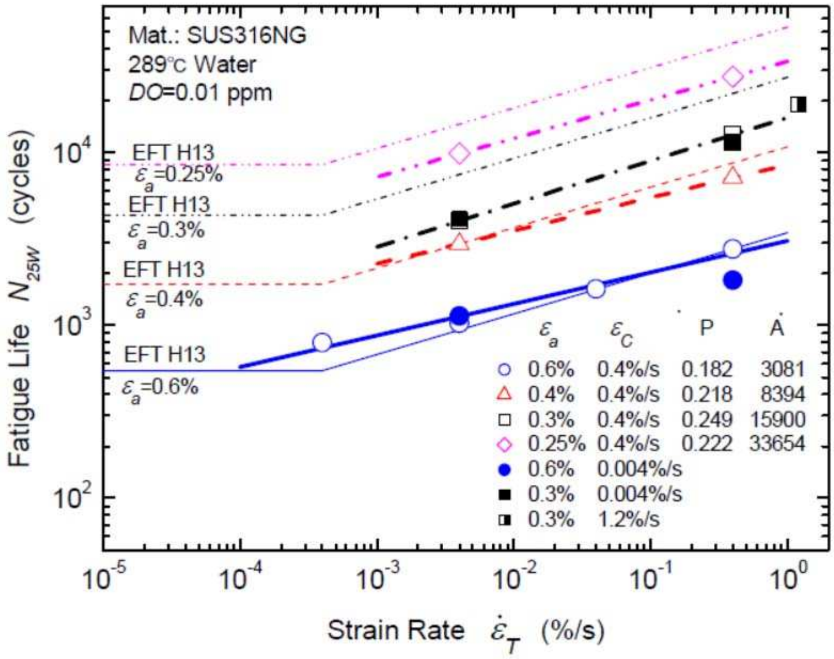

Figure 75 Effect of strain rate in compression on fatigue life of stainless steels in BWR conditions [8].

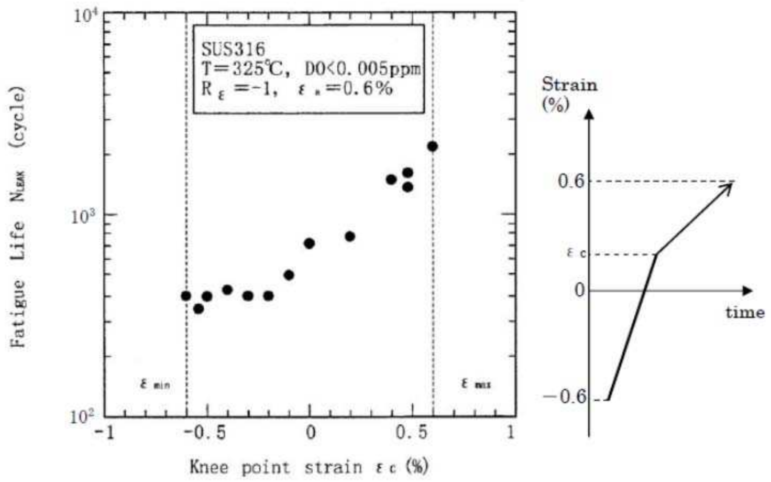

Figure 76 □Knee point strain effect on fatigue life [100].

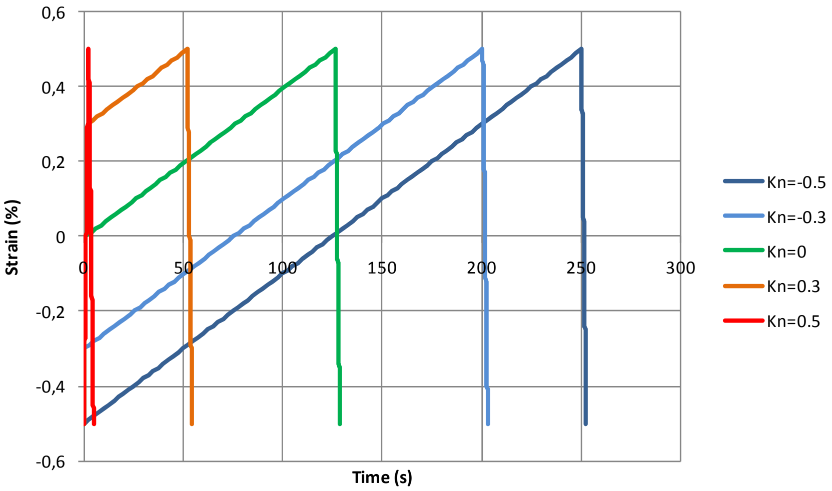

Figure 77 □Knee point signals [100].

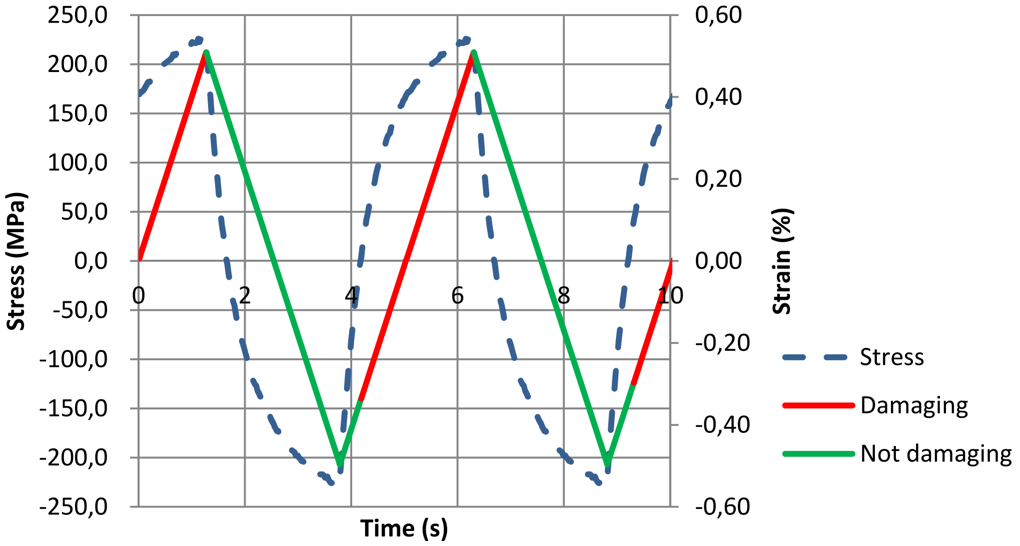

Figure 78 □Damaging areas where strain rate has an effect

Last, slow strain rate tensile tests (SSRTs) were performed by Totsuka [101] on pre strained 304 and 316 stainless steels in the range of strain rate 10^{-5} s^{-1} - 10^{-7} s^{-1}. As shown in Figure 79, in the case of 316 stainless steel, a decreasing strain rate resulted in a transition of stress corrosion cracking morphology from transgranular to intergranular. The strain rate of 10^{-7} s^{-1} promoting the intergranular stress corrosion cracking is in good agreement with the strain rate promoting intergranular EAF observed in Figure 74.

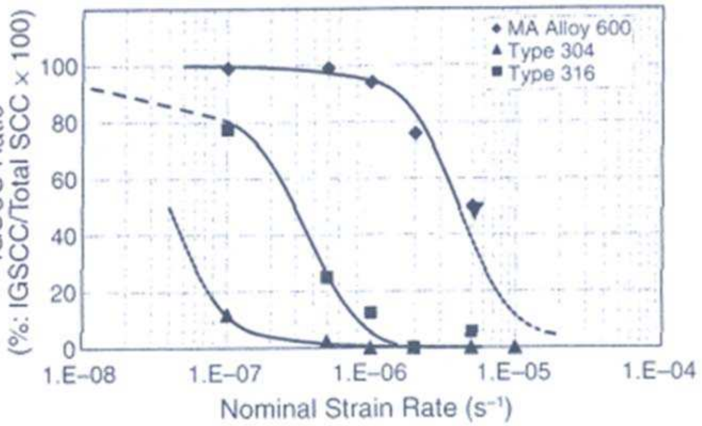

Figure 79 **- Evolution of intergranular stress corrosion cracking on austenitic alloy as a function of the applied strain rate SSRT in PWR primary environment at 360°C** [101].

6.3.3. Effect of the holding time

6.3.3.1. Effect of the strain holding at peak strain

This effect has been mainly investigated by Higuchi et al. [87]. These authors carried out trapezoidal waveform fatigue tests (see (*5) in Figure 80) in which strain was held at the peak tension of straining for type 316NG stainless steel, in order to study the effects of strain holding on fatigue life in simulated BWR and PWR primary environments [87]. The stress decrease during strain holding was less than 15%.

The test results in BWR water shown in Figure 81 examine the relation between logarithmic holding time and logarithmic fatigue life. The fatigue life reduction induced by strain holding up to 600 seconds was not observed at a strain rate faster than 0.04%/s at relatively large strain amplitude (0.6%), whereas there is a remarkable effect at a strain rate slower or equal to 0.004%/s.

Higuchi also performed the similar trapezoidal waveform strain holding fatigue tests for type 316 stainless steel in simulated PWR primary water. The test results are shown in

Figure 82. In the tested holding time range, no remarkable fatigue life reduction by strain holding was observed.

6.3.3.2. Effects of strain holding at sub-peak strain

In the previous section, it was shown that fatigue life reduces with strain holding in simulated BWR water. This reduction is not negligible and the effect of strain holding should be considered for evaluating environmental fatigue in power plant components. Based on this finding, Higuchi et al. conducted further tests [87].

In the sub-peak hold fatigue test (in simulated BWR water), the strain was held at the point reduced from the peak strain as shown in Figure 80 (*6). The strain was held at the value of 0.03% or 0.06% reduced from the peak strain. The holding time was of 600 seconds and two specimens were tested for each material. Test results are plotted in Figure 81 by half-solid symbol (peak strain - 0.03%) and solid symbol (peak strain - 0.06%) along with test data obtained from peak strain holding test mentioned above, revealing that the fatigue life reduction by strain holding disappears in sub-peak hold fatigue tests. The holding stress of peak strain 0.06% roughly corresponds to the yield stress of each material.

Based on the results of the peak strain hold and sub-peak strain hold fatigue tests, Higuchi et al. concluded that the effects of strain holding on fatigue life can be neglected under normal thermal transients but should be considered for transients in which the elastic follow-up stress such as internal pressure is held at the peak for a long period [87].

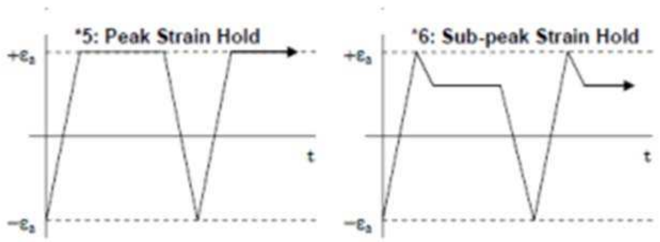

Figure 80 □Environmental fatigue test conditions [87].

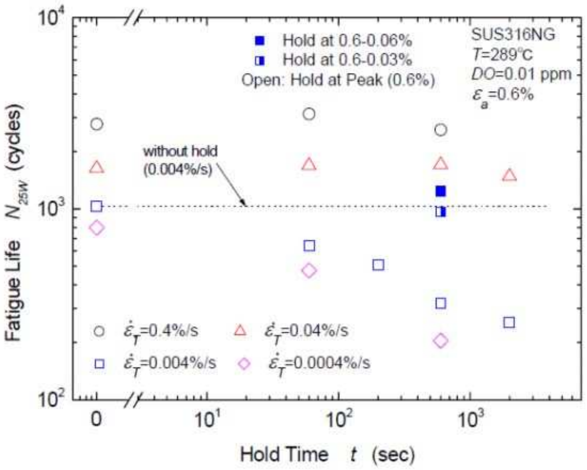

Figure 81 Correlation between Fen and holding time for SS in BWR environment [87].

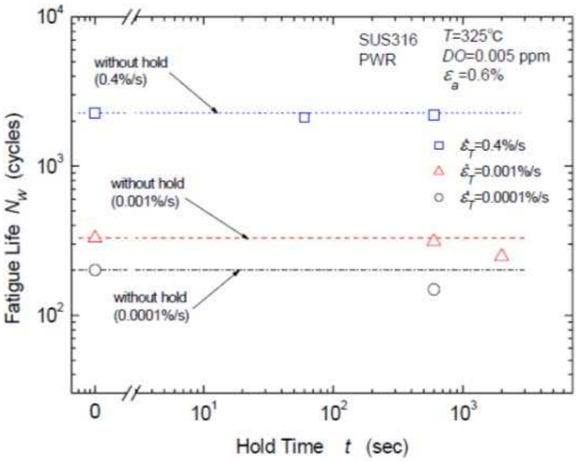

Figure 82 Correlation between Fen and holding time for SS in PWR environment [87].

6.4. Environmental factors

6.4.1. Effect of temperature

Figure 83 and Figure 84 represent the change in fatigue lives of austenitic stainless steels with temperature, for two strain amplitudes $\Delta\varepsilon_t/2$ = 0.3% and 0.6% [1]. At a high strain rate of 0.4%/s, we cannot see a clear temperature effect at both strain amplitudes, while at a low strain rate (0.01%/s) a significant decrease of fatigue life is observed when the temperature increases. Figure 85 shows the increasing dependency of the Fen to the increasing temperature at a strain rate of 0.001%/s [100].

These results are in good agreement with those obtained [96] on 304L (heat XY182) at 150°C and 360°C, for $0.1 < \Delta\varepsilon_p / 2\ (\%) < 0.6$ (Figure 86).

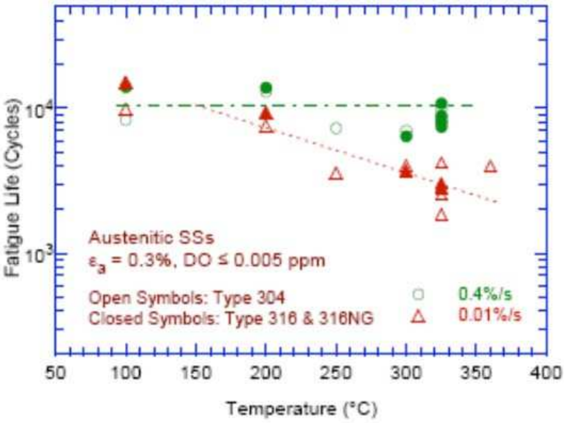

Figure 83 - Change in fatigue lives of austenitic stainless steels in PWR primary environment, $\Delta\varepsilon_t/2$= 0.3% [1].

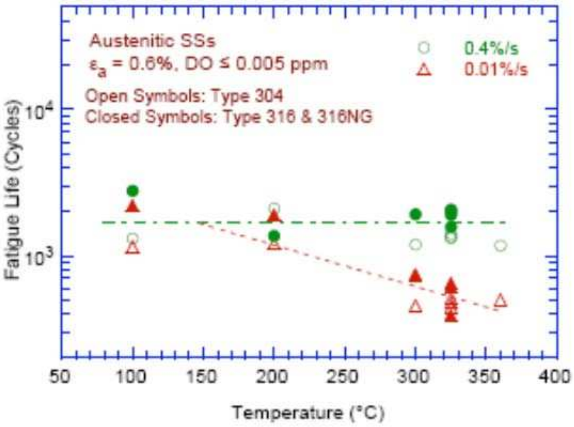

Figure 84 - Change in fatigue lives of austenitic stainless steels in PWR primary environment $\Delta\varepsilon_t/2$=0.6% [1].

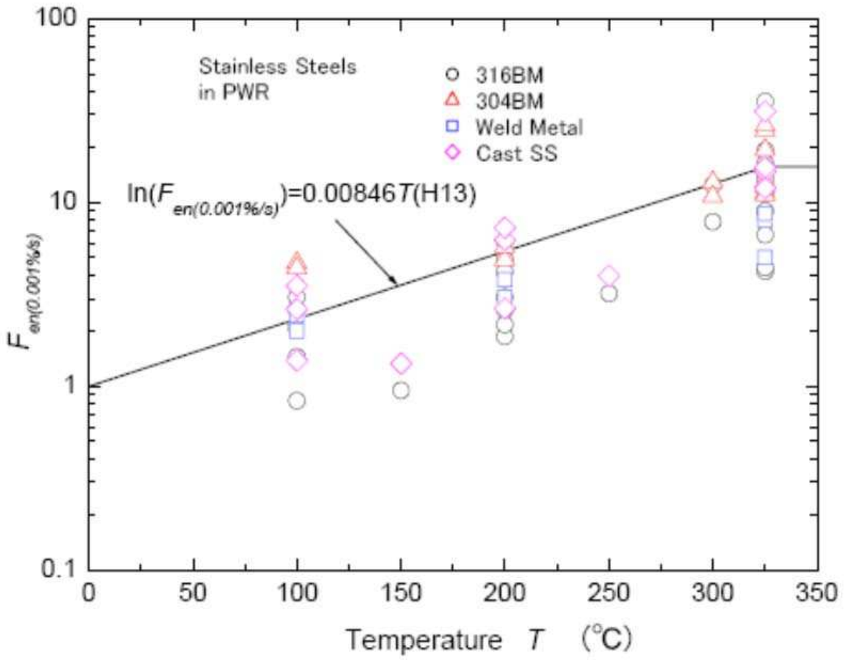

Figure 85 □Evaluation of the temperature effect on fatigue life of austenitic stainless steels in PWR primary environment. ($\Delta\varepsilon_t/2$=0.2% □0.6%, $\dot{\varepsilon}$ =0.001%/s) [100].

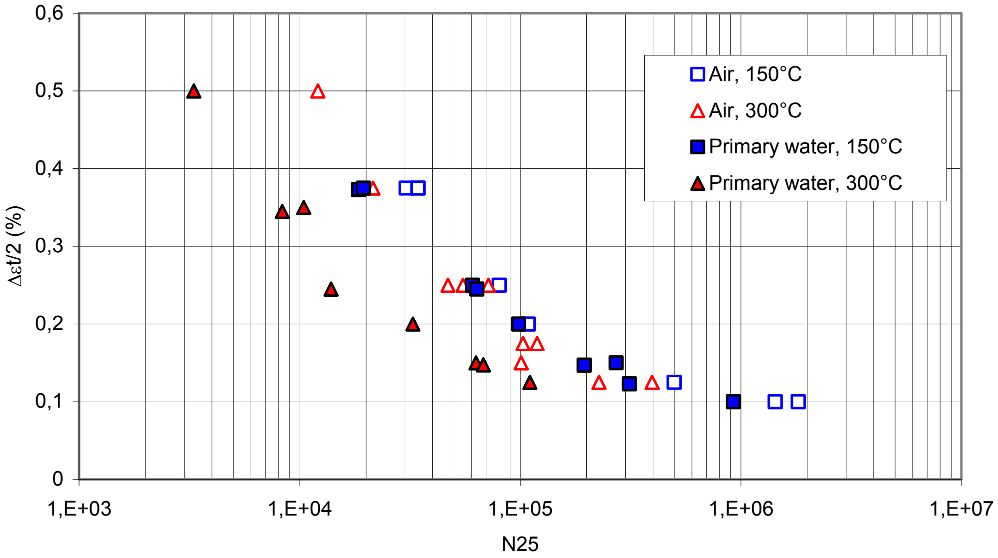

Figure 86 □Temperature effect in air and in primary water (1000ppm B, 2ppm Li, 25-35 $cm^3.kg^{-1}$) on fatigue life ($\dot{\varepsilon}$ = 0.4%/s, *R* = -1) [102].

6.4.2. Effect of dissolved oxygen content

In boiling water reactors (BWRs), radiolysis raises dissolved oxygen (DO) concentration up to 200 ppb and so the electrochemical potential up to +200mV (Figure 88). In light water reactor (LWR), the electrochemical potential controls the kinetics of corrosion reactions. Therefore, the increase in DO and ECP is accompanied with an increase of stress corrosion cracking growth rate (Figure 89).

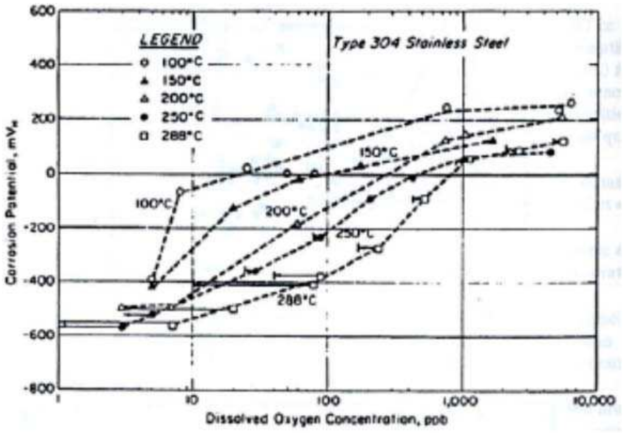

Figure 87 - Effect of dissolved oxygen content on electrochemical potential in BWR [103].

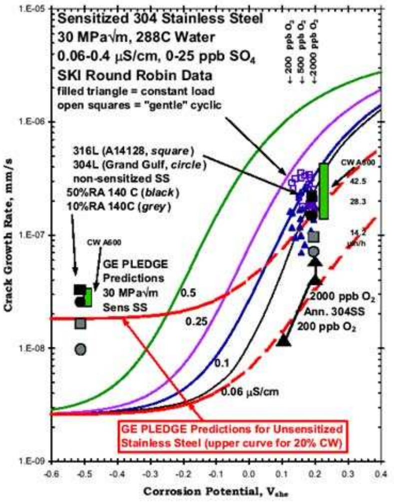

Figure 88 - Electrochemical potential effect on SCC crack growth rate in BWR primary environment [104].

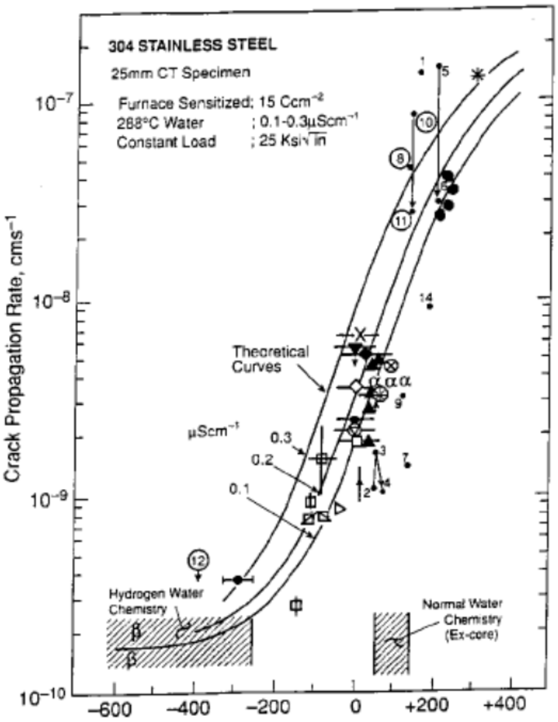

Figure 89 - Electrochemical corrosion potential effect on SCC crack growth rate in BWR environment [105].

In BWR environment (pure water), some results indicate that an increasing *DO* content decreases the F$_{en}$ (and increases the fatigue life) for austenitic stainless steels (Figure

90 and Figure 91) [100]. By contrast, results presented in Figure 92 indicate that the Fen (and associated fatigue lives) of austenitic stainless steel 304 does not depend on dissolved oxygen (DO) in PWR primary water within the range of 5 ppb □8 ppm. One possible explanation should be the favorable repassivation kinetics under high DO and cyclic loading resulting in a reduction of the sensitivity to cracking.

Consequently, in PWR primary environment, the effect of DO content on the fatigue life of austenitic SSs is explicitly considered in *Fen* equation (Equation 1, Equation 3) as a constant. However, the Fen dependency to DO suffers a lack of data between 5 ppb and 8 ppm of DO. In addition, a large discrepancy affects the current data set: further tests for intermediate DO and different strain rates (depassivation kinetics) would be necessary to clarify the effect of DO in PWR environment.

Based on previous studies on the effect of DO content on SCC growth rate (Figure 88), the DO content is supposed to have an influence on corrosion fatigue underlying mechanisms.

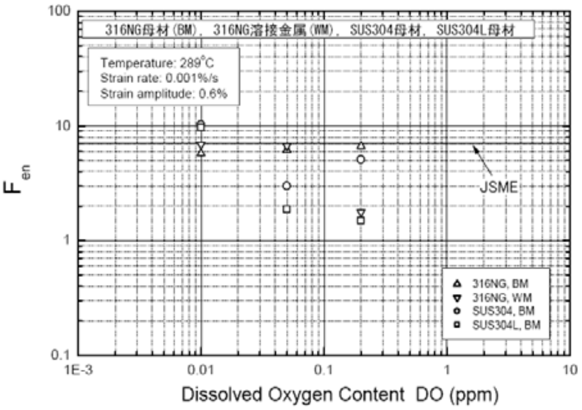

Figure 90 - Effect of dissolved oxygen on fatigue life in BWR environment [100].

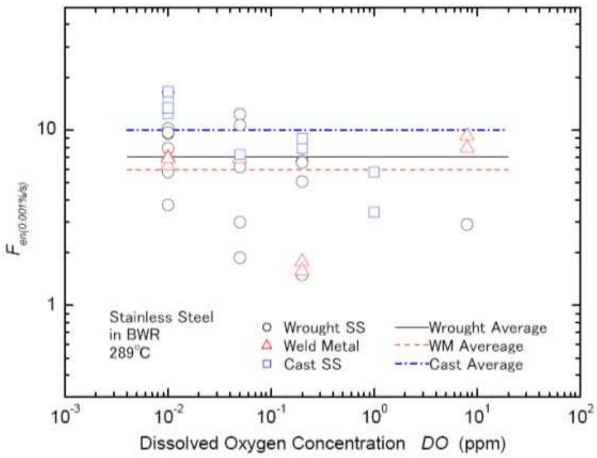

Figure 91 - Effect of dissolved oxygen on fatigue life in BWR environment [100].

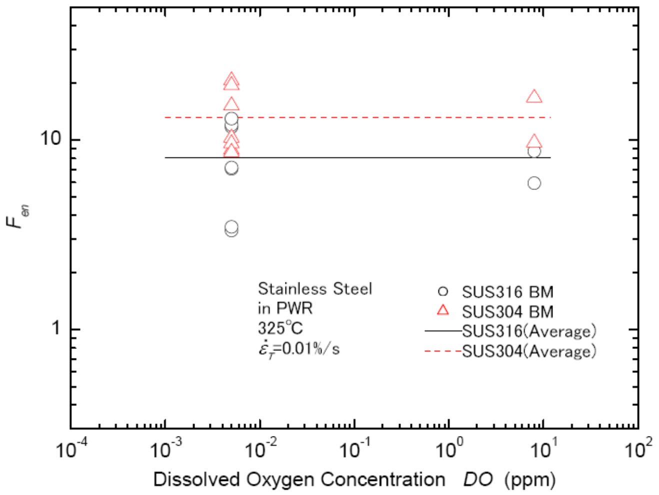

Figure 92 - Effect of dissolved oxygen concentration on fatigue life in PWR primary environment [11].

6.4.3. Effect of water conductivity

Though the effect of water conductivity has not been considered in the current Fen definition, NUREG-6909 discussed this parameter.

The effect of the conductivity of water and of the electrochemical potential (ECP) of the material on the fatigue life of austenitic stainless steels is shown in Figure 93 [1]. In high□DO water, fatigue life is decreased by a factor of ≈2 when the conductivity of water is increased from ≈0.07 to 0.4 µS/cm. Note that environmental effect on fatigue life appears more significant for the specimens that were soaked for only 24 h. For these tests, the ECP of steel was initially very low and increased during the test.

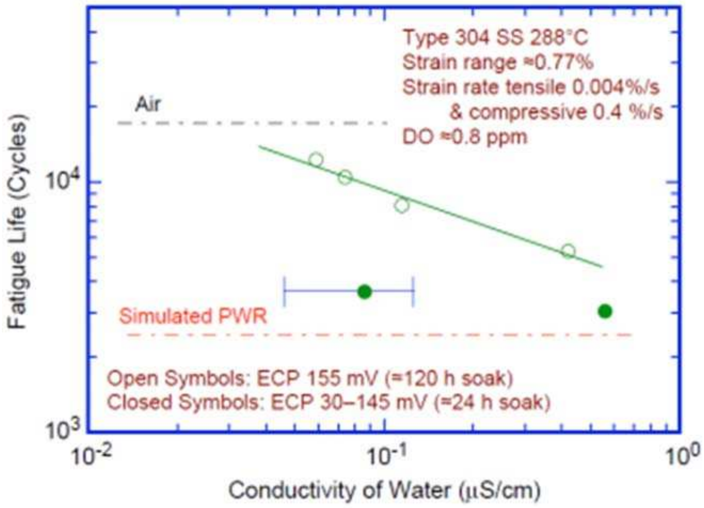

Figure 93 - Effects of conductivity of water and soaking period on fatigue life of Type 304 SS in high□DO water Effects of conductivity of water and soaking period on fatigue life of Type 304 SS in high□DO water [1].

6.4.4. Effect of dissolved hydrogen content

The effect of dissolved hydrogen (DH) content in water has not been taken into account in the Fen definition, mainly because no significant difference if fatigue life was observed (Figure 94) between DH = 30 cc/kg and 15 cc/kg. However, the available amount and range of data are quite limited. So, additional investigations may be needed to definitely conclude.

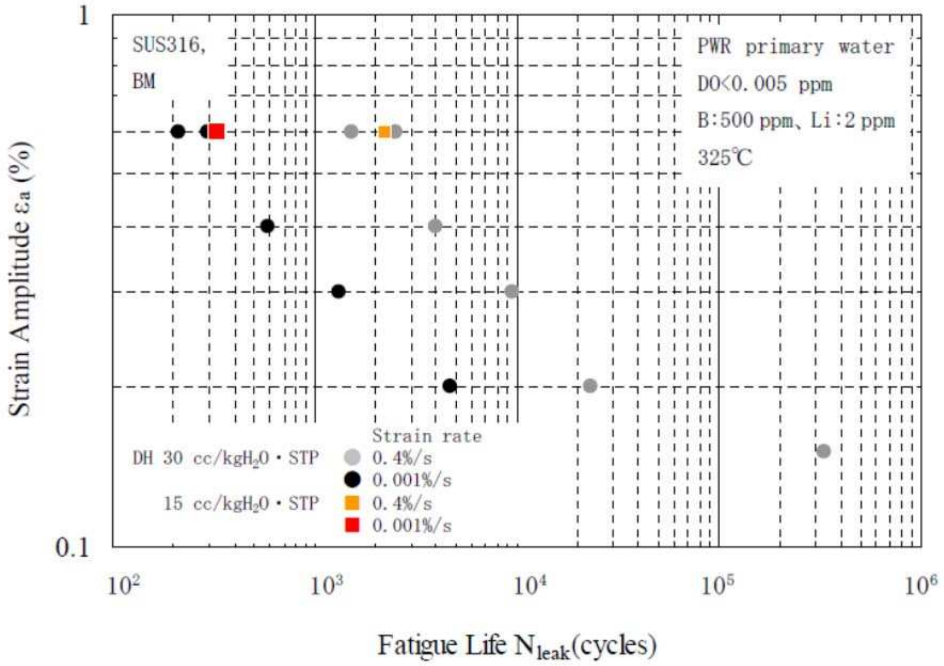

Figure 94 - Effects of DH of water on fatigue life of Type 316 SS in PWR water [8].

6.4.5. Effect of B/Li contents in primary water

As shown in Figure 95, tests were carried out for typical 2 ppm (corresponding to the center of a PWR cycle) and high 3.5 ppm (corresponding to the beginning of a PWR cycle) Li contents, for the same $pH_{320°C}$ of PWR primary water at 325°C [8]. Tests were carried out at strain rates of 0.4%/s and 0.001%/s. Despite the limited number of data (only two tests at $\Delta\varepsilon_t/2=0.6\%$ are available), it seems reasonable to assume a negligible effect of B/Li coordination for a given $pH_{320°C}$ (close to 7.2).

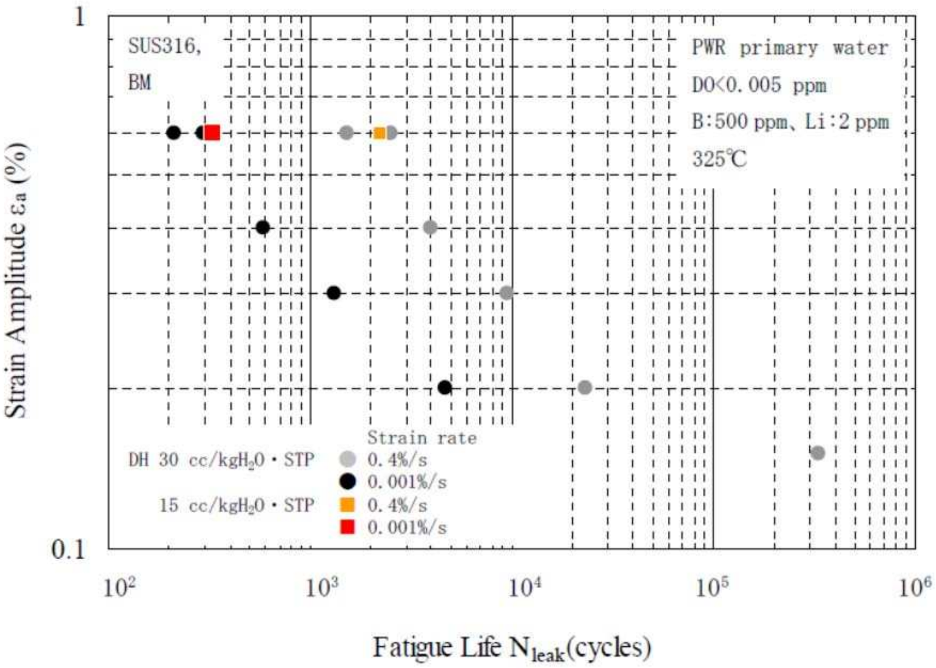

Figure 95 - Effects of B/Li contents on fatigue life of Type 316 SS in PWR primary water [8].

6.4.6. Effect of the water flow rate

Figure 96 and Figure 97 show the effect on Fen of water flow rate in PWR primary water and in BWR environment respectively. Results show a linear increase of Fen (i.e. shorter fatigue life) when the water flow rate increases in BWR environment (Figure 97). By contrast the Fen does not depend on the water flow rate in PWR primary environment (Figure 96). However, the range of flow rates tested in BWR environment (lower rates) was wider than that tested in PWR water. These results could be explained in terms of the effect of DO content on fatigue life. If the water flow rate is increased as an □oxygen supplier□, faster flow can supply much oxygen to specimen surface (or to the crack tip) during tests in BWR environment and consequently can shorten fatigue life.

Because of the uncertainties in the flow conditions at or near the location of crack initiation and also because its negligible effect on fatigue life, these effects are not presently considered in the NUREG fatigue evaluations [1]. By contrast, the effect has been taken into account in JNES equations for BWR environment [7].

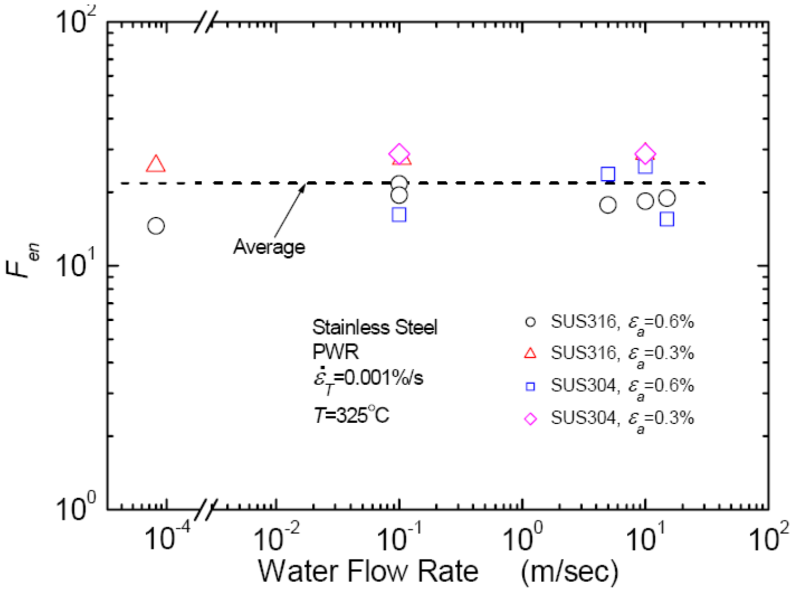

Figure 96 - Effect of water flow rate on Fen in PWR primary environment [100].

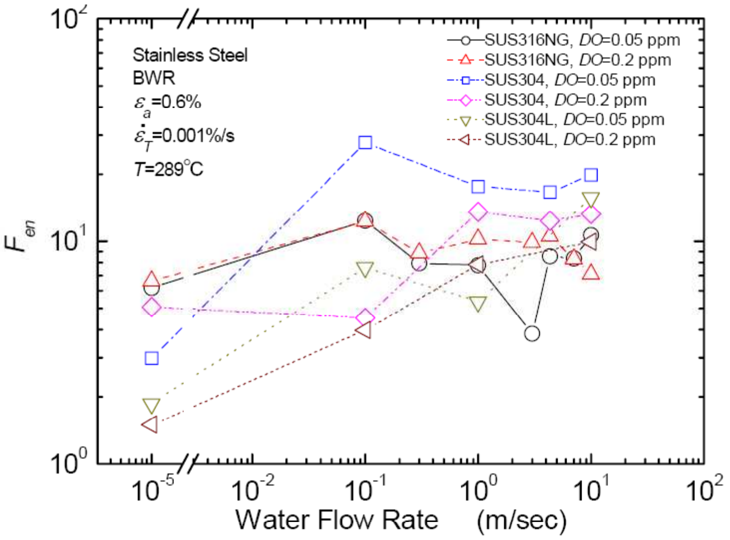

Figure 97 - Effect of water flow rate on Fen in BWR environment. [100].

7. Conclusion

The current status of researches and regulations on environmental fatigue in LWR water were reviewed and the following conclusions are listed. The codifications on environmental effect on fatigue life have been established in the US and in Japan based on a large amount of laboratory experiments which were performed over the last 30 years. Those methods are essentially comparable although many minor differences exist. Among the possible factors which may show deleterious effect on fatigue life, such as materials, strain amplitude, strain rate, temperature, DO, water conductivity, DH, B/Li contents, water flow rate, surface finishing, strain holding and cold work, only temperature and strain rate were selected as major parameters to define the penalty factor (Fen) in PWR condition.

The current evaluation includes a strain amplitude threshold below which it is assumed that there is no environmental effect. This threshold has been identified at a quite fast strain rate incompatible with corrosion kinetics. In other environments, it has been demonstrated that fatigue life as well as fatigue limit in the HCF region highly depends on the environment. **Therefore there is a need to work on the identification of a strain amplitude threshold at strain rates lower than 0.4%/s.** The second aspect is that the strain amplitude threshold has been obtained testing a various type of material such as base metals and welds. Mechanical behaviors of these materials are different, resulting in a difference of fatigue lives and limits. **As a consequence there is a need to identify more precisely material heat to heat the cyclic behavior in the HCF region in order to reach a more accurate fatigue curve.** Below a certain value, strain rate modify cracking mechanisms (TG to IG) reaching an assumed transition point with SCC. It seems reasonable to say that because the cracking mechanism are different, the associate cracking kinetics will be different. It is also well known that DO content has a strong effect on SCC cracking, then it seems also reasonable to say that, at least, DO content should have an effect on fatigue life at a low strain rate. Fatigue life are not well defined at low stress or strain amplitude, partly because of the long test times and complexity.

Strain rate is a very complex parameter to understand. It can depend and affect both the crack initiation and the micro crack propagation stage [99].

Pre hardening is a parameter, partly hidden in the □material effect□, that is not explicitly included in the current codification. The field experience related to fatigue highlighted that pre hardened areas such as welds exhibit an increased susceptibility to fatigue crack initiation (Genkai and Civaux). Moreover, the fatigue damage in air and PWSCC degradation processes are enhanced when considering pre hardened materials. In addition, the French RCC-M established in the RCC-M F 4000 that it is not necessary to justify and qualify any formed (4) component made of austenitic stainless steels under certain conditions (5). **There**

---

(4) The procedure of forming correspond to the mechanical or thermo-mechanical operations (bending, forging, rolling, welding,□), applied to a part or product in order to

is a need to clarify the pre hardening effect on fatigue life and cyclic behavior of austenitic stainless steels in PWR primary water and its reference in air environment.

Root causes that induce fatigue life reduction on austenitic stainless steels in LWR water environment have not necessarily been identified yet. According to NUREG-6909 [1], metallographic examination of the test specimens indicated that reduction in fatigue lives most likely is not caused by slip oxidation/dissolution but some other process, such as hydrogen□induced cracking. However, no clear evidences are provided in the report.

In addition, the Materials Degradation Matrix (MDM) provided by EPRI reports [106] that there is currently no adequate mechanism interpretation of significant reductions in the fatigue lives of stainless steels in simulated hydrogenated PWR environments, i.e., at low corrosion potential, and also suggests that there is a need for the industry to develop an improved understanding of this effects, especially with regards to modeling realistic plant strain patters and rates, complex variable amplitude fatigue cycle sequences, and chemical effects when considering 80-year operations.

Therefore, **it would be highly recommended not only to establish a realistic fatigue life evaluation model excluding current excess of conservatism but also to better understand the underlying mechanisms. At the moment that codes and predictions does not account for synergies between loadings, metallurgy and environment**. Mechanical centered codes persist in the current approach despite that environmental and materials factors can be as dominant as the mechanical loading.

8. Objectives and approach of the PhD thesis

In response to the above background, EDF R&D launched the environmentally-assisted fatigue studies in the framework of the COPRIN 2 and COFAT MAI projects.

The two main objectives of this work were separated into:

- A codification study

The current codification compares fatigue lives obtained in **PWR primary and air environments**. It is then proposed to evaluate the impact of a **prior strain hardening and a**

---

obtain a given component. and is still in good agreement with material specifications (chemistry, mechanical properties, □).

(5) It is not necessary to justify and qualify when the process, did not induce maximum residual strains higher than 10-15%, is perform at a temperature lower than 150°C, and is still in good agreement with material specifications (chemistry, mechanical properties, □).

reduced strain rate on the difference of fatigue life between the two environments (Chapter 3-4).

The approach on codification consists in obtaining, as a reference, the fatigue lives in air environment on pre hardened materials (Chapter 3) and to compare with those obtained in PWR primary environment (Chapter 4). Experimental results obtained in the present study will be discussed and compared in the Chapter 5 in addition to some results obtained in the same material but in the as-received condition (performed by GE and CEAT for EDF).

- A mechanism understanding study

It is proposed to progress in the understanding of the underlying mechanisms on environmentally-assisted fatigue (Chapter 3-4).

The approach on the understanding objective consists in the evaluation of the damage and cracking mechanisms in the air environment as a reference (Chapter 3) and in PWR primary environment (Chapter 4) for several loading and material conditions. The damage will be first evaluated macroscopically and then initiation and micro propagation will be studied more deeply up to the nm scale using several microscopic techniques presented in the Chapter 2. Results will be compared and discussed in the Chapter 5.

The following figure describes the general approach followed in this thesis

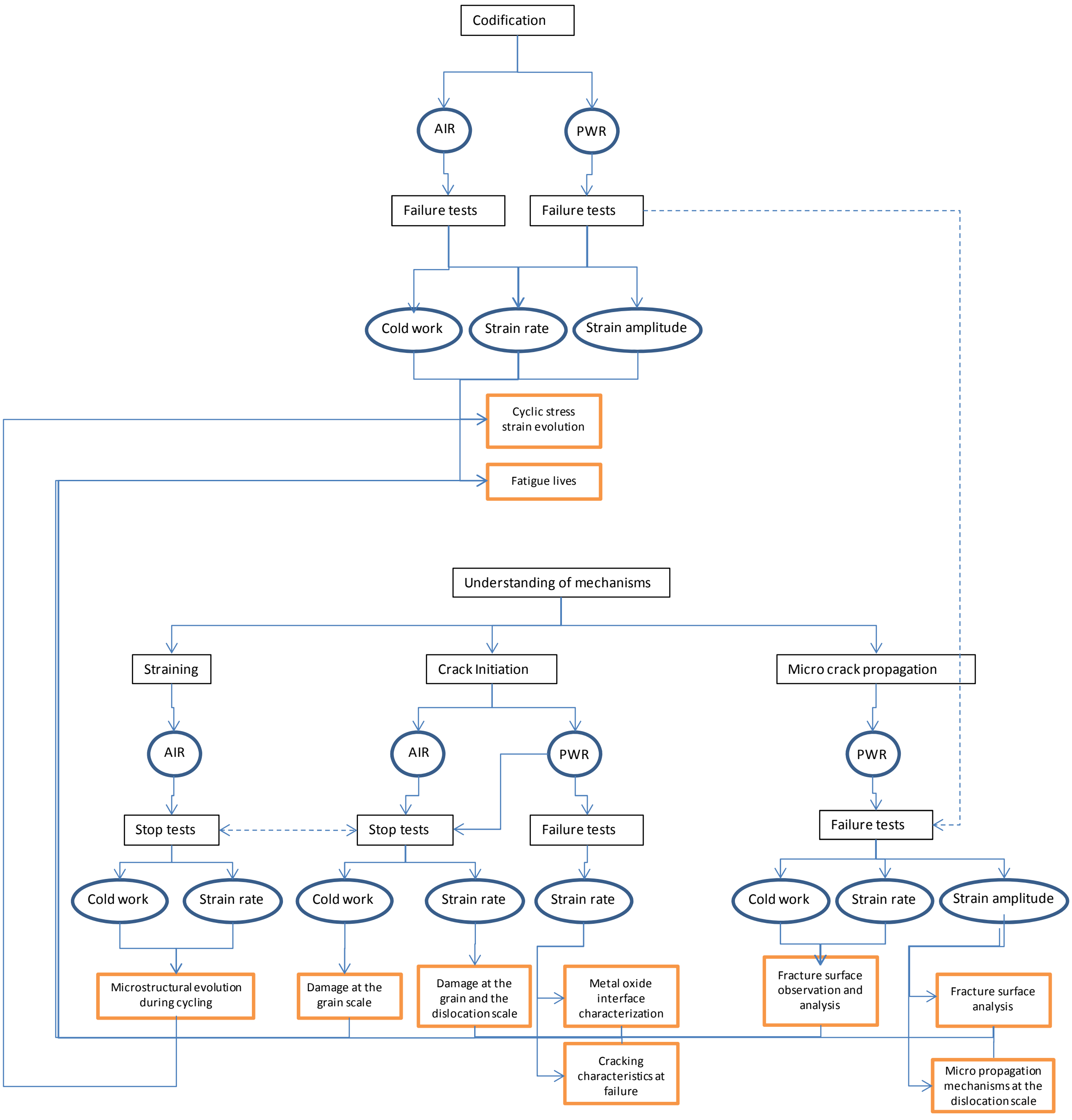
Codification
AIR
PWR
Failure tests
Failure tests
Cold work
Strain rate
Strain amplitude
Cyclic stress strain evolution
Fatigue lives
Understanding of mechanisms
Straining
Crack Initiation
Micro crack propagation
AIR
AIR
PWR
PWR
Stop tests
Stop tests
Failure tests
Failure tests
Cold work
Strain rate
Cold work
Strain rate
Strain rate
Cold work
Strain rate
Strain amplitude
Microstructural evolution during cycling
Damage at the grain scale
Damage at the grain and the dislocation scale
Metal oxide interface characterization
Cracking characteristics at failure
Fracture surface observation and analysis
Fracture surface analysis
Micro propagation mechanisms at the dislocation scale

---

[1] **O.K. CHOPRA, W.J. SHACK** , "Effect of LWR Coolant Environments on the Fatigue Life of Reactor Materials," Final Report, NUREG/CR-6909, ANL-06/08, Feb. 2007.

[2] **Regulatory Guide 1.207**, "Guidelines for Evaluating Fatigue Analyses Incorporating The Life Reduction of Metal Components Due to The Effects of The Light-Water Reactor Environment for New Reactors," U. S. Nuclear Regulatory Commission, March, 2007.

[3] **J.R. COLE, J.C. MINICHIELLO**, □Status Report on ASME Section III Subgroup on Design Plan for Code Changes to Implement Environmental Fatigue Evaluation Methods□, ASME PVP2010-25677.

[4] **Nuclear and Safety Management Division**, Agency for Natural Resources and Energy □Guidelines for Evaluating Fatigue Life Reduction in the LWR Environment□ in Japanese, September 2000.

[5] **Thermal and Nuclear Power Engineering Society (TENPES)** □Guidelines on Environmental Fatigue Evaluation for POWER Reactors□, 2002.

[6] **T. NAKAMURA, I. SAITO, Y. ASADA,** □Guidelines on Environmental Fatigue Evaluation for LWR Component□, ASME PVP-Vol. 453, PVP2003-1780, 2003.

[7] **The Japan Society of Mechanical Engineers**, □Codes for nuclear power generation facilities: Environmental fatigue evaluation method for nuclear power plants□, JSME S NF1-2006, JSME.

[8] **Japan Nuclear Safety Organization**, □Final report of EFT project□, 07-kizaiho-0002, 2007.(in Japanese)

[9] **M. HIGUCHI**, □Comparison of Environmental Fatigue Evaluation Methods in LWR Water□, ASME PVP 2008-61087, 2008.

[10] **O.K. CHOPRA**, "Environmental Effects on Fatigue Crack Initiation in Piping and Pressure Vessel Steels," Proceedings of International Conference on Fatigue of Reactor Components, July 31 - August 2, 2000, Napa California, USA

[11] **M. HIGUCHI, K. SAKAGUCHI, Y. NOMURA, A. HIRANO**, "Final Proposal of Environmental Fatigue Life Correction Factor (Fen) for Structural Materials in LWR Water Environment," ASME PVP 2007-26100.

[12] **L. MIDMORE** « Environmentally Assisted Fatigue Gap Analysis and Roadmap for Future Research » EPRI Report 1023012, 2011

[13] **R.G. BALLINGER**, “Light Water Reactors: Materials of Construction and their Performance: Characteristics that Impact Degradation”, International conference on plants materials degradations : Application to the stress corrosion cracking of Ni base alloys; The Materials Ageing Institute, EDF, Moret Sur Loing, France, November 2008

.

[14] **P. LACOMBE, B. BAROUX, G. BERANGER**, "Les aciers inoxydables", Les éditions de physique, Les Ulis, 1990.

[15] **T.COUVANT**, “Modélisation physique de la corrosion sous contraintes des aciers inoxydables austénitiques écrouis”EDF report, HT29-2007-01296-FR

[16] **J.P. MASSOUD, M. BETHMONT, J. CHAMPREDONDE**, “Long term aging of cast duplex stainless steel between 300 and 400°C Relationship between toughness properties and metallurgical parameters, Duplex Stainless Steels'91”, Vol. 1,p. 93, 1991.

[17] **B.S. RHO, H.U.HONG, S.W.NAM**, “The fatigue crack initiation at the interface between matrix and ferrite in 304L stainless steel”, Scripta Materialia, Vol. 39, No. 10, pp. 1407-1412, 1998.

[18] **F.B. PICKERING**, "Physical metallurgy and the design of steels", Applied Science Publishers, London, 1978.

[19] **M. GERLAND, J. MENDEZ, P. VIOLAN, B. AIT SAADI**, "Evolution of dislocation structures and cyclic behavior of a 316L-type austenitic stainless steel cycled in vacuum at room temperature", Materials Science and Engineering A, Vol. A118, pp. 83-95, Octobre 1989

[20] **G. BRUN, J.P. GAUTHIER, P. PETREQUIN**, "Etude de la fatigue oligocyclique d'un acier Z2 CND 17-12 (type AISI 316L) ", Journées Métallurgique d'Automne 1974, Mémoires Scientifiques Revue Métallurgie, pp. 461-483, Juillet-Août 1976.

[21] **M. GERLAND, J. MENDEZ, P. VIOLAN, B. AIT SAADI**, "Evolution of dislocation structures and cyclic behavior of a 316L-type austenitic stainless steel cycled in vacuum at room temperature", Materials Science and Engineering A, Vol.

A118, pp. 83-95, Octobre 1989

[22] **G. BRUN, J.P. GAUTHIER, P. PETREQUIN**, "Etude de la fatigue oligocyclique d'un acier Z2 CND 17-12 (type AISI 316L) ", Journées Métallurgique d'Automne 1974, Mémoires Scientifiques Revue Métallurgie, pp. 461-483, Juillet-Août 1976.

[23] **T. MAGNIN**, "Développements récents en fatigue oligocyclique sous l'angle de la métallurgie physique", Mémoires et Etudes Scientifiques Revue de Métallurgie, pp. 33-48, Janvier 1991.

[24] **P. LACOMBE, B. BAROUX, G. BERANGER**, "Les aciers inoxydables", Les éditions de physique, Les Ulis, 1990.

[25] **J.W. BROOKS, M.H. LORETTO, R.E. SMALLMAN**, "In situ observations of the formation of martensite in stainless steel", Acta Metallurgica, Vol. 27, No. 12, pp. 1829-1838, Décembre 1979.

[26] **R.G. TETERUK, H.J. MAIER, H.-J. CHRIST**, "Fatigue-induced martensitic transformation in metastable stainless steels", Proceedings of the 4th International Conference on Low Cycle Fatigue and Elasto-Plastic Behaviour of Materials, Garmisch-Partenkirchen, pp. 321-326, Septembre 1998.

[27] **C. BATHIAS, R.M. PELLOUX**, "Fatigue crack propagation in martensitic and austenitic steels", Metallurgical Transactions A, Vol. 4, No. 5, pp. 1265-1273, Mai 1973.

[28] **E. HORNBOGEN**, "Martensitic transformation at a propagating crack", Acta Metallurgica, Vol. 26, No. 1, pp. 147-152, Janvier 1978.

[29] **D. HENNESSY, G. STECKEL, C.ALTSTETTER**, "Phase transformation of stainless steel during fatigue", Metallurgical Transactions A, Vol 7, No. 3, pp. 415-424, Mars 1976.

[30] **J. STOLARZ, N. BAFFIE, T.MAGNIN**, "Fatigue short crack behaviour in metastable austenitic stainless steel with different grain sizes", Materials Science and Engineering A, Vol A319-321, pp. 521-526, December 2001.

[31] **TSL OIM Analysis**, Help, v5.1

[32] **K. OBRTLIK, T. KRUML, J. POLAK,** "Dislocation structures in 316L stainless steel cycled with plastic strain amplitudes over a wide interval", Materials Science and Engineering A, Vol A187, No. 1, pp. 1-9, October 1994.

[33] **A. GARCIA**, “Caractérisation microstructurales d'aciers inoxydables austénitiques de type AISI 304L sollicités en fatigue” These de doctorat de l’Institut National Polytechnique de Grenoble. 2009

[34] **N. JIN, C. ZHONG, X. CHEN**, “Cyclic deformation of AISI-310 stainless steel. II. Saturation dislocation structures”, Acta Metallurgica and Materialia, Vol. 38 No. 11, pp. 2141-2148, November 1990.

[35] **Y. LI, C. LAIRD**, "Cyclic response and dislocation structures of AISI 316L stainless steel. Part 2: polycrystals fatigued at intermediate strain amplitude", Materials Science and Engineering A, Vol. A186, No. 1-2, pp. 87-103, Octobre 1994.

[36] **H. MUGHRABI, F. ACKERMANN, K. HERZ**, "Persistent slip bands in fatigued face-centered and body-centered cubic metals", Proceedings of the ASTM-NBSNFS Symposium on Fatigue Mechanisms, Kansas City, Mai 1978, ASTM Special Technical Publication, Vol. 675, pp. 69-105, 1979.

[37] **R. ZAUTER, H.J. CHRIST, H. MUGHRABI**, "Some aspects of thermomechanical fatigue of AISI 304L stainless steel : Part II. Dislocation arrangements", Metallurgical and Materials Transactions A, Vol 25A, No. 2, pp. 407-413, Février 1994.

[38] **S. SURESH** “Fatigue of Materials 2nd edition”, Cambridge University Press, 2006

[39] **J.C. LE ROUX**, “Influence de paramètres métallurgiques et d’essai sir l’amorçage des fissures de fatigue en déformation impose des aciers inoxydables austénitiques”, EDF R&D report H-T26/03/056/B, 2004

[40] **M. POURBAIX** « Atlas d’équilibres électrochimiques » Gautier Villars et cie, 1963

[41] **J. CHENE, A.M. BRASS** « Interactions Hydrogène - Métal en relation avec le processus de corrosion sous contrainte » Corrosion Sous Contrainte –Phénoménologie et mécanismes, Les Éditions de Physique (1992).September 23-28, 1990.

[42] **D.H. LISTER, R.D. DAVIDSON, E. MCALPINE**, « The mechanism and kinetics of corrosion product release from stainless steels in lithiated high temperature water » Corrosion. Science, 1987

[43] **Z. SZKLARSKA-SMIALOWSKA, K.C. CHOU, Z. XIA,** « The composition and properties of oxide films on type 304 stainless steel on exposure to lithiated water at 100-350°C », Corrosion. Science, 1991

[44] **T. COUVANT, L. LEGRAS, A. HERBELIN, A. MUSIENKO, G. ILEVBARE, D. DELAFOSSE, G. CAILLETAUD, J. HICKLING**, "Development of understanding of the interaction between localized deformation and SCC of austenitic stainless steels exposed to PWR primary environment ", 14th International Conference on Environmental Degradation of Materials in Nuclear Power Systems Virginia Beach, August 23-27, 2009

[45] **PJE. FORSYTH**, "Slip band damage and extrusion", Proceeding of the Royal Society of London. vol. 242, pp198-202, 1957

[46] **P. PARIS**, "A critical analysis of crack propagation law", Journal of Basic Engineering, Trans ASME, pp 528-534, 1963

[47] **C. DEPRES**, "Crack initiation in fatigue: experiments and three-dimensional dislocation simulations ", Material science and engineering, pp 288–291, 2004

[48] **L. SABATIER** " Apport des techniques d'analyse locale EBSD et AFM à l'étude de l'émergence des bandes de glissements induites par fatigue dans l'acier inoxydable 316L. Influence des couches minces " University of Poitiers PhD Thesis, 2002.

[49] **M. MINEUR** « Conditions locales d'amorçage des fissures de fatigue dans un acier inoxydable de type 316L : aspects cristallographiques (EBSD » University of Poitiers PhD Thesis, 2000.

[50] **T. MAGNIN**, « Recent advances for corrosion fatigue mechanisms » ISIJ Internationnal, vol 35, 1995

[51] **T. COUVANT, F. VAILLANT, T. GHYS**, "Development of understanding of the interaction between localized deformation and SCC of austenitic stainless steels exposed to primary PWR environment" , EDF R&D report H-T29-2008-0945-EN, 2008.

[52] **T.COUVANT ET AL**, « Modeling intergranular stress corrosion cracking of austenitic alloys exposed to PWR primary water » Eurocorr 2012

[53] **T.COUVANT et al**. “Physical modeling of intergranular stress corrosion cracking in austenitic alloys exposed to PWR primary water” Workshop on Coupling Mechanisms to improve Lifetime Prediction of LWRs, EDF R&D, April 8 –9, 2010

[54] **F.P. FORD**, “Mechanism of environmental cracking in systems peculiar to the power generation industry”, Rapport de Electric Power Research Institute, EPRI NP-2589, p.22, 1982

[55] **F.P. FORD**, “Current understanding of the mechanism of stress corrosion and corrosion fatigue in environment sensitive fracture : evaluation and comparison of test methods”, ASTM STP 821, p22, 1984

[56] **F.P. FORD**, “Slip dissolution model”, corrosion sous contrainte : Phénoménologie et mécanisme, Eds, D. Desjardins et R. Oltra, Éditions de physique, Bombannes (France), 23-28 Septembre 1990

[57] **T. SHOJI** “Modeling and quantitative prediction of environmentally assisted cracking base upon a deformation oxidation mechanism” PVP vol 479, July 25-29 2004.

[58] **D. LANDLT**. “Corrosion et chimie des surfaces des métaux” Traité des matériaux, 2003

[59] **R.C. NEWMAN, M. SAITO** “Anodic stress-corrosion cracking : slip-dissolution and film-induced cleavage” Corrosion-Deformation Interactions - CDI’92, p. 3–26. Les Éditions de Physique Les Ulis (1993).Conférence internationale. Fontainebleau, France. 5-7 octobre 1992.

[60] **T. CASSAGNE** “Le modèle de clivage induit par un film”. Corrosion Sous Contrainte - phénoménologie et mécanismes, D. Desjardins et R. Oltra, p. 373–396. Les Éditions de Physique (1992). École d’Automne. Bombannes (Gironde), France. 23-28 septembre 1990.

[61] **J.R. GALVELE** “Surface mobility mechanism of stress-corrosion cracking. “Corrosion Sous Contrainte - phénoménologie et mécanismes” D. Desjardins et R. Oltra, p. 83-91. Les Éditions de Physique (1992). École d’Automne. Bombannes (Gironde), France. 23-28 septembre 1990.

[62] **K. SIERADZKI ET F.J. FRIEDERSDORF** “Notes on the surface mobility mechanism of stress-corrosion cracking”. Corrosion Science, 36(4) 669–675 (1994).

[63] **E.M. GUTMAN** "Notes on the discussion concerning the "surface mobility mechanism" of stress corrosion cracking". Corrosion Science, 45(9) 2105–2128 (2003).

[64] **P. SCOTT, M. LE CALVAR**, "Some possible mechanisms of intergranular stress corrosion cracking of alloy 600 in PWR primary water", 6th Int. Symposium on environmental degradation of materials in nuclear power system-water reactors, San Diego, USA, 1993

[65] **P. LAGHOUTARIS** "Corrosion sous contrainte de l'alliage 600 en milieu primaire : Apport à la compréhension des mécanismes" ENSMP PhD Thesis, 2009

[66] **C.A. ZAPPFE**, C.E. Sims Trans ASME, Vol 145, p225, 1941

[67] **R.A. ORIANI, P.H. JOSEPHIC**, " Equilibrium aspects of hydrogen-induced cracking of steels", Acta metallurgica, vol.22, p.1065, 1974

[68] **S.P. LYNCH** "A Commentary on Mechanisms of Environmentally Assisted Cracking". Corrosion-Deformation Interactions - CDI'96, p. 206–219. The Institute of Materials (1997). European Federation of Corrosion Publications num. 21. Nice, France. Septembre 1996

[69] **P. BASTIEN, P. AZOU**,C.R. Acad-Sciences Paris, 232, p1545, 1951

[70] **C.D. BEACHEM**, Metall. Trans, 3, p437,1972

[71] **N.J. PETCH**, Philosophical Magazine, 1, p331, 1956

[72] **L. COUDREUSE,** "Fragilisation par l'hydrogène et corrosion sous contrainte", Corrosion Sous Contrainte - phénoménologie et mécanismes, édité par D. Desjardins et R. Oltra, p. 397–424. Les Éditions de Physique (1992). École d'Automne. Bombannes (Gironde), France. 23-28 septembre 1990.

[73] **D.A. JONES**, "Localized surface plasticity during stress corrosion cracking", Corrosion Science, pp 356-362, 1996

[74] **T. MAGNIN,** "A unified model for trans and intergranular stress corrosion cracking", Corrosion-Deformation Interactions - CDI'92,1992

[75] **J.P. CHATEAU, D. DELAFOSSE, T. MAGNIN** « Numerical simulations of hydrogen–dislocation interactions in fcc stainless steels. Part II: hydrogen effects on crack tip plasticity at a stress corrosion crack», Acta Materialia 50 (2002) 1523–1538

[76] **J. LEPINOUX ,T. MAGNIN** , Mater. Sci. Engng A 1993;164:266–9.

[77] **A.N. STROH**, Proc. Roy. Soc. 1954, p223:404–14.

[78] **C.D. BEACHEM**, "A new model for hydrogen-assisted cracking (hydrogen embrittlement)", Metallurgical Transactions (1972), 3, p. 437-451.

[79] **H.K. BIRNBAUM , P. SOFRONIS**, "Hydrogen-enhanced localysed plasticity-a mechanism for hydrogen-related fracture", Materials Science and Engineering (1994), A176, p.191-202.

[80] **I. M. ROBERTSON, H. K. BIRNBAUM**, "An HVEM study of hydrogen effects on the deformation and fracture of nickel", Acta Metallurgica (1986), 34, p. 353-366.

[81] **P. ROZENAK, I. M. ROBERTSON, H. K. BIRNBAUM**, "HVEM studies of the effects of hydrogen on the deformation and fracture of ASI type 316 austenitic stainless steel", Acta Metallurgica et Materialia (1990), 38, p. 2031-2040.

[82] **E. SIROIS, H. K. BIRNBAUM**, "Effects of hydrogen and carbon on thermally activated deformation in nickel", Acta Metallurgica et Materialia (1992), 40, p. 1377-1385.

[83] **P. SOFRONIS**, "The influence of mobility of dissolved hydrogen on the elastic responseof a metal", Journal of the Mechanics and Physics of Solids (1995), 43, p. 1385-1407.

[84] **J.A. LE DUFF, ET AL.**, “Effects of surface finish and loading conditions on the low cycle fatigue behavior of austenitic stainless steel in PWR environment”, Proceedings of PVP2008, ASME PVP2008-61894, 2008.

[85] **J.A. LE DUFF, ET AL.**, “Effects of surface finish and loading conditions on the low cycle fatigue behavior of austenitic stainless steel in PWR environment for various strain amplitude levels”, Proceedings of PVP2009, ASME PVP2009-78129, 2009.

[86] **J.A. LE DUFF, ET AL.**, “Effect of loading signal shape and of surface finish on the low cycle fatigue behavior of 304L stainless steel in PWR environment.”, Proceedings of PVP2010, ASME PVP2010-26027, 2010.

[87] **M. HIGUCHI, ET AL.,** □Effects of strain holding and continuously changing strain rate on fatigue life reduction of structural materials in simulated LWR water□, Proceedings of PVP2007, ASME PVP2007-26101, 2007.

[88] **P. ANDRESEN**, □Introduction to degradation in Fe-Ni-Cr Alloys□, EPRI/NEI course on material reliability in nuclear power systems, 2008.

[89] **N. ISHIYAMA, M. MAYUZUMI, Y. MIZUTAN,** □Stress Corrosion Cracking of type 316 and 316L Stainless Steels in High Temperature Water□ 12th Environmental Degradation of Materials in Nuclear Power Systems, 2005.

[90] **J. KUNIYA, I. MASAOKA, R. SSAKI**. □Effect of cold work on the stress corrosion cracking of nonsensitized AISI 304 stainless steel in high-temperature oxygenated water□,Corrosion, 1998.

[91] **P. ANDRESEN** □Effects of yield strength, corrosion potential, stress intensity factor, silicon and grain boundary character on the SCC of stainless steels□, 11th International Conference Environmental Degradation of Materials in Nuclear Systems, 2003.

[92] **M.L. CASTANO, S. GARCIA, V.D. DIEGO, D. GOMEZ-BRICENO**, □Crack growth rate of hardened austenitic stainless steels in BWR and PWR environments□ 11th International Conference Environmental Degradation of Materials in Nuclear Systems, 2003.

[93] **F. VAILLANT et al.**, "Stress Corrosion Cracking Propagation of Cold□worked Austenitic Stainless Steels in PWR Environment," 14th Int. Conf. on Environmental Degradation of Materials in Nuclear Power Systems, 2009.

[94] **S. TAHERI et al**. « Micro□macro investigations about the fatigue behavior of pre-hardened 304L steel » International Journal of Plasticity, 2011

[95] **S. PETITJEAN**, "Influence de l'état de surface sur le comportement en fatigue a grand nombre

de cycles de l'acier inoxydable austenitique 304L", University of Poitiers PhD thesis, 2003.

[96] **H.D. SOLOMON, C. AMZALLAG, A.J. VALLEE AND R.E. DELAIR,** □Fatigue Limit and Hysteresis Behavior of 304L SS in Air and PWR Water at 150 °C and 300 °C □, rapport GE 2005GRC353, 2005.

[97] **C. AMZALLAG et al**, “Métallurgie : du minerai au matériau, ” Masson edition

[98] **P. COMBRADE**, “Fissuration assistée par l’environnement”, CACEMI, CNAM, 2005

[99] **L. DE BAGLION** “Comportement et endommagement en fatigue oligocyclique d’un acier inoxydable austénitique 304L en fonction de l’environnement (Vide, Air, Eau primaire REP) à 300°C” PhD Thesis, ENSMA, 2011

[100] **Japan Nuclear Energy Safety Organization** “The final report of EFT project”, 07kizaihou-0002, 2007.

[101] **N. TOTSUKA, Y. NISHIKAWA,Y. KANESHIMA**, “Effect of strain rate on primary water stress corrosion cracking fracture mode and crack growth rate of nickel alloy and austenitic stainless steel”, 2005, Corrosion, 61.

[102] **H.D. SOLOMON, C. AMZALLAG, A.J. VALLEE AND R.E. DELAIR,** “Fatigue Limit and Hysteresis Behavior of 304L SS in Air and PWR Water at 150 °C and 300 °C ”, rapport GE 2005GRC353, 2005.

[103] **HUIJBREGTS,** Corrosion, vol. 42, p. 456, 1986.

[104] **T. TSUKADA, Y. MIWA, S. JITSUKAWA, K. SHIBA, A. OUCHI**, “Effects of water and irradiation temperatures on IASCC susceptibility of type 316 stainless steel” Journal of Nuclear Materials, 329-333(Part 1), 657-662, 2004.

[105] **NELSON,** “Stress corrosion crack growth rate measurements on unsensitized type 304 stainless steel in 288°C water ”, EPRI, TR-113489, 2000.

[106] **EPRI**, “Primary System Corrosion Research Program; EPRI Materials Degradation Matrix, Revision 2”, Final Report, August 2010.

CHAPTER 2: EXPERIMENTAL PROCEDURES

List of acronyms

EBSD: Electron BackScaterred Diffraction
EDX: Energy Dispersive X-ray Spectroscopy
EELS: Electron Energy Loss Spectroscopy
EFTEM: Energy Filtered Transmission Electron Microscopy
ENSMA: Ecole Nationale Superieur de Mécanique et d'Aérotechnique
FEG: Field Emission Gun
FFT: Fast Fourier Transform
FIB: Focused Ion Beam
KAM: Kernel Average Misorientation
LCD: Linear Crack Density
LCF: Low Cycle Fatigue
MHI: Mitsubishi Heavy Industries
PWR: Pressurized Water Reactor
SCC: Stress Corrosion Cracking
SEM: Scanning Electron Microscope
STEM: Scanning Transmission Electron Microscopy
TEM: Transmission Electron Microscope

Summary

1. Introduction

This chapter addresses the different methods used in this study. For the codification support objective, the only required data corresponds to the cyclic strain-stress behavior and fatigue lifetimes. For the study of deformation, crack initiation and growth mechanisms on fatigue tested samples, several kinds of microscopic observations were used.

The main idea was to characterize the effect of relevant macroscopic parameters such as the loading strain rate and a degree/mode of pre hardening on the fatigue damage of the austenitic stainless steels at different scales from the nm scale up to the mm scale. Coarse analysis will consist in observations through optical and scanning electron microscopes. Fine observations will consist in observations of local deformation microstructures and chemistry using Transmission Electron Microscopy (TEM) (Bright Fields (BF)/ Dark Fields (DF), Diffraction, Electron Energy Loss Spectroscopy (EELS) / Energy Filtered Transmission Electron Microscopy (EFTEM) , Energy Dispersive X-ray Spectroscopy (EDX)). Basic fundamental knowledge of each technique will be described. All the techniques used are summarized in the Figure 50 in the end of this chapter.

2. Fatigue tests

2.1. Tests under PWR primary environment

Tests in PWR primary water were carried out at MHI Takasago R&D center.

Figure 1 shows the design of the hollow cylindrical specimens used for these tests. The gage length was 24 mm. The outer diameter was 12 mm and the wall thickness was 3 mm. Specimens were machined out from the mid wall of plates in the way that the lengthwise direction would match the rolling direction or the loading direction.

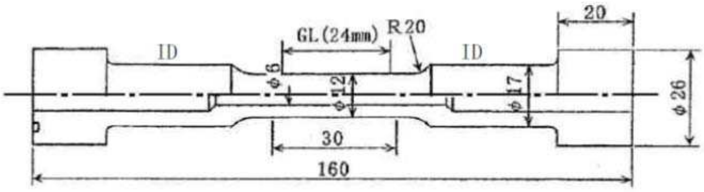

Figure 1 □Hollow type specimen, dimension in mm.

The temperatures on the outer and inner surfaces of tested portion were monitored by thermocouples. The difference between inner and outer temperatures were assessed to be lower than 1°C. Tests were conducted under fully reversed total axial strain control (R_ε= -1), using a contact-type extensometer attached to the outer surface of the specimen.

Figure 2 shows an outline of the test apparatus used for environmental testing. Water was heated by a pre-heater; it circulated thanks to a high-pressure pump through interior of the specimen. The maximum flow rate was approximately 10 liters/hour and the average fluid velocity was 0.1m/s into the hollow cylindrical area of the specimen.

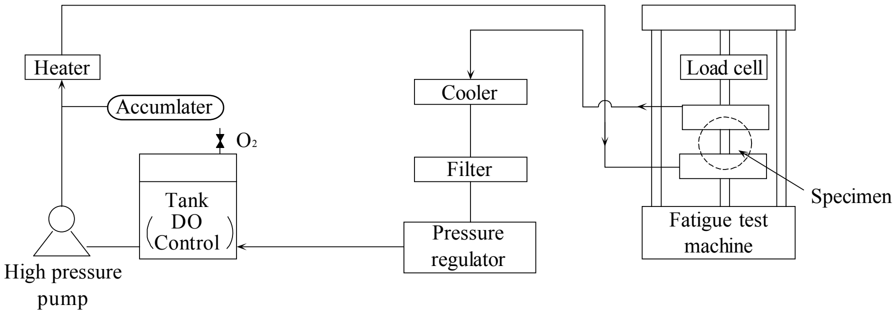

Figure 2 - Outline and overview of test apparatus in PWR primary water.

The environment was simulated PWR primary water with 1000 ± 100 ppm B as H_3BO_3, and 2 ± 0.2 ppm Li as LiOH, at 300°C. Dissolved oxygen (DO) was kept at a concentration lower than 5 ppb and dissolved hydrogen (DH) was kept at 30 ± 3 cc/kg·H2O. The water chemistry of the primary loop was controlled once per month. All specimens were exposed to the environment about 24 hours prior to the fatigue tests.

Codification-type tests:

The outer and inner surfaces of specimens were polished in the axial direction using emery papers of #100, #240, #400 and #800 in order to remove scratches caused by machining.

Understanding-type tests:

A protocol has been developed in order to get an inner surface finish without any residual cold work and scratches induced by machining and polishing:

- Prior drilling ϕ=3 mm.
- Enlargement of the hole using electro discharge machining up to ϕ=5.95 mm.
- Mechanical polishing with a FlexHone grid #2500 (Figure 3).
- Electrochemical polishing of the inner diameter.

Figure 3 □FlexHone.

2.2. Tests in air environment

2.2.1. Tests carried out at EDF MMC

Tests in air were perform using an electromechanical DMG-MAYES 100KN machine (Figure 4) and were conducted under fully reversed axial strain control, using a contact type extensometer attached to the outer surface of the specimen so that tests should be performed under equivalent operating condition to the tests in PWR primary water. Temperature was monitored with thermocouples.

Figure 5 shows the configuration of a modified FFL2-type specimen. Outer surfaces were polished in the axial direction using silicon paper #320, #500 and #800 in order to obtain the equivalent surface roughness compared to that on hollow type specimens used in the codification-type tests.

Figure 4 □DMG Mayes machine.

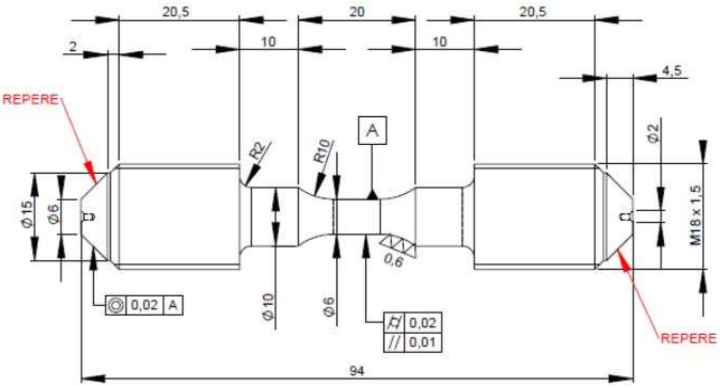

Figure 5 Modified FFL2 specimen, dimension in mm.

2.2.2. Tests carried out at ENSMA

In order to get some reference in air environment, some tests were performed at ENSMA using an electromechanical INSTRON 1362 50 kN fatigue machine (Figure 6). Tests were conducted under fully reversed total axial strain control with a high temperature INSTRON strain gage extensometer attached to the outer surface of the specimen using ceramic paste to avoid extensometer slip during the test. Strain amplitude was fixed at 0.5% and test temperature was set at 300°C in most of the tests.

Before testing, samples (Figure 8) were polished using paper grid #320, #500, #1200, #2400, #4000 followed by diamond paste 3 µm and 1 µm.

Figure 6 INSTRON 1362 fatigue machine [1].

Figure 7 High temperature strain gage extensometer [1].

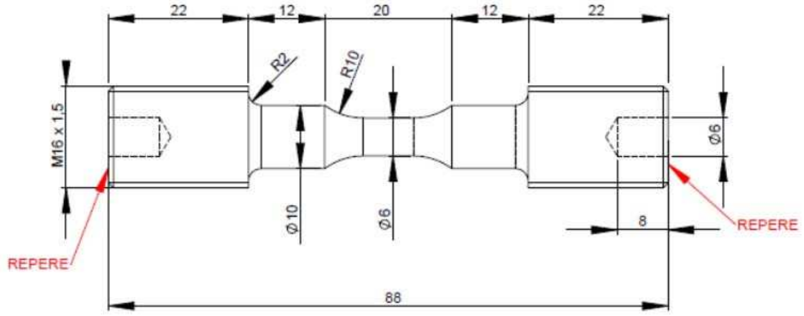

Figure 8 □Fatigue sample used at ENSMA, dimension in mm.

3. Mechanical behavior

The definitions of total strain ($\Delta\varepsilon_t$), non-elastic strain ($\Delta\varepsilon_p$) or a plastic strain, and elastic strain ($\Delta\varepsilon_e = \Delta\varepsilon_t - \Delta\varepsilon_p$) were illustrated in Figure 9. These parameters were used to describe the cyclic stress-strain evolution.

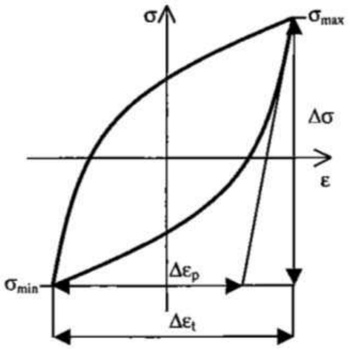

Figure 9 □Definition of total strain and non-elastic strain (plastic strain) in an hysteresis loop.

4. Microstructural observations

In this study, several kinds of microscopic observations were used at EDF R&D to characterize the damage of austenitic stainless steels at different scales.

4.1. Optical microscopes

Optical microscopy was used in order to control polishing scratches, global surface roughness, the quality of electropolished transmission electron microscopy (TEM) samples, etc...

In order to quantify the damage on each sample, crack length, crack depth, crack initiation angle and crack morphology (Figure 10) were measured on the cross sections using an optical microscope. The Linear Crack Density (LCD) was also quantified. This parameter represents the number of crack initiation sites observed on a cross section divided by the examined length. Fatigue samples were cut along the axial direction, polished up to diamond paste size 1 µm and then observed through an optical microscope.

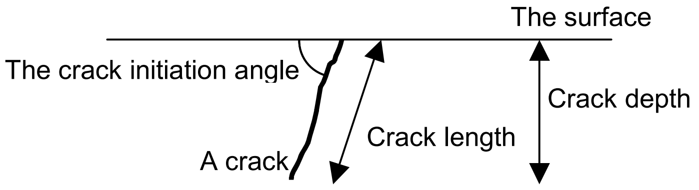

Figure 10 The definition of the crack depth and the crack initiation angle.

4.2. Introduction to electron matter interactions

An electron beam passing through the sample interacts with the atoms composing its structure and produces various types of interactions (Figure 11), usually classified into two families:

- The elastic interactions, if the electron has the same energy before and after the interaction (same kinetic energy and same wavelength).

Among the elastic electrons having crossed over the sample, it is possible to distinguish an electron beam transmitted parallel to the incident beam and diffracted beams following Bragg's law. The information contained in these diffracted and transmitted beams give information on the crystal structure and allows the formation of TEM images and diffraction patterns.

The electrons diffusing elastically, emerging from sample surface, are named backscattered electrons. The study of the diffraction of these electrons is the basis of the electron back scatter diffraction (EBSD) technique.

Both TEM and EBSD observations were used to characterize strain features at both the grain and the dislocation scales.

- The inelastic interactions occur when the electron energy kinetics and/or wavelength are modified during the interaction with the nuclei.

The attraction of the nuclei causes a deceleration of the electrons and thus a loss of energy. This lost energy is delivered in the form of X-rays. The collection of these X-ray emissions is the basis of energy dispersive X-ray spectroscopy (EDS or EDX) technique.

Furthermore, some displacement of internal electron resulting from the impact of the incident electron beam can occur. During this interaction these electrons lose some of their energy. In this case, the energy lost by electrons is characteristic of the ionized atomic element. The measurement of these energy losses can be achieved by a spectrometer. This spectrometric measurements are the basis of electron energy loss spectroscopy (EELS).

Both EDX and EELS were used to characterize local chemical compositions in the TEM.

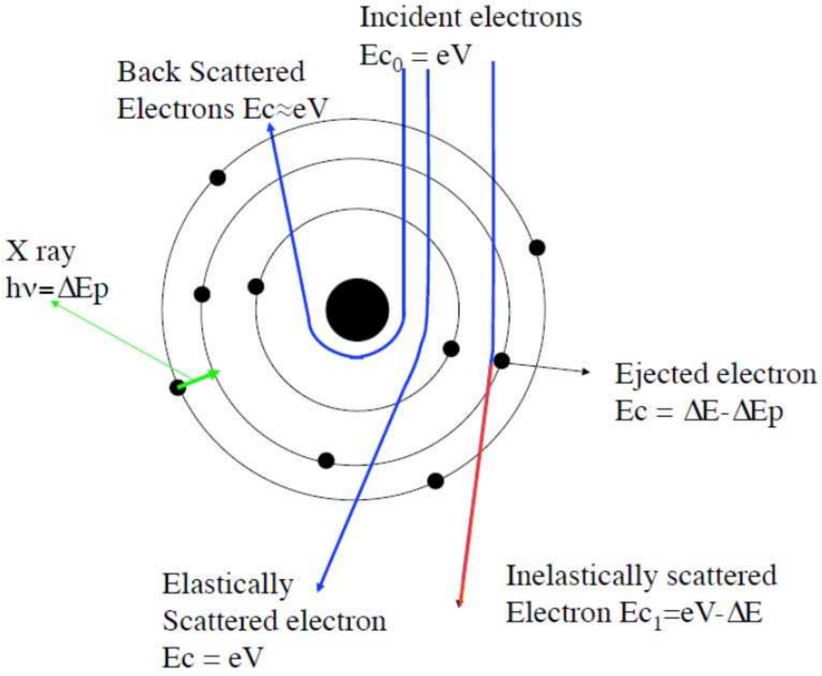

Figure 11 □Basis of electron matter interactions

4.3. Scanning Microscopy

4.3.1. Imaging

The analysis of samples and fracture surfaces were conducted on a scanning microscope (LEO SUPRA35) equipped with a Field Emission Gun (FEG). The acceleration voltage is set to approximately 15 kV, which corresponds to a resolution of about 1.5 nm.

- Protocol of crack propagation measurements

In a first approach, it was assumed that under loading, the stress at the crack tip has to reach a critical value to allow a crack extension, on a distance which is function of mechanical and environmental local conditions. The crack extension process involves the creation of successive fatigue striations (Figure 12) that correspond to each main crack advances. This assumption will be discussed in Chapter 4. Stress concentration at the site where each crack stops results in a plastic strain localization (misorientations in crystal lattice (Figure 13)) that remains even after the crack have propagated.

Fracture surface observations highlight some aspects of the environmental effects on fatigue. The quantification of propagation was performed by measuring the inter striation distances on fracture surfaces according to the following procedure:

- Identification of ductile fracture area and initiation site (Figure 14).
- Drawing of an arbitrary line from initiation area to the final ductile fracture (crack extension path).
- Measurement of spaces between striations along this line (red cross), as a function of the distance from the assumed initiation site. 10 interstriation distances were measured at each point and an average value was estimated.

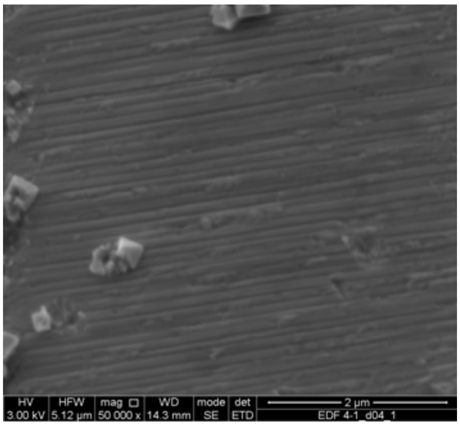

Figure 12 □Fracture surface, $\Delta\varepsilon_t/dt=0.4\%/s$, $\Delta\varepsilon_t/2=0.25\%$, 300°C, PWR (at 400 µm from initiation site).

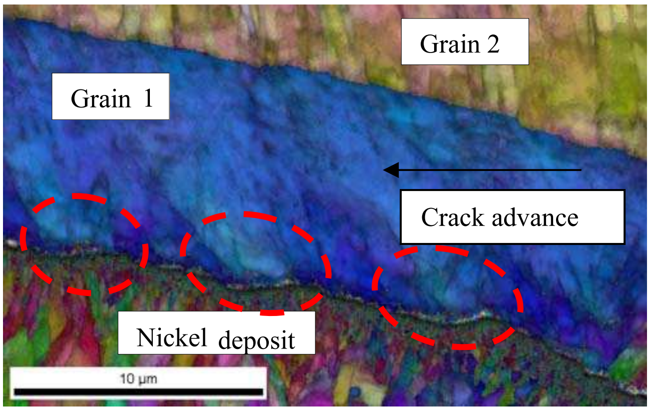

Figure 13 □Inverse pole figure, $\Delta\varepsilon_t/dt=0.4\%/s$ $\Delta\varepsilon_t/2=0.25\%$, 300°C, PWR, focusing on emerging striations on crack flanks.

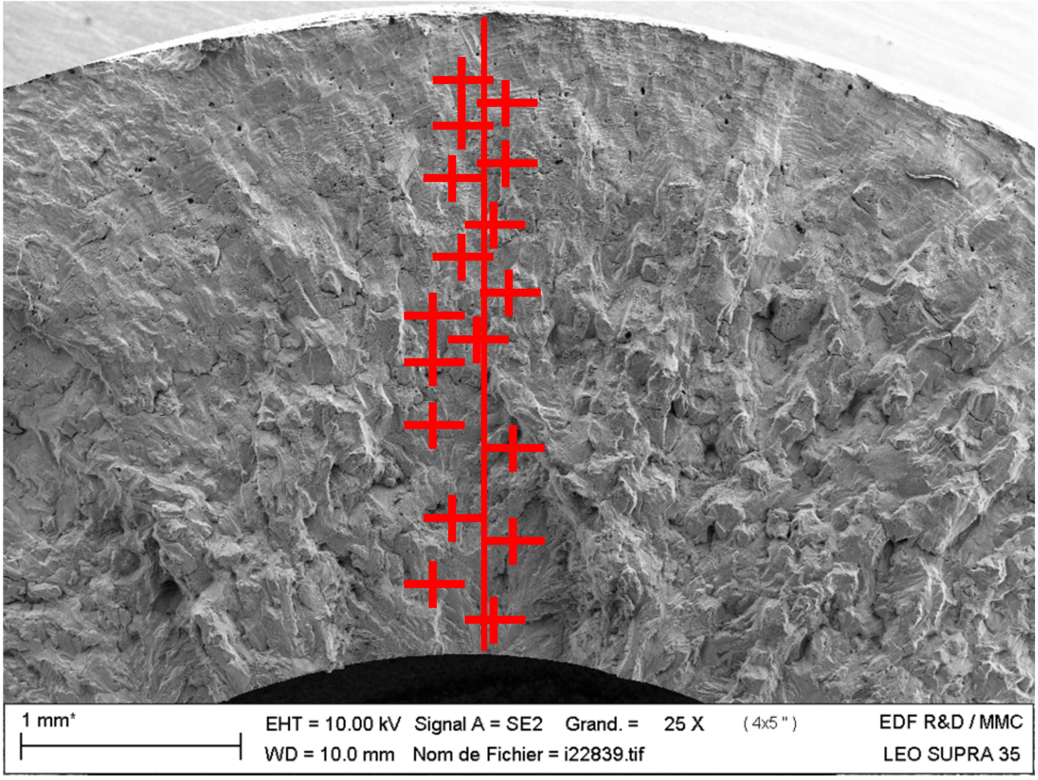

Figure 14 □Fracture surface of 1630 MHI 04, $\Delta\varepsilon_t/2=0.5\%$, 0.004%/s, As-received, PWR primary water at 300°C, general view.

4.3.2. Electron diffraction

Derived from the scanning electron microscopy, EBSD uses the ability of electrons to be diffracted on a crystal lattice. Indeed, the incident electrons diffuse into the material and those following Bragg law are diffracted by crystallographic planes forming Kikuchi lines. These lines provide information about the symmetry and the orientation of the crystal lattice.

The principle of EBSD is to focus a beam of electrons (at an acceleration voltage higher than 20 kV) on a polished sample tilted to 70° to the horizontal (Figure 15) in order to identify Kikuchi pattern formed projected on a phosphorus screen (Figure 16). Mapping of grain orientation can be obtained by scanning the electron beam at the surface of the sample. A surface finish without any residual cold work due to the polishing process is needed because electron/matter interactions occur below the first 300 nm in depth.

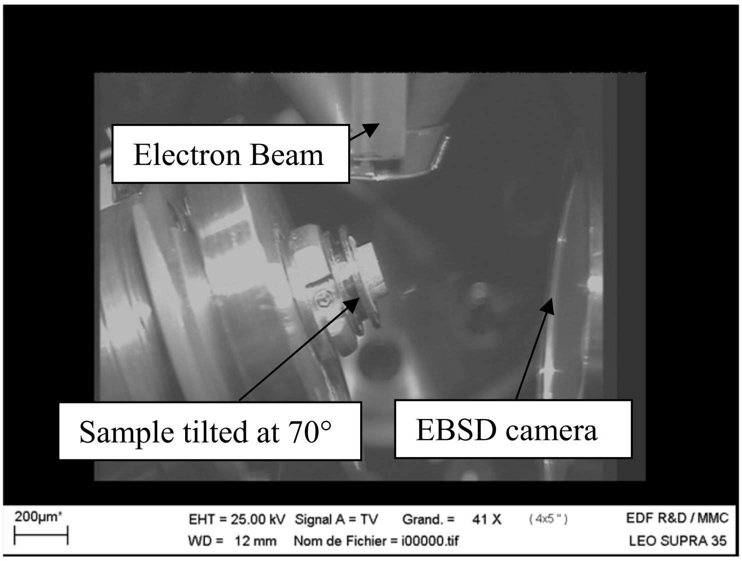

Figure 15 – SEM chamber with the EBSD camera.

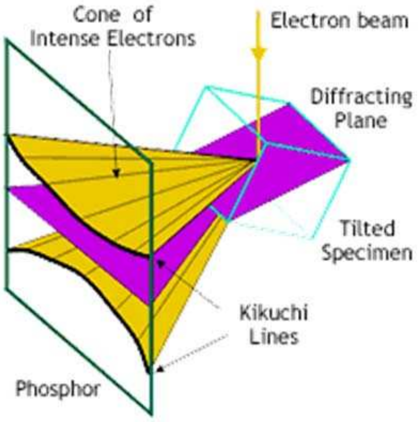

Figure 16 – Projection of Kikuchi lines on a phosphorus screen.

- Angles between slip emergence and loading axis measurements

In the LCF of FCC alloys, it is well known that fatigue crack initiation processes are often associated with slip band emergence at the free surface. It was widely shown that the emergence of persistent slip bands at free surfaces of single crystals in the form of extrusion–intrusion pairs are preferential sites for crack initiation.

A specific program was developed in order to characterize and qualify the most probable representative slip activity at the surface of a sample based on EBSD results. The aim of this program was to correlate slip activity in the near surface grains and the crack initiation angles measured on cross section. After each fatigue test, samples were cut and polished along the axial direction as presented in section 4.1. On the same cross section, a 1 mm² EBSD map (corresponding to more than 100 grains) was acquired with a 0.5 µm resolution in order to determine an average orientation per grain The higher Schmid factor of each slip systems presented in Table 1 was calculated for each grain. It was assumed that the most probable active slip system will be the one with the highest Schmid factor without taking into account the potential effect of grain interactions. The angle on an axial cross section between the free surface and each slip plane was also evaluated for each grain (Figure 17) and compared to the distribution of the emergence angle of cracks observed by optical microscopy (Figure 18).

Table 1- List of octahedral slip systems. Schmid and Boas notations are indicated into brackets.

System number *s* (Schmid & Boas notation)	Slip plane			Slip direction		
1 (B4)	1	1	1	$\bar{1}$	0	1
2 (B2)	1	1	1	0	$\bar{1}$	1
3 (B5)	1	1	1	$\bar{1}$	1	0
4 (D4)	1	$\bar{1}$	1	$\bar{1}$	0	1
5 (D1)	1	$\bar{1}$	1	0	1	1
6 (D6)	1	$\bar{1}$	1	1	1	0
7 (A2)	$\bar{1}$	1	1	0	$\bar{1}$	1
8 (A6)	$\bar{1}$	1	1	1	1	0
9 (A3)	$\bar{1}$	1	1	1	0	1
10 (C5)	1	1	$\bar{1}$	$\bar{1}$	1	0
11 (C3)	1	1	$\bar{1}$	1	0	1
12 (C1)	1	1	$\bar{1}$	0	1	1

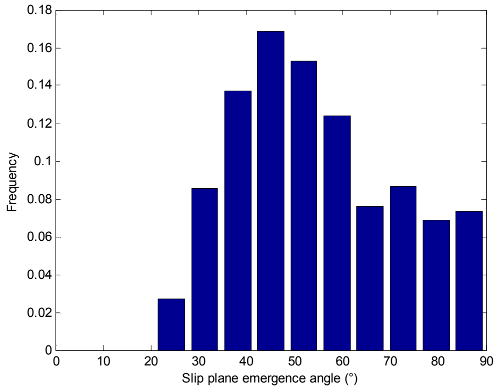

Figure 17 Slip plane emergence angles.

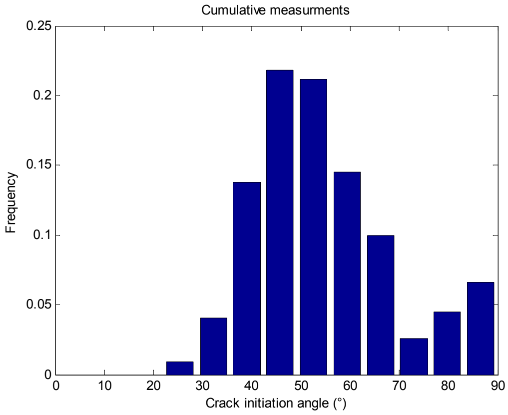

Figure 18 Distribution of crack initiation angles.

4.4. Transmission electron microscopy (TEM)

The TEM used for observations was a FEI TECNAI 200 kV, equipped with a Field Emission Gun (FEG). The electron source is a Schottky FEG. The accelerating voltage used is 200 kV and the spatial resolution of 0.27 nm.

The TEM used for Electron Energy Loss Spectroscopy (EELS) was a 80-300kV FEI TITAN, equipped with a FEG, a monochromator and a probe corrector.

4.4.1. Image and diffraction

The transmission electron microscopy (Figure 19) is based on the principle of electron diffraction. It consists of placing a sample thin enough to be traversed by a coherent electron beam. Elastic scattered electrons are then used to visualize the diffraction pattern projected in the focal plane of the objective lens and an image of the illuminated area (corresponding to a Fast Fourier transform (FFT) of the diffraction pattern) in the image plane of the same lens.

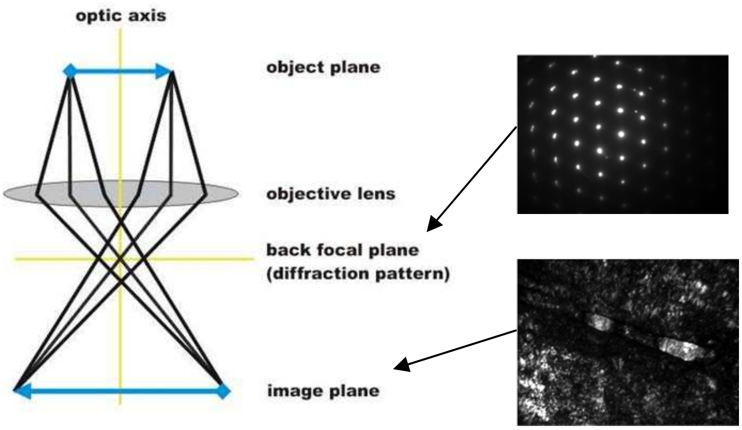

Figure 19 - TEM diffraction and image

The main contrast of crystalline materials in a TEM is a diffraction contrast. In order to achieve dislocation images, the sample is usually placed in a two-beam condition: the image was performed using the transmitted beam and only one diffracted beam.

In order to be in a two-beam condition, the studied area is first set in the zone axis. Then, the grain was tilted moving slightly away from the zone axis so as to have no more than the transmitted beam and one diffracted beam (vector g) excited. In this case a single family of crystallographic planes was then in diffraction conditions. A Bright Field image (BF) is obtained by selecting only the transmitted beam with an objective aperture (Figure 20). If only the diffracted beam is selected with the same objective aperture, a dark field image is obtained (Figure 21).

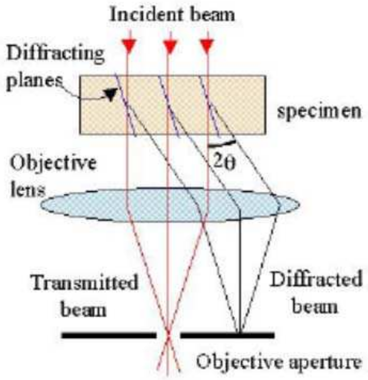

Figure 20 –Bright field image

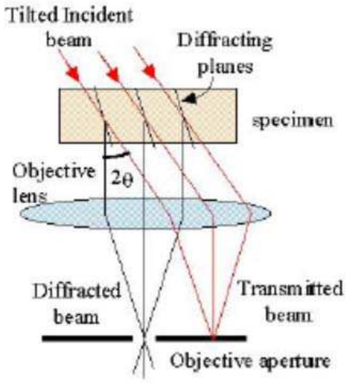

Figure 21 –Centered dark field image

4.4.1. Energy Dispersive X-ray analysis (EDX)

A sample, when interacting with an electron beam, generates characteristic X-rays which allow a local analysis of the chemical composition. In order to achieve an EDX analysis, the microscope was used in STEM mode to work with a focused probe which moved along profile. At each point of this profile, the exposure time is fixed between 60 and 120 s to obtain a result with a confidence index of about 90%. In addition, an image was automatically collected between two EDX pointing to control the possible drift of the sample. To optimize the detection of X-rays, the TEM sample must be inclined of 20 ° in the microscope, to face to the detector.

4.4.2. Electron Energy Loss Spectroscopy (EELS)

As previously shown, the inelastic scattering results from interactions between incident electrons and electrons of the sample. During this process, the kinetic energy of the incident electrons is transferred in the form of potential energy to the sample. During this exchange of energy, the trajectory of the incident electrons is deflected (a few mrad). A spectrum of energy losses represents the number of electrons detected as a function of the energy lost during crossing the sample. In the case of thin samples, the predominant peak, called zero loss, corresponds to electrons having passed through the sample without undergoing any interaction. After 35 ev of energy loss, the spectrum of energy (Figure 22) consists of a continuous background which is superimposed with characteristic edges of the elements present in the area and crossed by the electrons

By placing a slit at a specific value of energy loss, it was possible to get an Energy Filtered Transmission Electron Microscopic (EFTEM) image. This image contains the energy loss corresponding to the chemical element, but also the continuous background. In order to remove the continuous background from the image, a combination of three images was used: two images before the peak characteristic of the element (corresponding to Pre Edge 1 and Pre Edge 2 in Figure 23) to model the continuous background at the peak and an image after the studied edge (corresponding to Post Edge in Figure 23). The comparison of the different acquired images allows to qualitatively and quantitatively establish the local chemical composition (Figure 24 and Figure 25).

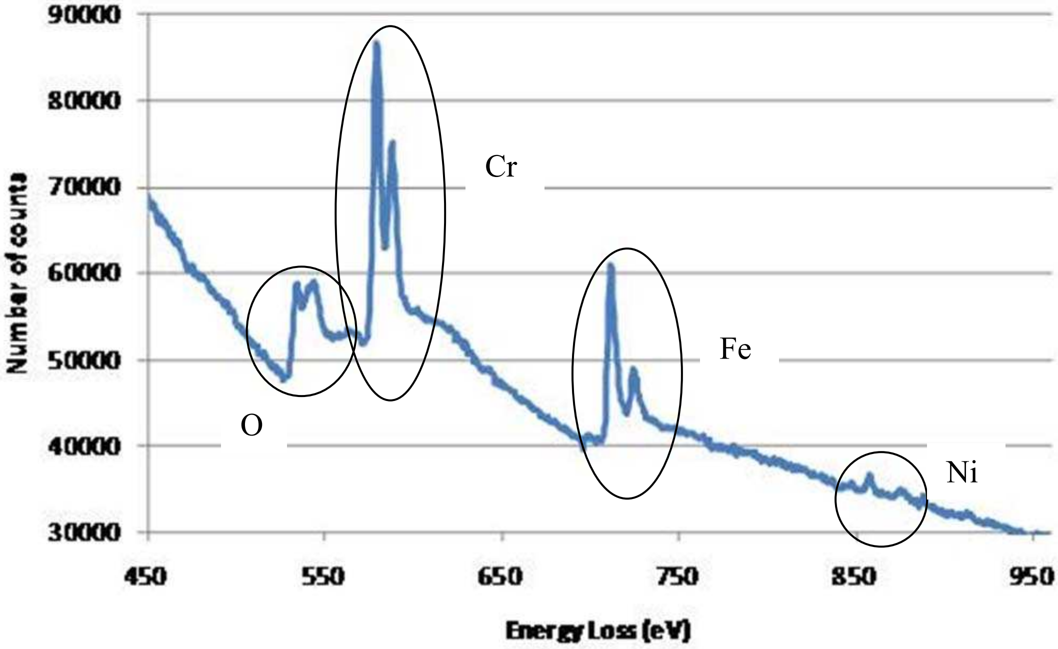

Figure 22 Typical EELS spectrum obtained on a 304L oxidized in PWR primary environment. EELS characteristics edges.

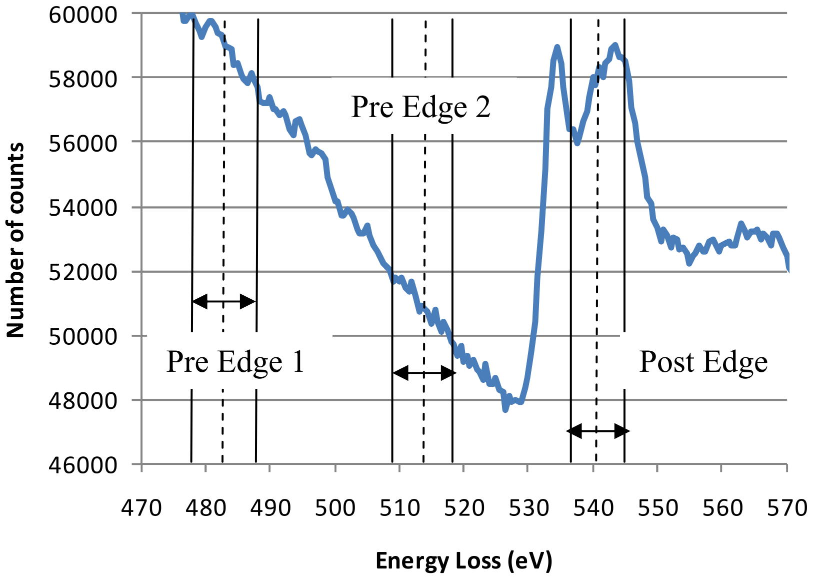

Figure 23 Typical EELS O edges obtained on a 304L oxidized in PWR primary environment.

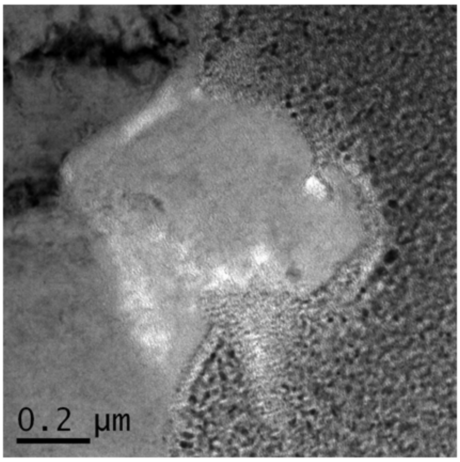

Figure 24 EFTEM Zero loss Image.

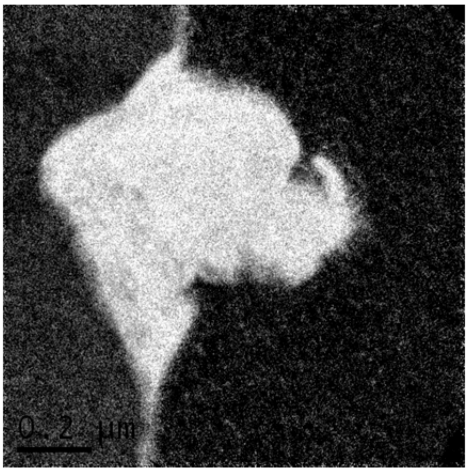

Figure 25 EFTEM O map.

4.5. Dual Beam

The combination of a SEM (electronic column) and a FIB (Focused Ion Beam) on the same instrument is named Dual Beam. This microscope allowed to slice the material or make a Pt/C deposition at its surface in order to prepare TEM samples, automatic slice and views and 3D EBSD. Such characterizations were performed on Helios Nanolab FEI dual beam. This dual beam has a Schottky field emission gun column, Ga ion beam column, Pt and C gas injection system, carbon selective etching system, 3D EBSD system, EDX detector and Autoprobe internal micromanipulator.

4.5.1. Dual beam TEM Sample preparation

The dual beam can be used in order to produce TEM sample in specific areas such as fatigue crack initiation, and specific locations on fracture surface with high accuracy. However, the size of the prepared blades cannot exceed 15-microns length and 10-15 microns in width in the case of the material of interest. LEGRAS presented a method to produce such TEM sample in this particular dual beam [2]. The TEM sample preparation protocol includes the following steps:

- Identification of an area of interest. (Figure 26).
- 0.5 µm Pt deposit using the electron beam. (Figure 27).
- 4-5 µm Pt deposit at the surface using the ion beam. (Figure 28).
- Rough milling around the area of interest using a 21 nA intensity (Figure 29).
- Cleaning of the sample at 2.8 nA up to a thickness of 2µm. (Figure 30).
- Preparation of the lift out at 0.92 nA (Figure 31).
- Approach and weld of the Omniprobe (Figure 32).

- Split (Figure 33) and lift out (Figure 34) of the TEM sample.
- Weld of the TEM sample on a copper made grid. (Figure 35).
- Split of the omniprobe (Figure 36).
- Thinning (Figure 37).

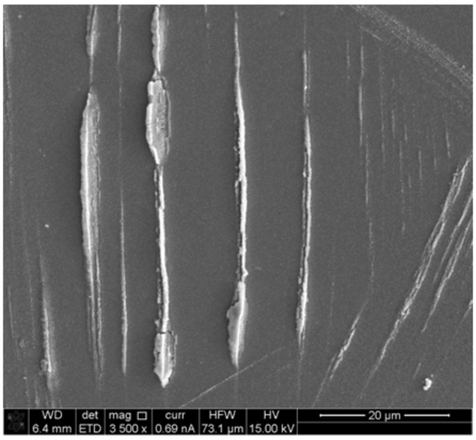

Figure 26 □Area of interrest

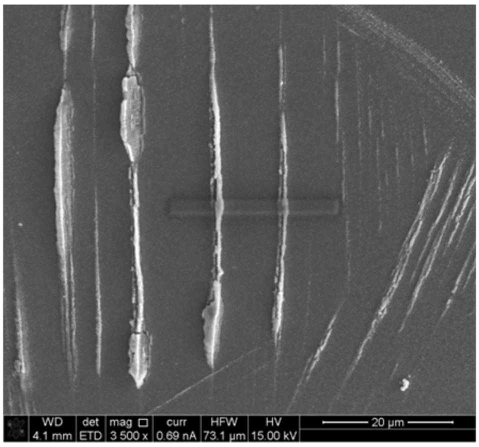

Figure 27 □Electronic Pt deposit

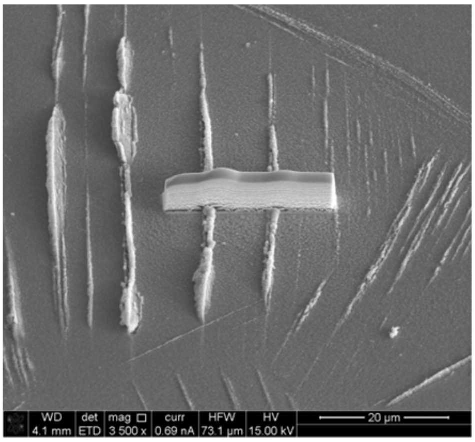

Figure 28 □Ionic Pt deposit

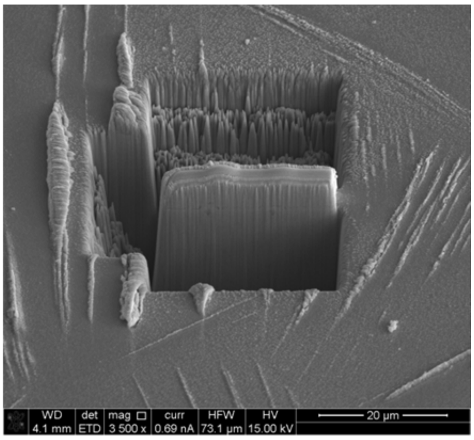

Figure 29 □Rough milling

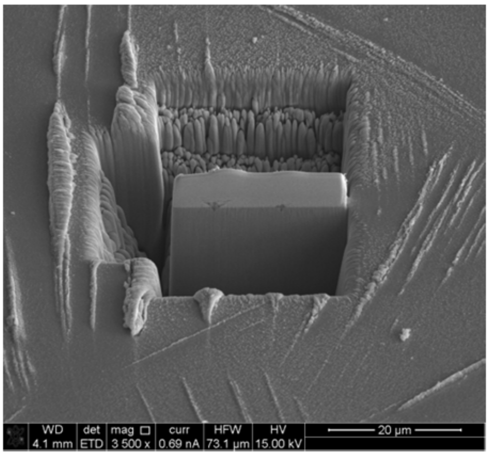

Figure 30 □Cleaning

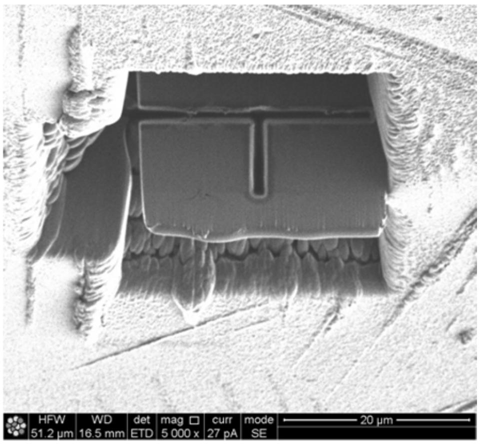

Figure 31 □Preparation of the lift out

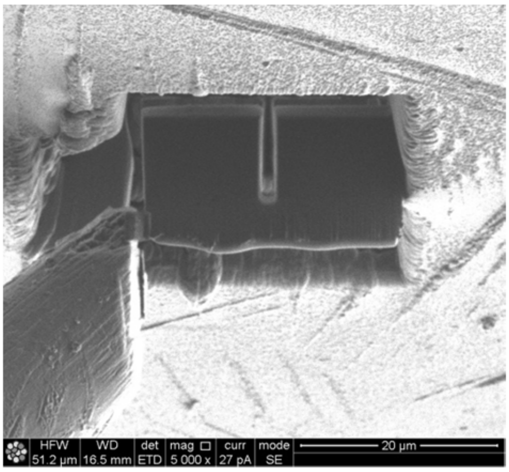

Figure 32 □Weld of the Omniprobe

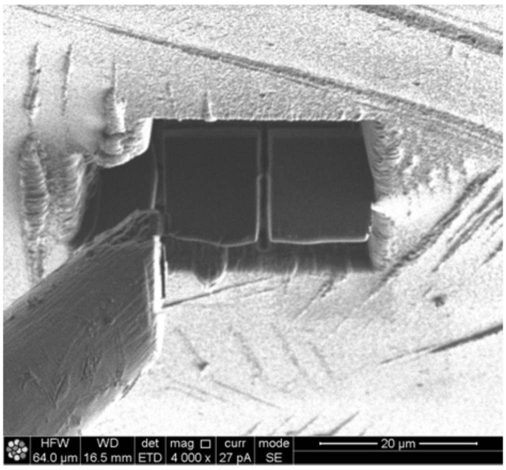

Figure 33 □Split of the TEM sample

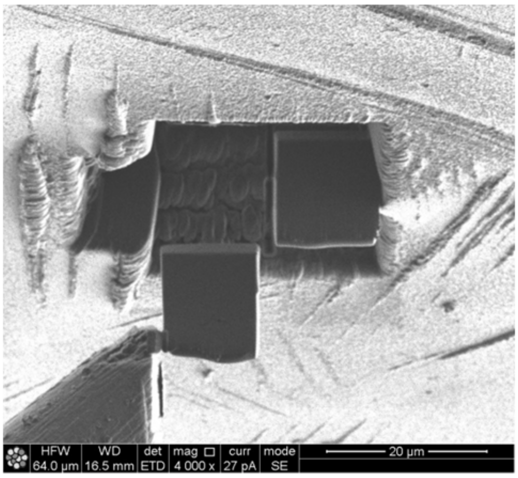

Figure 34 □Removal of the TEM sample

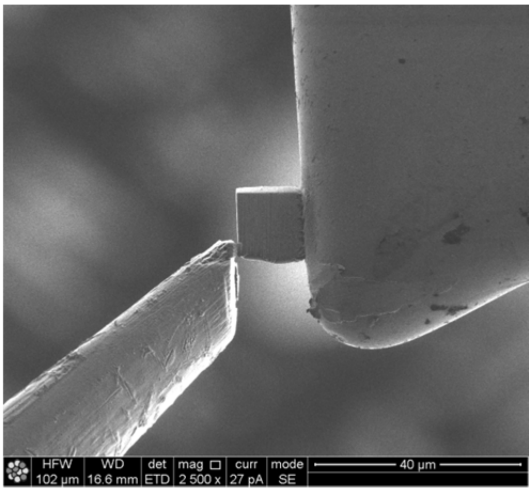

Figure 35 □Weld of the TEM sample on a Cu grid

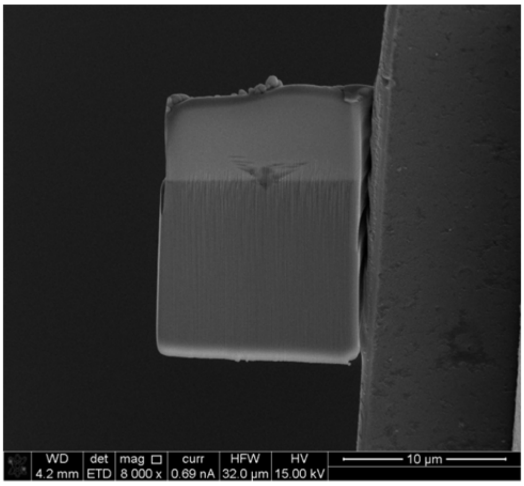

Figure 36 □Position of the TEM sample on the Cu grid

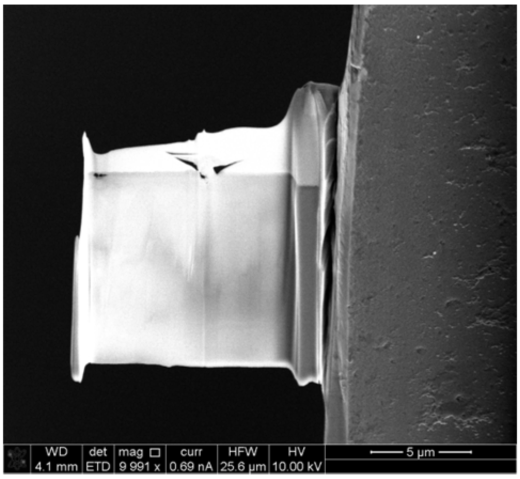

Figure 37 □View of the TEM sample after thinning

4.5.2. Dual beam 3D imaging

In the SCC field, several studies enlightened the significant effect of strain localization on SCC initiation [3]. This aspect was still not studied in terms of corrosion-fatigue of stainless steels in PWR Primary environment. Therefore this type of approach was duplicated in the current study for investigating mechanisms on fatigue crack initiation and crack propagation.

A possible way to qualitatively and quantitatively evaluate such interactions was done using the Helios microscope. The approach named “slice and view” consists in a succession of SEM pictures in SE mode, after removing a 10 nm thick slice with the ion beam. The 3D oxide reconstruction protocol included the following steps:

- Identification of a representative area.
- 0.5 µm Pt deposit using the electron beam (Figure 38).
- 2 µm Pt deposit at the surface using the ion beam (Figure 38).
- Rough milling around the area of interest at the highest ion beam current available on the ion beam (Figure 38).
- Slicing every 10 nm or 20 nm at 0.96 nA, 30 kV using the ion beam followed by a picture using the electron beam at 5 kV, 0.17 nA (corresponding to a spatial resolution of 1 nm) up to the end (Figure 39).

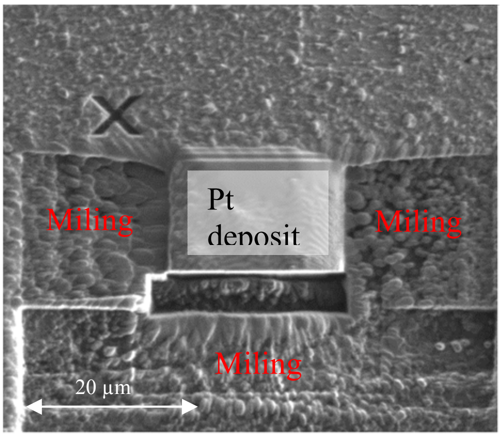

Figure 38 – Sample preparation, EDF 8-1, $\Delta\varepsilon_t/dt=0.4\%/s$, $\Delta\varepsilon_t/2=0.5\%$.

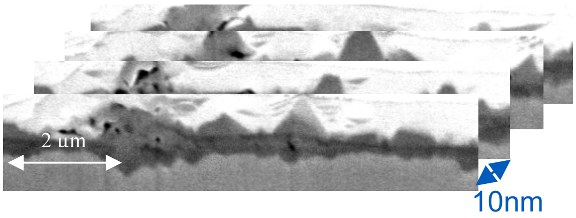

Figure 39 – Succession of SEM pictures, EDF 8-1, $\Delta\varepsilon_t/dt=0.4\%/s$, $\Delta\varepsilon_t/2=0.5\%$, (1.6µm * 20µm 10nm slice).

Series of pictures were combined in 3 dimensions using Amira software. Each separated different layers (Figure 40) were rebuilt into a 3D-image using their grayscale 8 bit values (Figure 41 and Figure 42). The main difficulty of this approach was to resolve the different layers using grayscale values which depend on the acquisition parameters. This reconstruction allowed quantifying the thickness of the Cr-rich layer. On the example presented in Figure 40, oxide penetrations have been measured and reported in the histogram (Figure 43). Using the 3D reconstruction, this preferential oxidation was observed where a significant oxide penetration along shear bands emerged on the surface (Figure 44).

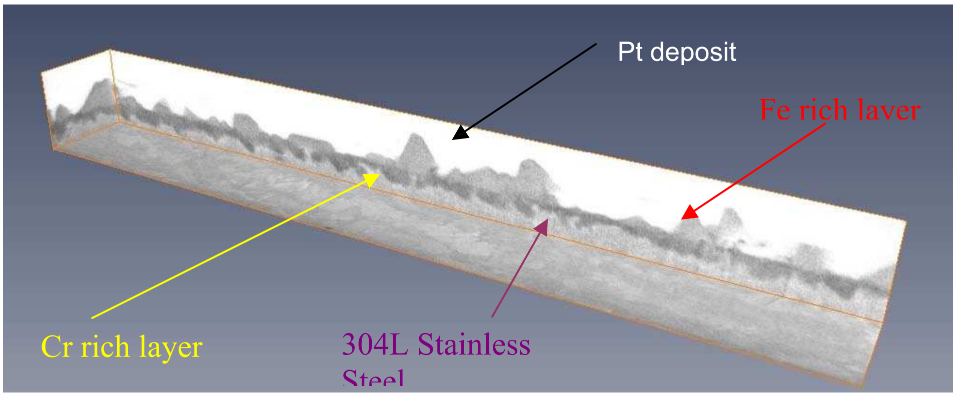

Figure 40 □Layers separation using grayscale, EDF 8-1, $\Delta\varepsilon_t/dt=0.4\%/s$, $\Delta\varepsilon_t/2=0.5\%$, (1.6 µm * 20 µm).

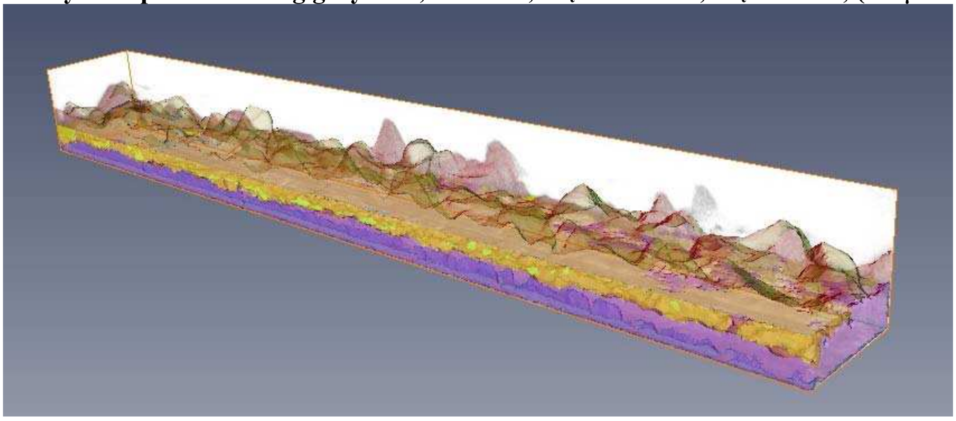

Figure 41 - 3D layer separation, EDF 8-1, $\Delta\varepsilon_t/dt=0.4\%/s$, $\Delta\varepsilon_t/2=0.5\%$, (1.6 µm * 2 µm * 20 µm, 10 nm per slice)

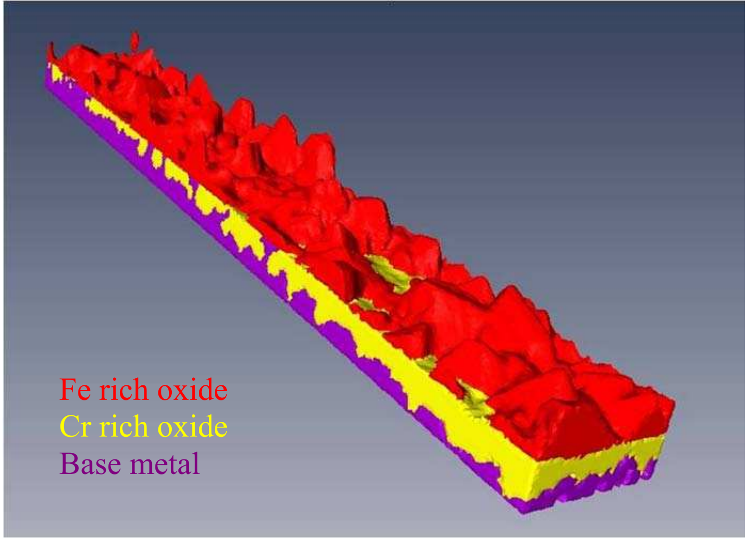

Figure 42 □3D reconstruction, EDF 8-1, $\Delta\varepsilon_t/dt=0.4\%/s$, $\Delta\varepsilon_t/2=0.5\%$, (1.6 µm * 2 µm * 20 µm, 10 nm per slice)

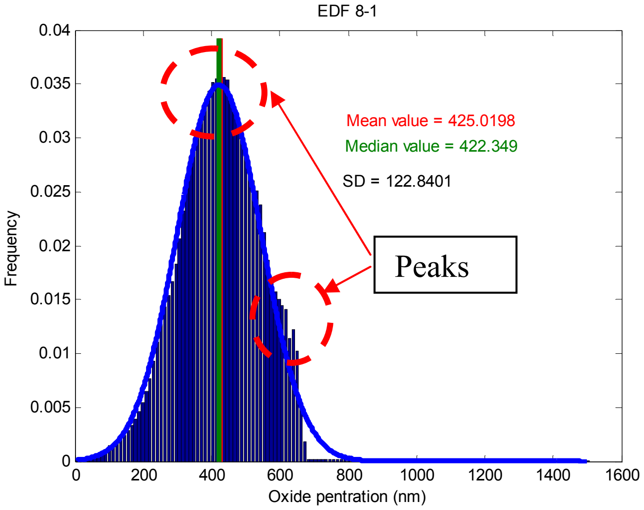

Figure 43 Cr-rich layer oxide penetration , EDF 8-1, $\Delta\varepsilon_t/dt=0.4\%/s$, $\Delta\varepsilon_t/2=0.5\%$, 32 µm².

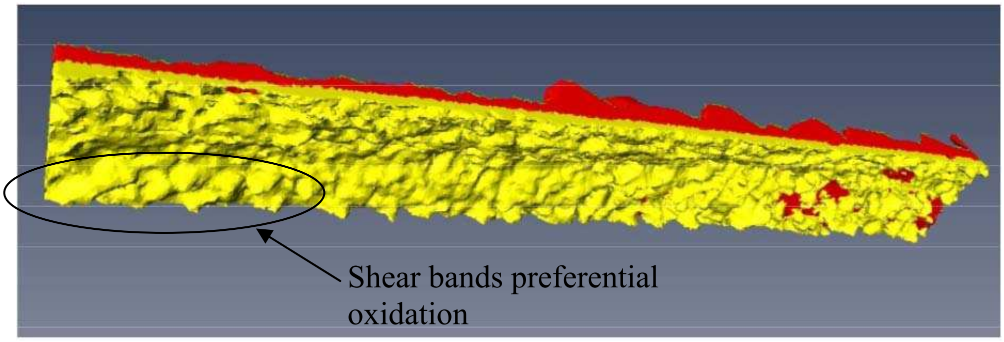

Figure 44 3D reconstruction focusing on Cr-rich layer, EDF 8-1, $\Delta\varepsilon_t/dt=0.4\%/s$, $\Delta\varepsilon t/2=0.5\%$, (1.6 µm * 2 µm * 20 µm, 10 nm per slice).

4.5.3. 3D EBSD

Interaction between strain localization (shear bands) and oxidation could promote fatigue crack initiation. In order to evaluate the environmental effect, 3D EBSD was coupled with 3D oxide reconstruction using a sample tested at $\Delta\varepsilon_t/2=0.5\%$ in PWR primary environment at 300°C and at a strain rate of $\Delta\varepsilon_t/dt=0.004\%/s$ using the following procedure:

Lift out of the cube:

- Electronic platinum deposit followed by an ionic deposition at the surface of the sample up to a 3 µm thickness.
- Slicing around the cube corresponding to a 15 µm * 15 µm surface for a 20 µm depth (30 kV, 21 nA).
- Slicing under 30 kV, 21 nA.
- Lift out of the cube using an Omniprobe and weld on a silicon wafer (Figure 45).

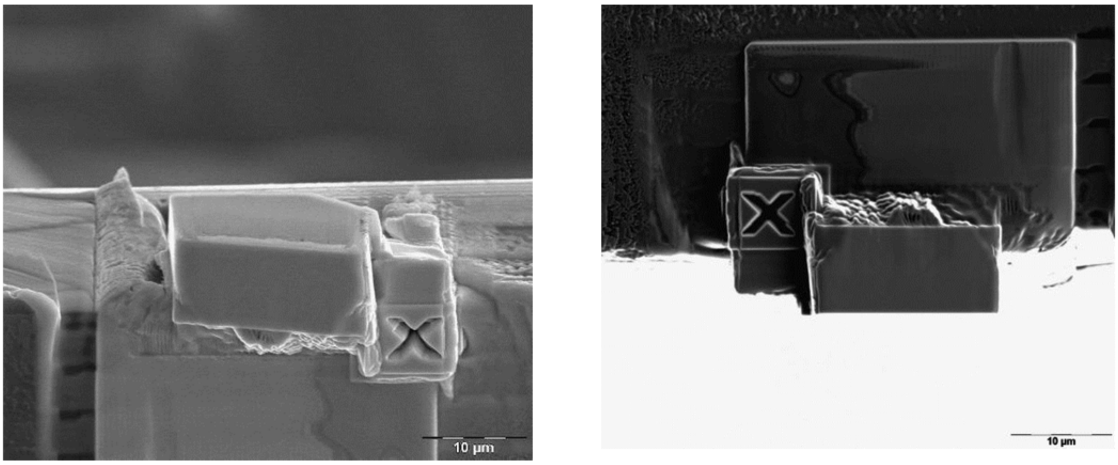

a) View from the electronic column. **b) View from the ionic column.**

Figure 45 □Sample vue before acquisition.

3D EBSD Acquisition

- 3D EBSD Acquisition was performed using EBS3 FEI software coupled with Oxford Fast camera. This method consists in acquiring an EBSD using a 50 nm-step size followed by a 50 nm-slice up to 55 slices in that particular test. EBSD acquisition parameters were binning 4x4, 13 ms waiting time, no frame averaging. Slicing was done using a 30 kV, 0.46, nA beam.

Data post analysis

- 3D EBSD
    - Conversion of 50 EBSD maps from Oxford HKL to OIM analysis, calculation of a kernel average misorientation (KAM) of the 5th order for each slice.
    - Separation of KAM using misorientation angles from 0° to 3° each 0.5° in grey scale values (Figure 46). In this analysis, no physical basis is given to misorientations values. The only purpose of these values is to be able to separate microstructural object.
    - Data export into images in order to conserve one data per pixel.
    - 3D reconstruction using AMIRA software (Figure 47).

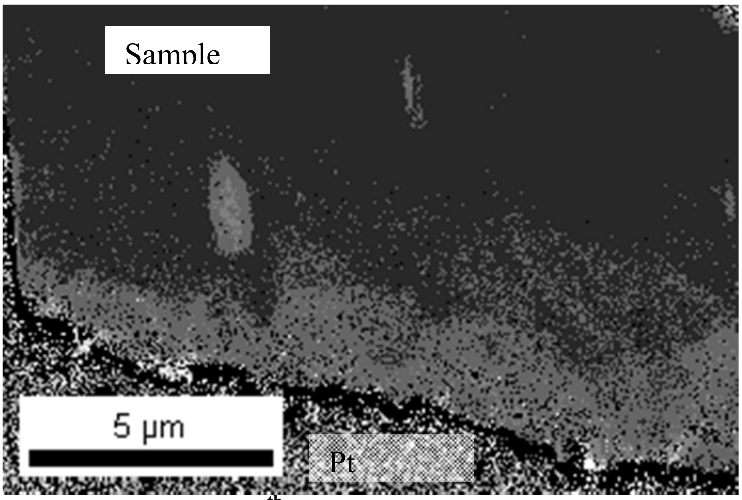

Figure 46 KAM at 5th order separate using grayscale values.

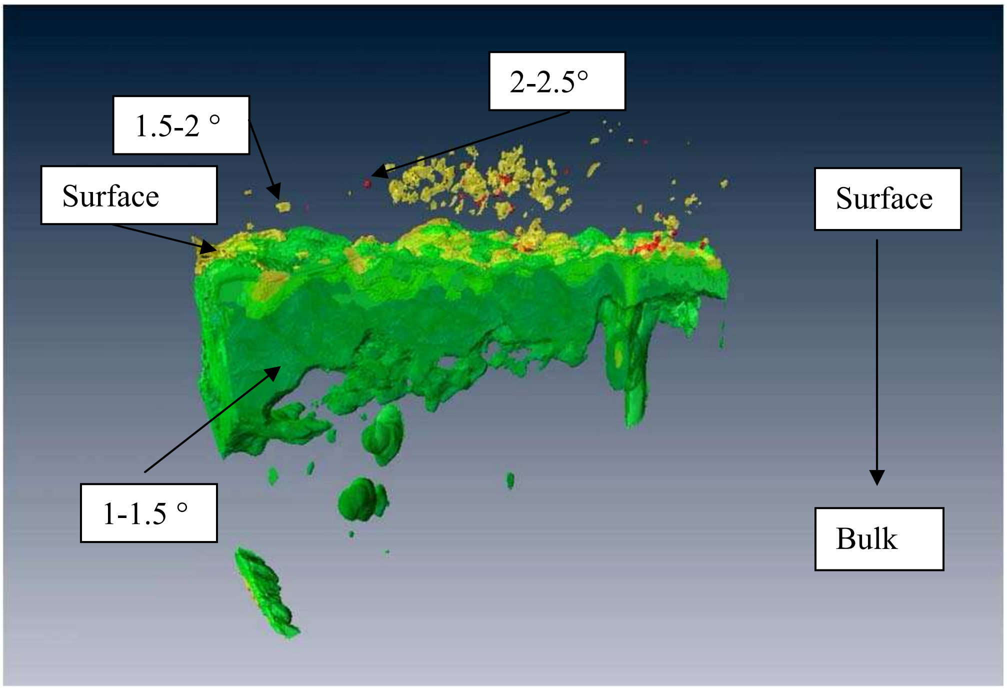

Figure 47 3D EBSD reconstruction of misorientations (12 µm * 3 µm).

- **3D oxyde reconstruction**
    - Acquisition of images using direct Backscattered detector of the EBSD camera. Images presenting an electronic noise were filtered using « Image J » software using a Fast Fourier Transform. It was impossible to separate the two oxide layers using this detector.

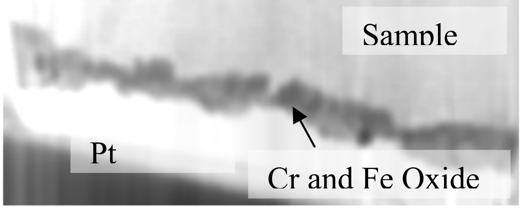

Figure 48 FFT filtered image.

- The 3D image was then reconstructed using Amira software (Figure 49)

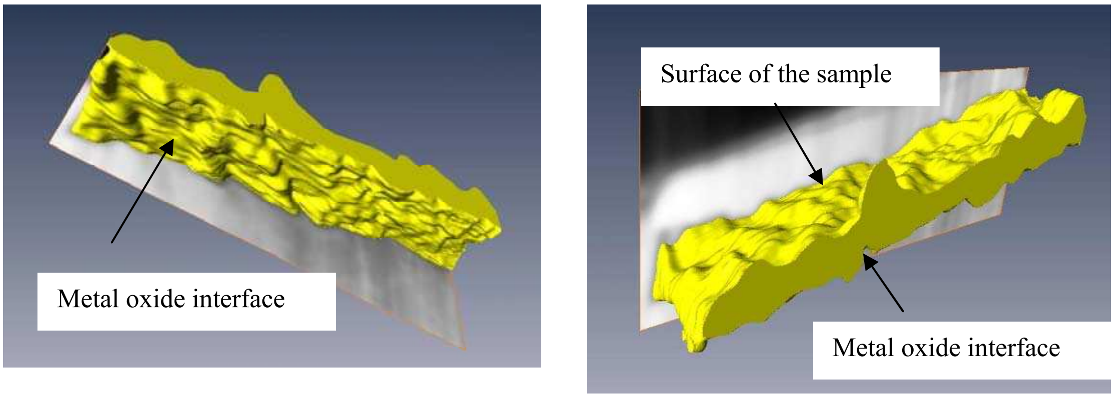

Figure 49 □3D oxyde reconstruction (12 µm * 3 µm).

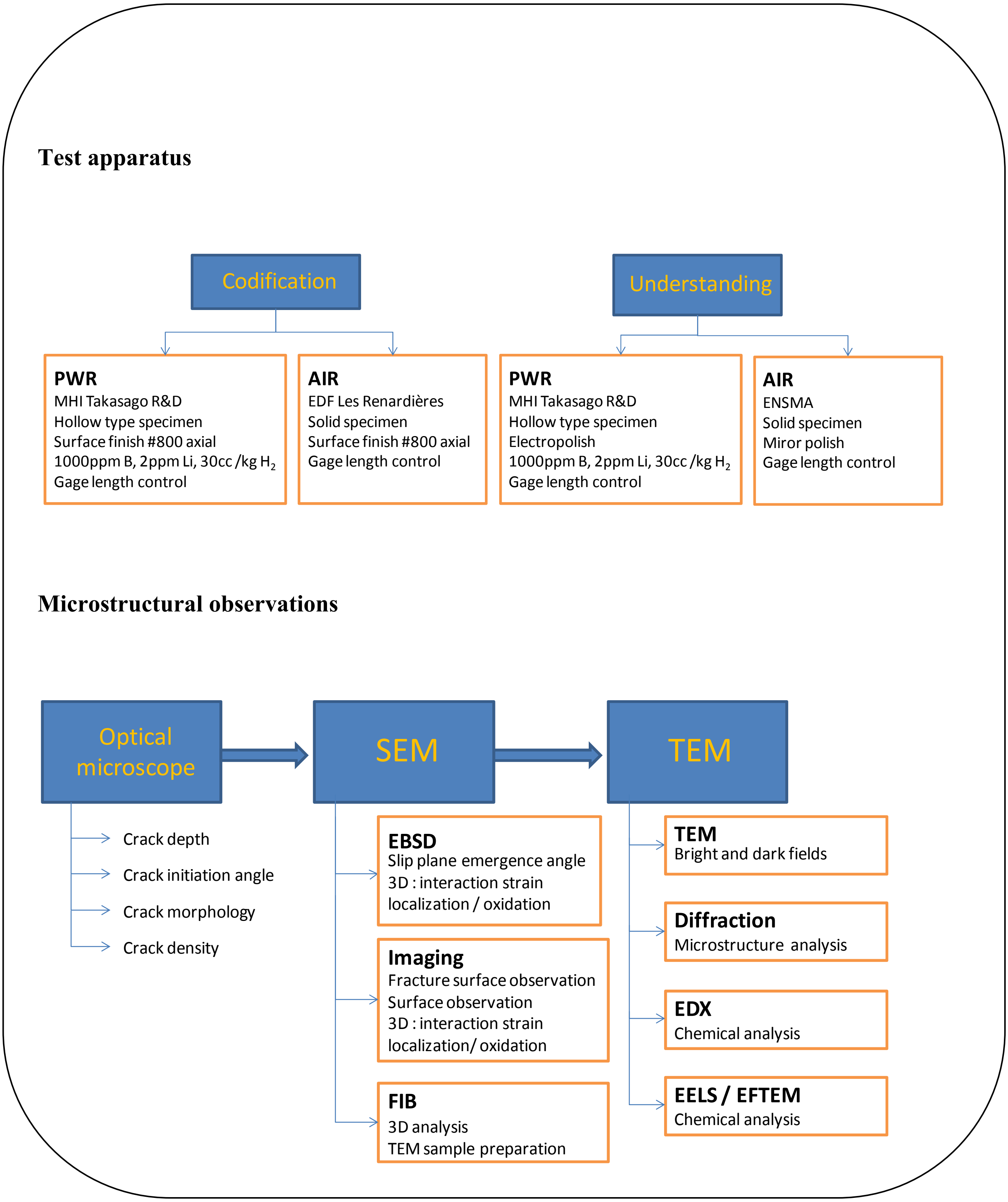

Figure 50 Global approach

---

[1] **L. DE BAGLION**, “Comportement et endommagement en fatigue oligocyclique d'un acier inoxydable austénique 304L en fonction de l'environement (air, vide primare REP) à 300°C”, PhD Thesis ENSMA, 06/2011.

[2] **L. LEGRAS** “Préparation d'échantillons par microscopie double faisceau pour observations par MEB équipé d'un detecteur STEM ou pour MET” Préparation des échantillons pour MEB et Microanalyses EDP Sciences, 2011

[3] **T. COUVANT, L. LEGRAS, A. HERBELIN, A. MUSIENKO, G. ILEVBARE, D. DELAFOSSE, G. CAILLETAUD, J. HICKLING**, “Development of understanding of the interaction between localized deformation and SCC of austenitic stainless steels exposed to PWR primary environment”, 14th International Conference on Environmental Degradation of Materials in Nuclear Power Systems Virginia Beach, August 23-27, 2009

CHAPTER 3: reference tests and characterizations

List of acronyms

AR: As-received
CEAT: Centre d'Essais Aeronautique de Toulouse
CR: Cold Rolling
CT: Cold Tension
EAF: Environmentally assisted fatigue
EBSD: Electron BackScattered Diffraction
EDF: Electricité de France
ENSMA: Ecole Nationale Supérieure de Mécanique et d'Aérotechnique
GE: General Electric
HAADF: High Annular Angular Dark Field
PSB: Persistent Slip Band
PWR: Pressurized Water Reactors
SFE: Stacking Fault Energy
SS: Stainless Steels
STEM: Scanning Transmission Electron Microscopy
TEM: Transmission Electron Microscope
TG: TransGranular
USNRC: United States Regulatory Commission

Summary

1. Introduction

The current codification considers the deleterious effect of the PWR primary water by introducing the Fen factor established at a given temperature into the design reference curve obtained in air at room temperature. Even if, its known that up to 300°C, the fatigue life in air environment is negligibly affected by the temperature [1], its contribution in the deformation mechanisms cannot be underestimated [2]. In order to evaluate the contribution of the environment (air or PWR primary water) on the cracking and deformation mechanisms, it is needed to evaluate them at a similar temperature (300°C). The first step consists in carrying out some tests in air environment on a 304L material:

- Concerning the codification support objective, the goal was to evaluate the effect of a prior cold rolling on both the cyclic stress-strain behavior and the fatigue life in air environment at 300°C.
- Concerning the objective of improving the understanding of EAF damage mechanisms, the first purpose was to examine the difference in deformation structure during cycling between the as-received and the strain-hardened 304L stainless steel at 300°C. The second purpose was to provide more information about the characteristics of the fatigue crack initiation mechanisms in the air environment at 300°C.

The results exposed in this chapter will be compared and discussed with the results obtained in chapter 4 in PWR primary environment within the chapter 5.

.

2. Material of interest

The tested material is an AISI 304L stainless steel rolled plate (European specification X2 Cr Ni 18-10, AFNOR specification Z2 CN 18-10), 30mm thick, manufactured by Creusot-Loire Industrie (Heat number XY182, EDF batch number T218), annealed at 1100°C and water-quenched. The chemical composition of the material given in Table 1 is in good agreement with nuclear French requirements RCC-M 220. Metallurgical properties such as residual delta ferrite (δ-Fe), stacking fault energy (SFE) and martensitic transformation temperatures (M_s, Md_{30}) calculated using empiric formula reported in Chapter 1 [3,4] are given in Table 2.

Two samples, cut off from the original plate, were cold-worked by 1D-cold rolling (CR) at EDF, up to 5% and 10% reduction of thickness respectively. The corresponding generalized plastic deformation (1) was estimated respectively to $\varepsilon_p = 0.06$ and $\varepsilon_p = 0.12$. Each CR pass corresponds to a reduction of 0.5 mm. Final dimensions were 650 mm*150 mm*26.9 mm for the 10% CR plate and 400 mm*100 mm*28.5 mm for the 5% CR one. The corresponding mechanical properties are given in Table 3. Some other samples were submitted to a 10% prior Cold Tension (CT) and polished up to #800 along the axial direction to remove transverse scratches.

Figure 1 shows the first stages of the stress-strain curves obtained at 300°C. The mechanical properties of the as-received Heat XY182 reported in Table 3 are in good agreement with the RCC-M 3307 requirements. The yield stress increases with an increasing prior hardening level.

Figure 2 and Figure 3 show pole figures obtained at mid thickness of the plates using EBSD, revealing that the cold worked materials did not exhibit any clear anisotropy.

Table 1 - Chemical composition of Heat XY182.

Heat	**C**	**Cr**	**Ni**	**Si**	**Mn**	**S**	**P**	**Mo**	**Cu**	**N**
RCCM-220	<0.03	17-20	8-12	<1	<2	<0.03	<0.045	-	<1	-
XY182	0.029	18.00	10.0	0.37	1.86	0.004	0.029	0.04	0.02	0.056

Table 2 □Metallurgical properties of Heat XY182.

Heat	**δ-Fe (%)**	**SFE (mJ. m^{-2})**	**Ms (°C)**	**Md30 (°C)**
XY182	3.0	30	-274	13

Table 3 □Tensile properties of XY182.

	T (°C)	**Direction**	**Ys(MPa)**	**UTS (MPa)**	**El (%)**	**E (GPa)**
RCC-M 3307	20	T	>175	>490	>45	-
	350	T	>105	-	-	-
XY182 As-received	20	L	220	555	68	196
		T	220	546	68	192
	300	L	138	401	48	168
		T	136	402	46	196
XY182 5% CR	300	L	248	435	37	167
		T	248	438	31	166
XY182 10% CR	300	L	333	462	28	169
		T	320	468	30	170

---

(1) Generalized plastic strain as a function of rolling: $\varepsilon_p = \frac{2}{\sqrt{3}} \mathrm{Ln} \frac{e_i}{e_f}$ where e_i and e_f are respectively the initial and final thickness of the plate.

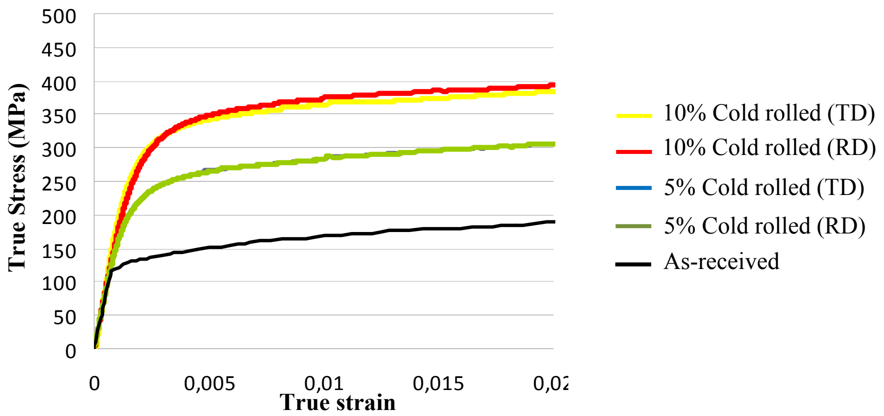

Figure 1 - Stress-strain curves of the different plates at 300°C.

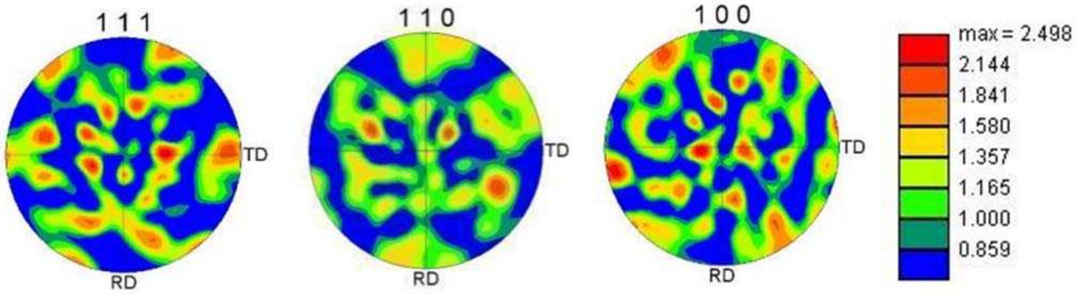

Figure 2 □Pole figure obtained on 5% cold rolled material along rolling direction. EBSD analysis.

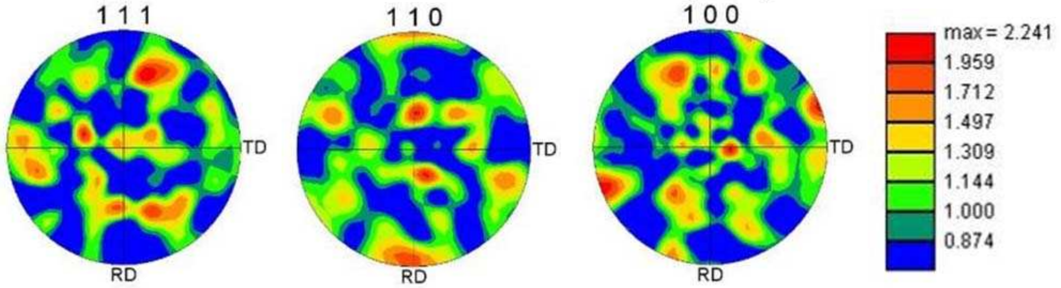

Figure 3 □Pole figure obtained on 10% cold rolled material along rolling direction. EBSD analysis.

3. Fatigue tests in air

For the purpose of the codification support objective, fatigue tests in air, were conducted until failure at EDF. The test conditions investigated are summarized in Table 4. Fatigue samples were cut off in the middle of the plate along the rolling direction. In the present study, the maximum strain amplitude at which specimen failure does not occur after 10^6 cycles was considered to be the fatigue limit. It is important to notice that, in the case of low strain rate tests, the unloading strain rate was kept equal to 0.4%/s (Figure 4).

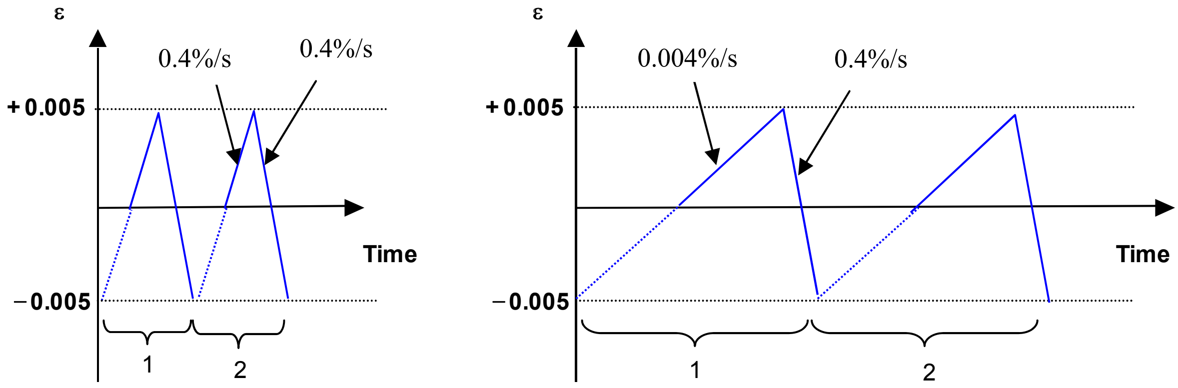

Figure 4 □Applied wave forms.

Table 4 - Codification tests in air at 300°C.

TP-ID		Strain rate (%/sec)		Strain amplitude (%)
		in tension	in compression	
As-received	1630-95	0.4	0.4	0.5
5% Rolling at EDF	1630-59	0.4	0.4	0.5
	1630-60	0.4	0.4	0.35
	1630-62	0.4	0.4	0.25
	1630-63	0.4	0.4	0.15
	1630-61	0.004	0.4	0.5
10% Rolling at EDF	1630-40	0.4	0.4	0.5
	1630-49	0.4	0.4	0.35
	1630-43	0.4	0.4	0.2
	1630-42	0.4	0.4	0.25
	1630-46	0.4	0.4	0.15
	1630-45	0.004	0.4	0.5
	1630-44	0.004	0.4	0.35
10% tension at EDF	1630-100	0.4	0.4	0.5
	1630-101	0.4	0.4	0.15

As for the understanding of microstructural and damage evolutions with cycling, tests were performed at ENSMA using polished samples.

Table 5 □Reference test matrix.

	TP-ID	Temperature	Strain rate (%/s)		Strain amplitude (%)	Number of cycle
		(℃)	in tension	in compression		
As-received	1630-70	300	0.4	0.4	0.5	10
	1630-71		0.004	0.4	0.5	10
	1630-78		0.4	0.4	0.5	100
	1630-83		0.004	0.4	0.5	100
	1630-76		0.4	0.4	0.5	300
	1630-84		0.004	0.4	0.5	300
	1630-75		0.4	0.4	0.5	600
	1630-74		0.004	0.4	0.5	600
10% cold rolled at EDF	1630-36		0.4	0.4	0.5	10
	1630-33		0.004	0.4	0.5	10
	1630-30		0.4	0.4	0.5	100
	1630-32		0.004	0.4	0.5	100
	1630-31		0.4	0.4	0.5	300
	1630-29		0.004	0.4	0.5	300
	1630-34		0.4	0.4	0.5	600
	1630-35		0.004	0.4	0.5	600
	1630-38	20	0.4	0.4	0.5	600

4. Cyclic stress-strain behavior

The following figures give the evolution of the maximum stress as a function of the number of cycles for various applied total strain amplitudes at a strain rate of 0.4%/s on the 10% CR (Figure 5), 10% CT (Figure 6) , 5% CR (Figure 7) and on the as-received (Figure 8) 304L material.

This figure reveals that all specimens, irrespective of the pre hardening level, experienced a primary hardening at the beginning of cycling followed by a noticeable softening. A secondary hardening was noticed in the case of tests conducted at a strain amplitude of 0.15%. The initial stress level is all the more important that the cold work level and the strain amplitude are high.

In the case of the two pre cold rolled materials, the stress level reached during softening seems to saturate at a quasi constant stress amplitude (240 MPa for the 10% CR and 220 MPa for the 5% CR).

The maximum hardening peaks (Figure 9), are reached at about 80-100 cycles in the case of the as-received material, regardless of the applied strain amplitude, and between 10-30 cycles and 3-5 cycles for the 5% and the 10% pre hardened materials respectively. No clear difference was noticed between the 10% CR and the 10% CT materials even if their respective plastic prior strain amplitude was slightly different (respectively 12% and 10%).

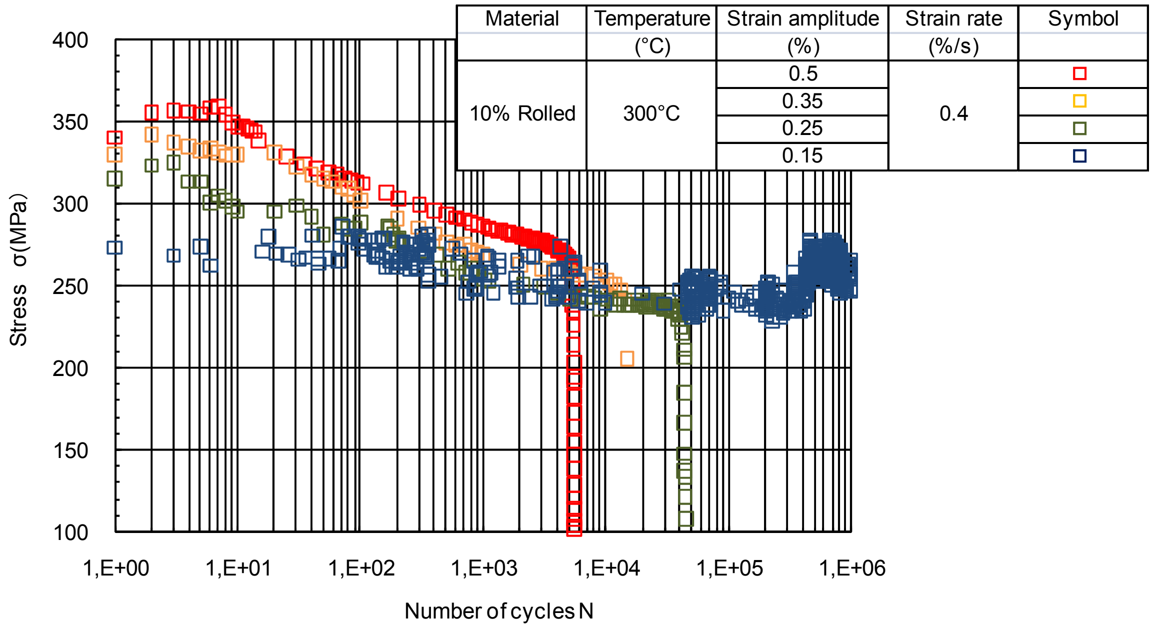

Figure 5 □Maximum stress evolution during cycling, 10% CR material.

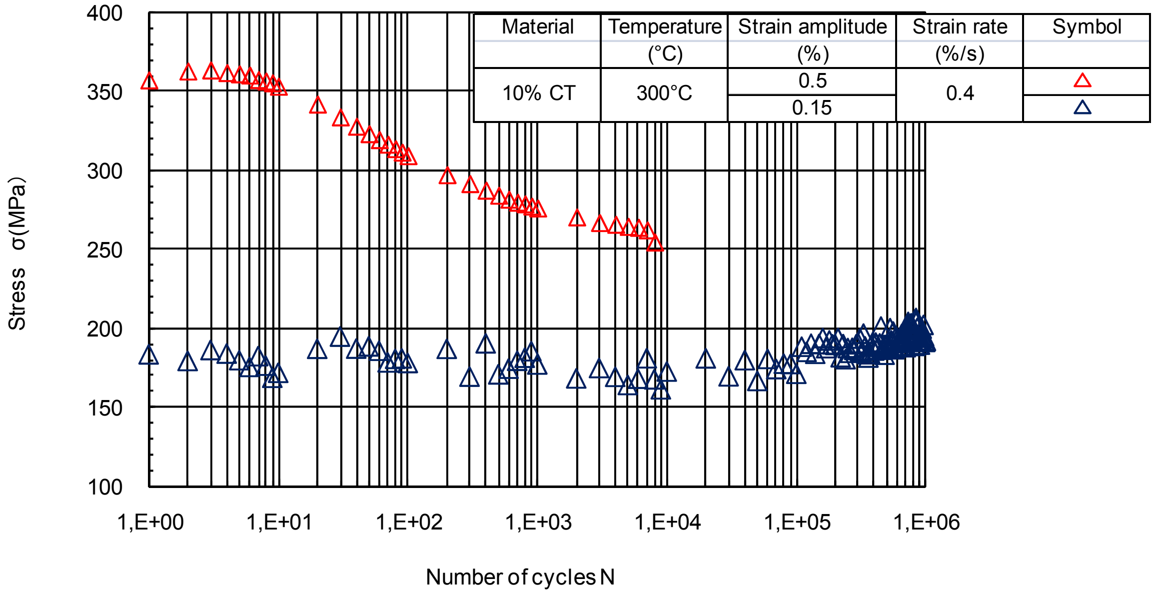

Figure 6 □Maximum stress evolution during cycling, 10% CT material.

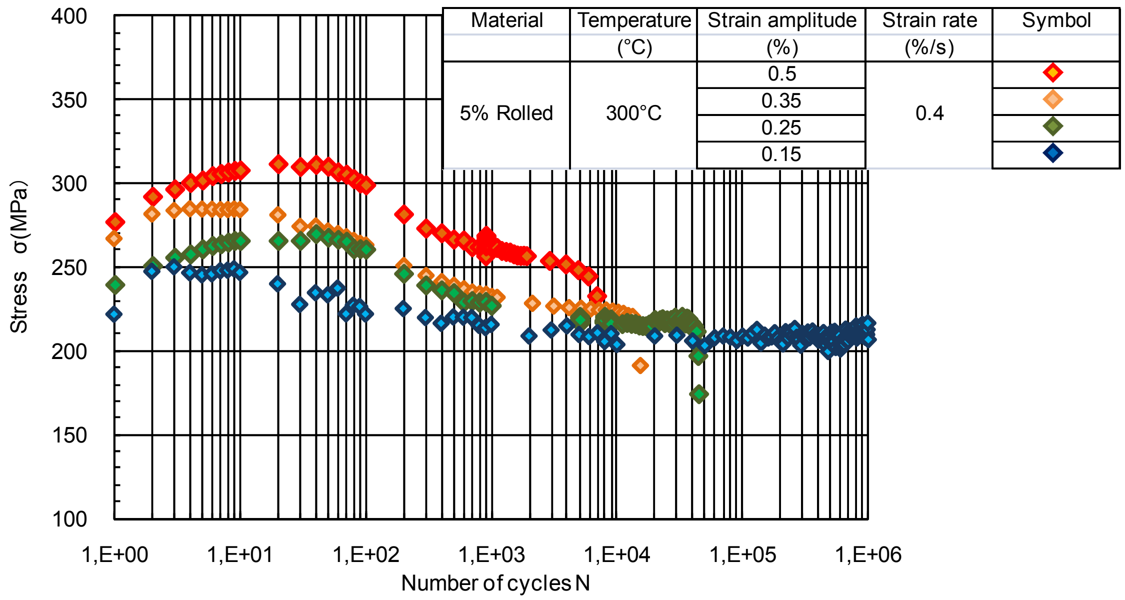

Figure 7 Maximum stress evolution during cycling, 5% CR material.

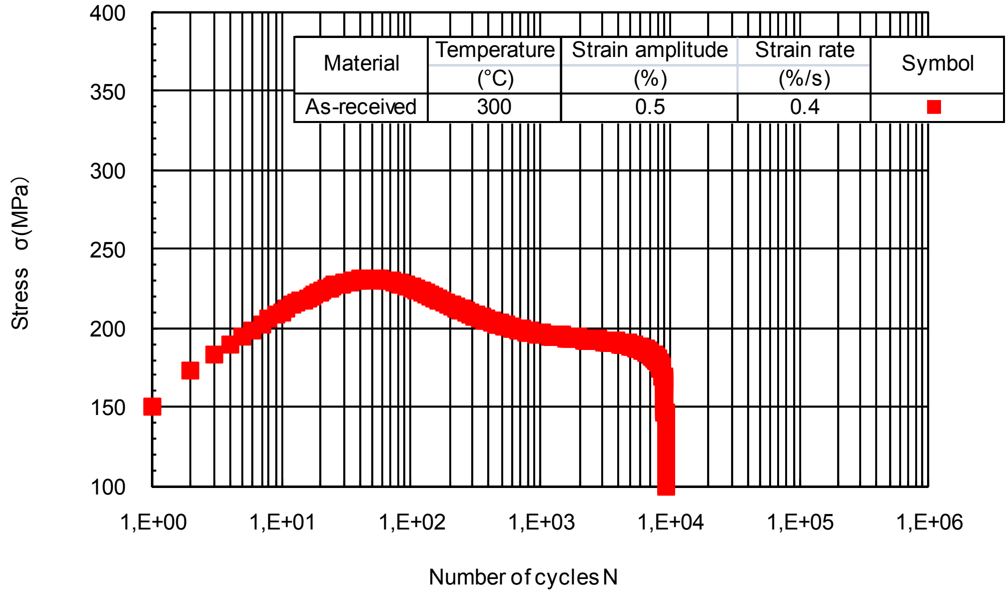

Figure 8 Maximum stress evolution during cycling, as-received material.

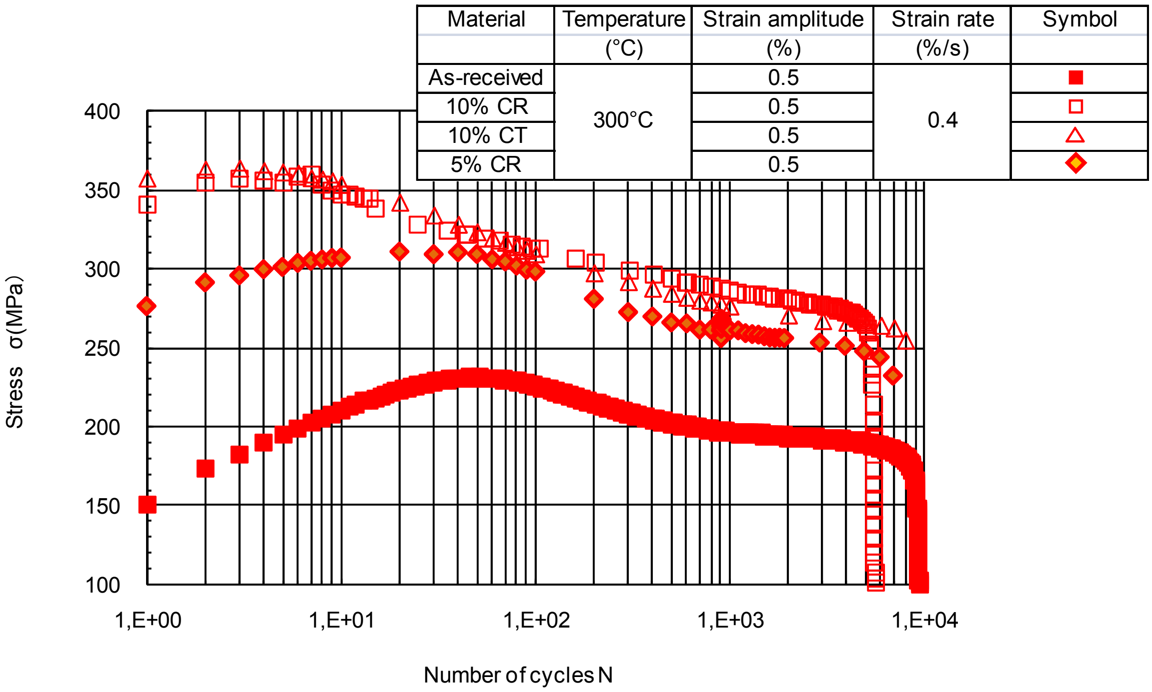

Figure 9 □Maximum stress evolution during cycling for the 10% CR, 10% CT, 5% CR and as-received material at a total strain amplitude of 0.5%.

Figure 10 and Figure 11 show the evolution of the mean stress as a function of the applied number of cycles in as-received and 10% CR material. Only at the lower strain amplitude, i.e. 0.15% and 0.25%, mean stresses of about 30-40 MPa are observed. When increasing the applied strain amplitude, these values decreased down to almost zero. The test conducted at an applied strain amplitude of 0.15% presents a lot of scattering. This scattering is due to the fact that the sample was tested almost in the elastic region and that in this region, the stress response is very sensitive to small variations of the imposed strain amplitude.

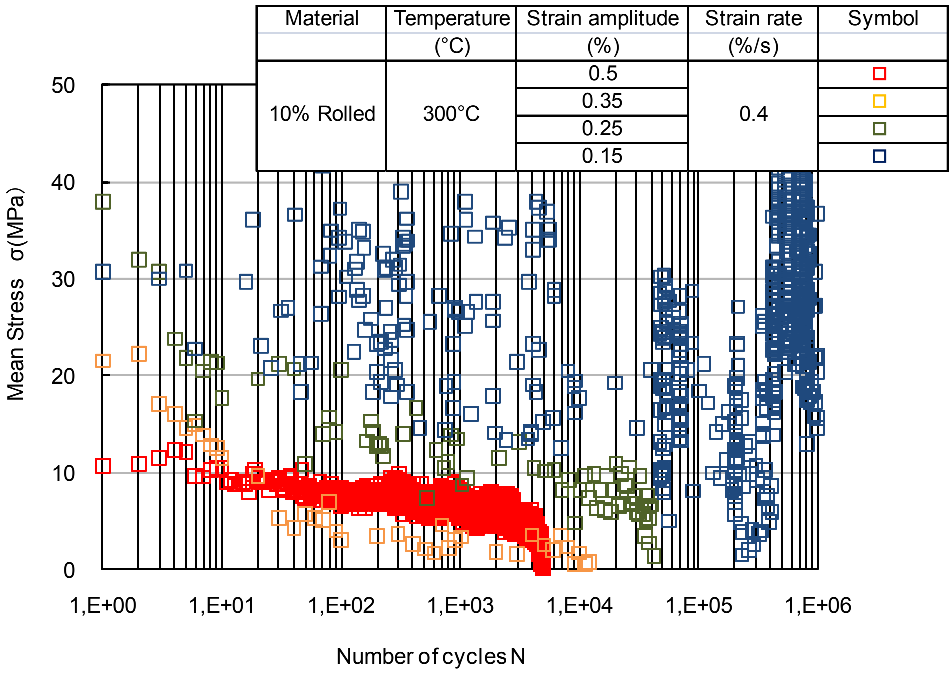

Figure 10 Evolution of mean stress as a function of number of cycles on the 10% CR material.

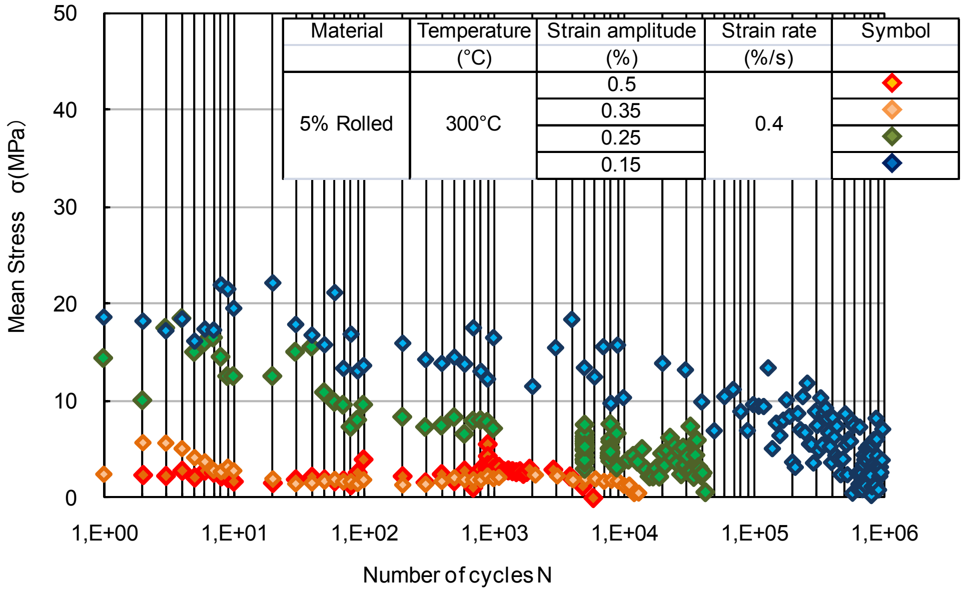

Figure 11 Evolution of mean stress as a function of number of cycles on the 5% CR material.

Figure 12 presents the curves obtained in the interrupted tests performed at ENSMA at $\Delta\varepsilon_t/2=0.5\%$ and $\Delta\varepsilon_t/dt=0.4\%/s$ or $\Delta\varepsilon_t/dt=0.004\%/s$ on the as-received and the 10% CR materials. Results obtained at ENSMA and EDF are in good agreement. The cyclic stress strain behavior will be interpreted through a characterization of the deformation structure in the bulk in the dedicated section.

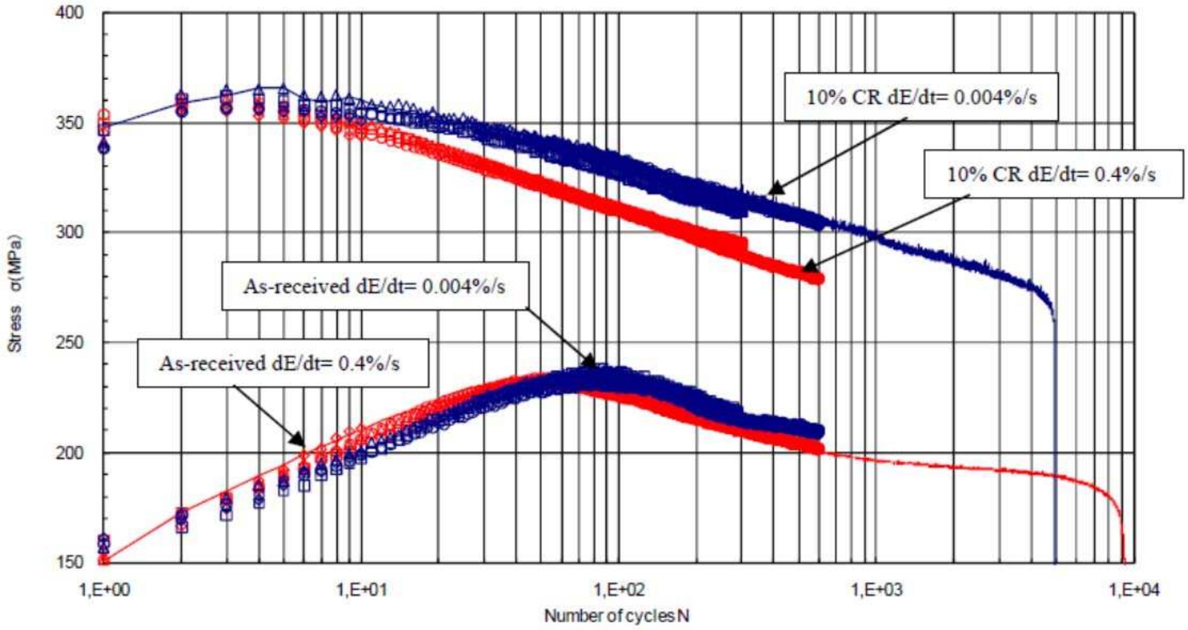

Figure 12 □Maximum stress evolution during cycling at $\Delta\varepsilon_t/2$ =0.5% at $\Delta\varepsilon_t/dt$ =0.4%/s and 0.004%/s.

5. Fatigue lives

The results obtained in air are summarized in Table 6 along with the data collected in a previous work [5] (heat XY182, same temperature, gage-type control extensometer, solid-type specimens) undertaken by GE and the CEAT for EDF, but using various strain amplitudes on the as-received material.

Fatigue ε_t-N data in air are presented in Figure 13, comparing the behavior of as-received and CR materials at different strain rates. The fatigue lives significantly increased when decreasing the strain amplitudes. As for the pre hardening effect on fatigue life in the air environment, within a range of total strain amplitude $\Delta\varepsilon_t/2$ = 0.2%-0.5%, fatigue lives of the 5%, 10% CR and 10% CT 304L are shorter than those of the as-received one. Below $\Delta\varepsilon_t/2$ ≈0.2%, the fatigue life of the pre hardened material becomes longer and an increase of the fatigue limit at 10^6 cycles, from 0.1% to at least 0.15%, was observed. By contrast, strain rate has a negligible effect on fatigue life. Figure 14 presents results comparing the as-received with the cold worked material at different strain rates using the plastic strain amplitude measured at mid-life. Conclusions on the fatigue life reduction related to a prior hardening, in the LCF regions are the same using plastic strain amplitude or total strain amplitude.

However, below a plastic strain amplitude of 0.04%, tests were found to be considered as run-out.

Table 6 Compendium of results obtained in air.

	Specimen		Temperature	Strain rate（%/sec）		Strain amplitude (%)	Fatigue life (N)	Comment
			(℃)	in tension	in compression			
AIR	As-received	1630-95	300	0,4	0,4	0,5	9800	
		XADL-26 (CEAT)		0,4	0,4	0,49	12520	
		XADL-104 (CEAT)		0,4	0,4	0,395	19210	
		XADL-69 (CEAT)		0,4	0,4	0,298	47470	
		XADL-45 (CEAT)		0,4	0,4	0,249	57460	
		XADL-15 (CEAT)		0,4	0,4	0,198	94530	
		XADL-49b (CEAT)		0,4	0,4	0,148	294300	
		EDF-7-1 (GE)		0,4	0,4	0,5	12100	
		EDF-6-20 (GE)		0,4	0,4	0,375	21500	
		EDF-6-19 (GE)		0,4	0,4	0,25	55000	
		EDF-3-19 (GE)		0,4	0,4	0,25	71815	
		EDF-6-12 (GE)		0,4	0,4	0,25	47000	
		EDF-6-3 (GE)		0,4	0,4	0,175	103000	
		EDF-4-19 (GE)		0,4	0,4	0,175	119344	
		EDF-6-6 (GE)		0,4	0,4	0,15	101000	
		EDF-6-13 (GE)		0,4	0,4	0,125	396000	
		EDF-3-21 (GE)		0,4	0,4	0,125	227438	
		EDF-5-41 (GE)		0,4	0,4	0,1	1885001	Run out
	5% CR	1630-59		0,4	0,4	0,5	6500	
		1630-60		0,4	0,4	0,35	16100	
		1630-62		0,4	0,4	0,25	45000	
		1630-63		0,4	0,4	0,15	1000000	Run out
		1630-61		0,004	0,4	0,5	6443	
	10% CR	1630-40		0,4	0,4	0,5	5400	
		1630-49		0,4	0,4	0,35	15000	
		1630-43		0,4	0,4	0,2	500000	
		1630-42		0,4	0,4	0,25	44000	
		1630-46		0,4	0,4	0,15	1000000	Run out
		1630-45		0,004	0,4	0,5	4930	
		1630-44		0,004	0,4	0,35	15220	
	10% CT	1630-100		0.4	0.4	0,5	4000	
		1630-101		0.4	0.4	0,15	1000000	Run out

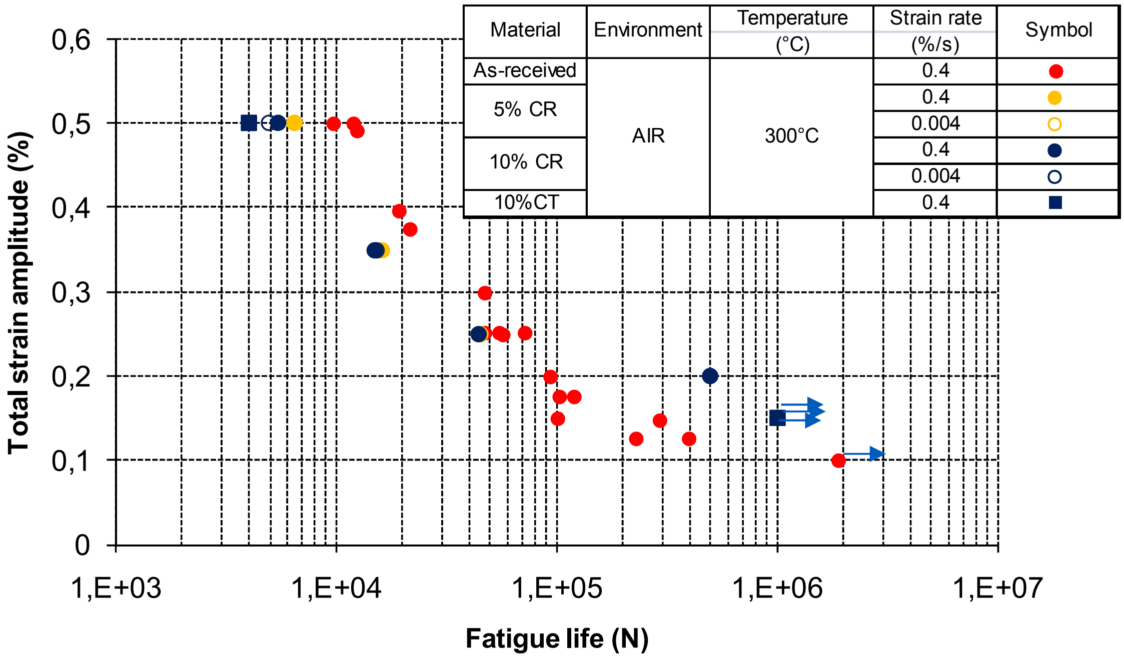

Figure 13 **Total strain amplitude vs. fatigue lives in air of as-received, 5% CR and 10% CR 304L.**

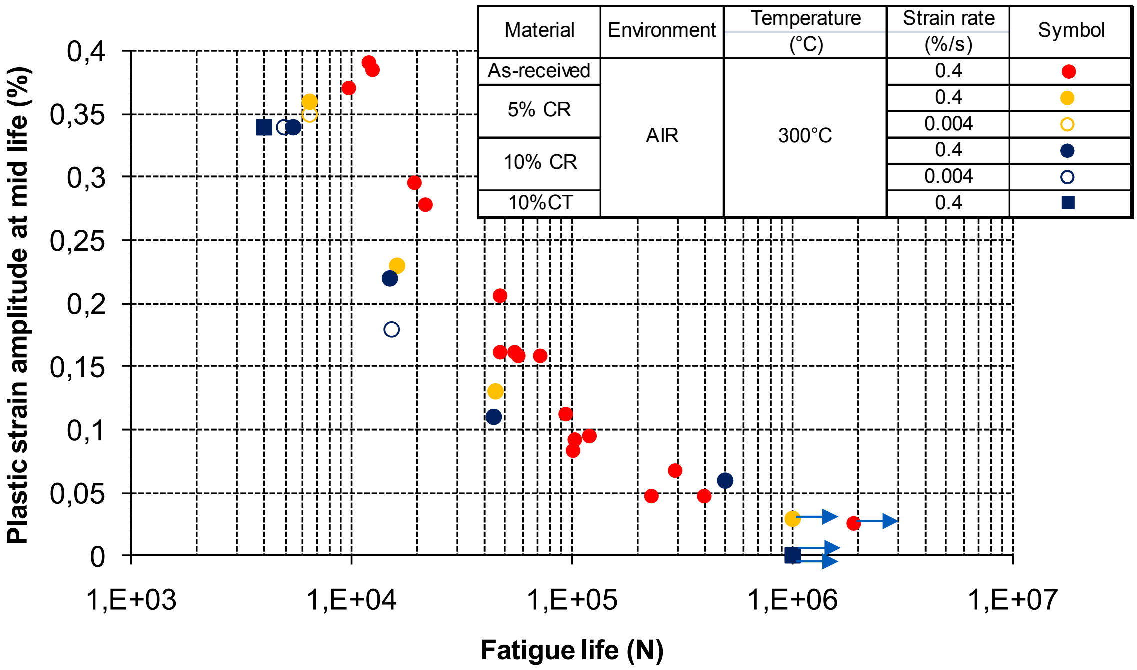

Figure 14 **Plastic strain amplitude at mid life vs. fatigue lives in air of as-received, 5% CR and 10% CR 304L.**

6. Evolution of damage during cycling

The fatigue life and the mechanical response of a given material can be related to the evolution of the damage process (crack initiation and growth) during cycling.

The two previous parts have highlighted the difference in cyclic stress-strain behavior in addition to a difference in fatigue life related to the level and the type of pre hardening. In addition, a modification of the loading strain rate was found to modify the mechanical response of the 10% CR material but less the as-received one. Since the mechanical response of a material is directly linked to the underlying deformation structure, it is proposed to evaluate the difference of microstructure induced by a pre hardening and a modified strain rate and their respective evolution during cycling. The damage will also be characterized using several techniques of microscopy. The main goal is to identify the difference in damage process between a pre hardened and an as-received material that may explain their difference of fatigue life in air environment. Because microstructural characterizations are time-consuming, only tests performed at a 0.5% of strain amplitude on the as-received and the 10% CR materials were considered.

6.1. Deformation structures within the bulk

6.1.1. As-received material

Figure 15 to Figure 30 present bright field STEM observations on samples in the as-received material tested at a loading strain rate of 0.4%/s.

- After 10 cycles, the main observation is the presence of numerous stacking faults (Figure 15). Figure 16 reveals stacking faults between 2 partial dislocations. Another type of microstructure is illustrated in Figure 17 and Figure 18 which indicate the presence of planar alignments and slip bands on 2 activated systems. Figure 18 also shows that the dislocation density increased close to a twin boundary, highlighting strain incompatibilities.
- After 100 cycles (Figure 19 to Figure 22) the deformation structures are mainly composed of planar dislocation alignments (Figure 19, Figure 20 and Figure 22) that evolved into cells or PSBs (Figure 19 and Figure 21). The density of stacking faults is drastically reduced compared to the sample tested up to 10 cycles. Figure 22 highlights the fact that deformation in the vicinity of grain boundaries results in a local increase of dislocation density due to strain

incompatibilities. Global dislocation density increased in agreement with the macroscopic stress increase.

- After 300 cycles (Figure 23 to Figure 26), 3D structures such as PSBs or cells are observed. The cell density is more pronounced close to grain boundaries (Figure 24). Some dislocation stacks and planar glide traces remain (Figure 23, Figure 26).
- After 600 cycles (Figure 27 to Figure 30), planar glide, stacking faults and dislocation stacks are preferred to the 3D structure observed after 100 cycles. This evolution in strain mechanisms is not expected because 3D dislocation structures such as cells are supposed to be more stable (minimizing stored energy). The apparent transition from 3D to planar dislocation structures is less advanced close to grain/twin boundaries (Figure 27 and Figure 30).

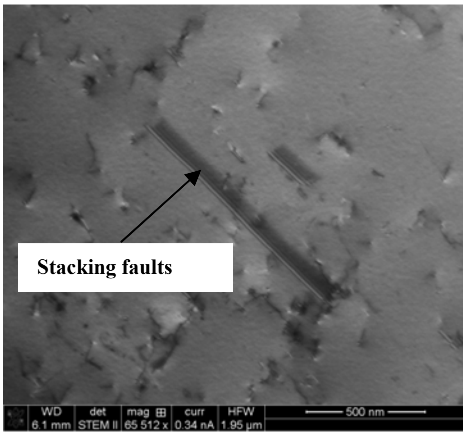

Figure 15 □Stacking fault on the bulk, $\Delta\varepsilon_t/2 = 0.5\%$, $\Delta\varepsilon_t/dt = 0.4\%/s$, 10 cycles, 300°C, as-received material.

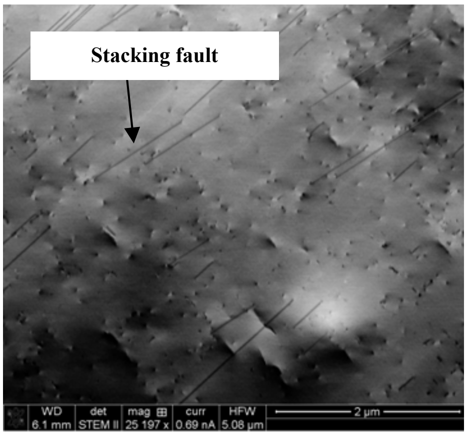

Figure 16 □Stacking fault with 2 partial dislocation on the bulk, $\Delta\varepsilon_t/2 = 0.5\%$, $\Delta\varepsilon_t/dt = 0.4\%/s$, 10 cycles, 300°C, as-received material.

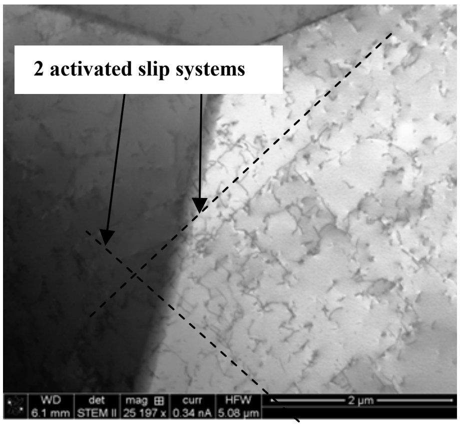

Figure 17 □Planar alignments and slip bands, 2 slip system activated on the bulk, $\Delta\varepsilon t/2 = 0.5\%$, $\Delta\varepsilon t/dt = 0.4\%/s$, 10 cycles, 300°C, as-received material.

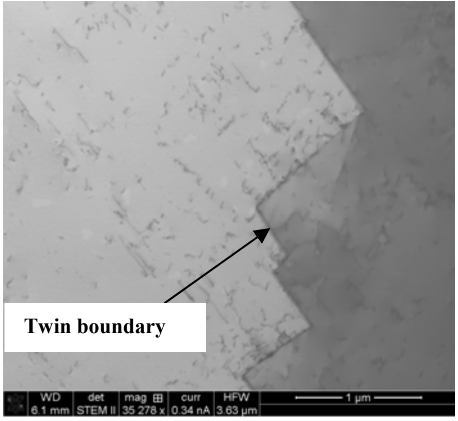

Figure 18 □Slip bands and increase of dislocation density close to a twin boundary on the bulk, $\Delta\varepsilon t/2 = 0.5\%$, $\Delta\varepsilon t/dt = 0.4\%/s$, 10 cycles, 300°C, as-received material.

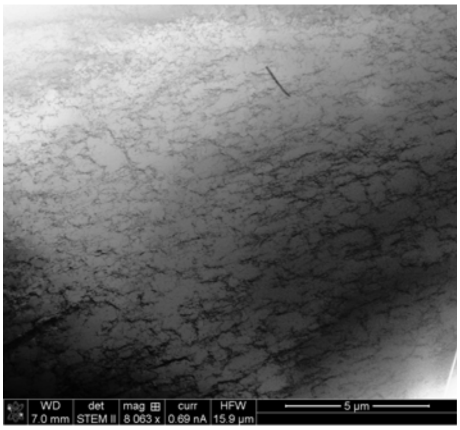

Figure 19 □Dislocation alignments evolving into cells or PSB, $\Delta\varepsilon t/2 = 0.5\%$, $\Delta\varepsilon t/dt = 0.4\%/s$, 100 cycles, 300°C, as-received material.

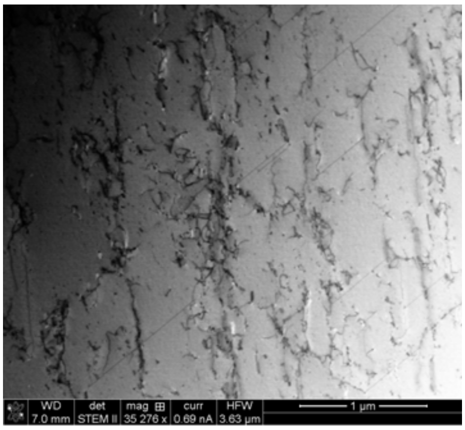

Figure 20 □Dislocation alignments and stacking faults, $\Delta\varepsilon t/2 = 0.5\%$, $\Delta\varepsilon t/dt = 0.4\%/s$, 100 cycles, 300°C, as-received material.

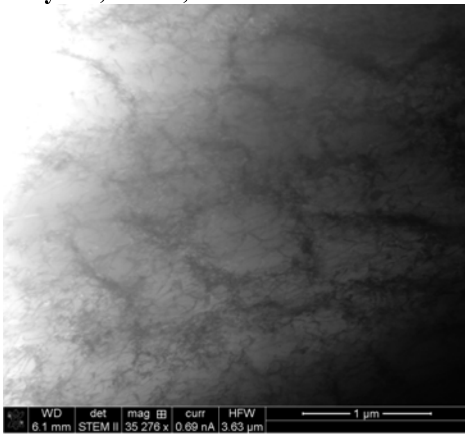

Figure 21 □Cells, $\Delta\varepsilon_t/2 = 0.5\%$, $\Delta\varepsilon_t/dt = 0.4\%/s$, 100 cycles, 300°C, as-received material.

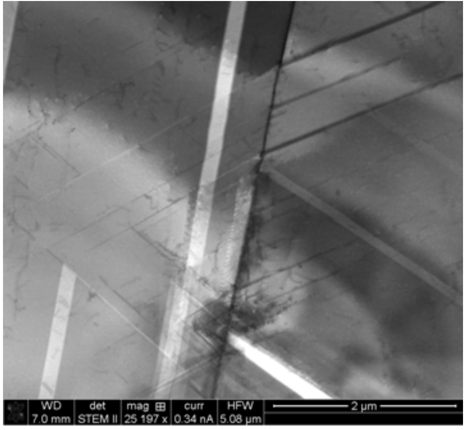

Figure 22 □Planar structure impacting grain boundary resulting in strain incompatibilities, $\Delta\varepsilon_t/2 = 0.5\%$, $\Delta\varepsilon_t/dt = 0.4\%/s$, 100 cycles, 300°C, as-received material.

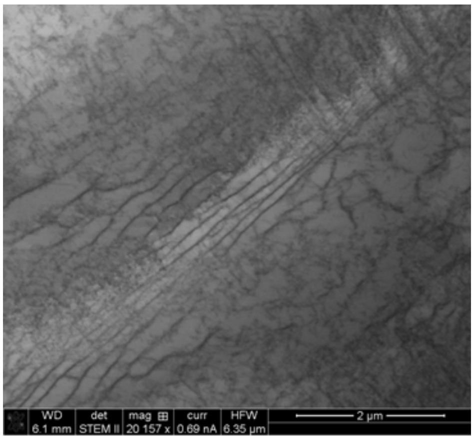

Figure 23 □Dislocation stacks evolving into PSBs, $\Delta\varepsilon_t/2 = 0.5\%$, $\Delta\varepsilon_t/dt = 0.4\%/s$, 300 cycles, 300°C, as-received material.

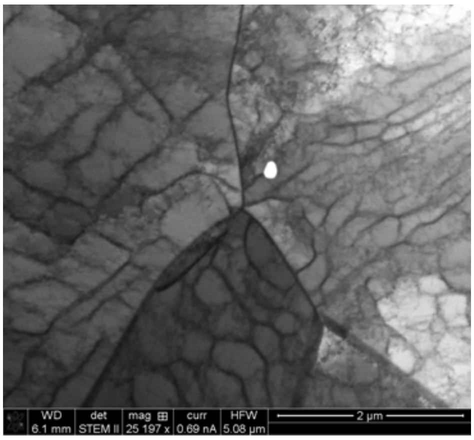

Figure 24 □PSB, cells, close to a triple junction, $\Delta\varepsilon_t/2 = 0.5\%$, $\Delta\varepsilon_t/dt = 0.4\%/s$, 300 cycles, 300°C, as-received material.

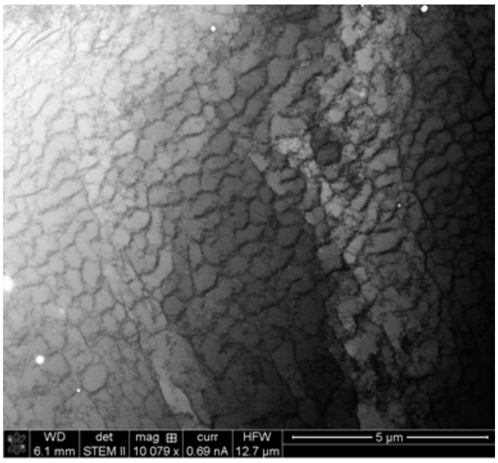

Figure 25 □PSBs and cells, $\Delta\varepsilon_t/2$ =0.5%, $\Delta\varepsilon_t/dt$=0.4%/s, 300 cycles, 300°C, as-received material.

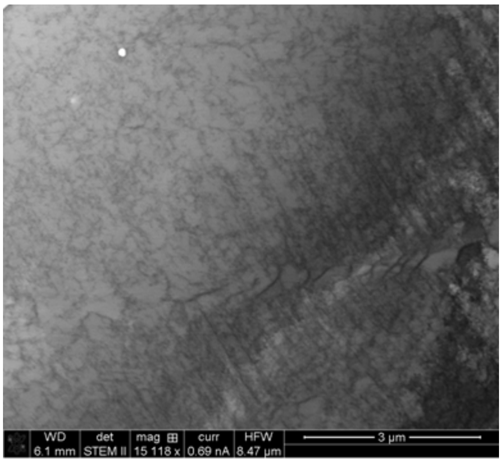

Figure 26 □Dislocation stacks and planar structure evolving into PSBs, $\Delta\varepsilon_t/2$ =0.5%, $\Delta\varepsilon_t/dt$=0.4%/s, 300 cycles, 300°C, as-received material.

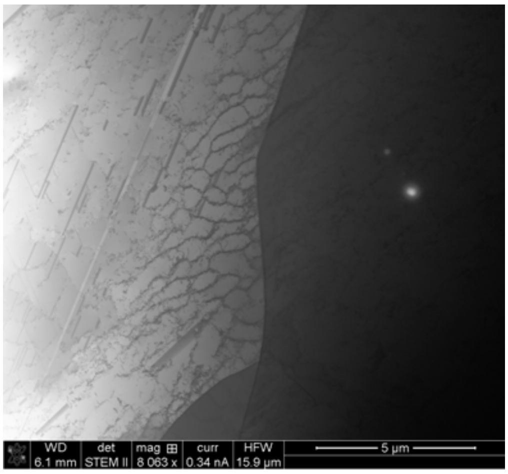

Figure 27 □PSBs close to a grain boundary and stacking fault, $\Delta\varepsilon_t/2$ =0.5%, $\Delta\varepsilon_t/dt$=0.4%/s, 600 cycles, 300°C, as-received material.

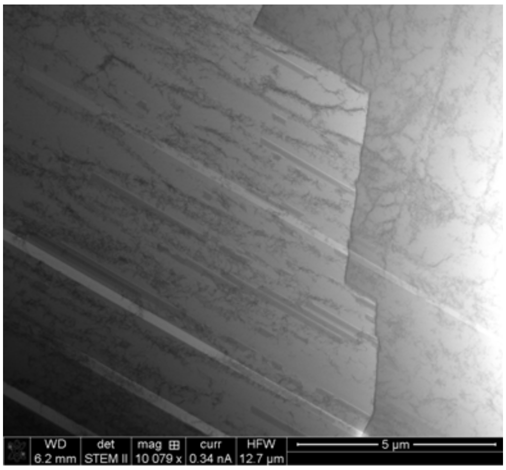

Figure 28 □Dislocation stacks and planar structure close to a twin boundary, $\Delta\varepsilon_t/2$ =0.5%, $\Delta\varepsilon t/dt$=0.4%/s, 600 cycles, 300°C, as-received material.

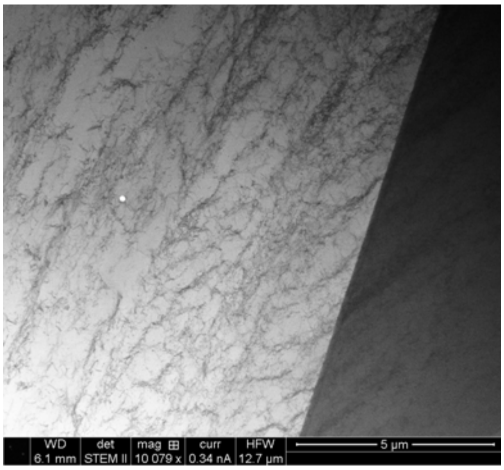

Figure 29 □Remains of 3D structures, $\Delta\varepsilon_t/2$ =0.5%, $\Delta\varepsilon_t/dt$=0.4%/s, 600 cycles, 300°C, as-received material.

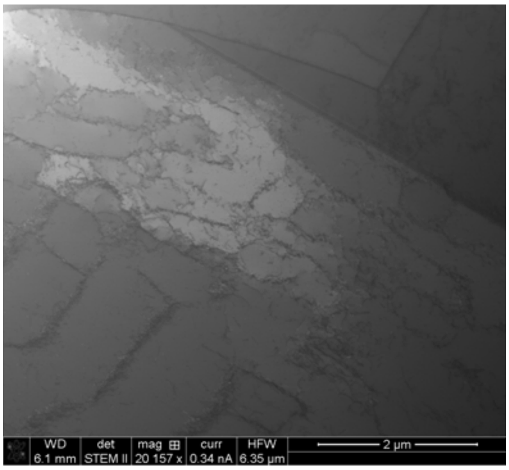

Figure 30 □Strain incompatibility close to a grain boundary, $\Delta\varepsilon_t/2$ =0.5%, $\Delta\varepsilon_t/dt$=0.4%/s, 600 cycles, 300°C, as-received material.

Figure 31 to Figure 45 present bright field STEM observations on samples in the as-received conditions tested at a strain rate of 0.004%/s. The overall microstructure is very similar to the one obtained at 0.4%/s but seems slightly more planar. A more statistical approach would be needed to make sure of this gliding aspect.

- After 10 cycles, (Figure 31 to Figure 34), observations are quite similar to those obtained at higher strain rate. The microstructure is mainly composed of planar alignments with 2 activated slip systems (Figure 31) and a very important density of stacking faults (Figure 32).
- After 100 cycles, (Figure 35 to Figure 37) planar alignments are the dominant organization for dislocations. Figure 37 presents strain incompatibilities between non-deformed δ-ferrite and austenite.
- After 300 cycles, (Figure 38 to Figure 41), the deformation structures are also very similar to those observed at high strain rate where dislocation stacks and planar structure evolved into 3D structures.
- After 600 cycles, (Figure 42 to Figure 45) most of the complex 3D structures are replaced by planar glide inside the grain while stacking fault and 3D structures remain close to grain boundaries.

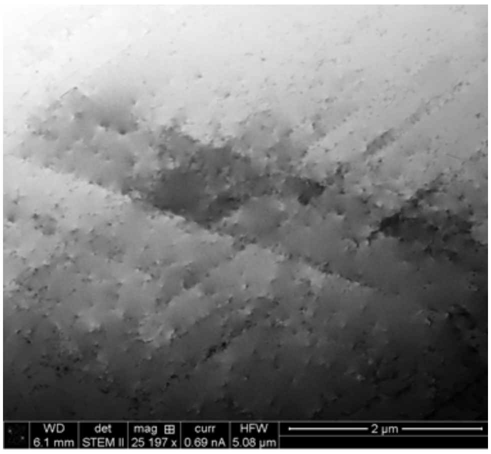

Figure 31 – Planar alignments, 2 slip systems activated, $\Delta\varepsilon_t/2$ =0.5%, $\Delta\varepsilon_t/dt$=0.004%/s, 10 cycles, 300°C, as-received material.

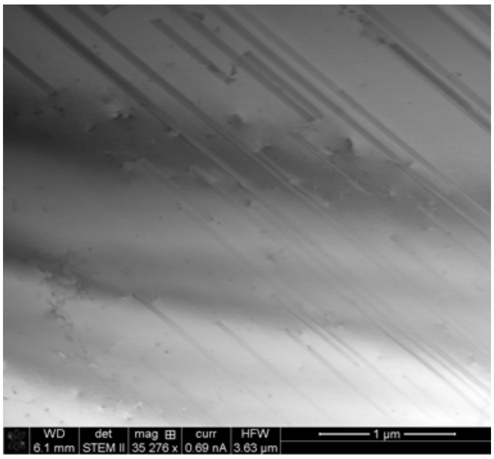

Figure 32 – Stacking faults, $\Delta\varepsilon_t/2$ =0.5%, $\Delta\varepsilon_t/dt$=0.004%/s, 10 cycles, 300°C, as-received material.

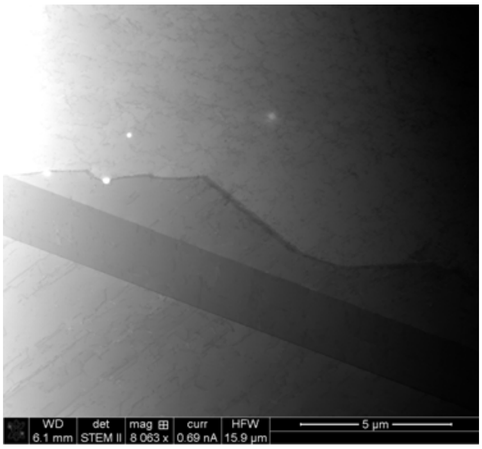

Figure 33 □Planar alignment crossing a twin boundary up to a grain boundary, $\Delta\varepsilon_t/2 = 0.5\%$, $\Delta\varepsilon_t/dt = 0.004\%/s$, 10 cycles, 300°C, as-received material.

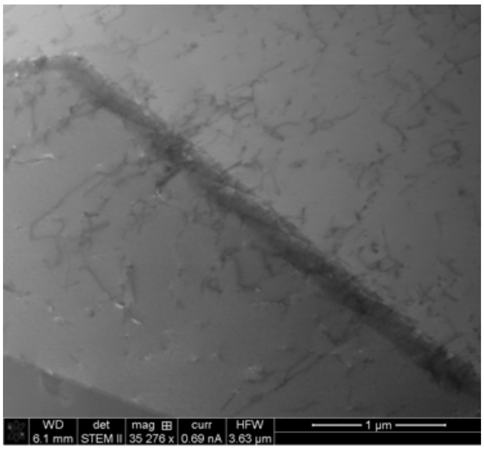

Figure 34 □Planar alignments emerging at a grain boundary, $\Delta\varepsilon_t/2 = 0.5\%$, $\Delta\varepsilon_t/dt = 0.004\%/s$, 10 cycles, 300°C, as-received material.

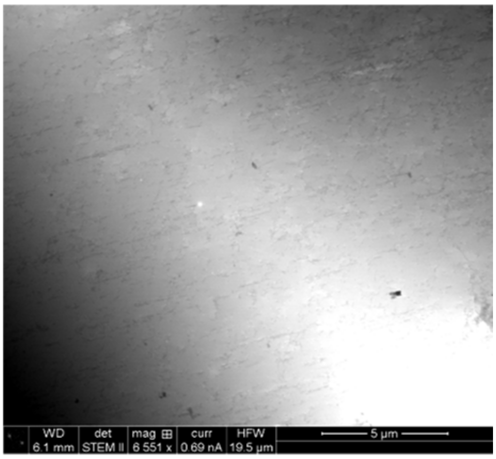

Figure 35 □Planar alignments, $\Delta\varepsilon_t/2 = 0.5\%$, $\Delta\varepsilon_t/dt = 0.004\%/s$, 100 cycles, 300°C, as-received material.

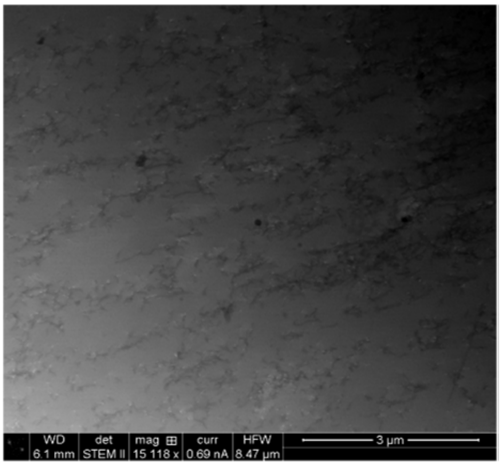

Figure 36 □Planar alignments, $\Delta\varepsilon_t/2 = 0.5\%$, $\Delta\varepsilon_t/dt = 0.004\%/s$, 100 cycles, 300°C, as-received material.

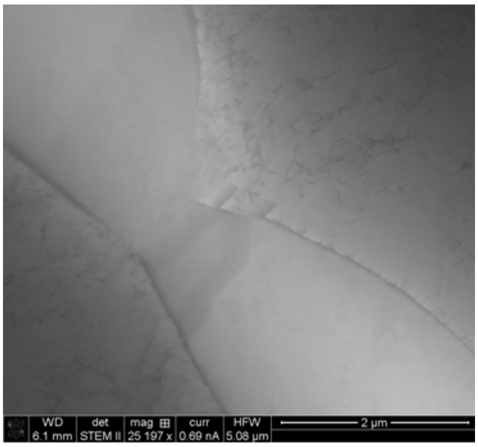

Figure 37 □Strain incompatibilities between ferrite and austenite, $\Delta\varepsilon_t/2 = 0.5\%$, $\Delta\varepsilon_t/dt = 0.004\%/s$, 100 cycles, 300°C, as-received material.

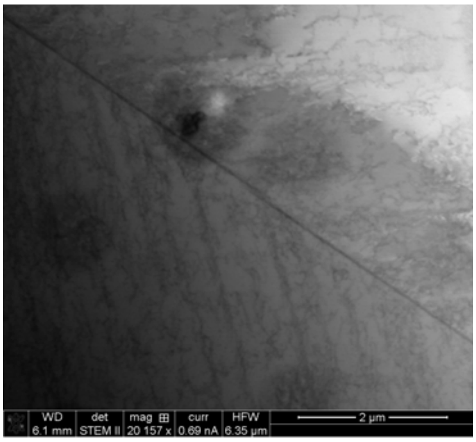

Figure 38 □Planar alignments emerging at a grain boundary, $\Delta\varepsilon_t/2$ =0.5%, $\Delta\varepsilon_t/dt$=0.004%/s, 300 cycles, 300°C, as-received material.

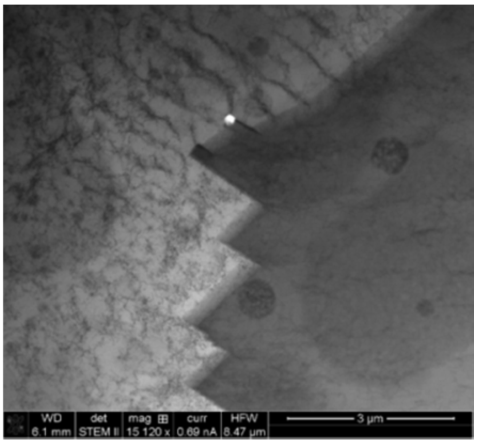

Figure 39 □Dislocation stacks evolving into 3D structures $\Delta\varepsilon_t/2$ =0.5%, $\Delta\varepsilon_t/dt$=0.004%/s, 300 cycles, 300°C, as-received material.

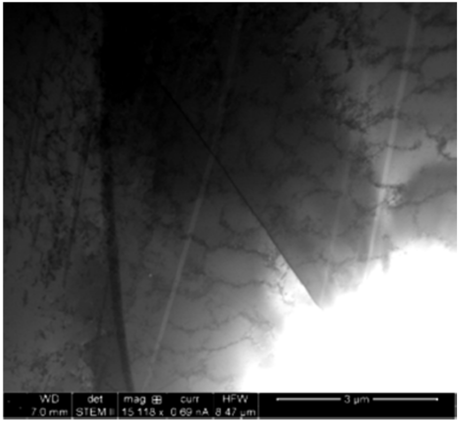

Figure 40 □Cells, $\Delta\varepsilon_t/2$ =0.5%, $\Delta\varepsilon_t/dt$=0.004%/s, 300 cycles, 300°C, as-received material.

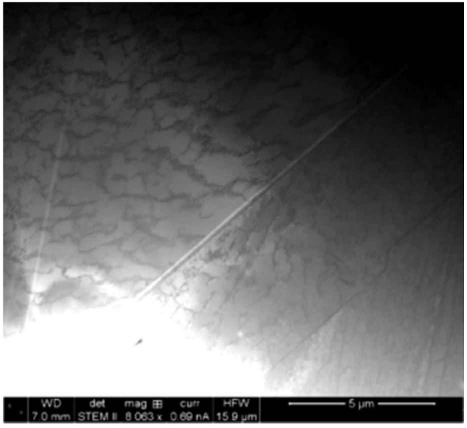

Figure 41 □3D structures, $\Delta\varepsilon_t/2$ =0.5%, $\Delta\varepsilon_t/dt$=0.004%/s, 300 cycles, 300°C, as-received material.

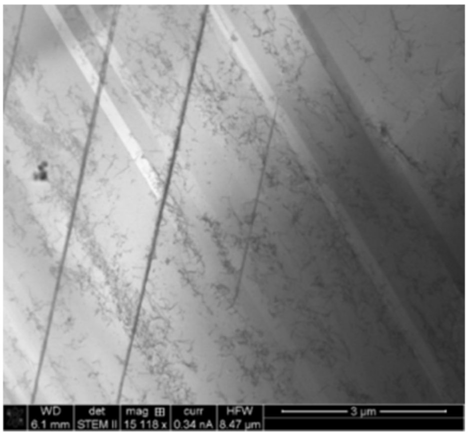

Figure 42 □Planar slip, $\Delta\varepsilon_t/2$ =0.5%, $\Delta\varepsilon_t/dt$=0.004%/s, 600 cycles, 300°C, as-received material.

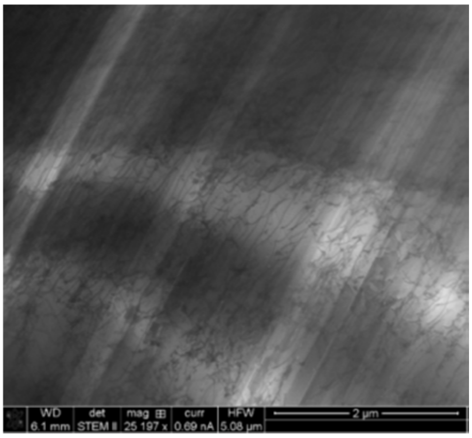

Figure 43 □Planar alignments with dislocation stacks, $\Delta\varepsilon_t/2$ =0.5%, $\Delta\varepsilon_t/dt$=0.004%/s, 600 cycles, 300°C, as-received material.

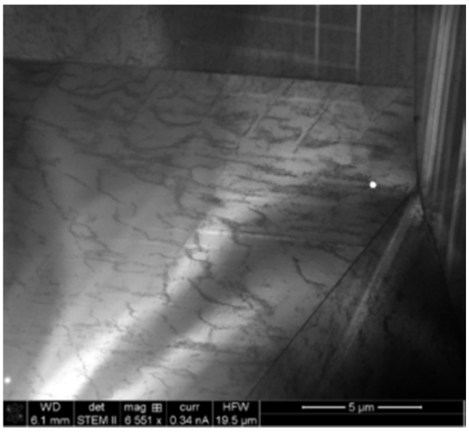

Figure 44 □Planar strcture ,3D structures and stacking faults close to grain boundary, $\Delta\varepsilon_t/2$ =0.5%, $\Delta\varepsilon_t/dt$=0.004%/s, 600 cycles, 300°C, as-received material.

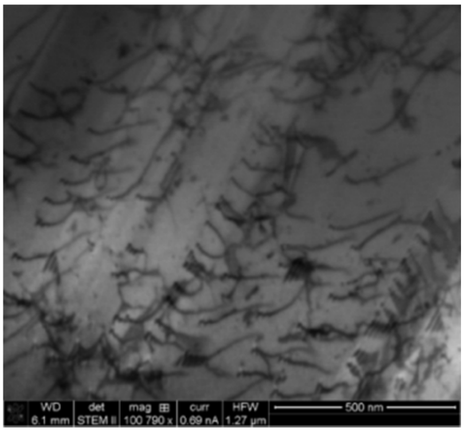

Figure 45 □Slip bands, $\Delta\varepsilon_t/2$ =0.5%, $\Delta\varepsilon_t/dt$=0.004%/s, 600 cycles, 300°C, as-received material.

6.1.2. 10% cold rolled material

Figure 46 present a bright field observation of the 10% CR material at the initial state. The material present a hard structure composed of planar structures. Some dislocation stacks can also be observed between planar glide. Such structures were not identified as micro twins using the diffraction mode in the TEM.

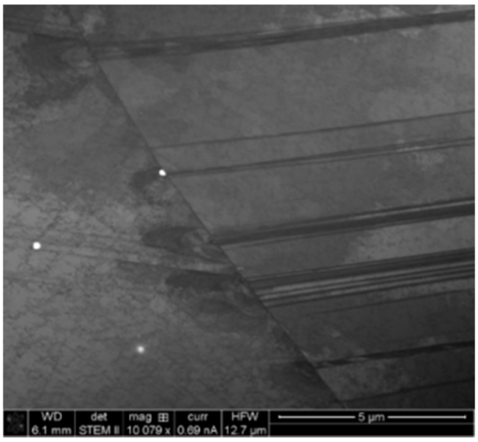

Figure 46 □Initial state of a 10% CW material composed of a planar structure.

Figure 47 to Figure 60 present bright field STEM observations on samples removed from a 10% cold rolled plate tested at a loading strain rate of 0.4%/s.

- After 10 cycles (Figure 47 and Figure 48), the microstructure is mainly composed of dislocations stacks. In addition, some traces of planar structure were observed (Figure 48).
- After 100 cycles (Figure 49 to Figure 52), a lot of dislocations in dense planar structures (Figure 49 and Figure 50) and 3D structures such as wall/channels

and cells were noticed (Figure 49 and Figure 51). Some traces of dislocation stacks were still observed (Figure 52).

- After 300 cycles (Figure 53 to Figure 56), the microstructure is mainly composed of 3D structures such as wall/channels and cells. Wall/channels are the dominant deformation structure in the bulk of the grain (Figure 53 and Figure 54) and seemed to evolve into dislocation cells close to grain boundaries, suggesting the presence of strain incompatibilities (Figure 55 and Figure 56).
- After 600 cycles (Figure 57 to Figure 60), 3D structures mostly compose the microstructure, contrary to the as-received material. The 3D structure (dislocation walls/channels) became thinner than at 300 cycles. Planar glide is also observed (Figure 59 and Figure 60).

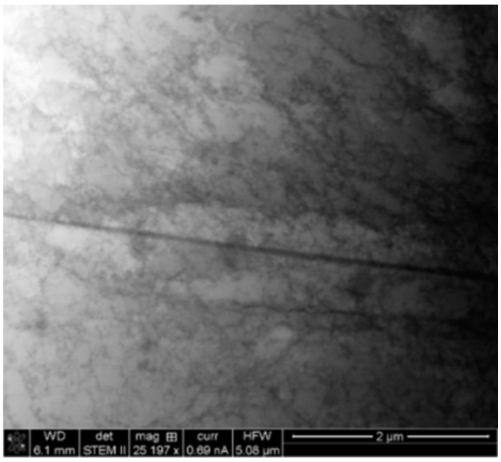

Figure 47 Dislocation stacks, $\Delta\varepsilon_t/2$ =0.5%, $\Delta\varepsilon_t/dt$=0.4%/s, 10 cycles, 300°C, the 10% cold rolled material.

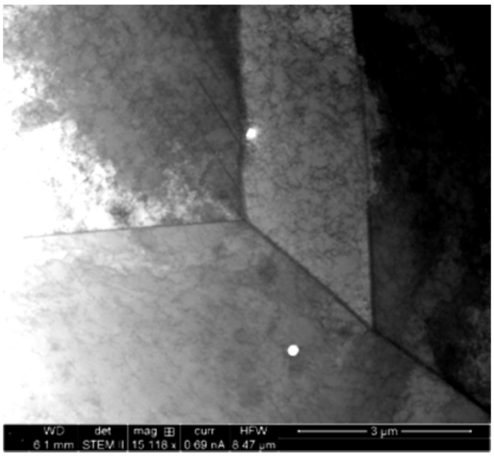

Figure 48 Dislocation stacks and planar structure, $\Delta\varepsilon_t/2$ =0.5%, $\Delta\varepsilon_t/dt$=0.4%/s, 10 cycles, 300°C the 10% cold rolled material.

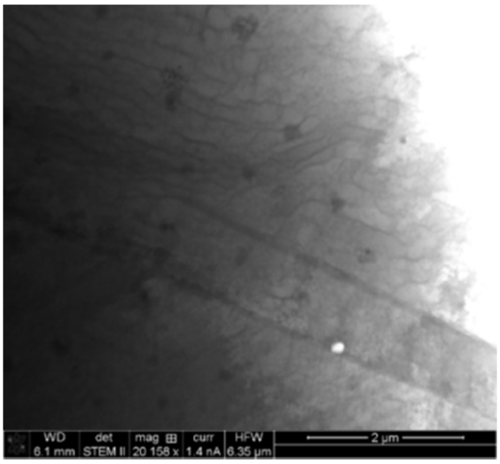

Figure 49 Planar structures and wall/channels, $\Delta\varepsilon_t/2$ =0.5%, $\Delta\varepsilon_t/dt$=0.4%/s, 100 cycles, 300°C the 10% cold rolled material.

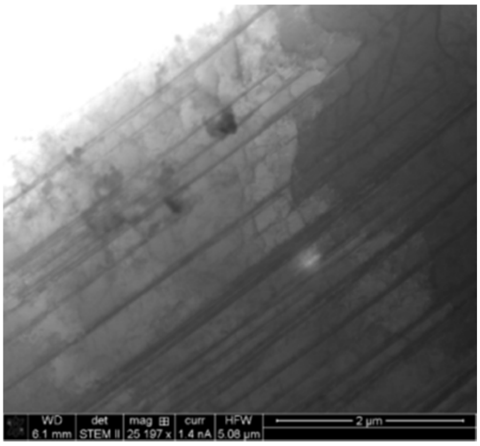

Figure 50 Planar structures, $\Delta\varepsilon_t/2$ =0.5%, $\Delta\varepsilon_t/dt$=0.4%/s, 100 cycles, 300°C the 10% cold rolled material.

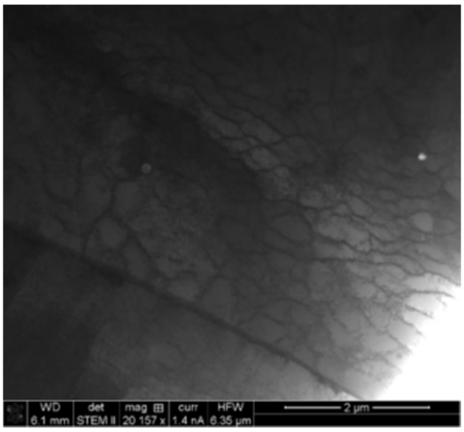

Figure 51 PSBs and cells, $\Delta\varepsilon_t/2$ =0.5%, $\Delta\varepsilon_t/dt$=0.4%/s, 100 cycles, 300°C the 10% cold rolled material.

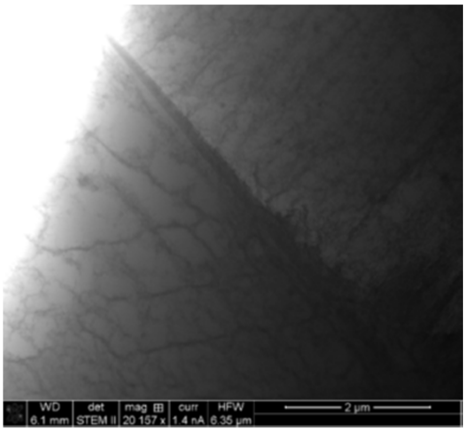

Figure 52 Planar slip and dislocation stacks $\Delta\varepsilon_t/2$ =0.5%, $\Delta\varepsilon_t/dt$=0.4%/s, 100 cycles, 300°C the 10% cold rolled material.

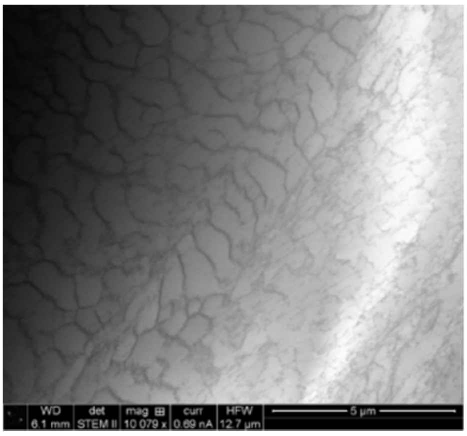

Figure 53 PSBs, $\Delta\varepsilon_t/2$ =0.5%, $\Delta\varepsilon_t/dt$=0.4%/s, 300 cycles, 300°C the 10% cold rolled material.

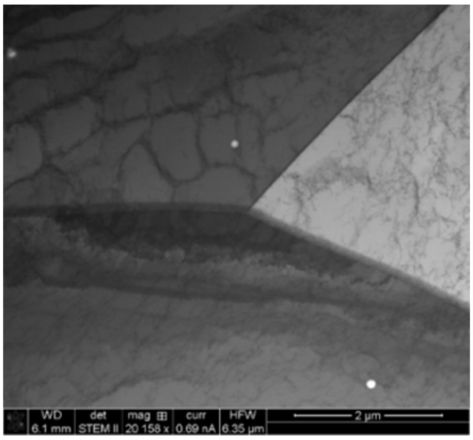

Figure 54 Cells and dislocation stacks $\Delta\varepsilon_t/2$ =0.5%, $\Delta\varepsilon_t/dt$=0.4%/s, 300 cycles, 300°C the 10% cold rolled material.

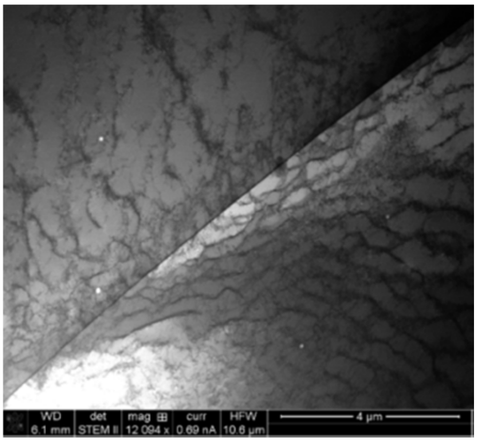

Figure 55 PSBs, PSB formation close to a grain boundary and strain incompatibilities, $\Delta\varepsilon_t/2$ =0.5%, $\Delta\varepsilon_t/dt$=0.4%/s, 300 cycles, 300°C the 10% cold rolled material.

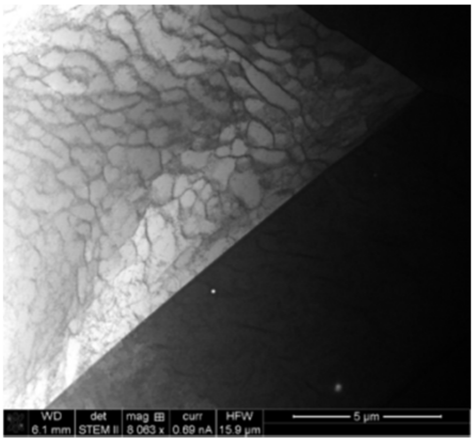

Figure 56 PSBs evolving into cells close to a triple junction, $\Delta\varepsilon_t/2$ =0.5%, $\Delta\varepsilon_t/dt$=0.4%/s, 300 cycles, 300°C the 10% cold rolled material.

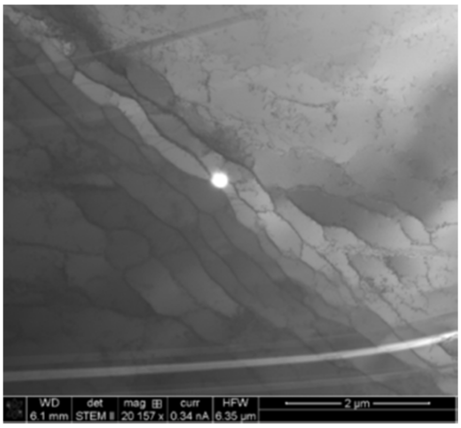

Figure 57 PSBs, $\Delta\varepsilon_t/2$ =0.5%, $\Delta\varepsilon_t/dt$=0.4%/s, 600 cycles, 300°C the 10% cold rolled material.

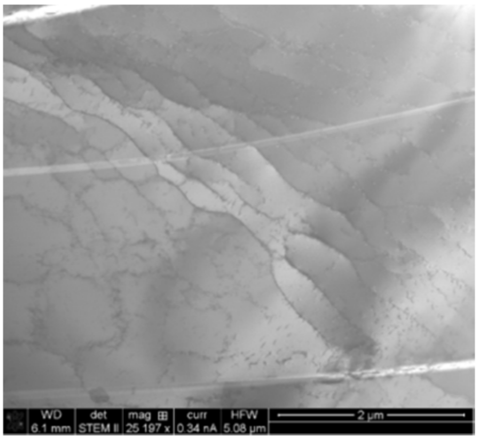

Figure 58 PSBs and cells, $\Delta\varepsilon_t/2$ =0.5%, $\Delta\varepsilon_t/dt$=0.4%/s, 300 cycles, 300°C the 10% cold rolled material.

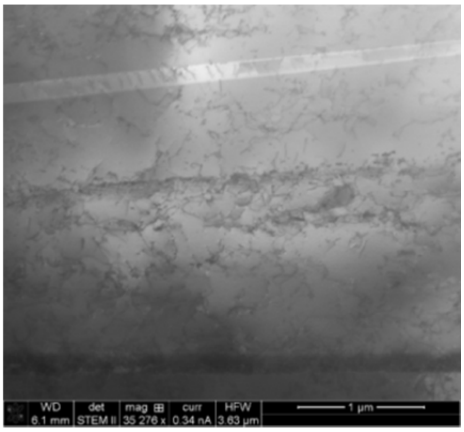

Figure 59 Planar slip, $\Delta\varepsilon_t/2$ =0.5%, $\Delta\varepsilon_t/dt$=0.4%/s, 600 cycles, 300°C the 10% cold rolled material.

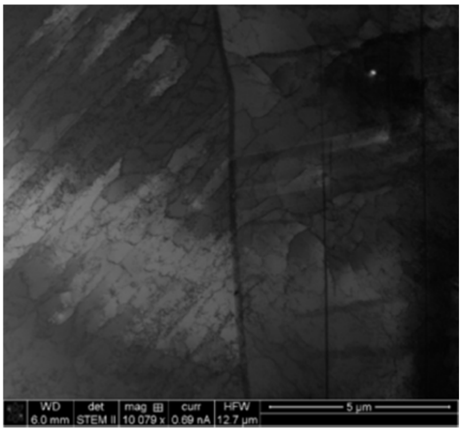

Figure 60 Planar slip and PSB, $\Delta\varepsilon_t/2$ =0.5%, $\Delta\varepsilon_t/dt$=0.4%/s, 600 cycles, 300°C the 10% cold rolled material.

Figure 61 to Figure 68 present bright field STEM observations on samples removed from a 10% cold work plate tested at a strain rate of 0.004%/s.

- After 10 cycles (Figure 61 and Figure 62), the microstructure is similar to the one obtained at a strain rate of 0.4%/s consisting in the co existence of planar structure induced by the pre hardening and of dislocation stacks.
- After 100 cycles (Figure 63 and Figure 64), the microstructure starts to evolve into dislocation cells.
- After 600 cycles (Figure 65 to Figure 68), 3D structures are mainly observed (Figure 65, Figure 66 and Figure 67). Planar structures are composed of stacking faults, dislocations and planar slips (Figure 68). Some dislocations (Figure 68) exhibited a non-equilibrium position highlighting the fact that they were pinned by solute atoms.

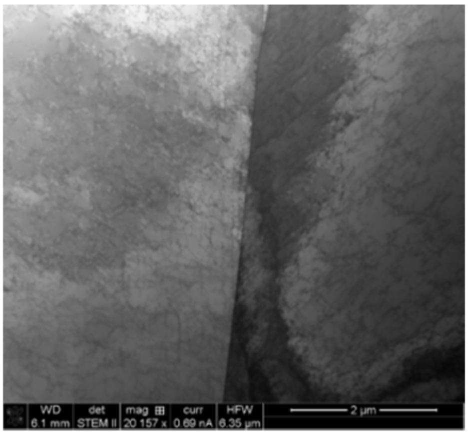

Figure 61 Dislocation stacks, $\Delta\varepsilon_t/2$ =0.5%, $\Delta\varepsilon_t/dt$=0.004%/s, 10 cycles, 300°C, the 10% cold rolled material.

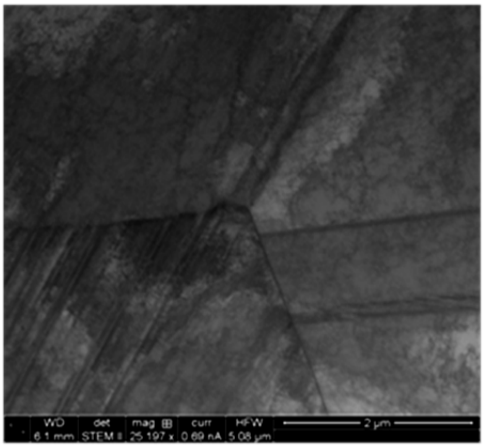

Figure 62 Planar glide, $\Delta\varepsilon_t/2$ =0.5%, $\Delta\varepsilon_t/dt$=0.004%/s, 10 cycles, 300°C, the 10% cold rolled material.

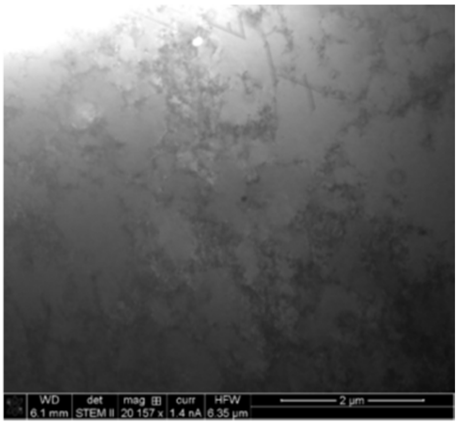

Figure 63 Dislocation stacks, $\Delta\varepsilon_t/2$ =0.5%, $\Delta\varepsilon_t/dt$=0.004%/s, 100 cycles, 300°C, the 10% cold rolled material.

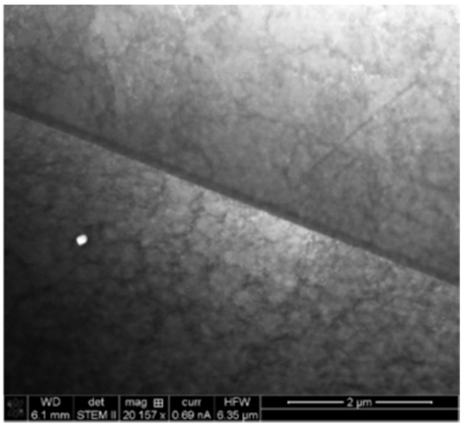

Figure 64 Beginning of cells organization, $\Delta\varepsilon_t/2$ =0.5%, $\Delta\varepsilon_t/dt$=0.4%/s, 100 cycles, 300°C, the 10% cold rolled material.

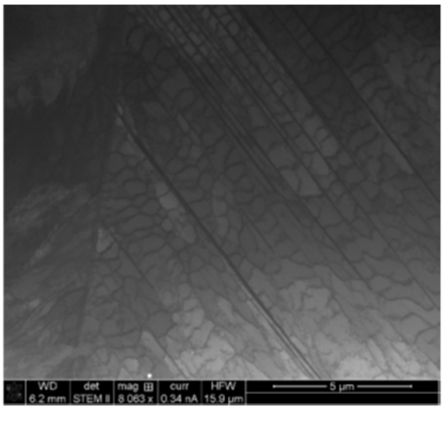

Figure 65 Planar structure, $\Delta\varepsilon_t/2$ =0.5%, $\Delta\varepsilon_t/dt$=0.004%/s, 600 cycles, 300°C, the 10% cold rolled material.

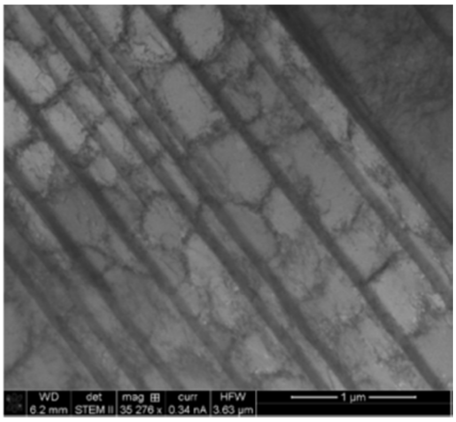

Figure 66 Planar structure crossed by cells, $\Delta\varepsilon_t/2$ =0.5%, $\Delta\varepsilon_t/dt$=0.004%/s, 600 cycles, 300°C, the 10% cold rolled material.

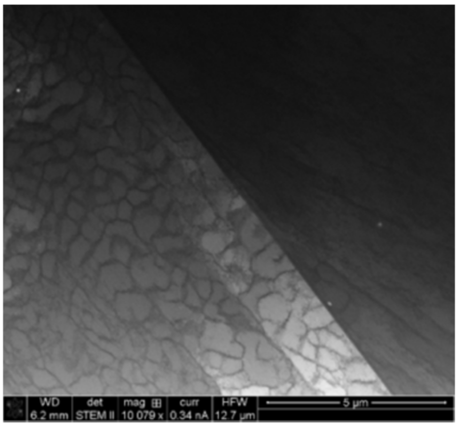

Figure 67 3D structures and alignments, $\Delta\varepsilon_t/2$ =0.5%, $\Delta\varepsilon_t/dt$=0.004%/s, 600 cycles, 300°C, the 10% cold rolled material.

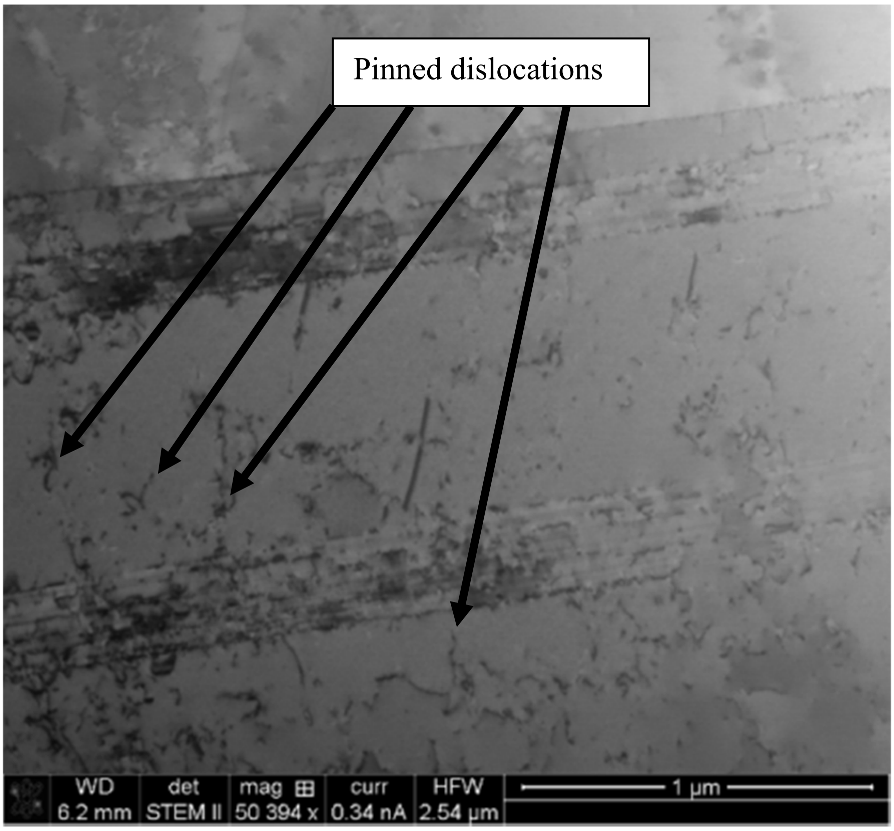

Figure 68 Planar glide composed of unorganized dislocations, stacking fault, alignment, $\Delta\varepsilon_t/2$ =0.5%, $\Delta\varepsilon_t/dt$=0.004%/s, 600 cycles, 300°C, the 10% cold rolled material.

6.1.3. Summary of observations

The microstructural evolutions are summarized in Figure 69 and Figure 70. In case of the as-received material (Figure 69), the primary hardening is linked to the generation of planar structures. The beginning of softening is related to the modification of the planar glide into 3D structures. Then the material softens by increasing the grain coverage by 3D structures. The softening continues by the reduction in the dislocation density on the 3D structure walls. At 600 cycles, it seems that the 3D structures are replaced by more planar glide structures. In addition, it seems that a reduction of the loading strain rate slightly modify the gliding properties that become more planar. However, our approach cannot clearly validate such assumption. Further observations are required. In the case of the 10% CR material (Figure 70), the initial microstructure of the material is composed of planar structures and dislocation stacks. During cycling the initial planar structures remain but the dislocation structure between the planar gliding starts to evolve into 3D structures. The material continues to soften by reducing the dislocation density of the 3D structures.

- **Effect of a pre hardening**

The primary hardening in the as-received material is related to the generation of dislocations, the dislocation generation rate is more important than the annihilation rate. In case of the pre hardened material, the pre hardening itself generates a high dislocation density and therefore there is no need to generate them by cycling but just to organize and annihilate them (the generation rate is lower than the annihilation rate).

Another aspect related to the pre hardening is that a part of the microstructure induced by the pre hardening consisting in dense planar glides remains during cycling.

- **Effect of the strain rate**

No clear modification of the microstructure was related to the strain rate (except a potential and slight modification of the gliding planarity) in the as-received material in agreement with the macroscopic mechanical behavior. However some trace of pinning was observed in the case of the 10% CR material. This pinning may result into an increase of the stress level in agreement with the mechanical behavior.

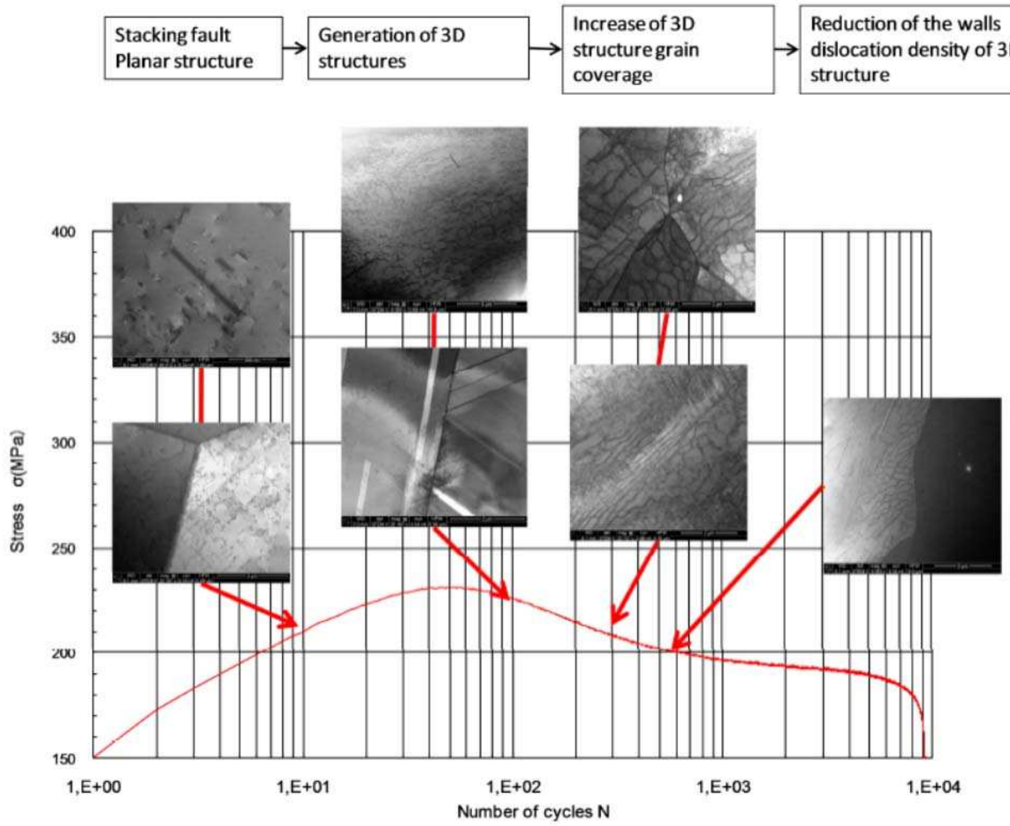

Figure 69 **Evolution of the microstructure during cycling at $\Delta\varepsilon_t/2 = 0.5\%$ and on the as-received material.**

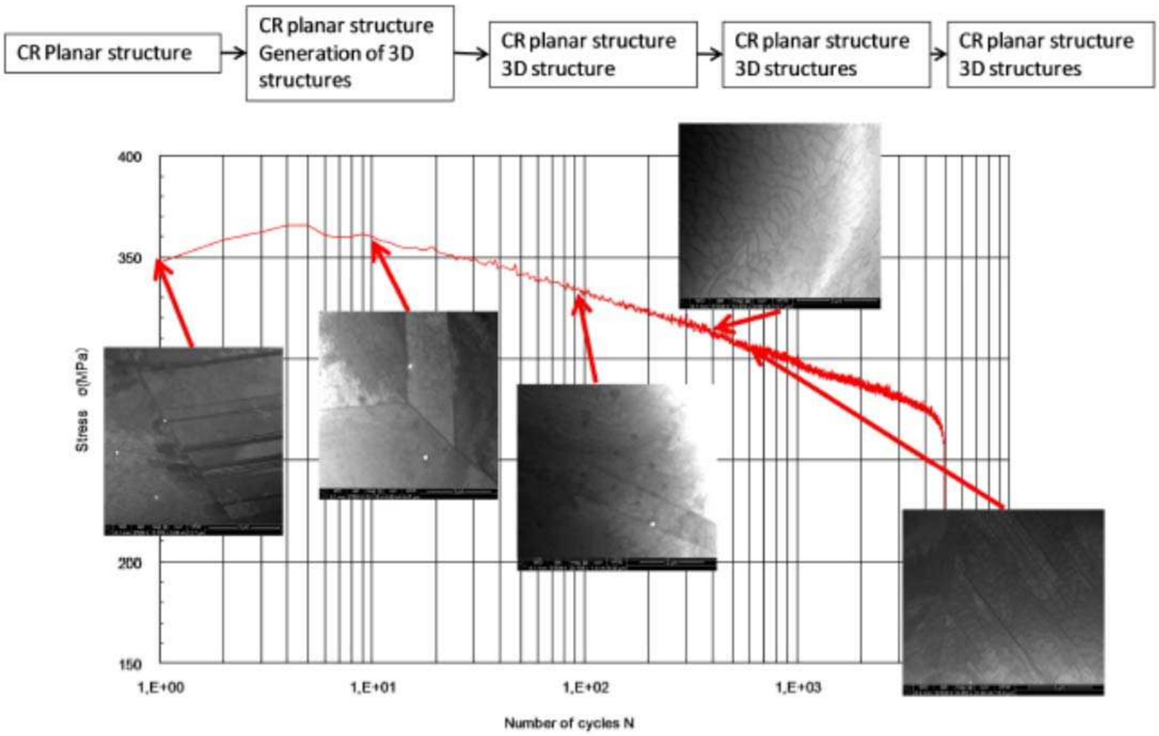

Figure 70 **Evolution of the microstructure during cycling at $\Delta\varepsilon t/2 = 0.5\%$ and on the 10% CR.**

6.2. Evolution of the fatigue damage at the specimen surface

The evaluation of cracking characteristics of the same previously tested sample is described in this section. A first part is dedicated to the evaluation of fatigue damage related to a prior strain hardening in relation with the applied strain rate. It consists in statistical observations coupling EBSD and optical microscopy of crack length and crack path evolutions during cycling as well as their relations with the local crystallography. The second section is dedicated to the TEM characterizations of cracking mechanisms at the dislocation scale of the as-received material and the effect of the loading strain rate on such mechanisms.

6.2.1. General observations

The investigations on deformation microstructure reveal that a pre hardening modifies the microstructural evolution during cycling: as-received and 10% CR 304L present different deformation structures and cyclic behaviors. In the analysis of the crack initiation mechanisms, it is important to check if differences in microstructures modify such mechanisms.

In order to quantify the damage on each sample, the crack length, the crack depth and the crack initiation angle as defined in chapter 2, were measured on the cross sections of the samples listed in Table 5. Figure 71 presents the evolution of the maximum crack depth as a function of the applied number of cycles at $\Delta\varepsilon_t/2 = 0.5\%$ and $\Delta\varepsilon_t/2 = 0.4\%$-0.004%/s for the as received and 10% CR materials.

At both strain rates and CR levels, after 100 cycles, some cracks were found. Though some scattering can be observed on each sample, from a cross section to another, the general evolution of the crack length (Figure 71) suggests that cracks initiates in air between 10 and 100 cycles. Figure 71 also indicates that this crack length increases with the number of cycles, without any influence of the strain rate and the pre-straining level.

Figure 72 presents the cumulative distribution of crack initiation angles for all data obtained on the interrupted tests. This plot points out a major peak in the range from 40° to 60° and also a smaller one in the range 80° to 90°. Furthermore, these histograms did not vary significantly with the number of cycles. This distribution has been compared to the most probable active slip plane emergence angle evaluated using EBSD analysis (Figure 73) that presents the same kind of distribution with a dominant range between 40° to 60° but not between 80° to 90°. The good agreement between the dominant ranges (crack orientation and the most probable activated slip plane, exhibiting the highest Schmid factors) reveals that most of the cracks, within the first grain, are in stage 1. The second range between 80° and 90° could be related to other type of crack initiation (for example along grain boundaries).

Because crack initiation kinetics and crack initiation angles on cold work material are similar, initiation mechanisms may be similar for AR and CR materials. The different evolutions of the dislocation structures did not seem to affect crack initiation mechanisms. The difference of fatigue life induced by a pre hardening in air environment cannot be related to a difference of crack initiation mechanism within the first grains. This difference may be related with a difference of crack growth kinetics.

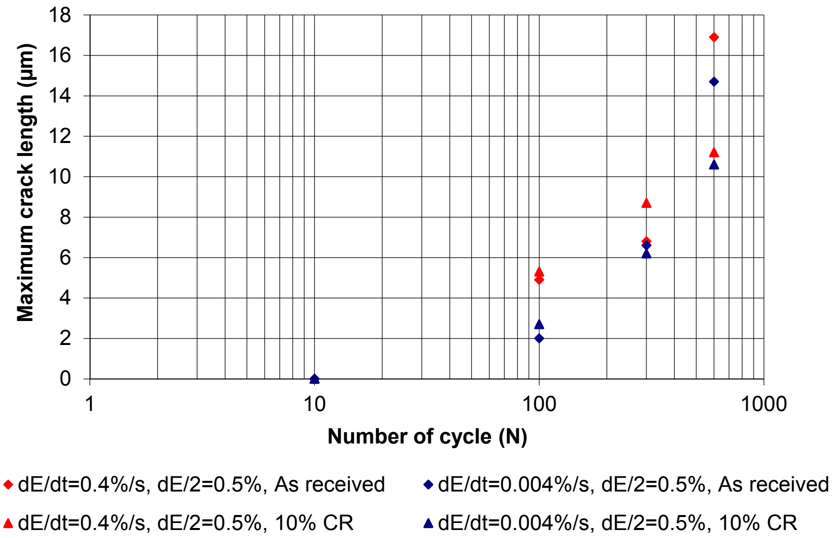

Figure 71 Evolution of maximum crack length at 300°C as a function of the applied number of cycles in the early stages of crack initiation and growth

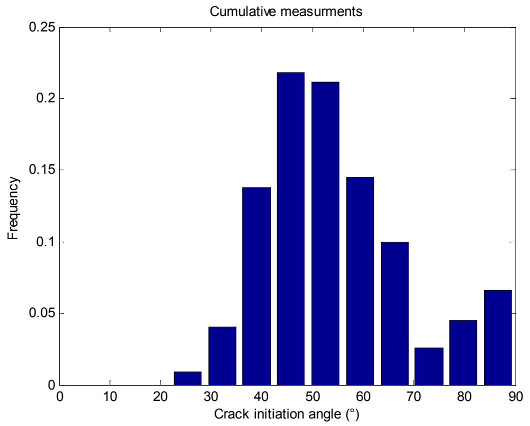

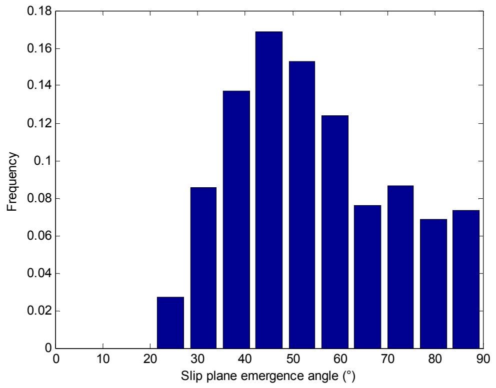

Figure 72 Distribution of crack initiation angles. **Figure 73 Slip plane emergence angles.**

6.2.2. Mechanisms of fatigue crack initiation

Strain localization at the free surface (with or without environmental effect) is well known [6] to be a relevant mechanism that promotes fatigue crack initiation. Therefore, TEM investigations on fatigue crack initiation sites have been undertaken.

Two samples (registered 1630-83 and 1630-78) tested at $\Delta\varepsilon_t/2$ =0.5% for 100 cycles in the air environment at 300°C at respectively 0.004%/s and 0.4%/s were analyzed.

Figure 74 illustrates a representative area at the surface of the sample 1630-83 ($\Delta\varepsilon_t/2$ =0.5%, $\Delta\varepsilon_t/dt$=0.004%/s, 100 cycles, air, 300°C) where the strain localization resulted in the initiation of a transgranular (TG) crack. The length of this crack measured at the outer surface was about 35 μm. SEM and STEM observations on cross section of this crack show that crack initiation occurred along a particular strain structure (Figure 75). In addition, it is possible to observe a modification of the surface roughness where crack initiated. At the bottom of the TEM sample, other structures following multiple slip planes were observed (Figure 76).

TEM observations in two-beam conditions were performed in order to characterize strain feature related to the crack initiation (Figure 77). These observations revealed the presence of alignments of dislocations cells just below the crack and of another structure consisting in slip bands. Other observations revealed the presence of dislocation cells along the crack (Figure 78). The shape of the crack seemed to follow the cell walls.

Figure 79 to Figure 81 present dark field images corresponding to sub spots in the diffraction pattern obtained placing the matrix in the <114> orientation (Figure 82). These dark field images reveal the presence of micro twins induced by the machining of the sample. This aspect must be kept in mind in a sense that the crack initiation process occurs in this pre hardened area and the results on the dislocation structures might be affected by its presence.

Figure 83 is a STEM-HAADF observation of the crack. This image suggests that areas of different chemical compositions (higher atomic level results in brighter contrast) exists within the crack, in the matrix and at the outer surface. Figure 84 corresponds to an EDX profile following the red line in Figure 83. This profile reveals the presence of oxygen enrichment inside the crack. The chemical composition evolves from the base metal to the crack vicinity: Ni enrichment followed by Cr/O enrichment (associated with a Fe depletion) then Fe/O enrichment. It must be noted that this chemical species profile is also representative of the chemical composition of oxide layers formed on SS exposed to PWR primary environment at high temperatures (> 320°C) [7]. Oxide thickness on crack flanks is about 35 □40 nm. At the outer surface, the oxide thickness is lower than 3-4 nm. The fact that oxide is thick at crack tip may be symptomatic of a strain induced oxidation mechanism (Chapter 1).

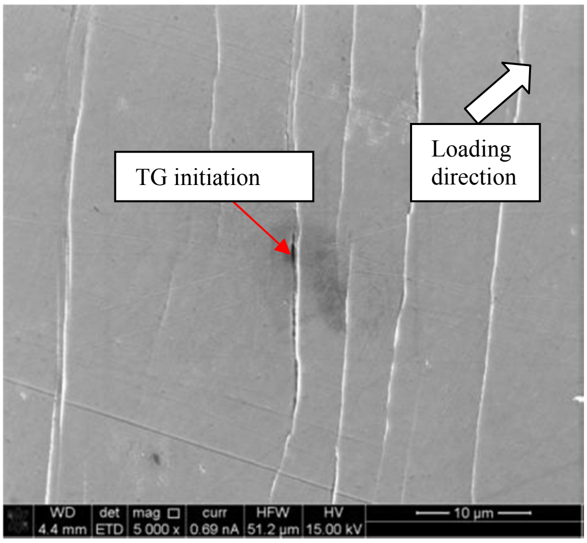

Figure 74 Fatigue crack initiation at the surface of sample 1630-83 $\Delta\varepsilon_t/2$ =0.5%, $\Delta\varepsilon_t/dt$=0.004%/s, 300°C

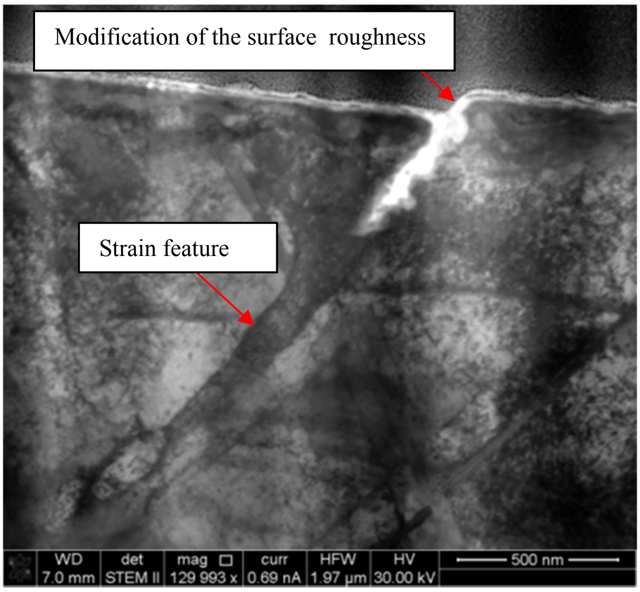

Figure 75 STEM cross section of sample 1630-83 $\Delta\varepsilon_t/2$ =0.5%, $\Delta\varepsilon_t/dt$=0.004%/s, 300°C

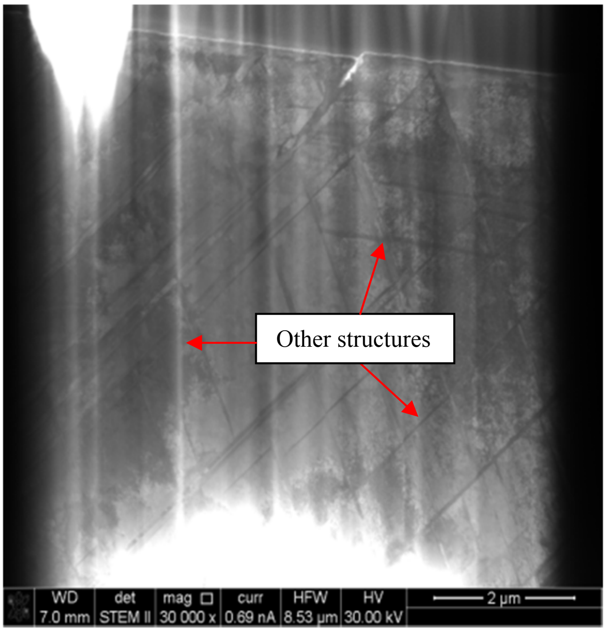

Figure 76 STEM cross section of sample 1630-83 $\Delta\varepsilon_t/2$ =0.5%, $\Delta\varepsilon_t/dt$=0.004%/s, 300°C.

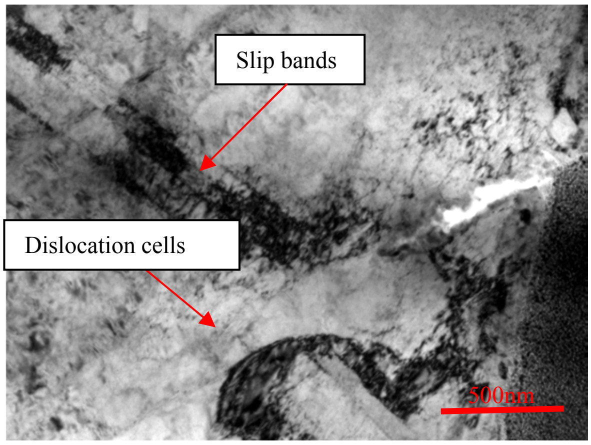

Figure 77 □TEM (2 beams conditions) of sample 1630-83 $\Delta\varepsilon_t/2 = 0.5\%$, $\Delta\varepsilon_t/dt = 0.004\%/s$, 300°C.

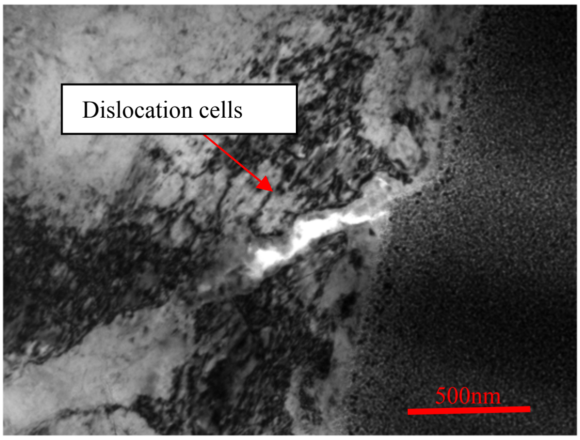

Figure 78 □TEM (2 beams conditions) of sample 1630-83 $\Delta\varepsilon_t/2 = 0.5\%$, $\Delta\varepsilon_t/dt = 0.004\%/s$, 300°C

Figure 79 □TEM Dark field image of sample 1630-83 $\Delta\varepsilon_t/2 = 0.5\%$, $\Delta\varepsilon_t/dt = 0.004\%/s$, 300°C. (spot 1)

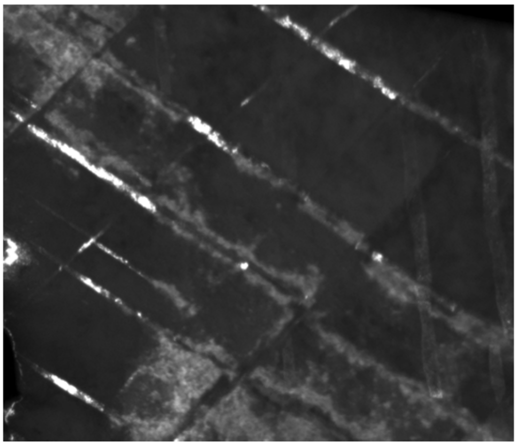

Figure 80 □TEM Dark field image of sample 1630-83 $\Delta\varepsilon_t/2 = 0.5\%$, $\Delta\varepsilon_t/dt = 0.004\%/s$, 300°C. (spot 2)

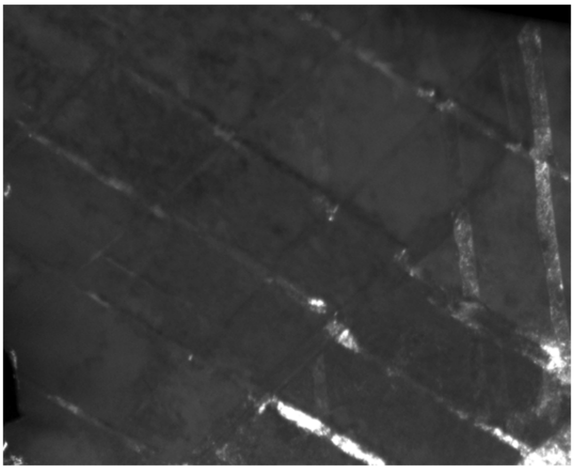

Figure 81 □TEM Dark field image of sample 1630-83, $\Delta\varepsilon_t/2 = 0.5\%$, $\Delta\varepsilon_t/dt = 0.004\%/s$, 300°C. (spot 3)

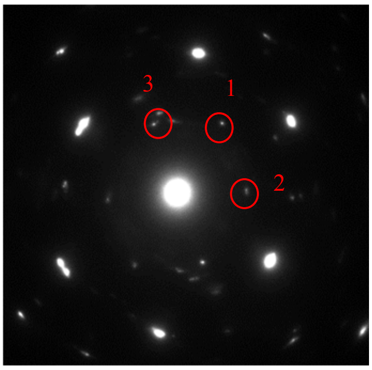

Figure 82 □Diffraction pattern of sample 1630-83 $\Delta\varepsilon_t/2 = 0.5\%$, $\Delta\varepsilon_t/dt = 0.004\%/s$, 300°C.

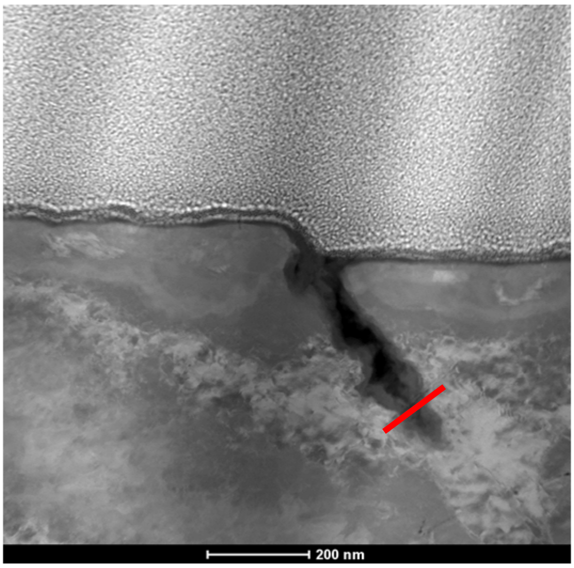

Figure 83 HAADF - STEM cross section of sample 1630-83 $\Delta\varepsilon_t/2$ =0.5%, $\Delta\varepsilon_t/dt$=0.004%/s, 300°C. EDX profile along red line.

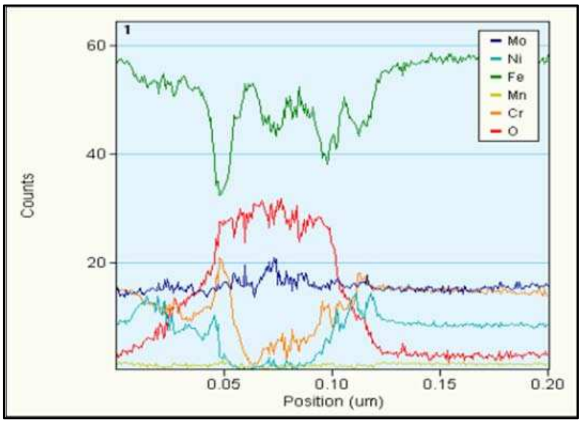

Figure 84 EDX profile, EDX profile along red line present in Fig 82.

Figure 85 gives a representative area of the surface of the sample 1630-78 tested at a higher strain rate ($\Delta\varepsilon_t/2$=0.5%, $\Delta\varepsilon_t/dt$=0.4%/s, 100 cycles, air, 300°C) where a TG fatigue crack initiated. The length of the main crack at the surface was about 15 µm. As previously observed, cracks initiated in preferential areas where strain localization occurred. Figure 86 is an STEM overview of the TEM sample revealing the presence of 2 cracks aligned with deformation features. Other features corresponding to micro twins induced by sample machining were observed (Figure 86).

Figure 87 corresponds to a TEM observation in two-beam conditions of crack #1 in Figure 86. This image confirms the presence of a dislocation cells alignments below the crack tip contained in a band. Figure 88 and Figure 89 correspond to TEM observations in two-beam conditions of crack #2 in Figure 86. Figure 88 suggests that crack initiation occurred at a site where there was a modification of the surface roughness induced by the microstructural evolution. Below the crack tip it is possible to observe two dislocation cell alignments lying in shear bands. A microtwin induced by machining was sheared by the cells alignment. Figure 89 reveals that the crack follows a first shear band and then deviates along another shear band. No specific oxidation was observed at this strain rate.

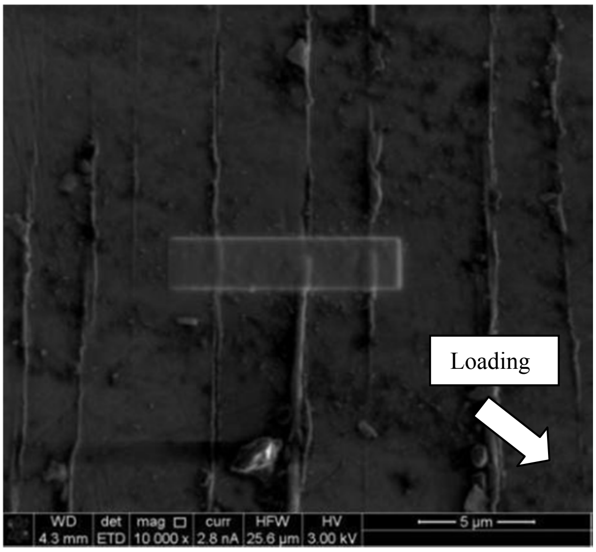

Figure 85 Fatigue crack initiation at the surface of sample 1630-78, $\Delta\varepsilon_t/2$ =0.5%, $\Delta\varepsilon_t/dt$=0.4%/s, 300°C.

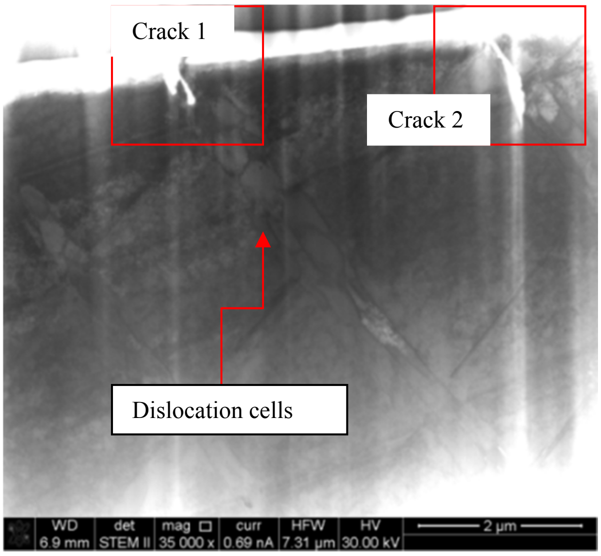

Figure 86 SEM-STEM cross section of sample 1630-78, $\Delta\varepsilon_t/2$ =0.5%, $\Delta\varepsilon_t/dt$=0.4%/s, 300°C.

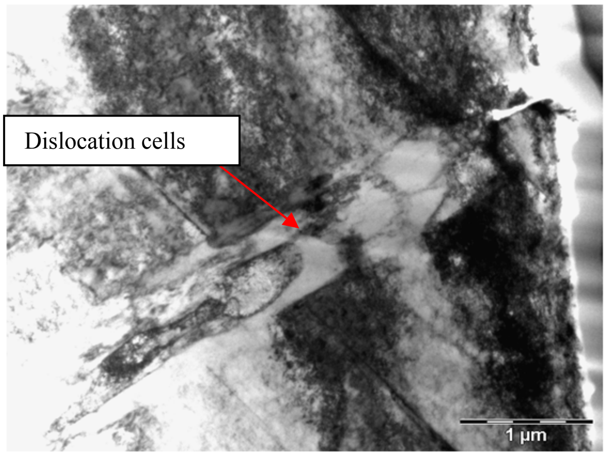

Figure 87 TEM (2 beams conditions) of sample 1630-78, $\Delta\varepsilon_t/2$ =0.5%, $\Delta\varepsilon_t/dt$=0.4%/s, 300°C (crack 1).

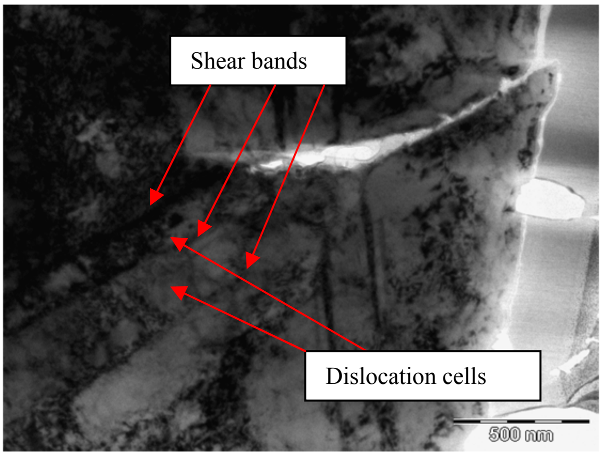

Figure 88 TEM (2 beams conditions) of sample 1630-78, $\Delta\varepsilon_t/2$ =0.5%, $\Delta\varepsilon_t/dt$=0.4%/s, 300°C (crack 2).

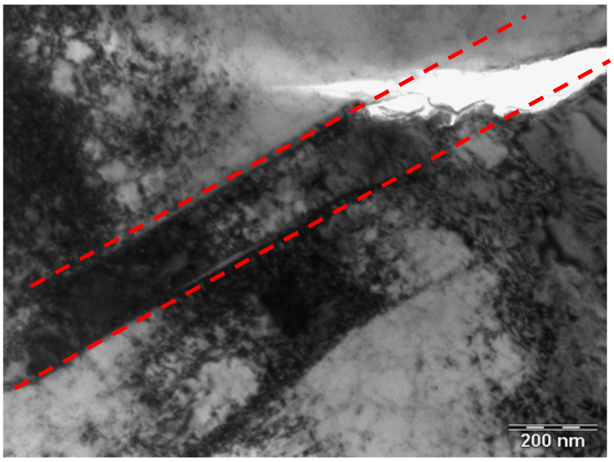

Figure 89 TEM (2 beams conditions) of sample 1630-78, $\Delta\varepsilon_t/2$ =0.5%, $\Delta\varepsilon_t/dt$=0.4%/s, 300°C (crack 2).

6.2.3. Summary of observations

The general evaluation of cracking characteristics of the as-received and the 10% CR material tested at different strain rates were found to be similar. Indeed in all cases, the cracking kinetics within the first 600 cycles were found to be highly similar. In addition, in all tests conditions, the crack initiation process followed the [111] slip plane of the slip system presenting the highest Schmid factor. Therefore the fatigue life reduction related to a prior hardening cannot be related to a modification of the crack initiation process.

Evaluation of crack initiation mechanisms at the dislocation scale leads to the following: during cycling, the strain within the first grain in air environment is accommodated by the generation of shear bands containing 3D dislocation structures such as PSB and cells, generating a modification of the surface roughness leading to a TG crack initiation.

These shear bands follow the slip system presenting the highest Schmid factor (Figure 90). Concerning the strain rate effect on the cracking process in air, it seems that this factor does not modify the cracking initiation kinetics. The dislocation structures are also similar between the two strain rates. The only noticeable difference is that it was possible to observe some interactions between the strain localization and the oxidation process at the lowest strain rate but this difference does not modify the cracking kinetics as well as the fatigue life in air environment.

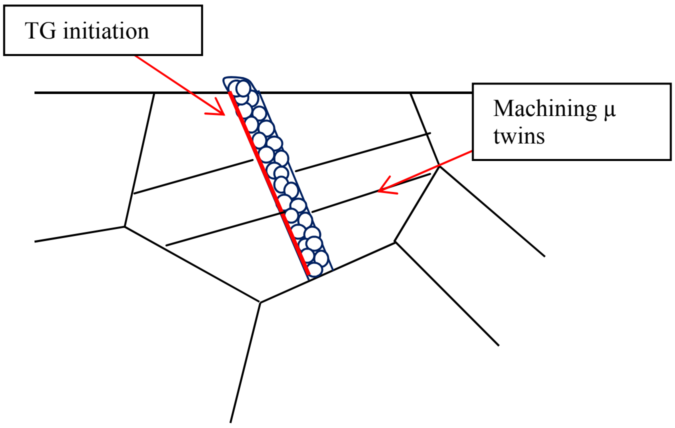

Figure 90 Summary view of the crack initiation mechanism in air environment.

7. Summary

To establish the difference in fatigue damage between the air and the PWR primary environment related to strain rate and a pre hardening, the behavior of the material in terms of macroscopic cyclic-stress strain behavior, the fatigue life and the damage processes were firstly studied in air. The main findings related to the cyclic stress-strain behavior, fatigue life and damage mechanisms can be summarized as follows.

- Cyclic stress-strain behavior

The mechanical behavior highly depends on the cold work level. An increasing cold work level results in an increase of the stress level and a reduction of the number of cycles in the primary hardening phase.

In the case of the as-received material, the primary hardening results in the generation of planar structures and the softening in the re arrangement of the planar structures into 3D structures. No clear effect of the loading strain rate was noticed. However, a tendency to an increase of planar glide might be considered at the lowest strain rate.

The microstructural evolution of the 10% CR, material consists in the evolution of dislocation structures from stacks into 3D structures between the planar structures generated by the pre hardening that remains during cycling. A reduced strain rate results in an increase of the stress level associated with the presence of pinned dislocations.

- Fatigue life

The prior strain hardening within a 0-10% range of 304L SS leads to a reduction of fatigue life in the low cycle regime and to an increase of fatigue life in the high cycle regime. The nature of pre hardening does not seem to modify this tendency.

- Damage mechanisms

No clear difference of crack initiation mechanisms (localization and kinetics) related to pre a hardening was found. Therefore the differences of fatigue lives induced by a pre hardening cannot be explained by a modification of the initiation phases but seems to be rather related to micropropagation.

Initiation mechanisms are related to the modification of the surface roughness induced by the emergence of 3D dislocation structure at the surface of the first grains. TG crack initiation occurs on grain presenting the highest Schmid factors. The only noticeable difference as a function of strain rate was observed in the case of a low strain rate, where the presence of interactions between strain localization and oxidation was highlighted, pointing out an important environmental effect even in air environment.

However the fact that an oxide was present at a lower strain rate does not seem to affect deformation structure, cracking mechanisms and the fatigue life in this environment.

---

[1] **O.K. CHOPRA, W.J. SHACK** , "Effect of LWR Coolant Environments on the Fatigue Life of Reactor Materials," Final Report, NUREG/CR-6909, ANL-06/08, Feb. 2007.

[2] **M. GERLAND, J. MENDEZ, P. VIOLAN, B. AIT SAADI**, "Evolution of dislocation structures and cyclic behavior of a 316L-type austenitic stainless steel cycled in vacuum at room temperature", Materials Science and Engineering A, Vol. A118, pp. 83-95, Octobre 1989

[3] **J.P. MASSOUD, M. BETHMONT, J. CHAMPREDONDE**, “Long term aging of cast duplex stainless steel between 300 and 400°C _ Relationship between toughness properties and metallurgical parameters, Duplex Stainless Steels'91”, 1991 Vol. 1,pp. 93.

[4] **F.B. PICKERING**, "Physical metallurgy and the design of steels", Applied Science Publishers, London, 1978.

[5] **H.D. SOLOMON** et al., “Comparison of the fatigue life of type 304L SS as measured in load and strain controlled tests”, 12th International Conference on environmental degradation of materials in nuclear systems-water reactors, Snowbird (Utah), 2005, pp1101-1110

[6] **S. SURESH** “Fatigue of Materials 2nd edition”, Cambridge University Press, 2006

[7] **T. COUVANT, F. VAILLANT, T. GHYS**, "Development of understanding of the interaction between localized deformation and SCC of austenitic stainless steels exposed to primary PWR environment" , EDF R&D report H-T29-2008-0945-EN, 2008.

CHAPTER 4: fatigue in simulated primary PWR water

List of acronyms

BF : Bright Field
BSED : BackScattered Detector
DF : Dark Field
EBSD : Electron BackScattered Difraction
EFTEM : Energy Filtered Transmission Electron Microscope
ETD : Everhart-Thornley Detector
GE : General Electric
HAADF : High Angular Anular Dark Field
ID : Inner Diameter
IG : Intergranular
LCD : Linear Crack Density
MHI : Mitsubishi Heavy Industries
OD : Outer Diameter
PWR : Pressurized Water Reactor
SCC : Stress Corrosion Cracking
SEM : Scanning Electron Microscope
STEM : Scanning Transmission Electron Microscope
TEM : Transmission Electron Microscope
TG : Transgranular

Summary

1. Introduction

The objective of this chapter is to present the results of fatigue tests conducted in PWR primary environment.

In a first part, the macroscopic cyclic stress-strain behavior of the 304L material is presented. A particular attention is given to the influence of a prior cold work level and of the strain rate on the fatigue life in PWR Primary environment. One of the objectives of this work is to provide new additional data to support codification. The obtained results will be then compared to those presented in chapter 3 within the chapter 5 in order to evaluate the effect of PWR environment on fatigue life for the different predeformation conditions investigated.

In a second part, the evolution and the characteristics of the fatigue damage will be characterized from the crack initiation stage up to failure. A specific test matrix was defined in order to investigate the cracking mechanisms during the first steps of a fatigue crack in PWR primary environment. A special attention is paid to the interactions between strain localization and oxidation processes at different observation scales. Additional data concerning the crack propagation behavior is given from the fracture surface observation focusing on fatigue striations.

As in the chapter 3, neither interpretation nor discussion will be given in this chapter. All the results will be discussed within the chapter 5.

2. Fatigue tests in PWR primary environment at 300°C

Table 1 shows the matrix of fatigue tests conducted up to failure in simulated PWR primary water at 300°C along with data obtained by GE [1]. The investigated factors were the mode (tension or cold rolling) and the level of cold working (5% and 10%), the strain rate in the tension part of the cycle and the total strain amplitude applied during the test.

The as-received 304L material was tested, as a reference, at the strain amplitude of 0.5%. Four total strain amplitudes were investigated in case of the pre hardened materials as $\Delta\varepsilon_t/2$=0.15%, 0.25%, 0.35% and 0.5%. The strain rate in compression was kept constant at 0.4%/s in all the tests conditions. Two types of waveforms were applied:

- ⇨ Triangle waveform with a strain rate of 0.4%/s both in tension and compression.

- ⇨ Saw tooth waveform with a low strain rate of 0.004%/s in tension ($d\varepsilon/dt > 0$) and a higher strain rate of 0.4%/s in compression ($d\varepsilon/dt < 0$).

Due to the presence of the primary water inside of the hollow cylindrical specimen, fatigue cracks initiated at the inner diameter (ID) and propagated towards the outer surface (OD). For these specimens, fatigue lives were defined as the number of cycles at which the crack growth through the wall thickness leading to a leakage (N_{leak}).

In order to obtain some information concerning the cracking mechanisms on the early steps of fatigue life, additional interrupted tests were undertaken. The main idea was to characterize crack extension during the fatigue life and the associated microstructures at the vicinity of the surface. These tests are listed in Table 2.

Table 1 □Results obtained in PWR primary environment at 300°C.

	TP-ID		Strain rate（%/sec）		Strain amplitude (%)	Fatigue life (N)	Comment
			in tension	in compression			
PWR primary water	As-received	1630 MHI 01	0.4	0.4	0.51	3114	
		1630 MHI 04	0.004	0.4	0.51	859	
		EDF-5-2 (GE)	0.4	0.4	0.49	2729	
		EDF-5-10 (GE)	0.4	0.4	0.5	3309	
		EDF-5-11 (GE)	0.4	0.4	0.345	8341	
		EDF-5-19 (GE)	0.4	0.4	0.35	10430	
		EDF-5-20 (GE)	0.4	0.4	0.245	13889	
		EDF-5-22 (GE)	0.4	0.4	0.2	32630	
		EDF-5-1 (GE)	0.4	0.4	0.15	63000	
		EDF-5-23 (GE)	0.4	0.4	0.1475	68109	
		EDF-5-34 (GE)	0.4	0.4	0.125	110670	
		EDF-5-25 (GE)	0.4	0.4	0.1	3437070	Run out
		EDF-5-39 (GE)	0.4	0.4	0.103	10000000	Run out
		EDF 5-29 (GE)	0.004	0.4	0.5	1328	
		EDF 5-38 (GE)	0.004	0.4	0.34	2781	
		EDF 5-33 (GE)	0.004	0.4	0.25	6029	
	10% tension at EDF	1630 MHI 02	0.4	0.4	0.52	2224	
		1630 MHI 03	0.004	0.4	0.51	827	
	5% Rolling at EDF	1630 MHI 05	0.4	0.4	0.51	2870	
		1630 MHI 07	0.004	0.4	0.51	953	
	10% Rolling at EDF	1630 MHI 11	0.4	0.4	0.52	2590	
		1630 MHI 12	0.4	0.4	0.36	7361	
		1630 MHI 13	0.4	0.4	0.26	16634	
		1630 MHI 17	0.4	0.4	0.15	1000000	Run out
		1630 MHI 14	0.004	0.4	0.51	887	
		1630 MHI 15	0.004	0.4	0.36	2162	
		1630 MHI 16	0.004	0.4	0.26	6864	

Table 2 □Stop test matrix in PWR primary environment at 300°C.

	TP-ID	Strain rate (%/s)		Strain amplitude (%)	Number of cycle
		in tension	in compression		
As-received	1630MHIST2	0.4	0.4	0.5	10
	1630MHIST5	0.004	0.4	0.5	10
	1630MHIST3	0.4	0.4	0.5	100
	1630MHIST6	0.004	0.4	0.5	100
	1630MHIST4	0.4	0.4	0.5	300
	1630MHIST7	0.004	0.4	0.5	300
10% Rolled	1630MHI18	0.004	0.4	0.5	10
	1630MHI19	0.004	0.4	0.5	100
	1630MHI20	0.004	0.4	0.5	300

3. Cyclic stress-strain behavior in PWR primary environment at 300°C

Figure 1 presents the maximum stress amplitude as a function of the number of cycles for specimens machined from a 10% CR 304L plate and tested in PWR primary environment at 300°C. All specimens, irrespective of strain rate, experienced a strain hardening only at the beginning of cycling (nearly up to 10 cycles). This initial hardening is followed a marked softening until failure, when the total imposed strain amplitude is higher than 0.26%. In contrast at a strain amplitude of 0.15%, the stress level remains stable, neither hardening nor softening occurred. Regarding the effect of the strain rate on these behaviors, it appears that a low strain rate (open symbols) leads to higher strain hardening with respect to a high strain rate (solid symbols).

Figure 2 shows the variations of the non-elastic strain as a function of the number of cycles. It illustrates the progressive softening during cycling, except for the 0.15% strain amplitude. In the case of the strain amplitude of 0.15%, the non-elastic strain remains almost zero up to the end of the test, so that this test was considered to have been performed almost in the elastic domain.

Figure 3 presents the evolution of the mean stress. A mean stress of about 20-30 MPa is only observed at the lowest strain amplitudes, i.e. 0.15% and 0.26%. When increasing the applied strain amplitude, the mean stress decreases down to almost zero. Finally, Figure 4 shows the evolution of stress as a function of the number of cycles. These results indicate that a high pre-hardening level results in an increase of cyclic stress level. No clear difference was observed between the 10% tensioned and the 10% cold rolled 304L, suggesting that the mode of pre straining does not affect the macroscopic behavior.

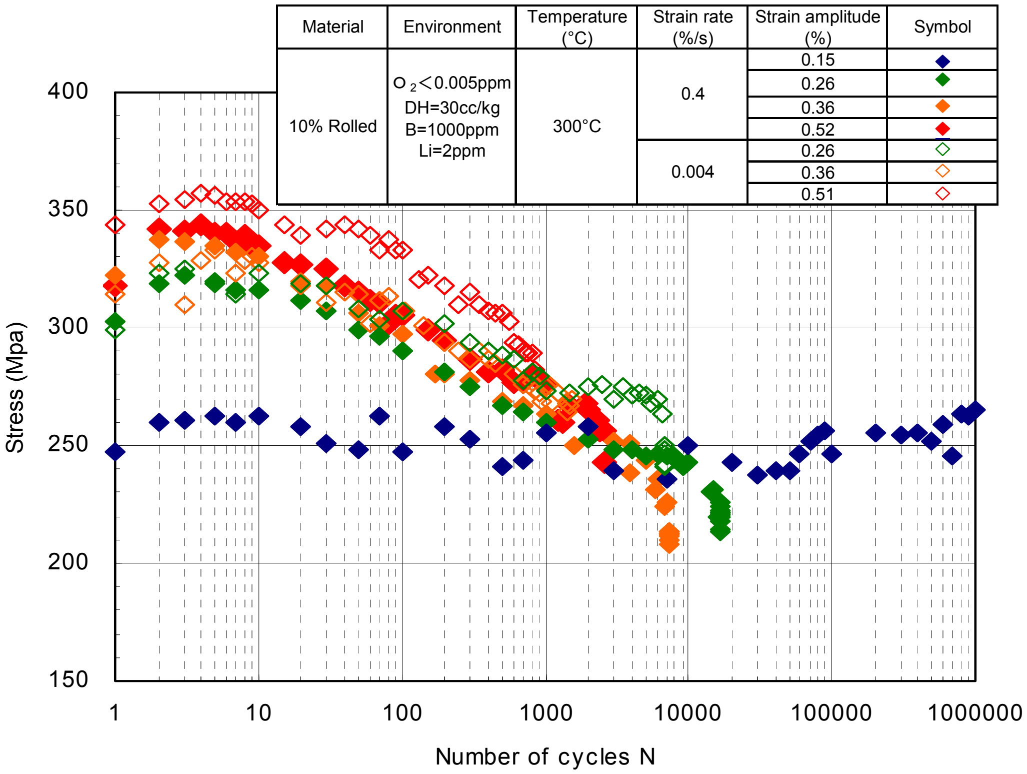

Figure 1 □Evolution of stress as function of number of cycles on the cold-worked material.

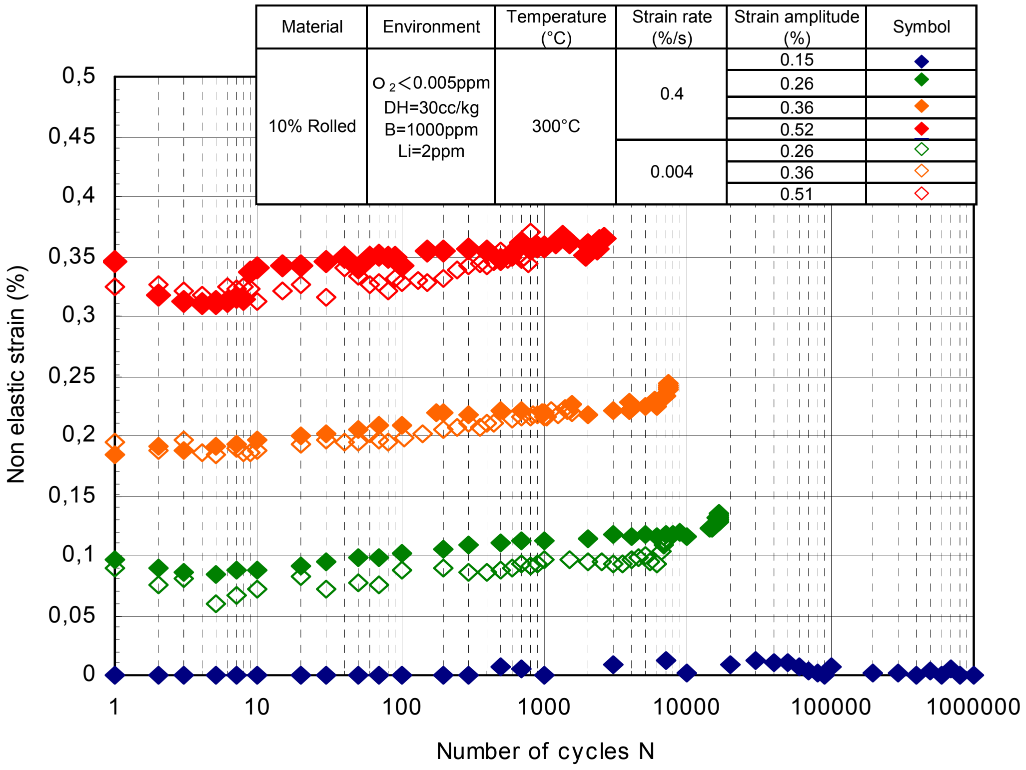

Figure 2 - Evolution of non-elastic strain as function of number of cycles.

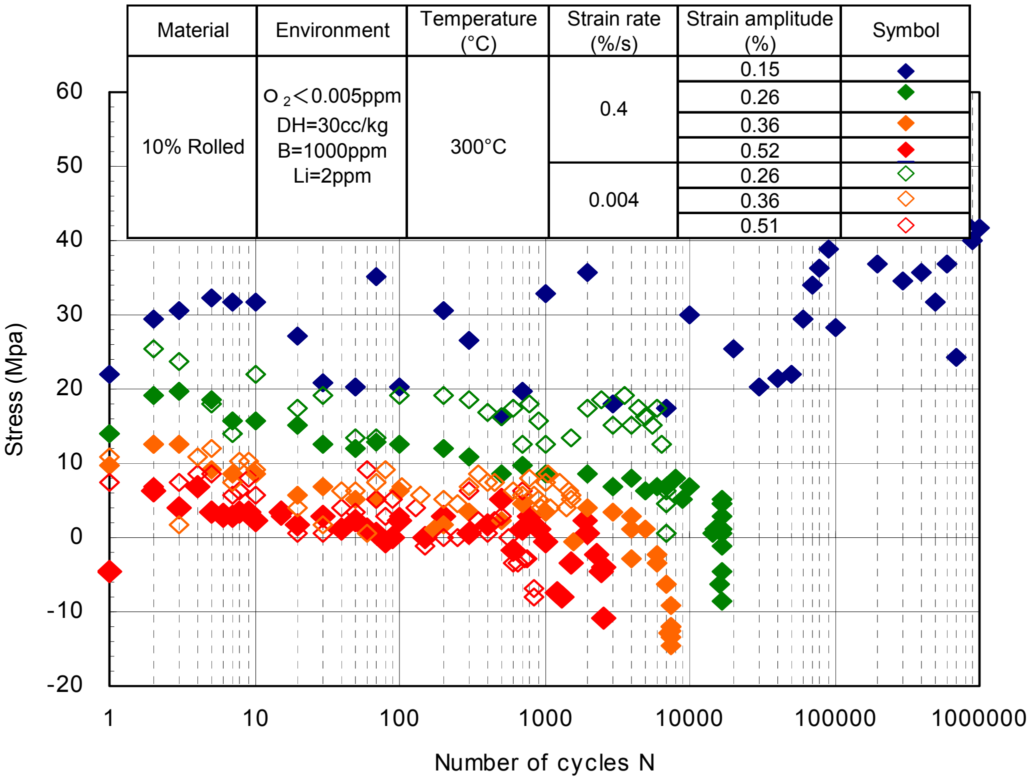

Figure 3 - Evolution of mean stress as function of number of cycles in primary water.

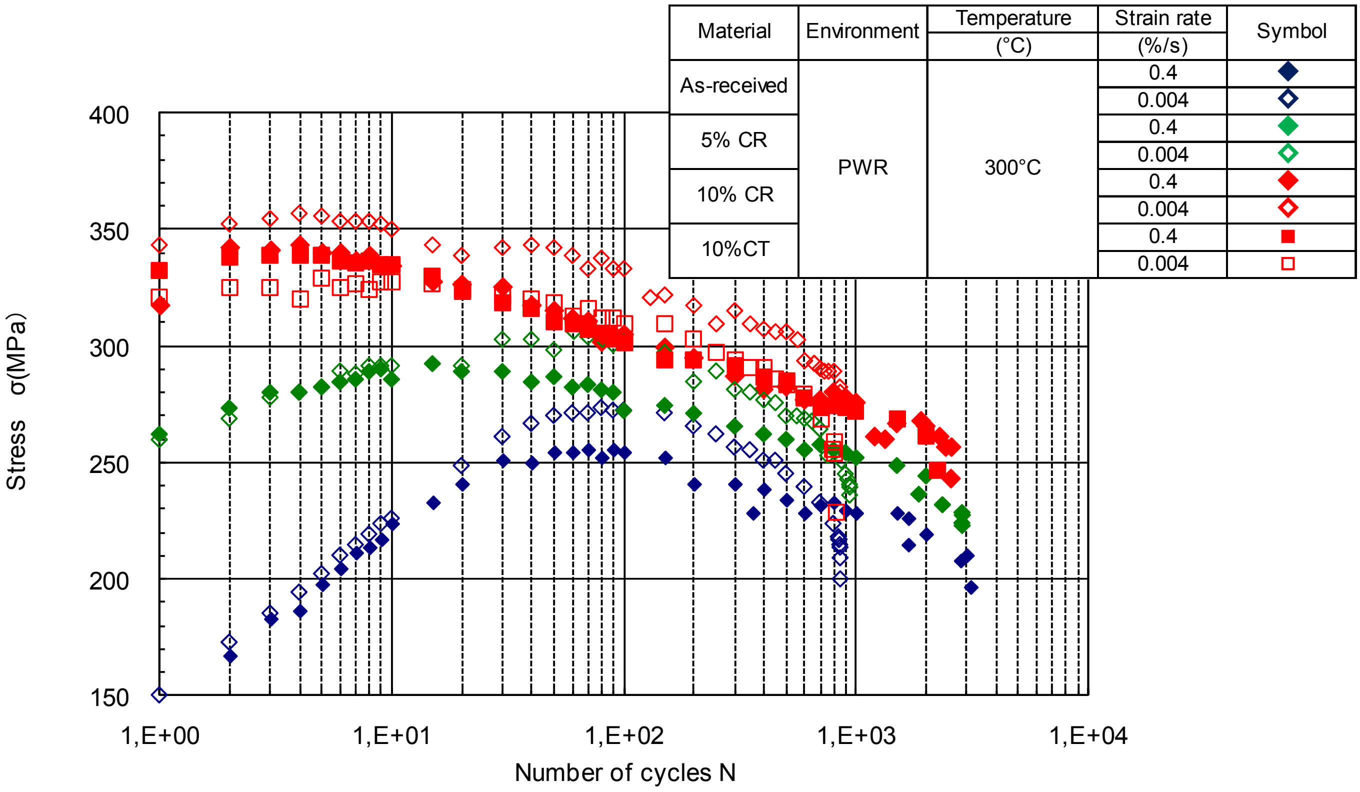

Figure 4 - Evolution of positive stress as a function of number of cycles.

4. Fatigue lives

Fatigue ε-N data obtained at two strain rates of 0.4%/s and 0.004%/s in PWR primary water are presented in Figure 5 along with data from GE, comparing the as-received with the cold worked materials.

In simulated PWR primary environment (Figure 5), fatigue lives of the cold-worked materials are almost the same as those of the as-received one at total strain amplitudes higher than 0.2%, indicating that the loss of ductility and the increase of stress level induced by a prior cold working do not necessarily affect the fatigue life in this environment. The fatigue limit of a 10% CR material at 10^6 cycles is clearly increased up to a strain amplitude of 0.15%. It should be noted that, in Figure 5, the plots at strain amplitude of 0.5% include the results obtained with hollow-type specimens (MHI) and with solid specimens (GE). The limited scatter suggests that the effect of specimen shape on fatigue life remains negligible in comparison with experimental data scatters.

As planned, a reduction strain rate results in a decrease of the fatigue life and a pre hardening does not seem to affect this tendency.

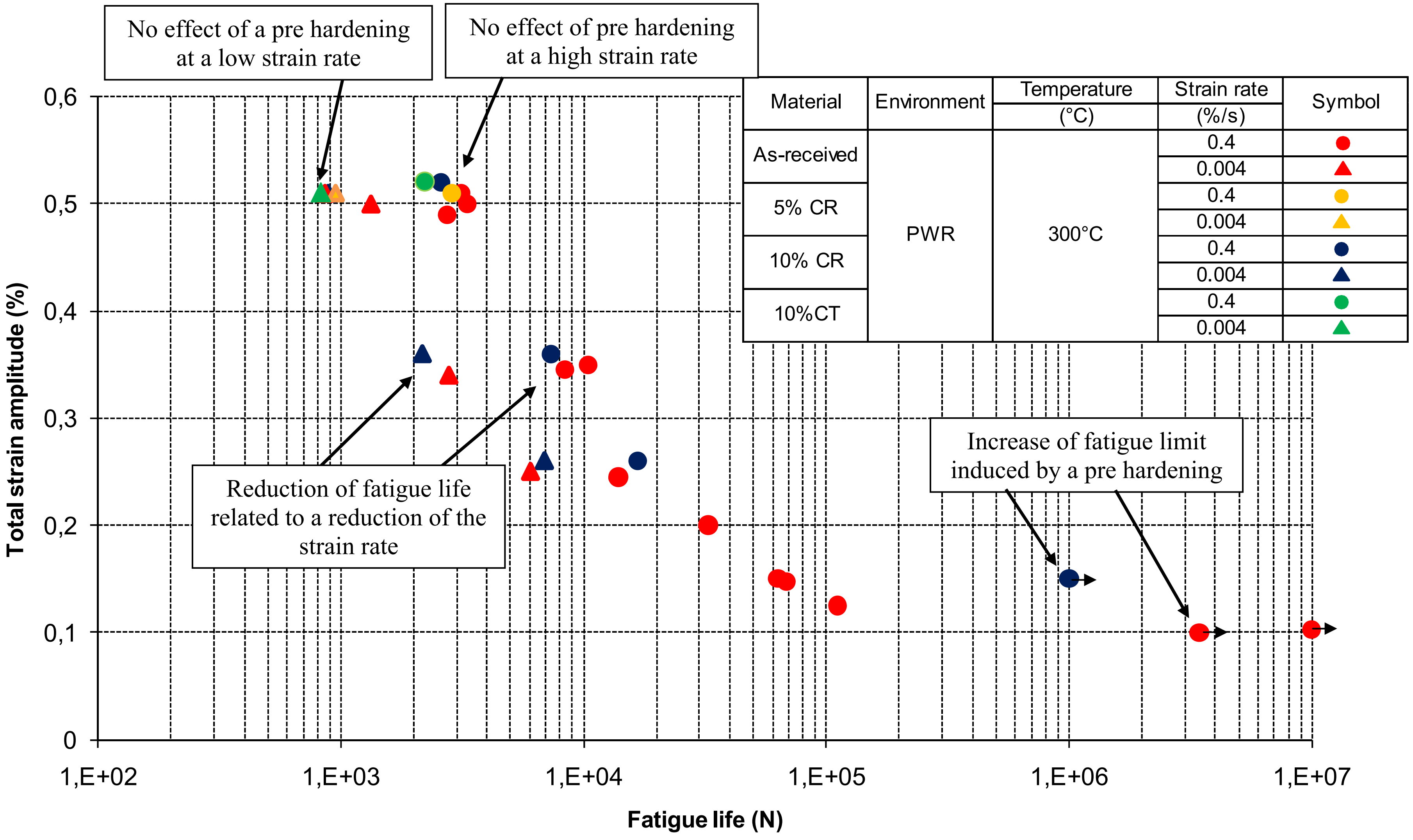

No effect of a pre hardening at a low strain rate

No effect of pre hardening at a high strain rate

Reduction of fatigue life related to a reduction of the strain rate

Increase of fatigue limit induced by a pre hardening

Material	Environment	Temperature (°C)	Strain rate (%/s)	Symbol
As-received	PWR	300°C	0.4	●
			0.004	▲
5% CR			0.4	●
			0.004	▲
10% CR			0.4	●
			0.004	▲
10%CT			0.4	●
			0.004	▲

Figure 5 - Strain amplitude vs. fatigue life data for XY182 at 300°C in simulated PWR water

5. Evolution of the fatigue damage in primary water

The main goal of this section is to identify typical characteristics of the fatigue damage in PWR primary environment, in the initiation stage and the propagation stage.

Concerning the crack initiation stage:

- In a first part some characteristics of fatigue cracks are observed on cross sections of specimens tested up to failure. Indeed such information can be useful in the failure analysis of nuclear components (see appendix 1). These observations take into account the potential effect of a prior cold working and strain rate.
- A second part aims in characterizing the EAF damage related to the interactions between strain localization and the PWR environment in the as-received material only. The influence of the loading strain rate will be investigated.

Concerning the crack propagation stage:

- A first part will focus on the characterization of fracture surfaces and the evaluation of crack growth rates using striation spacings. The potential effect of a prior strain hardening and of the strain rate will be considered. As for the crack initiation stage, such information can be useful in the failure analysis of nuclear components (see appendix 1).
- A second part will focus on TEM investigations on the fracture surfaces in order to identify some relevant aspects that may explain the differences in fatigue life induced by strain rate. As for the crack initiation stage, the effect of prior cold working will not be investigated here.

5.1. Crack initiation stage

5.1.1. Cracking morphology observed at the specimen failure

Figure 6 to Figure 15 give an overview of the aspect of fatigue crack paths on longitudinal cross sections obtained on different specimens using optical microscopy. The magnification was set to x200 and x1000. These figures reveal a significant branching of corrosion fatigue cracks. More precisely Figure 6 and Figure 7 show cross sections observed on samples in as-received and 10% CR conditions tested at $\Delta\varepsilon_t/2=0.5\%$ and $\Delta\varepsilon_t/dt=0.4\%/s$, up to failure. Branching occurs in annealed and in cold-rolled materials. Figure 8 to Figure 11 correspond to cross sections obtained on the sample tested at the same strain amplitude ($\Delta\varepsilon_t/2=0.5\%$), but at a lower strain rate (0.004%/s). In that case, even if branching is still observed, it seems less pronounced than at the high strain rate. It seems that crack branching reduces with a reduced strain rate.

It is generally admitted that the presence of crack branching is associated with a greater effect of the environment. However in low strain rate conditions (presenting a lower fatigue life) a linear crack which does not present any branching can also be affected by the environment, and in this case even more.

Figure 12 to Figure 15 present some smaller cracks observed on the same samples. It is possible to observe crack branching even inside the first grain (the mean grain size of this material is about 120 µm).

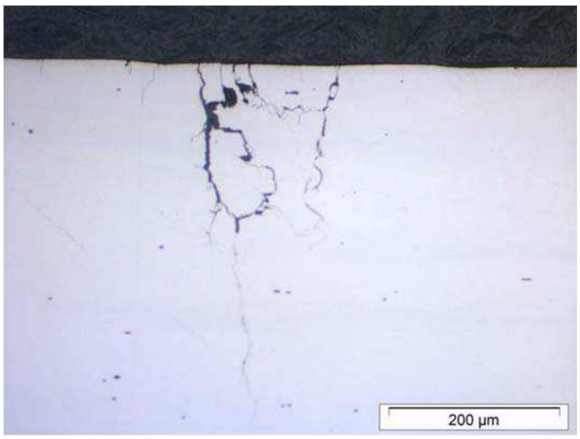

Figure 6 □Cross section of 1630 MHI 01, $\Delta\varepsilon_t/2=0.5\%$, $\Delta\varepsilon_t/dt=0.4\%/s$, 10% cold rolled, PWR primary water at 300°C.

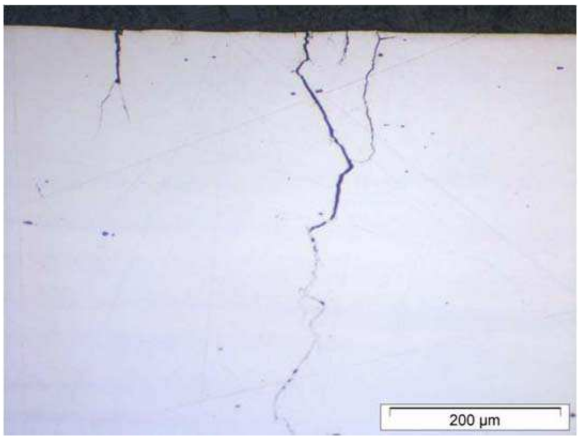

Figure 7 □Cross section of 1630 MHI 11, $\Delta\varepsilon_t/2=0.5\%$, $\Delta\varepsilon_t/dt=0.4\%/s$, 10% cold rolled, PWR primary water at 300°C.

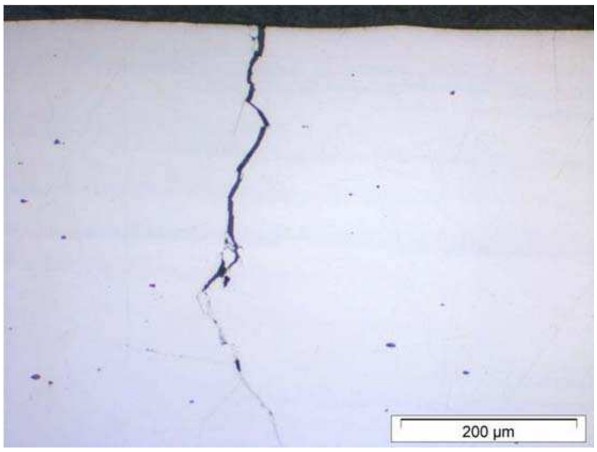

Figure 8 □Cross section of 1630 MHI 04, $\Delta\varepsilon_t/2=0.5\%$, $\Delta\varepsilon_t/dt=0.004\%/s$, as-received, PWR primary water at 300°C.

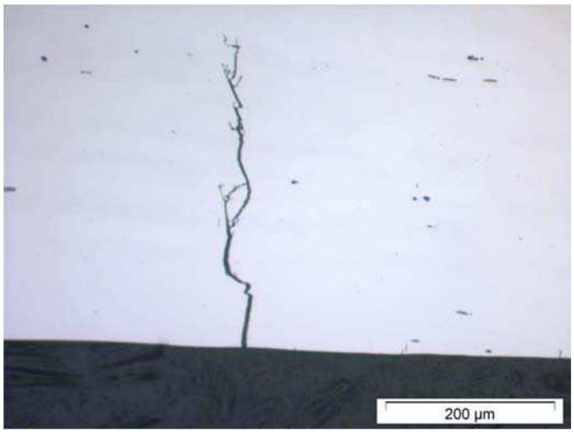

Figure 9 □Cross section of 1630 MHI 04, $\Delta\varepsilon_t/2=0.5\%$, $\Delta\varepsilon_t/dt=0.004\%/s$, as-received, PWR primary water at 300°C.

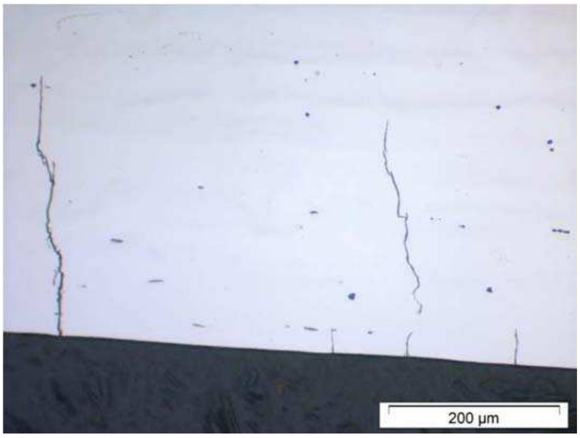

Figure 10 Cross section of 1630 MHI 04, $\Delta\varepsilon_t/2=0.5\%$, $\Delta\varepsilon_t/dt=0.004\%/s$, as-received, PWR primary water at 300°C.

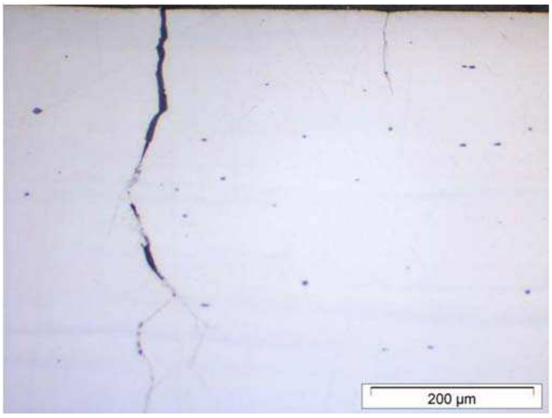

Figure 11 Cross section of 1630 MHI 14, $\Delta\varepsilon_t/2=0.5\%$, $\Delta\varepsilon_t/dt=0.004\%/s$, 10% cold rolled, PWR primary water at 300°C.

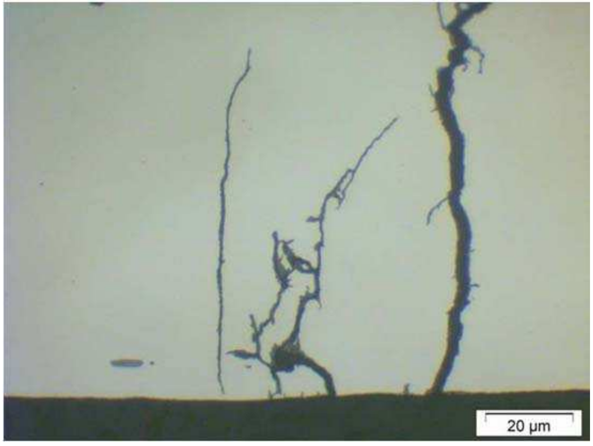

Figure 12 Cross section of 1630 MHI 01, $\Delta\varepsilon_t/2=0.5\%$, $\Delta\varepsilon_t/dt=0.4\%/s$, as-received, PWR primary water at 300°C. Focus on initiation.

Figure 13 Cross section of 1630 MHI 11, $\Delta\varepsilon_t/2=0.5\%$, $\Delta\varepsilon_t/dt=0.4\%/s$, 10% cold rolled, PWR primary water at 300°C. Focus on initiation.

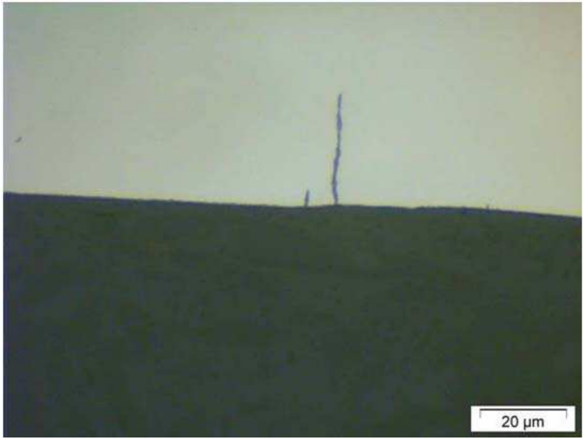

Figure 14 Cross section of 1630 MHI 04, $\Delta\varepsilon_t/2=0.5\%$, $\Delta\varepsilon_t/dt=0.004\%/s$, as-received, PWR primary water at 300°C. Focus on initiation.

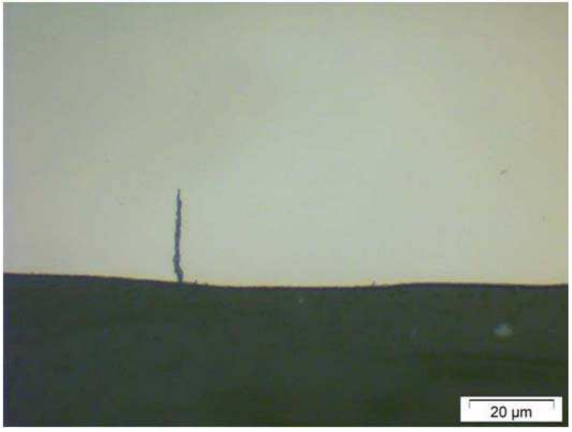

Figure 15 Cross section of 1630 MHI 14, $\Delta\varepsilon_t/2=0.5\%$, $\Delta\varepsilon_t/dt=0.004\%/s$, 10% cold rolled, PWR primary water at 300°C. Focus on initiation.

Figure 16 to Figure 18 represent the effect of strain rate on the Linear Crack Density (LCD) at three strain amplitudes ($\Delta\varepsilon_t/2=0.5\%$, $\Delta\varepsilon_t/2=0.34\%$, $\Delta\varepsilon_t/2=0.25\%$), using three different criteria of minimum crack depth (1 µm, 5 µm, 15 µm) presented along with additional data observed on GE tested samples. GE also performed some tests at the intermediate strain rate of 0.027%.

According to Figure 16 (crack depth criterion = 1 µm), at $\Delta\varepsilon_t/2=0.5\%$, LCD exhibits a remarkable strain rate dependency. Indeed, when the strain rate is increased, the LCD varies from 2 to 27 cracks/mm. This dependency seems less pronounced when the strain amplitude decreases. By increasing the crack depth criterion (15µm), this difference is reduced but the tendencies remain similar. Figure 19 shows that the previous conclusions on LCD still hold when considering the 10% cold rolled material.

Therefore, it appears that strain rate modifies both the crack density and morphology. A low strain rate induces a low LCD of sharp (straight) cracks, whereas a high strain rate increases the LCD while promoting crack branching.

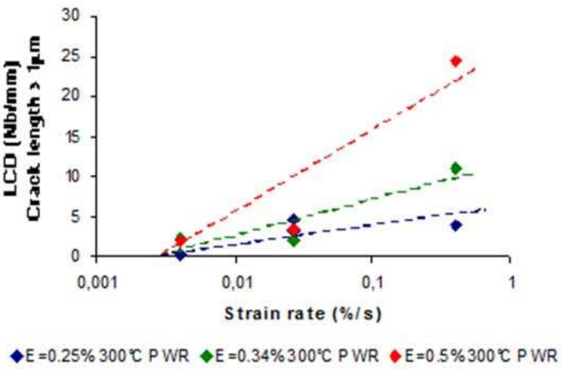

Figure 16 □Effect of strain rate on crack density at different strain amplitude 300°C PWR primary on the as receive material, minimum crack detection criteria 1µm.

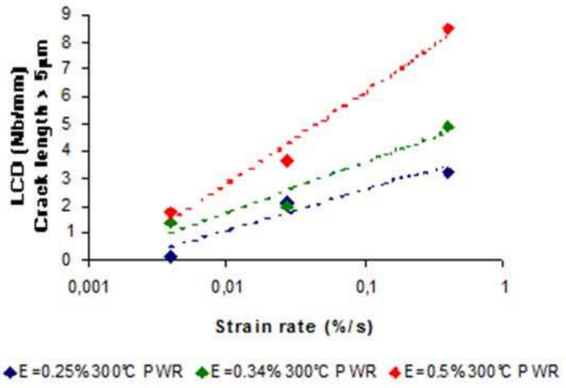

Figure 17 □Effect of strain rate on crack density at different strain amplitude 300°C PWR primary on the as receive material, minimum crack detection criteria 5µm.

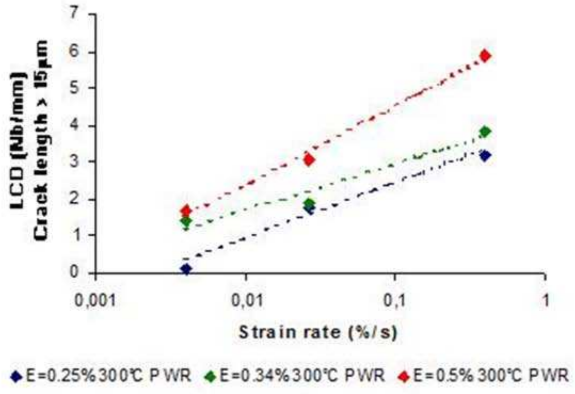

Figure 18 □Effect of strain rate on crack density at different strain amplitude 300°C PWR primary on the as receive material, minimum crack detection criteria 15µm.

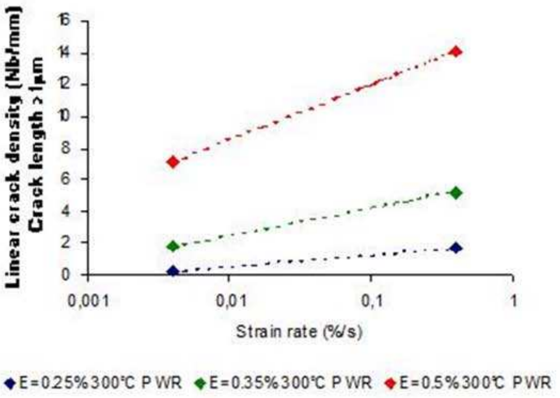

Figure 19 □Effect of strain rate on crack density at different strain amplitude 300°C PWR primary on the 10% Rolled material, minimum crack detection criteria 1µm.

As for the observations performed on the specimens tested in air (Chapter 3), an analysis of crack emergence angles at initiation was carried out (Figure 20). The data collected in all the samples (including as-received as well as rolled materials) tested in PWR primary environment are compared in Figure 21 to the most probable slip plane emergence angle evaluated using EBSD analysis. In PWR primary environment, most of the cracks deeper than 5µm (regardless of strain rate, strain amplitude and cold work degree) emerged with a 85°-90° angle independently of the orientation of the [111] slip plane exhibiting the highest Schmid factor. This specific aspect will be explained on the basis of fine observations that will be presented in the dedicated section.

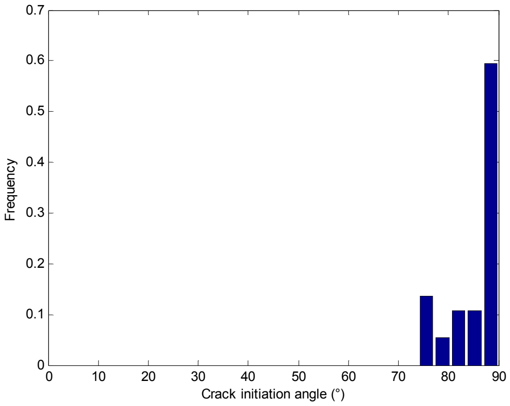

Figure 20 Crack emergence angles.

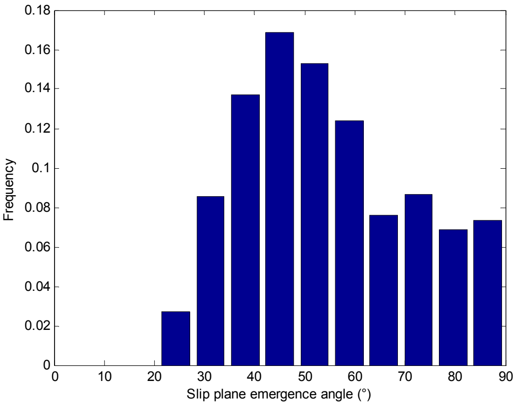

Figure 21 Most probable slip plane emergence angles.

5.2. Interactions between strain localization and oxidation

When considering environmentally assisted cracking (EAC), a major concern is the underlying mechanisms and the interactions between the PWR primary environment and the localized deformation. Indeed, in the case of SCC, such interactions were found to be one of the most relevant mechanisms leading to crack initiation [2].

It is proposed in this section to apply an approach similar to the one used in the SCC field and to investigate the interactions between strain localization and oxidation on fatigue crack initiation process on GE tested samples.

Figure 22 is a representative view of the morphology of the oxide formed at the surface of a sample tested at a strain rate of 0.004%/s in PWR primary environment at 300°C. It can be seen that some of the shear bands that emerge at the free surface are preferentially oxidized as indicated by the red squares.

Area #1 in Figure 22 shows a crack initiation site where a shear band emerges. The crack is aligned with the shear band and exhibits an oxidation involving Cr-rich layer (the inner layer) and a Fe-rich oxide layer (the outer layer). It was not possible to conclude whether this crack initiated and was subsequently filled by oxide, or if cracking occurs along a shear band that has endured a prior oxidation . In Area #2, a preferential oxidation along a shear band is observed, without any clear evidence of crack opening in the metal. Last, it has also to be noticed that several emerging shear bands are not oxidized. Further investigations using 3D EBSD will help us to understand this aspect.

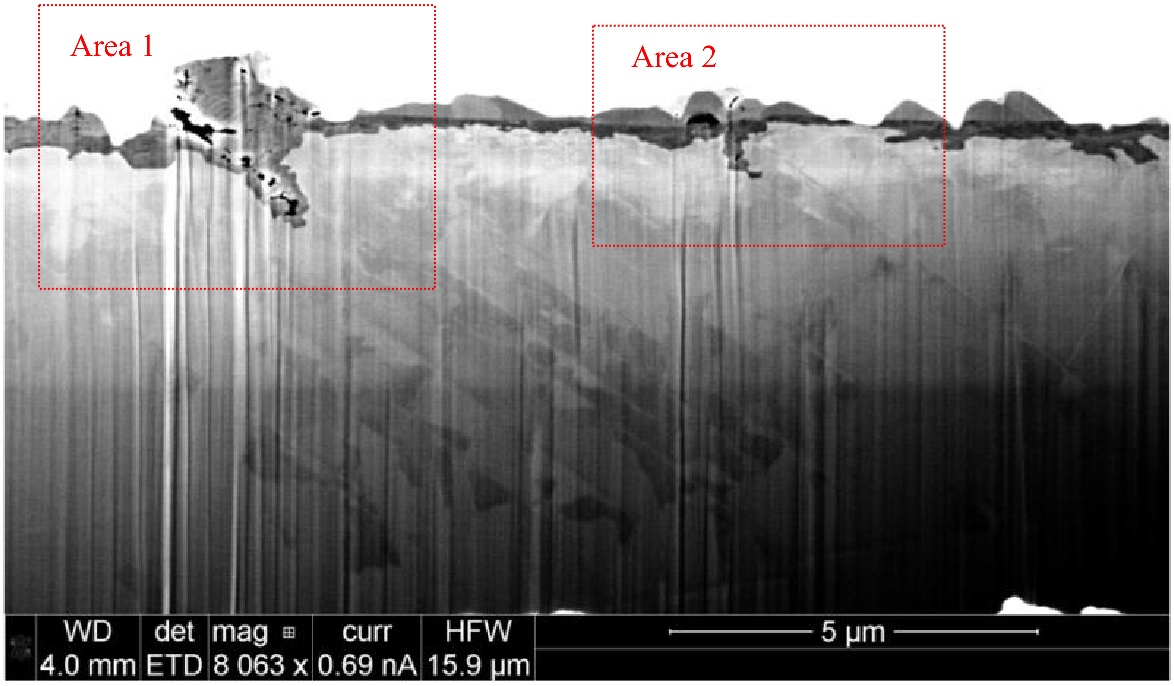

Figure 22 □Cross section on a sample tested in PWR primary environment at 300°C, at $\Delta\varepsilon_t/dt=0.004\%/s$, $\Delta\varepsilon_t/2=0.5\%$, as-received, failure. Observed with electronic beam at 5 kV.

In order to quantify and to characterize the interactions between strain localization and the oxidation, 3D reconstructions of the oxide layers were performed on two different samples both tested at $\Delta\varepsilon_t/2=0.5\%$ in PWR primary environment at 300°C but at different strain rates, namely $\Delta\varepsilon_t/dt=0.004\%/s$ and $\Delta\varepsilon_t/dt=0.4\%/s$ tested by GE. 3D oxide reconstructions are presented in Figure 23 and Figure 24 where yellow parts correspond to the Cr-rich inner layer (at the interface with the metal) and the red parts refer to the Fe-rich layer. In the following, only Cr-rich (passive protective layer) oxide will be considered.

Figure 23, corresponding to the sample cycled with the highest strain rate, shows that some emerging shear bands are more oxidized than the matrix as confirmed by Figure 25.

Typically, the mean Cr-rich oxide layer thickness in the matrix was 420 nm deep and 600 nm deep along shear bands, corresponding to an aspect ratio of 1.5 (Figure 25). Distances between oxidized slip bands were around 600 nm. At the lowest strain rate (Figure 24) the Cr-rich oxide penetration was much more pronounced: 770 nm into the matrix and 1150 nm along emerging shear bands (Figure 26). However, the aspect ratio remains of the order of 1.5. The distance between oxidized slip bands is about 4.5 µm, which is much larger than in the previous sample tested at a higher strain rate.

In order to get some statistical measurements of the distance between oxidized shear bands, some complementary analyses were performed. The typical distance separating oxidized slip bands was more precisely measured (Figure 27) using the Everhart-Thornley Detector (ETD), in secondary electron mode, in order to enhance topographic contrast. In Figure 28, the BackScattered Electron Detector (BSED) detector was used in Z-contrast mode to enhance the chemical contrast at the surface (a higher atomic number results in a whiter level). Figure 27 clearly shows emergence of shear bands at the surface and Figure 28 confirms that the oxide layer is particularly thick at the emergence of these bands.

Inter shear-band distances were measured following the red line drawn in Figure 28. The results obtained on 200 assumed shear bands randomly selected at the surface of the two same samples are presented in Figure 29 and Figure 30. They indicate that the distance between oxidized shear bands increases when the strain rate is reduced, from 3.5 µm and 6 µm. The results obtained using 3D oxide reconstructions (Figure 23 and Figure 24) are within the scatters of such data.

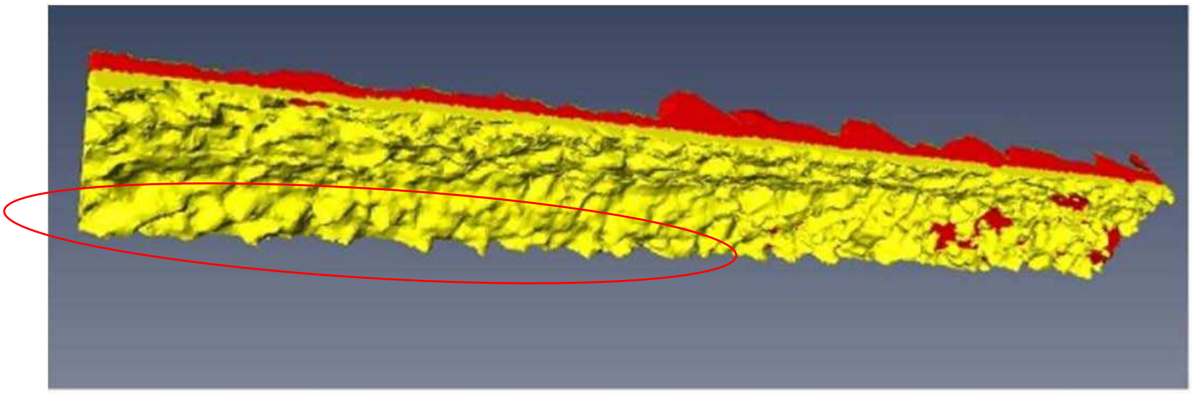

Figure 23 3D oxide reconstruction, $\Delta\varepsilon_t/dt=0.4\%/s$, $\Delta\varepsilon_t/2=0.5\%$, 300°C in PWR Primary environment (1.6 µm*20 µm).

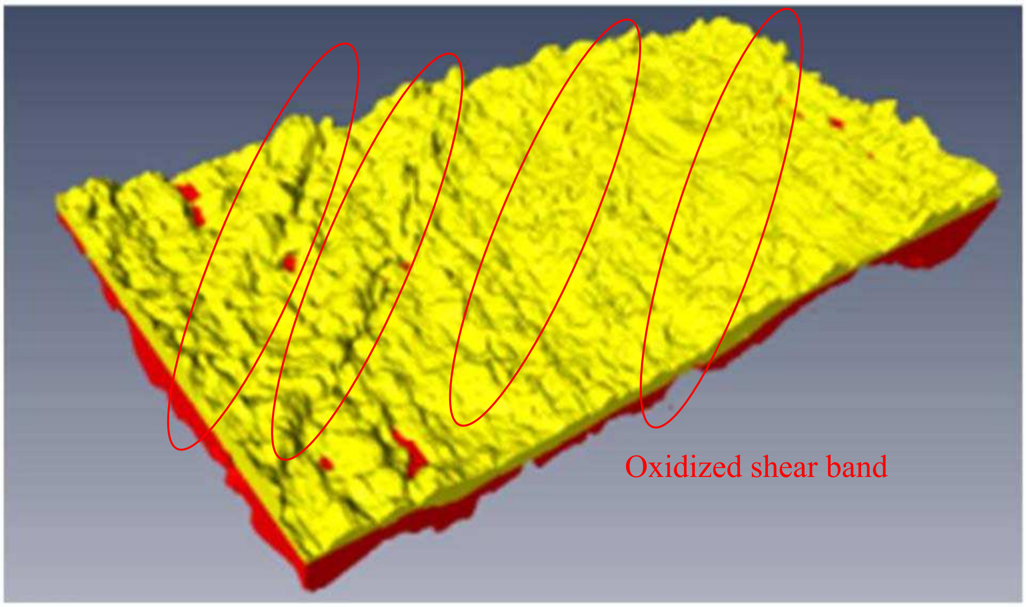

Figure 24 - 3D oxide reconstruction, $\Delta\varepsilon_t/dt=0.4\%/s$, $\Delta\varepsilon_t/2=0.5\%$, 300°C in PWR primary environment (16 µm*9 µm).

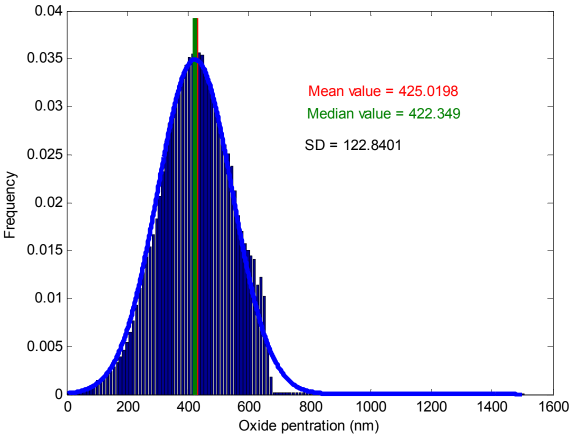

Figure 25 □Cr-rich oxide penetration, $\Delta\varepsilon_t/dt=0.4\%/s$, $\Delta\varepsilon_t/2=0.5\%$, 300°C in PWR primary environment (1.5 µm*20µm). Nf=3309 cycles.

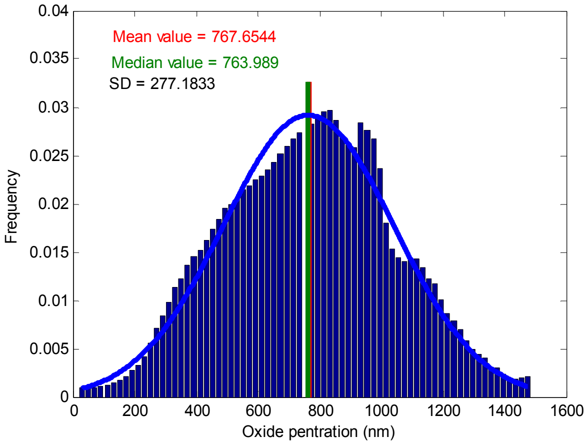

Figure 26 - Cr-rich oxide penetration, $\Delta\varepsilon_t/dt=0.004\%/s$, $\Delta\varepsilon_t/2=0.5\%$, 300°C in PWR primary environment (16 µm*9 µm). Nf= 1328 cycles.

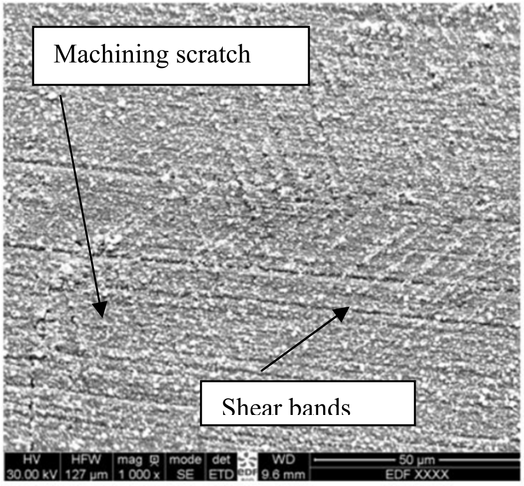

Figure 27 □ETD, $\Delta\varepsilon_t/dt=0.4\%/s$, $\Delta\varepsilon_t/2=0.5\%$, 300°C in PWR primary environment.

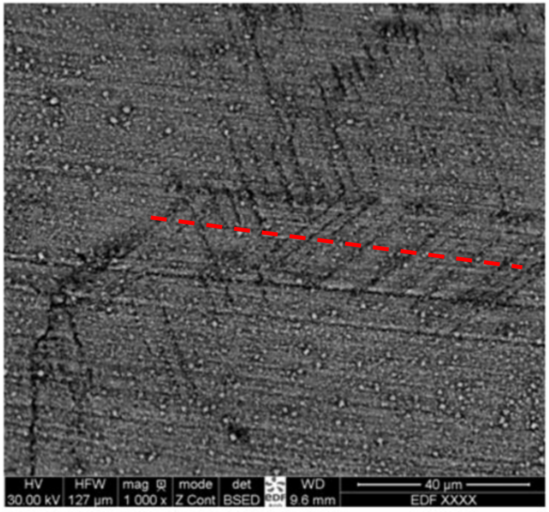

Figure 28 □BSED, $\Delta\varepsilon_t/dt=0.4\%/s$, $\Delta\varepsilon_t/2=0.5\%$, 300°C in PWR primary environment.

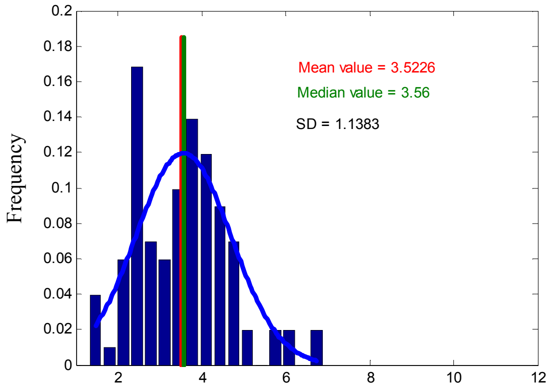

Figure 29 Distance between oxidized shear bands (µm) $\Delta\varepsilon_t/dt$=0.4%/s, $\Delta\varepsilon_t/2$=0.5%, 300°C in PWR pPrimary environment, 200 intersected shear bands.

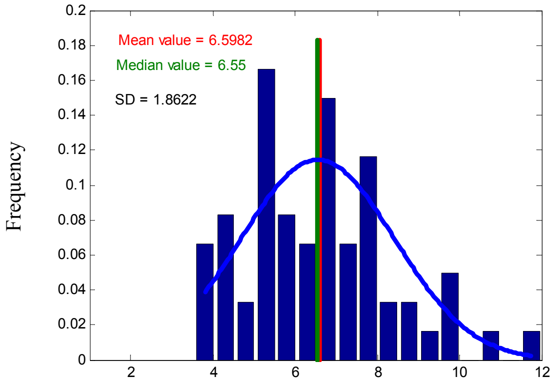

Figure 30 Distance between oxidized slip bands (µm) $\Delta\varepsilon_t/dt$=0.004%/s, $\Delta\varepsilon_t/2$=0.5%, 300°C in PWR primary environment, 200 intersected shear bands.

The interaction between strain localization (shear bands) and oxidation seems to be a key factor in fatigue crack initiation in PWR environment. However an important point from Figure 22 remains unanswered. Indeed, it was noticed that only some emerging shear bands present such a preferential oxidation.

In order to address this issue, 3D EBSD was coupled with 3D oxide reconstruction using a sample tested at $\Delta\varepsilon_t/2$=0.5% in PWR primary environment at 300°C and at a strain rate of $\Delta\varepsilon_t/dt$=0.004%/s.

Figure 31 and Figure 32 present the 3D oxide reconstruction and the 3D EBSD of the same area, respectively. The oxide reconstruction revealed a preferential oxidation along shear bands as previously shown in Figure 24, without separating Fe-rich layer and Cr-rich layer. The image quality is less than the previous reconstruction due to the lower of spatial resolution (from 20 nm to 50 nm) and to a reduction of resolution on the EBSD camera. However, the image reveals a preferential oxidation along four parallel bands. Meanwhile, four parallel misorientated bands are also observed in case of 3D EBSD shown in Figure 32, corresponding to preferential oxidation where misorientations vary from 0.5° to 1°. At the beginning of this section, the examination of a cross section revealed that many bands emerge at the surface. However, only a few of them are oxidized (Figure 22). As a conclusion, it is possible to assume that preferential oxidation occurs on shear bands presenting the highest misorientations, i.e. the highest accumulated plastic strain.

It is also important to notice that the minimum spatial resolution of EBSD, without any interactions between each acquisition steps, at 30 kV in Fe lattice is about 150 nm. In addition, minimum angular resolution of classical EBSD is about 0.5°. This experiment reaches the minimum spatial and angular resolution of EBSD.

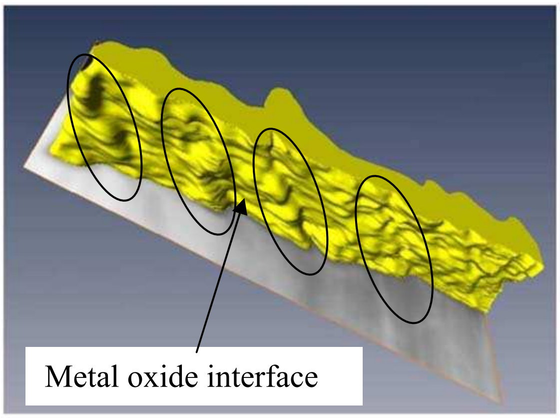

Figure 31 3D oxide reconstruction of the oxide layer: Presence of 4 preferential oxidations bands, $\Delta\varepsilon_t/dt$=0.004%/s, $\Delta\varepsilon_t/2$=0.5%, 300°C in PWR primary environment, (12 µm * 3 µm).

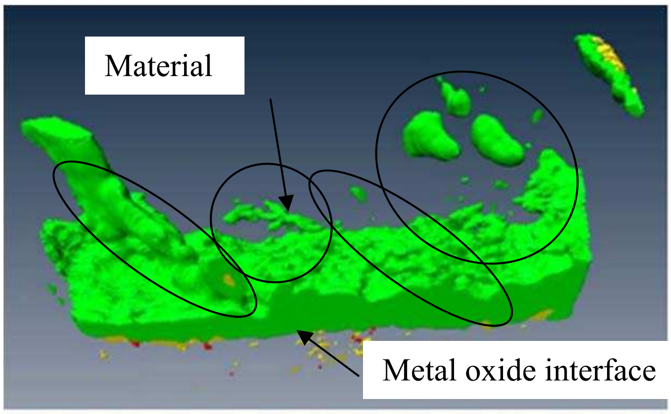

Figure 32 3D EBSD: Presence of 4 bands of higher misorientations, $\Delta\varepsilon_t/dt$=0.004%/s, $\Delta\varepsilon_t/2$=0.5%, 300°C in PWR primary environment, (12 µm * 3 µm).

5.2.1. Summary of observations

The main characteristics of cracks in PWR primary environment at failure were described in this section and can be summarized as:

- Crack initiation occurs at the metal oxide interface where strain localization occurs. Only the emerging shear bands presenting misorientations higher than 0.5° were oxidized.
- After initiation, the crack directly propagates along a 90°orientation representative of stage 2 cracking mode.

Concerning the effect of strain rate, results indicate several differences:

- Lowering strain rate induces a low LCD of sharp cracks, whereas a high strain rate that tends to increase the LCD with branched cracks.
- The strain localization process also depends on the applied strain rate. Indeed, a low strain rate induces deeper oxide penetration than at a high strain rate. In addition, the distance between oxidized shear bands is larger when strain rate decreases.

The observations are summarized in Figure 33.

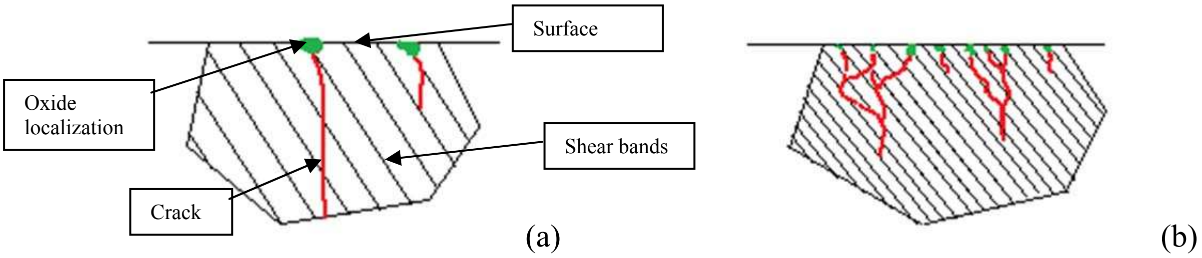

Figure 33 Difference in cracking morphologies and their relations with the environment and microstructure as a function of strain rate. (a) Low strain rate (b) High strain rate

The analysis has revealed differences in cracking mechanisms due to strain rate on the basis of observations carried out after failure of the test piece. However it might not be relevant to compare results at failure since the applied number of cycles and the exposure to environment are different from one specimen to another and these factors control the kinetics of crack initiation and growth. Therefore, in order to clarify this point, it would be more valuable to perform the same kind of analysis at the same number of cycles by conducting tests interrupted at selected numbers of cycles. This analysis is presented hereunder.

5.3. Observations of cracking features at different stages of fatigue life.

5.3.1. Cracking kinetics

Figure 34 presents the evolution of the maximum crack depth measured on cross sections as a function of the applied number of cycles tested in PWR primary environment on the as-received and the cold-rolled material.

Though some scattering can be observed on a given sample, the general evolution of the crack length (Figure 34) suggests that early cracks initiated between 10 cycles and 100 cycles. Figure 34 also indicates that, at 300 cycles and at a low strain rate, the maximum crack length reaches 55-60 µm for both materials while at higher strain rate the maxium length after 300 cycles is only a few microns, which is in good agreement with the fatigue life reduction observed for this lower strain rate in PWR primary environment. Regarding the cold work level, no difference in crack growth kinetics was observed with the as-received material within the 10-300 s cycle range.

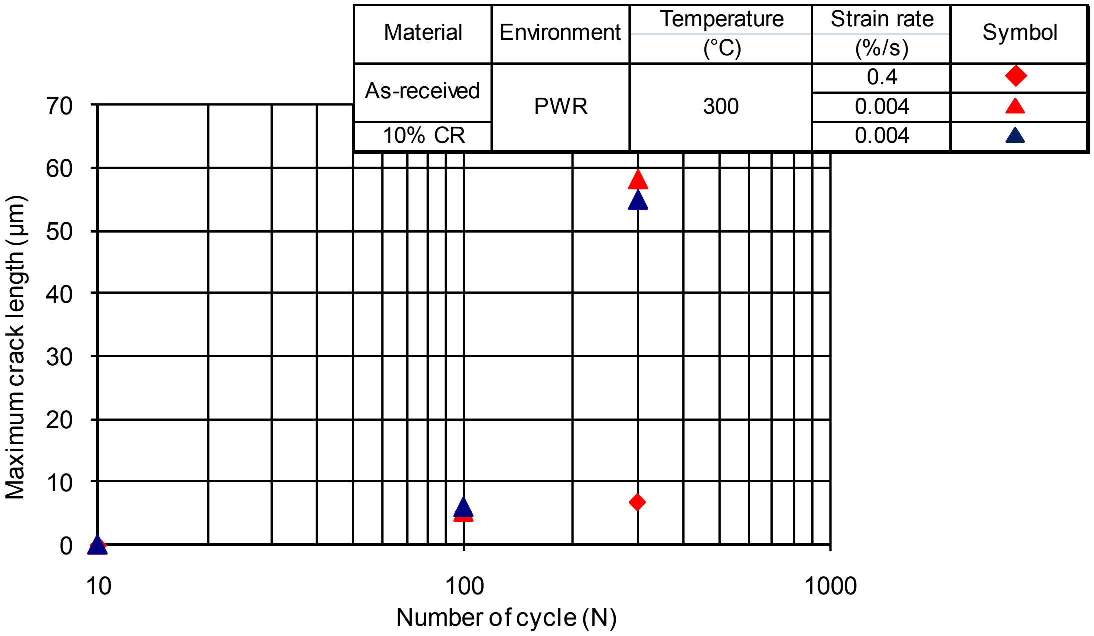

Figure 34 Evolution of maximum crack length as a function of number of cycles in PWR primary environment.

5.3.2. Characterization of cracking mechanisms

This specific aim of this section to investigate the cracking mechanisms within the first 10 to 300 cycles using various SEM and TEM based characterizations focusing in the evolution of the interactions between strain localization and the oxidation process during cycling. Indeed in a previous dedicated section these interactions were found to be the driving force of the crack initiation process in PWR primary environment. Three samples were selected, registered 1630MHIST5, 1630MHIST6, 1630MHIST7 and tested at $\Delta\varepsilon t/2=0.5\%$, $\Delta\varepsilon t/dt= 0.004\%/s$, 300°C in PWR primary water at 10, 100 and 300 cycles, respectively. In order to evaluate the effect of the strain rate at a fixed strain amplitude, an additional specimen registered 1630MHIST3 tested at $\Delta\varepsilon_t/2=0.5\%$, $\Delta\varepsilon_t/dt=0.4\%/s$, 300°C in PWR primary water during 100 cycles was analyzed.

5.3.2.1. 10 cycles at $\Delta\varepsilon_t/dt =0.004\%/s$

Figure 35 shows a representative image of the surface of specimen 1630MHIST5 ($\Delta\varepsilon t/2=0.5\%$, $\Delta\varepsilon t/dt= 0.004\%/s$, 300°C in PWR primary water, 10 cycles). The grains present parallel localized bands. These bands exhibit preferential oxide localization as shown in Figure 36. They are aligned with a preferential activated slip system (Figure 37). Electron diffraction patterns revealed that the corresponding gliding structure is composed of stacking faults (Figure 38 and Figure 39) lying in {111} planes. No micro twins induced by the machining process were observed. EFTEM characterizations (Figure 40 to Figure 44) indicate the oxide localization by the presence of oxygen (Figure 41). The thickness of this localized oxide is about 400 nm while the thickness of the native oxide film (film away from the strain localization) is less than 15 nm. Figure 42 and Figure 43 reveal that this localized oxide is composed of 8-9 double Cr and Fe rich layers. The respective average thickness is about 30 nm for Cr-rich layer and 42 nm in case of Fe-rich layer. No clear variation in Ni content was noticed (Figure 44). All these observations are summarized in the schematic morphology presented in Figure 45.

The number of layers is in good agreement with the applied number of cycles. This agreement allows us to postulate that one double layer is generated at each fatigue cycle.

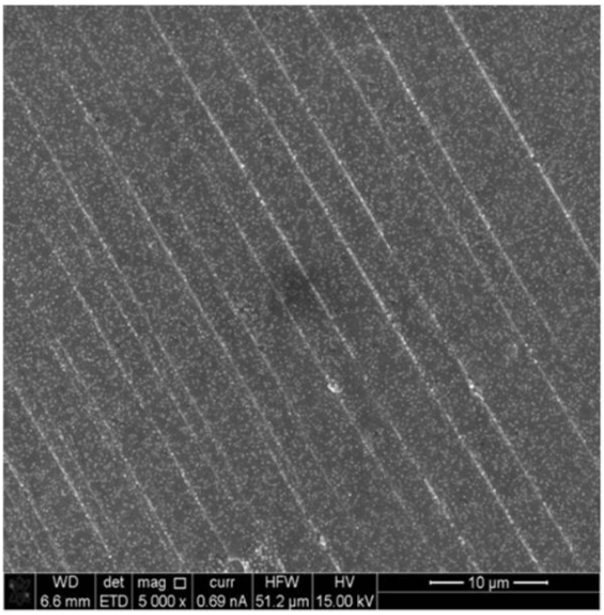

Figure 35 Surface of 1630MHIST5, $\Delta\varepsilon_t/dt=0.004\%/s$, $\Delta\varepsilon_t/2=0.5\%$, 10cycles, top view.

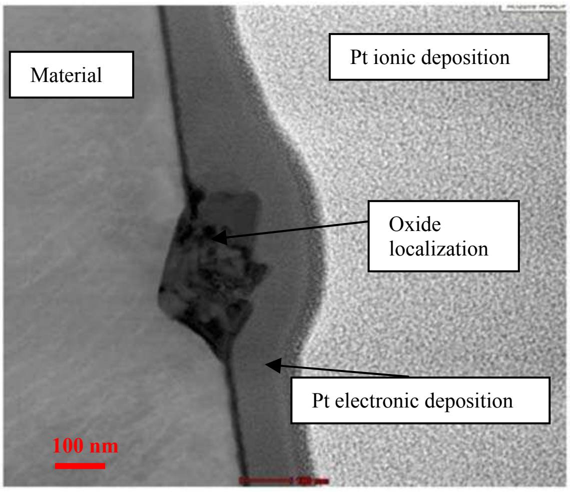

Figure 36 Preferential oxidation localization 1630MHIST5, STEM HAADF, $\Delta\varepsilon_t/dt=0.004\%/s$, $\Delta\varepsilon_t/2=0.5\%$, 10 cycles, cross section.

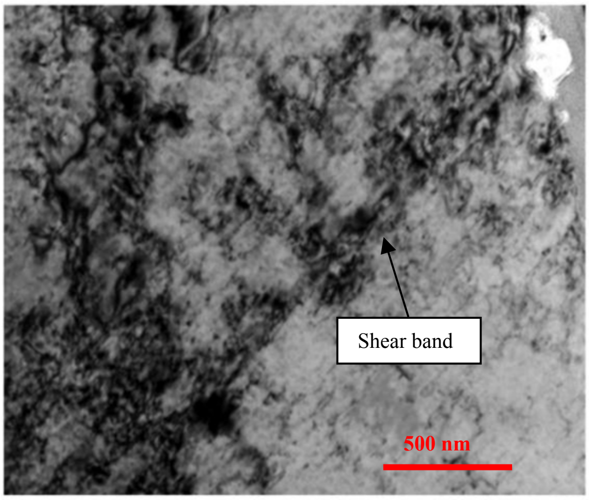

Figure 37 Oxidation localization along gliding bands 1630MHIST5, TEM BF, $\Delta\varepsilon_t/dt=0.004\%/s$, $\Delta\varepsilon_t/2=0.5\%$, 10cycles.

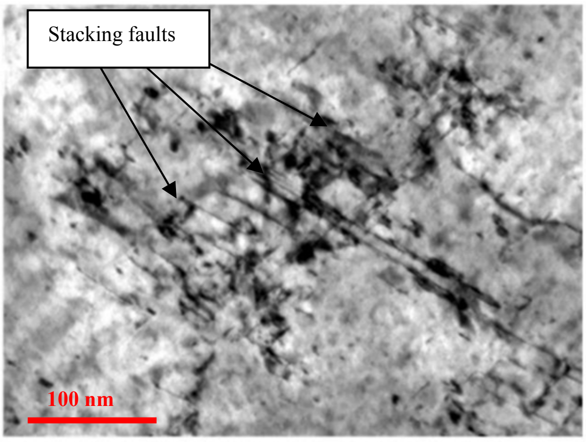

Figure 38 □Stacking fault composing gliding bands 1630MHIST5, TEM BF, $\Delta\varepsilon_t/dt=0.004\%/s$, $\Delta\varepsilon_t/2=0.5\%$, 10cycles.

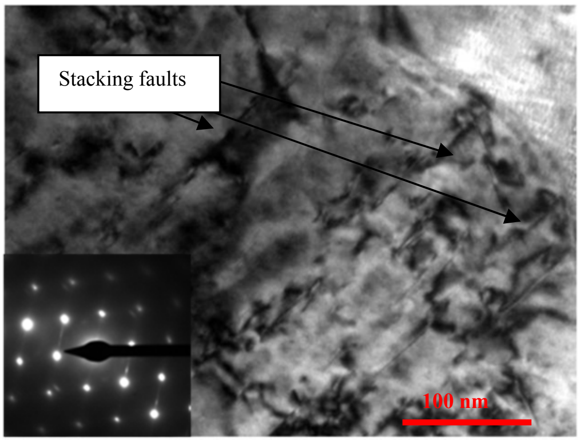

Figure 39 □Stacking fault composing gliding bands below the oxide penetration 1630MHIST5, TEM BF, $\Delta\varepsilon_t/dt=0.004\%/s$, $\Delta\varepsilon_t/2=0.5\%$, 10cycles.

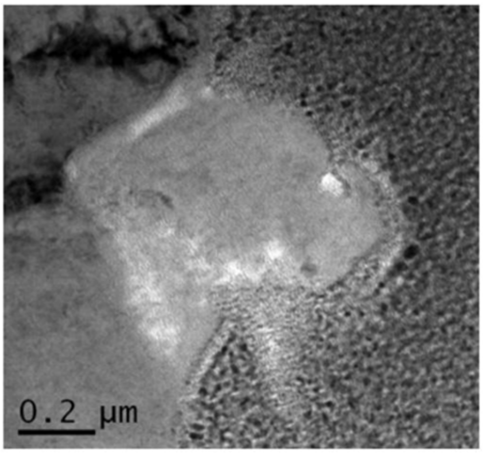

Figure 40 □Oxide penetration 1630MHIST5, EFTEM zero loss, $\Delta\varepsilon_t/dt=0.004\%/s$, $\Delta\varepsilon_t/2=0.5\%$, 10cycles.

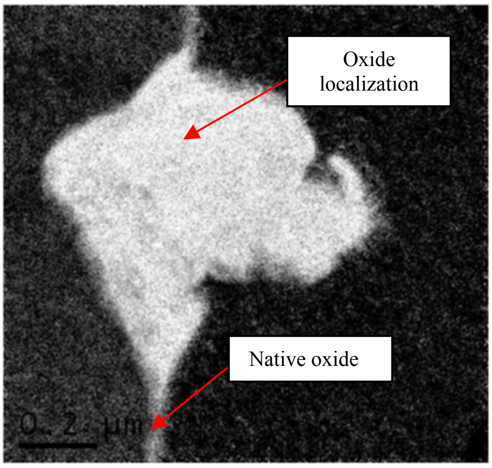

Figure 41 □Oxide penetration 1630MHIST5, EFTEM Oxygen, $\Delta\varepsilon_t/dt=0.004\%/s$, $\Delta\varepsilon_t/2=0.5\%$, 10cycles.

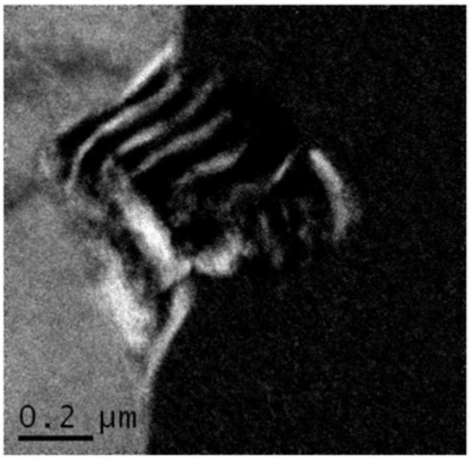

Figure 42 □Oxide penetration 1630MHIST5, EFTEM Chromium, $\Delta\varepsilon_t/dt=0.004\%/s$, $\Delta\varepsilon_t/2=0.5\%$, 10cycles.

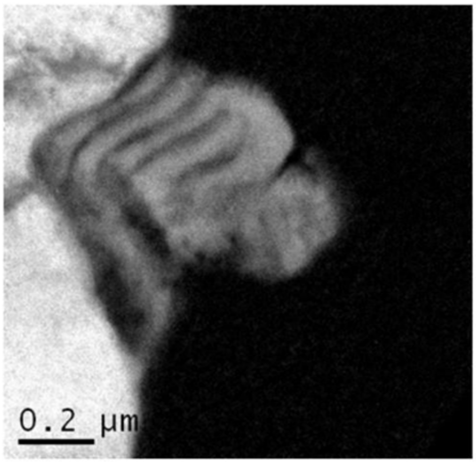

Figure 43 □Oxide penetration 1630MHIST5, EFTEM Iron, $\Delta\varepsilon_t/dt=0.004\%/s$, $\Delta\varepsilon_t/2=0.5\%$, 10cycles.

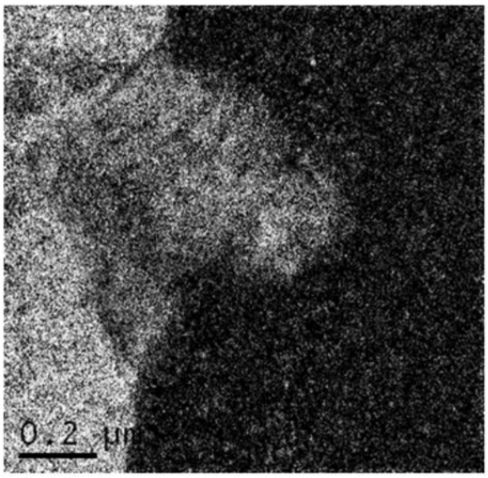

Figure 44 Oxide penetration 1630MHIST5, EFTEM Nickel, $\Delta\varepsilon_t/dt=0.004\%/s$, $\Delta\varepsilon_t/2=0.5\%$, 10cycles.

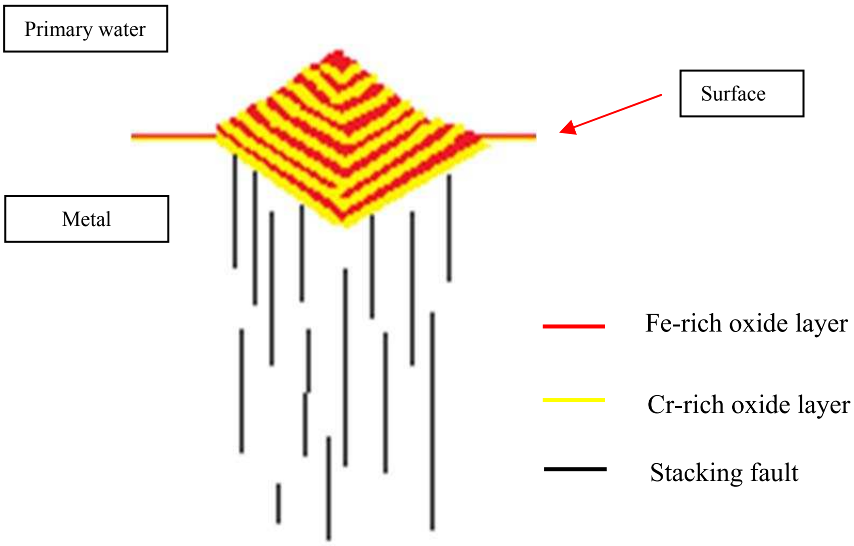

Figure 45 Morphology scheme corresponding to 10 cycles at , $\Delta\varepsilon_t/dt=0.004\%/s$, $\Delta\varepsilon_t/2=0.5\%$, 10cycles, in PWR primary environment

5.3.2.1. 100 cycles at $\Delta\varepsilon_t/dt=0.004\%/s$

Figure 46 shows a representative image of the surface of specimen 1630MHIST6 ($\Delta\varepsilon_t/dt=0.004\%/s$, $\Delta\varepsilon_t/2=0.5\%$, 300°C in PWR primary water, 100 cycles). The surface is similar to the one observed after 10 cycles, consisting in grains presenting interaction between strain localization and oxidation in localized bands. In some areas it is possible to observe that some cracks have already initiated (around 20 µm at the surface). Figure 47 and Figure 48 correspond to a cross section of the crack presented in Figure 46, crack initiation depth is about 1 µm. The crack initiation is aligned with a typical deformation feature which was identified as microtwinning (Figure 49 and Figure 50). Figure 51 is a TEM Bright Field image obtained in a 2-beam condition showing the metal/oxide interface at the crack tip with pores in the crack. Figure 52 corresponds to the Area 1 in Figure 51. In this figure it is possible to see an emerging microtwin shearing the oxide. Figure 53 shows a dislocation cell under oxidation. Preferential oxidation occurs along the cell walls, suggesting diffusion rates are increased by the presence of dislocations (diffusion shortcuts [2]). Figure 54 is an EFTEM oxygen map indicating that the crack initiation site is completely filled up by an oxide. Figure 55 corresponds to a chromium map indicating that the oxide is composed of two structures. The first structure is similar to the one observed at 10 cycles with a superposition of 30 layers. The typical size of a single Cr-rich layer is also close to 30 nm in agreement with the observations made after 10 cycles. The second oxidized structure follows the micro twinned structure. The mouth of the crack is covered by a Cr-rich layer while the oxide penetration does not present any clear organization. Figure 56 to Figure 60 are EFTEM characterizations focused at the crack tip. Figure 56 correspond to the zero loss image where it is possible to see the emerging microtwins at the metal/oxide interface. Figure 57 corresponds to the EFTEM oxygen map. This image clearly highlights the metal oxide interface. No preferential oxygen diffusion is observed below the crack tip. Figure 58 is an EFTEM chromium map revealing that the metal/oxide interface is mainly covered by a Cr-rich layer. The thickness of this layer varies from 30 to 60 nm. Area 1 presents an emerging microtwin, corresponding to the one presented in Figure 52. This emergence may have resulted in the rupture of the protective Cr-rich layer. Area 2 shows a local decrease of the Cr enrichment corresponding to other emerging microtwins presented in the zero loss image (Figure 56). In that case the damage process may be related to the progressive rupture of this passive layer by the microstructure. Figure 59 reveals that the crack tip is filled by a Fe-rich oxide. No Nickel enrichment was found ahead of the crack tip (Figure 60). All these data are summarized in the morphologic scheme presented in Figure 61.

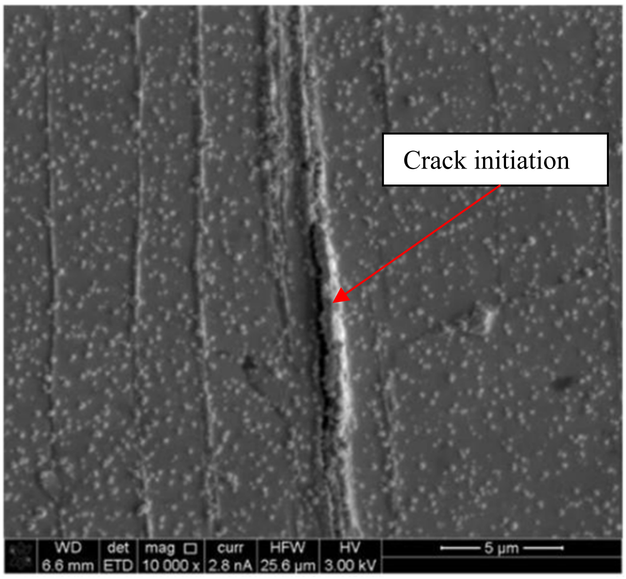

Figure 46 □Surface of 1630MHIST6, $\Delta\varepsilon_t/dt=0.004\%/s$, $\Delta\varepsilon_t/2=0.5\%$, 100 cycles.

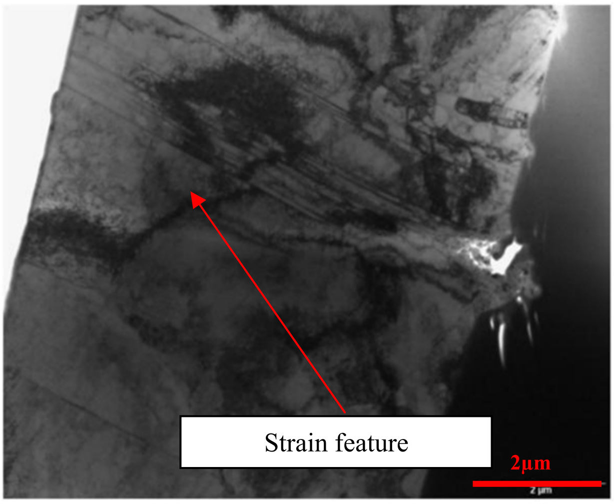

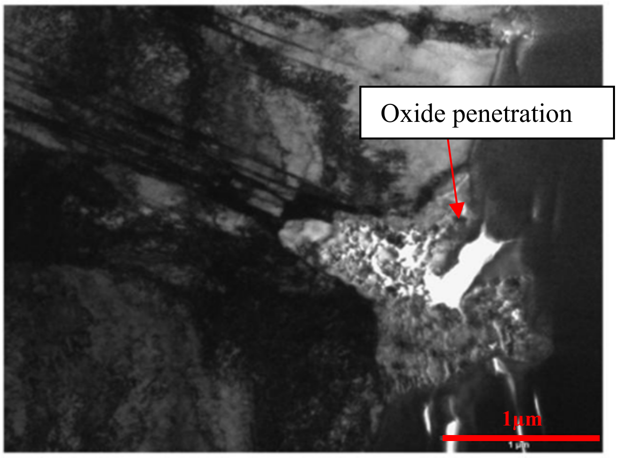

Figure 47 □Cross section of crack initiation in 1630MHIST6, TEM BF, $\Delta\varepsilon_t/dt=0.004\%/s$, $\Delta\varepsilon_t/2=0.5\%$, 100 cycles.

Figure 48 □Focus of crack initiation area 1630MHIST6, TEM BF, $\Delta\varepsilon_t/dt=0.004\%/s$, $\Delta\varepsilon_t/2=0.5\%$, 100 cycles.

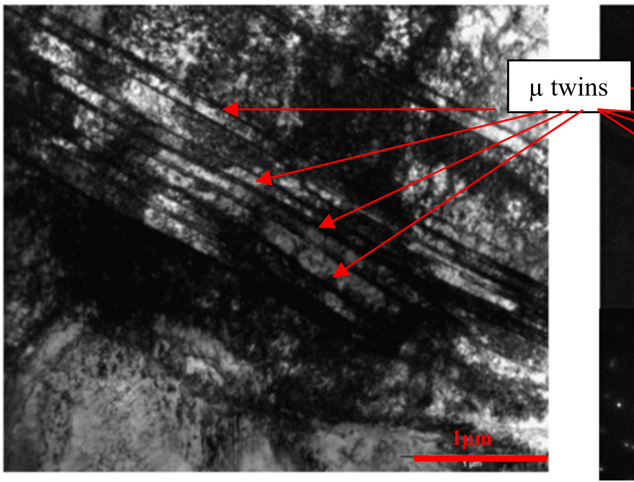

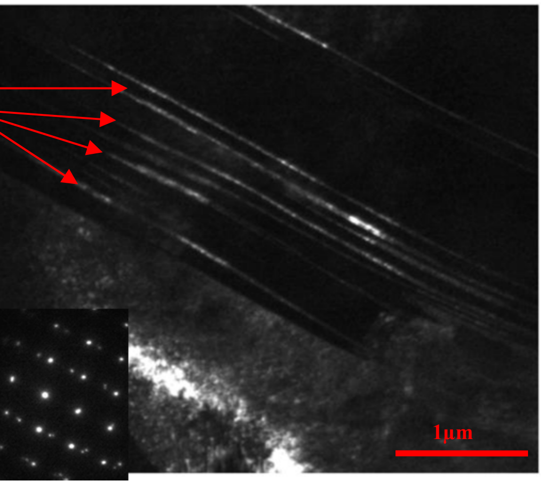

Figure 49 □µ twins in 1630MHIST6, TEM BF, $\Delta\varepsilon_t/dt=0.004\%/s$, $\Delta\varepsilon_t/2=0.5\%$, 100 cycles.

Figure 50 □µ twins in 1630MHIST6, TEM DF, $\Delta\varepsilon_t/dt=0.004\%/s$, $\Delta\varepsilon_t/2=0.5\%$, 100 cycles.

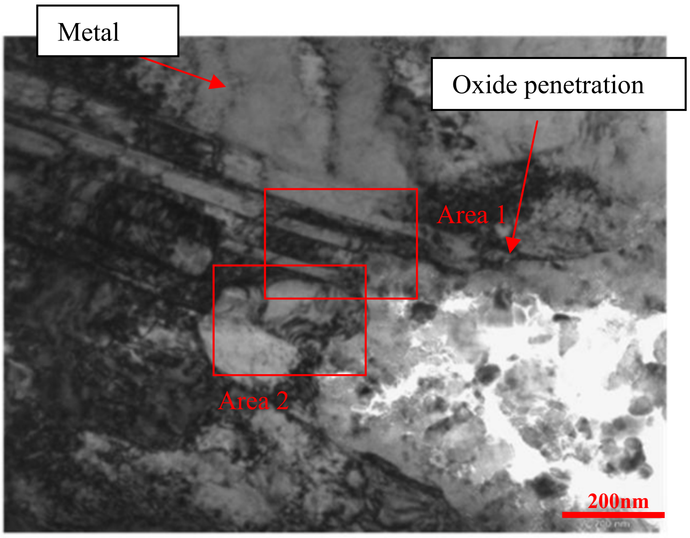

Figure 51 Crack tip 1630MHIST6, TEM BF, 2 beam conditions, $\Delta\varepsilon_t/dt=0.004\%/s$, $\Delta\varepsilon_t/2=0.5\%$, 100 cycles.

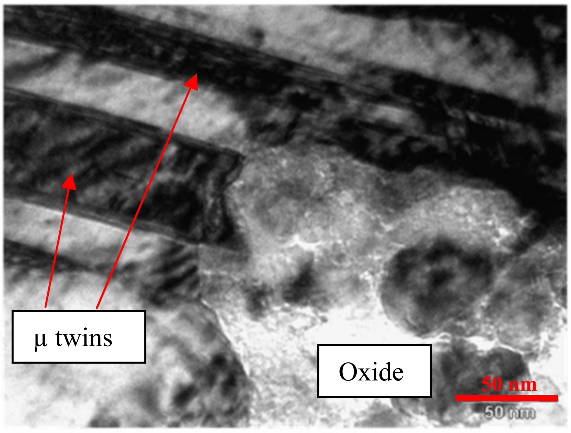

Figure 52 Crack tip 1630MHIST6, TEM BF, 2 beams conditions, $\Delta\varepsilon_t/dt=0.004\%/s$, $\Delta\varepsilon_t/2=0.5\%$, 100 cycles.

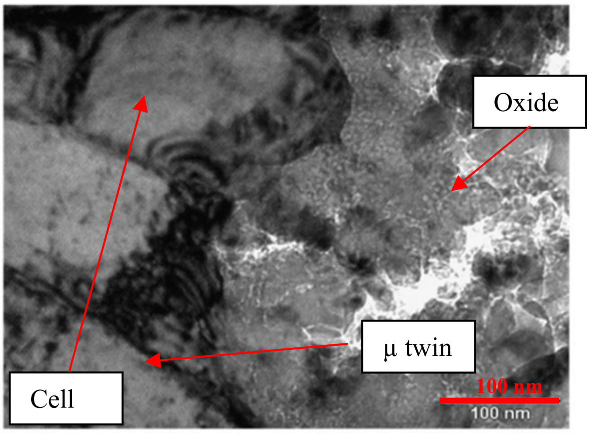

Figure 53 Crack tip 1630MHIST6, TEM BF, 2 beams conditions, $\Delta\varepsilon_t/dt=0.004\%/s$, $\Delta\varepsilon_t/2=0.5\%$, 100 cycles.

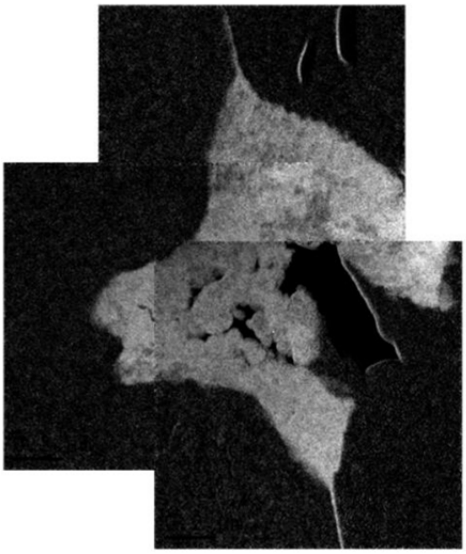

Figure 54 Oxide penetration 1630MHIST6, EFTEM Oxygen map, $\Delta\varepsilon_t/dt=0.004\%/s$, $\Delta\varepsilon_t/2=0.5\%$, 100 cycles.

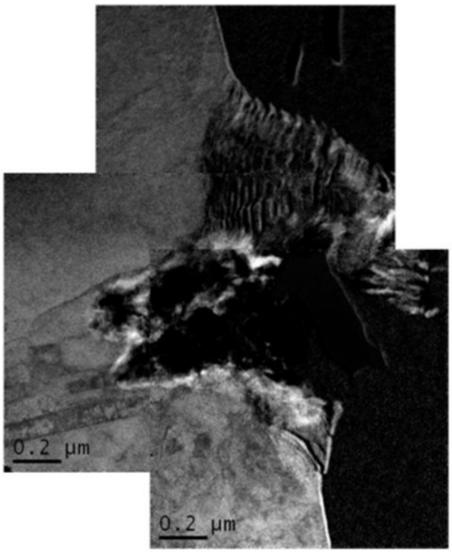

Figure 55 Oxide penetration 1630MHIST6, EFTEM Chromium map, $\Delta\varepsilon_t/dt=0.004\%/s$, $\Delta\varepsilon_t/2=0.5\%$, 100 cycles.

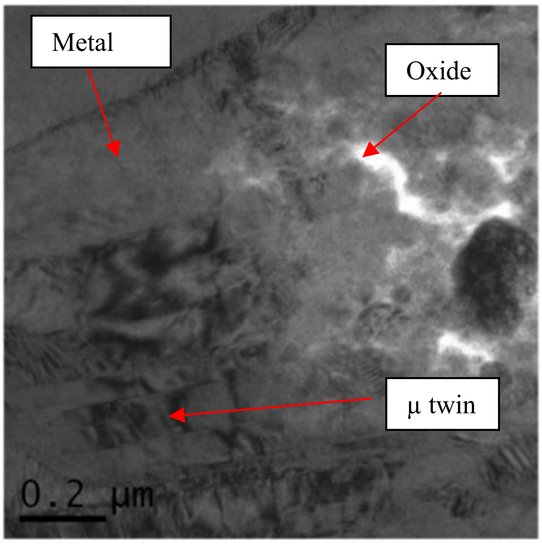

Figure 56 □Crack tip 1630MHIST6, EFTEM zero loss, $\Delta\varepsilon_t/dt=0.004\%/s$, $\Delta\varepsilon_t/2=0.5\%$, 100 cycles.

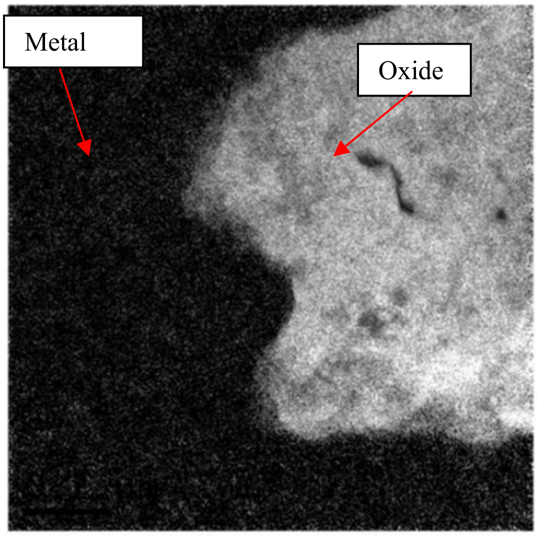

Figure 57 □Crack tip 1630MHIST6, EFTEM Oxygen map, $\Delta\varepsilon_t/dt=0.004\%/s$, $\Delta\varepsilon_t/2=0.5\%$, 100 cycles.

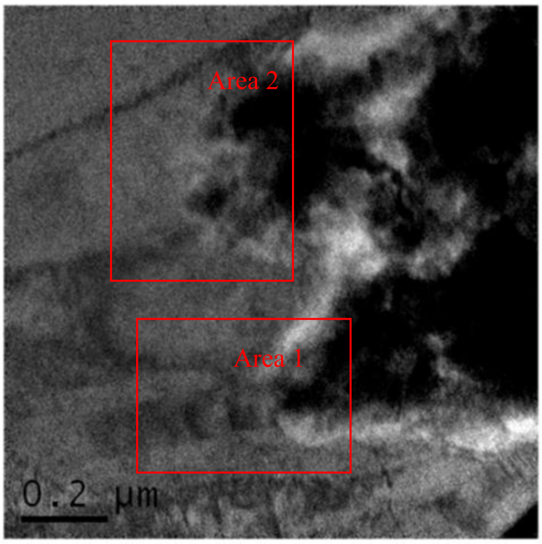

Figure 58 □Crack tip 1630MHIST6, EFTEM Chromnium map, $\Delta\varepsilon_t/dt=0.004\%/s$, $\Delta\varepsilon_t/2=0.5\%$, 100 cycles.

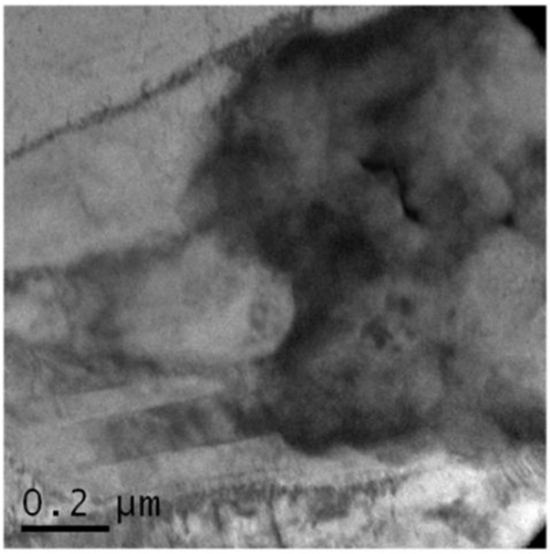

Figure 59 □Crack tip 1630MHIST6, EFTEM Iron map, $\Delta\varepsilon_t/dt=0.004\%/s$, $\Delta\varepsilon_t/2=0.5\%$, 100 cycles.

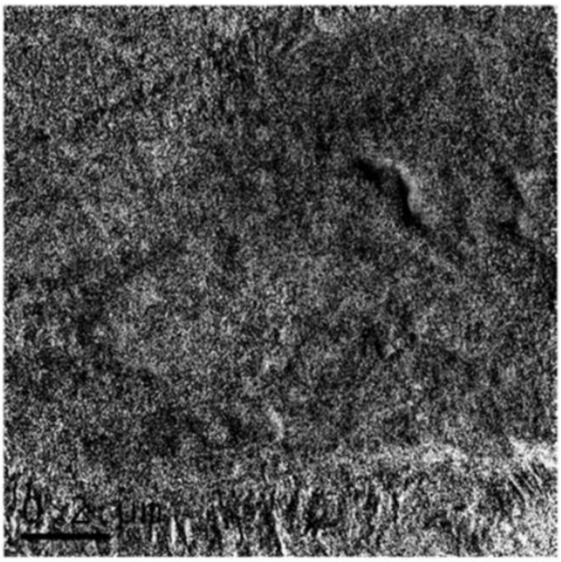

Figure 60 Crack tip 1630MHIST6, EFTEM Nickel map, $\Delta\varepsilon_t/dt=0.004\%/s$, $\Delta\varepsilon_t/2=0.5\%$, 100 cycles.

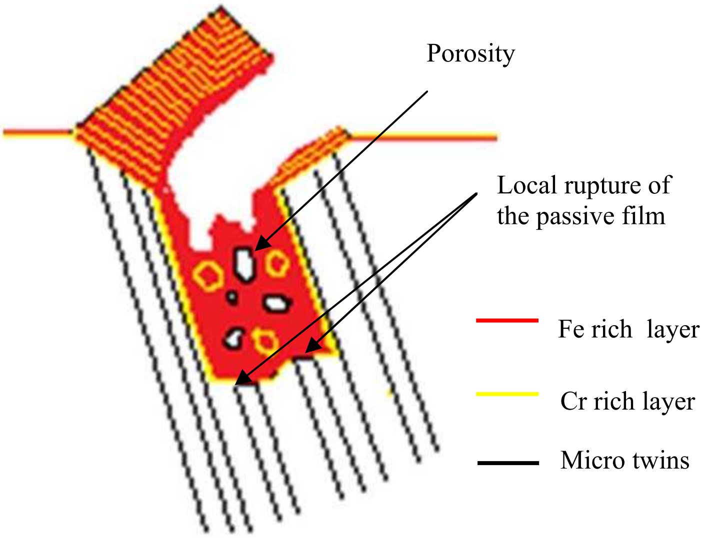

Figure 61 Morphology scheme of a crack initiation, $\Delta\varepsilon_t/dt=0.004\%/s$, $\Delta\varepsilon_t/2=0.5\%$, 100cycles, in PWR primary environment

5.3.2.1. 300 cycles at $\Delta\varepsilon_t/dt=0.004\%/s$

Figure 62 to Figure 64 show a representatives types of crack developed at the surface of 1630MHIST7 ($\Delta\varepsilon_t/2=0.5\%$, $\Delta\varepsilon_t/dt=0.004\%/s$, 300°C in PWR primary water, 300 cycles). Most of the cracks present at the surface of the sample are transgranular. Cracks can have different sizes as shown in Figure 62 and Figure 63. In some areas it was also possible to observe some IG cracks (Figure 64). Figure 65 and Figure 66 corresponds to two different cracks observed on cross sections of the sample. In Figure 65 and Figure 66, close to the surface, the crack presents a morphology similar to what has been observed in the case of the specimen tested at 100 cycles. However after a few microns, the two crack paths change their orientations to 90° from the surface representative of a crack in stage 2.

Figure 67 corresponds to an EBSD map of Figure 65. Each line of the red star presented in this figure corresponds to a {110} plane trace. With this characterization it is possible confirm that the crack path is TG and that the crack initiated along the main active slip system (presence of gliding trace on the {111} planes). After a few microns, the crack path changed and followed another{110} plane close to a 90° angle from the surface. Some other observations show that the crack can follow major crystallographic {111}, {110}, and {100} planes. The propagating plane must be the closest to the 90° angle from the surface. The fact that the crack propagation propagates along a major gliding plane allows to assume that the early stage of propagation seems to be crystallographic. A complementary analysis of this point will be done on fracture surface analysis hereunder.

Due to the important crack depth, no TEM sampling succeeded, except the one presented in Figure 68. This cross section corresponds to the middle of the crack presented in Figure 64. In this cross section, it is possible to see that the initiation occurred at a grain boundary. Just after initiation the crack path did not follow the grain boundary anymore but directly extended in depth with an angle close to 90° from the surface. Figure 69 is a focus of Figure 68 close to the crack. On the left of the image it is possible to see the initial deformed microstructure of the grain consisting in dislocation cells close to the grain boundary. On the right of the image it is possible to observe planar gliding. However, close to the crack, the microstructure evolved into a succession of parallel bands representative of crack propagation features (activation of 2 <110> {111} slip systems and crack advance on a mean plane). The average distance between such bands is close to 300 nm. This specific propagation microstructure aspect will be studied more deeply on the fracture surface analysis hereunder.

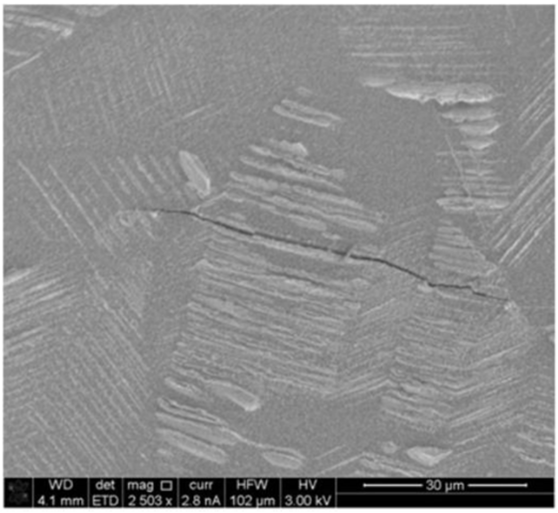

Figure 62 Surface of 1630MHIST7. Large TG crack, $\Delta\varepsilon_t/dt=0.004\%/s$, $\Delta\varepsilon_t/2=0.5\%$, 300 cycles.

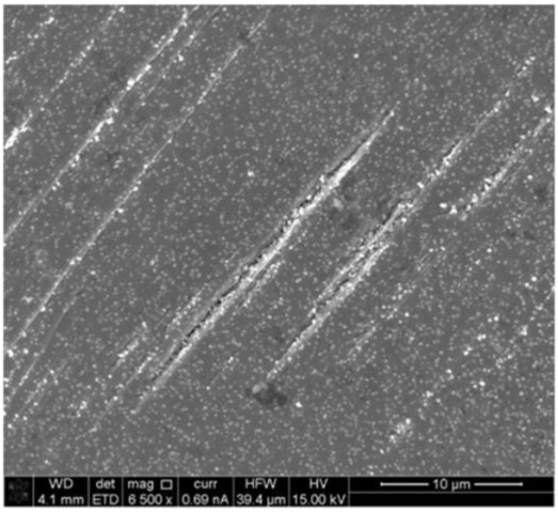

Figure 63 Surface of 1630MHIST7. Small TG crack, $\Delta\varepsilon_t/dt=0.004\%/s$, $\Delta\varepsilon_t/2=0.5\%$, 300 cycles.

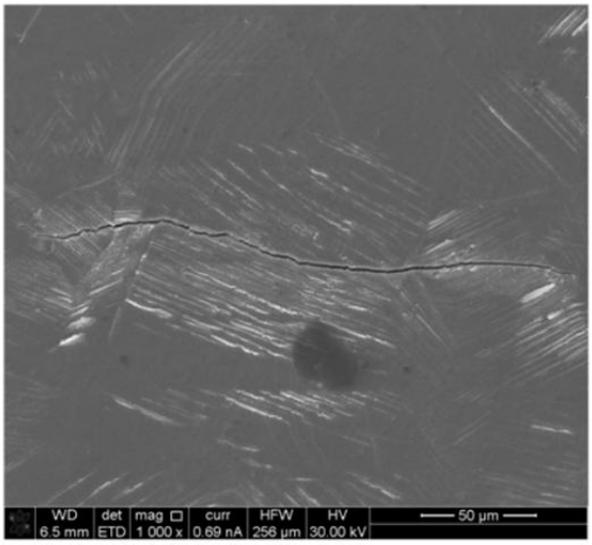

Figure 64 Surface of 1630MHIST7 Large IG crack, $\Delta\varepsilon_t/dt=0.004\%/s$, $\Delta\varepsilon_t/2=0.5\%$, 300 cycles.

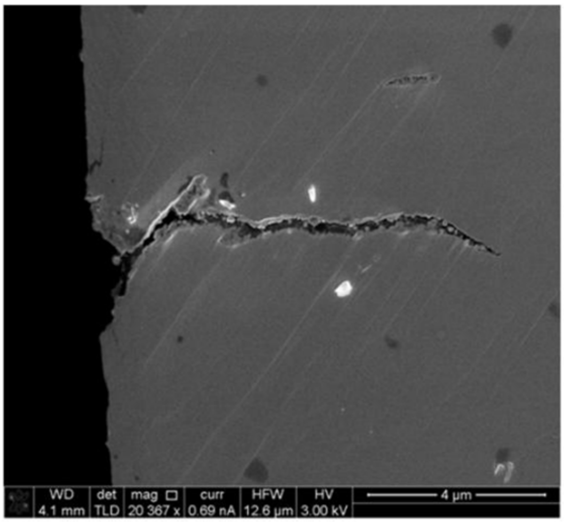

Figure 65 Cross section 1 of a TG crack on 1630MHIST7, $\Delta\varepsilon_t/dt=0.004\%/s$, $\Delta\varepsilon_t/2=0.5\%$, 300 cycles.

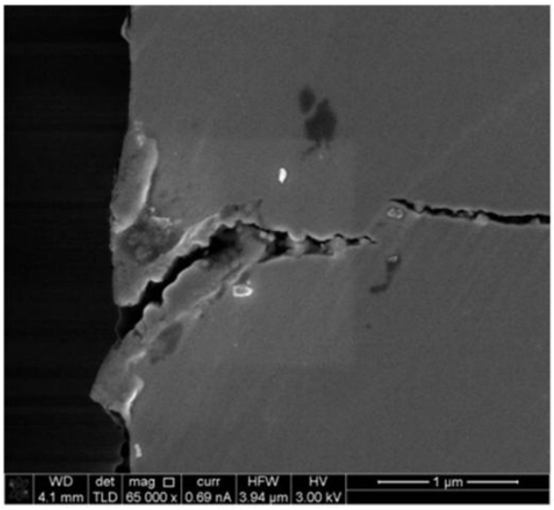

Figure 66 Cross section 2 of a TG crack on 1630MHIST7, $\Delta\varepsilon_t/dt=0.004\%/s$, $\Delta\varepsilon_t/2=0.5\%$, 300 cycles.

Figure 67 EBSD map of Cross section 1 of a TG crack on 1630MHIST7 with {110} plan traces, $\Delta\varepsilon_t/dt=0.004\%/s$, $\Delta\varepsilon_t/2=0.5\%$, 300cycles..

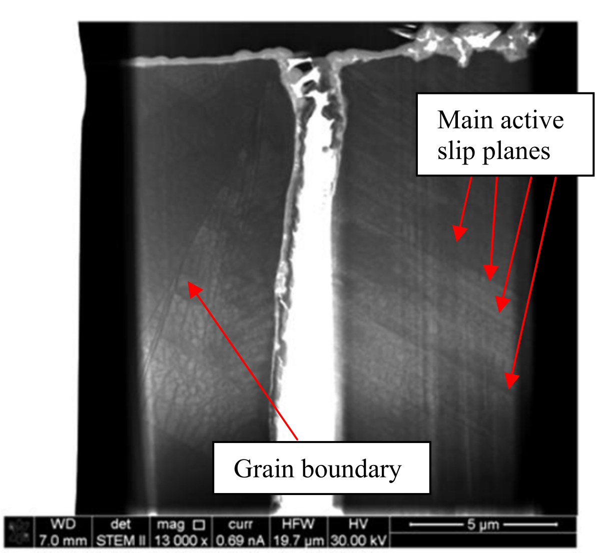

Figure 68 Cross section of an IG crack in 1630MHIST7, STEM, $\Delta\varepsilon_t/dt=0.004\%/s$, $\Delta\varepsilon_t/2=0.5\%$, 300cycles.

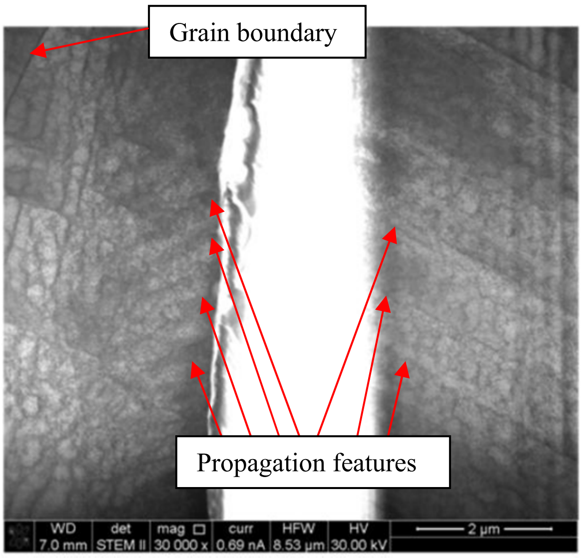

Figure 69 Focus on propagation feature in Figure 68, 1630MHIST7, STEM, $\Delta\varepsilon_t/dt=0.004\%/s$, $\Delta\varepsilon_t/2=0.5\%$, 300cycles.

5.3.2.1. 100 cycles at $\Delta\varepsilon_t/dt=0.4\%/s$

The same type of characterizations has been done in the case of the specimen 1630MHIST3 ($\Delta\varepsilon_t/dt=0.4\%/s$, $\Delta\varepsilon_t/2=0.5\%$, 300°C in PWR primary water, 100 cycles) to evaluate the impact of the loading strain rate on the initiation mechanisms. A representative image of the surface is given in Figure 70. As at a lower strain rate, the surface was composed of parallel localized bands, where some TG cracks initiated. Figure 71 is a cross section view of a crack initiation site. The crack initiation depth is close to 400 nm and seems to be full of oxide. The deformation structure leading to the crack is shown in Figure 72. This corresponds, as at a lower strain rate, to microtwinning (Figure 73, Figure 74 and Figure 75). Figure 76 is a bright field image in a 2-beam condition focusing on the crack tip. This image revealed the presence of stacking faults just below the crack tip. Figure 77 is a STEM image showing the same area at a lower magnification. It is possible to observe that stacking faults are only located close to the crack tip. Figure 78 to Figure 81 presents EFTEM characterizations of the crack initiation. Figure 78 reveals that the inner part of the oxide contains porosities. Figure 79 reveals that the crack initiation is full of oxide. Figure 80 corresponds to an EFTEM map of chromium of this area. It shows that, at this high strain rate, the passive layer is not uniform and not homogeneous within the crack.

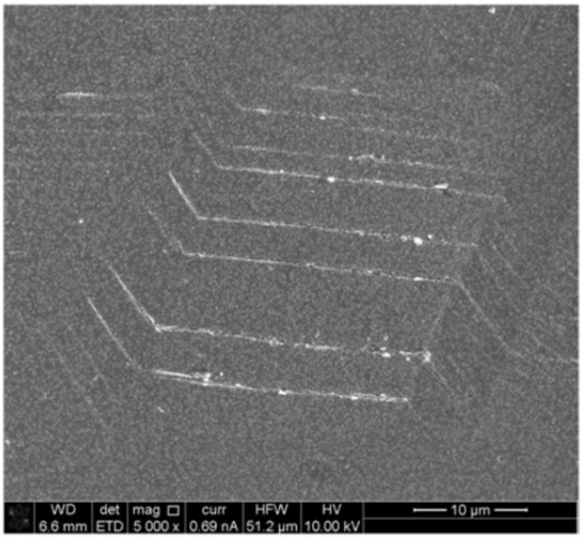

Figure 70 Surface of 1630MHIST3, $\Delta\varepsilon_t/dt=0.4\%/s$, $\Delta\varepsilon_t/2=0.5\%$, 100 cycles.

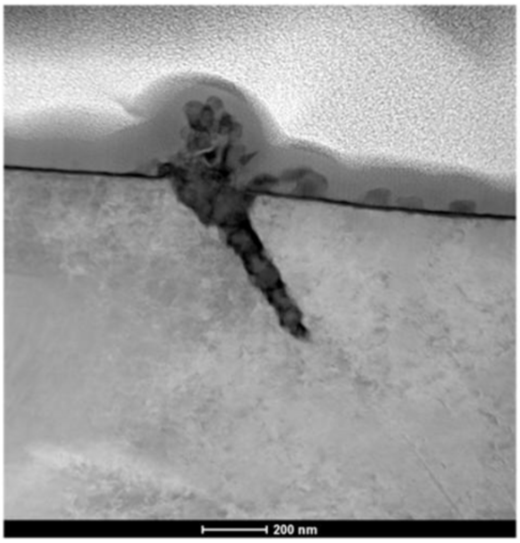

Figure 71 Cross section of crack initiation in 1630MHIST3, STEM HAADF, $\Delta\varepsilon_t/dt=0.4\%/s$, $\Delta\varepsilon_t/2=0.5\%$, 100 cycles.

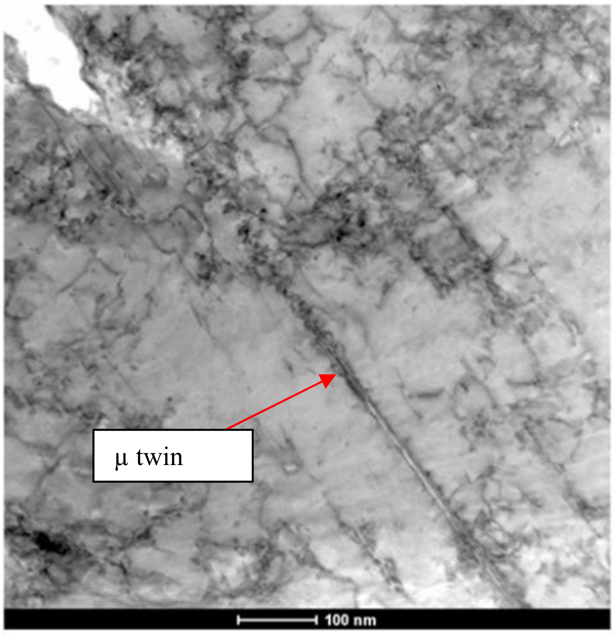

Figure 72 Cross section of crack initiation in 1630MHIST3, STEM, $\Delta\varepsilon_t/dt=0.4\%/s$, $\Delta\varepsilon_t/2=0.5\%$, 100 cycles.

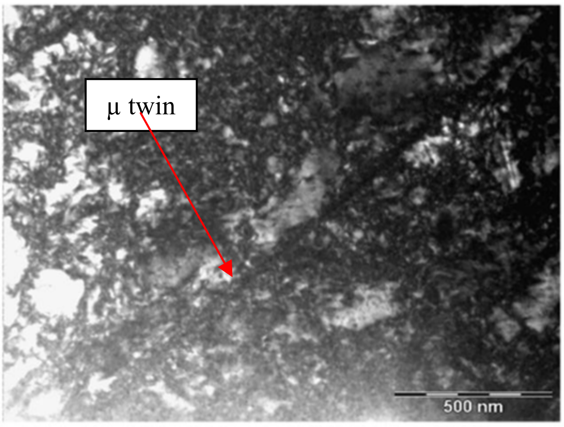

Figure 73 micro twin, 1630MHIST3, TEM BF, $\Delta\varepsilon_t/dt=0.4\%/s$, $\Delta\varepsilon_t/2=0.5\%$, 100 cycles.

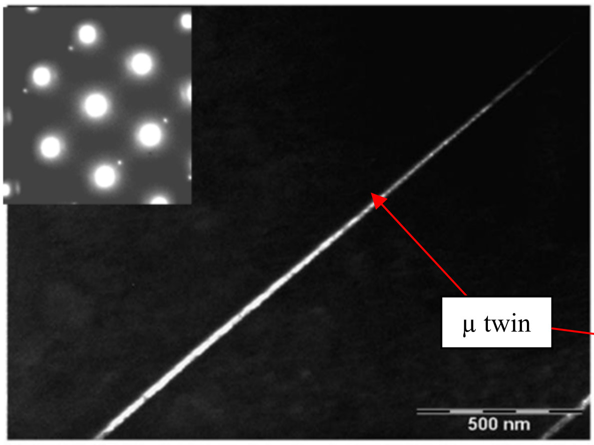

Figure 74 micro twin, 1630MHIST3, TEM dark field, $\Delta\varepsilon_t/dt=0.4\%/s$, $\Delta\varepsilon_t/2=0.5\%$, 100 cycles.

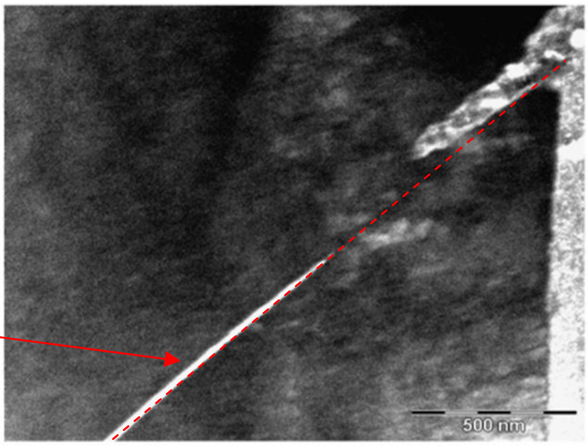

Figure 75 micro twin close to the crack initiation area, 1630MHIST3, TEM dark field, $\Delta\varepsilon_t/dt=0.4\%/s$, $\Delta\varepsilon_t/2=0.5\%$, 100 cycles.

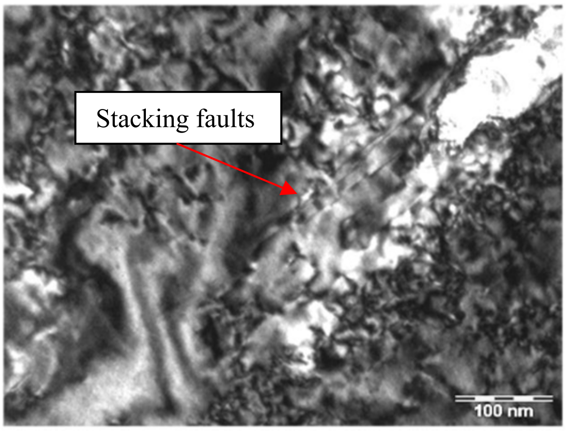

Figure 76 Stacking fault below the crack tip initiation area, 1630MHIST3, TEM BF, $\Delta\varepsilon_t/dt=0.4\%/s$, $\Delta\varepsilon_t/2=0.5\%$, 100 cycles.

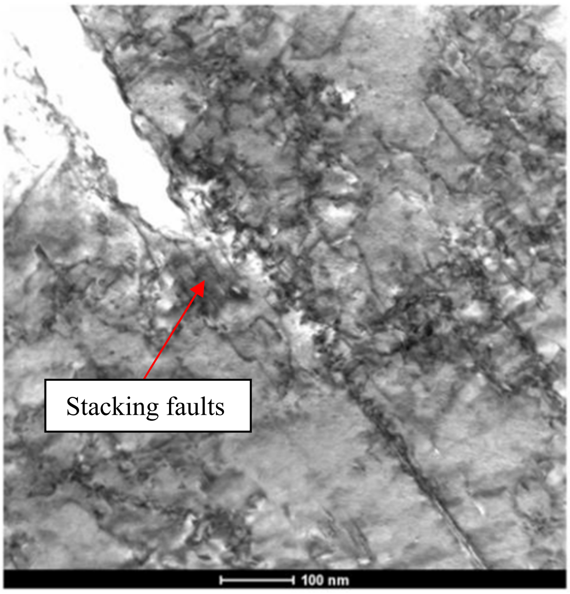

Figure 77 Stacking fault below the crack tip initiation area, 1630MHIST3, STEM, $\Delta\varepsilon_t/dt=0.4\%/s$, $\Delta\varepsilon_t/2=0.5\%$, 100 cycles.

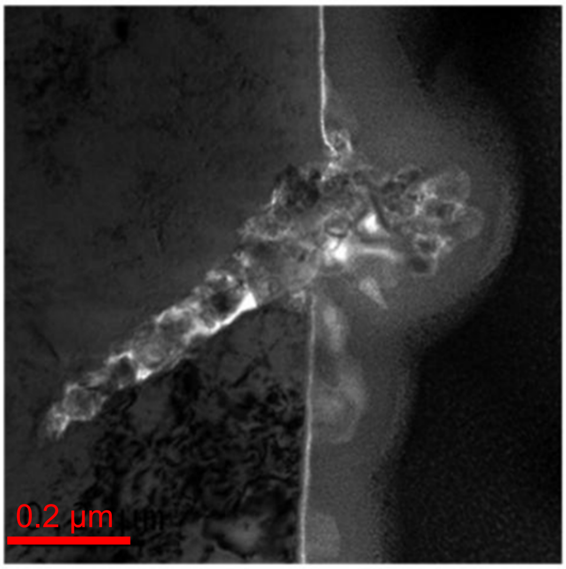

Figure 78 Crack tip 1630MHIST3, EFTEM zero loss, $\Delta\varepsilon_t/dt=0.4\%/s$, $\Delta\varepsilon_t/2=0.5\%$, 100 cycles.

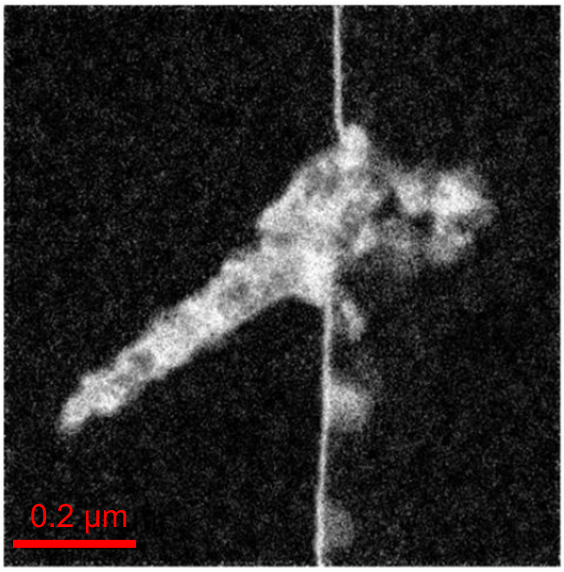

Figure 79 Crack tip 1630MHIST3, EFTEM Oxygen map, $\Delta\varepsilon_t/dt=0.4\%/s$, $\Delta\varepsilon_t/2=0.5\%$, 100 cycles.

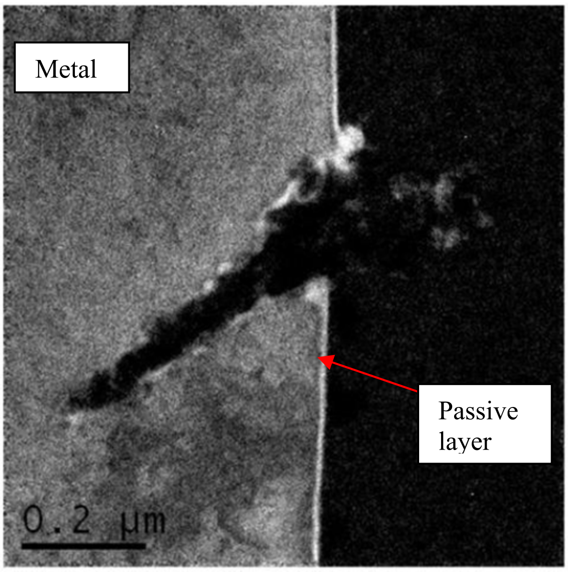

Figure 80 Crack tip 1630MHIST3, EFTEM Chromium map, $\Delta\varepsilon_t/dt=0.4\%/s$, $\Delta\varepsilon_t/2=0.5\%$, 100 cycles.

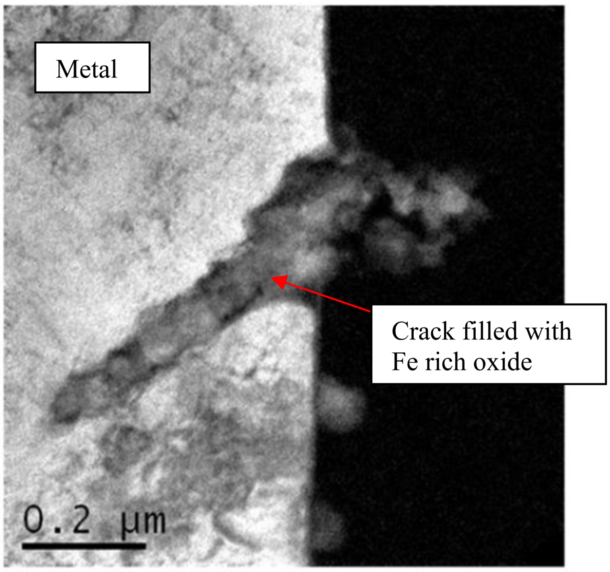

Figure 81 Crack tip 1630MHIST3, EFTEM Iron map, $\Delta\varepsilon_t/dt=0.4\%/s$, $\Delta\varepsilon_t/2=0.5\%$, 100 cycles.

5.3.3. Conclusion on the evolution of the crack initiation stage during cycling

The observations presented so far suggest that Fatigue crack initiation in PWR primary environment is directly related to the interaction between the localized plasticity and the environment.

Indeed, at the early stage of the fatigue life (below 10 cycles), the material surface presents some preferential oxidation on emerging dissociated dislocation along {111} planes (Figure 82-a). Each cycle generates a new C-rich/Fe-rich oxide layer. With an increasing applied number of cycles, the deformation microstructure evolves from stacking fault into micro twinning (Figure 82-b). The crack extends by repeating by continuous shearing and dissolution of the passive film up to a certain depth (<3µm). At this depth, the crack starts to propagate along other crystallographic planes close to a 90° angle from the surface (Figure 82-c). An increase of the applied strain rate mainly results in a reduction of the Cr-rich layer homogeneity and a decrease of the micro twinned structure width.

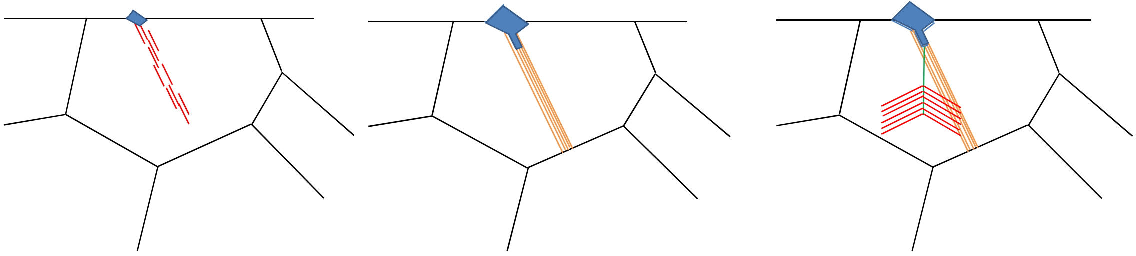
Oxidation localization (a) Crack initiation (b) Beginning of micro crack propagation (c)

Figure 82 Summary of observations of fatigue crack initiation

5.4. Crack propagation stage

The fatigue life of a given material is generally separated into the crack initiation and a crack propagation phase. The previous study of the evolution of cracking during cycling allows us to describe the first step of initiation and early stage of crack propagation. This section will focus on the examination of the propagation mechanisms. Many useful information on the crack propagation stage can be derived from observations of the fracture surface.

The propagation stage will be first described qualitatively by a description of the fracture surfaces, and then an evaluation of crack growth rates derived from measurements of fatigue striation spacings will be performed.

5.4.1. Fractographic aspects

Figure 83 is an overview of the fracture surface obtained on specimen 1630MHI01 ($\Delta\varepsilon_t/2=0.5\%$, $\Delta\varepsilon_t/dt= 0.4\%/s$, 300°C in PWR primary water). Crack initiation occurred on the inner diameter and propagated up to the outer diameter. Thanks to a sufficient ligament at a cracked section when a leakage occurred on a hollow type specimen, a limited hammering was experienced by the fracture surfaces, allowing the observation of striations close to the assumed initiation site (< 200 µm). The crack initiation (Figure 84) area is very smooth and similar to a TGSCC crack initiation. The initiation area presents relatively flat facets separated by steps also named shear ligaments. Because of its appearance very similar to the cleavage fracture of ferritic materials at low temperatures, this morphology, commonly encountered in case of SCC and corrosion fatigue, is qualified of “pseudo-cleavage” [3]. These observations are in agreement with EBSD characterization presented in the previous section where it was possible to say that, the first steps of propagation follow the crystallographic planes (Previous section on crack initiation).

At 500 µm in depth, the crack presents clear striation features (Figure 85). This feature remains present up to the sample failure.

Figure 86 presents a general view of the fracture surface obtained on specimen 1630MHI04 ($\Delta\varepsilon_t/2=0.5\%$, $\Delta\varepsilon_t/dt= 0.004\%/s$, 300°C in PWR primary water) and its associated initiation area (Figure 87). The initiation area does not exhibit any clear difference between the two strain rate conditions. The main crack remains TG in good agreement with the observations performed on interrupted tests. Figure 88 reveals the same fatigue striation features than in the case of a higher strain rate condition. It seems however that the distance between striations is higher at this lower strain rate conditions for a crack depth of 500 µm. In addition, it is also possible to see “sub-striations” markings between 2 main striations (Figure 89). Detailed investigations of these differences are described below.

Figure 90 and Figure 91 respectively present initiation areas in the pre tensioned specimen 1630MHI03 and the pre cold rolled specimen 1630MHI14 ($\Delta\varepsilon_t/2=0.5\%$, $\Delta\varepsilon_t/dt=0.004\%/s$, 300°C in PWR primary water). Initiation areas look very similar to the as-received material, consisting of “pseudo-cleavage” features. No presence of IG cracking was noticed. It seems that prior pre hardening does not modify initiation and propagation mechanisms.

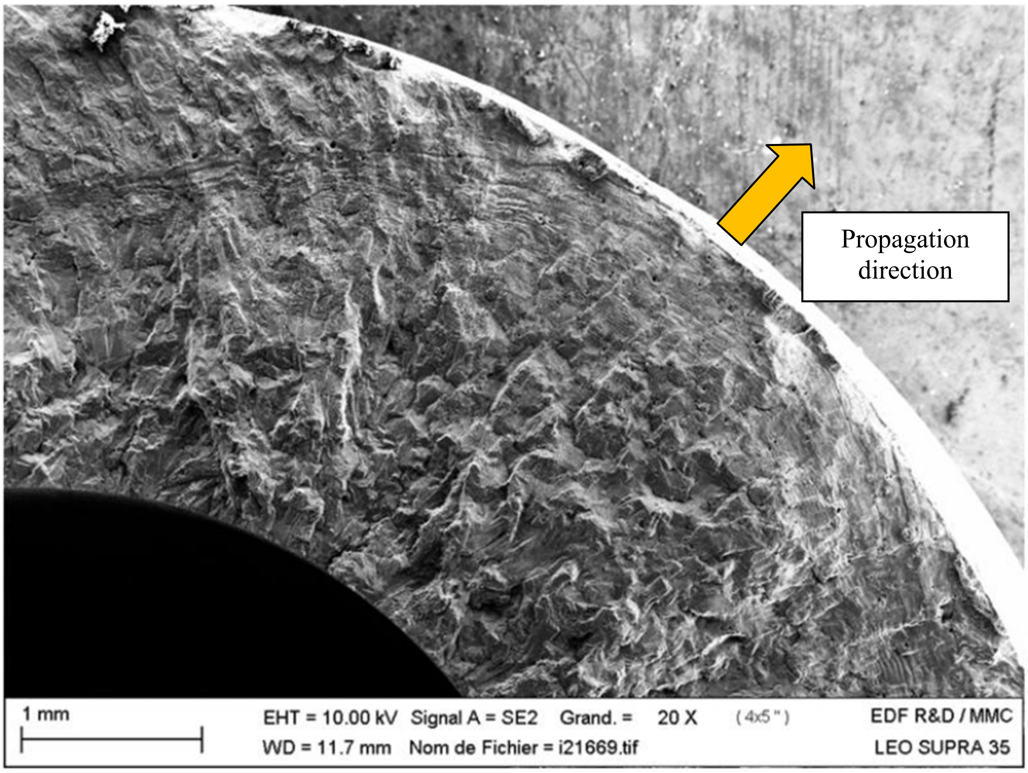

Figure 83 – Fracture surface of 1630 MHI 01, $\Delta\varepsilon_t/2=0.5\%$, $\Delta\varepsilon_t/dt=0.4\%/s$, as-received, PWR primary water at 300°C, general view.

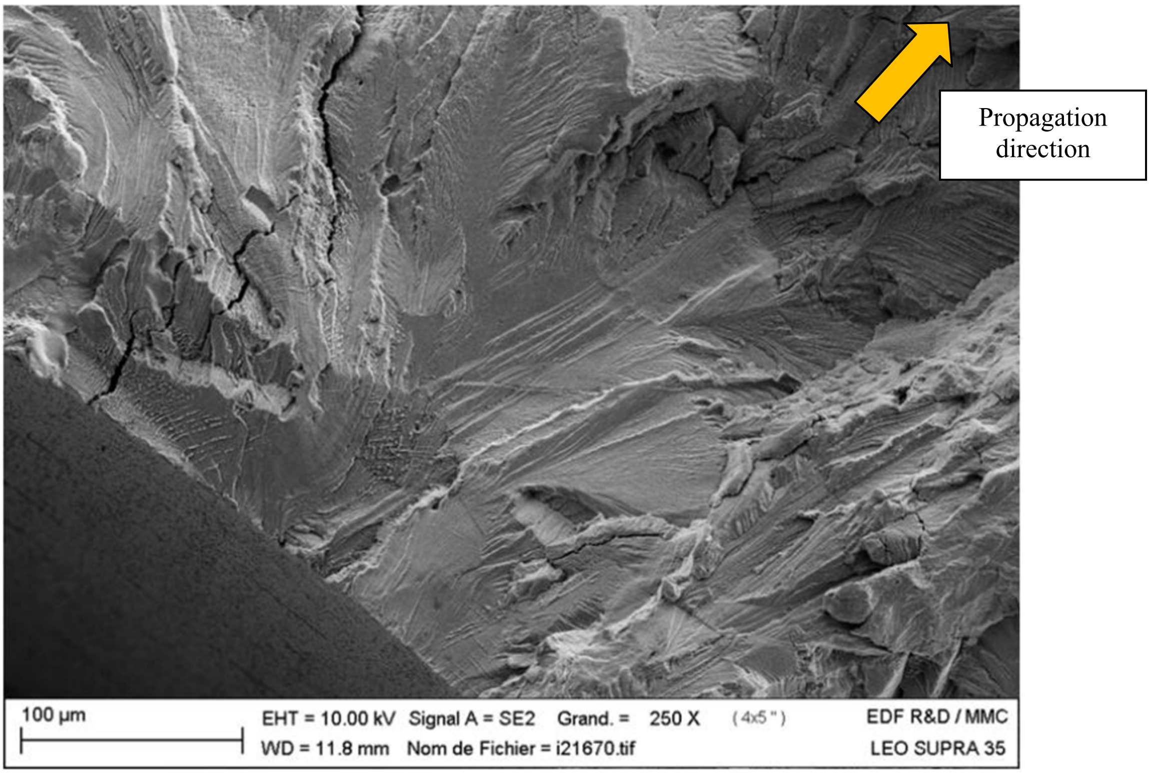

Figure 84 □Fracture surface of 1630 MHI 01, $\Delta\varepsilon t/2=0.5\%$, $\Delta\varepsilon_t/dt=0.4\%/s$, as-received, PWR primary water at 300°C, initiation area.

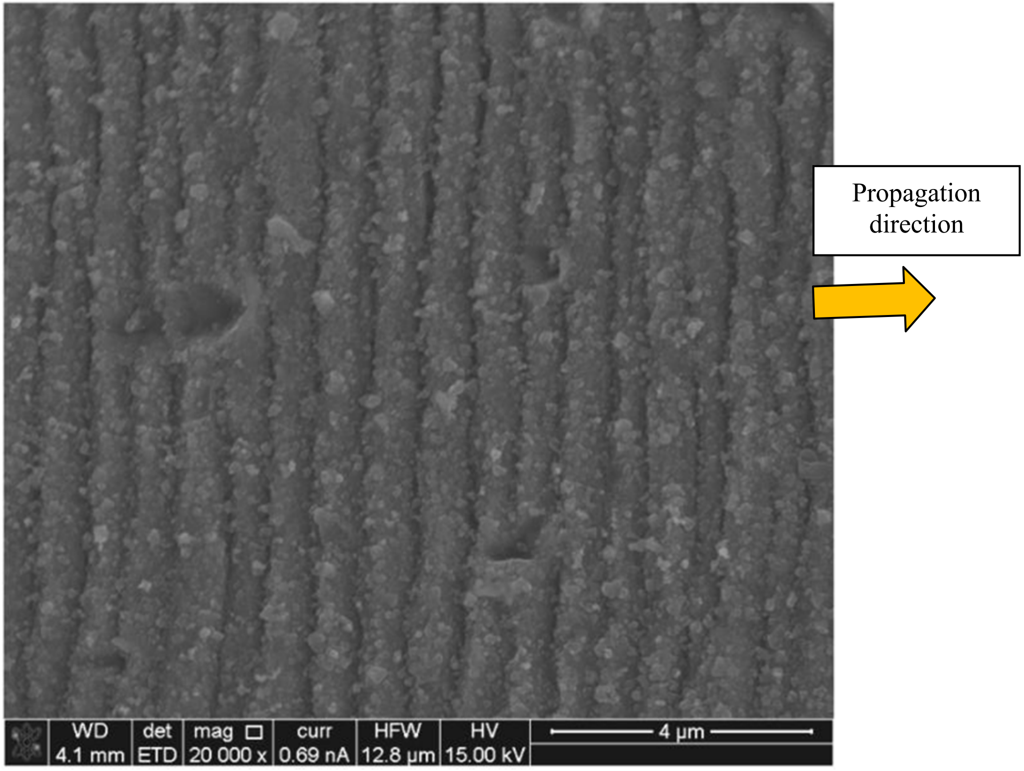

Figure 85 □Fracture surface of 1630 MHI 01, $\Delta\varepsilon t/2=0.5\%$, $\Delta\varepsilon_t/dt=0.4\%/s$, as-received, PWR primary water at 300°C, 500µm from initiation area.

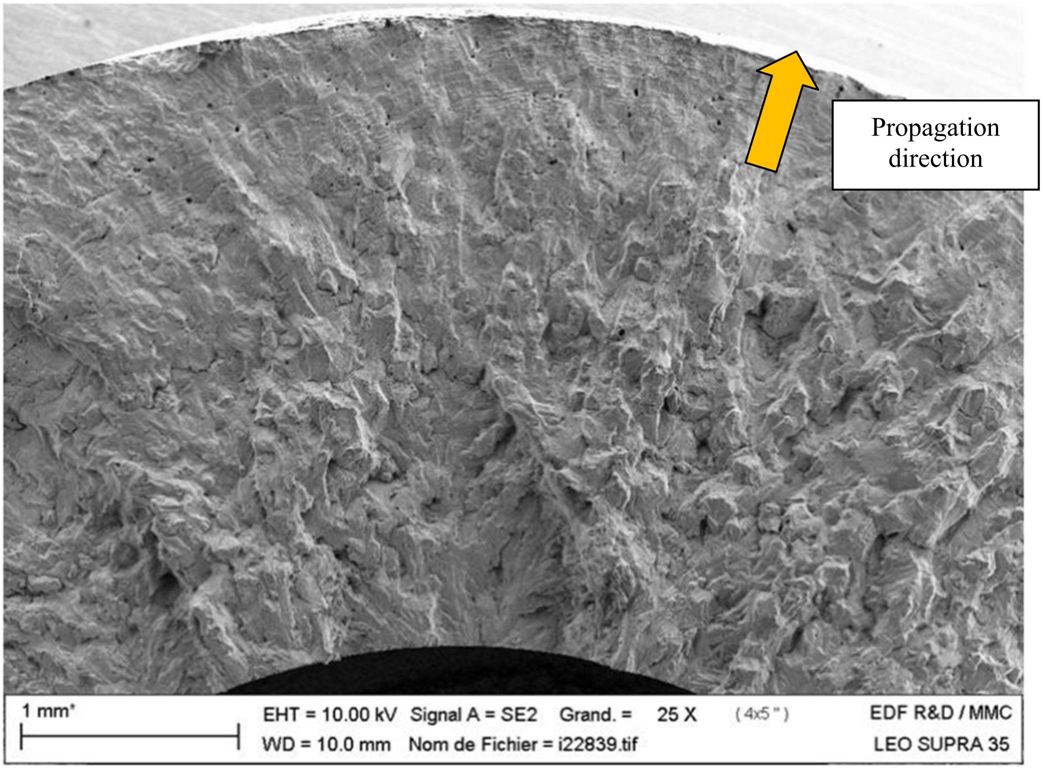

Figure 86 Fracture surface of 1630 MHI 04, $\Delta\varepsilon t/2=0.5\%$, $\Delta\varepsilon_t/dt=0.004\%/s$, as-received, PWR primary water at 300°C, general view.

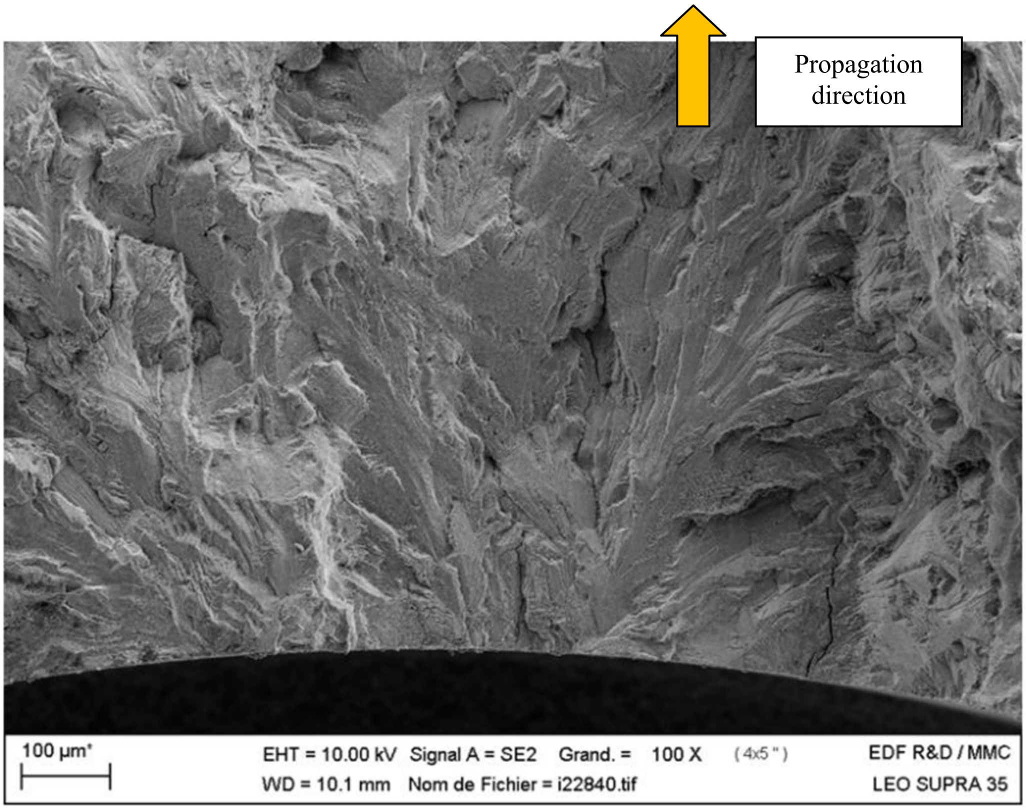

Figure 87 Fracture surface of 1630 MHI 04, $\Delta\varepsilon t/2=0.5\%$, $\Delta\varepsilon_t/dt=0.004\%/s$, as-received, PWR primary water at 300°C, initiation area.

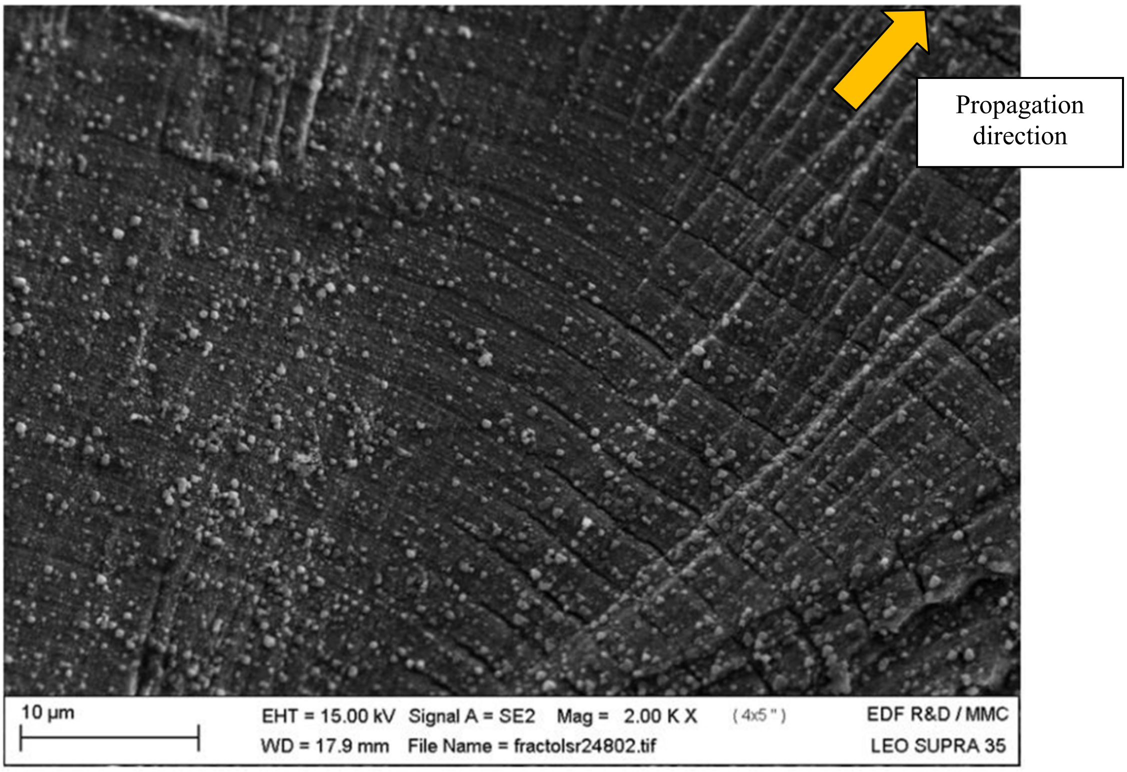

Figure 88 Fracture surface of 1630 MHI 04, $\Delta\varepsilon t/2=0.5\%$, $\Delta\varepsilon_t/dt=0.004\%/s$, as-received, PWR primary water at 300°C, 500µm from initiation area.

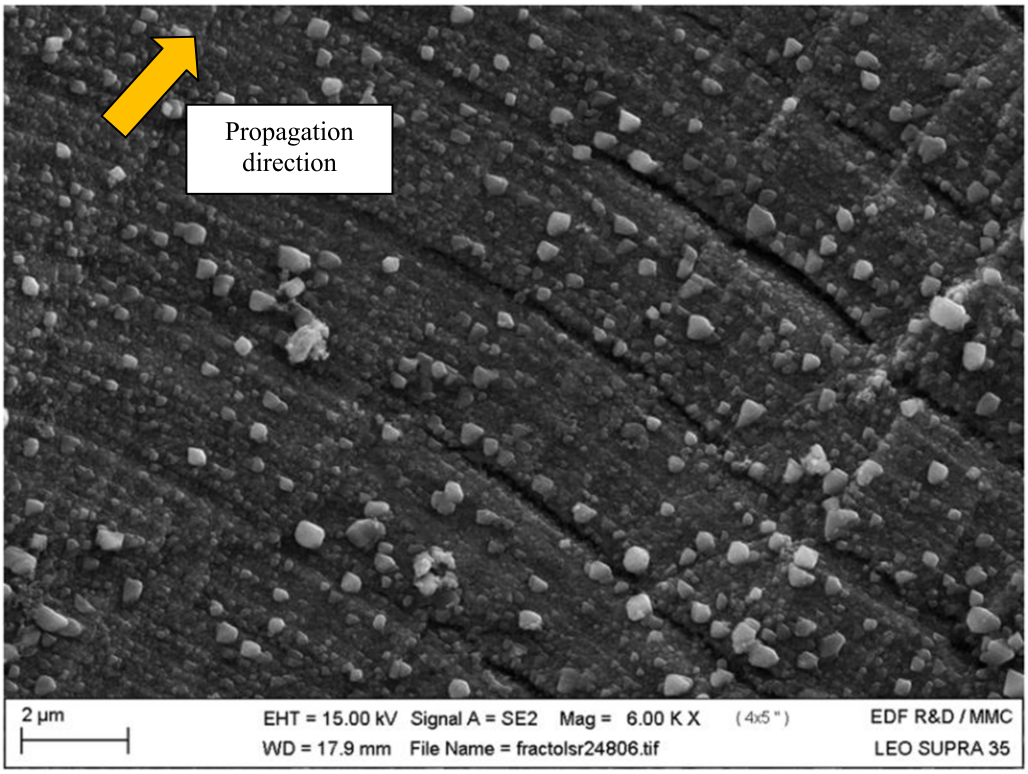

Figure 89 Fracture surface of 1630 MHI 04 focusing on sub striations, $\Delta\varepsilon t/2=0.5\%$, $\Delta\varepsilon_t/dt=0.004\%/s$, as-received, PWR primary water at 300°C, 500µm from initiation area.

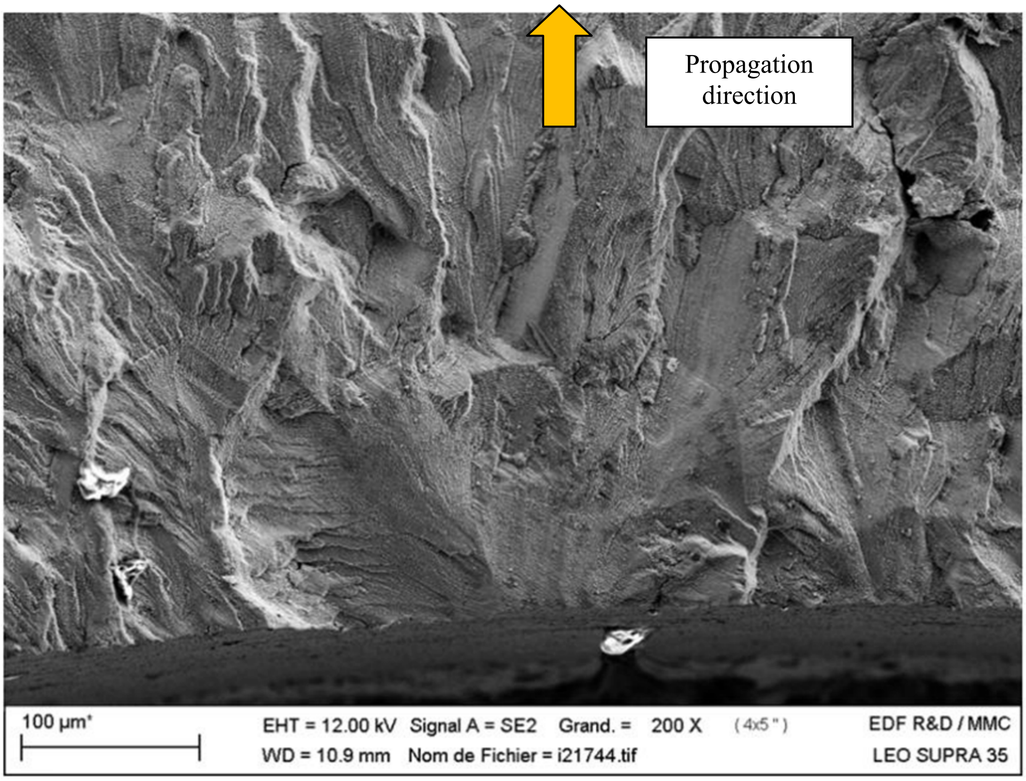

Figure 90 Fracture surface of 1630 MHI 03, $\Delta\varepsilon t/2=0.5\%$, $\Delta\varepsilon_t/dt=0.004\%/s$, 10% Tension, PWR primary water at 300°C, initiation area.

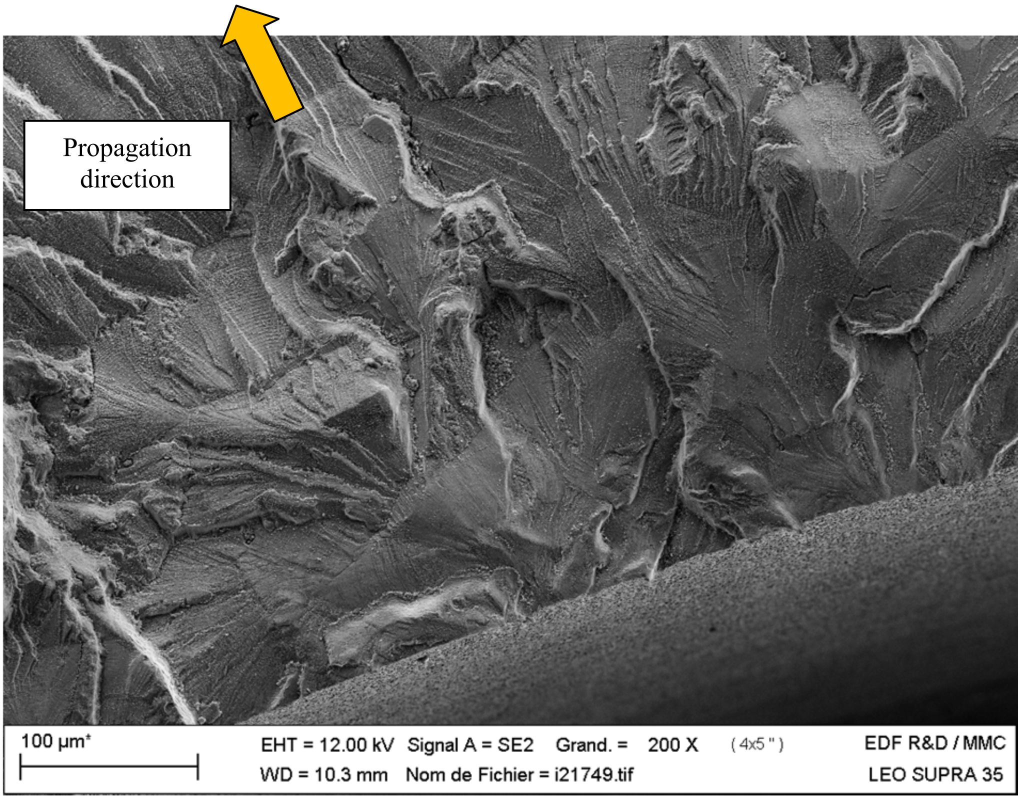

Figure 91 Fracture surface of 1630 MHI 14, $\Delta\varepsilon t/2=0.5\%$, $\Delta\varepsilon_t/dt=0.004\%/s$, 10% Rolled, PWR primary water at 300°C, initiation area.

5.4.2. Evaluation of propagation kinetics

Qualitatively, the fracture surface observations did not differ so much between each other when pre hardening conditions and applied strain rate vary except the presence of substriations in the low strain rate conditions. The next section addresses a quantitative evaluation of the crack propagation step.

5.4.2.1. Validation of method

The NUREG CR/6878 [145] considered that, in PWR primary environment, each cycle generates a fatigue striation. It is thus proposed to verify the equivalence between the distance between striations measured on the fracture surface and the crack growth rate in PWR primary environment in the case of the sample 1630MHI04 ($\Delta\varepsilon t/2=0.5\%$, $\Delta\varepsilon t/dt=0.004\%/s$, as-received, PWR primary water at 300°C). Data collected on fracture surface are supported with data obtained on cross section on samples tested at a fixed number of cycles (10-300) used in the study of crack initiation mechanisms. Indeed it is assumed that the maximum crack length measured on these cross sections corresponds to the main crack depth. Thus, by a simple fit with a power law (Figure 92) and by derivation of the calibrated equation, it was possible to evaluate the crack growth rate as a function of the crack depth. Results are presented in Figure 93 along with data obtained on fracture surfaces. The global curve was then fitted with a power law (Equation 1) and by its integration it was possible to evaluate the number of cycles covered by the micro propagation stage between an initial main crack depth (a0) and a final crack depth (af). a0 was chosen equal to 3 µm because the results from the crack initiation investigations revealed that the transition between crack initiation and the microcrack propagation seems to occur close to this crack depth. The results are presented in Table 1. The evaluation of the number of cycles between 3 µm and 2 mm is in good agreement with the fatigue life obtained on this sample (859 cycles). Therefore, it is possible to conclude that, for this set of parameters in PWR primary environment, the crack growth rate matches with the distance between striations.

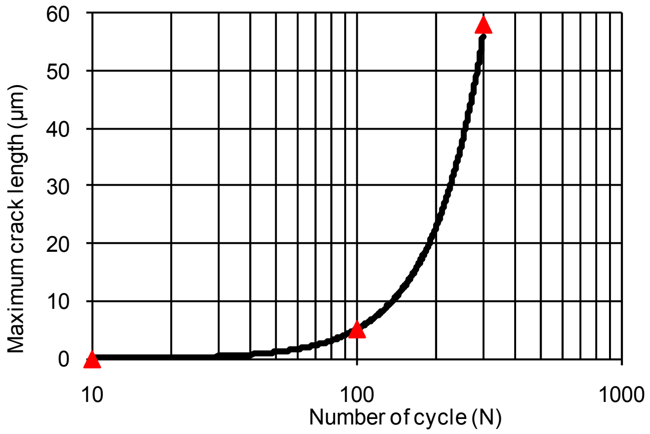

Type of equation	R	W	R²
$a = R \times N^{W}$	$2.1*10^{-4}$	2.19	99.74

Figure 92 □Evolution of the maximum crack length as a function of the number of cycle of 1630 MHI 04, $\Delta\varepsilon_t/2=0.5\%$, $\Delta\varepsilon_t/dt=0.4\%/s$, As-received, PWR primary water at 300°C

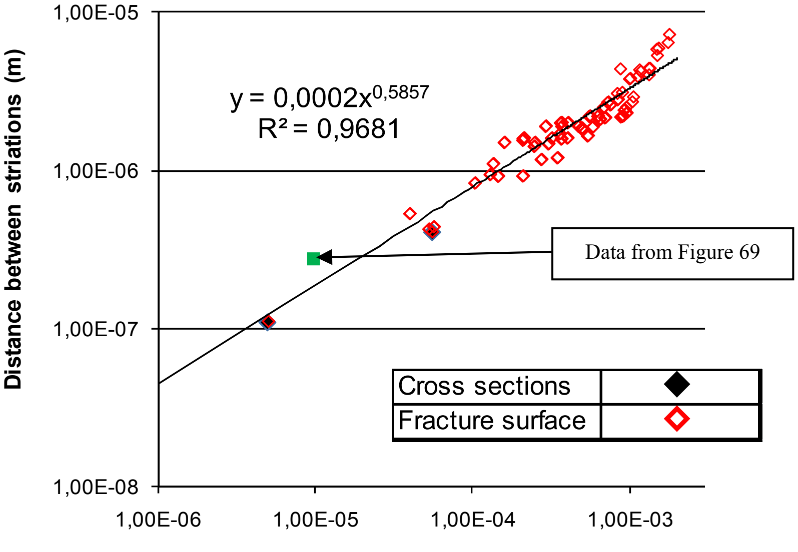

Figure 93 □Evolution of the distance between striations as a function of the distance from initiation point of specimen 1630 MHI 04, $\Delta\varepsilon_t/2=0.5\%$, $\Delta\varepsilon_t/dt=0.004\%/s$, as-received, PWR primary water at 300°C.

$$\frac{da}{dN} = C \times a^{n}$$

Equation 1

$$N = \frac{1}{C \times (1-n)} \times \left[a_f^{(1-n)} - a_0^{(1-n)}\right]$$

Equation 2

Table 1 Evaluation of the number of cycles

C	n	a_0 (m)	a_f (m)	N (cycles)
2.10^{-4}	0.5857	3.10^{-6}	2.10^{-3}	864

5.4.2.2. Effect of strain amplitude and strain rate on microcrack propagation rate

The results presented in Figure 94 correspond to the 10% cold-worked material tested at $\Delta\varepsilon_t/2=0.5\%$, $\Delta\varepsilon_t/2=0.35\%$ and $\Delta\varepsilon_t/2=0.25\%$ and also $\Delta\varepsilon_t/dt=0.004\%/s$ and $\Delta\varepsilon_t/dt=0.4\%/s$.

The crack growth rate seems affected by the strain amplitude: the larger the strain amplitude, the faster the crack growth rate. In addition, Figure 94 indicates that a lower strain rate leads to an increase of micro crack growth rate for all the strain amplitudes considered up to a 1-2 mm crack depth. For deeper crack depths, no clear strain rate effect on crack propagation rate can be noticed, except at a strain amplitude of 0.5%. Results obtained at totally different strain amplitude/strain rate couples ($\Delta\varepsilon_t/2=0.5\%$ under $\Delta\varepsilon_t/dt=0.4\%/s$ and $\Delta\varepsilon_t/2=0.35\%$ under $\Delta\varepsilon_t/dt=0.004\%/s$) exhibited similar crack propagation rates and fatigue lives (2590 cycles and 2162 cycles respectively). The same conclusion is reached comparing the two tests at $\Delta\varepsilon_t/2=0.35\%$, $\Delta\varepsilon_t/dt=0.4\%/s$ and $\Delta\varepsilon_t/2=0.25\%$, $\Delta\varepsilon_t/dt=0.004\%/s$ for which fatigue lives are respectively 7361 cycles and 6864 cycles.

These results support the hypothesis of the good correlation between the observed distance between striations and the calculated crack growth extensions.

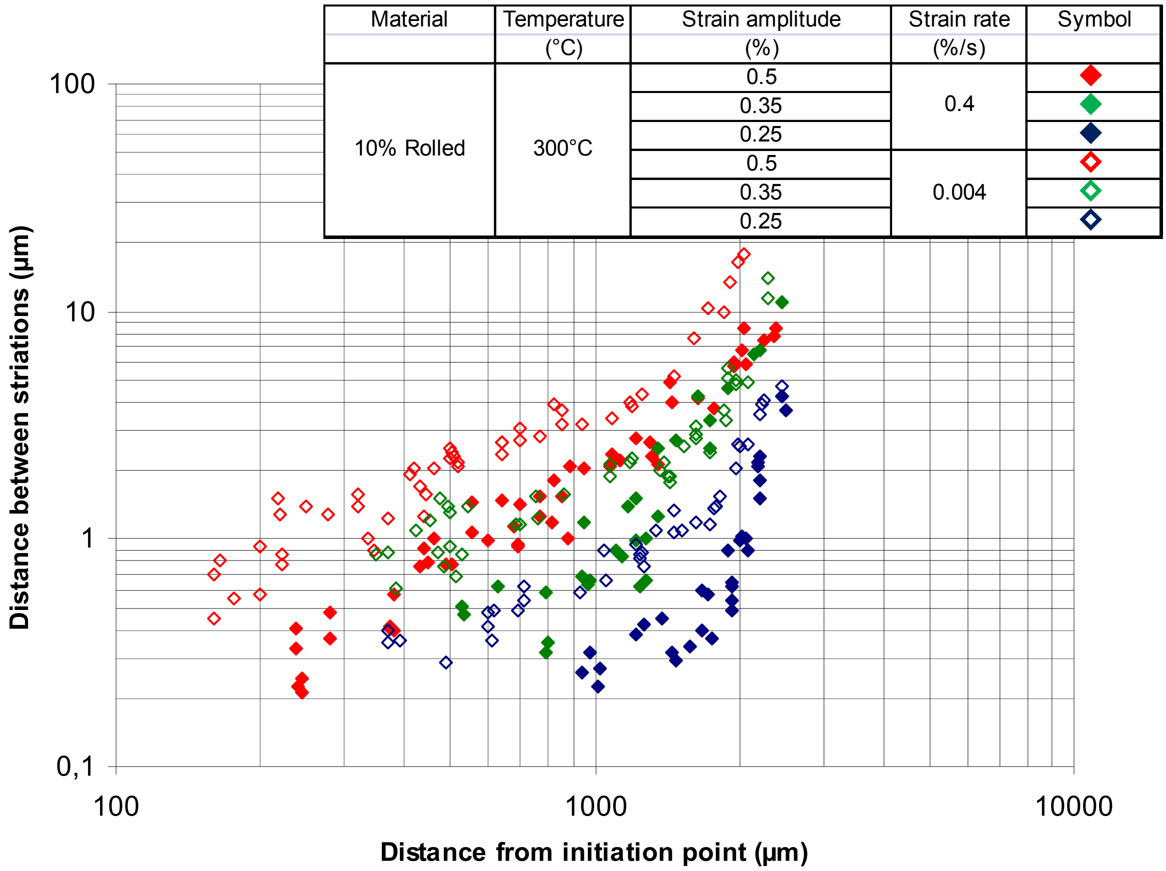

Material	Temperature (°C)	Strain amplitude (%)	Strain rate (%/s)	Symbol
10% Rolled	300°C	0.5	0.4	◆
		0.35		◆
		0.25		◆
		0.5	0.004	◇
		0.35		◇
		0.25		◇

Figure 94 - Effect of strain rate and strain amplitude on crack propagation of 10% rolled material, 300°C, PWR Primary environment.

Figure 95 corresponds to results obtained on the 10% prior cold rolled, 10% prior tensioned and as-received 304L. No clear difference in crack growth rates is noticed between the different degrees of cold working at both strain rates, in good agreement with their similar fatigue lives.

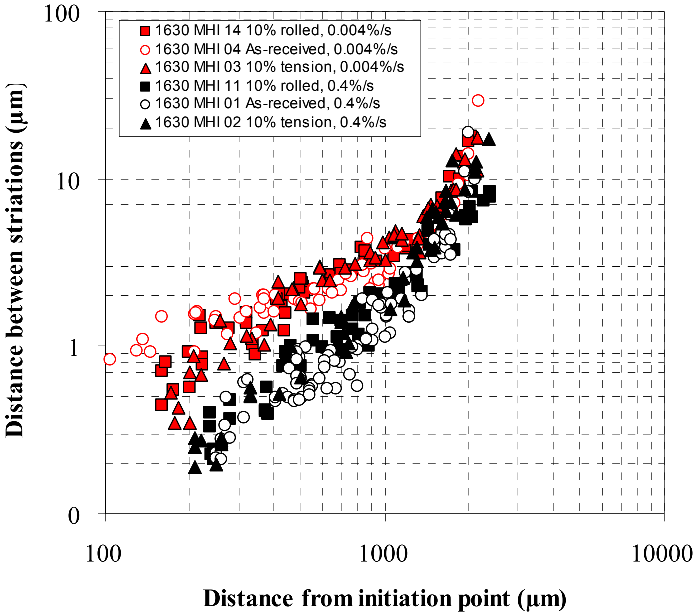

Figure 95 - Effect of a prior strain hardening on crack propagation, $\Delta\varepsilon_t/2=0.5\%$, $\Delta\varepsilon_t/dt=0.004\%/s$ and 0.4%/s, 300°C, PWR Primary environment.

5.4.3. Mechanisms of crack propagation behavior related to strain rate

The previous section has highlighted major differences in crack growth rates between 0.4%/s and 0.004%/s. Crack growth rate increased under lower strain rate. This section focuses on a potential explanation of this effect through some microstructural observations of the fracture surface.

In order to simplify the problem, only the as-received material was observed. The two considered tests are presented in Figure 96. Tests conditions were $\Delta\varepsilon t/2=0.5\%$ in PWR primary environment on the as-received material at 300°C using two different strain rates 0.004%/s and 0.4%/s. TEM cross section sampling was performed on fracture surface in order to study fatigue striation generation mechanisms in PWR primary environment. Four different areas were selected corresponding to crack depths of 500 µm and 1 mm. At least 2 TEM samples were cut per selected area up to 7 in the case of the 1 mm crack in low strain rate conditions.

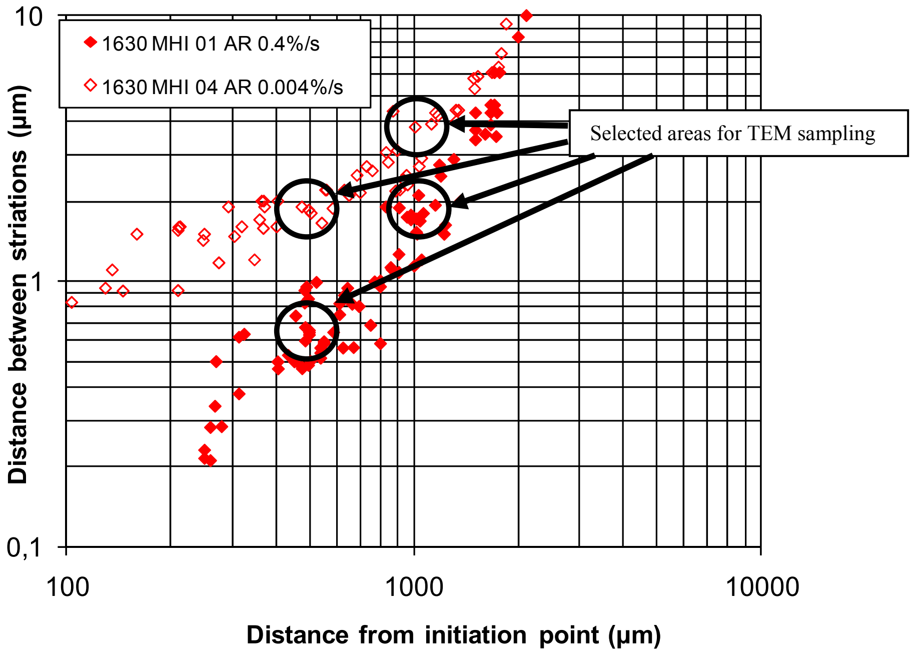

Figure 96 □Propagation curves of 1630MHI01 and 1630MHI04 ($\Delta\varepsilon_t/2=0.5\%$, $\Delta\varepsilon_t/dt=0.004\%/s$ and 0.4%/s, as-received, PWR primary water at 300°C).

5.4.3.1. At 500 µm from initiation point

Figure 97 presents a characteristic fracture surface with typical fatigue striations, observed on specimen 1630MHI01 tested at 0.4%/s for a crack depth of 500 µm. The mean distance between striations was close to 600 nm. Figure 98 is STEM image of the sample cross section. In this figure it is possible to see striations in addition to shear bands that are localized below each striation. In this case, the mean distance between shear bands is highly similar to the distance between striations.

Figure 99 presents typical fatigue striations observed on the fracture surface of specimen 1630MHI04 tested at 0.004%/s for a crack depth of 500 µm. The mean distance between striations was close to 2 µm. In addition to commonly observed striations, it was possible to see □sub striations□ Figure 100 corresponds to a STEM general view of the sample cross section where it is possible to identify the fatigue striations. Figure 101 is a detailed view of Figure 100. In this figure, it is possible to observe the same structure than the one observed at higher strain rate. Structures consist in the emission of shear bands at each striation. However, between two striations, it was possible to observe some other shear bands corresponding to the sub striations observed at the surface. It is also important to mention that all of the 7 TEM samples observed at this strain rate and at this crack depth presents the same type of substructures.

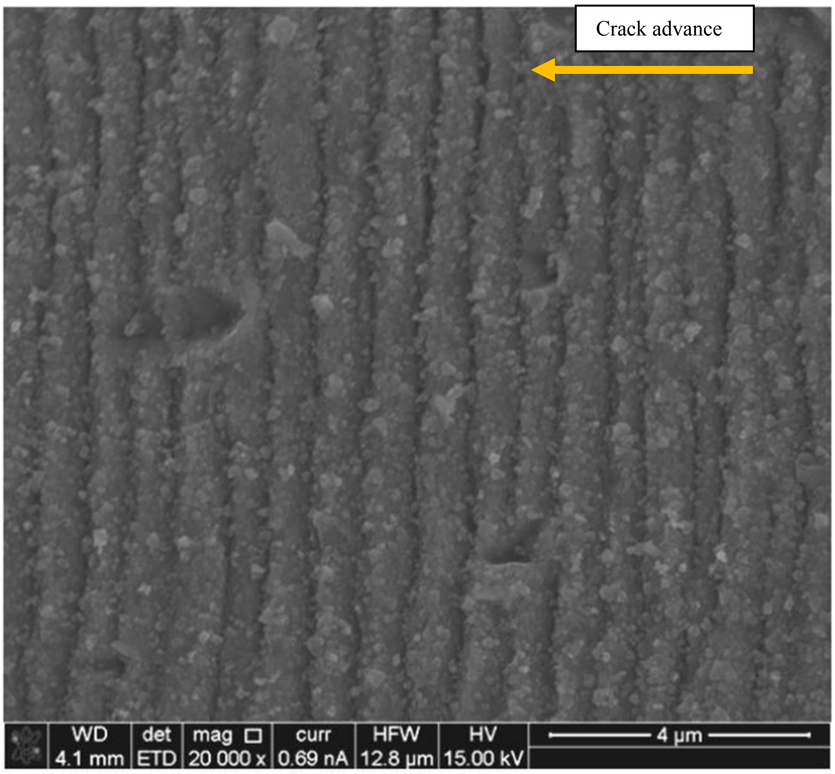

Figure 97 Fatigue striations 1630MHI01 $\Delta\varepsilon_t/2=0.5\%$, $\Delta\varepsilon_t/dt=0.4\%/s$, as-received, PWR primary water, 300°C, 500µm crack depth.

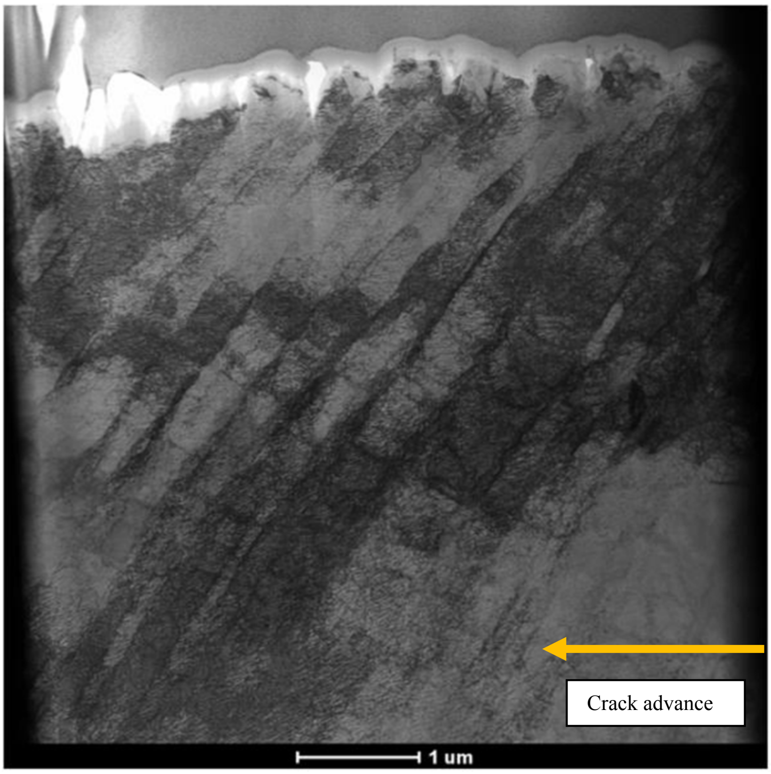

Figure 98 Fatigue striations 1630MHI01 $\Delta\varepsilon t/2=0.5\%$, $\Delta\varepsilon_t/dt=0.4\%/s$, as-received, PWR primary water, 300°C, 500µm crack depth, STEM.

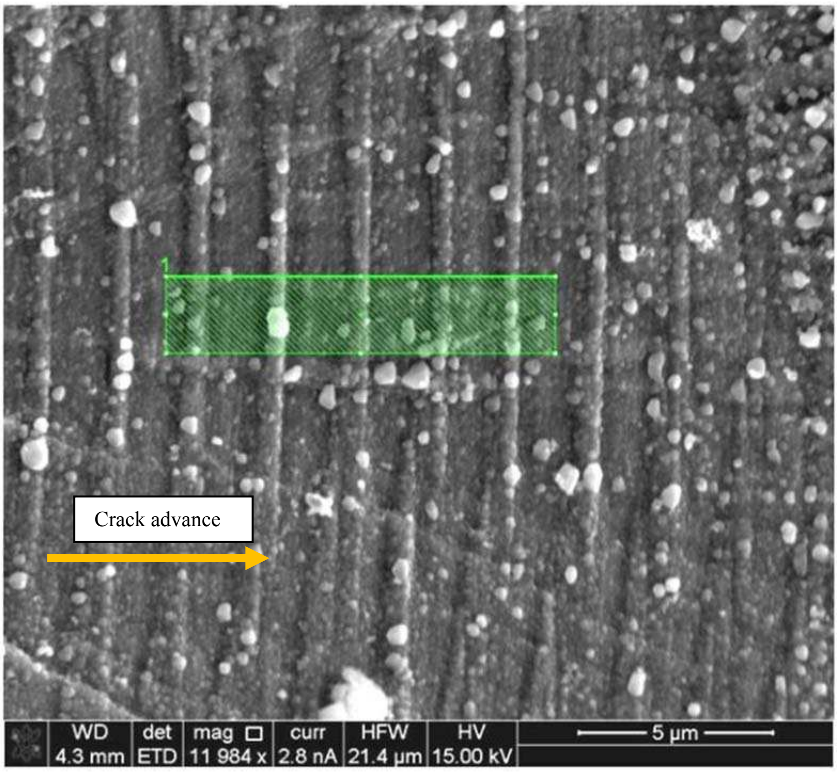

Figure 99 □Fatigue striations 1630MHI04 Δεt/2=0.5%, $\Delta\varepsilon_t/dt$=0.004%/s, as-received, PWR primary water, 300°C, 500 µm crack depth.

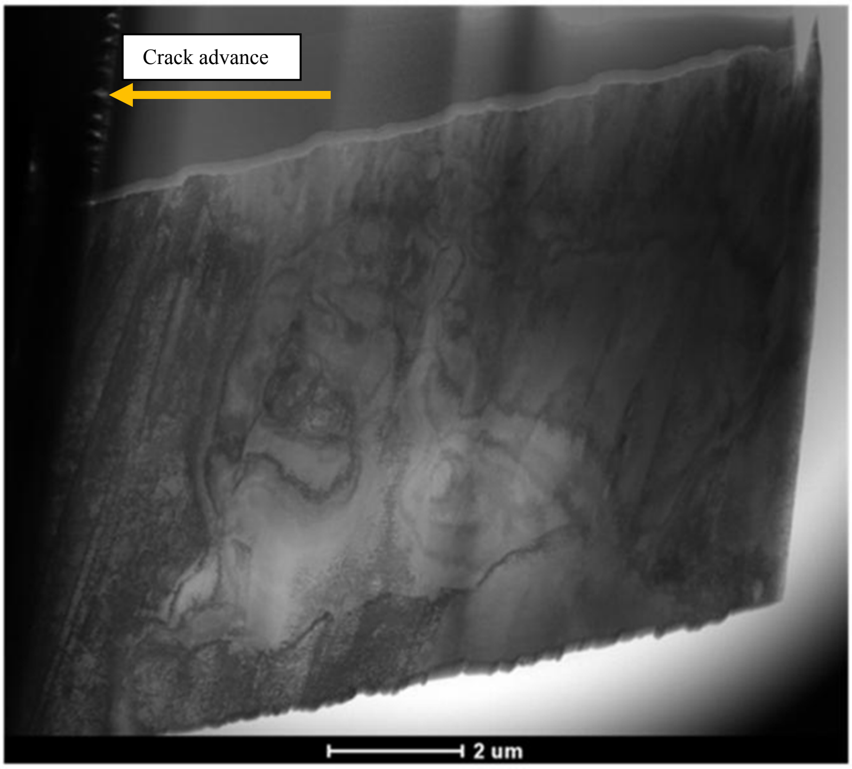

Figure 100 □Fatigue striations 1630MHI04 Δεt/2=0.5%, Δεt/dt=0.004%/s, as-received, PWR primary water, 300°C, 500 µm crack depth, STEM

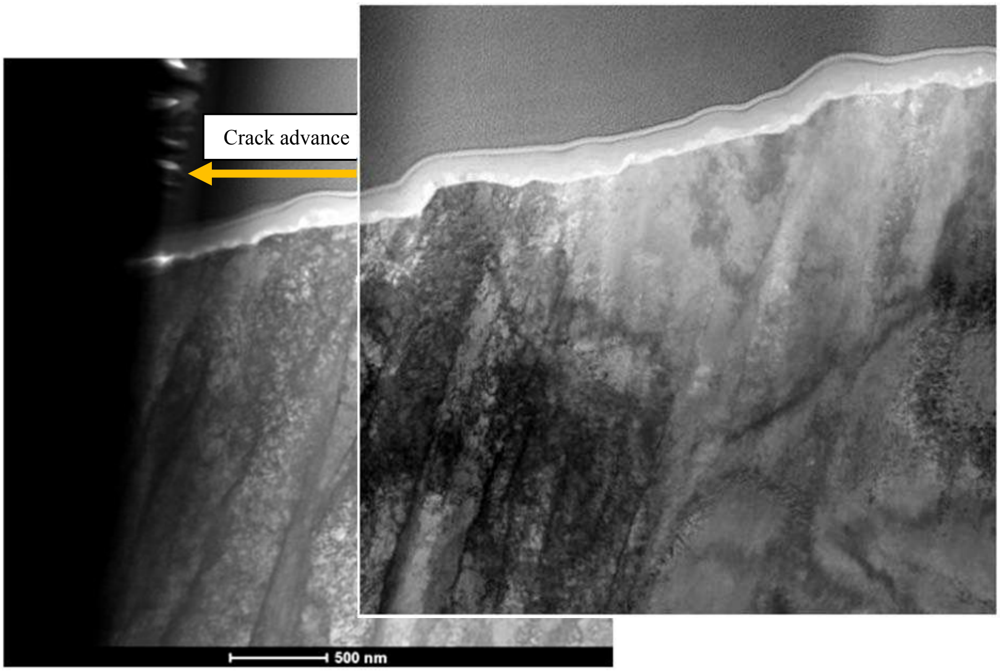

Figure 101 – Fatigue striations 1630MHI04 $\Delta\varepsilon t/2=0.5\%$, $\Delta\varepsilon t/dt=0.004\%/s$, as-received, PWR primary water, 300°C, 500 µm crack depth, STEM, focusing on striations

5.4.3.1. At 1mm from initiation point

Figure 102 is a STEM general view of a cross section obtained on specimen 1630MHI01 tested at 0.4%/s for a crack depth of 1 mm. The average distance between striations is close to 2 µm. Figure 103 is a detailed view of Figure 102. In this image it is possible to see two types of deformation structures. One is generated at each striation, and the other one is present between each striations. Some characteristics of these bands were measured using EBSD (Figure 104). It is possible to see that, close to the surface, the two features seem to have different orientation. However, when similar observations are performed deeper in the bulk, this difference in orientation is less pronounced. This difference of orientation is close to disappear at the bottom of the sample. This result suggesting that residual misorientations i.e. residual strains are more important close to the fracture surface may indicate that this structure was not present before the crack proceeded through this area but has been generated by the crack.

Figure 105 presents typical fatigue striations observed on the fracture surface of specimen 1630MHI04 tested at 0.004%/s for a crack depth of 1 mm. The mean distance between striations was close to 4 µm. As for a 500 µm crack depth, it was possible to see some other “sub striations”. STEM investigations revealed that the microstructure is highly similar to what has been observed in case of a 500 µm-depth crack. At each striation, it was possible to observe shear bands. In addition to these bands, others are generated at each □sub-striation□ Therefore the propagation mechanism at a 1mm depth seems similar to the one observed at 500µm, that means at a lower crack growth rate.

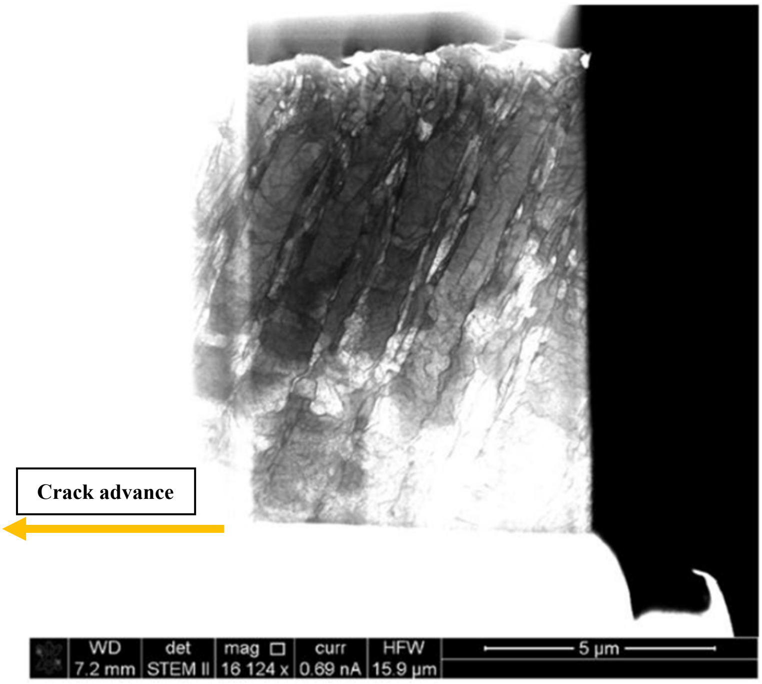

Figure 102 □Fatigue striations on specimen 1630MHI01 Δεt/2=0.5%, Δεt/dt=0.4%/s, as-received, PWR primary water, 300°C, 1 mm crack depth, STEM.

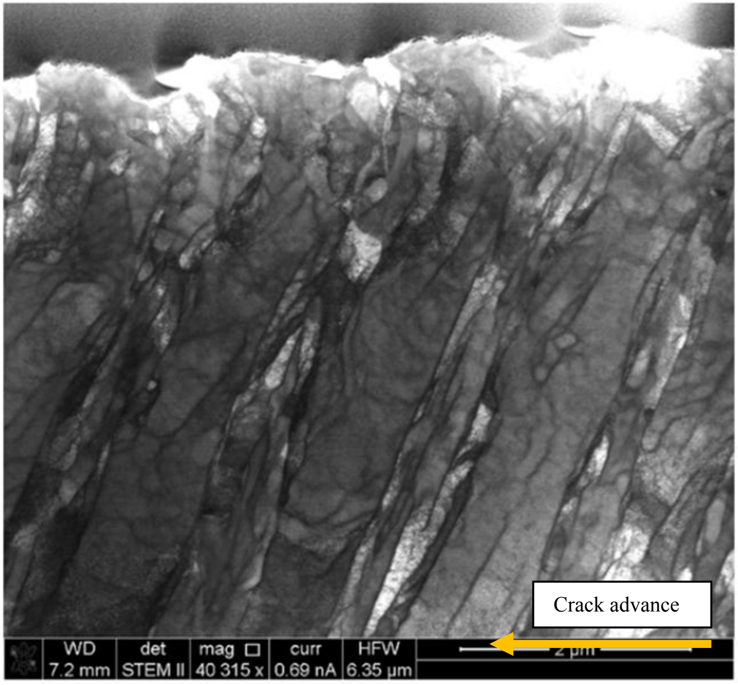

Figure 103 □Fatigue striations on specimen 1630MHI01 Δεt/2=0.5%, Δεt/dt=0.4%/s, as-received 304L, PWR primary water, 300°C, 1 mm crack depth, STEM, focused area.

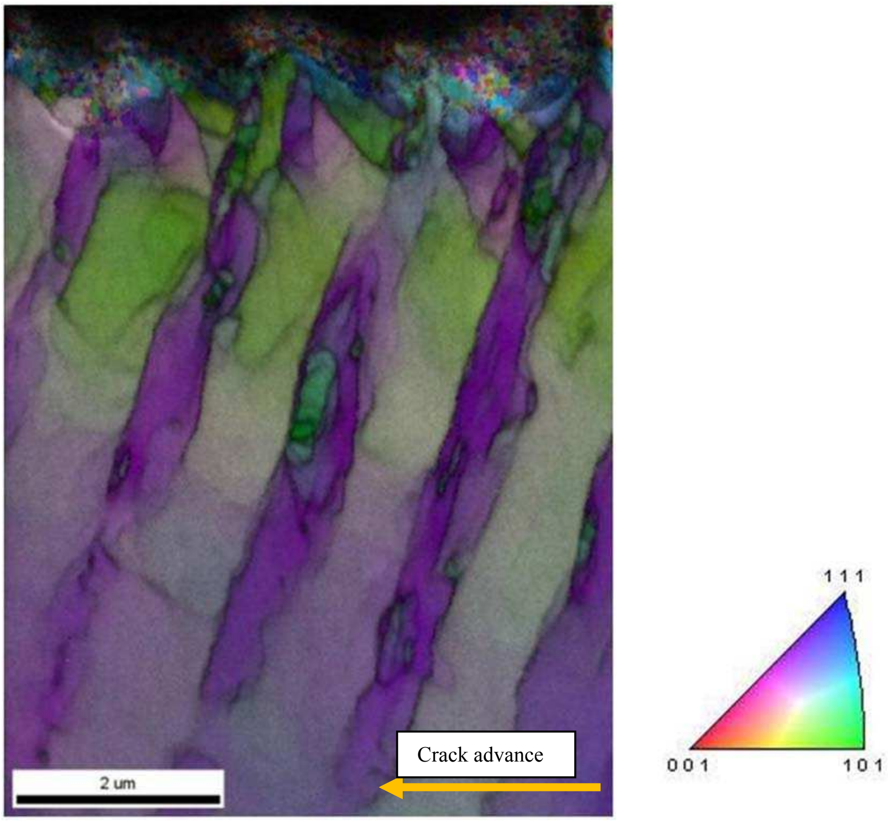

Figure 104 Fatigue striations on specimen 1630MHI01 Δεt/2=0.5%, Δεt/dt=0.4%/s, As-received, PWR primary water, 300°C, 1 mm crack depth, EBSD.

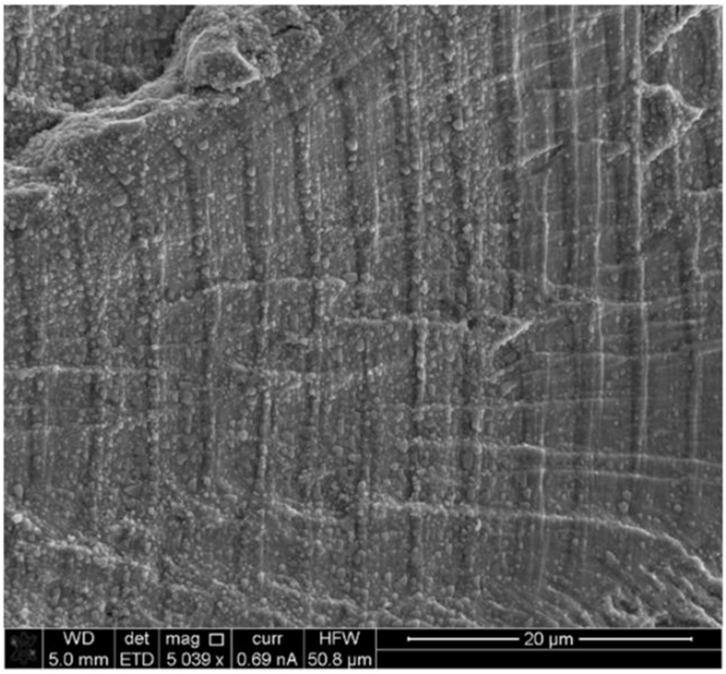

Figure 105 Fatigue striations on specimen 1630MHI04 Δεt/2=0.5%, Δεt/dt=0.004%/s, As-received 304L, PWR primary water, 300°C, 1 mm crack depth.

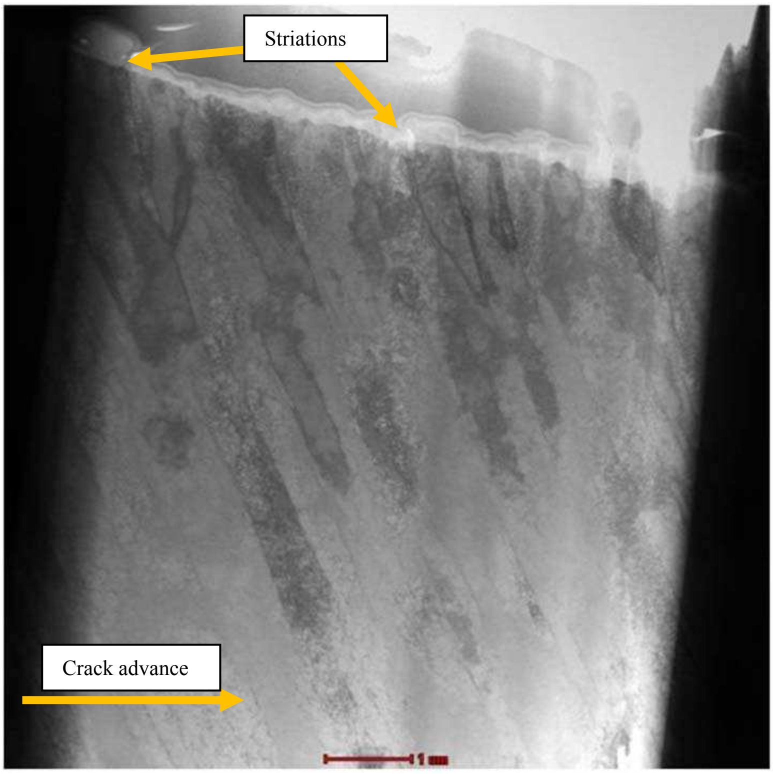

Figure 106 Fatigue striations on specimen 1630MHI04 Δε/2=0.5%, Δε/dt=0.004%/s, as-received, PWR primary water, 300°C, 1 mm crack depth, STEM.

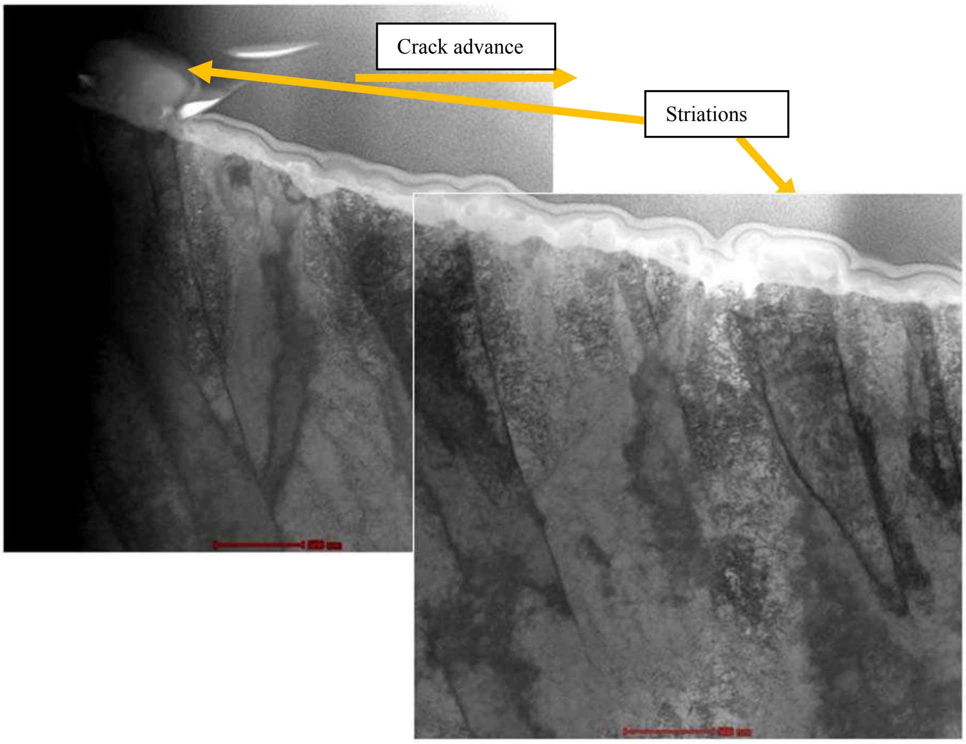

Figure 107 Fatigue striations on specimen 1630MHI04, Δε/2=0.5%, Δε/dt=0.004%/s, as-received 304L, PWR primary water, 300°C, 1 mm crack depth, STEM, focused area.

6. Summary

- Cyclic stress strain behavior

  The mechanical behavior highly depends on the cold-work level. An increasing cold work level results in an increase of the stress level and a reduction of the number of cycle in the primary hardening phase. A reduction of the loading strain rate result in an increase of the stress level developed during cycling.

- Fatigue life

  In PWR primary environment, the prior strain hardening within a 0-10% range of 304L SS does not lead to a reduction of fatigue life in the low cycle region with respect to the as-received condition and an increase of fatigue life in the high cycle region. A reduction of the loading strain rate reduces the fatigue life but no additional effect related to a prior hardening can be observed.

- Damage mechanisms

  Fatigue life of a 304L material in PWR primary environment can be summarized as:

  Preferential oxidation along emerging dissociated dislocation at the surface along [111] planes. Each cycle generates a new C-rich/Fe-rich oxide layer (Figure 108 - a).

  The deformation microstructure evolves from stacking fault into micro twinning. Layered preferential oxidation continues along this microstructure by repeated shearing and dissolution of the passive film up to a certain depth (<3µm). (Figure 108 - b).

  At this depth, the crack starts to propagate along other crystallographic planes that can be [100], [110] and [111] which are close to a 90° angle from the surface. The crack continues its propagation by successive generation of shear bands and fatigue striations at each cycle up to failure. The distance between striation increases with the crack depth (Figure 108 □c and Figure 108 - d).

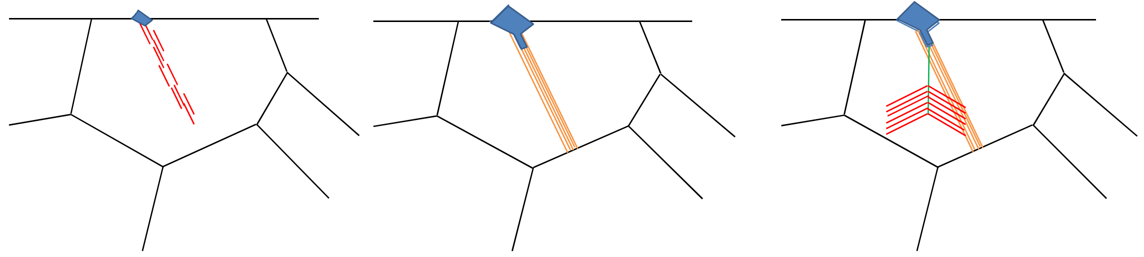

Oxidation localization (a) Crack initiation (b) Beginning of micro crack propagation (c)

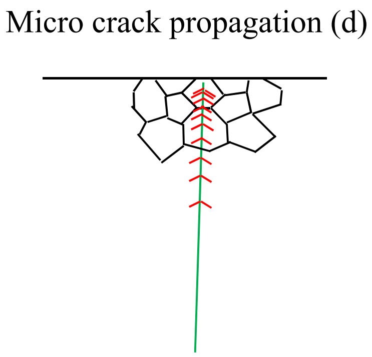

Figure 108 □Fatigue life description

- Effect of a pre hardening

A prior pre-hardening whether it is a pre tension or a pre rolling, does not seem to affect the initiation and propagation stages in agreement with observed fatigue lives.

- Effect of strain rate

These mechanisms can be affected by strain rate. Indeed a high strain rate can limit the generation of the oxide double layer structure. Strain rate also modifies the cracking morphology. Indeed, a high density of branched cracks is observed at a high strain rate and a low density of straight cracks at a low strain rate.

In the micropropagation regime, a lower strain rate results in an increase of crack growth rate in agreement with the fatigue life reduction. In this regime, some additional shear bands were observed, in addition to the one generated at each striations. This suggests that under such loading conditions, the crack growth proceeds through different steps within one cycle.

The next chapter will address the comparison and discussion of the results obtained in air in air (chapter 3) and in PWR primary environment (chapter4).

---

[1] **H.D. SOLOMON, C. AMZALLAG, A.J. VALLEE AND R.E. DELAIR,** “Fatigue Limit and Hysteresis Behavior of 304L SS in Air and PWR Water at 150 °C and 300 °C ”, rapport GE 2005GRC353, 2005.

[2] **T. COUVANT, F. VAILLANT, T. GHYS**, "Development of understanding of the interaction between localized deformation and SCC of austenitic stainless steels exposed to primary PWR environment" , EDF R&D report H-T29-2008-0945-EN, 2008.

[3] **E. HERMS** « Etude fractographique de la corrosion sous contrainte et de la fatigue corrosion d'alliages austénitiques : incidence sur l'expertise et les mécanismes » PhD Thesis, University of Bordeaux 1, 2000

CHAPTER 5: Synthesis and discussion

List of acronyms

BF : Bright Field
CT : Cold Tension
CR : Cold Rolled
DF : Dark Field
DSA : Dynamic Strain Ageing
EAC : Environmental Assisted Cracking
EAF : Environmentally Assisted Fatigue
FCC : Face Centered Cubic
GE : General Electric
HAADF : High Angular Anular Dark Field
HCF : High Cycle Fatigue
IG : Intergranular
LCD : Linear Crack Density
LCF : Low Cycle Fatigue
MHI : Mitsubishi Heavy Industries
PSB : Persistant Slip Bands
PWR : Pressurized Water Reactor
SCC : Stress Corrosion Cracking
SEM : Scanning Electron Microscope
SFE : Stacking Fault Energy
STEM : Scanning Transmission Electron Microscope
TEM : Transmission Electron Microscope
TG : Transgranular

Summary

1. Introduction

The environmentally assisted fatigue current approach in the US and in Japan consider the potential deleterious effect of the PWR primary water using a fatigue life reduction factor Fen with regard to a fatigue curve obtained in the air environment at room temperature. At the moment, there is still a lack of knowledge about the various mechanisms and stages of damage which lead to the significant reductions in the fatigue lives observed for stainless steels in simulated hydrogenated PWR environments.

A potential way to improve our knowledge on the EAF field is to consider the commonly used approach in the Environmentally Assisted Cracking field consisting in studying the synergy between three main parameters: the environment, the material and the mechanical loading.

- **Material: effect of a pre-hardening**

Pre-hardening is a parameter, more or less implicitly taken into account in the "material effect", that is not explicitly included in the current evaluation NUREG 6909. A prior work-hardening may results in some detrimental or positive effect. Indeed, the field experience related to fatigue highlighted that formed areas such as welds exhibit an increased susceptibility to fatigue crack initiation (Genkai and Civaux see appendix 1). In addition, it has been established that the SCC sensitivity drastically increases with increasing pre hardening [1,2,3].

- **Mechanical loading: Strain amplitude and strain rate**

The strain rate and the strain amplitude are two main loading parameters that are well-known to affect the fatigue life in air and in PWR primary environment at 300°C. In a first approach, in the LCF regime, the effect of strain amplitude can be considered through the modification of the applied plastic strain which controls fatigue behavior and damage. However the fatigue life reduction related to a modification of strain rate is less clear since for stainless steels there are several coupled factors which may govern fatigue damage rates involving environmental time-dependent interactions but also dynamic strain ageing effects.

- **Environment: Air and PWR primary environment**

Most of the knowledge of the fatigue mechanisms comes from the analysis of data and observations obtained in air and more seldom in an inert environment like vacuum. At the moment, no clear understanding of the mechanisms of the deleterious effect of the PWR primary environment has been proposed in the literature, mainly due to the limited set of available data.

The main objective of this discussion is to try and examine the respective influence of each parameter and their interactions using the following approach.

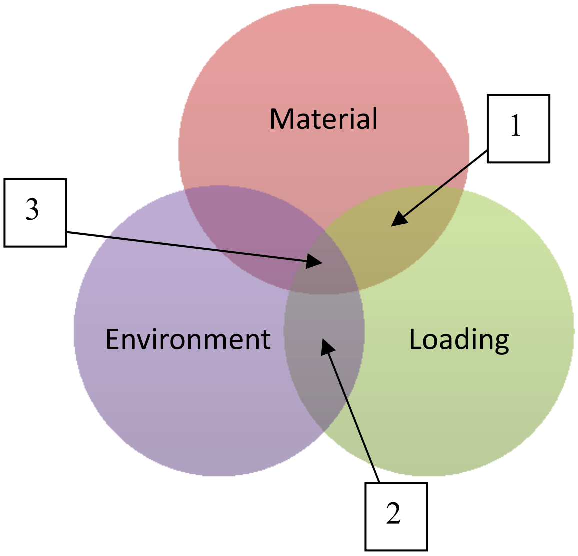

(1) Interactions between material and mechanical loading

This specific aspect will focus on a potential explanation of the cyclic stress strain behavior and fatigue life related to the degree of prehardening or the strain rate level using the microstructural characterizations presented in chapter 3

(2) Interactions between mechanical loading and environment

This aspect will focus on a comparison of oxidation data in air and in PWR primary environment, established under cyclic and static loading partly coming from the litterature.

(3) Interactions between material, loading and environment

This section constitutes the main body of this chapter. It is devoted to the evaluation of the PWR primary environment effect on cyclic stress strain behavior, fatigue life and cracking mechanisms.

2. Interactions between material and loading

2.1. Effect of a pre hardening on the cyclic stress strain behavior

Figure 1 presents some of the results obtained in the air environment among those presented in chapter 3. The first point is that increasing the pre hardening level results, for a given total strain amplitude, in an increase of the stress level which implies a decrease of the plastic strain amplitude.

It appears that the initial hardening is not erased during cycling and that the 304L material tends to conserve a memory of the pre-hardening even for the less severe pre-hardening conditions. Such "memory effect" behavior in fatigue is well-known in the case of low SFE FCC materials [4]. The key point of this "memory effect" in austenitic stainless steels is related to the formation of a hard deformation structure during pre hardening [5]. In order to erase such hard structure, the subsequent deformation has to exceed a threshold stress value.

In the case of other 10% 304L pre hardened material investigated here, this threshold value was not exceeded [6,7]. Indeed STEM observations of the bulk deformation structure confirm the presence of a hard structure composed of shear bands presenting a very high dislocation density, which remains all along cyclic deformation. Moreover, In addition to the higher stress level developed during cycling, it has to be noted that increasing the pre-hardening level also results in a decrease of the number of cycles needed to reach the softening region.

This specific region corresponds to the domain where the dislocation annihilation rate becomes greater than the generation rate. In addition, in the softening region, the rearrangement of dislocation by the constitution of 3D structures locally allows a better accommodation of plastic deformation. In the case of pre hardened materials, the high dislocation density generated by the pre hardening directly increases the annihilation rate that become directly higher than the generation rate [8,9]. In addition the dislocations also directly reorganize into 3D structures, thus favoring softening.

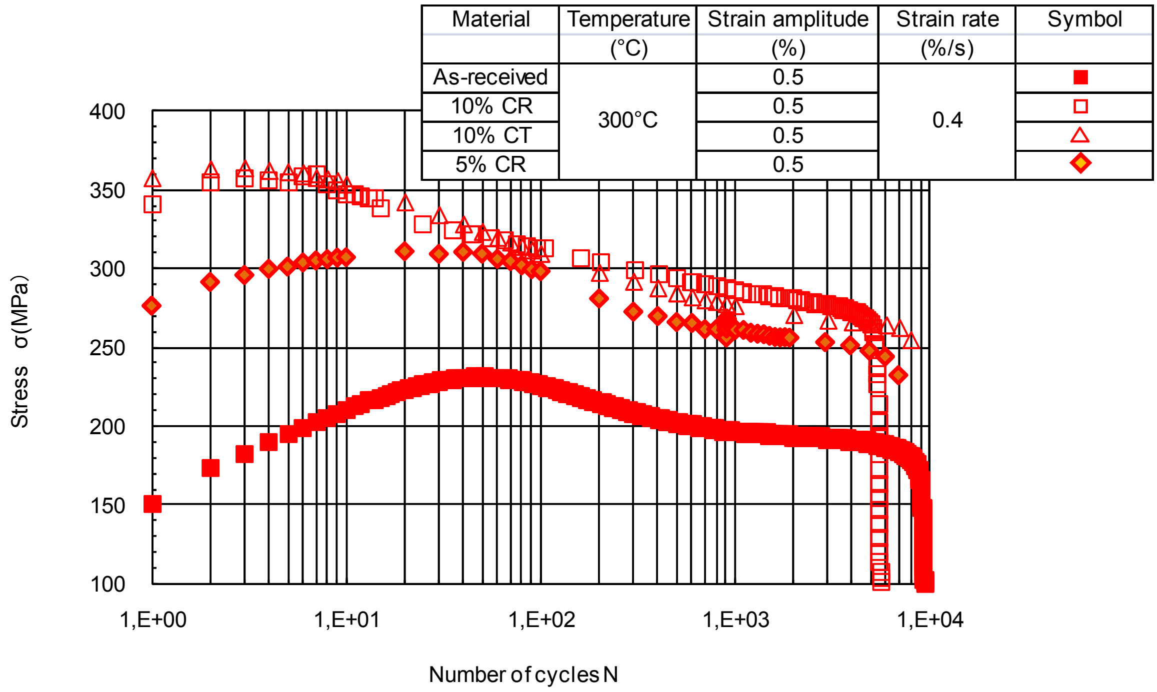

Figure 1 □Maximum stress evolution during cycling for the 10% CR, 10% CT, 5% CR and as-received material at a total strain amplitude of 0.5%.

2.2. Effect of the strain rate and the wave form

Figure 2 presents the results obtained on the as-received and the 10% CR material tested at $\Delta\varepsilon_t/2=0.5\%$ in air at $\Delta\varepsilon_t/dt=0.4\%/s$ and $0.004\%/s$.

In the case of the 10% CR material, regardless of the loading strain rate, the material exhibits a negligible hardening period and the cyclic stress strain behavior almost exhibits only softening. A reduction of the strain rate from 0.4%/s to 0.004%/s results in an increase of the stress level (20 MPa at 300 cycles). In both strain rates conditions, the dislocation structure in the bulk was characterized, indicating the presence of dislocation pinning in the case of low strain rates conditions (Figure 3).

The negative sensitivity to the strain rate is usually explained by Dynamic Strain Aging (DSA) that modifies the deformation substructure and consequently the macroscopic stress [10]. Actually DSA during cyclic deformation results from the locking of dislocations by substitutional solute atoms (C, N) [11]. This locking results in an increase of the stress level. The observed dislocation pinning observed in low strain rate conditions in the case of the 10% CR material can be a signature of the DSA (Chapter 3).

In contrast, in the same conditions (air environment, 300°C, investigated strain rate range, strain amplitude at $\Delta\varepsilon_t/2=0.5\%$, saw tooth wave form) the as-received material did not present any clear sensitivity to the strain rate (only about 5MPa). In addition, in the current study, no evidence of pinning, symptomatic of DSA, was noticed in the dislocation microstructure of the as-received material deformed at the different strain rates. Yet, in the case of triangle wave forms and in very similar conditions (as-received material, 300°C, same testing apparatus) de Baglion [12] found a negative sensivity to strain rate. This suggests that the sensitivity to DSA might be also controlled by the waveform. Indeed the modification of the stress response related to the wave form was recently confirmed by Poulain [13].

This indicates that applying a high strain rate in the compression part of the cycle limits the effect of DSA on the cyclic strengthening (Figure 4). It can be proposed that during the tension part, the propensity of solute atoms and dislocations to interact is the same between triangles and saw tooth waveforms due to the similar strain rate. However, in compression, the higher strain rate used in saw tooth signals may facilitate the unlocking of dislocations, and as a consequence reduce the stress during the following loading sequence.

The higher sensitivity to DSA related to a pre hardening can basically be explained by the fact that pre hardened materials present a higher dislocation density which is a key parameter in the DSA mechanism. Even if there is no data using triangle waveforms in the case of the 10% CR material, it can be assumed that the stress level would be higher in such a case.

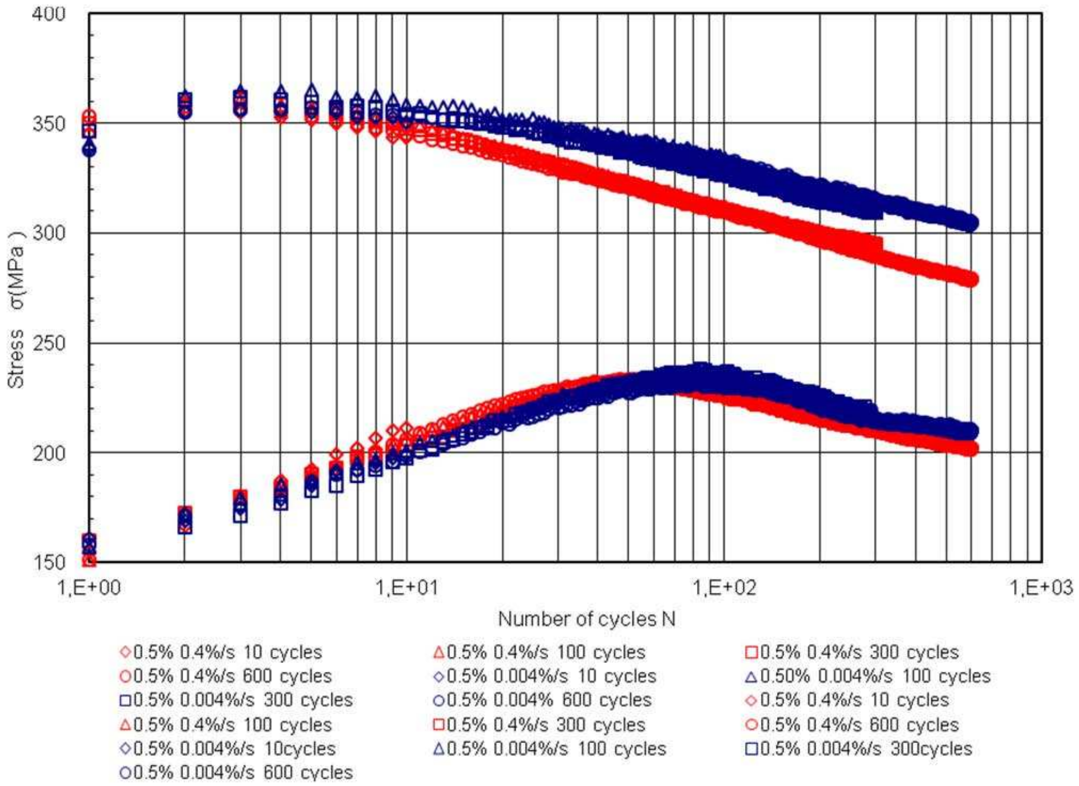

Figure 2 □Evolution of maximum stresses as a function of number of cycles at $\Delta\varepsilon t/2=0.5\%$, $\Delta\varepsilon t/dt=0.4\%/s$ and 0.004%/s, 300°C.

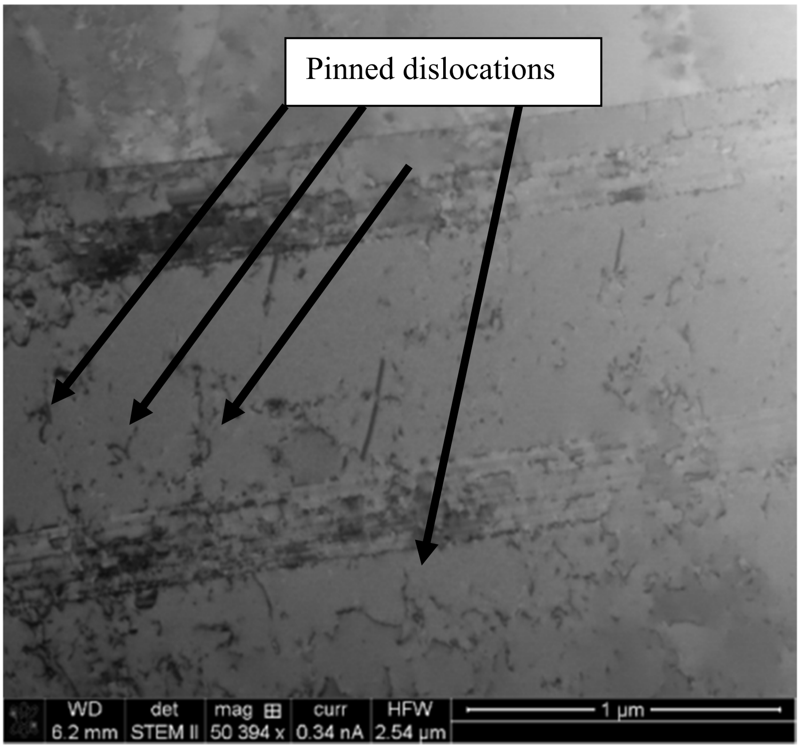

Figure 3 Planar glide composed of unorganized dislocations, stacking fault, alignment, $\Delta\varepsilon t/2=0.5\%$, $\Delta\varepsilon t/dt=0.004\%/s$, 600 cycles, 300°C, the 10% cold rolled material.

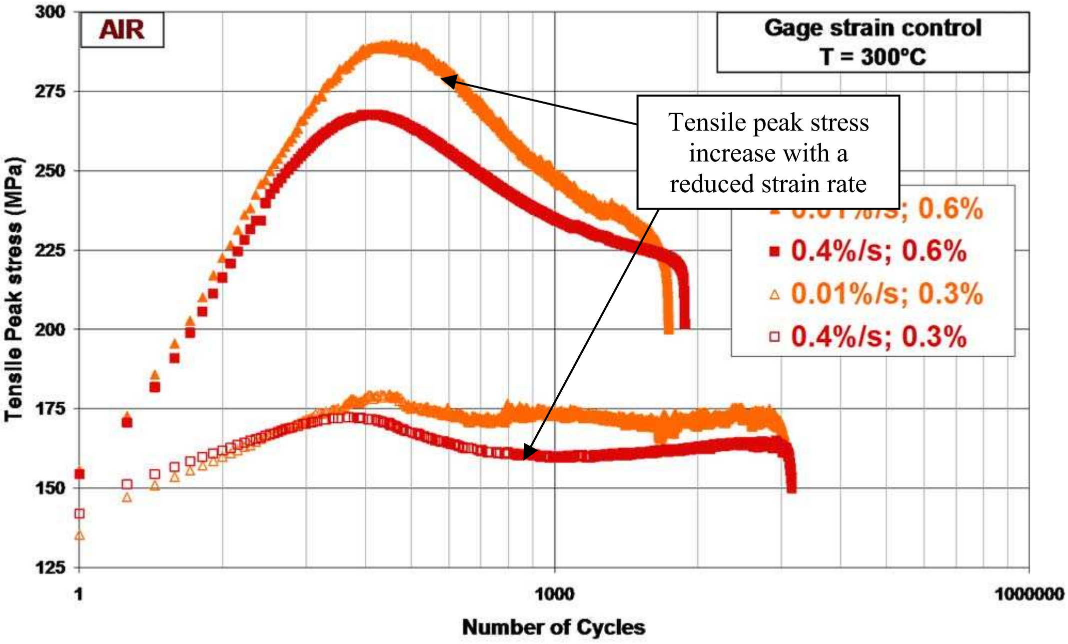

Figure 4 Evolution of peak stresses as a function of number of cycles, Heat XY182, 300°C, triangle wave form [12].

3. Interactions between cyclic loading and environment effects

In contact with an aqueous environment, austenitic stainless steels protect themselves by the formation of a thin and adherent Cr-rich passive film, which prevents the material from corrosion. However, the passive film may be damaged under local stress or strain.

3.1. Effect of the environment

Figure 5 presents a compilation of results on the evolution of the Cr-rich inner layer obtained in the case of various cyclic loadings in air and in PWR primary environment at 300°C. The data comes from measurements on 3D oxide reconstructions and from TEM observations on cross sections. Data obtained in both environments are arbitrarily plotted versus the oxidation time to compare them. This figure reveals that the contribution of the environment on the oxidation process is much higher (two orders of magnitude) in PWR primary environment than in air. Indeed, the Cr-rich layer can reach up to 460 nm in PWR primary water while it remains below 4-5 nm for both the Fe-rich and Cr-rich layer in air (Chapter 3).

The entry of hydrogen is related to the cathodic reaction at the surface of the material and the hydrogen production is a function of the amount of oxidized metal. Therefore, the quantity of cathodic hydrogen generated at the cyclically deformed 304L specimen surface is much higher in the PWR primary environment than in the air environment. This aspect might be a major consequence of the influence of the PWR primary environment that will be discussed in the dedicated section.

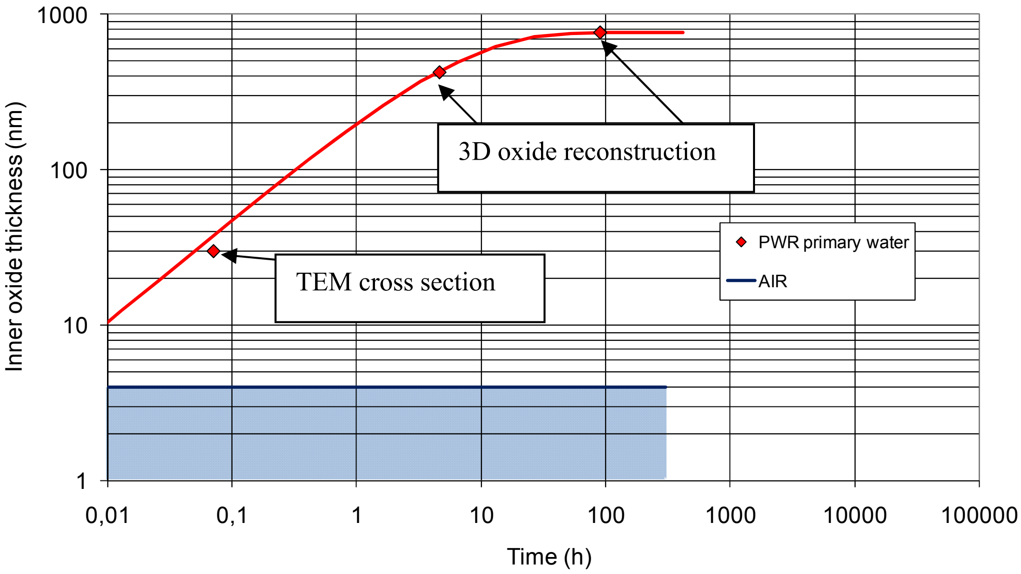

Figure 5 Mean inner Cr-rich oxide penetration against time to exposure to PWR primary water and air at 300°C cyclic loadings. Best fit of Evans-type law in PWR primary environment.

3.2. Effect of cyclic loading

Figure 6 presents the evolution of the mean Cr inner rich layer thickness as a function of time in the case of observations performed at EDF using TEM and SIMS based techniques on 304L, 316L, 304L CW materials [14] mechanically tested under various static loads in PWR environment. In addition to these data, TEM and SEM observations performed in the present study for fatigue tests and reported in Chapter 4 are presented. This figure reveals that cyclic loads drastically increase corrosion kinetics to a factor of 10 to 30 for a given time of exposure to the PWR primary environment. In addition, the time required to form a 30 nm thickness oxide layer is 2000 times lower under cyclic than under static loading.

As discussed in the previous section, the amount of cathodic hydrogen depends on the quantity of oxidized metal. That means that a cyclic loading drastically increases the kinetics of cathodic hydrogen production. In the case of static loading (SCC tests mainly) of stainless steels in PWR primary environment, it has been suggested that the cathodic hydrogen trapped in the material reached up to 20-40 ppm where strain localization occurs [15,16,17]. Nevertheless, its effect on the increase of the SCC crack growth rate remains unclear [18,19].

These observations suggest that the amount of produced hydrogen may be much more important in the case of cyclic loadings.

The enhanced oxidation kinetics under cyclic loading may be due to the increase in diffusion shortcuts at the metal oxide interface. Another potential explanation is given by Soulas et al [20] on a non-strained 316L material in PWR primary environment concerning the oxide structure. According to these authors, during the first minute of the oxidation process, the inner Cr-rich layer oxide is amorphous. The diffusion of Cr and Fe is pretty rapid. From 1min to 10 min and also depending on the crystallographic orientation of the grain with respect to the surface, the layer is not completely crystallized and presents a nano crystalline structure. After 10 minutes, the Cr-inner layer is completely recrystallized and the diffusion process is highly reduced. From these considerations, it is possible to postulate that in the case of a sample tested at $\Delta\varepsilon_t/dt=0.004\%/s$ and $\Delta\varepsilon_t/2=0.5\%$ (corresponding to a period close to 4.2 min) the oxide film at each cycle may not have the time to completely recrystallize and therefore the oxidation process may mainly be governed by diffusion through an amorphous layer.

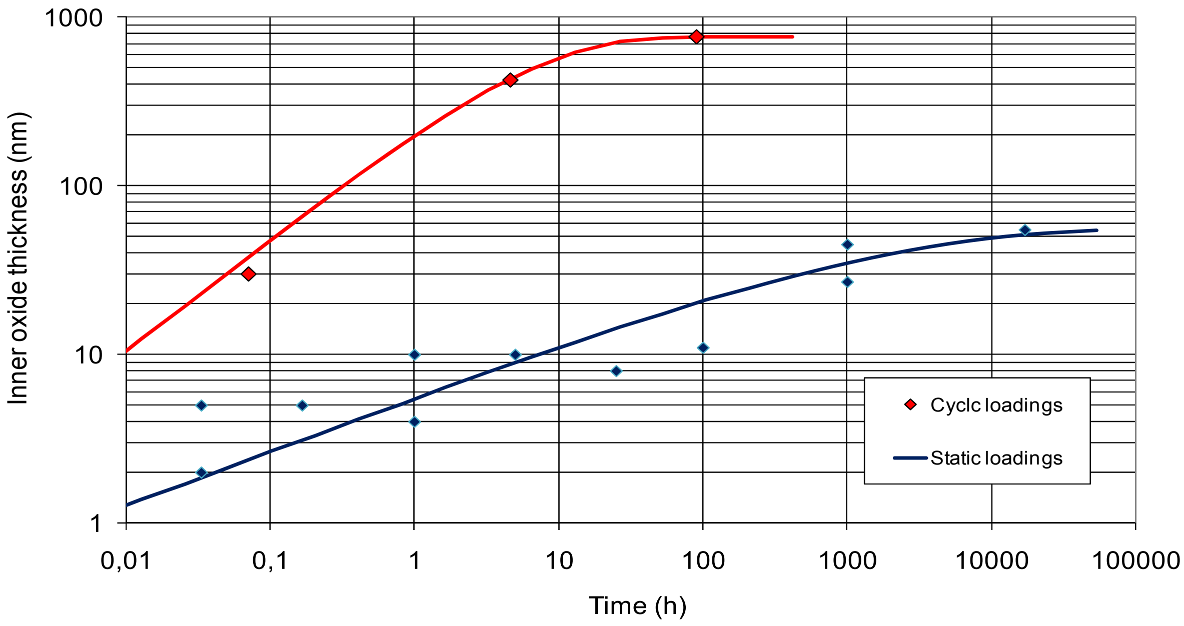

Figure 6 Mean inner Cr-rich oxide penetration against time to exposure to primary water. Austenitic stainless steels (304L and 316L) for various static deformation < 30% and in the case of cyclic loading. Saturating law (Evans-type) (red and blue curve) [21]

4. Interactions between loading, environment and material behavior and damage

Interactions between deformation localization in materials and environment reactions play an important role in cracking processes and therefore in the integrity of LWR components. Thus, a detailed understanding of strain localization during plastic deformation and of the underlying mechanisms is of great importance for the manufacturing and design against fatigue of components exposed to the environment of the primary circuit of PWRs.

This specific section aims in the understanding of Environmental Assisted Cracking EAC mechanisms related to the strain rate and a pre hardening in air and in PWR primary water.

4.1. Cyclic stress strain behavior

Figure 7 presents the evolution of the stress amplitude with the number of cycles under various strain rates in air and in PWR primary environment at strain amplitude of 0.5% on the as-received material using the same type of signals. Data in PWR primary environment include the results of tests conducted to failure in addition to those corresponding to the interrupted tests. Datasets in PWR primary environment come from two different laboratories (MHI and GE). Data in air come from 4 different laboratories (CEAT, EDF, GE, and

ENSMA). All these 22 tests have been carried out on the same material (304L, Heat XY182) using different sample designs but with a total strain amplitude always controlled with extensometers directly fixed on the specimen gage length. All the results obtained in the same loading and environment conditions in the different laboratories are in good agreement.

An effect of the environment on the evolution of the cyclic behavior is noted (Figure 7). The maximum stress peak varies from 230 MPa in air to 255 MPa in PWR primary water at $\Delta\varepsilon t/dt=0.4\%/s$ and from 235 MPa in air to 270 MPa in PWR primary water in the case of $\Delta\varepsilon t/dt=0.004\%/s$.

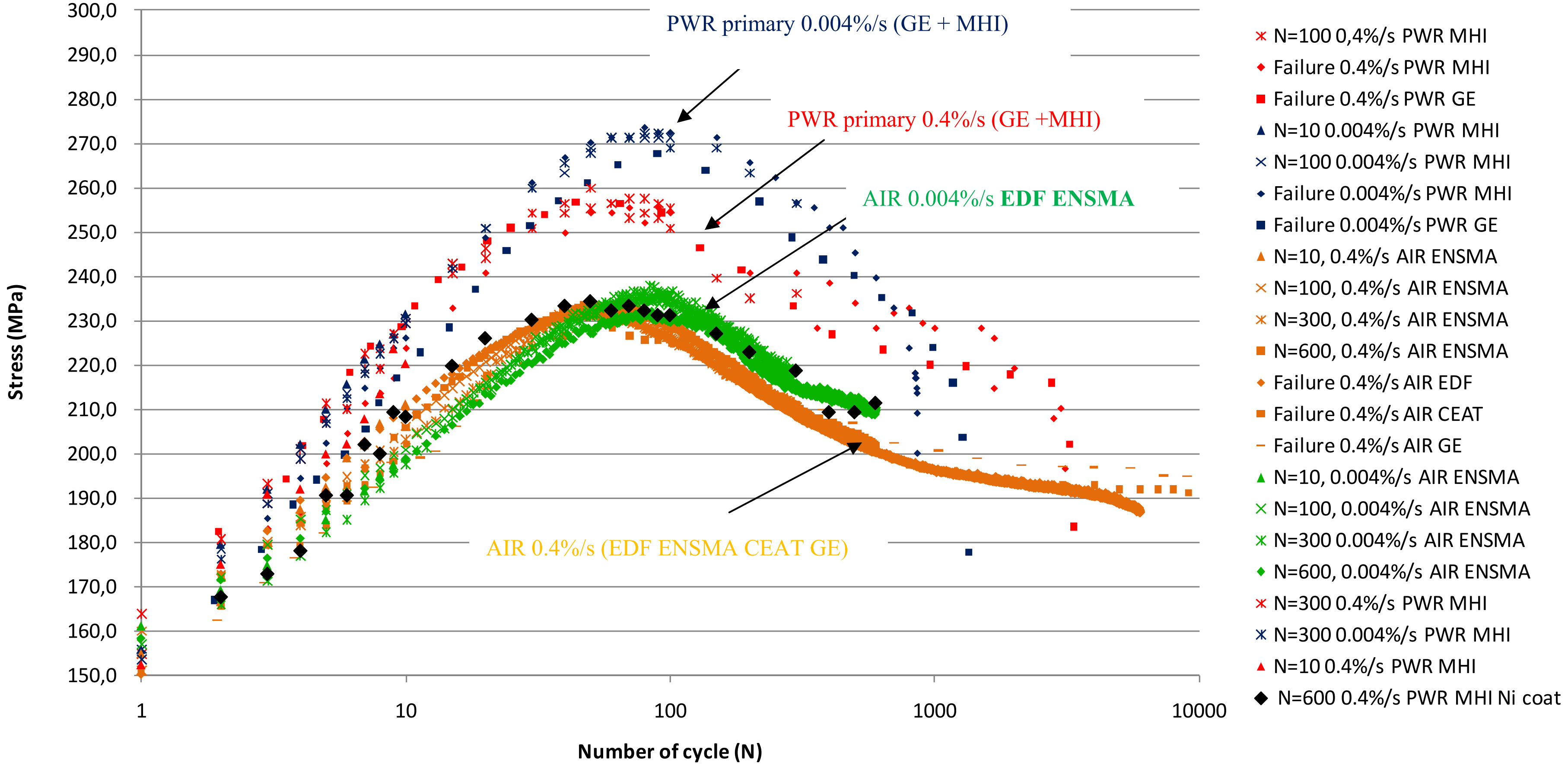

Figure 7 - Evolution of maximum stress as a function of number of cycles, Δεt/2=0.5%, 300°C, as-received material.

However it should be noted that de Baglion [22] did not observe such an effect in very similar conditions ($\Delta\varepsilon_t/2=0.6\%$ and $\Delta\varepsilon_t/2=0.3\%$). Indeed he observed in tests performed at AREVA NP (Le Creusot) the same cyclic stress strain response in both air and PWR environment and also in vacuum. This is illustrated in Figure 8 where scattering in cyclic behavior is particularly low; in other tests a difference in cyclic behavior is observed but in some cases the cyclic curve in air can be above the curve in the PWR primary environment, in other cases it can be situated below. Now, as in our case, in the work of de Baglion, tests in air and in PWR environment are performed using two different equipments and the question of the equivalence of the experimental conditions remains open. To remove the ambiguity on an effect of the PWR primary environment on the macroscopic mechanical behavior under cyclic deformation, it would be essential to lead the fatigue tests in both environments (air/PWR) on the same tests apparatus in order to limit as far as possible the experimental uncertainties, in particular with regard to strain and temperature control.

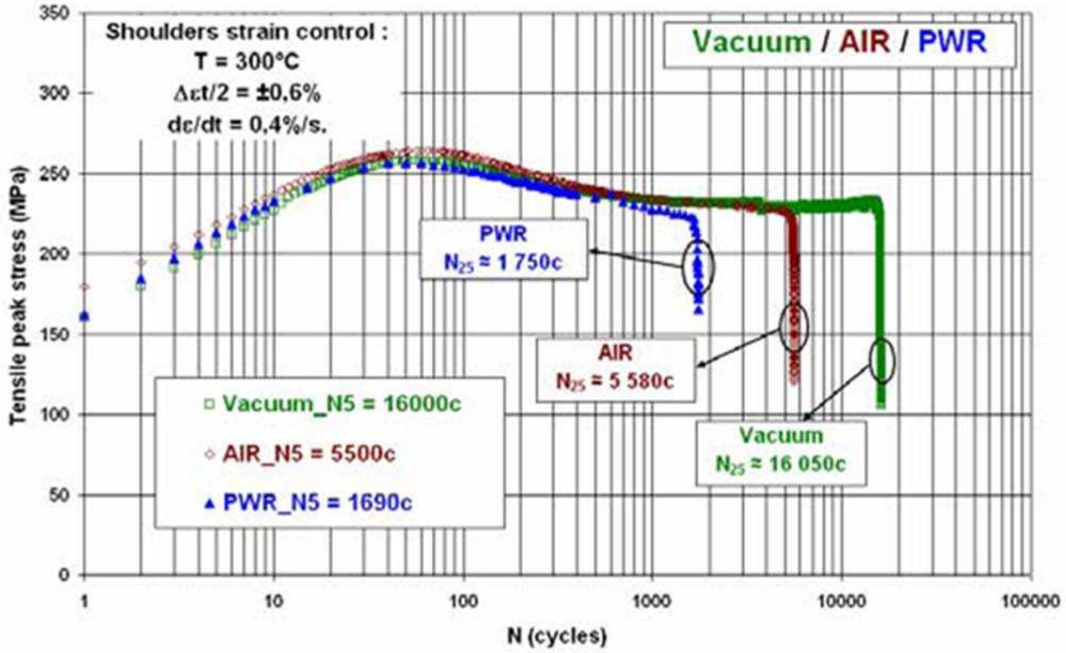

Figure 8 □**Tensile Peak Stress versus cycles for LCF tests conducted at T = 300°C, Δεt/dt = 0,4%/s and Δεt /2 = ±0.6%; Comparison between Vacuum, Air and PWR water [22]**

However, both results from GE and MHI tend to independently confirm the higher hardening in PWR primary environment. We can add that this increase of hardening due to the PWR environment was already observed in the GE dataset for other strain amplitudes at 300°C (Figure **9**). In contrast, it seems that the difference of hardening between the air and the PWR primary water was reduced at 150°C

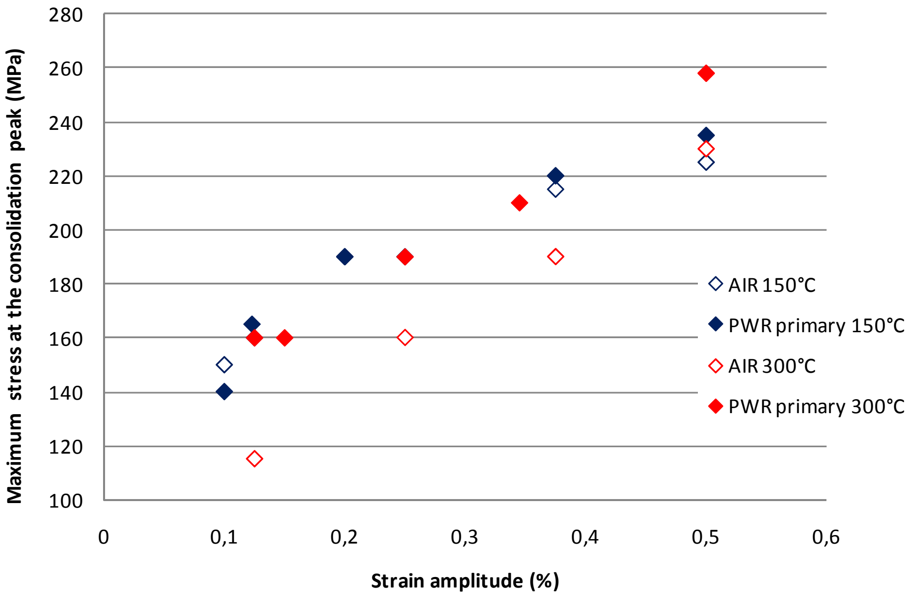

Figure 9 **Evolution of the maximum stress reaches at the consolidation peak for different loading strain amplitude at T = 300°C and 150°C, Δεt/dt, Comparison between air and PWR primary environment**

None of test equipment at MHI facilities did not allow to perform tests in air and in PWR primary water using the same machine, indeed the primary environment is used to heat the sample up to 300°C and without its presence the sample cannot reach this temperature.

In order to clarify this effect, additional test has been designed and carried out at MHI using a Ni-coated sample. The goal of this test was to launch a test in PWR primary environment without any contact between the base metal and the environment. A 500 µm thick adherent Nickel layer was then electrodeposited at the inner surface of one sample in order to avoid any chemical reactions between the PWR primary environment and the base metal. Mechanical properties of the Nickel layer used were the one given by the manufacturer [23]. They are similar to the base metal. To evaluate the cyclic behavior of this composite, the stress is calculated considering the total section including the section of the deposit. However, in the literature, a large variety of mechanical properties are assigned to electrodeposited Ni. In order to evaluate the difference of mechanical properties between the Ni layer and the stainless steel, $HV_{0.5}$ hardness tests were performed at room temperature on both materials (Table 2). Hardness results indicate that the mechanical properties of the Ni layer are higher than the base metal, indicating that our calculation overestimates the real mechanical response of the base metal (supposing that the hardness at 300°C of the Ni layer remains higher than the base metal).

The corresponding result to this test is included in Figure 7 (black diamonds).

Table 1 □Tensile properties.

	T (°C)	Direction	Ys(MPa)	UTS (MPa)	El (%)	E (GPa)
XY182 As-received	300	L	138	401	48	168
		T	136	402	46	196
Nickel 200	300	L	140	450	45	190

Table 2 □Micro hardness properties.

	T (°C)	HV0.5
XY182 As-received	20	155
Nickel 200	20	260

The cyclic stress-strain behavior appears to be similar to the those observed in air under the same strain amplitude and strain rate. Therefore, it tends to support that the environment affects the mechanical response of the material in the PWR primary environment. However, additional experiments must be done to definitively confirm such phenomenon.

Two physical processes, commonly proposed in the literature to account for EAC, can also be considered to explain this hardening, namely vacancies and hydrogen.

- Vacancies are well known to enhance the mobility of dislocations [24]. However, this enhancement may facilitate the rearrangement of dislocations and as a consequence softening. Therefore the difference of hardening cannot be explained by vacancy diffusion.
- The effect of hydrogen in austenitic stainless steels was found to lead to an increase of the yield stress under static and cyclic loadings [25,26,27]. In addition, the presence of hydrogen can play an important role on both static and dynamic strain aging [28]. Indeed, the viscous dragging of Cotrell atmospheres leads to a positive contribution to the yield stress. In other words, the presence of hydrogen tends to pin the dislocations, resulting in an increase of the resolved shear stress needed to accommodate plastic strains.

The hypothesis of the effect of the cathodic hydrogen is in agreement with the fact that results obtained at 150°C at GE do not present any clear difference of hardening between air and PWR primary conditions. Indeed the oxidation process and therefore the production of cathodic hydrogen is reduced at 150°C. In addition, at this specific temperature, the material is less sensitive to DSA [11].

In the PWR primary environment, the reduction of strain rate results in a significant increase of the consolidation peak in contradiction with results obtained in air. As previously discussed, the sensitivity to DSA may be affected by the presence of cathodic hydrogen. In addition, a reduction of the loading strain rate results in an increase in the oxide thickness and therefore an increase of the production of cathodic hydrogen. In the case of low strain rate conditions, the decrease of dislocation velocity combined with a higher concentration of cathodic hydrogen may lead to an increase of the stress level.

In opposition to the as-received material, the 10% rolled material did not present any effect of the PWR primary environment (Figure 10).

In the case of the as-received material, the additional contribution of hydrogen on the stress level may be induced by the dislocation pinning mainly. Pre hardened material presents a higher stress level than the as-received one due to the multiple interactions between dislocations. The presence of hydrogen, pinning dislocation may also occur in this case but it may be hidden by these dislocations-dislocations interactions. In addition some authors mentioned that a prior hardening decreases the effect of hydrogen on the mechanical behavior in tension [29],[30].

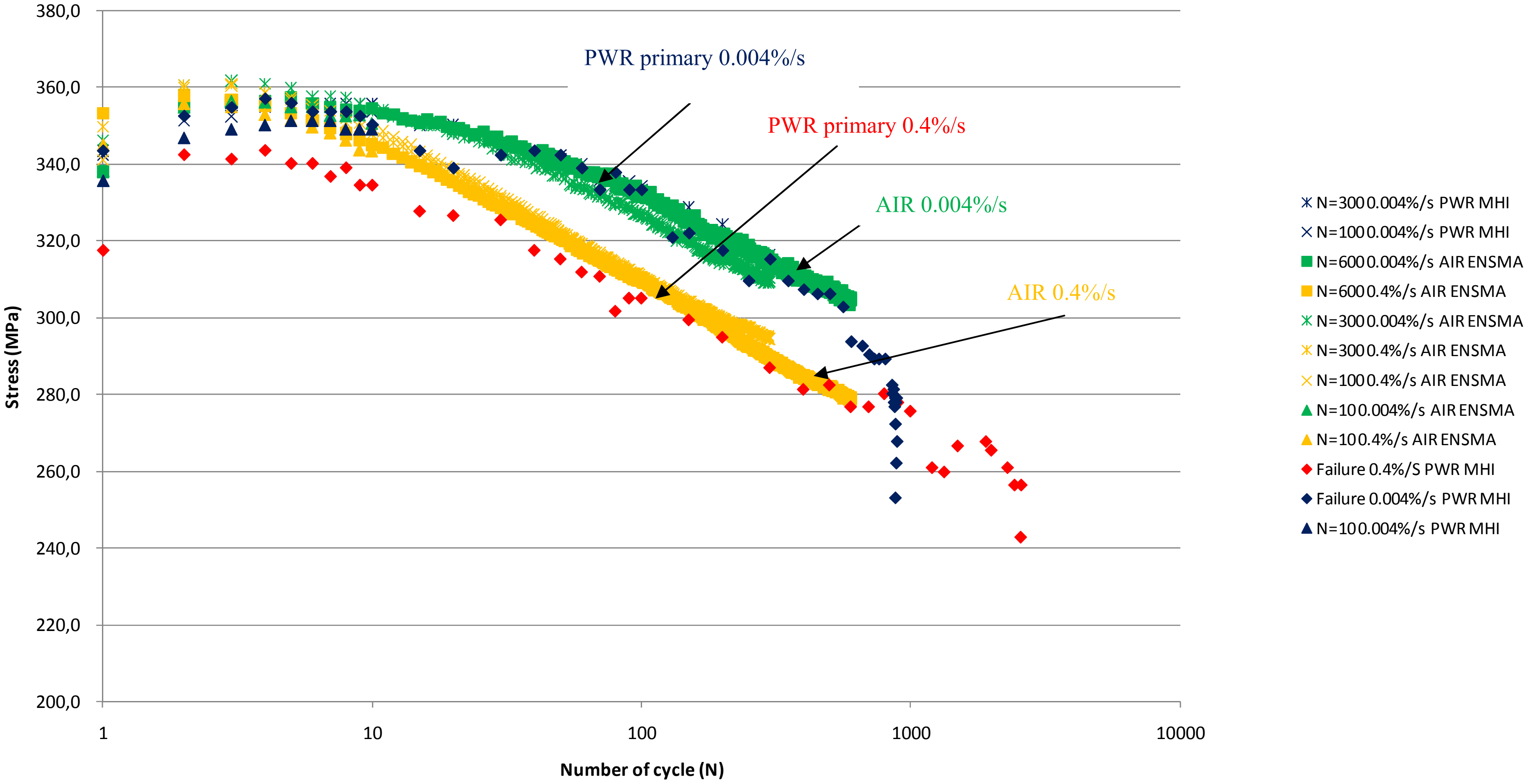

Figure 10 - Evolution of maximum stress as a function of number of cycles, Δεt/2=0.5%, 300°C, 10% rolled material.

4.2. Evaluation of the fatigue damage

4.2.1. Fatigue life

Fatigue ε-N and ε_p-N results obtained for all tests conditions are presented in Figure 11 and Figure 12 respectively. Results are compared to the Nureg 6909.

4.2.1.1. Effect of pre hardening

In the air environment, a prior strain hardening within a 0-10% cold work degree range leads to a reduction of fatigue life (up to a maximum of 50%) within a range of total strain amplitude of 0.2%-0.5%. A similar reduction of fatigue life in the LCF region induced by a prior hardening has been observed by Raman et al. and Taheri et al. [31,32]. Their conclusion was also that a pre hardening increases the internal stresses, for a given strain amplitude. Such an increase of stress level leads to an increase of the total energy leading per cycle to a higher damage. However, we have shown that, for strain amplitudes lower than ≈0.2%, the fatigue life in air of the cold worked material is longer and leads to an increase of the fatigue limit at 10^6 cycles, from 0.1% for the as-received 304L to at least 0.15% in the case of the 10% CR 304L.

In air environment and in the LCF, pre hardened materials fatigue tests present good agreements with the Nureg 6909 while the as-received material exhibits a longer fatigue life. In the HCF range our pre hardened materials exhibit a longer fatigue life than predicted by the Nureg 6909 while the as-received material presents a shorter one. Such codifications considerations are described in Appendix 2.

At 10^6 cycles, the increase in fatigue life induced by pre-hardening that has been observed is in good agreement with the literature in the case of low alloy steels [33,34] and stainless steels [31]. In these studies, the pre hardening was obtained by straining the base material prior to sample manufacturing, in order to have completely similar samples for all tests. In contrast, Taheri found that a pre hardening results in a fatigue life reduction in the high cycle fatigue regime [32]. However, in Taheri study, the pre hardening was obtained by a prior tension (12%) of the sample, directly followed by a fatigue test keeping the surface roughness induced by the pre hardening. It is commonly assumed that a modification of surface roughness can have some strong deleterious effect on fatigue life, especially in the HCF region [35].

In simulated PWR primary environment (Figure 11), fatigue lives of the cold-worked material are almost the same as those on the as-received one at strain amplitude above 0.2%. These results indicate that the loss of ductility and the increase of stress level induced by a prior cold working does not affect the fatigue life in PWR primary environment. The fatigue limit at 10^6 cycles clearly increased up to a strain amplitude of 0.15%.

In both environment it seems that the fatigue limit is reached independently of the pre hardening level, when considering a critical $\Delta\varepsilon_p/2<0.03\%$ (Figure 12).

In PWR primary environment, the plastic strain amplitude measured at mid life seems to be a good parameter to predict fatigue life (Figure 12). Indeed, even if the material has been pre hardened and therefore present a higher stress level during cycling in addition to a different microstructural evolution, the fatigue life remains the same for a given plastic strain amplitude.

These results suggests that the fatigue damage process induced by cold work, should involve additional contributions in primary water and that energetically models, based on the contribution of the stress level and the plastic strain, may not be relevant in primary water. Indeed, application of that kind of model is partly based on the deleterious effect of a high total stress level during cycling. However, the use of energetically based models in air environment cannot be excluded and and it would be valuable to examine the relevancy of such models in this environment.

In the LCF, all results present a good agreement with the Nureg 6909 while the fatigue lives in the HCF are lower than predicted by the Nureg 6909.

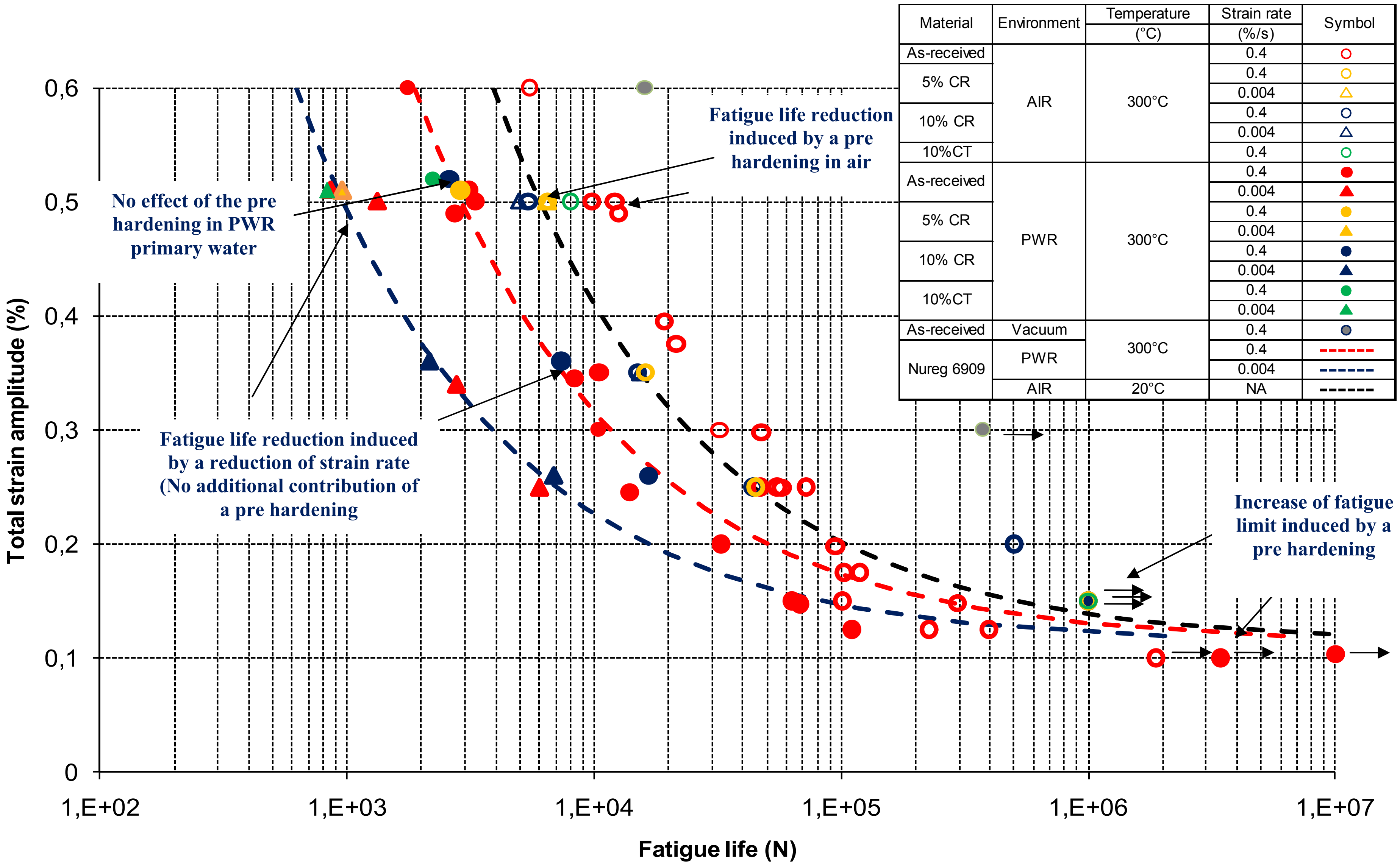

Figure 11 - Total amplitude vs. fatigue life data for XY182 at 300°C in simulated PWR water.

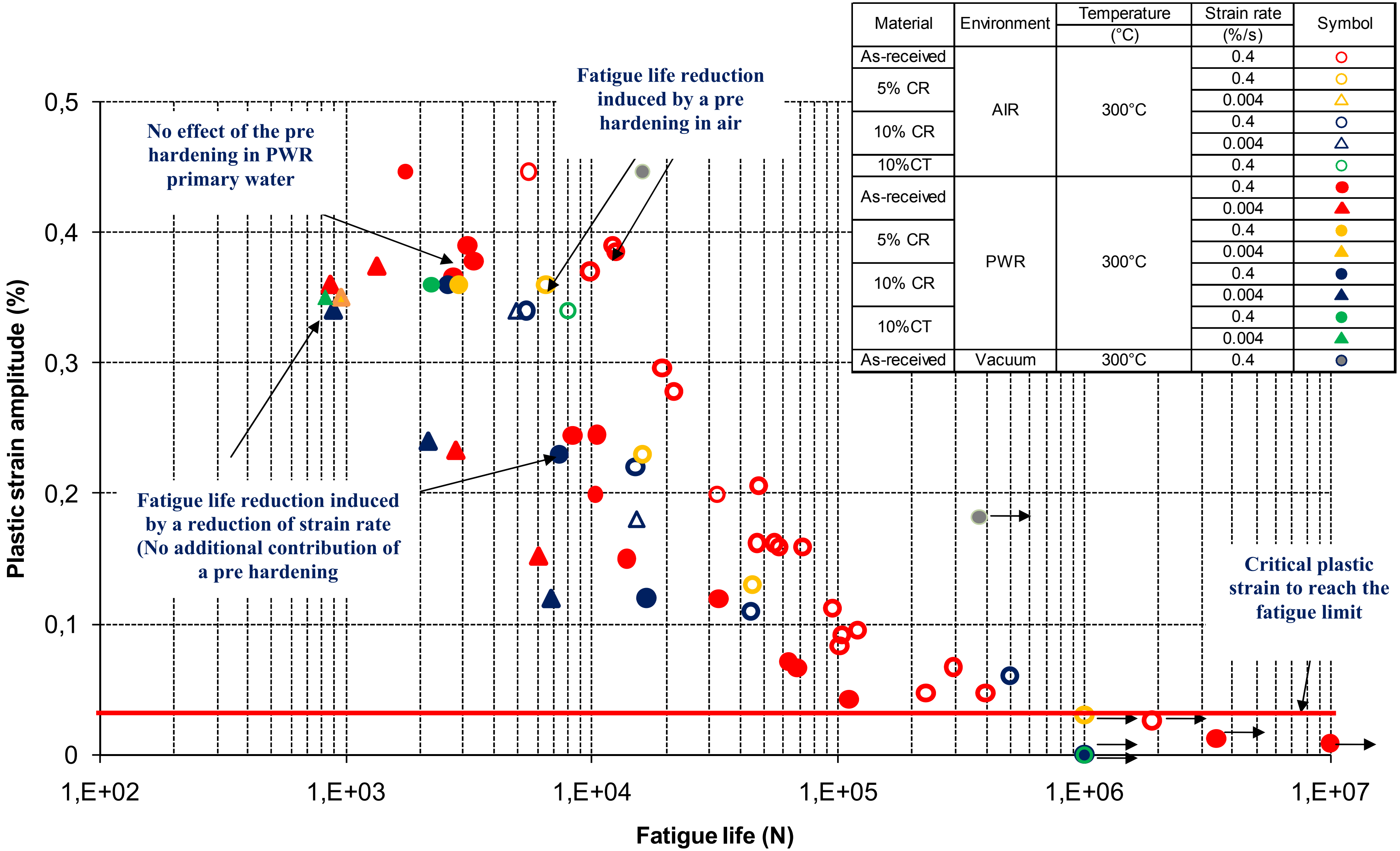

Figure 12 - Plastic amplitude vs. fatigue life data for XY182 at 300°C in simulated PWR water

4.2.1.2. Effect of strain rate

In the air environment, no clear modification of fatigue life was observed related to the loading strain rate. In PWR primary environment, typical fatigue life reduction was attributed to the reduction of the strain rate. As for the cold working effect on fatigue life in simulated PWR primary water at strain rates of 0.4%/s and 0.004%/s, Figure 11 shows that pre hardened materials exhibit the same sensitivity to the loading strain rate than the as-received materials. A pre hardening does not additionally contribute even if the stress level developed during cycling is higher in this condition.

4.2.2. Crack initiation mechanisms

TEM observations reveal several differences between crack initiation mechanisms in air and in PWR primary environment.

4.2.2.1. Effect of the environment

Initiation in air environment is related to the modification of the surface roughness induced by the emergence of 3D dislocation structure at the surface of the first grains (Figure 13). TG cracks mostly initiate on the most activated slip system, i.e. exhibiting the largest Schmid factor (Chapter 3) (Figure 15). Such crack initiation mechanism is commonly encountered in the case of FCC materials [36,37]. Even if it was possible to observe some oxidation in the air environment, it does not affect the underlying microstructure.

In PWR primary water, cracks initiate at the metal oxide interface. Preferential oxidation occurs by local and successive growth and rupture of the passive Cr-rich film induced firstly by dissociated dislocations evolving into micro twins (Figure 14). Using EBSD analysis at the surface of polished fatigue samples, de Baglion [38] has shown that crack initiation (in air or PWR primary water) is mainly transgranular (>80%) and occurs on grains presenting high Schmid factors (>0.41), i.e. experiencing active plasticity under simple glide. In PWR primary environment, after a short initiation stage along [111] planes (2-3μm in depth), the cracks directly follow a 90° orientation to the loading axis, in good agreement with observations reported in the NUREG 6787 (Figure 16).

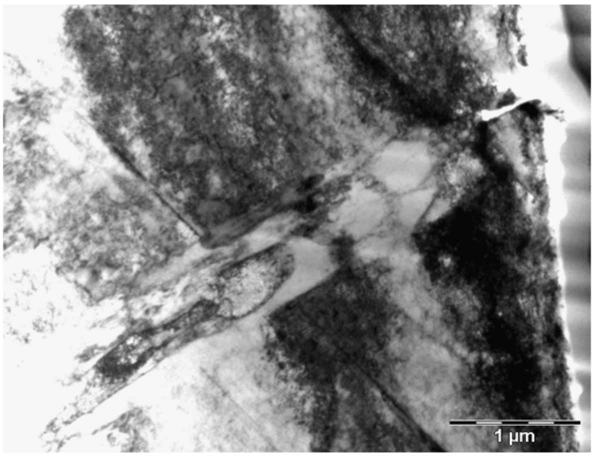

Figure 13 TEM (2 beams conditions) as-received $\Delta\varepsilon_t/2=0.5\%$, $\Delta\varepsilon_t/dt=0.4\%/s$, 300°C, 100 cycles, air.

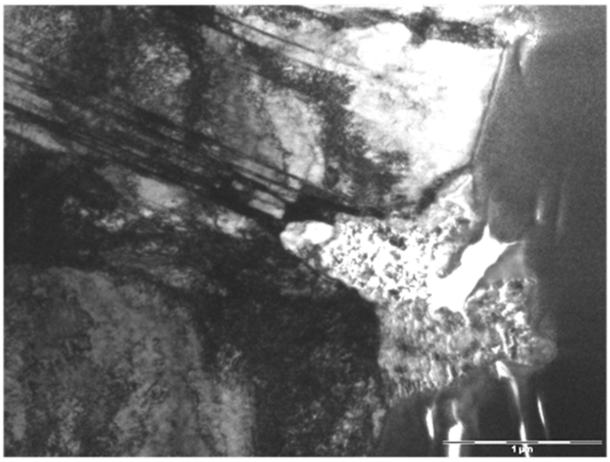

Figure 14 Focus of crack initiation area as-received, $\Delta\varepsilon_t/2=0.5\%$, $\Delta\varepsilon_t/dt=0.4\%/s$ 300°C, TEM BF, PWR primary water.

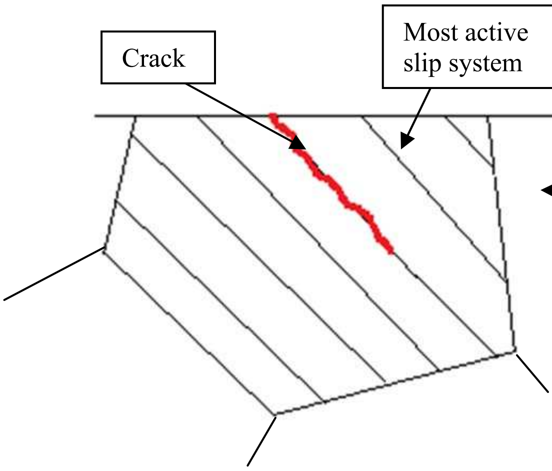

Figure 15 Crack initiation along emerging shear bands in air environment.

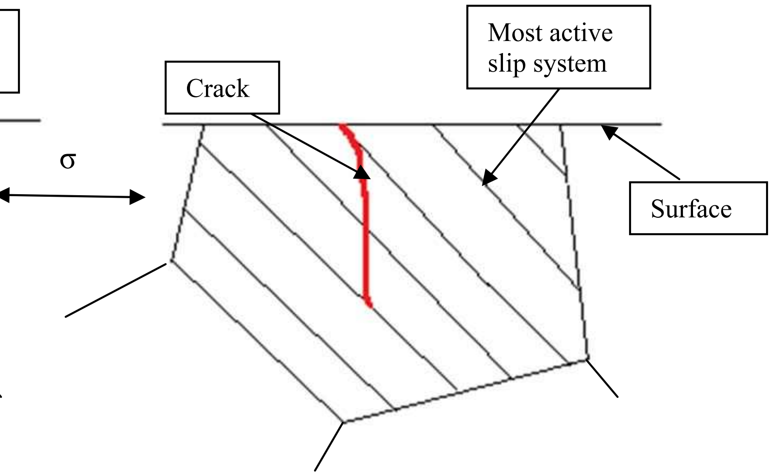

Figure 16 Crack initiation along emerging shear bands and early transitioning at 90° from the surface in PWR primary environment.

Concerning the evolution of the crack length, even though some scattering can be observed on a given sample, the general evolution of the crack length (Figure 17) suggests that early cracks initiated between 10 cycles and 100 cycles in both air and PWR primary environment. Figure 17 also shows that, in high strain rate conditions, cracking kinetics within the 10-300 cycles range are similar (below 10 µm at 300 cycles) between air and PWR primary environment. At 300 cycles and at a lower strain rate in the PWR primary environment, the maximum crack depth increases up to 55-60 µm, while in air it reaches only a few micron even at low strain rate which is in good agreement with the fatigue life reduction induced by a lower strain rate in PWR primary environment.

Regarding the cold work level, no difference was observed suggesting that cracking kinetics within the 10-300 cycle range are similar.

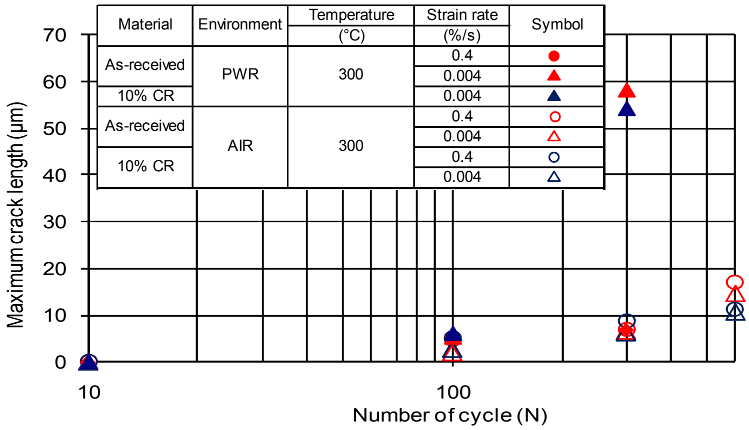

Figure 17 □Evolution of maximum crack length as a function of number of cycles in air and PWR primary environment.

In addition to the earliest transition from stage I to stage II in the crack path, the environment is also responsible for a modification of the deformation mechanisms within the first grain at the vicinity of the specimen surface.

In PWR primary environment, the strain is first accommodate by a dense structure of stacking faults at 10 cycles evolving into micro twins at 100 cycles.

It can be argued that the potential presence of hydrogen induced by cathodic discharge may locally modify the straining mechanisms of the material by a reduction of the stacking fault energy [39,40,41,42]. Fatigue crack initiation observations reveal a constant and high density of stacking faults at the oxidation localization tip (Chapter 4). This is consistent with the fact that, in FCC alloys, the presence of hydrogen was found to reduce the probability to activate deviated slip and to increase the probability of dislocation dissociation and therefore the density of stacking faults [43,28,44]. The increase of stacking fault density in PWR primary environment may be due to the presence of hydrogen induced by cathodic discharge resulting from the oxidation process.

In the PWR primary environment, the stacking fault structure present at 10 cycles evolves into micro twinning at 100 cycles. Such micro twinning generation was reported by Cottrel et al. [45] and confirmed by Venables [46], in the case of sufficiently low stacking fault energy materials. The assumed mechanism is the continuous growth of both a Shockley and a Franck partials resulting from an initial dissociated dislocation. Indeed, under an applied stress, the relative and successive movement of the two types of partial dislocarions leads to the generation of a twin [46,47]. In other words, a twin may be defined as a stack of stacking faults. The generation of micro twins by stacking faults can be facilitated when the SFE is low (due to the increase of dislocation dissociation probability). Low SFE materials such as Fe-Mn-C alloys or low SFE stainless steels mainly accommodate deformation by mechanical twinning [48,49].

4.2.2.2. Effect of strain rate

Modifying strain rate, cold work and its associated strain path may affect EAC mechanism. Ranaivoarisoa [50] has conducted several observations on the fracture surface of austenitic stainless steels samples after corrosion fatigue tests in boiling $MgCl_2$ environment. The author found that, in the case of very low frequencies ($6.5.10^{-5}$ Hz), it is possible to observe a transition from TG to IG, similar to that observed in SCC.

As for the effect of strain rate in PWR environment, the results of the present study indicate several points:

- Lowering strain rate induces a low linear crack density (LCD) of sharp cracks in opposition to high strain rate that tends to increase the LCD with branched cracks.
- Strain localization also depends on the strain rate. Indeed, a low strain rate induces a deeper oxide penetration than at a high strain rate. In addition, the distance between oxidized shear bands tends to increase at a low strain rate.

The observations are summarized in Figure 18.

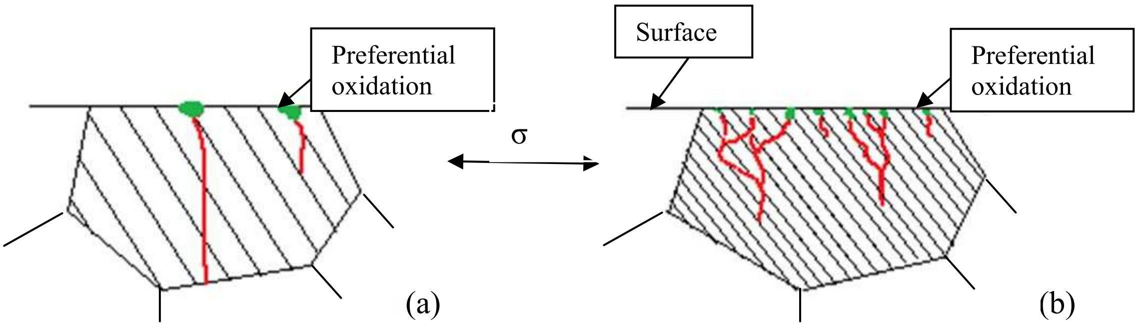

Figure 18 Difference of cracking morphology in PWR primary environment as a function of strain rate. (a) Low strain rate (b) High strain rate.

A possible explanation for the strain rate effect is the following.

- First, during low strain rate tests, oxide has much more time to grow along emerging shear bands, reducing the number of cycles needed to obtain a strain localization reaching a critical configuration to initiate a crack.
- Secondly, the distance between shear bands, is higher at low strain rates, higlighting an enhancement of strain localization at low strain rate in these conditions.

Both factors tend to favor the crack nucleation in the case of low strain rates leading to a low crack density.

4.2.2.3. Effect of a pre hardening

Couvant [51] mentioned that in, PWR primary environment, monotonic strain paths lead to pure TGSCC, while complex strain paths (reverse and cross-directional) favor IGSCC due to the enhancement of stress concentration at grain boundaries. However, in the present case of EAF, no difference in crack initiation mechanisms induced by the difference of pre hardening (pre tensioned or pre rolled), was observed and most of the cracks observed were TG. Cyclic deformation induces a sufficient reorganization of dislocations to limit the presence of strain incompatibilities at grain boundaries.

4.2.3. Crack propagation mechanisms

De Baglion [38] mentioned that the evaluation of crack growth rate in the air environment using fatigue striations leads to an overestimation of the crack growth kinetics. Therefore, in this work none of such characterizations were done on specimens tested in the air environment. In this study it is confirmed that the evaluation of crack growth rate in PWR primary environment using fatigue striation gives a good estimation of fatigue life (Chapter 4).

4.2.3.1. Effect of cold work

A prior hardening results on the creation of a hard structure that is not erased during cycling even if some rearrangements are observed. In air environment, this structure was found to affect the propagation behavior (Chapter 3). At the opposite, in PWR primary environment such hard structure is completely ignored by the main crack since no differences in crack growth rates (measured using striations) and crack morphology were found in pre hardened or in as-received material (chapter 4). In addition, the fatigue life is governed by

Δεp/2. As crack initiation occurs very early in the fatigue life, this would imply that the crack growth rate is also mainly controlled by Δεp/2 and not by a ΔJ type parameter dependent to the stress amplitude

4.2.3.2. Strain rate effect in PWR primary environment

The loading strain rate was found to highly affect the propagation behavior in PWR primary environment. Indeed low strain rates induce higher crack growth rates. Additionally the microstructure below the fracture surface revealed the presence of shear bands at each fatigue striation. This structure is generated by the crack and it was never been observed in the bulk (Chapter 3). Takahashi et al. [52] found the same relationship between shear bands and fatigue striations in the case of BCC iron alloys and confirmed that the shear bands are emitted from the fatigue crack tip.

The presence of shear bands observed below fracture surface allows drawing possible micro propagations schematics for a given signal (Figure 19):

- At a high strain rate (Figure 20 - a), the crack propagates in a single step during each cycle. Each crack arrest corresponds to the generation of a shear band.
- In the case of low strain rates (Figure 20 - b), it was possible to observe some additional sub-striations and corresponding underlying shear bands within an intense striation. This observation suggests that, during one cycle, the main crack propagates discontinuously and at each crack arrest, it generates another shear band.

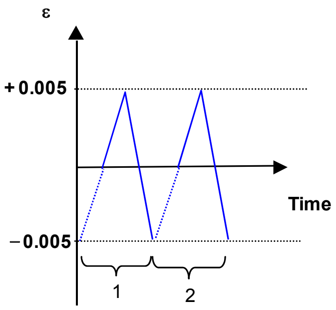

Figure 19 Reference signal

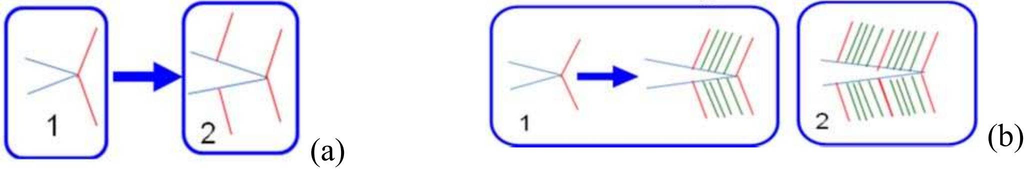

Figure 20 Difference of propagation mechanisms. (a) High strain rate (b) Low strain rate (red: shear bands generated at the end of a load cycle, green: shear band generated during the load cycle, blue: crack).

Similar observations performed in air tested specimens would have been necessary in order to determine the specific role of the environment in the deformation features at the crack tip.

4.2.3.3. Modeling of the strain rate effect on propagation mechanisms in PWR primary water

The influence of the PWR primary environment on crack initiation and propagation stages has been analyzed. Several model and theories modeling the EAC were reviewed in the chapter 1. In the next section, the ability of different EAF models to account for the observed phenomena is thus discussed.

4.2.3.3.1. Slip dissolution

Quantitatively speaking, the slip dissolution model developed by Ford [53] [54] [55] can be hardly directly applied to the results represented here. Indeed, one of the main parameter of this model, i.e. the charge density factor Qf, is highly related and affected by the corrosion kinetics. In the case of static conditions, the evaluation of this parameter is highly time-consuming and constitutes a delicate task [56]. Furthermore, in the case of cyclic loadings, the corrosion kinetics are highly affected by the loading and the evaluation of a relevant Qf might be even more difficult because the microstructure evolve during cycling. In addition, the expression of the crack tip strain rate proposed by Shoji [57] is expressed as a function of a K in the elastic plastic conditions whereas in our study it occurs in generalized plasticity conditions.

In the early stage of the fatigue life, the results presented in chapter 4 highlighted that the crack expansion occurs due to regular and continuous shear and passivation of the material, without any preferential diffusion of oxygen, chromium and iron into these shear bands. The Ford mechanism seems to be relevant but its expression appears to be hard to apply.

4.2.3.3.2. Film induced cleavage

The film induce cleavage model [58] is similar to the slip dissolution model but it also considers a potential brittle fracture ahead of the crack tip. Since no clear evidence of such brittle fracture was found during the present investigations. This model is not relevant in our case.

4.2.3.3.3. Surface mobility mechanism

The surface mobility mechanism [59] postulates the presence and the coalescence of vacancies at the crack tip. The model is expressed as a function of a tensile stress reducing the free energy for the formation of vacancies. It would imply a difference of environment deformation interaction for as-received and pre hardened material with a vacancy generation rate higher for pre hardened materials. In our study and at a strain amplitude of 0.5%, we did not observe any clear difference of fatigue life (crack initiation and crack propagation) induced by a prior cold working despite of the higher tensile stress which should enhance vacancy generation

4.2.3.3.4. Internal oxidation

The internal oxidation model proposed by Scott [60] in the case of IGSCC is based on the embrittling action of oxygen at grain boundaries by preferential diffusion was observed. In the case of our TG cracks, no preferential diffusion was observed ahead of the crack tip.

4.2.3.3.5. Hydrogen enhanced decohesion

This theory proposed by Oriani [61] is related to the diffusion of mono atomic hydrogen on the crystal lattice at the crack tip assuming that the hydrogen reduces the energy required for the separation of two atomic planes increasing the brittleness of the material. Even if in our study no brittle fracture was observed on fracture surfaces a weakening of atomic bonds by hydrogen increasing crack growth rate cannot be excluded.

4.2.3.3.6. Hydrogen adsorption induces dislocation emission

This theory proposed by Lynch [62] relies on the presence of micro cavities at intersection of shear bands at the crack tip due to hydrogen precipitation. This precipitation results in the micro cavities coalescence contributing to the crack extension. The only way to confirm this model is to observe the crack front of a propagating crack in order to observe the presence or not of micro cavities. None of our results can confirm nor negate this model. One solution to evaluate the potential presence of hydrogen would have been to make some hydrogen content characterizations at the crack tip as those performed Lagoutharis [63] using nanoSIMS.

4.2.3.3.7. Corrosion enhanced plasticity model

This model proposed by Magnin [64] considers this effect of localized anodic dissolution of the material at the crack tip generating hydrogen and vacancies. The diffusion zone near the crack tip is then softens, while a hardened zone is created further away. Hydrogen lowers the decohesion energy on the {111} planes and the crack propagate on the soften zone. This process is expected to present a zigzag aspect involving the {111} planes.

In our study the crack propagation does not present any zigzag planes. In addition the crack does not propagate along crystallographic orientation. None of our results can support the CEPM.

4.2.3.3.8. Hydrogen enhanced localized plasticity.

This model [65,66,67] is based on potential hydrogen enrichment at crack tip. The presence of hydrogen promotes the emission and the motion of dislocations. The plasticity increase ahead of the crack tip is followed by an extremely localized brittle fracture. Indeed a succession of very localized brittle fracture may have the same aspect than a ductile fracture.

4.2.3.3.9. Conclusion on the modeling of EAF

Most of the existing models present some strong incompatibilities with our observations. The most relevant models with regards to the EAF mechanisms may be the slip dissolution model proposed by Ford and the hydrogen adsorption induced dislocation emission by Lynch. Concerning the slip dissolution it cannot be applied directly without any complex tests to identify relevant parameters for the faraday law. In addition several attempts of applying the slip dissolution model to EAC in PWR primary environment of stainless steels and Ni base alloy did not succeed [68,69]. In order to verify the applicability of the Lynch, HELP and Oriani models it is needed to observe the microstructure ahead of the crack tip and our observations at on the fracture surface are not sufficient. The potential presence of hydrogen may be observed by SIMS based techniques.

5. Conclusion

The main objectives of the current study were the following:

- To quantify the possible effect of a prior hardening and the strain rate on the fatigue life in air and PWR primary water.
- To progress in the understanding of the mechanisms on environmental fatigue in PWR primary environment.

After testing on as-received and cold worked 304L stainless steel in air and in PWR primary environment, the following conclusions were drawn:

Codification objective:

- ✓ A prior hardening does not modify the fatigue life in The PWR environment in the LCF range when it reduces the fatigue life in air. However, the fatigue limit defined at 10^6 cycles of the hardened material was increased up to at least 0.15% compared to 0.112% in as-received stainless steel. These aspects with regard to the codification challenges will be detailed in Appendix 2.
- ✓ The plastic strain amplitude is the main factor governing fatigue life in PWR primary environment, but is not sufficient to predict fatigue life in the air.
- ✓ A reduction of the fatigue life induced by a decrease of the strain rate was confirmed. No additional contribution of a pre hardening was noticed in the LCF region for pre hardened material.

EAF Mechanisms:

Cyclic stress-strain behavior

- ✓ An increase of the hardening peak was observed in the PWR primary environment. This hardening was discussed in terms of potential hardening induced by hydrogen produced by cathodic reactions at the surface. This behavior needs to be experimentally confirmed by conducting additional critical experiments in particular using a unique test machine that can have the capacity to perform experiments in air and in PWR primary environment to minimize experimental uncertainties.

- ✓ A small increase of the hardening peak induced by DSA was found in air environment when considering low strain rates saw tooth signals. In the PWR primary environment, a higher hardening peak was related to a reduction of strain rate. These results have been discussed through a potential hydrogen effect on DSA in addition to commonly considered solute atoms (C, N).
- ✓ A prior strain hardening results in an important increase of stress level developed during cycling. Furthermore, the loading strain rate affects the cyclic stress-strain behavior. The presence of an additional increasing hardening peak due to the environment was not found as in the case of the pre hardened material. These aspects were discussed through the respective role of DSA and would imply a reduction of hydrogen effects on pre hardened materials.

There is a strong need to evaluate the difference of bulk deformation structure the between the air and the PWR primary environments. Indeed, if the hydrogen resulting from the corrosion affects the bulk deformation, it would be possible to observe some modifications of the microstructure such as an increase in the planar slip, an increase of the stacking fault density, the formation of micro twins, and the presence of martensite.

EAC mechanisms

- ✓ Cyclic loadings highly enhance the corrosion kinetics compared to static loadings (factor of 30). Such modification of corrosion behavior may be related to the presence of diffusion shortcuts.
- ✓ In agreement with the literature, crack initiation in the air environment was found to be related to the evolution of dislocation structures near the surface. These structures modify the surface roughness and this modification results in the crack initiation. After initiation, a crack in air environment follows the most activated slip system.
- ✓ In the PWR primary environment, crack initiation presents several differences with the air environment. During the first cycles, preferential oxidation occurs along

emerging dissociated dislocation and each cycle generates a new C-rich/Fe-rich oxide layer. Then, the microstructure evolves from stacking fault into micro twinning and preferential oxidation occurs by continuous shearing and dissolution of the passive film. After a crack deeper than (<3 µm), the crack starts to propagate along crystallographic planes close to a 90° angle from the surface. The crack continues its propagation by the generation of shear bands and fatigue striations at each cycle up to failure.

- ✓ The difference of straining mechanisms of the first grain was attributed to the potential action of hydrogen on the stacking fault energy that tends to reduce cross slip and to increase the probability dislocation dissociation generating stacking faults. The presence of micro twins in PWR primary environment was discussed on the basis of a potential action of hydrogen on the stacking fault energy.
- ✓ The most relevant models to be applied to the EAF mechanisms may be the slip-dissolution model proposed by Ford, the hydrogen-adsorption induced dislocation emission proposed by Lynch, the HELP and Oriani model mechanism. However, no direct experimental evidence was found to support most of the models available in the literature. Moreover none of them can be directly applied to ^predict fatigue life in PWR environment.

First of all, most of the results on the PWR environmental effect are based on a potential effect of hydrogen on the microstructural evolution during cycling. This hydrogen results from the cathodic reactions at the surface of the material especially where the strain is localized. The impressive difference of corrosion kinetics related to cyclic loadings can directly have an effect on the production of cathodic hydrogen. The study of the nature and the structure of the oxide film can be a relevant way to explain this production. The potential presence of hydrogen have to be confirmed by SIMS based techniques characterizations.

Concerning the crack propagation mechanisms in PWR primary environment the loading strain rate clearly modifies the propagation mechanism but none of our results can bring a clear physical explanation. Most of the relevant mechanisms models are related to crack tip interactions between the environment and the cyclic loading. Therefore further experiments consisting in crack tip observations of the microstructure may be valuable to confirm a potential mechanism and the applicability of these models.

---

[1] **J. KUNIYA, I. MASAOKA, R. SSAKI**. □Effect of cold work on the stress corrosion cracking of nonsensitized AISI 304 stainless steel in high-temperature oxygenated water□,Corrosion, 1998.

[2] **P. ANDRESEN** □Effects of yield strength, corrosion potential, stress intensity factor, silicon and grain boundary character on the SCC of stainless steels□, 11th International Conference Environmental Degradation of Materials in Nuclear Systems, 2003.

[3] **F. VAILLANT et al**., "Stress Corrosion Cracking Propagation of Cold□worked Austenitic Stainless Steels in PWR Environment," 14th Int. Conf. on Environmental Degradation of Materials in Nuclear Power Systems, 2009.

[4] **J.COLIN, A.FATEMI, S.TAHERI,** □Fatigue Behavior of Stainless Steel 304L Including Strain Hardening, Prestraining, and Mean Stress Effects□ J. Eng. Mater. Technol., Vol.132, 2010.

[5] **H.D.CHANDLER, J.V.BEE**. □Cell structures in polycristalline copper undergoing creep at room temperature□ Acta Metall., Vol 33, pp 1121□1127, 1985.

[6] **C.GAUDIN, X.FEAUGAS**, □Cyclic creep process in AISI 316L stainless steel in terms of dislocation patterns an internal stress□ Acta Mater. 52, 3097□3110, 2004.

[7] **C.GAUDIN, C.GUILLEMER-NEEL, X.FEAUGAS**,□Hardening rate under reverse loading in 316L: Back stress and effective stress evolutions□J. Phys. IV France 11, 285□292, 2001.

[8] **S.G.S. RAMAN, K.A. PADMANABHAN**, □Effect of prior cold work on the room-temperature low- cycle fatigue behaviour of AISI 304LN stainless steel□, International Journal of Fatigue, 18 (1996) 71-79.

[9] **S. TAHERI ET AL,** □Micro□macro investigations about the fatigue behavior of pre-hardened 304L steel□International Journal of Plasticity, 2011

[10] **K.PRASAD ET AL**. □Effects of strain waveform an low cycle fatigue behaviour of near α Timetal 834 titanium allow□Material and design 32, 2011

[11] **S.L. MANNAN** □Role of dynamic strain ageing in low cycle fatigue□Bull. Mater. Sci vol 16, 1993

[12] **L. DE BAGLION, J. MENDEZ**, □Low cycle fatigue behavior of a type 304L austenitic stainless steel in air or in vacuum, at 20°C or at 300°C: relative effect of strain rate and environment□Fatigue 2010, Procedia Engineering 2 (2010) pp 2171□ 2179

[13] **T.POULAIN,** « Étude des mécanismes physiques gouvernant l'évolution du dommage en fatigue oligocyclique d'un acier inoxydable austénitique 304L en milieu eau primaire REP » ENSMA PhD thesis, in progress

[14] **T.COUVANT ET AL. «** Modeling intergranular stress corrosion cracking of austenitic alloys exposed to PWR primary water » Eurocorr, n°1149, 2012

[15] **TOTSUKA, SZKLARSKA-SMIALOWSKA,** « Hydrogen induced IGSCC of two unsensitized austenitic stainless steels in high temperature water », Corrosion Nace, pp. 124-126, 1987.

[16] **TOTSUKA, SZKLARSKA-SMIALOWSKA**, « Hydrogen induced IGSCC of Ni-containing fcc alloys in high temperature water », Environmental Degradation of Materials in Nuclear Power Systems-Water Reactors, pp. 691-696, 1988.

[17] **P. LAGHOUTARIS** Corrosion sous contrainte de l'alliage 600 en milieu primaire : Apport à la compréhension des mécanismes ENSMP PhD Thesis, 2009

[18] **ARIOKA**, « Effect of temperature, hydrogen and boric acid concentration on IGSCC susceptibility of annealed 316 stainless steel », Corrosion, 2002.

[19] **F.MENG ET AL.** « Stress corrosion cracking of uni-directionally cold worked 316NG stainless steel in simulated PWR primary water with various dissolved hydrogen concentrations » Corrosion Science, Volume 53, Issue 8, August 2011, pp 2558-2565

[20] **R.SOULAS ET AL** « TEM investigation of the oxide layer formed on a 316L alloy in simulated PWR environment » Journal of Material Science, 2012, accepted

[21] **T.COUVANT ET AL**, « Modeling intergranular stress corrosion cracking of austenitic alloys exposed to PWR primary water » Eurocorr 2012

[22] **L.DE BAGLION**, influence of pwr primary water on lcf behavior of type 304l austenitic stainless steel at 300°C - comparison with results obtained in vacuum or in air PVP 2012-78767, 2012

[23] http://www.specialmetals.com/documents/Nickel%20200%20&%20201.pdf, pp5.

[24] **J.R. GALVELE** Surface mobility mechanism of stress-corrosion cracking. Corrosion Sous Contrainte - phénoménologie et mécanismes D. Desjardins et R. Oltra, p. 83-91. Les Éditions de Physique (1992). École d'Automne. Bombannes (Gironde), France. 23-28 septembre 1990.

[25] **D. P. ABRAHAM, C. J. ALTSTETTER**, The effect of hydrogen on the yield and flow stress of an austenitic stainless steel, Metallurgical and Materials transactions A (1995), 26A, p. 2849-2858.

[26] **D. G. ULMER, C. J. ALTSTETTER**, □Hydrogen-induced strain localization and failure ofaustenitic stainless steels at high hydrogen concentrations□, Acta Metallurgica et Materialia (1991), 39, p. 1237-1248.

[27] **G. R. CASKEY**, "Effect of hydrogen on work hardening of type 304L austenitic stainless steel", Scripta Metallurgica (1981), 15, p. 1183-1186.

[28] **G.GIRARDIN** □Interactions hydrogène-plasticité dans le Nickel et dans ses alliages□ ENSM-SE PhD Thesis, 2004

[29] **S.OHIMIYA, H.FUJII** « Mechanical properties of cold work type 316L stainless steel in high pressure gaseous hydrogen » ASME Pressure Vessel and Piping conference, n°pvp2007-26492, 2007

[30] **C. SAN MARCHI ET AL.** « On the physical differences between tensile testing of type 304 and 316 austenitic stainless steels with internal hydrogen and in external hydrogen » international journal of hydrogen energy, pp 9736-9745, 2010

[31] **S.G.S. RAMAN, K.A. PADMANABHAN**, □Effect of prior cold work on the room-temperature low- cycle fatigue behaviour of AISI 304LN stainless steel□, International Journal of Fatigue, pp 71-79, 1996.

[32] **S. TAHERI ET AL,** □Micro□macro investigations about the fatigue behavior of pre-hardened 304L steel□International Journal of Plasticity, 27, pp 1981□2004, 2011.

[33] **AM. SHERMAN**, □Fatigue properties of high strength-low alloysteels□ Metall Trans 1975;6A:1035□40

[34] **H. MUGHRABI** , □Dislocations and Properties of Real Materials□, The Institute of Metals, London, 1985, pp. 244-262

[35] **S. PETITJEAN**, □Influence de l'etat de surface sur le comportement en fatigue a grand nombre de cycles de l'acier inoxydable austenitique 304L□, University of Poitiers PhD Thesis, 2003.

[36] **L. SABATIER** □Apport des techniques d□analyse locale EBSD et AFM à l□étude de l□émergence des bandes de glissements induites par fatigue dans l□acier inoxydable 316L. Influence des couches minces□University of Poitiers PhD Thesis, 2002.

[37] **M. MINEUR** □Conditions locales d□amorçage des fissures de fatigue dans un acier inoxydable de type 316L : aspects cristallographiques (EBSD)□University of Poitiers PhD Thesis, 2000.

[38] **L. DE BAGLION** □Comportement et endommagement en fatigue oligocyclique d□un acier inoxydable austénitique 304L en fonction de l□environnement (Vide, Air, Eau primaire REP) à 300°C□ PhD Thesis, ENSMA, 2011

[39] **A. PONTINI ET AL.** « X-Ray diffraction measurement of the stacking fault energy reduction induced by hydrogen in an AISI 304 steel » Scripta Materialia, Volume 37, Issue 11, 1 December 1997, pp 1831–1837.

[40] **J.D.HERMIDA,** « Stacking fault energy decrease in austenitic steels induced by hydrogen pairs formation » Scripta Materialia, vol 39, pp 1145-1149

[41] **M.L.HOLTZWORTH, M.R.LOUTHAN,** “Hydrogen-Induced Phase Transformations in Type 304L Stainless Steels” Corrosion 24, pp 110, 1968.

[42] **A.INOUE,Y.HOSOYA,T.MATSUMOTO**, Trans ISIJ, 19, pp170, 1979

[43] **A. GŁOWACKA, W.A. SWIATNICKI** “Effect of hydrogen charging on the microstructure evolution of duplex stainless steel” Materials Chemistry and Physics 81 (2003) 496–499

[44] **M.I. BASKES** « An atomistic study of the relationship between stacking fault energy and partial dislocation splitting » Materials Science and Engineering: A, Volume 108, February 1989, Pages 289-290.

[45] **A.H. COTTREL et al.**, Phil Mag.42 , pp 573, 1951

[46] **J.A.VENABLES**, Phil Mag 6, pp 379, 1961

[47] **J.W.CHRISTIAN, S.MAHAJAN**, « deformation twinning » Material Science 39, pp1-157, 1995

[48] **M.KOYAMA et al.** « Hydrogen embrittlement in a Fe-Mn-C ternary twinning induced plasticity steel » Corrosion science 54 pp 1-4, 2012

[49] **T.H. LEE ET AL.** « Correlation between stacking fault energy and deformation microstructure in high-interstitial-alloyed austenitic steels » Acta Materialia 58 (2010) 3173–3186

[50] **A.RANAIVOARISOA** “Etude des couplages entre les processus de fatigue corrosion et de corrosion sous contrainte d’un acier inoxydable austenitique en milieux chloruré chaud” University of Bordeaux PhD Thesis, 1996

[51] **T. COUVANT**, “Corrosion sous contrainte en milieu primaire nominal REP de l'acier inoxydable austénitique AISI 304L écroui”, ENSM-SE PhD Thesis 2004

[52] **Y.TAKAHASHI ET AL.** “High-voltage electron-microscopic observation of cyclic slip behavior around a fatigue crack tip in an iron alloy” Scripta materialia 2009

[53] **F.P. FORD**, “Mechanism of environmental cracking in systems peculiar to the power generation industry”, Rapport de Electric Power Research Institute, EPRI NP-2589, p.22, 1982

[54] **F.P. FORD**, "Current understanding of the mechanism of stress corrosion and corrosion fatigue in environment sensitive fracture : evaluation and comparison of test methods", ASTM STP 821, p22, 1984

[55] **F.P. FORD**, "Slip dissolution model", corrosion sous contrainte : Phénoménologie et mécanisme, Eds, D. Desjardins et R. Oltra, Éditions de physique, Bombannes (France), 23-28 Septembre 1990

[56] **A. AMBARD**, "Des modèles de tribocorrosion des aciers inoxydables en milieu primaire", 2005, Rapport EDF HT29/05/084/A.

[57] **T. SHOJI** "Modeling and quantitative prediction of environmentally assisted cracking base upon a deformation oxidation mechanism" PVP vol 479, July 25-29 2004.

[58] **R.C. NEWMAN, M. SAITO** "Anodic stress-corrosion cracking : slip-dissolution and film-induced cleavage" Corrosion-Deformation Interactions - CDI'92, p. 3–26. Les Éditions de Physique Les Ulis (1993).Conférence internationale. Fontainebleau, France. 5-7 octobre 1992.

[59] **J.R. GALVELE** "Surface mobility mechanism of stress-corrosion cracking. "Corrosion Sous Contrainte - phénoménologie et mécanismes" D. Desjardins et R. Oltra, p. 83-91. Les Éditions de Physique (1992). École d'Automne. Bombannes (Gironde), France. 23-28 septembre 1990.

[60] **P. SCOTT, M. LE CALVAR**, " Some possible mechanisms of intergranular stress corrosion cracking of alloy 600 in PWR primary water", 6th Int. Symposium on environmental degradation of materials in nuclear power system-water reactors, San Diego, USA, 1993

[61] **R.A. ORIANI, P.H. JOSEPHIC**, " Equilibrium aspects of hydrogen-induced cracking of steels", Acta metallurgica, vol.22, p.1065, 1974

[62] **S.P. LYNCH** "A Commentary on Mechanisms of Environmentally Assisted Cracking". Corrosion-Deformation Interactions - CDI'96, p. 206–219. The Institute of Materials (1997). European Federation of Corrosion Publications num. 21. Nice, France. Septembre 1996

[63] **P. LAGHOUTARIS** "Corrosion sous contrainte de l'alliage 600 en milieu primaire : Apport à la compréhension des mécanismes" ENSMP PhD Thesis, 2009

[64] **T.MAGNIN**, "A unified model for trans and intergranular stress corrosion cracking", Corrosion-Deformation Interactions - CDI'92,1992

[65] **C.D. BEACHEM**, "A new model for hydrogen-assisted cracking (hydrogen embrittlement)", Metallurgical Transactions (1972), 3, p. 437-451.

[66] **I. M. ROBERTSON, H. K. BIRNBAUM**, "An HVEM study of hydrogen effects on the deformation and fracture of nickel", Acta Metallurgica (1986), 34, p. 353-366.

[67] **P. ROZENAK, I. M. ROBERTSON, H. K. BIRNBAUM**, "HVEM studies of the effects of hydrogen on the deformation and fracture of ASI type 316 austenitic stainless steel", Acta Metallurgica et Materialia (1990), 38, p. 2031-2040.

[68] **L.TRIBOUILLOY** « Etude de la propagation par corrosion sous contrainte des aciers inoxydables austénitiques écrouis en milieu primaire de REP. Vers un modèle d'amorçage » PhD thesis, University of Bordeaux, 2007

[69] **C.BOSCH,** « Etude de la relation entre la corrosion sous contrainte et la fatigue corrosion basse fréquence de l'alliage 600 en milieu primaire des réacteurs à eau sous pression » PhD thesis, University of Bordeaux, 1998

General conclusion

The aim of this work was to contribute to the understanding of the role of several parameters such as the strain rate or the initial cold-working conditions, with regard to the effects induced on the fatigue behavior of a 304L SS in a PWR primary environment. The work intends to give some additional support for codification rules and also to bring new analysis on fundamental environment-deformation interactions. The codification support objective mainly addresses the influence of a reduced strain rate and a prior hardening on fatigue life in air and in PWR primary environment. The approach developed in the understanding part consists in the evaluation of the damage and cracking mechanisms in the air environment as a reference and in PWR primary water using multiscale characterizations. A first type of analysis is thus based on observations using optical and scanning electron microscopy of cross sections in order to get some statistical data on the cracking characteristics and its kinetics as a function of the testing parameters. Then finer observations are performed to understand synergies between deformation, local microstructure and local chemistry using TEM (BF/DF, Diffraction, EELS/EFTEM, and EDX) which control initiation and growth of cracks.

Concerning the codification support objective, the present study has shown that a prior hardening reduces the fatigue life in air in the LCF region, but slightly improves the fatigue resistance in the HCF region in terms of total strain amplitude. Furthermore, it was found that in the case of high strain rate conditions, the fatigue limit was similar in air and in PWR primary environment, for the as-received material, suggesting that the environmental effect is limited when the plastic strain amplitude is small. However, none of the present results or data presented in the literature allows concluding that the fatigue limit at very low strain rates would still remain similar. In air, the plastic strain amplitude is not sufficient to account for differences in fatigue lives of as-received and pre-hardened materials; the stress level or energy based models taking into account the differences in stress levels for a given total strain amplitude may be a better candidate to account for the observed behaviors. On the contrary, in PWR primary environment, the plastic strain by itself can relatively well correlate the fatigue life of all pre strained or as received materials, for a given stain rate. Thus, the plastic strain is a key factor governing fatigue life in PWR primary environment.

In the air environment, the use of saw tooth signals presenting a low strain rate in the tension part and a fast strain rate in the compressive part, results in a small increase of the stress level during cycling. When comparing with the results found in the literature concerning triangle signals, it seems that the use of saw tooth signals reduces the negative sensitivity to the strain rate induced by dynamic strain aging. Compared to the results obtained in air, in the PWR primary environment, it appears that the environment modifies the mechanical response of the material by increasing the stress level developed during cycling. The potential action of cathodic hydrogen can be suspected because it can play a hardening role, provided that a large amount of hydrogen atoms can diffuse into the bulk, even after a small number of cycles. However the role of cathodic hydrogen in the mechanical behavior in PWR environment requires confirmation. In particular TEM investigations of the bulk deformation structure of samples tested in PWR primary environment may be of interest to evaluate the role of hydrogen by comparing with structures produced in an inert environment.

Considering the pre-hardened materials, only a limited cyclic strain hardening phase is observed and most of the fatigue behavior consists in softening. Before cycling, a pre hardened material presents mainly planar structures and dislocation stacks. The presence of the hard structure was found to be the root cause of the increase of stress level related to a prior hardening. When considering a low strain rate saw-tooth signal, a pre-hardened material presents an increase of stress level compared to high strain rate conditions. This increase was associated with the presence of pinned dislocations symptomatic of DSA. It thus seems that a pre hardening increases the susceptibility to DSA. In opposition with the results obtained for the as-received material, no modification of the mechanical behavior was noticed in PWR primary environment. This aspect is supported by reports from literature indicating that pre-hardened materials are less sensitive to hydrogen than as-received materials during tensile tests.

It is however worth noticing that all these results concerning a potential effect of hydrogen in the cyclic behavior of 304LSS at a macroscopic scale still have to be confirmed by conducting tests using a unique machine that can have the capacity to perform experiments in air and in PWR primary environment or by designing new critical experiments in order to minimize experimental uncertainties.

The results presented in this thesis also bring some new elements about fatigue cracking processes in the PWR primary environment, in particular as regards the difference in the initiation mechanisms between this environment and air. In the air environment, initiation mechanisms were found to be related to the modification of the surface roughness induced by the emergence of 3D dislocation structure intense bands at the surface of grains presenting a high Schmid factor. No clear difference of crack initiation mechanisms (localization and kinetics) related to pre hardening and strain rate were noticed. Therefore, the difference of fatigue life induced by a prior hardening in the air environment may be related to a difference in the propagation stage. Crack initiation mechanisms in PWR primary environment can be analyzed as follows. During the first cycles, a preferential oxidation occurs along emerging dissociated dislocation at the surface along {111} planes presenting high Schmid factors. Then each cycle generates a new C-rich/Fe-rich oxide layer. During cycling, in the subsurface regions, the deformation microstructure evolves from stacking faults into micro twins. Preferential oxidation progresses along this microstructure by continuous shearing and dissolution of the passive film up to a certain depth (<3μm). Beyond this critical depth, the crack propagates along other crystallographic planes that can be {100}, {110} and {111} close to a 90° angle from the surface. The crack continues its propagation by generating shear bands and ductile fatigue striations at each cycle up to failure. The distance between fatigue striations increases with an increasing crack depth. A good prediction of the fatigue life can be derived from such inter-striation measurements, revealing a negligible contribution of the initiation stage to the total fatigue life.

Besides, it was shown that the loading strain rate highly modifies the propagation behavior in PWR primary environment. On the basis of TEM observations of the microstructure below the fracture surface, the following mechanism was proposed. At a high strain rate, the crack propagates in a single step during each cycle. Each crack arrest corresponds with the generation of a shear band. In case of low strain rates, additional sub-striation markings are observed and correspond with shear bands within a striation. This observation suggests that, during one cycle, the main crack propagates in a discontinuous mode and at each crack arrest; it generates another shear band up to the point when the loading signal goes into compression. To explain this difference related to strain rate, it would be interesting to examine the difference in deformation microstructure at the crack tip between the high and low strain rates conditions in the PWR environment but also in the air tested material Such evaluation may allow us to identify a relevant propagation mechanism in relation with the environment.

The difference in deformation mechanisms in the first grains between the air and the PWR primary environment was attributed by the potential action of cathodic hydrogen on the stacking fault energy. Indeed, hydrogen can decrease the SFE leading to a reduction of cross slip and increase the probability of dislocation dissociation generating stacking faults.

Perspectives

In this study, different aspects of interactions between fatigue damage and environmental effects have been addressed using a large panel of innovative techniques of characterisation. The research field has now to be focussed on specific issues that need further assessment due to the limited amount of test results and observations. Indeed well-controlled tests in PWR environment are particularly difficult to realize. Besides the processes responsible for the environmental effect take place at a very fine scale and are extremely localized while a statistical view of the global process is required. For instance, all the results presented have been established for a strain amplitude of 0.5%. Their extension to different strain amplitude values needs to be verified.

More precisely, on the basis of the present work, different points that need clarification can be listed.

First the observed hardening effect in PWR and attributed to an hydrogen effect needs to be confirmed, either by performing experiments in air and in PWR on the same equipment as previously mentioned, either by using the same type of critical experiments like the one using the Ni layer that should be repeated.

The reproducibility of oxide layer characterisation should also be examined, in particular by paying a special attention to the control of initial surface characteristics (residual stresses, roughness, hardening,).

Furthermore the analysis of sub-striation deformation structure that has been presented here should be also performed on a fracture surface produced in air in order to determine the specific contribution of the PWR environment, especially on the shear-band generation process with respect to strain rate.

Finally, since the role of hydrogen is often proposed to account for the observed phenomena, it would be valuable to investigate the possibility of quantifying the amount of hydrogen present in the bulk after cyclic deformation in PWR environment and at the crack tip.

EXTENDED ABSTRACT

CHAPITRE 0 - INTRODUCTION

L’augmentation de la durée de vie des centrales nucléaires est un point clef dans la gestion de l’énergie. En effet, d’ici à 2020, le tiers de la flotte nucléaire mondiale aura plus de 40 ans. Le parc de réacteurs mondial vieillit relativement bien, et de nombreux électriciens dans le monde envisagent de faire fonctionner les réacteurs existants au-delà de la durée de vie pour laquelle ils ont été initialement conçus. Cette extension de durée de vie nécessite, de la part du constructeur et de l’utilisateur de la centrale, une démonstration auprès de l’ASN de la maîtrise et de la prévisibilité du vieillissement des composants. Dans ce but, l’ASN impose la surveillance et la validation des comportements mécaniques des composants des centrales REP soumis à des sollicitations cycliques. Le retour d’expérience international actuel ne présente pas de cas identifiés clairement comme étant liés à de la fatigue assistée par le milieu primaire REP. Néanmoins, il est important de dire que ce type de fissuration peut être facilement confondu lors d’expertises avec des cas de CSC ou de fatigue. Cet aspect est en partie lié au manque de visibilité sur les mécanismes de fissuration assistée par l’environnement comme souligné récemment par l’EPRI.

Actuellement, la NRC a pris en compte les effets de l’environnement REP sur la fatigue mécanique dans le Nureg 6909 en introduisant de nouvelles variables dans les courbes de conception. Une réflexion sur la prise en compte de ces effets d’environnent est en cours en France et de nombreux programmes de R&D ont été lancés par EDF, le CEA et AREVA pour comprendre le comportement des aciers inoxydables austénitiques soumis à la fatigue sous milieux REP à haute température.

Dans ce contexte, EDF R&D a lancé une étude ayant pour premier volet l’identification et l’étude de paramètres non pris en compte dans la codification actuelle NUREG6909 sur un acier inoxydable 304L. Ces paramètres sont identifiés dans le Chapitre 1 et leurs effets sur la durée de vie seront étudiés en air (Chapitre 3) et en milieu primaire (Chapitre 4). Ces résultats seront confrontés et discutés dans le Chapitre 5. Le second volet de l’étude tend à promouvoir la compréhension des mécanismes d’endommagement, de ce même matériau, liés au milieu primaire REP et à l’air. Dans cette partie de l’étude, les mécanismes d’amorçage et de micro propagation de fissure de fatigue seront développés dans le Chapitre 3 pour ce qui est de la référence air, puis dans le Chapitre 4 en milieu primaire REP.

CHAPITRE 1 – LITTERATURE REVIEW

Les courbes de durée de vie sont une des bases de conception des composants des centrales REPs. A ce jour, l'ASN française ne demande pas explicitement de justifier des effets du milieu primaire REP sur ces courbes de durée de vie. Aux USA et au Japon, ces effets sont introduis sous la forme d'un paramètre « Fen » défini comme étant le rapport entre la durée de vie obtenue en déformation totale imposée en air à 20°C et celle obtenue en milieu primaire REP. Ce rapport de durée de vie a été paramétré en fonction de la vitesse de déformation, de la température et de la quantité d'oxygène dissous présent dans le milieu. D'autres facteurs peuvent également s'appliquer pour prendre en compte un état de surface dégradé (2-3.5), un effet de taille,… Actuellement aucune piste n'est donnée concernant la compréhension des mécanismes de fissuration.

Dans le domaine de la CSC, et plus généralement dans celui de la fissuration assistée par l'environnement, de nombreuses études ont pointé les effets de couplages plus ou moins complexes entre les trois paramètres que sont la microstructure, l'environnement et le chargement. Il semble opportun de dire que ces mêmes synergies peuvent avoir un effet dans le cas de la fatigue environnementale. Ce chapitre porte principalement sur la description de chacun de ces paramètres et sur leur influence sur l'endommagement et le comportement cyclique en fatigue.

Matériau : acier austénitique 304L

Le matériau de l'étude est un acier inoxydable de type austénitique. Les composants en acier inoxydables austénitiques présentant un retour d'expérience en rapport avec la fatigue sont principalement localisés dans les tuyauteries auxiliaires. Ces composants nécessitent d'avoir un matériau présentant une faible limite d'élasticité et une résistance à la rupture relativement élevée. Ces propriétés mécaniques sont directement liées à la structure CFC de l'austénite. Pour réduire les phénomènes de corrosion généralisée, il est nécessaire d'introduire du Chrome dans la matrice austénitique. Ce chrome ayant tendance à favoriser une structure CC, il faut également introduire du Nickel pour stabiliser la structure CFC. D'autres phases peuvent être présentes dans l'austénite, la ferrite de type CC qui peut dans certaines conditions favoriser l'amorçage de fissures de fatigue et la martensite. Des formes de martensite de type CC ou HC, habituellement observées à basse température, peuvent résulter de la déformation plastique du matériau et modifier les mécanismes de propagation de fissures de fatigue. Un autre paramètre relativement important dans le cas des aciers inoxydable austénitiques est l'énergie de faute d'empilement. En effet, ce paramètre peut modifier les caractéristiques de glissement des dislocations de par la facilité qu'ont ces dislocations à se dissocier. Les matériaux à faible énergie de défaut d'empilement (EDE) vont avoir tendance à activer principalement du glissement planaire alors que des matériaux présentant une plus forte EDE vont plutôt avoir tendance à favoriser le glissement dévié.

Comportement mécanique : Propriétés en fatigue à faible nombre de cycles

Sous chargement cyclique, les aciers inoxydables austénitiques accommodent la déformation plastique par des organisations de dislocations très spécifiques. Ces structures peuvent être de type alignement de dislocations, dipôles, structures veines, bandes de glissement permanentes, labyrinthe, cellules et Corduroy. Dans le cas d'un polycristal de 304L cyclé en déformation imposée, ces évolutions de structures contrôlent la réponse en contrainte tout au long de la durée de vie. Le comportement typique d'un 304L cyclé comporte une phase de durcissement résultant de la création et du début d'organisation des dislocations sous forme de bandes de glissement puis de structure veines. Peu après cette phase de durcissement, le matériau va avoir tendance à déconsolider. Cette phase est associée à l'évolution des structures veines, qui accommodent mal la déformation plastique, sous forme de bandes de glissement permanentes. Une seconde phase de durcissement peut se produire dans le cas des faibles amplitudes de déformation liée à l'apparition de la structure dite Corduroy.

Environnement : le milieu primaire REP

Dans les centrales REP, le milieu primaire nominal (hors conditions d'arrêt et de redémarrage) est composé d'eau, d'acide borique (1000ppm) comme modérateur de la réaction de fission, de d'hydroxyde de lithium (2ppm) pour stabiliser le pH et de l'hydrogène (30cc/kg d'eau). Ce dernier a pour objectif de diminuer fortement la quantité d'oxygène dissout dans le milieu et de maintenir le potentiel électrochimique relativement bas (-600mV/NHE) afin de limiter les problèmes de corrosion généralisée. La température est maintenue entre 320°C et 360°C à une pression de 155bars.

La plupart des matériaux en contact avec ce milieu aqueux sont thermodynamiquement instables et ont une tendance à s'oxyder. Les aciers inoxydables austénitiques vont produire une couche d'oxyde duplex avec une couche supérieure riche en fer et une couche interne riche en chrome. C'est cette couche interne qui est responsable de la passivation du matériau et qui le protège contre les effets de l'environnement. Ces réactions électrochimiques peuvent amener dans certains cas à la production d'hydrogène dit cathodique.

Fatigue et fissuration assistée par l'environnement

L'endommagement par fatigue se sépare en deux phases : l'amorçage et la propagation de fissures.

D'un point de vue physique, l'amorçage des fissures correspond à la création de microfissures à la surface. Ces fissures apparaissent localement dans des zones ayant accumulés une déformation plastique elevée, les PSB, les joints de grains et de macles. Les environnent air et REP ont tendance à favoriser l'amorçage dans les PSB.

- En air l'activité de glissement à la surface de ces bandes génère des extrusions et des intrusions. Ces dernières semblent être responsables de l'amorçage des fissures. Les PSBs émergentes à la surface de grains préférentiellement orientés avec un facteur de Schmid élevé ont tendance à promouvoir ce type d'amorçage.
- En milieu primaire REP, la stabilité du film passif peut être compromise par le chargement. En effet l'émergence de bandes de glissement tend à rompre ce film et à promouvoir une dissolution locale du matériau.

L'autre phase dans l'endommagement par fatigue est la propagation. De nombreuses théories cherchent à modéliser cette phase de propagation. Ces modèles reposent principalement sur l'action de la dissolution locale en pointe de fissure. Cette dissolution peut générer de l'hydrogène, des lacunes ou de l'oxygène modifiant localement les propriétés du matériau.

Les effets du milieu primaire REP sur l'amorçage de fissures ont longuement été étudiés avec une approche purement phénoménologique au Japon et aux USA. Le principe de ces études repose sur le lancement de matrices d'essais portant sur divers paramètres et de regarder l'influence de ceux-ci sur la durée de vie d'un échantillon sollicité en traction compression en déformation imposée. Il est possible de classer ces différents paramètres de la façon suivante.

Facteurs technologiques :

Paramètres	**Gammes d’étude dans les codifications**	**Prise en compte dans le Nureg 6909**	**Notes**
Design d’éprouvette	Eprouvettes solides et tubulaires	Pas d’influence	
Etat de surface	#50	Réduction de la durée de vie d’un facteur 2 à 3.5	Areva considère et démontre que ces valeurs sont trop conservatives

Facteurs matériaux

Paramètres	**Gammes d’étude dans les codifications**	**Prise en compte dans le Nureg 6909**	**Notes**
Nuance	304, 304L, 316, 316L, soudure 304 et 316	Pas d’influence	Les matériaux soudés présentes des durées de vie différentes des matériaux à l’état de réception
Traitement de sensibilisation	1100°C et hypertrempe 100min à 750°C puis 1700h à 400°C	Pas d’influence	
Pré écrouissage	Non étudié	Non étudié	Forte influence dans le cas de la CSC, quid de la fatigue

Facteurs chargement

Paramètres	**Gammes d’étude dans les codifications**	**Prise en compte dans le Nureg 6909**	**Notes**
Amplitude de déformation	0.1% - 0.6%	Paramètre majeur. Une diminution de l’amplitude augmente la durée de vie	Il est établi qu’en dessous d’une valeur de 0.112%, il n’y a pas d’effets d’environnement. Hors aucunes données à faibles vitesse de déformation ne permet de le confirmer
Vitesse de déformation	10-4%/s – 0.4%/s	Diminution de la durée de vie liée à une diminution de la vitesse de déformation puis saturation	La vitesse de déformation semble modifier les mécanismes d’amorçage passant de transgranulaire à intergranulaire pour les très faibles vitesses
Effet du temps de maintien	0-2000s	Pas d’influence	

Facteurs environnementaux

Paramètres	**Gammes d’étude dans les codifications**	**Prise en compte dans le Nureg 6909**	**Notes**
Température	20-300°C	Diminution croissant de la durée de vie entre 150°C et 300°C	
Oxygène dissous	5ppb – 8ppm	Pas d’effet	Les mécanismes d’oxydation et de CSC sont fortement influencés par la quantité d’oxygène. Les données présentes des lacunes importantes.
Conductivité	0.05µS/cm-0.6µS/cm	Pas d’influence	
Hydrogène dissous	15cc/kg – 30cc/kg	Pas d’influence	
Bore / Lithium	1000ppm/2ppm 1800ppm/3.5ppm	Pas d’influence	
Débit	10-4m/s – 10m/s	Pas d’influence	

A la suite de cette revue bibliographique, deux objectifs principaux ont été identifiés pour cette étude. :

- Un premier objectif de support à la codification pour la prise en compte des effets de pré écrouissage sur la durée de vie en air et en milieu primaire REP.
- Un deuxième objectif portant sur la compréhension des mécanismes d’amorçage et de propagation de fissures de fatigue dans l’air (chapitre 3) et en milieu primaire REP (chapitre 4). L’endommagement sera caractérisé par différentes techniques de microscopie (chapitre 2).

Tous les résultats seront confrontés et comparés dans le chapitre 5.

CHAPITRE 2 - EXPERIMENTAL PROCEDURE

Ce chapitre porte sur les différentes techniques expérimentales utilisées dans ces travaux de thèse.

Essais de fatigue

Deux types d’essai de fatigue ont été réalisés. Pour ce qui est du premier objectif de support à la codification, les données importantes à obtenir sont les durées de vie en milieux air et primaire REP d’un acier inoxydable austénitique 304L. Les essais à rupture en air ont été effectués sur le site EDF des Renardières sur des éprouvettes cylindriques polies #800 de façon à supprimer les fissures circonférentielles. Les essais portés à rupture en milieu primaire REP ont été réalisés au centre de recherche MHI de Takasago sur des éprouvettes tubulaires présentant des états de surface identiques à ceux des éprouvettes testées en air (#800). Le milieu primaire est fourni par une boucle de recirculation dans un milieu primaire simulé contenant 1000ppm de bore, 2 ppm de lithium et 30cc/kg d’hydrogène. Tous les échantillons ont été pré-oxydés 24h avant essai.

Les essais portant sur l’objectif de compréhension des mécanismes ont été réalisés dans l’air à l’ENSMA sur des éprouvettes progressivement polies jusqu’au micron. Les essais en milieu primaire REP ont été réalisés chez MHI utilisant un procédé d’usinage limitant fortement l’écrouissage de surface avec une finition de type polissage électrolytique.

Observations microstructurales

Plusieurs techniques de caractérisation ont été utilisées. La première est la microscopie optique permettant de quantifier des densités linéiques de fissures et des angles d’émergence de fissures.

Deux types de microscopie électronique nous ont servi à caractériser l’endommagement. La microscopie électronique à balayage en mode imagerie a été utilisée pour les observations courantes de surfaces d’échantillon ainsi que de faciès de rupture. Ce mode a notamment servi à évaluer des cinétiques de propagation de fissures à partir des mesures d’interstrie.

La technique de diffraction des électrons rétrodiffusés (EBSD) en microscopie à balayage nous a permis de déterminer l’orientation cristallographique locale de nos échantillons par rapport à l’axe de sollicitation. Un programme spécifique a été conçu à partir de ces orientations dans le but d’établir une corrélation entre les angles d’émergence de fissures et l’activité de glissement à la surface des échantillons à partir de la loi de Schmid.

Des techniques basées sur de la microscopie en transmission on été utilisées afin d’établir finement des structures de déformation ainsi que de mesurer localement la chimie via des mesures d’émission de rayons X (EDX) et de spectroscopie en perte d’énergie (EELS/EFTEM). Les échantillons prélevés en surface on été préparé avec un « dual beam » (colonne ionique et électronique). Le « dual beam » nous a permis d’étudier l’influence de localisation de déformation sur les mécanismes d’oxydation via des reconstructions d’oxyde en 3 dimensions. Ce procédé consiste à prendre une image en coupe de la zone d’intérêt puis de faire une succession d’abrasion et d’image permettant de reconstruire la couche d’oxyde en 3D. Ce procédé a été couplé à une acquisition successive de cartographie EBSD afin de combiner les mesures de désorientations locales à une acquisition de la couche d’oxyde.

CHAPITRE 3 – RESULTS IN AIR

Dans le but d'établir les différences de durée de vie entre les environnements air et primaire REP en relation avec la vitesse de déformation et un pré-écrouissage, le comportement cyclique et les mécanismes d'endommagement ont été préalablement étudiés en air à 300°C.

Le matériau de l'étude est un acier inoxydable austénitique 304L hypertrempé fourni sous forme de tôle. Certaines parties de cette tôle ont été prélevé et laminé uni axialement à froid à 5% et 10% de réduction d'épaisseur. Les échantillons ont été ensuite usinés dans ces tôles.

Deux types de signaux sont utilisés :

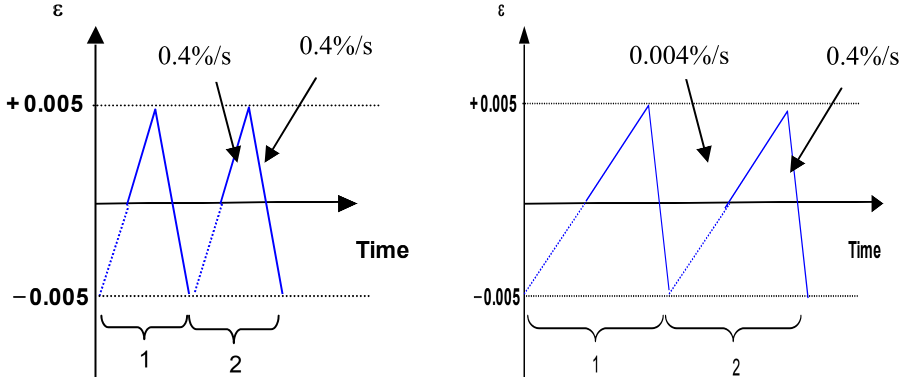

Figure 1 – Signaux de chargement.

Comportement cyclique

Le comportement cyclique dépend fortement du niveau de pré-écrouissage. Une augmentation de ce niveau de pré-écrouissage diminue le nombre de cycle nécessaire pour atteindre le pic de consolidation.

Dans le cas du matériau à l'état de réception, le durcissement résulte de la création de structures de dislocations planaires et la phase de déconsolidation de la réorganisation de ces structures sous forme de structures planaires. La vitesse de déformation n'affecte que peu le comportement cyclique malgré une légère tendance à l'augmentation de la planéité du à faible vitesse de déformation.

L'évolution microstructurale du matériau laminé 10% consiste en la réorganisation d'empilements de dislocations sous forme de structures 3D. Cette évolution se déroule au milieu de structures planaires induites par la pré-déformation qui restent tout au long de la durée de vie. Une diminution de la vitesse de déformation induit une augmentation du niveau de contrainte associé à la présence de dislocations épinglées.

Durée de vie

Un pré-écrouissage induit une réduction de durée de vie dans le domaine de la fatigue olygocyclique et une augmentation de la durée de vie dans le domaine du grand nombre de cycle.

Mécanismes d’endommagement

Aucune différence en termes de mécanismes et de cinétiques d’amorçage de fissures lié à un pré-écrouissage n’a été détectée. C’est pourquoi les différences de durée de vie ne peuvent pas s’expliquer par ces phases, mais plutôt par une différence de cinétiques au niveau de la propagation.

Les mécanismes d’amorçage en air sont liés à la modification de l’état de surface induite par l’émergence de structure 3D de dislocations à la surface des premiers grains. L’amorçage se produit suivant des systèmes de glissement présentant un fort facteur de Schmid

CHAPITRE 4 – RESULTS IN PWR PRIMARY ENVIRONMENT

L'objectif de ce chapitre est de présenter les résultats des essais de fatigue effectués en milieu primaire REP en terme de comportement cyclique et de mécanisme d’endommagement en lien avec un pré écrouissage et une modification de la vitesse de déformation. Une attention particulière est portée aux mécanismes de fissuration lors des premières étapes de vie d'une fissure de fatigue en milieu primaire REP se focalisant sur les interactions entre localisation des déformations et oxydation à des échelles d'observation différentes.

Comportement cyclique

Le comportement mécanique dépend fortement du niveau de pré-écrouissage. Une augmentation du niveau de pré-écrouissage conduit à une augmentation du niveau de contrainte et à une réduction du nombre de cycles en phase de consolidation. Une réduction de la vitesse de chargement conduit à une augmentation du niveau de contrainte développée au cours du cyclage pour les matériaux à l’état de réception comme les écrouis.

Durées de vie

En milieu primaire REP un pré-écrouissage dans la gamme 0-10% ne modifie en rien la durée de vie dans le domaine de la fatigue olygocyclique. Néanmoins, dans le domaine du grand nombre de cycle, les matériaux pré-écrouis présentent une durée de vie plus grande. Une réduction de la vitesse de déformation modifie la durée de vie comme prédit par les codifications en vigueur mais sans effet supplémentaire d’un pré écrouissage.

Mécanismes d’endommagement

La durée de vie en fatigue d’un acier inoxydable austénitique 304L en fatigue peut être résumée par :

- Une oxydation préférentielle dans l’alignement d’une bande de cisaillement évoluant dans les plans {111} denses en faute d’empilement. Chaque cycle génère une double structure d’oxyde riche en Fer et riche en Chrome (Figure 2 - a).
- Puis, au cours du cyclage, la microstructure évolue d’une structure dense en fautes d’empilement vers une structure principalement constituée de micro-maclage. L’oxydation se poursuit par cisaillement répété de la couche d’oxyde en fond de fissure jusqu’à une profondeur de l’ordre de 3µm. (Figure 2 - b).

- A partir de cette profondeur et au cours du cyclage, la fissure va se réorienter et se propager selon un plan cristallographique de type {100}, {111}, {110} le plus près d’un angle de 90° par rapport à la direction de sollicitation. La fissure se propage par génération successive de bandes de cisaillement et de strie de fatigue à chaque cycle. La distance inter strie augmente avec la profondeur de la fissure (Figure 2 – c and Figure 2 - d).

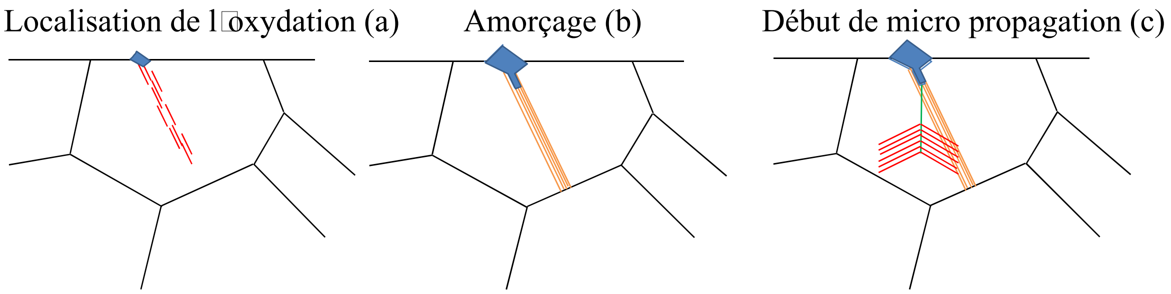
Localisation de l’oxydation (a) Amorçage (b) Début de micro propagation (c)

Propagation (d)

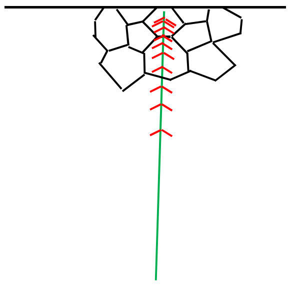
Figure 2 – Fatigue life description

- Effets d’un pré écrouissage

Un pré-écrouissage, qu’il soit sous forme de traction ou de laminage, ne semble pas modifier les phases d’amorçage et de propagation. Ceci est en accord avec les durées de vie similaires.

- Effets de la vitesse de déformation

Ces mécanismes de fissuration peuvent être affectés par la vitesse de déformation. En effet une plus forte vitesse de déformation tend à limiter la génération de la structure d’oxyde en double couche riche en Fe et Cr. La vitesse de déformation affecte aussi les mécanismes de fissurations dans le sens ou une plus forte vitesse de déformation à tendance à augmenter le nombre d’amorce et à favoriser le branchement de fissures même si la durée de vie dans ces conditions est plus importante. Dans le domaine de la micro propagation, une diminution de la vitesse de déformation augmente sensiblement les cinétiques de propagation de fissures en accord avec les durées de vie observées. Cette augmentation de vitesse de propagation est associée à la présence de plans de glissement activés entre plusieurs stries de fatigue, suggérant une propagation continue de la fissure au cours d'un cycle contrairement à ce qui est observé à plus forte vitesse de déformation.

CHAPITRE 5 : SINTHESYS AND DISCUSSION

L’objectif de ce chapitre est de confronter et de discuter les résultants obtenus sous air et en milieu primaire REP.

Les principaux objectifs de cette étude sont de:

- Quantifier les effets d’un pré écrouissage et de la vitesse de déformation sur la durée de vie en air et en milieu primaire REP dans une optique de support à la codification.
- Progresser dans la compréhension des mécanismes de fissuration de fissures de fatigue en milieu primaire REP.

Support à la codification

- Comportement cyclique

Dans le cas du matériau à l’état de réception, une augmentation du pic de consolidation est observée en milieu REP par rapport à l’air. Cet effet est discuté en termes d’effet potentiel de l’hydrogène cathodique. Ce résultat devra toutefois, être confirmé par des essais complémentaires réalisés à l’air et en milieu REP sur une seule et même machine afin de minimiser les erreurs expérimentales.

Dans le cas du matériau à l’état de réception, une augmentation du pic de durcissement est aussi observée en milieu REP à faible vitesse de déformation par rapport à une vitesse plus rapide. Cet effet est analysé sur la base d’un effet de l’hydrogène cathodique sur les mécanismes de vieillissement, notamment le vieillissement dynamique.

Une augmentation du niveau de pré-écrouissage induit une forte augmentation du niveau de contrainte développée au cours du cyclage. De plus, les matériaux pré-écrouis présentent une sensibilité positive à une diminution de la vitesse de déformation. Aucune modification du comportement cyclique n’est liée à la présence du milieu primaire. Cet aspect est discuté en termes de diminution de la sensibilité à l’hydrogène des matériaux pré-écrouis.

- Durées de vie

Un pré écrouissage réduit la durée de vie en air dans le domaine de la fatigue olygocyclique mais ne la modifie pas en milieu primaire. Dans tous les cas, la limite de fatigue des matériaux écrouis est augmentée par rapport au matériau à l’état de réception.

L’amplitude de déformation plastique est un paramètre clef pour prédire la durée de vie en milieu primaire REP, mais ne semble pas suffisant en milieu air.

Compréhension des mécanismes de fissurations en milieu primaire REP

En accord avec la littérature, les mécanismes d'amorçage de fissures en air sont à l'émergence de structures 3D de dislocations à la surface. Ces structures modifient l'état de surface et cette modification engendre l'amorçage de la fissure. Après l'amorçage, la fissure poursuit sa propagation en suivant le plan de glissement activé.

En milieu primaire, les mécanismes présentent de nombreuses différences par rapport à l'air. Durant les premiers cycles se produit une oxydation préférentielle le long de dislocation dissociées émergentes à la surface. Chaque cycle génère une double structure d'oxyde riche en Cr et Fe. La microstructure sous jacente évolue vers une structure de type micro maclage. La fissure se propage par cisaillement et dissolution successive du matériau. Après une profondeur de l'ordre de 3µm les fissures se propagent selon des plans cristallographiques proche d'un angle de 90° par rapport à la direction de sollicitation jusqu'à la rupture de l'éprouvette.

La différence de mécanisme de déformation dans les premiers grains liés à l'environnent REP est analysée en relation avec l'action de l'hydrogène cathodique sur la modification de l'énergie de faute d'empilement. En effet l'hydrogène tend à augmenter la planéité du glissement et la probabilité de dissociation des dislocations, et donc celle du micro maclage.

La plupart des résultats en milieu PWR sont basées sur un effet potentiel de l'hydrogène cathodique sur l'évolution de la microstructure au cours du cyclage. En effet, l'impressionnante différence des cinétiques de corrosion entre les chargements cycliques et statiques peut avoir un effet direct sur la production de l'hydrogène cathodique. L'étude de la nature et de la structure de la couche d'oxyde peut être un moyen pertinent pour expliquer cette production.

En ce qui concerne les mécanismes de propagation des fissures en milieu primaire REP, la vitesse de déformation modifie les mécanismes de propagation, mais aucun des résultats ne permet d'appuyer tel ou tel modèle. En effet, la plupart des modèles existants portant sur la propagation de fissures présentent de nombreuses incompatibilités avec les observations présentées ici. Les modèles les plus pertinents pouvant être appliqués aux mécanismes d'EAF semblent être le modèle de Ford, le modèle de Lynch et le HELP. Cependant, aucun d'entre eux ne peut être directement appliqué. Par conséquent, des analyses complémentaires, consistant par exemple en des observations de fond de fissures pour caractériser l'action de l'environnement sur les mécanismes de propagation et ainsi confirmer l'applicabilité potentielle d'un modèle.

Conclusion

Ces travaux de thèse contribuent à la compréhension du rôle de plusieurs paramètres tels que la vitesse de déformation et un pré écrouissage d'un acier inoxydable austénitique 304L en milieu primaire REP. Ce travail a été divisé en une étude de support à la codification et une étude plus fondamentale portant sur la compréhension des mécanismes de fissuration par fatigue en air ainsi qu’en milieu primaire REP via des techniques de caractérisation microscopiques multi échelles.

En ce qui concerne l'objectif de support à la codification, la présente étude a montré qu'un pré écrouissage réduit la durée de vie dans le domaine du LCF en air mais ne n’affecte pas la durée de vie en milieu primaire REP. Dans tout les cas la limite de fatigue des matériaux pré écrouis se retrouve augmentée par rapport aux matériaux à l’état de réception. La déformation plastique mesurée à mi vie est un bon paramètre prédictif de la durée de vie milieu REP mais n’est pas suffisant en air. Une approche de type énergétique peut être envisagée dans ce milieu.

L’influence du milieu primaire REP sur le comportement cyclique peut être suspectée. En effet le niveau de contrainte développé au cours du cyclage est plus important dans ce milieu qu’en air. L’action potentielle de l’hydrogène cathodique est suspectée car sa présence peut modifier les propriétés mécaniques et provoquer un durcissement. Néanmoins d’autres études sont nécessaires pour confirmer cet aspect. Une caractérisation fine des structures de déformation à cœur d’échantillons testés en milieu REP peut permettre de progresser dans la compréhension de ce phénomène. Le comportement mécanique des matériaux pré écroui sont peu sensible à la présence du milieu primaire. En accord avec la littérature il semble que les matériaux pré écrouis sont peu sensibles à l’action de l’hydrogène.

Dans tous les cas il apparait comme nécessaire de valider ces comportements par des essais utilisant une seule machine pouvant travailler en milieu primaire REP et en air afin de minimiser les erreurs expérimentales.

Les résultats présentés dans cette thèse permettent également d'améliorer la compréhension du processus de fissuration d'un acier inoxydable 304L en milieu primaire REP ainsi qu’en air. Ainsi les mécanismes d’amorçage en air sont liés à une modification de la rugosité induite par l’émergence de structures 3D de dislocations. En milieu primaire l’amorçage des fissures se produit à l’interface métal oxyde via l’émergence de micromacle. Cette différence de microstructure au sein des premier grains peut s’expliquer par une action de l’hydrogène sur l’énergie de faute d’empilement.

Les mécanismes de propagation de fissures en milieu REP sont fortement affectés par la vitesse de déformation. En effet une réduction de a vitesse de déformation tends à favoriser la propagation de la fissure au cours d’un cycle. Une étude plus approfondie de ces différences permettrait de trouver une explication physique à ce phénomène.

Toutes les caractérisations précédentes ont été établies à un 0,5% de l'amplitude de déformation, il semble pertinent de procéder à la même approche pour d’autres amplitudes.

Appendix 1

Field experience related to thermal fatigue

Summary

1. Civaux 1

The Residual Heat Removal System (RHRS) of PWRs provides a minimum amount of fluid in the primary circuit during shutdown and startup phases (maintenance or refueling), to cool primary loop. These circuits experience temperature variations caused by turbulent mixing of hot and cold fluids in the mixing zones (Figure 1, Figure 2). These variations may induce through-wall cracks leading to the leakage of cooling medium. Such an incident occurred in May 1998 at Civaux 1, where a loss of coolant was detected on the RHRS circuit. Following this incident, many studies have been undertaken [1].

The reactor stopped when a water leakage of 30 m^3/h was detected on the elbow of the RHRS circuit (Figure 2) made of 304L stainless steel. Because this system consists of two independent and redundant circuits, the leaking portion was isolated, and the reactor cooled thanks to the second [2].

Approximative operating conditions of CIVAUX 1 RHRS were:

- Fluid pressure of 27 bars.
- Hot flow temperature of 180°C.
- Cold flow temperature of 90°C.
- ΔT_{metal} =°C.
- 3767 hours in service, including 1500 h at ΔT = 150°C in PWR water.

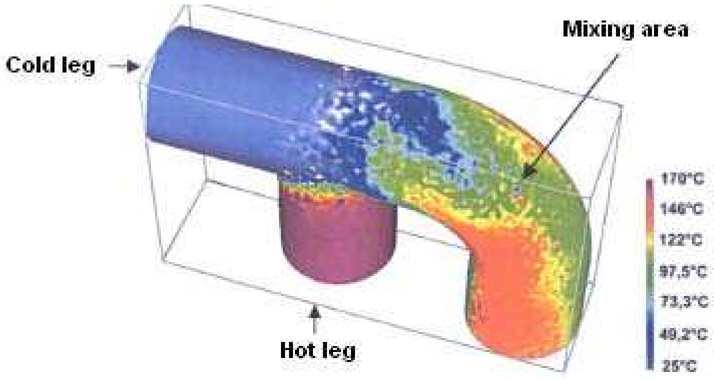

Figure 1 □Thermohydraulic simulation of temperature of Civaux 1 RHRS [1].

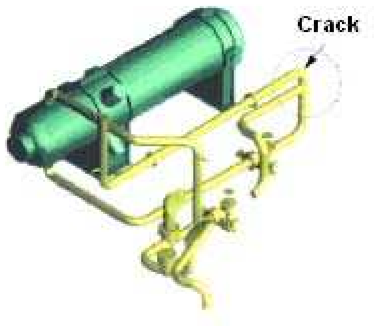

Figure 2 □Civaux 1 RHRS [2].

1.1. Assumed root cause

A portion of RHRS was examined at EDF in order to determine the root cause of failure and to look for the presence of eventual manufacturing defect. This elbow is composed of a round welded tube made of AISI 304L stainless steel measuring 273 mm of diameter and

9.3 mm of thickness. It is composed of two welded half-shells (Figure 3). The crack which caused the leakage was located at the upper side of the weld elbow (Figure 4). It reached a length of 180 mm at the outer surface and 250 mm at the inner surface of the weld. Initiation sites of thermal fatigue cracks were highlighted (Figure 5) by liquid penetrant testing (PT).

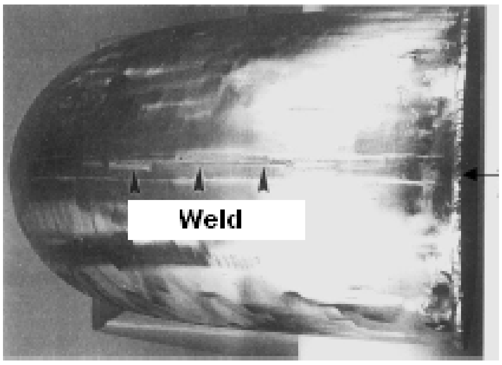

Figure 3 - Civaux 1 RHRS crack location [3].

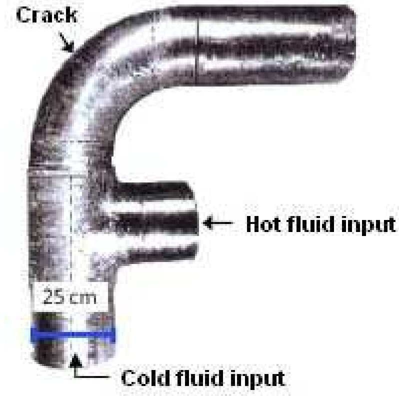

Figure 4 - Civaux 1 elbow location [3].

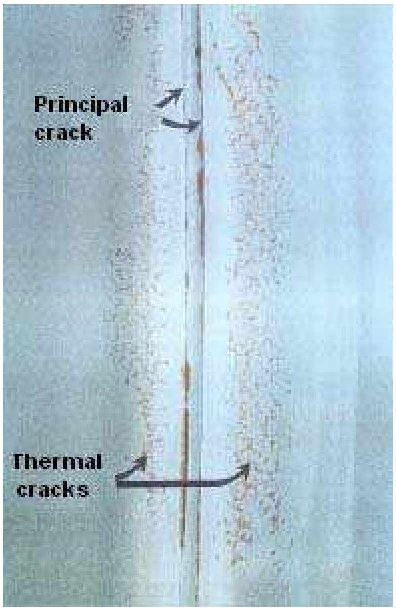

Figure 5 □Cracks on Civaux 1 elbow [3].

Based on X-ray diffraction (XRD) measurements, residual stresses at the inner diameter (ID) were estimated about □400 MPa. Stresses increased in the heat affected zone (HAZ) to reach +139 MPa. The surface roughness was evaluated to 1 µm<Ra<5 µm and 8 µm<Rt <35 µm. No abnormal residual δ ferrite content was observed. Optical examination of the main and secondary cracks revealed a transgranular cracking morphology. No evidence of manufacturing defect was observed. Moreover, a crack network representative of thermal fatigue phenomenon was noticed at the ID of the weld.

Scanning electron microscopy (SEM) examinations of the elbow surface were performed by Garcia [4] at EDF R&D. A grain boundary attack resulting from contamination cleaning was reported (Figure 6). In addition, a TEM/EDX observation revealed the presence of oxides at fatigue crack tip. However, the eventual contribution of the environment on the degradation was not demonstrated.

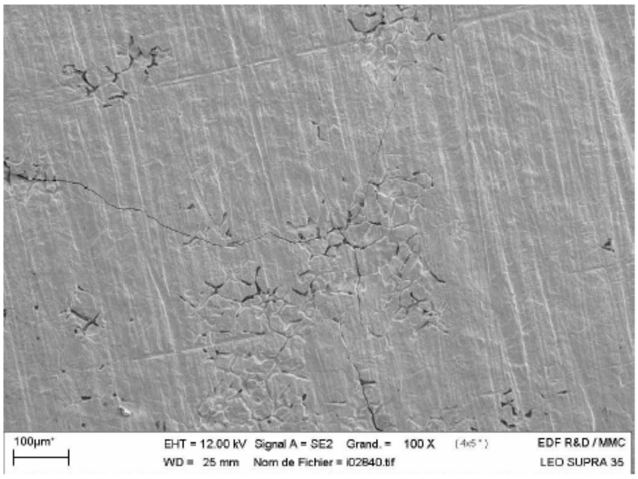

Figure 6 □Grain boundary attack at the surface of Civaux 1 RHRS ID [4].

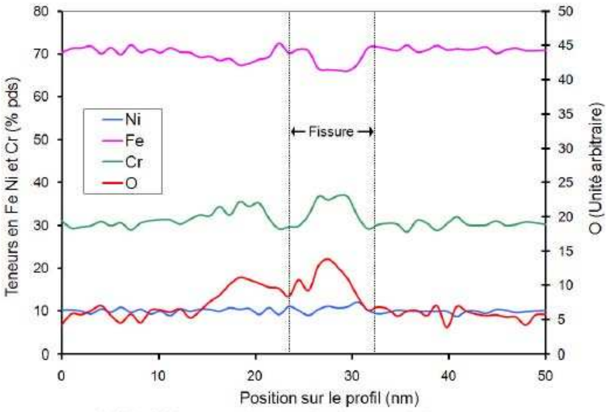

(a) Profil de composition en fer chrome nickel et oxygène.

Figure 7 □Elemental analysis (EDS) along line 1 [4].

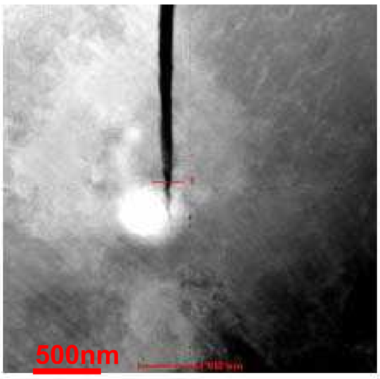

Figure 8 □TEM / HAADF observation. Red line 1 represents EDS line scan location [4].

1.2. Corrective actions

To prevent such cracking, several counter measures were taken, including a modification of the design of the circuit. Improvements on the welds were also made. EDF carried out replacement of all 128 RHRS mixing zones; crack with depth limited to 3 mm were found.

2. Genkai 1

On June 6, 1988 the containment sump water level of Genkai Unit 1 was found to have risen. Since this was judged to be due to leakage from the primary cooling system, the reactor was shutdown manually for inspection.

Inspections revealed a slight leakage through a crack in the weld of the horizontal pipe upstream of the RHRS line inlet isolation valve of loop A. The diameter of the pipe, made of AISI 316 stainless steel, was 200 mm and 20.6 mm thick. A through-wall crack was located at the top of the circumferential weld seam between the horizontal piping and the elbow. Other examination of adjacent welds revealed a non through-wall crack at the top of the weld seam between the horizontal pipe and the inlet isolation valve (Figure 9) [5].

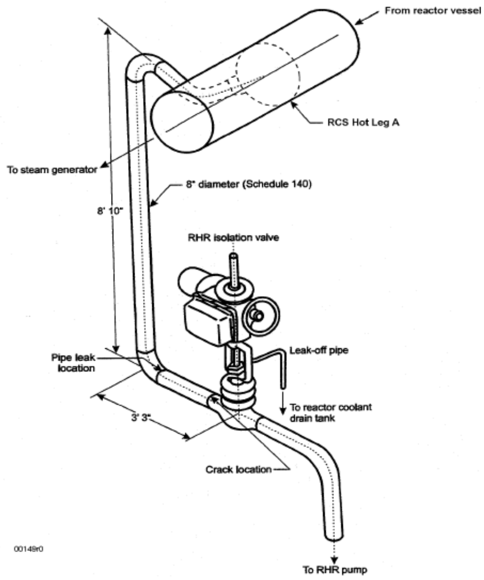

Figure 9 □Genkai 1: Cracks locations [6].

2.1. Assumed root cause

The through-wall crack initiated between the weld metal and the base metal and propagated perpendicularly to the pipe axis. On the inner surface, the crack length was about 97 mm long. On the outer surface, it was about 1.5 mm long. The non-through wall crack was similar in shape to through-wall crack except that crack depth was only 60% of wall thickness (Figure 10).

Scanning electron microscopy (SEM) investigation of the fracture surface through-wall crack revealed a flat transgranular fatigue crack. Observations also highlighted fatigue striations. Assuming that the distance between striations corresponds to the crack growth rate, the fatigue life of the component was estimated to 10^4 -10^5 cycles, corresponding to a stress amplitude within the range 70 - 110 MPa.

No abnormalities were found into the material and the structures. X-Ray diffraction analyses on deposits observed at the inner surface of the valve revealed a spinnel structure, similar to those usually observed on materials exposed to primary environment at high temperature. The stress concentration factor at the crack initiation location was estimated to 3.

Further analysis on mock-up revealed that the stress level may have reached 180 MPa at the weld/metal transition and that the loading period was of 20 minutes. These facts suggested that the pipe had been subjected to unexpected stresses induced by thermal stratification resulting from cold water in the pipe (93°C) and hot water leaking from the valve gland (315°C) [5, 6].

Based on Japanese and US codifications (see Chapter 1), and also on Genkai 1 characteristics (temperature, loading, period and fatigue life), the effect of environment on fatigue cannot be excluded in this degradation.

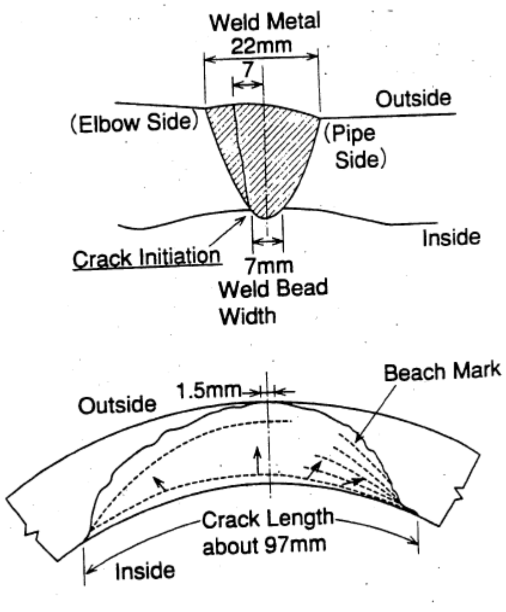

Figure 10 Genkai 1: illustration of fracture surface of the through wall crack [5].

2.2. Corrective actions

The following corrective actions were taken to prevent the recurrence of the degradation [5]:

- The gland packing was replaced to stop the gland leak.
- The position of the valve disc was increased to secure a sufficient seat gap, so that if thermal stratification forms, it will not fluctuate.
- The leak-off pipe was thermally insulated to enhance detectability of small gland leak.

3. Loviisa 2

On May 1994, a leakage was observed in the body of a control valve of a pressurizer auxiliary spray line at Loviisa 2. The plant was manually shutdown and inspections revealed an axial through-wall crack in the valve body. The valve was replaced with an equivalent one and the unit restarted-up 6 days afterwards. Non-destructive examinations (NDE) revealed the same kind of crack in the body of the corresponding valve on Loviisa 1. Valve structure and crack location are presented in Figure 11. The inlet nozzle of the Z-type valve is located higher than the outlet nozzle. After the valve, the pipe is almost horizontal up to the bent, then turning down to the vertical part of the piping going to the pressurizer. So, the cold water (250°C) comes down while the steam (325°C) comes up from the pressurizer, into horizontal part of the pipe. Valve body material is a A321 titanium stabilized stainless steel [7].

3.1. Assumed root cause

Crack dimensions were 80 mm along the horizontal surface and 25 mm along the vertical surface of the valve body. According to the investigations, the crack in the valve of Loviisa 2 initiated from a titanium inclusion that enhanced the crack nucleation. Fatigue striations and transgranular crack advances were observed on the fracture surface. The fact that there were only one major and a few more minor parallel cracks suggested that a low cycle rather than a high cycle fatigue mechanism was involved.

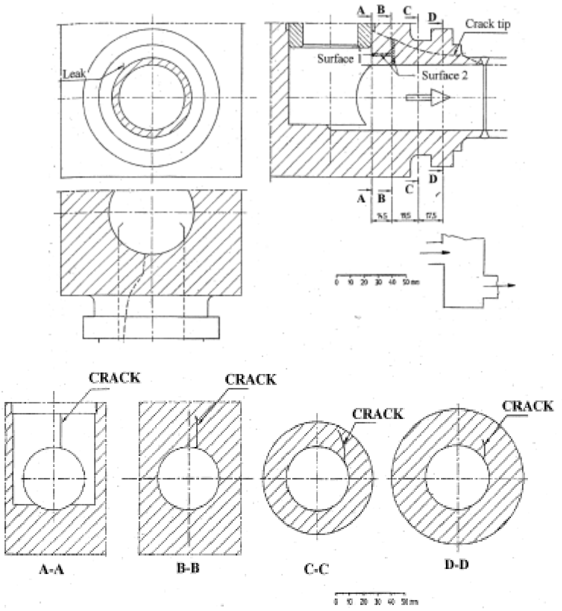

Figure 11 Crack location in the Loviisa spray line control body [7].

3.2. Corrective actions

The following corrective actions were taken to prevent recurrence of these phenomena:

- The damage in the valve body at Loviisa units 1 and 2 were removed and identical valve bodies from one of the primary letdown pipe were installed in the shutdown spray line.
- In 1996 valves were replaced with another type of valve and pipelines were modified at both units. The direction of the outlet nozzle is now downwards, and followed by a bend.

4. Mihama 2

In April 1999, at Mihama 2, while the plant was operating at 65% fuel power, a small leak was discovered in an elbow down to the reactor coolant system (RCS) crossover leg made of AISI 316 stainless steel. The crack (Figure 12) was located 380 mm from the reactor coolant loop inside surface and was in the center extrados of the elbow, oriented at 45° from the pipe centerline. It measured 25.4 mm long at the inner surface, and 6.4 mm long at the outer surface. Another 12.7 mm long through-wall crack was also found [6].

4.1. Assumed root cause

The cause of the cracking was supposed to be the turbulence penetration of the hot RCS fluid extending into the horizontal run resulting in thermal stratification. Cycling was induced by fluctuations in the turbulence penetration distance above and below the elevation of the horizontal run. The Mihama 2 elbow also exhibited high tensile residual stresses induced in the manufacturing process.

Test on mock-up revealed a temperature variation within the range 150°C to 260°C at a period of 100 s/cycle. Based on finite element modeling (FEM) stresses were evaluated to 150 MPa [6].

Based on Japanese and US codifications, and on Mihama 2 characteristics (temperature, loading, period), this degradation may have been due to environmentally-assisted fatigue.

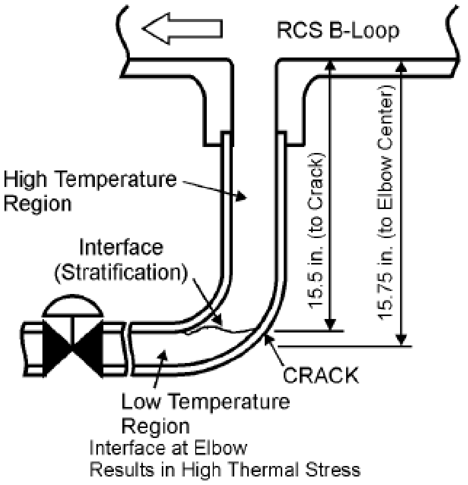

Figure 12 □Mihama 2 leak location [6].

4.2. Corrective actions

The corrective action for this event was to shorten the vertical pipe to 254 mm, in order to guaranty that the interface between the low and the high temperature regions be away from the elbow (Figure 13). This modification limited thermal cycling and stress concentration in the elbow. Thus, the vertical pipe and the elbow will experience a constant source of heat, eliminating thermal stratification cycling. In addition, an elbow with reduced residual stresses was used in the replacement [6].

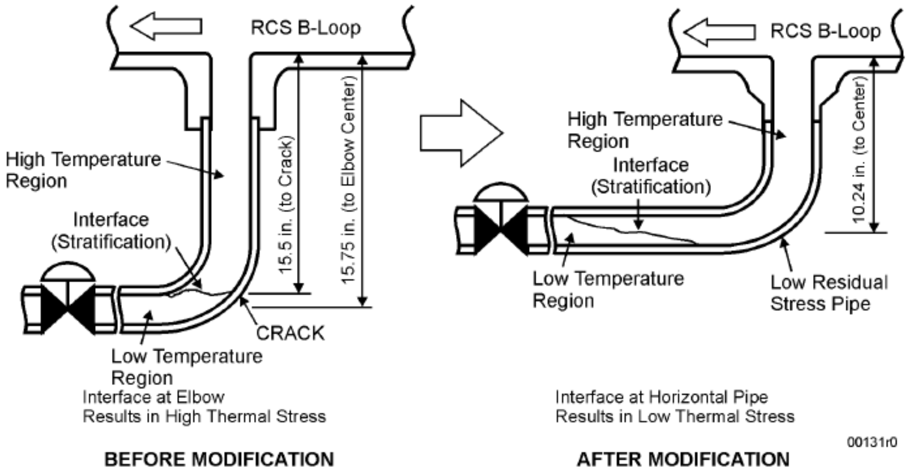

Figure 13 □Mihama 2 RCS loop modifications [6].

5. Conclusion on field experience

The international field experience includes cases of fatigue crack initiation in austenitic stainless steels exposed to PWR primary water. Nevertheless, after examinations, it was never concluded that the root cause of the degradations was environmentally assisted fatigue. However, loading and environmental conditions are in good agreement with the current international codification (Figure 14). It can be noticed that Mihama 2 and Genkai 1 cases occurred under low strain amplitude (long fatigue life area in Figure 14).

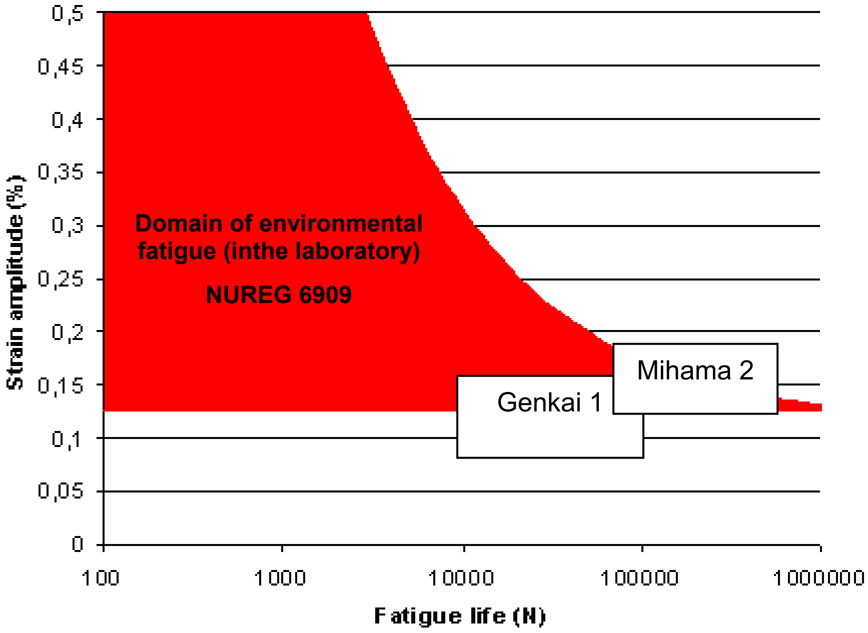

Figure 14 Field experience compared to the NUREG 6909.

---

[1] **V. MAILLOT**, « Amorçage et propagation de réseaux de fissures de fatigue thermique dans un acier inoxydable austénitique de type X2 CrNi18-09 (AISI 304L) », Ecole Centrale de Lille PhD Thesis, 2003.

[2] **DRIRE** : Direction Régionale de l'Industrie, de la Recherche et de l'Environnement, Anomalies génériques concernant les tuyauteries du circuit de refroidissement à l'arrêt. Adresse URL : http ://www.aquitaine.drire.gouv.fr/surete/RRA_N4.html.

[3] **O. GOLTRANT**, "CNPE de CIVAUX - Tranche 1 - Expertise du coude RRA situé en aval de la vanne RRA071VP" Note EDF (GDL) D5710/ECH/1998/008136/00, Août 1998.

[4] **A. GARCIA**, “Caractérisation microstructurales d'aciers inoxydables austénitiques de type AISI 304L sollicités en fatigue” These de doctorat de l’Institut National Polytechnique de Grenoble. 2009.

[5] **S. SHIRAHAMA**, “Failure to the RHRS suction line pipe in Genkai unit 1 caused by thermal stratification cycling”, Experience with thermal fatigue in LWR piping caused by mixing and stratification, 1998.

[6] **P. HIRSCHBERG**, “Operating Experience Regarding Thermal Fatigue of Unisolable Piping Connected to PWR Reactor Coolant Systems” (MRP-25), EPRI, Palo Alto, CA: 2000. 1001006.

[7] **Y. HYTÖNEN**, "Two leakeages induced by thermal stratification at the Loviisa power plant ", Experience with thermal fatigue in LWR piping caused by mixing and stratification, 1998.

Appendix 2: Benefits of mechanisms understanding for the engineering

Summary

1. Introduction

The objective of this specific chapter is to provide more information related to the environmental fatigue aspects.

- A first part will focus on the codification aspect with a specific discussion concerning the Fen with pre hardened material and a discussion on the apprehension of other factors governing fatigue life in PWR primary environment.
- The second part will focus on the specific signatures of EAF that may help on the identification of EAF field experience from basic optical microscopic observations up to TEM.

2. Codification

2.1. Environmental effect: Fen evaluation

Figure 1 summarizes the experimental Fen data established in this work as a function of strain rate. The Fen was calculated as defined in Equation 1, where state is “annealed” or “10% cold worked”. The evaluated Fen by NUREG 6909 codification and the JSME code are, moreover, given with the solid line and the dot line, respectively. The effect of cold working is not considered in these codes.

$$F_{en,experimental} = \frac{N_{air,T,state}}{N_{water,T,state}}$$ **Equation 1**

where $N_{air,T,state}$ and $N_{water,RT,state}$ were observed after fatigue tests in air and primary water, under the same waveform, at the same strain rate and the same strain amplitude.

It clearly appears that Fen increases with a decrease of strain rate for both materials, and that the Fen value of the cold-worked material is almost half of that of the as-received one. This difference is only due to the fact that fatigue life of the cold-worked material in air is half than that of the as-received (annealed) one, consequently leading to the reduced Fen. As far as only Fen values are considered, it could be concluded that the environmental effect can be reduced by 10% cold working compared to the as-received condition, even if fatigue lives of both materials in water are almost the same.

Observed Fen values are in good agreement with codifications. Nevertheless, it should be noticed that the evaluation provided by NUREG 6909 is not enough restrictive for the as-received material, whereas the Japanese code seems sufficient to predict environmental factors for the annealed material and relatively conservative for the cold-worked material.

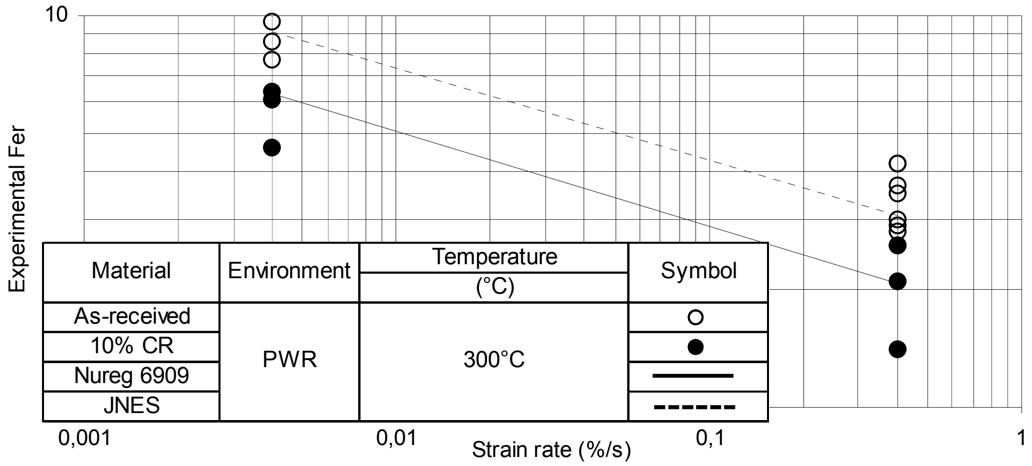

Figure 1 □Experimental Fen for cold-worked and as-received materials in simulated PWR environment at 300°C

Figure 2 and Figure 3 compare the expected fatigue lives evaluated using the current US or Japanese models with the experimental fatigue lives determined in the current study. Both figures indicate that the codifications predict accurate fatigue lives (lower than a factor of 2) as long as fatigue lives are lower than 60,000 cycles. For higher numbers of cycles, the experimental fatigue lives are much lower than the prediction (up to a factor of 20). It points out that both models are not conservative for this material in the high cycle fatigue regime.

Figure 4 and Figure 5 compare the experimental Fen and the predicted Fen with NUREG 6909 and the JSME codification, respectively, revealing that both models can predict the Fen with a good accuracy (factor of 2). However, it can be also pointed out that the JSME model tends to give conservative prediction on the cold-worked material, while the NUREG model seems less conservative on the as-received material. In addition, Figure 6 and Figure 7 propose similar comparisons for the weld metal data previously reported in the JNES. These models show the same tendency on the weld metal as on the cold-worked material. Therefore, it could be possible to improve the accuracy of the predicted Fen based on material considerations.

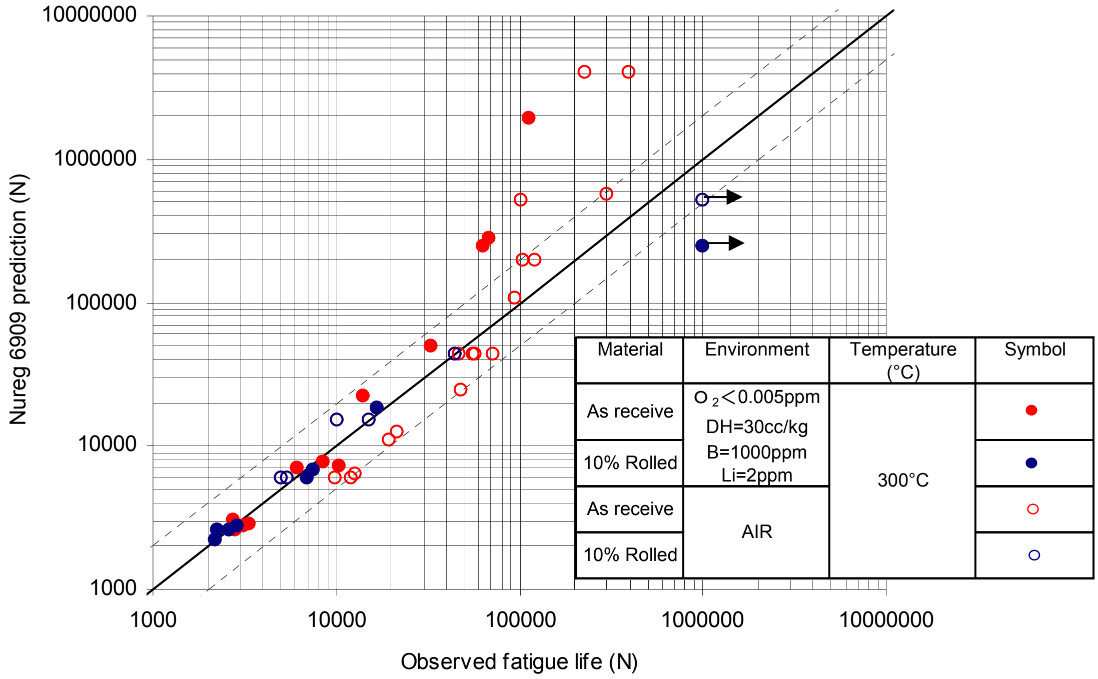

Figure 2 NUREG 6909 fatigue life prediction compared to experimental data.

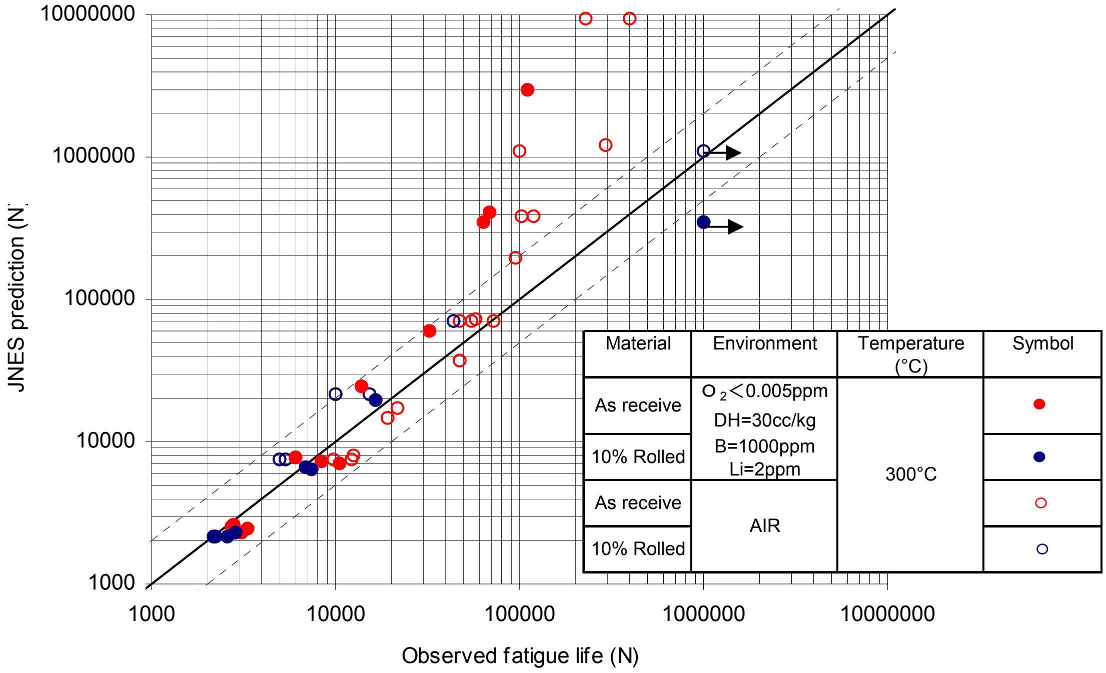

Figure 3 JSME fatigue fatigue life prediction compared to experimental data.

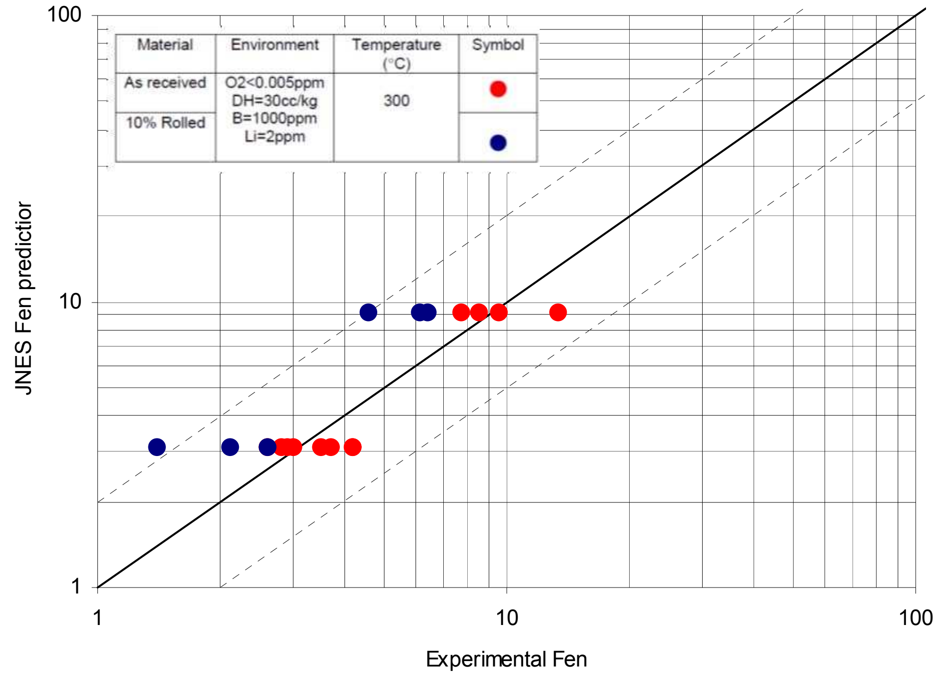

Figure 4 □JSME Fen prediction as a function of experimental Fen.

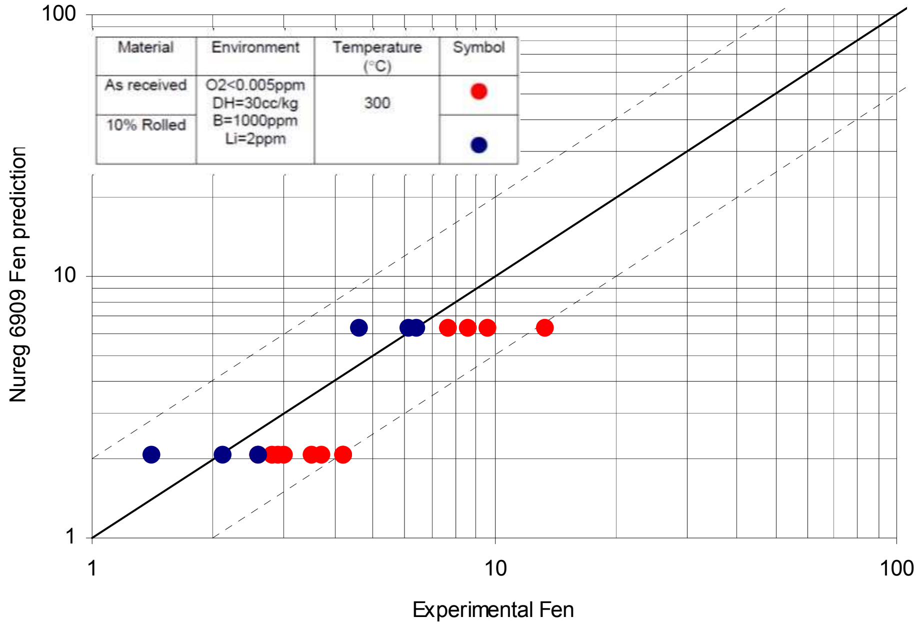

Figure 5 □NUREG 6909 Fen prediction as a function of experimental Fen.

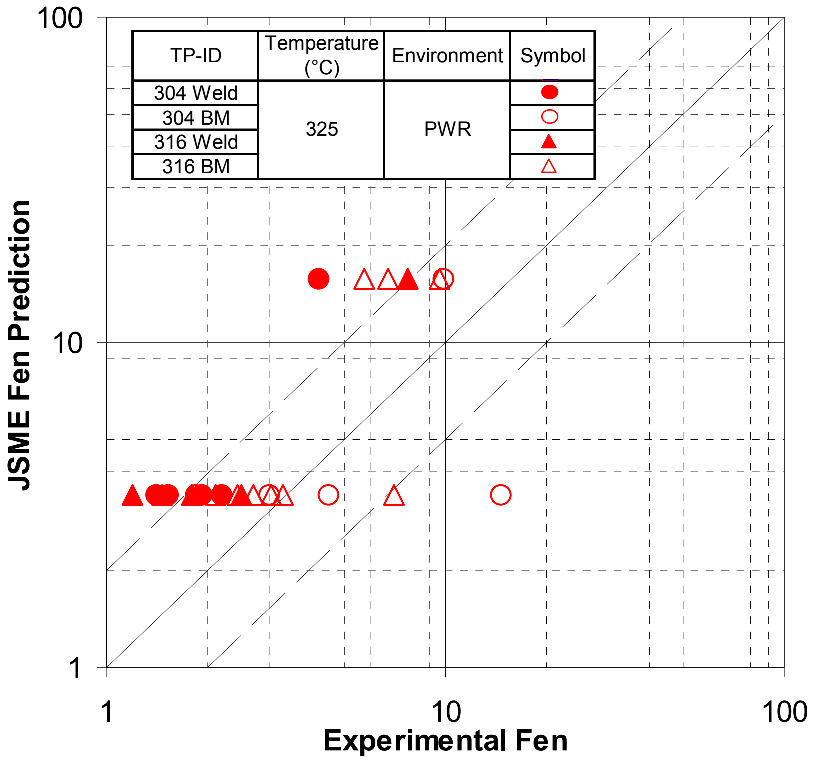

Figure 6 - JSME Fen prediction as a function of experimental Fen for weld metals.

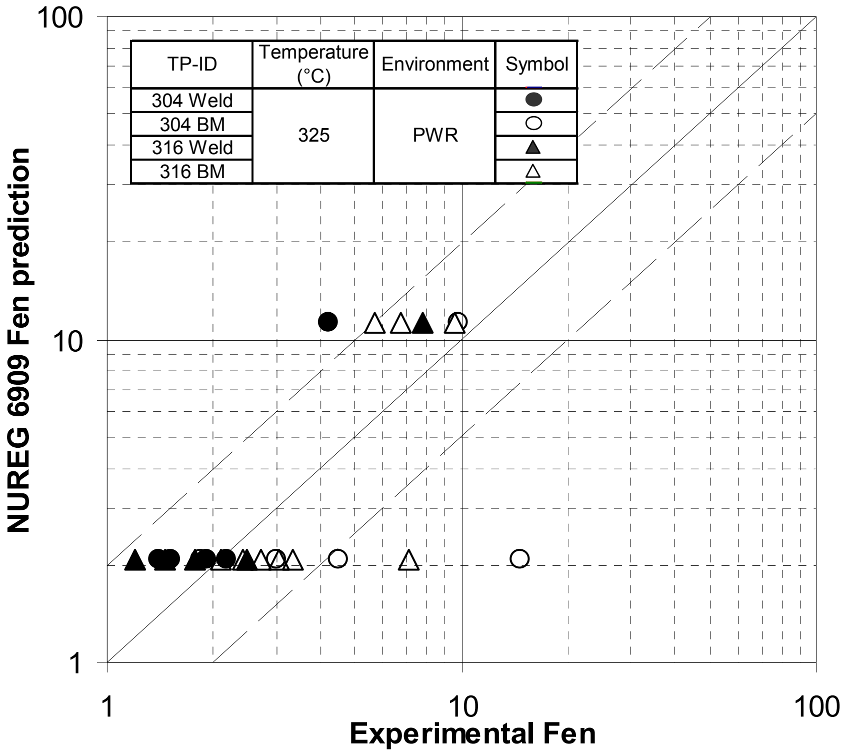

Figure 7 - NUREG 6909 Fen prediction as a function of experimental Fen for weld metals.

2.2. Apprehension of other parameters governing fatigue life

Observations are limited to a restricted number of test conditions. Understanding of the underlying mechanisms is a way to try and extrapolate results beyond the boundaries of the phenomenological test matrix towards more complex in-service conditions.

2.2.1. Effects of strain amplitude and strain rate

It has been shown in chapter 4 that the fatigue life in nominal PWR primary environment can be accuretaly estimated using by the micro crack growth rates derived from striations measurements. However plants in operation experienced several types of loadings at different strain amplitudes and strain rate conditions. The influence of these parameters are analyzed in the next sections.

2.2.1.1. Damage accumulation induced by strain rate

The loading history induced by a pre strain hardening did not affect the fatigue life and the propagation behavior (Chapter 4). In this section, it is proposed to evaluate another type of loading history with a varying strain rate within the fatigue life of a sample. In that kind of test, the loading history during one cycle is composed of several segments as shown in Figure 8.

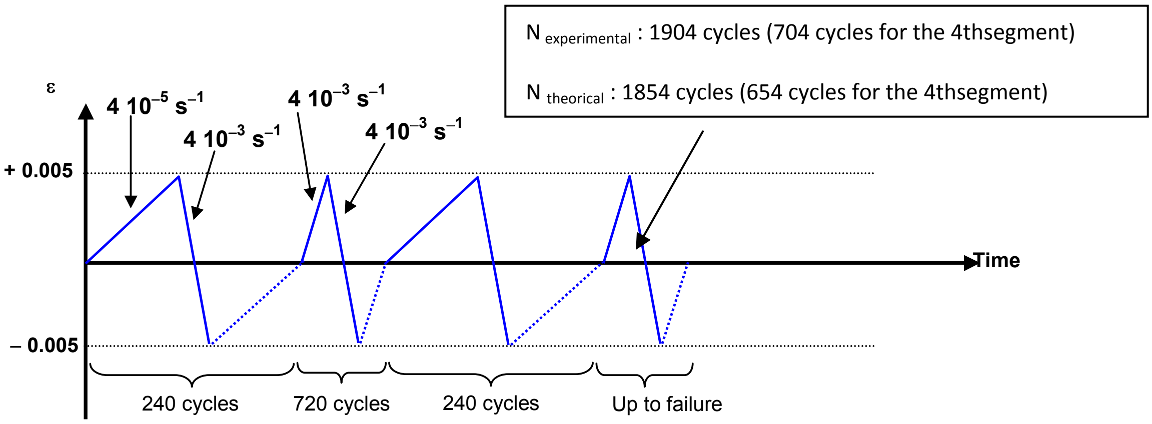

Figure 8 □Test conditions of the varying strain rate test

In the case of the total fatigue life during the test (Nexp) is equivalent to the sum of fatigue life fraction of each sequence (Ntheorical), the ratio between Nexp and Ntheorical namely Cumulative Usage Factor (CUF) become close to 1. In that case the damage accumulation is qualified as being linear.

Such evaluation was carried out using results obtained at a fixed strain rate (Chapter 4) and the following equations:

$$\mathrm{f_{sequence\ 1}} = \mathrm{f_{sequence\ 3}} = \frac{\mathrm{N_{segment1}}}{\mathrm{N}_{0.004\%/\mathrm{s}}} = \frac{240}{859} = 0.28$$

$$\mathrm{f_{sequence\ 2}} = \frac{\mathrm{N_{sequence\ 2}}}{\mathrm{N}_{0.4\%/\mathrm{s}}} = \frac{720}{3114} = 0.23$$

$$\mathrm{f_{sequence\ 4}} = \frac{\mathrm{N_{sequence\ 4}}}{\mathrm{N}_{0.4\%/\mathrm{s}}} = \frac{654}{3114} = 0.21$$

Each segment corresponds to a fraction of the estimated fatigue life. The sum of each fraction must be equal to 1. The estimation of the predicted fatigue can be achieved and compared to the experimental one:

$$\mathrm{N_{theorical}} = 0.28 \times \mathrm{N}_{0.004\%/\mathrm{s}} + 0.23 \times \mathrm{N}_{0.4\%/\mathrm{s}} + 0.28 \times \mathrm{N}_{0.004\%/\mathrm{s}} + 0.21 \times \mathrm{N}_{0.4\%/\mathrm{s}}$$

$$\mathrm{N_{theorical}} = 1854 \text{ cycles}$$

$$\mathrm{CUF} = \frac{\mathrm{N_{experimental}}}{\mathrm{N_{theorical}}} = 1.03$$

This result indicates a good agreement between predicted fatigue life and experimental fatigue life and that the damage accumulation induced by strain rate is linear.

A potential explanation can be given by crack propagation rates evaluation (Figure 9). In this curve it is possible to observe the last 3 segments. It was impossible to observe the 1st segment and the beginning of the 2nd due to the very small size of striations.

It is also possible to observe that each segment tested at a specific strain rate follow the mastercurve obtained at a fixed strain rate. The good agreement between $\mathrm{N_{experimental}}$ and $\mathrm{N_{theorical}}$ can be explained by the fact that each segment of the varying strain rate test follows a specific crack propagation master curve. This behavior is only function of loading conditions and not by loading history.

In addition, in case of sequence 2, 3 and 4, the good agreement between the applied number of cycles and the measured distance between striations (Figure 9) suggests that the hypothesis of equivalence between crack growth rates and distance between striations is verified.

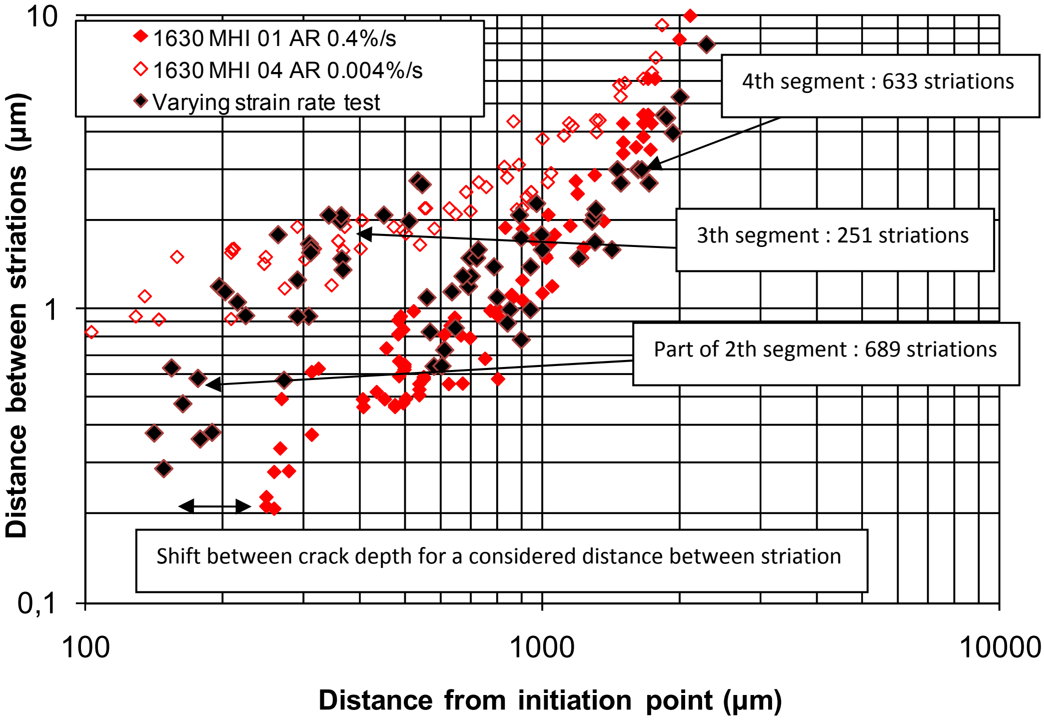

Figure 9 **Effect of a varying strain rate test conditions on crack growth rate behavior, As-received conditions, 300°C, PWR primary environment.**

2.2.1.1. Damage accumulation induced by strain rate and strain amplitude

The damage accumulation corresponds to the successive loading involving different strain amplitude and strain rates. The results presented in chapter 4 highlighted that linear damage accumulation can be used in case of strain rate variation during cycling. Such results were also observed by Higuchi (Figure 10). The explanation was that for each portion of the fatigue life, the crack follows a propagation mastercurve (Figure 9). Higuchi also performed some other tests using varying strain rates and strain amplitudes during cycling (Figure 11). The result suggests that it is also possible to apply the linear damage accumulation in case of strain amplitude. It is then possible to say that the explanation for the strain rate damage accumulation can also be applied to strain amplitude.

(SUS316NG Temp. : 289℃ DO : 0. 01 ppm Strain Ratio R = -1)

No.	Strain Amp.(%) ε_a	Loading Mode	Step	Strain Wave Form	Strain Rate(%/s) $\dot{\varepsilon}_T$	$\dot{\varepsilon}_C$	ΔN (Cycles)	Stress σ_a (MPa)	Fatigue Life N_{25} (Cycles)	CUF
EIHS-05	0.3	–	–	F-F*1	0.4	0.4	–	459	2470	
EIHS-06	0.3	–	–	S-F*2	0.004	0.4	–	501	261	
CIHS-1	0.3	1*3	1/4	S-F*2	0.004	0.4	65			0.25
			2/4	F-F*1	0.4	0.4	617			0.50
			3/4	F-F*1	0.4	0.4	617			0.75
			4/4	F-F*1	0.4	0.4	965		2264	1.14
CIHS-2	0.3		1/4	F-F*1	0.4	0.4	617			0.25
		2*4	2/4	S-F*2	0.004	0.4	65			0.50
			3/4	F-F*1	0.4	0.4	617			0.75
			4/4	F-F*1	0.4	0.4	892		2191	1.11
CIHS-3	0.3		1/4	F-F*1	0.4	0.4	617			0.25
			2/4	F-F*1	0.4	0.4	617			0.50
		3*5	3/4	S-F*2	0.004	0.4	65			0.75
			4/4	F-F*1	0.4	0.4	645		1944	1.01
CIHS-4	0.3		1/4	F-F*1	0.4	0.4	617			0.25
			2/4	F-F*1	0.4	0.4	617			0.50
			3/4	F-F*1	0.4	0.4	617			0.75
		4*6	4/4	S-F*2	0.004	0.4	76		1927	1.04
EIHS-01	0.6	–	–	F-F*1	0.4	0.4	–	495	974	
EIHS-02	0.6	–	–	S-F*2	0.004	0.4	–	552	134	
CIHS-5	0.6	1*3	1/4	S-F*2	0.004	0.4	33			0.25
			2/4	F-F*1	0.4	0.4	243			0.50
			3/4	F-F*1	0.4	0.4	243			0.75
			4/4	F-F*1	0.4	0.4	311	497	830	1.06
CIHS-6	0.6		1/4	F-F*1	0.4	0.4	243			0.25
		2*4	2/4	S-F*2	0.004	0.4	33			0.50
			3/4	F-F*1	0.4	0.4	243			0.75
			4/4	F-F*1	0.4	0.4	257	510	776	1.01
CIHS-7	0.6		1/4	F-F*1	0.4	0.4	243			0.25
			2/4	F-F*1	0.4	0.4	243			0.50
		3*5	3/4	S-F*2	0.004	0.4	33			0.75
			4/4	F-F*1	0.4	0.4	305	503	824	1.06
CIHS-8	0.6		1/4	F-F*1	0.4	0.4	243			0.25
			2/4	F-F*1	0.4	0.4	243			0.50
			3/4	F-F*1	0.4	0.4	243			0.75
		4*6	4/4	S-F*2	0.004	0.4	29	493	758	0.96

*1: Fast-Fast (triangle) *2: Slow-Fast (saw tooth)

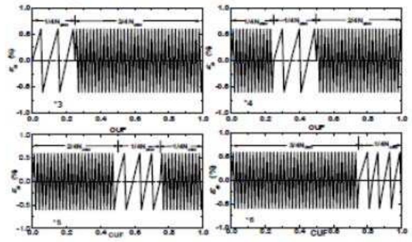

Figure 10 Damage accumulation induced by the loading strain rate.

(SUS316NG Temp. : 289℃ DO: 0. 01 ppm R = -1)

Test No.	DO (ppm)	Strain Amp. (%)	Strain Rate High (%/s)	Low (%/s)	Cycles at One Block *1	Order of Block *2	Actual Cycles at Block	Partial CUF at Block	N_{25} (Cycles)	Total CUF
EIEB-14	0.05	0.6	0.4		-	-	-	-	2775	-
EIEB-13		0.6		0.004	-	-	-	-	1032	-
EIEB-01		0.3	0.4		-	-	-	-	12645	-
EIEB-02		0.3		0.004	-	-	-	-	4024	-
CIEB-1	0.01	0.3	0.4		1/4*N_{f1}	1	3161	0.25		
		0.6	0.4		1/4*N_{f2}	2	694	0.25		
		0.3		0.004	1/4*N_{f4}	3	1006	0.25		
		0.6		0.004	1/4*N_{f3}	4	275	0.27	5136	1.02
CIEB-2	0.01	0.3		0.004	1/4*N_{f4}	1	1006	0.25		
		0.6		0.004	1/4*N_{f3}	2	258	0.25		
		0.3	0.4		1/4*N_{f1}	3	3161	0.25		
		0.6	0.4		1/4*N_{f2}	4	860	0.31	5285	1.06

Figure 11 Damage accumulation induced by the loading strain rate and strain amplitude.

2.2.2. Surface roughness

Surface roughness is considered in the Nureg 6909 as being a subfactor that can reduce the fatigue life in PWR primary environment by a factor 2 to 3.5.

Le Duff [1] [2] [3] performed some fatigue tests using grinded samples (Rt >70µm) (Table 1). The variation of fatigue life in PWR primary environment between a polished sample and a grinded sample was 1.16 at a strain amplitude of 0.55% and a strain rate of

0.01%/s. Using propagation curves obtained (Equation 1 and Equation 2) with loadings parameters close to the one used by Le Duff and a simple hypothesis that a surface roughness just corresponds to the fatigue life obtained with an initial crack (70µm) (Table 2 and Table 3). It was possible to say that in our case the difference of fatigue life induced by a theorical modification of surface roughness is 1.24. This result is very close to the one obtained by Le Duff and it seems that surface roughness effect on fatigue life can be considered using a deeper initial crack and a micro propagation curve.

Using our hypothesis, it is possible to say that the 2 and 3.5 margin presented in the Nureg, can be reach by having an initial crack of 450µm for the factor 2 and 1mm for the factor 3. Such initial crack seems to be completely over estimated and the 2-3.5 factors may leads to over conservatism.

Table 1 □Surface roughness effect on fatigue life in PWR primary environment [1]

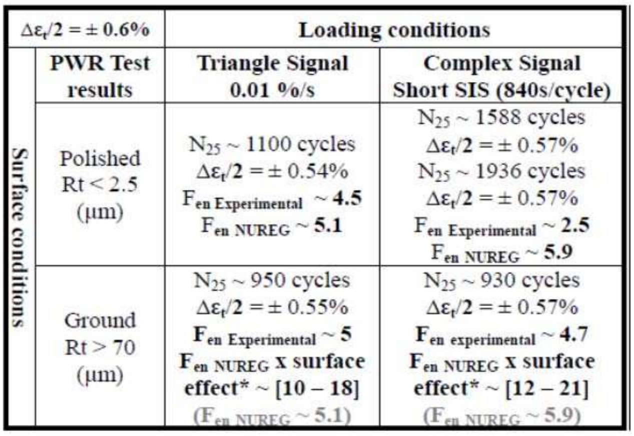

$\Delta\varepsilon_t/2 = \pm 0.6\%$		**Loading conditions**	
Surface conditions	**PWR Test results**	**Triangle Signal 0.01 %/s**	**Complex Signal Short SIS (840s/cycle)**
	Polished Rt < 2.5 (µm)	N_{25} ~ 1100 cycles $\Delta\varepsilon_t/2 = \pm 0.54\%$ $F_{en\ Experimental}$ ~ **4.5** $F_{en\ NUREG}$ ~ **5.1**	N_{25} ~ 1588 cycles $\Delta\varepsilon_t/2 = \pm 0.57\%$ N_{25} ~ 1936 cycles $\Delta\varepsilon_t/2 = \pm 0.57\%$ $F_{en\ Experimental}$ ~ **2.5** $F_{en\ NUREG}$ ~ **5.9**
	Ground Rt > 70 (µm)	N_{25} ~ 950 cycles $\Delta\varepsilon_t/2 = \pm 0.55\%$ **$F_{en\ Experimental}$ ~ 5** **$F_{en\ NUREG}$ x surface effect* ~ [10 – 18]** ($F_{en\ NUREG}$ ~ 5.1)	N_{25} ~ 930 cycles $\Delta\varepsilon_t/2 = \pm 0.57\%$ **$F_{en\ experimental}$ ~ 4.7** **$F_{en\ NUREG}$ x surface effect* ~ [12 – 21]** ($F_{en\ NUREG}$ ~ 5.9)

$$\frac{da}{dN} = C \times a^n$$	**Equation 1**
$$N = \frac{1}{C \times (1-n)} \times \left[a_f^{(1-n)} - a_0^{(1-n)}\right]$$	**Equation 2**

Table 2 □Evaluation of the number of cycles to failure, no initial deflect

C	n	a_0 (m)	a_f (m)	N (cycles)
2.10^{-4}	0.5857	3.10^{-6}	2.10^{-3}	864

Table 3 □Evaluation of the number of cycles to failure, initialcrack depth = 70µm

C	n	a_0 (m)	a_f (m)	N (cycles)
2.10^{-4}	0.5857	7.10^{-5}	2.10^{-3}	690

2.3. Conclusion on codification

Results concerning the fatigue lives both in air and in PWR primary environment in the LCF region are in a good agreement with current Nureg 6909 and Japanese codifications. However for higher numbers of cycles, the experimental fatigue lives for the as received material are much lower than the predicted ones. This aspect points out that both models are not conservative for this material in the high cycle fatigue regime. On the basis of Fen calculated with fatigue lives in air and in primary water, it reveals that the Fen on the strain hardened material is smaller than that on the as-received one, meaning less environmental effect on the hardening material. Results presented in the literature shows that weld metals follow the same tendency than prior hardened materials and therefore, it could be possible to improve the accuracy of the predicted Fen based on material considerations. This approach is currently under consideration in Japan[1].

Currently the approach on the environmentally assisted fatigue is based on some macroscopic considerations. However in this section we have shown that some of the results can be apprehended with some basic understanding knowledge such as the assumption of an initial crack and a micro propagation master curve to predict the effect of the surface roughness on the fatigue life. It is clearly needed to progress in such a way to be able to apprehend more carefully the environmentally assisted fatigue.

3. Environmentally-assisted fatigue signatures

Environmental fatigue cracks of 304L stainless steel have some specific characteristics that may help to conclude on the contribution of the PWR primary water in fatigue of actual components.

3.1. Evaluation on cross sections

Figure 12 to Figure 21 present short representative overviews of cross sections obtained on different specimens observed through an optical microscope. Magnification was fixed to x200 or x1000. A rapid examination of these figures allows us to identify the major characteristic of corrosion fatigue crack that is branching. Indeed, such branching seems less pronounced without any environmental effect.

---

[1] MHI report not published

Figure 12 to Figure 14 show cross sections observed on samples tested at $\Delta\varepsilon t/2=0.5\%$ and at a strain rate of 0.4%/s, and cut in as-received and the 10% cold rolled materials. These figures clearly indicate that branching occurs in both annealed and cold-rolled materials. Figure 15 to Figure 17 correspond to cross sections obtained on the sample tested at the same strain amplitude, namely $\Delta\varepsilon t/2=0.5\%$, but at the lower strain rate of 0.004%/s. In that case, a less pronounced branching is observed than at the high strain rate.

It is generally admitted that the presence of crack branching is associated with a greater effect of the environment. However in low strain rate conditions (presenting a lower fatigue life) a linear crack which does not present any branching can also be affected by the environment, and in this case even more.

Figure 18 to Figure 21 present some smaller cracks observed on the same samples. The detail views highlight two other characteristics of a corrosion fatigue crack in PWR primary environment: first, only transgranular branching occurs using different activate slip systems, regardless of its orientation from the surface (the mean grain size for these samples is about 120 µm). Second, cracks do not initiate in the same angle range than in air. Indeed, in PWR environment, cracks mainly initiate mainly at 90° from the axis of loading. In addition, the angle is not affected by cold work and strain rate.

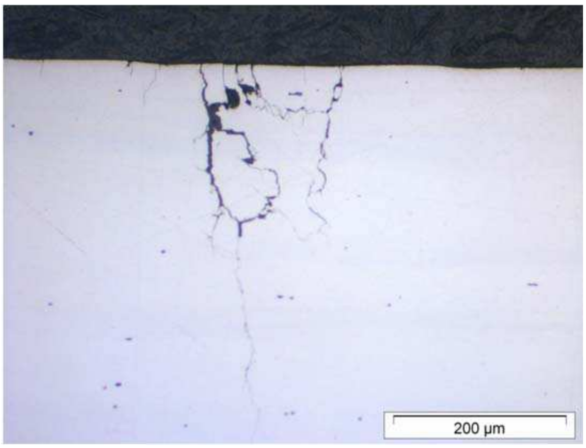

Figure 12 Cross section of 1630 MHI 01, $\Delta\varepsilon t/2=0.5\%$, 0.4%/s, 10% cold rolled, PWR primary water at 300°C.

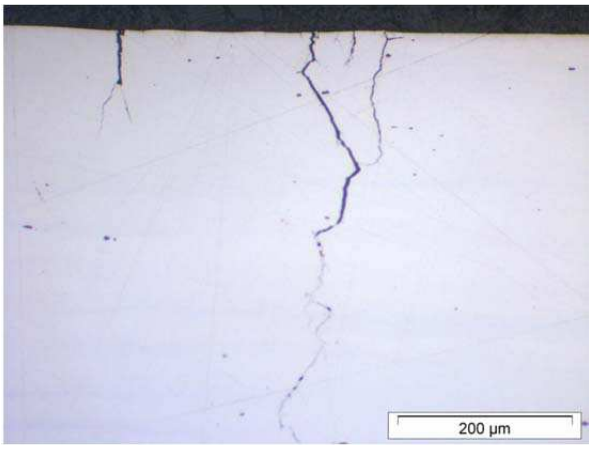

Figure 13 Cross section of 1630 MHI 11, $\Delta\varepsilon t/2=0.5\%$, 0.4%/s, 10% cold rolled, PWR primary water at 300°C.

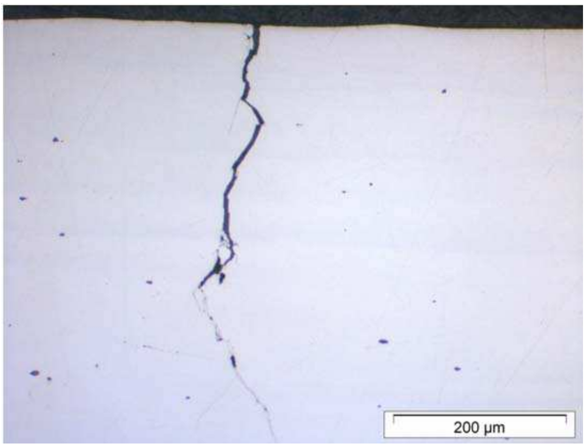

Figure 14 **Cross section of 1630 MHI 01, Δεt/2=0.5%, 0.4%/s, as-received 304L, PWR primary water at 300°C.**

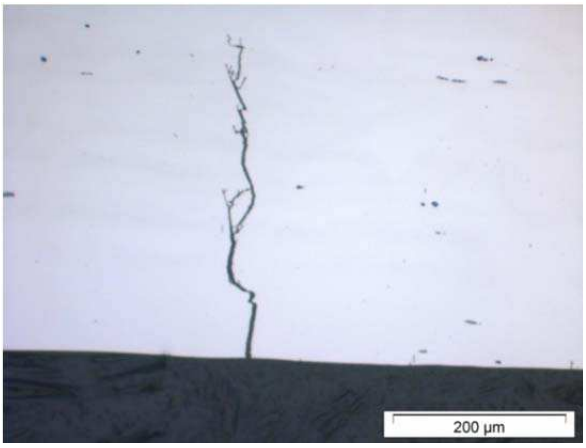

Figure 15 **Cross section of 1630 MHI 04, Δεt/2=0.5%, 0.004%/s, as-received 304L, PWR primary water at 300°C.**

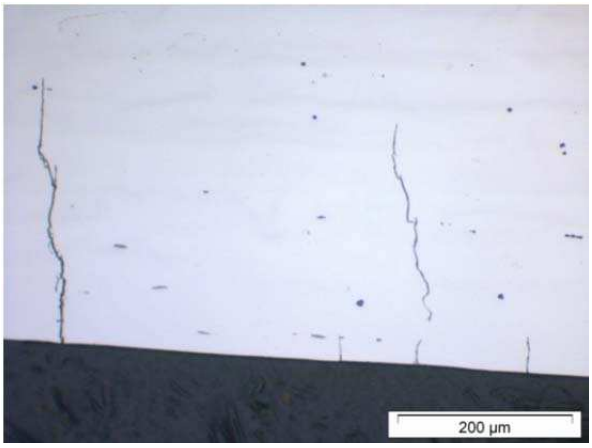

Figure 16 **Cross section of 1630 MHI 04, Δεt/2=0.5%, 0.004%/s, as-received 304L, PWR primary water at 300°C.**

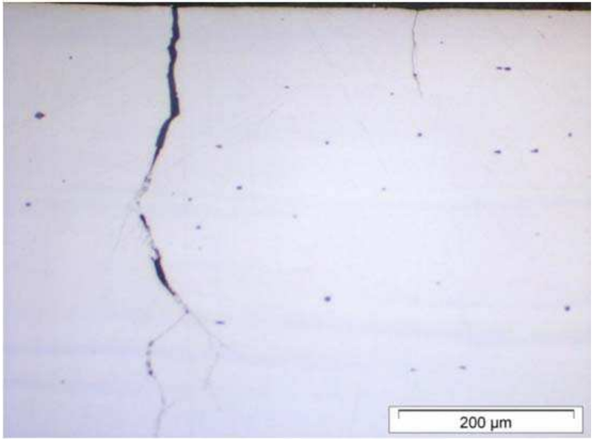

Figure 17 **Cross section of 1630 MHI 14, Δεt/2=0.5%, 0.004%/s, 10% cold rolled 304L, PWR primary water at 300°C.**

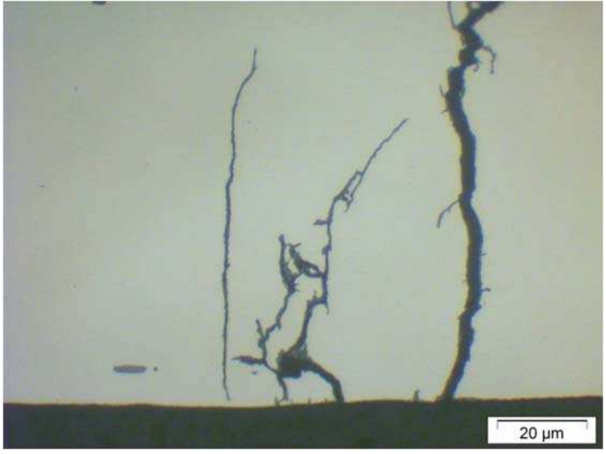

Figure 18 **Cross section of 1630 MHI 01, Δεt/2=0.5%, 0.4%/s, as-received 304L, PWR primary water at 300°C. Focus on initiation.**

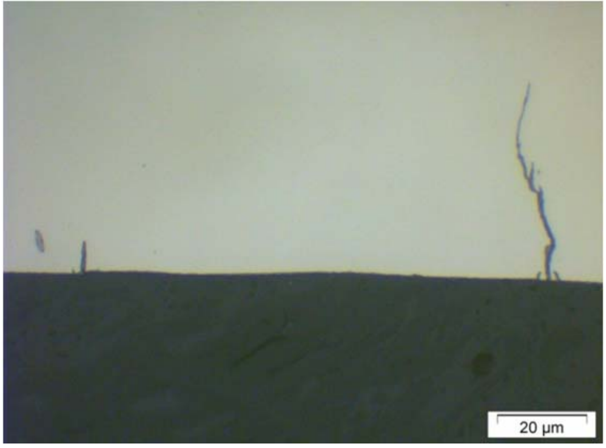

Figure 19 **Cross section of 1630 MHI 11, Δεt/2=0.5%, 0.4%/s, 10% cold rolled 304L, PWR primary water at 300°C. Focus on initiation.**

Figure 20 Cross section of 1630 MHI 04, Δεt/2=0.5%, 0.004%/s, as-received 304L, PWR primary water at 300°C. Focus on initiation.

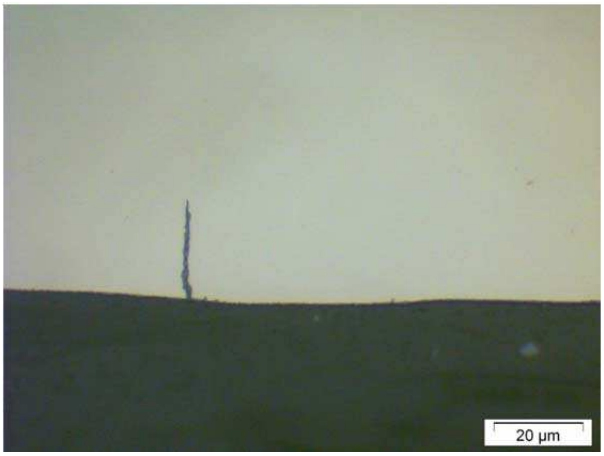

Figure 21 Cross section of 1630 MHI 14, Δεt/2=0.5%, 0.004%/s, 10% cold rolled 304L, PWR primary water at 300°C. Focus on initiation.

3.2. Evaluation on fracture surface

Figure 22 and Figure 23 present typical initiation areas on the samples tested in PWR primary water. Crack initiation areas are very smooth as observed after testing in air. Figure 24 to Figure 26 present typical fatigue striations obtained on the fracture surfaces. In these figures, it is possible to see that branching occurs mainly at striation tip. Crack growth rates can be then different between the main crack and sub-cracks. One other main characteristic of corrosion fatigue crack in PWR primary water is presented in Figure 27. It corresponds to the fact that the main crack can also interact with twins and grain boundaries, leading to a different local propagation direction.

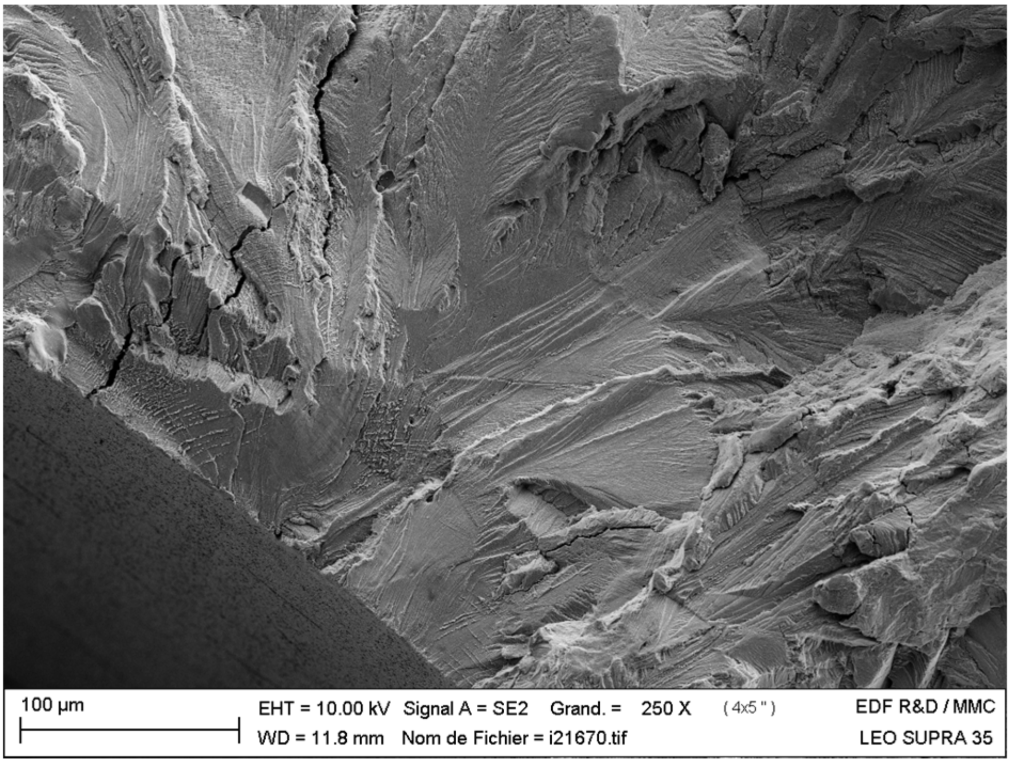

Figure 22 Fracture surface of 1630 MHI 01, Δεt/2=0.5%, 0.4%/s, as-recieved, PWR primary water at 300°C, initiation site.

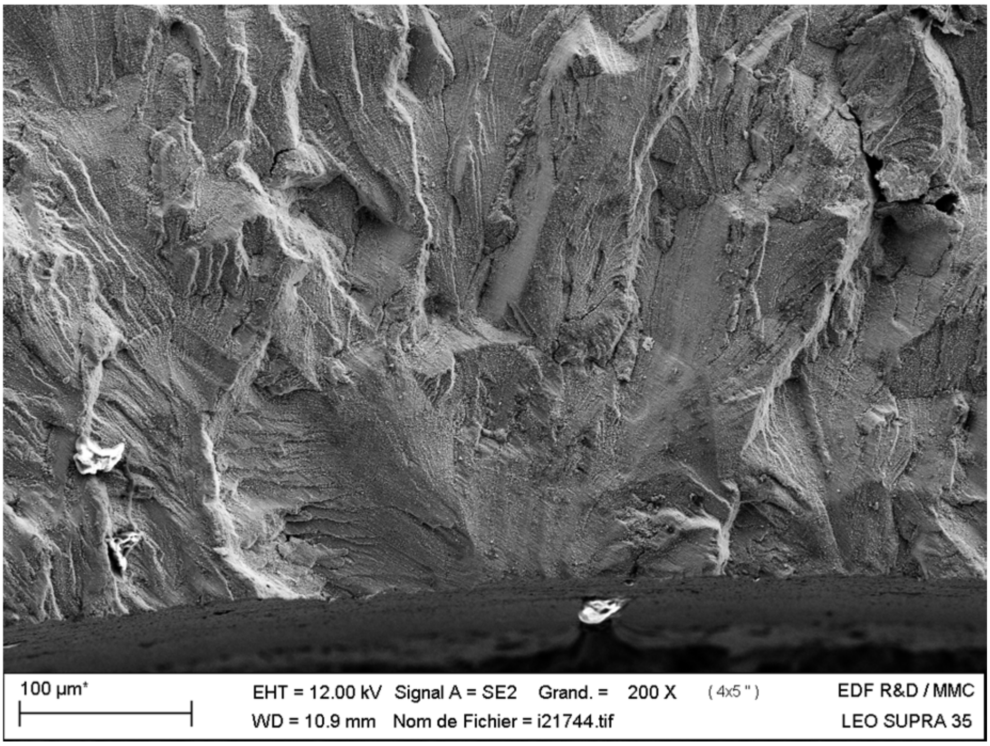

Figure 23 Fracture surface of 1630 MHI 03, Δεt/2=0.5%, 0.004%/s, 10% prior tensile strain, PWR primary water at 300°C, initiation site.

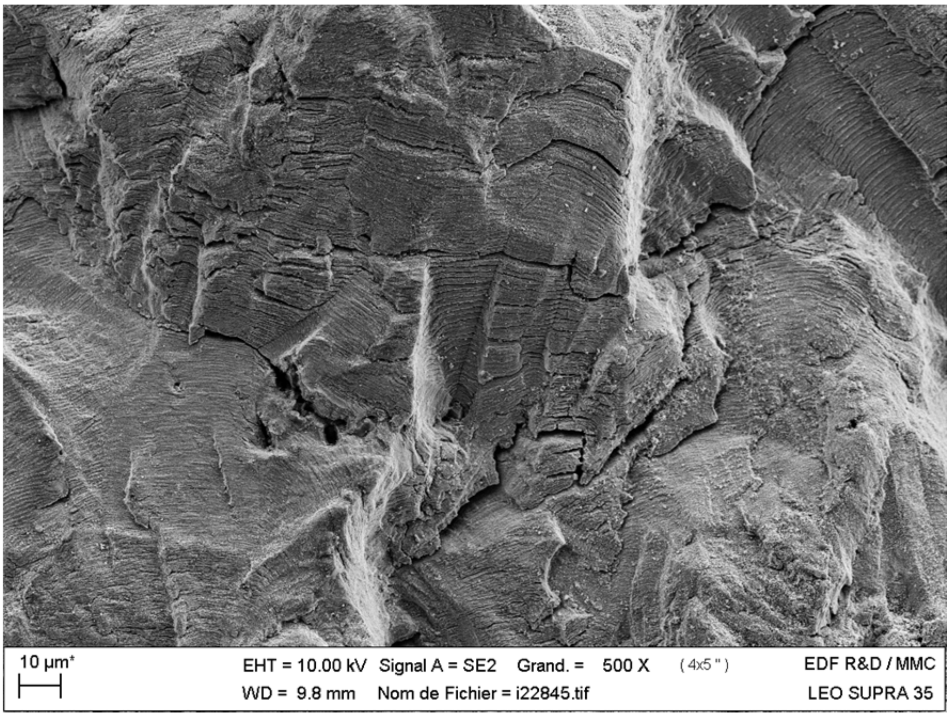

Figure 24 – Fracture surface of 1630 MHI 01, $\Delta\varepsilon t/2=0.5\%$, 0.4%/s, 300°C. As-received 304L, PWR, branching.

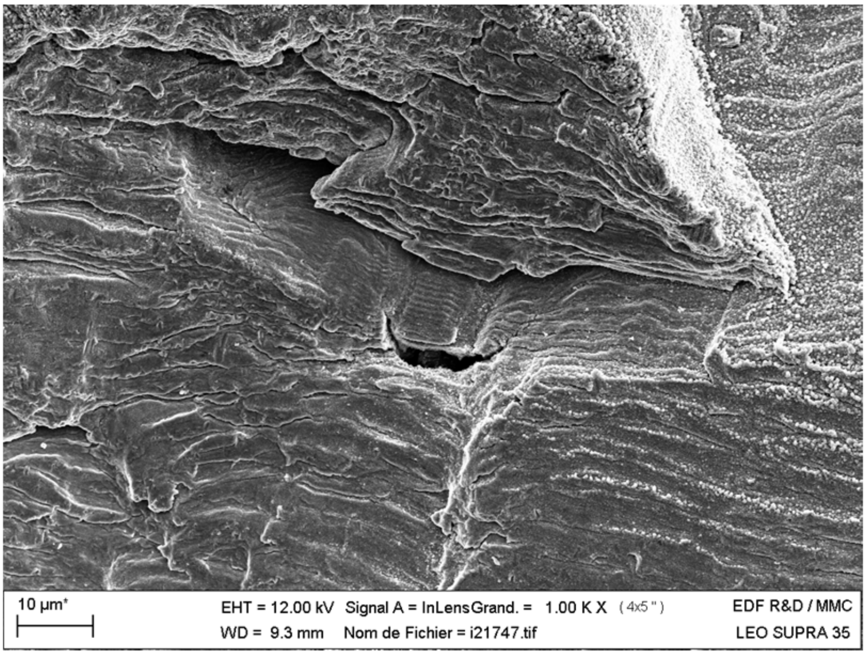

Figure 25 – Fracture surface of 1630 MHI 04, $\Delta\varepsilon t/2=0.5\%$, 0.004%/s, 300°C. As-received 304L, PWR, branching with 2 crack growth rates.

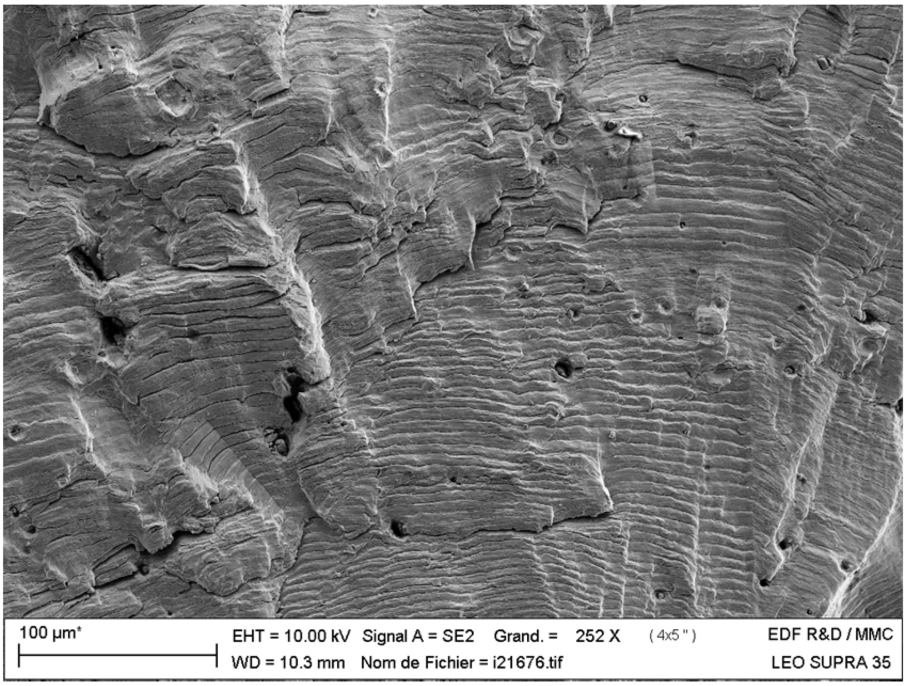

Figure 26 Fracture surface of 1630 MHI 01, Δεt/2=0.5%, 0.4%/s, 300°C. As-received 304L, branching.

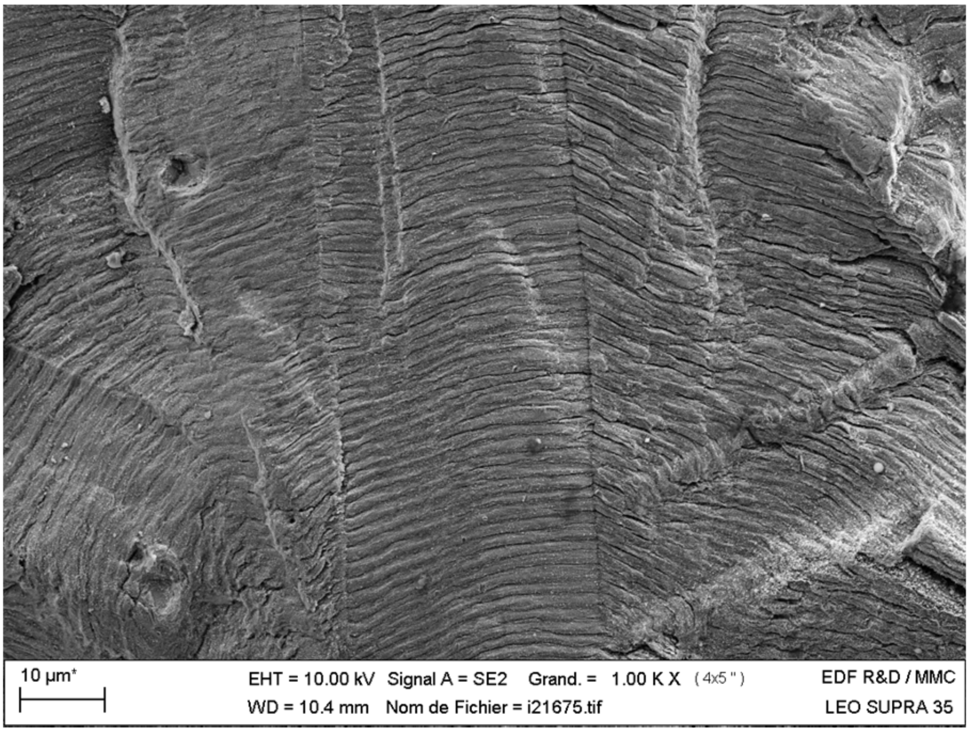

Figure 27 Fracture surface of 1630 MHI 02, Δεt/2=0.5%, 0.4%/s, 300°C. 10% tension, PWR, twin boundary.

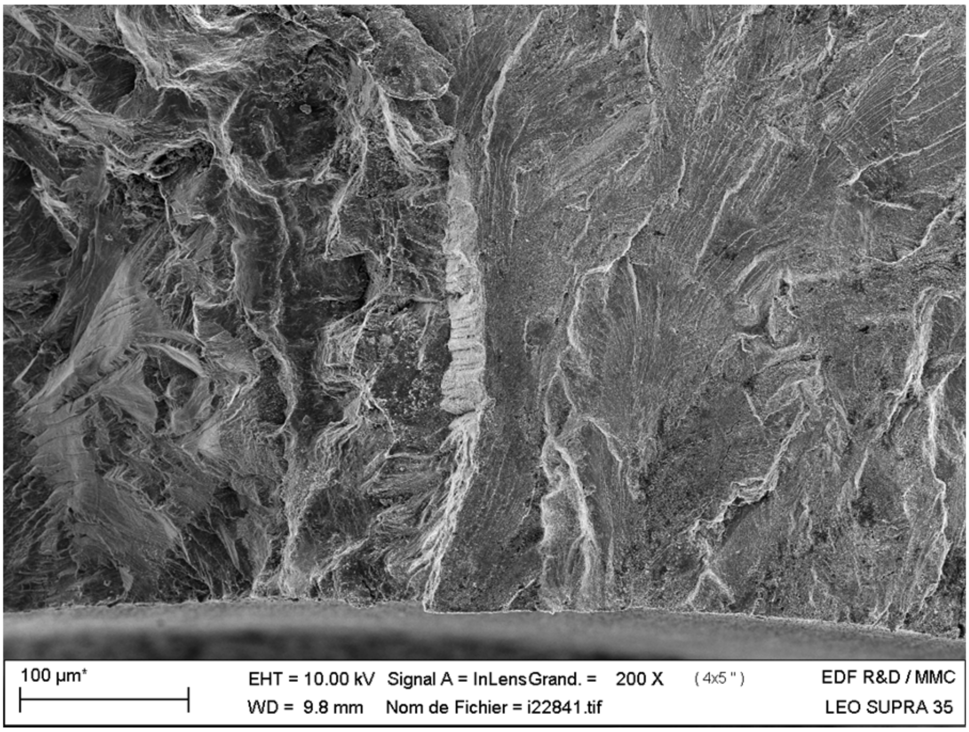

Figure 28 Fracture surface of 1630 MHI 04, $\Delta\varepsilon t/2$=0.5%, 0.004%/s, 300°C. As-received 304L, PWR. Residual delta ferrite.

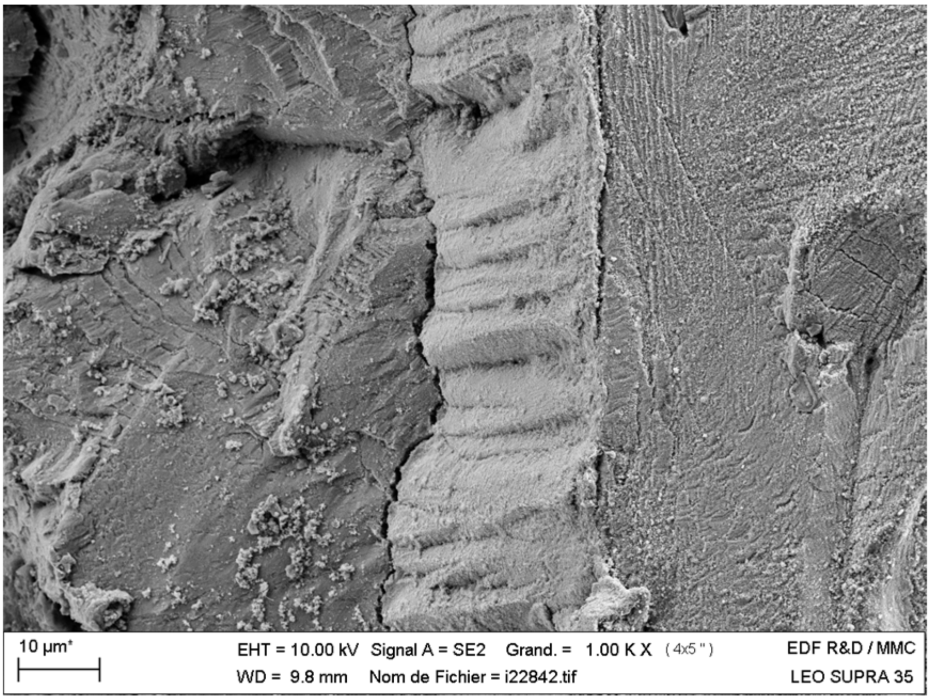

Figure 29 Fracture surface of 1630 MHI 04, $\Delta\varepsilon t/2$=0.5%, 0.004%/s, 300°C. As-received 304L, PWR, focusing on the austenite/ferrite interface.

3.3. Evaluation of microstructure by TEM

Fatigue loadings generate some very typical dislocation structures that cannot be confounded with other types of loadings. The following figures present typical observations of fatigue microstructures. In these figures it is possible to observe vein-like, cells, PSBs and corduroy structures. These observations of these structures in the bulk is a good signature of fatigue and may be applied to make the distinction between SCC and EAF.

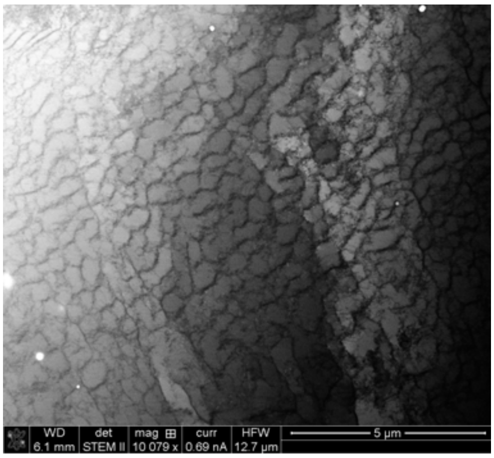

Figure 30 □3D structures, Δεt/2=0.5%, Δεt/dt=0.4%/s, 300 cycles, 300°C, the as-received material.

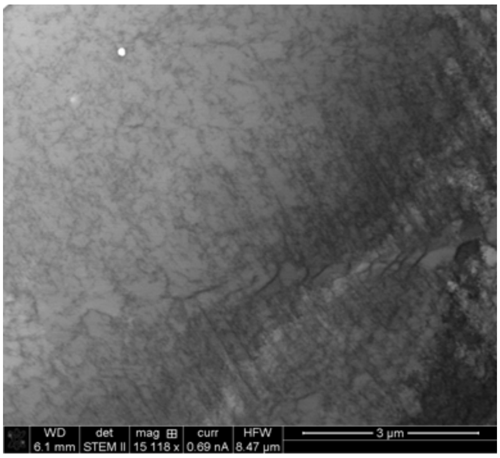

Figure 31 □Dislocation stacks and planar slip evolving into 3D structures, Δεt/2=0.5%, Δεt/dt=0.4%/s, 300 cycles, 300°C, the as-received material.

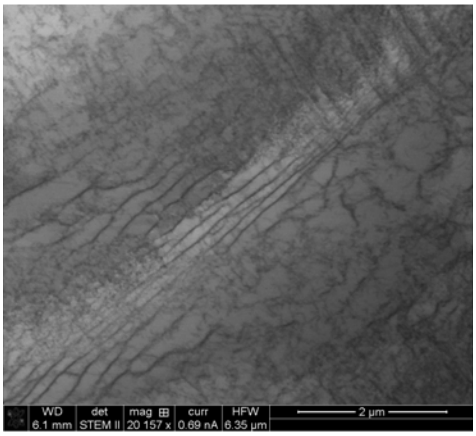

Figure 32 □Dislocation stacks evolving into PSBs, Δεt/2=0.5%, Δεt/dt=0.4%/s, 300 cycles, 300°C, the as-received material.

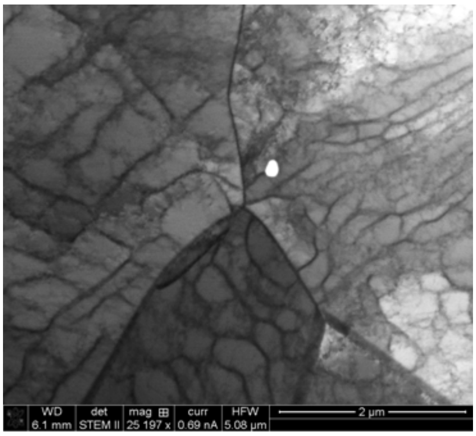

Figure 33 □PSB, cells, close to a triple junction, Δεt/2=0.5%, Δεt/dt=0.4%/s, 300 cycles, 300°C, the as-received material.

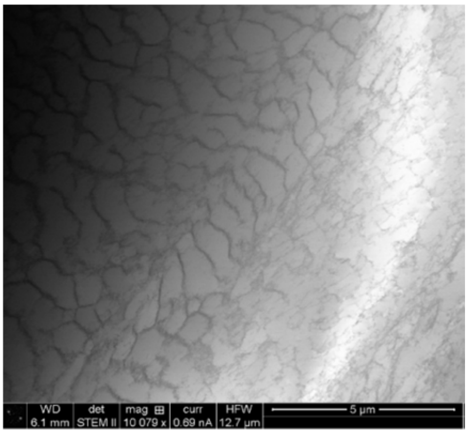

Figure 34 □PSBs, Δεt/2=0.5%, Δεt/dt=0.4%/s, 300 cycles, 300°C the 10% cold rolled material.

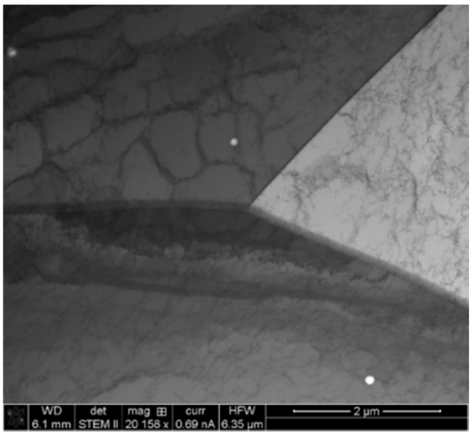

Figure 35 □Cells and dislocation stacks Δεt/2=0.5%, Δεt/dt=0.4%/s, 300 cycles, 300°C the 10% cold rolled material.

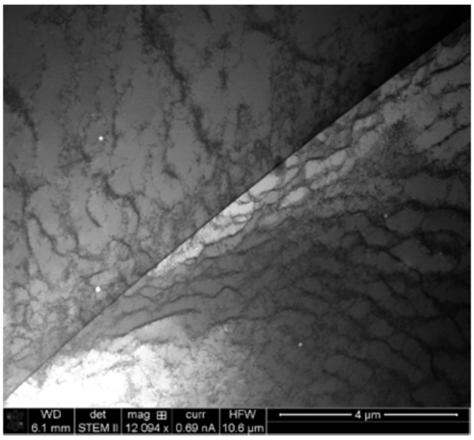

Figure 36 □PSBs, PSB formation close to a grain boundary and strain incompatibilities, Δεt/2=0.5%, Δεt/dt=0.4%/s, 300 cycles, 300°C the 10% cold rolled material.

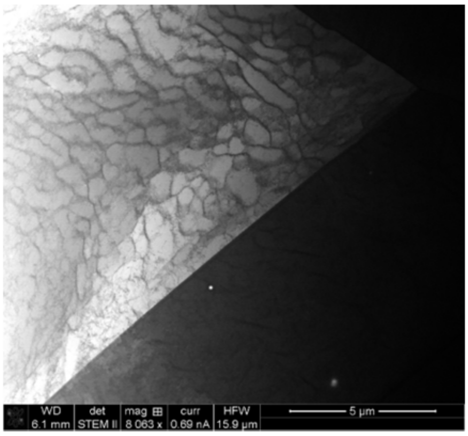

Figure 37 □PSBs evolving into cells close to a triple junction, Δεt/2=0.5%, Δεt/dt=0.4%/s, 300 cycles, 300°C the 10% cold rolled material.

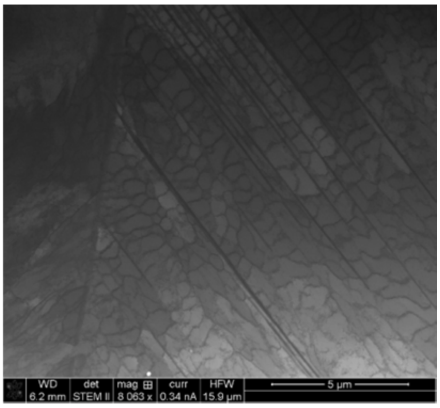

Figure 38 □PSBs, Δεt/2=0.5%, Δεt/dt=0.004%/s, 600 cycles, 300°C, the 10% cold rolled material.

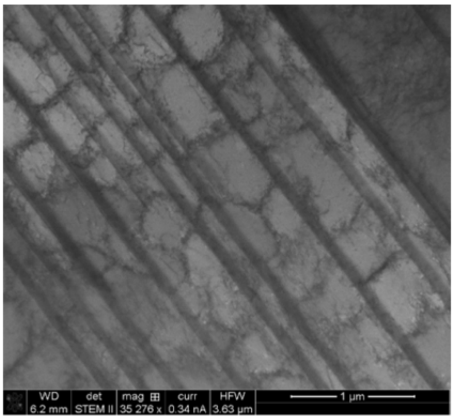

Figure 39 □Cells, Δεt/2=0.5%, Δεt/dt=0.004%/s, 600 cycles, 300°C, the 10% cold rolled material.

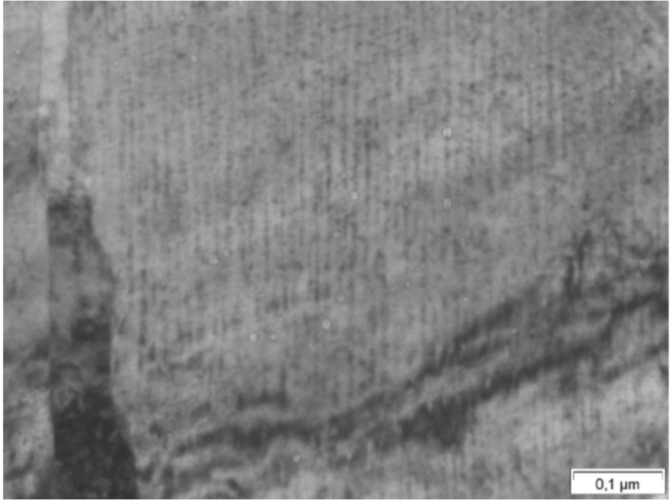

Figure 40 □Corduroy structure, Δεt/2=0.1%, Δεt/dt=0. 4%/s, as-received at failure [4] .

---

[1] **J.A. LE DUFF ET AL.**, “Effects of surface finish and loading conditions on the low cycle fatigue behavior of austenitic stainless steel in PWR environment”, Proceedings of PVP2008, ASME PVP2008-61894, 2008.

[2] **J.A. LE DUFF ET AL.**, “Effects of surface finish and loading conditions on the low cycle fatigue behavior of austenitic stainless steel in PWR environment for various strain amplitude levels”, Proceedings of PVP2009, ASME PVP2009-78129, 2009.

[3] **J.A. LE DUFF ET AL.**, “Effect of loading signal shape and of surface finish on the low cycle fatigue behavior of 304L stainless steel in PWR environment.”, Proceedings of PVP2010, ASME PVP2010-26027, 2010.

[4] **A. GARCIA**, “Caractérisation microstructurales d'aciers inoxydables austénitiques de type AISI 304L sollicités en fatigue” These de doctorat de l’Institut National Polytechnique de Grenoble. 2009.

La présente étude a donc été entreprise afin d'obtenir de nouvelles informations sur les mécanismes de fissuration d’un acier inoxydable 304L en milieu primaire REP en fatigue.

Plus précisément, le premier objectif de cette étude est d'évaluer l'effet de différentes conditions de pré écrouissage sur le comportement cyclique et sur la durée de vie en air et en milieu primaire. En air, un pré écrouissage tend à réduire la durée de vie dans le domaine de la fatigue oligocyclique et à l’augmenter dans le domaine du grand nombre de cycles. En milieu primaire cette diminution de durée de vie n’apparaît pas

Le second objectif porte sur l'effet de l'air et du milieu primaire sur les mécanismes de fissuration (amorçage et propagation) dans le cas du matériau recuit dans le domaine de la fatigue oligocyclique. Ainsi, des cinétiques d’amorçage et de propagation de fissures ont été évaluées via une approche microscopique multi échelles dans ces deux environnements. En milieu primaire au cours des premiers cycles, une oxydation préférentielle en couche se produit dans l’alignement d’une bande de cisaillement dense en dislocations dissociées. Puis, au cours du cyclage, la microstructure évolue vers une structure de type micromaclage. Le processus d’oxydation progresse par cisaillement de l’oxyde et dissolution du métal en pointe de fissure. Au-delà d'une certaine profondeur de fissure (<3 µm), la fissure se réoriente à un angle de 90° par rapport à la surface. La fissure continue sa propagation par génération successive de bandes de cisaillement à chaque cycle jusqu'à la rupture.

Ces processus de fissuration ont ensuite discutés au travers du rôle potentiel de l’hydrogène de corrosion.

Mots clefs:

- Fatigue environnementale
- Amorçage de fissure
- Oxydation en milieu primaire REP
- Propagation des fissures
- Pré écrouissage
- Mécanismes de déformation

The present study was undertaken in order to get further insights on cracking mechanisms in a 304L stainless steel.

More precisely, a first objective of this study was to evaluate the effect of various cold working conditions on the cyclic stress-strain behavior and the fatigue life in air and in PWR primary environment. In air a prior hardening was found to reduce the fatigue life in the LCF regime but not in primary environment. In both environments, the fatigue limit of the hardened materials was increased after cold working.

The second objective addresses the effect of the air and the PWR primary environments on the cracking mechanisms (initiation and propagation) in the annealed material in the LCF regime. More precisely, the kinetics of crack initiation and micro crack propagation were evaluated with a multi scale microscopic approach in air and in primary environment.

In PWR primary environment, during the first cycles, preferential oxidation occurs along emerging dissociated dislocation and each cycle generates a new C-rich/Fe-rich oxide layer. Then, during cycling, the microstructure evolves from stacking fault into micro twinning and preferential oxidation occurs by continuous shearing and dissolution of the passive film. Beyond a certain crack depth (<3µm), the crack starts to propagate with a direction close to a 90° angle from the surface. The crack continues its propagation by successive generation of shear bands and fatigue striations at each cycle up to failure.

The role of corrosion hydrogen on these processes is finally discussed.

Key words

- Environmentally assisted fatigue
- Crack initiation
- Oxidation in PWR primary environment
- Crack propagation
- Pre hardening
- Strain mechanisms